UCRL-ID-146907

Proceedings of the 3rd US-Japan Workshop on Plasma Polarization Spectroscopy

P. Beiersdorfer, T. Fujimoto

June 18, 2001

U.S. Department of Energy
Lawrence Livermore National Laboratory

DISCLAIMER

This work was performed under the auspices of the U. S. Department of Energy by the University of California, Lawrence Livermore National Laboratory under Contract No. W-7405-Eng-48.

Proceedings of the 3rd US-Japan Plasma Polarization Spectroscopy Workshop

Livermore, California
June 18–21, 2001

P. Beiersdorfer and T. Fujimoto, Editors

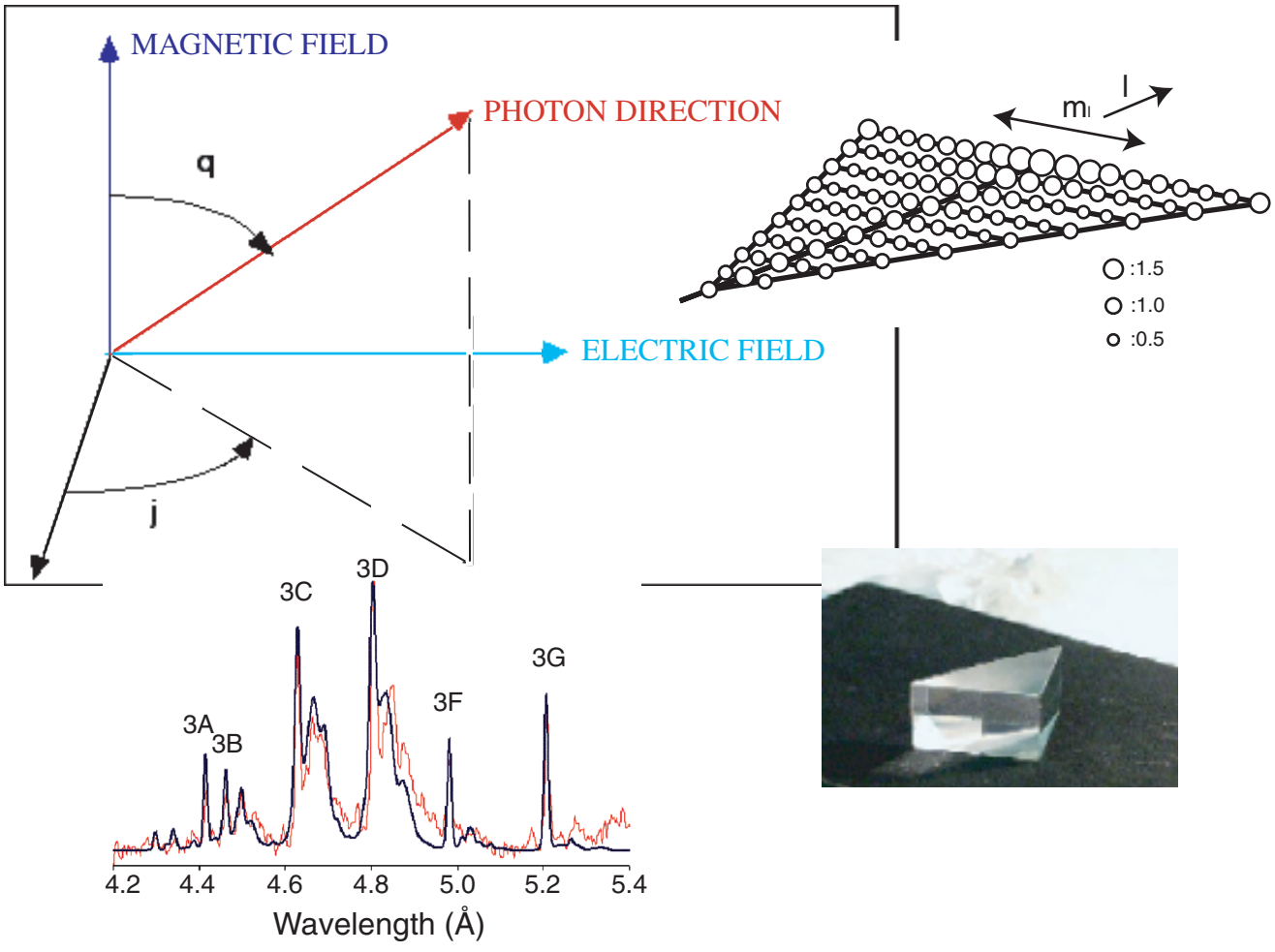

University of California Lawrence Livermore National Laboratory
Report UCRL-ID-146907

DISCLAIMER

Proceedings

Of

The 3rd US-Japan Workshop on Plasma Polarization Spectroscopy

Livermore, California, June 18-21, 2001

edited by
Peter Beiersdorfer
Takashi Fujimoto

Abstract

The third US-Japan Workshop on Plasma Polarization Spectroscopy was held at the Lawrence Livermore National Laboratory in Livermore, California, on June 18 – 21, 2001. The talks presented at this workshop are summarized in these proceedings. The papers cover both experimental investigation and applications of plasma polarization spectroscopy as well as the theoretical foundation and formalisms to understand and describe the polarization phenomena. The papers give an overview of the history of plasma polarization spectroscopy, derive the formal aspects of polarization spectroscopy, including the effects of electric and magnetic fields, discuss spectra perturbed by intense microwave fields, charge exchange, and dielectronic recombination, and present calculations of various collisional excitation and ionization cross sections and the modeling of plasma polarization spectroscopy phenomena. Experimental results are given from the WT-3 tokamak, the MST reverse field pinch, the Large Helical Device, the GAMMA 10 mirror machine, the Nevada Terrawatt Facility, the Livermore EBIT-II electron beam ion trap, and beam-foil spectroscopy. In addition, results were presented from studies of several laser-produced plasma experiments and new instrumental techniques were demonstrated.

Preface

The US-Japan Workshop on Plasma Polarization Spectroscopy was held during June 18 – 21, 2001, in Livermore. This was the third meeting of its kind following the first US-Japan Workshop at Los Alamos in 1994 and the second such workshop in 1998 in Kyoto. The Third US-Japan Workshop on Plasma Polarization Spectroscopy was attended by 22 US and 6 Japanese participants. In addition, there were 6 participants from Russia, South Korea, and Germany.

The purpose of the three and a half day workshop was to review the current applications and assess the future scope of polarization spectroscopy as a diagnostic tool for fusion plasmas in MFE and ICF, for short-pulse laser-generated plasmas, Z-pinch produced plasmas, electron-ion beam interactions, and for astrophysical sources. The workshop addressed both experimental and theoretical issues pertaining to the emission of polarized radiation from plasmas.

Workshop topics were:

- Reviews of the plasma environments that create polarized ensembles of atoms, electrons, and ions resulting in polarized radiation
- A review of the current status of theories that describe the creation and destruction of ensembles of polarized atoms, electrons, and ions
- Diagnostic techniques for identifying polarized radiation and plasma processes creating polarized ensembles
- Effects of magnetic and electric fields
- Assessment of relevancy to fusion energy plasmas
- Needs for atomic data for proper descriptions of plasma polarization phenomena

The presentations covered the three main classes of Plasma Polarization Spectroscopy. The first class deals with the polarization of atomic radiation caused by the effects of electric and/or magnetic fields. An example of this class of Plasma Polarization Spectroscopy is the Motional Stark effect (MSE), which has become a prime field

diagnostic of magnetically confined plasmas. The second class deals with the polarization caused by the anisotropic excitation of atoms and ions. An example of this class are x-ray spectra excited by electrons in an electron beam. Polarization can thus be a diagnostic of the electron velocity distribution function, for example in magnetic mirror machines, X pinches, or laser-produced plasmas. The third class represents phenomena caused by a mixture of Class 1 and Class 2. An example is the radiation produced by light ions excited by beam electrons embedded in mega-Gauss transient fields.

In the spirit of a workshop, the program consisted primarily of long and medium-length oral presentations given by workshop attendees, allowing for ample discussions.

As organizers we feel that the Third Workshop marks a milestone in the progress in Plasma Polarization Spectroscopy. While the field was still in the development phase during the first and second Workshops, it has now matured into an established area of research. The presentations during the Third Workshop showed that Plasma Polarization Spectroscopy has found wide application in both low and high temperature plasma research and that it has become an indispensable diagnostic tool for many experiments.

This Proceedings describes the many different aspects and applications of Plasma Polarization Spectroscopy. We hope the reader will find the topics in these papers interesting and stimulating.

Finally, we would like to acknowledge many people who have contributed to the success of the Workshop. Our thanks goes foremost to the conference secretary, Bertie Gros-Baumgartner, who made the many arrangements necessary for a smooth event. We thank Carl Bruns for the Monday night barbecue, Phil D'Antonio for setting up the computer room, Eryn Davis and Daniel Thorn for helping with the Proceedings, as well as Ed Magee, Vickie McFadden, Ida Hartman, and Terry Strahl for their varied contributions. Last but not least, we thank Bill Goldstein and Ron McKnight for their financial support.

Work by the University of California Lawrence Livermore National Laboratory was performed under the auspices of the Department of Energy under Contract No. W-7405-Eng-48.

December 2001,

Peter Beiersdorfer
Takashi Fujimoto

List of Participants

M. Adams: Lawrence Livermore National Laboratory, P.O. Box 808, L-018, Livermore, California 94551-9900 USA; adams48@llnl.gov

E. Baronova: Kumamoto University, Kurokami, 2-39-1, Kumamoto, 860-8555, Department of Electrical and Computer Engineering, Faculty of Engineering, JAPAN: baronova@eecs.kumamoto-u.ac.jp

P. Beiersdorfer: Lawrence Livermore National Laboratory, P.O. Box 808, L-260, Livermore, California 94551-9900 USA; beiersdorfer@llnl.gov

L. Bureyeva: Scientific Council on Spectroscopy of the RAS, Leninski Pr. 53, Moscow, 119991, RUSSIA; bureyeva@sci.lebedev.ru

H. Chen: Lawrence Livermore National Laboratory, P.O. Box 808, L-260, Livermore, California 94551-9900 USA; chen33@llnl.gov

G. Csanak: Los Alamos National Laboratory, Los Alamos, New Mexico, 87545 USA; gc@t4.lanl.gov

D. Den Hartog: Department of Physics, University of Wisconsin, Madison USA; djdenhar@facstaff.wisc.edu

T. Fujimoto: Department of Engineering Physics and Mechanics, Graduate School of Engineering, Kyoto University, Kyoto 606-8501, JAPAN; a53080@sakura.kudpc.kyoto-u.ac.jp

M. Goto: National Institute of Fusion Science, Toki 509-5292, JAPAN; goto@nifs.ac.jp

A. Iwamae: Department of Physics and Mechanics, Graduate School of Engineering, Kyoto University, Kyoto 606-8501, JAPAN; iwamae@kues.kyoto-u.ac.jp

V. Jacobs: Complex Systems Theory Branch, Code 6693, Condensed Matter and Radiation Sciences Division, Naval Research Laboratory, Washington, D.C. 20375, USA; jacobs@dave.nrl.navy.mil

J. Lepson: University of California, Space Sciences Laboratory, 1 Grizzly Peak Blvd., Berkeley, CA 94720-7450; lepson@ssl.berkeley.gov

T. Kawachi: The Institute of Physical and Chemical Research, RIKEN, Wako 351-01, JAPAN; kawachi@apr.jaeri.go.jp

D. P. Kilcrease: Los Alamos National Laboratory, Los Alamos, New Mexico, 87545 USA; dpk@t4.lanl.gov

D.E. Kim: Department of Physics, Pohang University of Science and Technology, San 31, Hyojadong, Namgu, Pohang, KyungBuk, 790-784, Republic of Korea; kimd@vision.postech.ac.kr

J. Kim: Department of Physics, Pohang University of Science and Technology, San 31, Hyojadong, Namgu, Pohang, KyungBuk, 790-784, Republic of Korea; jhoon@anyon.postech.ac.kr

Y. W. Kim: Department of Physics, Lehigh University, Bethlehem, PA, 18015, USA; ywk0@lehigh.edu

R. Mancini: Department of Physics, University of Nevada-Reno, Reno, Nevada 89557, USA; rcman@physics.unr.edu

M. May: Lawrence Livermore National Laboratory, P.O. Box 808, L-260, Livermore, California 94551-9900 USA; may13@llnl.gov

R. More: National Institute for Fusion Science, Data and Planning Center, Gifu-ken, Toki-shi, Oroshi-cho, Japan 509-5292; more@nifs.ac.jp

P. Neill: University of Nevada Reno, Department of Physics, MS 200, Reno, Nevada, 89557 USA; pan@scs.unr.edu

A. Osterheld: Lawrence Livermore National Laboratory, P.O. Box 808, L-047, Livermore, California 94551-9900 USA; osterheld1@llnl.gov

A. Petrashen: S-Petersburg Institute of the Fine Mechanics and Optics, 199101, S-Petersburg, Russia; Alexei.Rybkin@pobox.spbu.ru

K. Reed: Lawrence Livermore National Laboratory, P.O. Box 808, L-041, Livermore, California 94551-9900 USA; reed5@llnl.gov

D.H. Sampson: Department of Astronomy and Astrophysics, The Pennsylvania State University, University Park, Pennsylvania 16802; sampson@lonestar.astro.psu.edu

J. Scofield: Lawrence Livermore National Laboratory, P.O. Box 808, L-043, Livermore, California 94551-9900 USA; scofield1@llnl.gov

H. Scott Lawrence Livermore National Laboratory, P.O. Box 808, L-018, Livermore, California 94551-9900 USA; scott6@llnl.gov

A. Shlyaptseva: University of Nevada Reno, Department of Physics, MS 200, Reno, Nevada, 89557 USA; alla@physics.unr.edu

G. Smith: Department of Physics, Morehouse College, Atlanta, CA 30314 USA; smith144@llnl.gov

D. Thorn: Lawrence Livermore National Laboratory, P.O. Box 808, L-260, Livermore, California 94551-9900 USA; thorn3@llnl.gov

E. Traebert: University de Liege, Belgium, Ruhr University Bochum, Germany; traebert@ep3.ruhr-uni-bochum.de

C. Weatherford: Florida A&M University, Department of Physics, Professor of Physics, 301C Science Research Building, Tallahassee, FL 32307 weatherf@cennas.nhmfl.gov

M. Yoshikawa: Plasma Research Center, University of Tsukuba, Tsukuba, Ibaraki 305, JAPAN; yosikawa@prc.tsukuba.ac.jp

H. Zhang: Los Alamos National Laboratory, Los Alamos, New Mexico, 87545 USA; zhang@lanl.gov

Monday

8:15 - 9:00 Badging at West Badge Office, Registration in B219
9:15 - 9:30 Welcome (Beiersdorfer)
9:30-10:15 Session I (Fujimoto)
10:15-10:30 Break
10:30-12:30 Session II (J. Kim, Y. Kim, Jacobs)
12:30-14:00 Lunch, email
14:00-16:00 Session III (Petrashen, Iwamaee, Csanak)
16:00-16:30 Break
16:30-19:30 Session IV (Mancini, Bureyeva; barbecue dinner provided)

LIST OF TALKS MONDAY
in order of presentation
(only presenter is listed)

"Plasma Polarization Spectroscopy---Past, Present and future Scope"
Takashi Fujimoto, Kyoto University, Japan

"Measurement of the degree of polarization of the spectra from laser produced Al plasmas"
Jaehoon Kim, POSTECH, South Korea

"Analysis of charge separation in neutral gas confined laser produced plasmas by polarization spectroscopy"
Yong Kim, Lehigh University, USA

"Density-Matrix description of Atomic Radiative Emission from Autoionizing States in Electric and Magnetic Fields"
Verne L. Jacobs, Naval Research Laboratory, USA

"Theoretical principals of spectropolarimetric sensing"
Alexander G. Petrashen, St. Petersburg, Russia

"Plasma Polarization Spectroscopy on Magnetic Confinement Plasmas and Population-Alignment Collisional-Radiative model"
Atsushi Iwamae, Kyoto University, Japan

"Plasma Polarization Spectroscopy for the O V Ion: Relevant Collision Cross Sections and Kinetic Modeling"
George Csanak, Los Alamos National Laboratory, USA

"Polarized X-ray satellite line emission in non-equilibrium, transient Si plasmas"
Roberto Mancini, University of Nevada, Reno, USA

"Quasiclassical Theory of Dielectronic Recombination in Plasmas"
Lyudmila Bureyeva, Scientific Council on Spectroscopy of the
RAS, Russia

Barbecue dinner will be served in the park area across the street from B219.

Tuesday

9:00 - 10:30 Session I (Sampson, Chen)
10:30-10:50 Break
10:50-12:15 Session II (Beiersdorfer, Bureyeva, Sampson)
12:15-13:45 Lunch, email
13:45-15:40 Session III (Yoshikawa, Shlyaptseva, Goto)
15:40-16:00 Break
16:00-17:45 Session IV (More, Yoshikawa, Den Hartog)

LIST OF TALKS TUESDAY
in order of presentation
(only presenter is listed)

"Relativistic Cross Sections for Excitation and Ionization of Ions by an Electron Beam and Applications to the Polarization of the Subsequent Radiation"
Douglas H Sampson, Pennsylvannia State University, USA

"The effect of polarization on electron impact excitation cross-section measurements using an EBIT source"
Hui Chen, LLNL, USA

"Determining the electron temperature in an EBIT using x-ray plasma polarization spectroscopy"
Peter Beiersdorfer, LLNL, USA

"Effect of Charge Exchange on Spectral Line Intensity of Multicharge Ions in Plasmas"
Lyudmila Bureyeva, Scientific Council on Spectroscopy of the
RAS, Russia

"Effect of Innershell Ionization on the Linear Polarization of Se XXV Lines"
Douglas H Sampson, Pennsylvannia State University, USA

"Measurement of polarization of atomic helium lines due to strong caviton fields caused by IREB-plasma interactions"
Masayuki Yoshikawa, University of Tsukuba, Japan

"Theoretical development of x-ray line polarization spectroscopy: polarization database and influence of magnetic fields"
Alla Shlyaptseva, University of Nevada Reno, USA

"Determination of the line emission locations in the LHD on the basis of the Zeeman effect"
Motoshi Goto, NIFS, Japan

Hydrogen spectra in microwave fields
Richard More, NIFS, Japan

"Plasma polarization spectroscopy in the tandem mirror GAMMA 10"
Masayuki Yoshikawa, University of Tsukuba, Japan

Spectral Motional Stark Effect Measurements of Magnetic Field in Low-Field (< 0.5 T) Plasma Confinement Devices"
Daniel Den Hartog, University of Wisconsin, USA

Wednesday

9:00 - 10:50 Session I (Shlyaptseva, Baronova, Smith)
10:50-11:10 Break
11:10-12:10 Session II (Beiersdorfer, Reed)
12:10-13:45 Lunch
13:45-15:45 Session III (Kawachi, Fujimoto, Petrashen)
15:45-16:00 Break
16:00-17:30 Session IV (Baronova, Träbert, Neill)

18:00-21:30 Dinner at Garré Winery

LIST OF TALKS WEDNESDAY
in order of presentation
(only presenter is listed)

"X-ray spectropolarimetry studies at the Nevada Terawatt Facility and LLNL EBIT"
Alla Shlyaptseva, University of Nevada Reno, USA

"An X-ray polarimeter based on quartz crystal"
Elena Baronova, RRC Kurchatov Institute, Russia

"Measurement of the Polarization of the Kß2 Line of heliumlike V21+"
Augustine Smith, Morehouse College, USA

"Some problems with determing the polarization of H-like ions"
Peter Beiersdorfer, LLNL, USA

“Plasma polarization spectroscopy in an optical field ionization plasma"
Tetsuya Kawachi, JAERI, Japan

"Electron collisions of highly excited atoms:
Toward the population-alignment collisional-radiative model for recombining plasma"
Takashi Fujimoto, Kyoto University, Japan

"Quantitative spectropolarimetric sensing of the different ionized media"
Alexander G. Petrashen, St. Petersburg, Russia

"Characterization of large spherical crystals on optical contact"
Elena Baronova, RRC Kurchatov Institute, Russia

"Polarization studies in fast-ion beam spectroscopy"
Elmar Träbert, LLNL, USA

"Polarization measurements at EBIT using Calorimeter and Crystal Spectrometer data"
Paul Neill, University of Nevada, USA

The workshop dinner will take place at the Garré Winery (opens at 18:00).
The winery is located on Tesla Road at the intersection of Greenville Road and Tesla Road:

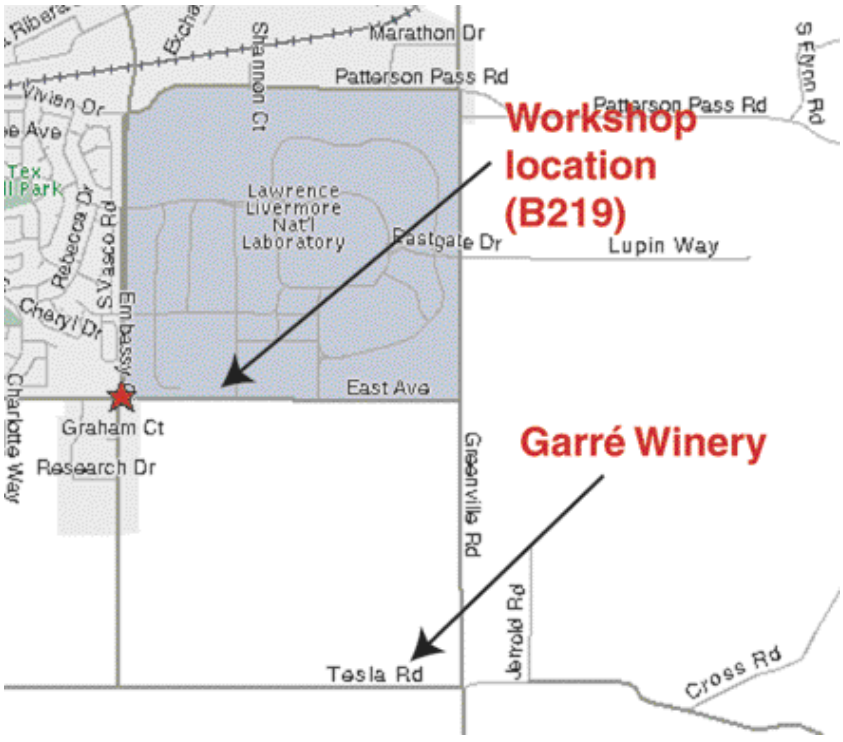

Thursday

We will meet for buses in B219.

9:00 - bus leaves B219

9:15–11:00 Tour of magnetic fusion research facilities in Building B435
Hosts: Bick Hooper (Spheromak)
David Hwang (Davis Divertor Tokamak)

11:15-12:30 Tour of EBIT facility, Building B194
Host: Peter Beiersdorfer

12:30-14:00 Lunch, email

Content

Abstract …… iii

Preface …… v

List of Participants …… vii

Program …… x

Table of Contents …… xvii

Plasma Polarization Spectroscopy: Past, Present and future Scopes ……..…….....1
T. Fujimoto

Theoretical Principles of Spectropolarimetric Sensing ……..……11
S.A. Kazantsev and A.G. Petrashen

Quantitative Spectropolarimetric Sensing of Ionized Media ……39
S.A. Kazantsev, A.G. Petrashen and Pudovkin M.I.

Density-Matrix Description of Atomic Radiative Emission from Autoionizing States In Electric and Magnetic Fields ….……69
V. L. Jacobs

Theoretical Development of X-Ray line Polarization Spectroscopy: Polarization Database and influence of magnetic fields ……93
A.S. Shlyaptseva, S. Hansen, V.L. Kantsyrev, S.A. Kazantsev, A.G. Petrashen and U.I. Safronova

Quasiclassical Theory of Dielectronic Recombination in Plasmas ……..121
L.A. Bureyeva, T. Kato, V.S. Lisitsa and C. Namba

Effect of Charge Exchange on Spectral Line Intensity of Multicharge Ions in Plasmas.143
L. Bureyeva, V. Lisitsa, V. Sergeev, R. Stamm and S. Sudo

Plasma Polarization Spectroscopy for the OV Ion: Relevant Collision Cross Sections for Kinetic Modeling …… 153
G. Csanak, D.P. Kilcrease, Honglin Zhang, D.V. Fursa, I Bray, T. Fujimoto and A. Iwamae

Contents contd.

Polarization of Emission Lines from Beryllium-like oxygen OV: Analysis based on the Population-Alignment Collisional-Radiative model ……. 165
A. Iwamae, A. Tanaka, T. Inoue, T. Fujimoto, Honglin Zhang, D. Kilcrease and G. Csanak

Monte Carlo calculation of Collisions of Directionally-Incident Electrons on highly excited hydrogen atoms …… 187
K. Kawakami and T. Fujimoto

Hydrogen Spectra in microwave fields
R. More ……..... 201

Spectral Motional Stark Effect Measurement of B in Low-Field Devices ….…… 205
D. J. Hartog, D. Craig, G. Fiksel, The MST Group, V.I. Davydenko, A.A. Ivanov and A.A. Lizunov

Determination of the line emission locations in the LHD on the basis of the Zeeman effect ……. 209
M. Goto and S. Morita

Plasma Polarization Spectroscopy in the tandem mirror GAMMA 10 ……. 215
M. Yoshikawa, T. Furukawa, A. Tanaka, A. Iwamae and T. Fujimoto

Plasma Polarization Spectroscopy on an Optical-Field-Ionization Plasma ……. 221
T. Kawachi, A. Iwamae and T. Fujimoto

Measurement of Polarization of atomic helium lines due to strong cavaton fields caused by IREB-plasma interactions ……. 227
M. Yoshikawa, F. Osawa, R. Ando, K. Kamada and M. Masuki

Analysis of Charge Separation in Neutral Gas-Confined Laser-Produced Plasmas by Polarization Spectroscopy ……. 231
Y. W. Kim

Polarized X-Ray Satellite line Emission in Non-Equilibrium transient Si plasmas . 249
P. Hakel, R. Mancini, J. Gauthier, E. Minguez, J. Dubau and M. Cornille

Measurement of the degree of Polarization of the Spectra from laser produced Al Plasmas ……. 263
Jaehoon Kim and Dong-Eon Kim

Relativistic Cross Sections for Excitation and Ionization by an Electron Beam and Application to the Polarization of the Subsequent Radiation……. 271
D. H. Sampson, H.L. Zhang, M.K. Inal and C.J. Fontes

Contents contd.

Measurement of the Polarization of the K 2 Line of heliumlike V^{21+} 299
A.J. Smith, P. Beiersdorfer, K.L. Wong and K.J. Reed

Relativistic effects on the Polarization of line radiation emitted from He-like and H-like ions following electron-impact excitation 305
K.J. Reed and M.H. Chen

Measurement of the relative intensity of the Ly- lines in Fe^{25+} 311
K. L. Wong, P. Beiersdorfer, K.J. Reed and A.L. Osterheld

Effect of Polarization on the measurements of Electron Impact Excitation Cross-Section of L-shell Fe in an Electron Beam Ion Source 319
H. Chen

Measurement of the Electron Cyclotron Energy Component of the EBIT II Electron Beam 329
P. Beiersdorfer and M. Slater

X-Ray Spectropolarimetry studies at the Nevada Terawatt Facility and LLNL EBIT 339
A.S. Shlyaptseva, V.L. Kantsyrev, B.S. Bauer, P. Neill, C. Harris, D.A. Fedin S. Hansen, N. Ouart, P. Beiersdorfer, A.G. Petrashen, U.I. Safronova

Polarimeter, based on one quartz crystal 359
E.O. Baronova and M.M. Stepanenko

Polarization studies in Fast-Ion Beam Spectroscopy 363
E. Träbert

Plasma Polarization Spectroscopy: Past, Present and future Scopes

Takashi Fujimoto
Kyoto University

Abstract: The developments of the plasma polarization spectroscopy (PPS) research over the last 35 years are reviewed, and an overview of its present status is given. It is noted that, at present, one of the important tasks is quantitative interpretation of the observed polarization data in terms of the plasma anisotropy. As a background for that direction the population kinetics of excited levels are reviewed on the basis of the collisional-radiative model for the ionizing plasma and for the recombining plasma. It is pointed out that, for the purpose of relating the observed polarization to the anisotropic velocity distribution of plasma electrons, the population-alignment collisional-radiative model is a basic tool.

1. History and present status of PPS

In the middle 1960's, spontaneous polarization of emission lines from plasma was discovered by three groups. This was the starting point of Plasma Polarization Spectroscpy (PPS). The first was the observation of polarization of neutral helium lines from a high-frequency discharge by Lombardi and Pebay-Peyroula in 1965. A little later, Kallas and Chaika (1969), and Carrington and Corney (1969), almost simultaneously, reported polarization of neon lines from DC discharge plasmas. Interestingly, they had little knowledge of other groups' work. This new phenomenon was named as *the self alignment*. The origin of polarization of light, or of the alignment in the upper-level 'population', was attributed to directional collisional excitation by electrons or to radiation trapping in the anisotropic geometry.

In the 1970's – 80's the self alignment phenomena of various origins were discovered and investigated vigorously on various discharge plasmas, mainly in the former Soviet Union. Gradually it became realized that PPS is a promising new technique which would give us valuable information of the plasma, *i.e.*, its anisotropy, to which no other ordinary spectroscopic technique has an access. Thus, the target of PPS observations expanded to a variety of plasmas, and this trend continues still now. These developments are summarized in Fujimoto and Kazantsev (1997).

In such a circumstance, the first US-Japan Workshop on PPS was held in 1994 in Los Alamos. In 1998 a joint Workshop on PPS was held in Kyoto (Fujimoto and Berierdorfer, 1998). The present Workshop is the continuation of this series.

In the following we will have a brief look at the historical developments and the present status

of PPS.

An element always important in PPS research is the instrumentation. For stationary discharge plasmas, an experimental setup, based on the Hanle effect, was developed which was capable of measuring polarization as low as 10^{-4} (Kazantsev, 1983a). For a variety of discharge conditions, self alignment produced by anisotropic electron impacts, ion collisions, or trapped radiation was realized, and even the self alignment due to the ion drift motion was discovered (Kazantsev *et al.*, 1987). By using the Hanle effect, the lifetime and an alignment destruction rate coefficient (cross section) of excited atoms by atom collisions were determined for many atomic species. Various possibilities of plasma diagnostics were demonstrated: obtaining the quadrupole moment of the electron velocity distribution (Kazantsev, 1983b); determining the energy input in a high-frequency discharge (Drachev *et al.*, 1991a); determining the electric field (Demkin and Kazantsev, 1995). The term *Plasma Polarization Spectroscopy* was first introduced by Kazantsev *et al.* (1983). An interesting observation was on an atmospheric-pressure argon arc plasma; ionized argon lines showed polarization and this was quantitatively interpreted as due to the anisotropic velocity distribution of electrons (Margolin *et al.*, 1983).

An important target of PPS is the solar atmosphere; Atoms in the solar prominence is illuminated by the light from the solar disk, and the photoexcitation is anisotropic. The alignment thus produced is perturbed by the magnetic field present there. From the direction and the magnitude of the observed polarization of a helium line, for example, the direction and the strength of the magnetic field is deduced (Sahal-Bréchot *et al.* 1977, Bommier *et al.*, 1981). Solar flares, in which anisotropic excitation of atoms and ions by electrons having a directional motion would produce alignment, are also the subject of PPS observation (Hénoux and Chambe, 1990). Vacuum sparks and plasma focuses are also the target of PPS research. Polarization is observed on heliumlike lines in the x-ray region (Walden *et al.*, 1999). However, the difficulty stemming from the observation geometry sometimes makes the interpretation complicated, and efforts to improve the instrumentation are being continued (Baronova, 2001). The so-called x-pinch is now being investigated vigorously (Mancini, 2001, Shlyaptseva, 2001).

The first PPS observation on a laser-produced plasma was made by Kieffer *et al.* (1992) on heliumlike aluminum lines. They interpreted the polarization as due to the nonlocal spatial transport of hot electrons from the superdense plasma to the underdense plasma. Another observation was performed by Yoneda *et al.* (1997) on heliumlike fluorine lines. The intensity distribution pattern of the resonance-series lines and the presence of the recombination continuum clearly indicates that the observed plasma is in the recombining phase. Interesting findings are that the recombination continuum is polarized, and that the resonance-series lines ($1^1S - n^1P$) are also polarized. The first point indicates that the velocity distribution of the low-energy electrons which make radiative recombination is anisotropic: more directional to the direction of the target surface normal. This is

against the general understanding that low-energy electrons thermalize very rapidly. The second point indicates that owing, probably, to the anisotropic elastic collisions by electrons, n^1P upper-level populations are aligned: among the $m_J = 0, \pm 1$ magnetic sublevels, the $m_J = 0$ level is more populated. No interpretation of this experiment has been made so far. A new experiment is being performed (Kim and Kim, 2001). Kawachi *et al.* (1995) examined polarization of the neonlike germanium x-ray laser line of 19.6 nm. The transition was $2p^5 3p \rightarrow 2p^5 3s$ ($J = 0 \rightarrow 1$), so that the spontaneous emission of this line is never polarized. The observed polarization was ascribed to the alignment of the $2p^5 3s$ lower-level population, which was due to the anisotropic radiation trapping, $2p^6 \leftrightarrow 2p^5 3s$.

Magnetically confined plasmas including tokamak plasmas are also the target of PPS observations. MSE (motional Stark effect) is now a standard technique to determine the direction of the local magnetic field, and thus to determine the current distribution in the plasma (Levinton *et al.*, 1989, Den Hartog, 2001). The Zeeman effect is also utilized for plasma diagnostics (Goto, 2001). Fujimoto *et al.* (1996) first reported the polarization observation on carbon and oxygen impurity emission lines from a tokamak plasma. They used a calcite plate incorporated into the spectrometer as a polarization resolving element. Anisotropic distributions of electron velocities were suggested as the origin of the observed polarizations.

Polarization of emission lines and continuum may be attributed to several origins. Class 1 polarization is the result of anisotropy of space, or the presence of an electric field or a magnetic field: this class is nothing but the well known Stark effect or the Zeeman effect. The MSE mentioned above falls in this category. Recently, another possibility of this kind is proposed (More, 2001), but in this case, the field is an anisotropic electromagnetic waves that are resonant with the Zeeman splitting of the level. Class 2 is the polarization resulting from directional excitation of atoms and ions. The colliding agent would be electrons, ions, photons or even atoms. Radiation trapping in an anisotropic geometry is included in this category. In the next section we will concentrate on the Class 2 polarization of atoms and ions produced by directional collisions of electrons in an anisotropic plasma.

2. Quantitative interpretation

For the purpose of plasma diagnostics, for instance, quantitative interpretation of the observed polarization is essential. With the aim of quantitative interpretation of polarization, we first review the population kinetics of atoms and ions in plasma under various plasma conditions. We assume the Maxwell distribution for electron velocities with a certain electron temperature and varying electron density. In this regard, the following pictures have nothing to do with the polarization problem. We take neutral hydrogen as an example of atoms and ions in plasma.

Figure 1 shows schematically the structure of excited level populations of atoms or ions in

plasma. The population of an excited level p consists of two components: $n_1(p)$, the ionizing plasma component which is proportional to the ground-state population $n(1)$, and $n_0(p)$, the recombining plasma component which is proportional to the ion density n_z. Here p=1 means the ground state and

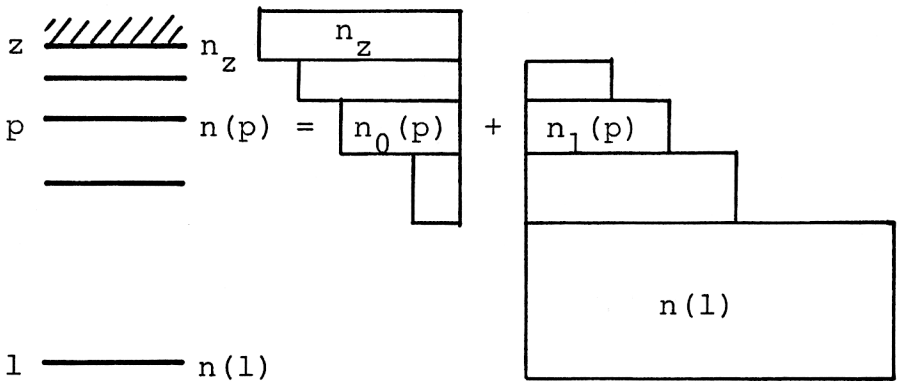

Figure 1. The structure of excited-level populations in plasma.

z means the ion. Both the distribution of $n_1(p)$ over p and that of $n_0(p)$ are functions of electron temperature and density. An important point is that, in the majority of laboratory plasmas, either of the components is predominant and the other component is negligibly small. This is the result of the gross departure of $[n_z/n(1)]$ from the value the plasma would take if the plasma were in ionization balance. In other words, both the components could be of similar magnitudes only when the plasma is in ionization balance. Thus, many plasmas are classified into either *the ionizing plasma* or *the recombining plasma.* We simply call the system of $n_1(p)$ the ionizing plasma and that of $n_0(p)$ the recombining plasma. Figures 2 and 3 show the overall pictures of the population fluxes among the energy-level diagram for the ionizing plasma and the recombining plasma, respectively (Fujimoto, 1979a, 1979b, 1980a, 1980b); In Fig. 2, we assume T_e = 1.28 x 10^5 K, n_e = 10^{12} m^{-3} (top), 10^{18} m^{-3} (middle) and 10^{22} m^{-3} (bottom), and n_z = 0. In Fig. 3, we assume T_e = 10^3 K, $n_e \rightarrow 0$ (top), 10^{20} m^{-3} (middle) and $n_e \rightarrow \infty$ (bottom) and $n(1)$ = 0. The blank arrows indicate the transitions induced by electron collisions and the hatched arrows the radiative transitions. The thickness of each arrow is proportional to the magnitude of the flux, or the number of the events per unit time and unit volume, of the transition. It is seen that, except for the cases of low density as shown at the top of Figs. 2 and 3, the population kinetics are rather complicated in both the plasmas. They are essentially of a collective nature.

We now suppose that the velocity distribution of our electrons is anisotropic. Even in this case, the overall population kinetics are expected to be much the same as those given in Figs. 2 and 3, and now new features would appear that are due to the anisotropy of the distribution. When we observe an emission line and find it to be polarized, its upper level would be in a situation similar to the one as

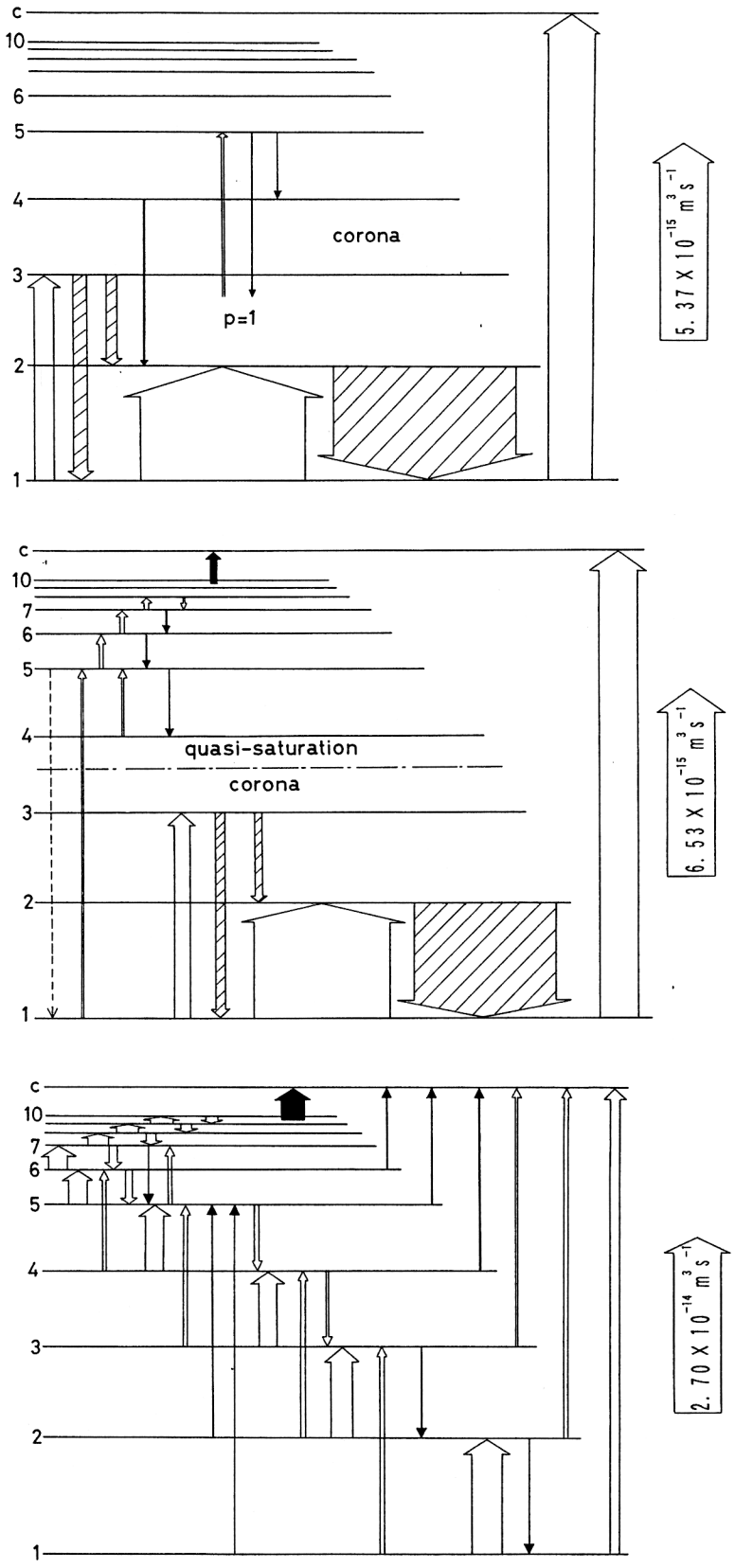

Figure 2. Population fluxes in the energy-level diagram in the ionizing plasma. $T_e = 1.28 \times 10^5$ K. top: $n_e = 10^{12}$ m^{-3}, middle: $n_e = 10^{18}$ m^{-3}, and bottom: $n_e = 10^{22}$ m^{-3}.

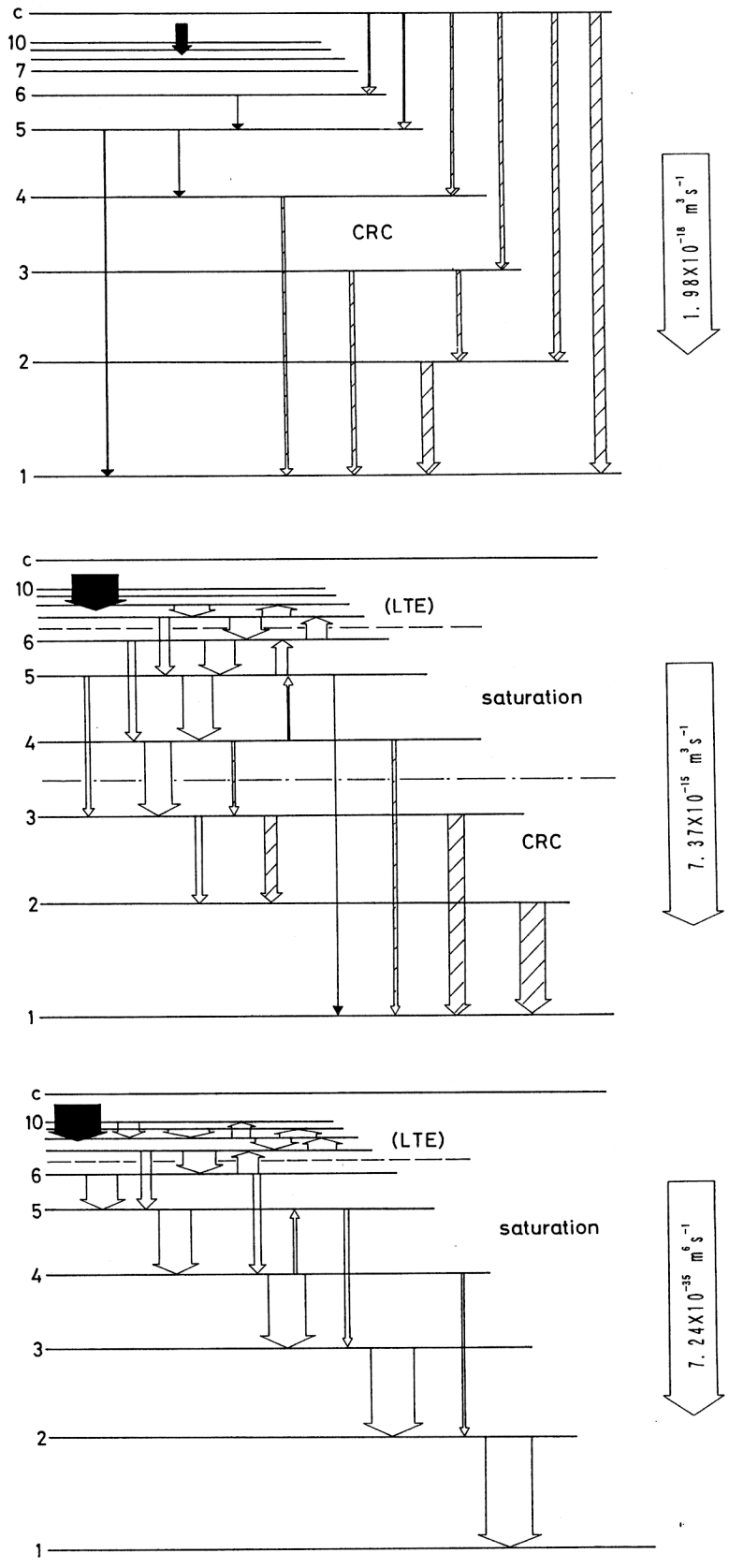

Figure 3. Population fluxes in the energy-level diagram in the recombining plasma. T_e = 1 x 10^3 K. top: $n_e \rightarrow 0$, middle: $n_e = 10^{20}$ m^{-3}, and bottom: $n_e \rightarrow \infty$.

shown in these figures. Thus, for the purpose of quantitative interpretation of the observed polarization, we have to ask two questions first;

Question 1: *Is this plasma ionizing or recombining ?*

Question 2: *Is this plasma density low enough or rather high ?*

Depending on the answer to these questions the plasma is classified into one of the four situations:

Various situations of polarization phenomena

Q2 \ Q1	low density	high density
ionizing plasma	1	2
recombining plasma	3	4

We investigate below each situation.

Situation 1

As Fig. 2, top, shows excited levels are in corona equilibrium, and the important process in the population kinetics is the direct excitation from the ground state. Substantial body of atomic data of the relevant cross sections exists now (Sampson, 2001; Beiersdorfer, 2001, Neil, 2001; Csanak, 2001). The interpretation of polarization is rather straightforward, but if the produced alignment is relaxed by electron or atom collisions these effects should be properly taken into account. Sometimes, radiation trapping, especially to the lines terminating on the ground state, tends to destroy the alignment. It could also produce alignment as noted at the beginning of this article.

Situation 2

Besides the direct excitation from the ground state, the indirect excitation from the metastable levels or from closely-lying adjacent lower levels become important, or they even predominate. These intermediate levels may be aligned, too, and this alignment may be transferred to the level with which we are concerned. Elastic collisions may destroy the alignment, but they could also create alignment, because they are directional. Almost no atomic data exist for these processes. In a theoretical interpretation, all these effects should be treated self-consistently. The population-alignment collisional-radiative (PACR) model is the kinetic model which is intended for this. Recently, an almost complete formulation of the PACR model has been constructed for berylliumlike oxygen (OV) and it is applied to the PPS observation on a tokamak plasma (Iwamae *et al.*, 2001).

Situation 3

Radiative recombination and radiative transitions are only the processes involved. Radiative

recombination of directionl electrons has been investigated by several workers, and a few atomic data can be found (Scofield, 1989; Scofield, 1991).

Situation 4

As in Situation 2, the population kinetics are essentially collective. A PACR model would be a method to cope with this situation, but no model has been constructed so far. One of the difficulties is with the three-body recombination, which is the starting point in the population fluxes. Almost nothing is known when the electron velocity distribution deviates from the Maxwell distribution. A formulation is needed in which the anisotropic three-body recombination is expressed quantitatively. Another difficulty is the presence of a large number of rydberg states. In contrast to the case of the Maxwell distribution, we cannot assume LTE populations. Rather, these levels would be less populated, and these populations would be aligned. Other problems are essentially the same as in Situation 2. In this case, alignment relaxation and alignment creation by trapped radiation should not be forgotten. The experiment by Yoneda *et al.* falls in this situation, and, naturally, its interpretation is yet to be done. An attempt in this direction is being made (Kawakami and Fujimoto, 2001).

References

Baronova, E., 2001, (this Workshop).

Beiersdorfer, P., 2001 (this Workshop).

Bommier, V., Leroy, J.L. and Sahal-Bréchot, S., 1981, Astron. Astrophys. **100**, 231.

Carrington, C.G. and Corney, A., 1969, Opt. Comm. **1**, 115.

Csanak, G., 2001 (this Workshop).

Demkin, V.P. and Kazantsev, S.A., 1995, Opt. Spectrosc. **78**, 337.

Den Hartog, D., 2001 (this Workshop).

Drachev, A.I., Kazantsev, S.A, Rys, A.G. and Subbotenko, A.V., 1991, Opt. Spectrosc. **71**, 527.

Fujimoto, T. 1979a, J. Phys. Soc. Japan **47**, 265.

Fujimoto, T. 1979b, J. Phys. Soc. Japan **47**, 273.

Fujimoto, T. 1980a, J. Phys. Soc. Japan **49**, 1561.

Fujimoto, T. 1980b, J. Phys. Soc. Japan **49**, 1569.

Fujimoto, T. and Beiersdorfer, P., 1998, *Proceedings of the Japan-US Workshop on Plasma Polarization Spectroscopy and The International Seminar on Plasma Polarization Spectroscopy* (NIFS-PROC-37, Nagoya).

Fujimoto, T. and Kazantsev, S.A., 1997, Plasma Phys. Control. Fusion **39**, 1267.

Fujimoto, T., Sahara, H., Kawachi, T., Kallstenius, T., Goto, M., Kawase, H., Furukubo, T., Maekawa, T. and Terumichi, Y., 1996, Phys. Rev. E **54**, R2240.

Goto, M., 2001 (this Workshop).

Hénoux, J.C. and Chambe, G., 1990, J. Quant. Spectrosc. Radiative Transfer **44**, 193.

Iwamae, A., Tanaka, A., Inoue, T., Fujimoto, T., Zhang, H., Kilcrease, D.P. and Csanak, G., 2001 (this Workshop).

Kallas, Kh. and Chaika, M., 1969, Opt. Spectrosc. **27**, 376.

Kawachi, T., Murai, K., Yuan, G., Ninomiya, S. Kodama, R., Daido, H., Kato, Y. and Fujimoto, T., 1995, Phys. Rev. Lett. **75**, 3826.

Kawakami, K. and Fujimoto, T., 2001 (this Workshop).

Kazantsev, S.A., 1983a, Sov. Phys. Usp. **26**, 328.

Kazantsev, S.A., 1983b, JETP Lett. **37**, 158.

Kazantsev, S.A., Margolin, L.Ya., Polynovskaya, N. Ya., Pyatnitskii, L.N., Rys, A.G. and Edelman, S.A., 1983, Opt. Spectrosc. **55**, 326.

Kazantsev, S.A., Petrashen', A.G., Polezhaeva, N.T., Rebane, V.N. and Rebane, T.K,. 1987, JETP Lett. **45**, 17.

Kieffer, J.C., Matte, J.P., Pépin, H., Chaker, M., Beaudoin, Y., Johnston, T.W., Chien, C.Y., Coe, S., Mourou, G. and Dubau, J., 1992, Phys. Rev. Lett. **68**, 480.

Kim, J. and Kim, D.E., 2001 (this Workshop).

Levinton, F.M., Fonck, R.J., Gammel, G.M., Kaita, R., Kugel, H.W., Powell, E.T. and Roberts, D.W., 1989, Phys. Rev. Lett. **63**, 2060.

Lombardi, M. and Pebay-Peyroula, J.-C., 1965, C. R. Acad. Sc. Paris **261**, 1485.

Mancini, R., 2001 (this Workshop).

Margolin, L.Ya., Polynovskaya, N.Ya., Pyatnitskii, L.N., Timergaliev, R. Sh. and Édel'man, S.A., 1983, High Temp. **22**, 149.

More, R, 2001 (this Workshop).

Neil, P., 2001 (this Workshop).

Sahal-Bréchot, S., Bommier, V. and Leroy, J.L., 1977, Astron. Astrophys. **59**, 223.

Sampson, D., 2001 (this Workshop).

Scofield, J.H., 1989, Phys Rev. A **40**, 3054.

Scofield, J.H., 1991, Phys. Rev. A **44**, 139.

Shlyaptseva, A. 2001 (this Workshop).

Walden, F., Kunze, H.-J., Petoyan, A., Urnov, A. and Dubau, 1999, J., Phys. Rev. E **59**, 3562.

Yoneda, H., Hasegawa, N., Kawana, S. and Ueda, K., 1997, Phys. Rev. E **56**, 988.

THEORETICAL PRINCIPLES OF SPECTROPOLARIMETRIC SENSING

S.A. Kazantsev *, A.G.Petrashen **

* Observatoire de Paris, DASOP, F-92195,Meudon Cedex, France

** St-Petersburg Institute of the Fine Mechanics and Optics,199101, St-Petersburg, Russia.

Contents

Introduction

1. Polarization moments and its physical meaning.

2. The evolution of the density matrix.

3. The polarization characteristics of emission excited by collisions with counter-propagating beams.

3.1 Collisional transformation of the momentum ordering in the counter-propagating beams at low relative velocities.

3.2 Collisional transformation of the momenta ordering in the counter-propagating beams at high relative velocities.

3.3 The polarization characteristics of the emission of atomic ensembles interacting with a monoenergetic beam.

3.4 Low velocity case - mixing of the sublevel populations of the primarly excited state.

3.5 High velocity case - direct excitation of a quantum state.

4. Spectropolaremetric effects in angular correlation experiments.

5. Spectropolarimetric manifestation of the higher polarization moments.

6. Collisional relaxation of polarization moments excited by a monochromatic laser beam.

7. The evolution of polarization moments in the presence of a magnetic field.

0.1 Introduction

Polarization spectrometry of ionized media was actively developed during last two to three decades. New theoretical approaches have been elaborated and extensive experimental data have been obtained as well. These experimental data stimulated the theoretical studies of polarization phenomena. Basic theoretical principles of the polarization spectroscopy and a number of applications of these principles are described in the books [1, 2, 3].

Methods of the polarization spectroscopy were successfully applied for the description of processes in the gas discharge plasmas [4], the hydrogen ionized medium of the Solar chromosphere [5], the high temperature plasma [6], and the diluted plasma of the higher Earth Atmosphere [7].

The polarization of emission stems from non-equilibrium distribution of the populations of the magnetic sublevels of atoms or ions. Many physical processes may be

responsible for creation of non-equilibrium distribution of these populations. These processes lead to the anisotropy and polarization of the emission. Therefore the spectropolarimetric and angular data, can give new information about the processes that take place in plasma.

The present report is mainly focused on the description of the polarization properties of the emission that results from the general properties of atomic ensembles undergoing different types of interactions.

1 Polarization moments and its physical meaning

The wave function of an atom of the ensemble can be represented as the decomposition over the complete set of eigen functions of the operator of the square of the momentum and its projection $\psi_{j,m}$

$$\Psi(r,t) = \sum_{j,m} c_{j,m}\psi_{j,m}e^{-iE_jt/\hbar}, \tag{1.1}$$

where the symbol r denotes the set of space coordinates and E_j is the energy of the state with the momentum j.

The description of the properties of an atomic ensemble is best done using the density matrix formalism. the density matrix is defined as an ensemble averaged products $\Psi(r,t)\Psi(r,t)^*$

$$\widehat{\rho} = \sum_{j,m,j'.m'} \left\langle c_{j,m}c^*_{j',m'} \right\rangle \psi_{j,m}\psi^*_{j',m'} = \sum_{j,m,j',m'} \rho_{j,m;j',m'}\psi_{j,m}\psi^*_{j',m'} \tag{1.2}$$

where the angular brackets denote the average over the ensemble and $\rho_{j,m;j',m'}$ are the matrix element of the density operator in the j,m representation.

It is well known [8] that that with the products of functions $\psi_{j,m}\psi^*_{j',m'}$ the direct product of the representations $D^{(j)} \otimes D^{(j')^*}$ is realized.. It is convenient to introduce a new basis (that is often named as the $k-q$ base) on which this direct product is decomposed into the irreducible parts. Elements of this basis are expressed in terms of the linear combinations of the products $\psi_{j,m}\psi^*_{j',m'}$, whereas the coefficients of these combinations are given by the Clebsch-Gordan coefficients [9]. Elements of the density matrix in this new $k-q$ basis are known as the polarization moments

$$\rho^k_q(j,j') = \sum_{m,m'} (-1)^{j'-m'} \begin{bmatrix} j & j' & k \\ m & -m' & q \end{bmatrix} \rho_{j,mj',m'} \tag{1.3}$$

The polarization moments may be considered as the decomposition coefficients of the density operator over the set of irreducible tensor operators T^k_q [9]:

$$\widehat{\rho}(j) = \sum_{k,q} \rho^k_q(j)\widehat{T}^k_q \tag{1.4}$$

Since the irreducible tensor operators satisfy the orthogonality property

$$Sp_j\left(\widehat{T}^k_q\widehat{T}^{k_1\dagger}_{q_1}\right) = 0 \quad if \quad k \neq k_1 and \quad q \neq q_1, \tag{1.5}$$

where the trace is spread over the state with total momentum j, the polarization moments may be defined by the formula

$$\rho_q^k(j) = Sp_j\left(\rho\widehat{T}_q^{k\dagger}\right) \tag{1.6}$$

This relation coincides with (1.3) if the reducible matrix element of the operator T_q^k is chosen such that

$$\left\langle j \left\| \widehat{T}^k \right\| j' \right\rangle = \sqrt{\frac{2k+1}{2j+1}} \tag{1.7}$$

Polarization moments have a deeper physical meaning with respect to the density matrix elements in jm representation. They describe the ordering of angular moments of exited atomic ensemble.

The zero rank polarization moment that is diagonal with respect to the angular moments is proportional to the population of the state n_j under consideration.

$$\rho_0^0\left(j,,j\right) = \frac{\sum_m \rho_{j,m;j,m}}{\sqrt{2j+1}} = \frac{n_j}{\sqrt{2j+1}} \tag{1.8}$$

The physical meaning of polarization moments of the higher rank can be inferred by considering of the ensemble average at the state with total momentum j equal to irreducible tensor operator of rank k:

$$\left\langle \widehat{T}_q^k \right\rangle = Sp_j\left(\rho\widehat{T}_q^k\right) = \sum_{j,j'} \left\langle j' \left\| \widehat{T}^k \right\| j \right\rangle \sqrt{\frac{2j+1}{2k+1}} \left(-1\right)^{j-j'+q} \rho_{-q}^k\left(j,j'\right) \tag{1.9}$$

One can see from this relation, that the ensemble average at the state with the total momentum j value equal to $q-$component of the irreducible tensor operator of the rank k is a linear combination of polarization moments of the same rank.

As the Hamiltonian and the operator of the square of the angular momentum $\widehat{j^2}$ and its projections $\widehat{j}_i$ $(i = x, y, z)$ commute, the matrix elements of $\hat{J}_q^k$, which is an irreducible tensor operator, constructed from components of the total angular momentum are diagonal in terms of values of the angular momentum. Therefore if $\widehat{J}_q^k$ is the operator of the type mentioned above, the relation (1.9) will take the form

$$\left\langle \widehat{J}_q^k \right\rangle = \left\langle j \left\| \widehat{J}^k \right\| j \right\rangle \sqrt{\frac{2j+1}{2k+1}} \left(-1\right)^q \rho_{-q}^k\left(j,j\right) \tag{1.10}$$

Or, in the other words, the mean value of a irreducible tensor operator $\widehat{J}_q^k$ is the linear combination of the polarization moments of the same rank. Hence, the mean value of the tensor $\widehat{J}_q^1$, which is transformed as a vector under the space rotationsis, is the linear combination of the quantities ρ_q^1 $(q = 0, \pm 1)$,. With the help of the last formula one can obtain the relation for the mean values of circular components of the total momentum

$$\begin{aligned} \left\langle \widehat{j}_z \right\rangle &= \sqrt{\frac{2j(2j+1)(2j+2)}{12}} \rho_0^1\left(j.j\right) \\ \left\langle \widehat{j}_\pm \right\rangle &= \pm\sqrt{\frac{2j(2j+1)(2j+2)}{6}} \rho_{\mp 1}^1\left(j.j\right) \end{aligned} \tag{1.11}$$

Three components of the tensor ρ_q^1 are named as the orientation vector. The values ρ_q^1 $(q = 0, \pm 1)$ are closely linked to the vector of the magnetic dipole moment of an atomic ensemble. It depends on Lande factor g_j , Bohr magneton μ_0, and and the mean value of the total angular momentum $\langle j \rangle$ according to

$$\overrightarrow{\mu} = -g_j \mu_0 \langle j \rangle \tag{1.12}$$

Five elements of ρ_q^2 $(q = 0, \pm 1, \pm 2)$ are named the alignment tensor. Under the space rotations this tensor transforms over the $D^{(2)}$ representation of group of three dimension rotations, and the components of this tensor define the averaged over the ensemble linear combination of the pair products of components of the angular momentum, as illustrated below:

$$\left\langle 3j_z^2 - j^2 \right\rangle = \frac{\sqrt{(2j-1)2j(2j+1)(2j+2)(2j+3)}}{2\sqrt{5}} \rho_0^2(j) \tag{1.13a}$$

$$\langle j_z j_\pm + j_\pm j_z \rangle = \mp \frac{\sqrt{(2j-1)2j(2j+1)(2j+2)(2j+3)}}{2\sqrt{15}} \rho_{\mp 1}^2(j) \tag{1.13b}$$

$$\left\langle j_\pm^2 \right\rangle = \frac{\sqrt{(2j-1)2j(2j+1)(2j+2)(2j+3)}}{\sqrt{30}} \rho_{\pm 2}^2(j) \tag{1.13c}$$

The quantities $\rho_q^1(j, j'; t)$ are $\rho_q^2(j, j'; t)$ are known as the orientation an alignment of the state with the total atomic momentum j. Components of the alignment tensor $\rho_0^2(j, j'; t)$, $\rho_{\pm 2}(j, j'; t)$, and $\rho_{\pm 2}^2(j, j'; t)$ can be named as longitudinal, inclined, and transverse alignment respectively. Formulas (1.13) are schematically illustrated at the fig. 1 (plots a-c).

The physical meaning of the first formula of last relations can be illustrated at the fig. 1 (a), where the angular dependence of the quantity is represented:

$$\frac{3\cos^2\vartheta - 1}{2} = \frac{\left\langle 3\widehat{j}_z - \widehat{j}^2 \right\rangle}{2} \Big|_{j=1} \tag{1.14}$$

According to formula (1.13a), this value is proportional to the longitudinal alignment ρ_0^2 of the state with angular momentum $j = 1$. If all moments are parallel to the OZ axis ($\langle \cos\vartheta \rangle = 1$), the degree of alignment is a maximum and equal to 1. If the momenta are perpendicular to this axis ($\langle \cos\vartheta \rangle = 0$) the alignment will be minimized and equal to $-1/2$. For $\langle \cos\vartheta \rangle = 1/\sqrt{3}$ $(\vartheta \sim 54.73^o)$, the longitudinal alignment is absent, while the atomic ensemble is ordered. This angle is often named as the "magic" one. For the axially symmetric system at the "magic" angles only the population and the zero-order components of the higher-rank polarization moments can exist. It means that for axially symmetric ensemble of particles with the angular moments $j = 1$ at the "magic" angle, only population present, although the moments are ordered. This phenomenon may be used to create nonaligned ensembles under typical experimental conditions with the axial symmetry in excitation process [10].

If the system a certain symmetry, the polarization moments should be invariant with respect to operations of the some group. Under the set of operations of

the rotation group $\{g\}$ the eigenfunctions of the Hamilton operator $\psi_{j,m}$ transform according to the representations of this group:

$$\widehat{g}\psi_{j,m} = \sum_{j} D^{(j)}_{m',m}\psi_{j.m'} \tag{1.15}$$

Polarization moments, as it was mentioned above, transform according to one of the representations used to decompose the direct product $D^{(j)} \otimes D^{(j)*}$.

In the case of the spherical symmetry, polarization moments transform over the representation of the rotation group $D^{(j)}$:

$$\widehat{g}\rho^k_q = \sum_{q'} D^{(k)}_{q'.q}\rho^k_{q'} \tag{1.16}$$

Because $D^{(0)}_{0,0} = 1$, only polarization moment of zero rank will be invariant under the operations of the rotation group. This means, that in spherically symmetric ensemble only the population can be induced.

In the case of the axial symmetry, the polarization moments are invariant over the operation of the C_v group [8]. The transformation of polarization moment under the operation of rotation with angle φ around the axis of symmetry may be written as

$$\widehat{g}\rho^k_q = e^{iq\varphi}\rho^k_q. \tag{1.17}$$

From this relation it is clear, that in the axial symmetry ensemble only the polarization moments with the zero components are not zero,

If the system has a plane of symmetry [$\varphi \to -\varphi$; see fig. 2], the wave functions under the reflection operation are transformed as $\widehat{\sigma}_{zy}\psi_{l,m} = (-1)^m\psi_{l,-m}$. Therefore the transformation of the polarization moments takes the form

$$\widehat{\sigma}_{zx}\rho^k_q = (-1)^{k+q}\rho^k_{-q} \tag{1.18}$$

This relation together with the properties of the polarization moments with respect to the operation of complex conjugation, $(\rho^k_q)^* = (-1)^q\rho^k_{-q}$, results to the relation

$$\rho^k_q = (-1)^k\rho^k_q \tag{1.19}$$

from which one can see that all polarization moments of the odd rank are purely imaginary whereas even rank polarization moments are real.

In analogy, the symmetry of the system over the operation of reflection in the ZY plane (the transformation of polar angle $\varphi \to \pi - \varphi$) leads to the symmetry property

$$\rho^k_q = (-1)^{k-q}\rho^k_q \tag{1.20}$$

With the help of relation (1.19) one have that in this case the moments with even $k - q$ are real and with odd $k - q$ are purely imaginary.

If an atomic ensemble is excited to a state which is characterized by the value of the total momentum j, then the intensity of the radiation emitted by the transition

$j \to j_0$ will be polarized in the direction defined by the unit vector $\overrightarrow{e_\lambda}$ and may be written

$$I_\lambda = I_o \sum_{m_0,m,m'} \left\langle j_0, m_0 \left| \left(\overrightarrow{e_\lambda}, \overrightarrow{d}\right) \right| j, m \right\rangle \left\langle j_0, m_0 \left| \left(\overrightarrow{e_\lambda}, \overrightarrow{d}\right) \right| j, m' \right\rangle^* \rho_{j,m;j,m'} \qquad (1.21)$$

Here I_0 is a constant that depends on the fundamental constants and $\overrightarrow{d}$ is the vector of dipole moment. Decomposing the unit vector of polarization over the circular unit vectors [9]

$$\overrightarrow{e_\lambda} = \sum_q a_q^{(\lambda)} \overrightarrow{e_q}, \qquad (1.22)$$

one can obtain a more convenient relation for the intensity of the dipole emission:

$$I_\lambda = I_0 \sum_{k,q} (-1)^k \left\{ \begin{array}{ccc} 1 & 1 & k \\ j & j & j_0 \end{array} \right\} \Phi_{k,q}\left(\overrightarrow{e_\lambda}\right) \rho_q^k, \qquad (1.23)$$

Here the expression in $\{\}$ is the Wigner $6j$ symbol. I_0 is the factor that contains the constant I_0 and the oscillator strengths and $\Phi_{k,q}\left(\overrightarrow{e_\lambda}\right)$ is known as the polarization tensor.

$$\Phi_{k,q}\left(\overrightarrow{e_\lambda}\right) = \sum_{q,q'} (-1)^{1-q} a_q^{(\lambda)} a_{q'}^{(\lambda)*} \left[\begin{array}{ccc} 1 & 1 & k \\ q' & -q & q \end{array} \right]. \qquad (1.24)$$

The significance of this formula comparing with (1.21) is that (1.23) is represented by two principally different parts. The first is the geometry of the observation, that is defined by the polarization tensor and the second is the dynamical characteristics of emitting system, that are defined by polarization moments.

From the relation (1.23) one can see that due to the properties of $6j$ symbol, the intensity of the polarized dipole radiation is given by the linear combination of the polarization moments with rank not higher than two. The moments of the higher orders are named as the "hidden" ones. They are not presented in the dipole radiation, but they can influence indirectly on the polarization characteristics of an atomic ensemble.

Detaching in formula (1.23) the term with $k = 0$ one have

$$I_\lambda = I_0 \left[\frac{(-1)^{j+j_0+1}}{3\sqrt{2j+1}} \rho_0^0 + \sum_{k=1}^{2} \sum_q (-1)^k \left\{ \begin{array}{ccc} 1 & 1 & k \\ j & j & j_0 \end{array} \right\} \Phi_{k,q}\left(\overrightarrow{e_\lambda}\right) \rho_q^k \right] \qquad (1.25)$$

Now one can see that the expression for dipole emission intensity consists of the isotropic part, which contains the polarization moment of zero rank as a multiplier, and the anisotropic part, which contains the polarization moments of higher order. Therefore, in the dipole approximation, the anisotropic part contains only components of the orientation vector and the alignment tensor. Or, in other words, the components of these tensors define completely the intensity of the dipole emission.

Measuring of the anisotropic part of the dipole intensity may give information about the ordering of the angular moments in the ensemble under consideration,

and therefore information about dynamical processes that lead to such an ordering. As is clear from (1.25), the anisotropic part of intensity may by obtained as the difference of intensities measured in two orthogonal directions. For instance, if OX axis is selected as an axis of observation, then one can measure two unequal differences and the sum of intensities:

$$I_y - I_z = I_0 K_2 \left[\sqrt{\frac{3}{2}} \rho_0^2(j) + Re\rho_2^2(j) \right] \tag{1.26a}$$

$$I_{zy+} - I_{zy-} = 2 I_0 K_2 Im\rho_1^2(j) \tag{1.26b}$$

$$I_+ - I_- = I_0 K_1 Im\rho_1^1(j) \tag{1.26c}$$

$$I_z + I_z = I_0 \left\{ \frac{2}{\sqrt{3}} \rho_0^0(j) K_0 + K_2 \left[-\sqrt{\frac{1}{6}} \rho_0^2(j) + Re\rho_2^2(j) \right] \right\} \tag{1.23d}$$

where introduced a factor

$$K_k^{-1} = (-1)^{j+j_0+1} \sqrt{3\,(2j+1)} \left\{ \begin{array}{ccc} 1 & 1 & k \\ j & j & j_0 \end{array} \right\} \tag{1.27}$$

The notations I_y and I_z denote the intensities polarized in the directions of OY and OZ axis; I_+ and I_- - intensities polarized clockwise and counterclockwise around OX axis; I_{yz+} and I_{yz-} are the intensities polarized over the diagonals of the first and the second squares of the YZ plane.

The first of expressions (1.26a) is illustrated by fig. 1 (plots a and c). If OX axis is selected as the direction of observation, then the imaginary part of the inclined alignment (fig.1 (b)) will be invariant to the replacement OY and OZ axis therefore this term did not present in the difference of the intensities. By contrast, the longitudinal and the transverse alignments are not invariant under this substitution, and these types of ordering are present in the differences of the intensities. As for formula (1.26c), according relation (1.11), $Im\rho_1^1(j) \sim \langle j_y \rangle$, and the value $j_{y|j=1} = \sin\vartheta \sin\varphi$. The plot of this value is represented at the fig. 1 (d). Since the plotted figure is not invariant under rotations around the OX axis, the difference $I_+ - I_-$ is not zero. The difference of intensities (1.26a) and (1.26b) may be called the signals of longitudinal and inclined alignment, respectively, whereas the difference (1.26c) may be called the orientation signal.

The signals of alignment are not normally used because they contain unknown parameters through the factor I_O. Instead, the Stokes parameters, that are ratios of the difference and the sum of intensities are measured. The relations (1.26a)-(1.26d) give the opportunity of constructing three parameters:

$$\begin{aligned} Q &= \frac{I_y - I_z}{I_z + I_z} = \frac{3\rho_0^2(j) + \sqrt{6} Re\rho_2^2(j)}{2\sqrt{2}\rho_0^0(j)\frac{K_0}{K_2} - \rho_0^2(j) + \sqrt{6} Re\rho_2^2(j)} \\ U &= \frac{I_{zy+} - I_{zy-}}{I_{zy+} + I_{zy-}} = \frac{2 Im\rho_1^2(j)}{2\sqrt{2}\rho_0^0(j)\frac{K_0}{K_2} - \rho_0^2(j) + \sqrt{6} Re\rho_2^2(j)} \\ V &= \frac{I_+ - I_-}{I_+ + I_-} = \frac{2\sqrt{6} Im\rho_1^1(j)}{2\sqrt{2}\rho_0^0(j)\frac{K_0}{K_1} - \left(\rho_0^2(j) - \sqrt{6} Re\rho_2^2(j)\right)\frac{K_2}{K_1}} \end{aligned} \tag{1.28}$$

2 The evolution of the density matrix.

If $\Psi(r,t)$ is the wave function of a particular atomic ensemble under consideration, then this function is the solution of Schrodinger equation

$$i\hbar\frac{\partial}{\partial t}\Psi(r,t) = \left(\widehat{H}_0 + \widehat{V}\right)\Psi(r,t) \tag{2.1}$$

where $\widehat{H}_0$ is the Hamilton's operator of an isolated atom and $\widehat{V}$ describes the interaction of this atom with the environment.

If $\psi_{j,m}$ is the set of eigenfunctions of the square of the total momentum and projection, the wave function $\Psi(r,t)$ can be decomposed over this set its

$$\Psi(r,t) = \sum_{j,m} c_{j,m}(t)\psi_{j,m}(r)e^{-iE_jt/\hbar} \tag{2.2}$$

Substituting last decomposition into (2.1), the system of differential equations over the coefficients $c_{j,m}(t)$ takes the form

$$i\hbar\frac{d}{dt}c_{j,m}(t) = \sum_{j',m'} V_{j,m;j',m'}c_{j',m'}(t) \tag{2.3}$$

Now we introduce the density operator

$$\widehat{\rho}(r,r';t) = \langle\Psi(r,t)\Psi^*(r',t)\rangle \tag{2.4}$$

Here the angular brackets denotes the averaging over the ensemble, with the help or relation (2.3) one can obtain the equation for the density operator

$$i\hbar\frac{\partial}{\partial t}\widehat{\rho} = \left[\widehat{V},\widehat{\rho}\right] \tag{2.5}$$

which is known as the Liouville equation. In the representation of the polarization moments for a single-level approximation the relation (2.5) takes the form

$$i\hbar\frac{\partial}{\partial t}\rho_q^k(j) = \sum_{k_1,q_1} W_{q,q_1}^{k,k_1}(j)\rho_{q_1}^{k_1}(j) \tag{2.6}$$

where the relation for matrix elements W_{q,q_1}^{k,k_1} may be given by the formula first obtained by Fano [11]

$$W_{q,q_1}^{k,k_1}(j) = 2\sum_{k_2,q_2}(-1)^{k+2j}\sqrt{(2k_1+1)(2k_2+1)}\left\{\begin{array}{ccc} j & j & k \\ k_1 & k_2 & j\end{array}\right\}V_{q_2}^{k_2}(j)\left[\begin{array}{ccc} k_1 & k_2 & k \\ q_1 & q_2 & q\end{array}\right] \tag{2.7}$$

Here $V_{q_2}^{k_2}(j)$ is the decomposition coefficient of the interaction operator over the irreducible tensor operators, and the sum is spread over those values of k_2 that cause the sum (k_1+k_2+k) to be odd.

It should be mentioned that the equation (2.5) is not suitable for consideration of the collisional problems, that are usually connected with the redistributions of populations between atomic levels. Therefore examining the collisional problems it

is more convenient to proceed from equation (2.3), the solution of which give an opportunity to construct the element of the density matrix by the formula

$$\rho_{j,m;j',m'} = \left\langle c_{j,m} c^*_{;j',m'} \right\rangle \tag{2.8}$$

For the solution of equation (2.3) the "following" system of reference $\widetilde{X}\widetilde{Y}\widetilde{Z}$ is always introduced. The axis $O\widetilde{Z}$ of this system is directed at the projectile and the $\widetilde{X}\widetilde{Z}$ plane coincides with XZ of collisional system XYZ. The OZ axis of the collisional system is directed antiparallel to the direction of relative velocity of colliding particles (see fig .) In the system $\widetilde{X}\widetilde{Y}\widetilde{Z}$ the eigenfunctions of the square of momentum and its projection $\psi_{j,m}$ will depend on t. The last leads to the appearance of additional term connected with the rotation of the system of reference:

$$\frac{d}{d\alpha}\widetilde{c}_{j,m} = -i\frac{(v/v_0)}{b}\sum_{j'}\langle j,m\,|V|\,j',m\rangle\,\widetilde{c}_{j',m} + \tag{2.9}$$

$$\frac{1}{2}\left[\sqrt{(j-m)(j+m+1)}\widetilde{c}_{j,m+1} - \sqrt{(j+m)(j-m+1)}\widetilde{c}_{j,m-1}\right]$$

Here α is the angle between OZ and $O\widetilde{Z}$ axis (see fig. 3) , v is the value of velocity of relative motion, v_0 is the atomic velocity, b is impact parameter and the index tilde denotes that this value is refers to the following system of reference.

The symmetry property of the system should be considered for averaging the product $c_{j,m}c^*_{;j',m'}$ over the atomic ensemble and the successive transformation to the basis of the polarization moments. Five problems will be considered below in this connection:

1. Polarization characteristics of emission excited by collisions in counterpropagating beams.
2. Polarization characteristics of the emission of atomic ensemble bombarded by the monoenergetic beam.
3. Spectropolaremetric effects in angular correlation experiments.
4. Spectropolarimetric manifestations of the higher order polarization moments
5. Collisional relaxation of polarization moments excited by a laser beam.

3 Polarization characteristics of emission excited by collisions with the counter-propagating beams.

3.1 Collisional transformation of the momentum ordering in the counter-propagating beams at low relative velocities.

If an isolated level is excited an effect of the collision is reduced to "mixing" of the populations between magnetic sublevels. The collisional evolution of polarization moments is described thereby by the equation

$$\frac{\partial}{\partial t}\rho^k_q(j) = n_0 v \sum_{k_1,q_1}\sigma^{k,k_1}_{q,q_1}(j)\rho^{k_1}_{q_1}(j), \tag{3.1}$$

where n_0 is the density of the projectiles and v is the relative velocity of motion.

Owing to the axial symmetry of collision process in counter-propagating beams, $\sigma^{k,k_1}_{q,q_1} = \delta_{q,q'}\sigma^{k,k_1}_q$, and equation (3.1) takes the form

$$\frac{\partial}{\partial t}\rho^k_q(j) = n_0 v \sum_{k_1} \sigma^{k,k_1}_q(j)\rho^{k_1}_q(j) \tag{3.2}$$

From last relation one can see, that the equation that describes the evolution of polarization moments splits into blocks and every block is associated with the particular value of $\dot{q}$. Collisions mix the rank of polarization moments within each block. This leads to an opportunity of transformation between the types of the angular momentum ordering. In particular, within the block with $q = 1$ where $\sigma^{1,2}_1 \neq 0$ the inclined alignment is transformed into an orientation [12, 13]. Following the symmetry property of polarization moments with respect to complex conjugation $\rho^{k*}_q = (-1)^q \rho^k_{-q}$, one has from the relation (3.2)

$$\left(\sigma^{k,k_1}_q\right)^* = \sigma^{k,k_1}_q \tag{3.3}$$

and now it is clear, that diagonal over upper indexes cross sections are real, $Im\left(\sigma^{k,k}_q\right) = 0$.

From the symmetry property of polarization moment over the operation of reflection in the collisional plane $\widehat{\sigma}_{xz}\rho^k_q = (-1)^{k-q}\rho^k_{-q}$ ( ) , follows the symmetry property for cross section

$$\sigma^{k,k_1}_q = (-1)^{k+k_1}\, \sigma^{k,k_1}_{-q} \tag{3.4}$$

It follows from the last relation that $\sigma^{k,k_1}_0 \neq 0$, if $k + k_1$ is even. Or in other words the block with $q = 0$ splits into two subblocks within which the collisions mix the polarization moments with rank of definite parity. In particular, the mutual relaxation of polarization moments ρ^0_0 and ρ^2_0 leads to an opportunity of transformation of the population and the longitudinal alignment [3].

In the end of this section let us consider an isolated level j to be populated by the external excitation source

$$n_j = \sqrt{2j+1}\rho^0_0 \tag{3.5}$$

Hence for the derivative of the right hand part of the last relation

$$\frac{d}{dt}n_j = n_0 v\sqrt{2j+1}\sum_{k_1}\sigma^{0.k_1}_0(j)\rho^{k_1}_0(j) = 0. \tag{3.6}$$

Then, according to the linear independence of polarization moments one has

$$\sigma^{0.k_1}_0(j) = 0 \tag{3.7}$$

and, if the cross section has the symmetry property $\sigma^{k,k'}_q = \sigma^{k',k}_q$, then

$$\sigma^{k,0}_0 = 0 \tag{3.8}$$

That means that for an isolated level the transformation of the population into other types of ordering is forbidden.

3.2 The collisional transformation the ordering in the counter-propagating beams at the high relative velocities.

In this case atoms are excited by the collisional impact at a certain state with the momentum j. The evolution of polarization moments in this case is described by the expression

$$\frac{\partial}{\partial t}\rho_q^k(j) = n_0 v \sigma_q^k(j) \tag{3.9}$$

where cross section $\sigma_q^k(j)$ characterize the efficiency of excitation. The fact that the indexes k and q on both sides of (3.9) are equal follows from the necessity of transformation of both sides of (3.9) by means of the same representation of the rotation group.

From the relation (3.9) one can see, that the character of momentum ordering stipulated by the excitation process of an atomic ensemble is entirely determined by its symmetry. In the particular case of isotropic excitation $\sigma_q^k(j) \sim \delta_{k,0}\delta_{q,0}$ only the ordering of population type will be induced. In the case of axially symmetry excitation $\sigma_q^k(j) \sim \delta_{q,0}\sigma_0^k(j)$ only zero-order components of the polarization moments will be induced in the system. It the last case the equation (3.9) takes the form

$$\frac{\partial}{\partial t}\rho_0^k(j) = n_0 v \sigma_0^k(j) \tag{3.10}$$

From the relation (3.9) it is clear that the cross section of excitation is symmetric with respect to the operation of complex conjugation

$$\left(\sigma_q^k\right)^* = (-1)^q \, \sigma_{-q}^k \tag{3.11}$$

and to the reflection in the collisional plane

$$\sigma_{xz}\sigma_q^k = (-1)^{k-q} \, \sigma_{-q}^k \tag{3.12}$$

It is clear from last two relations, that all cross sections σ_0^k are $real$ and $\sigma_0^k = -\sigma_0^k$, if k is odd. This means that excitation processes with axial and reflection symmetry can not create any orientation of the momenta.

4 Polarization characteristics of emission of atomic ensemble bombarded by the monoenergetic beam.

Let the ensemble of particles "a" is characterized by the distribution of velocities described by the function $f_a(\overrightarrow{v_a})$. It is bombarded by the monokinetics beam of particles "b". If OZ axis of the laboratory frame of reference XYZ is directed along the incident beam, the velocity of the particles of this beam is $\overrightarrow{v}_b = v_0 \overrightarrow{e}_z$. We suppose a low density of particles in the incident beam so that each atom of the sort "a" undergoes no more then one collision act during the lifetime. Collisions thus lead to the mixture of populations of the primary exited state (low velocities), or to the impact excitation of atoms of the sort "a" (high velocities).

4.1 The case of low velocities, that leads to mixing the populations of the sublevels of the primary excited state.

For description of this collisional process, one additional system of reference should be introduced. Let $O\widetilde{Z}$ axis of the system $\widetilde{X}\widetilde{Y}\widetilde{Z}$ be the axis of symmetry of the solid angle that contains the particles with the velocities which belong to the interval $[v, v+dv]$.(see fig. 4). In the system $\widetilde{X}\widetilde{Y}\widetilde{Z}$ the evolution of polarization moment $\widetilde{\rho}_q^k$ is described by the equation (3.2)

$$\frac{\partial}{\partial t}\widetilde{\rho}_q^k(j) = n_0 v \sum_{k_1} \widetilde{\sigma}_q^{k,k_1}(j,v)\widetilde{\rho}_q^{k_1}(j) \tag{4.1}$$

where indexes tilde denotes that this value is referred to the system $\widetilde{X}\widetilde{Y}\widetilde{Z}$.

Evolution of polarization moments ρ_q^k in the laboratory frame of reference can be obtained by summing inputs from all solid angles

$$\frac{\partial}{\partial t}\rho_q^k(j) = n_0 \sum_{k_1} \left\langle v\sigma_q^{k,k_1}(j)\right\rangle \rho_q^{k_1}(j) \tag{4.2}$$

Here the values $\left\langle v\sigma_q^{k,k_1}(j)\right\rangle$ are called as the rate constants of the process of the collisional relaxation for which one can write the expression

$$\left\langle v\sigma_q^{k,k_1}(j)\right\rangle = \sum_{q'.L} (-1)^{q+q'} \begin{bmatrix} k & k' & L \\ q & -q & 0 \end{bmatrix} \begin{bmatrix} k & k' & L \\ q' & -q' & 0 \end{bmatrix} \tag{4.3}$$

$$\int d\overrightarrow{v}\, v f(\overrightarrow{v})\widetilde{\sigma}_q^{k,k_1}(j,v)P_L(\cos\vartheta)$$

Here $\overrightarrow{v} = \overrightarrow{v}_a - \overrightarrow{v}_b$ is the vector of relative velocity, and $f(\overrightarrow{v})$ denotes the distribution function of relative velocities. Decomposing the distribution function of relative velocity vectors over Legendre polynomials

$$f(\overrightarrow{v}) = \sum_L f_L(v)P_L(\cos\vartheta) \tag{4.4}$$

and suggesting that the cross sections depend only on the absolute value of the velocity vector of relative motion, the expression (4.3) can be written as

$$\left\langle v\sigma_q^{k,k_1}(j)\right\rangle = \sum_{q'.L} (-1)^{q+q'} \begin{bmatrix} k & k' & L \\ q & -q & 0 \end{bmatrix} \begin{bmatrix} k & k' & L \\ q' & -q' & 0 \end{bmatrix} F_L(v_0) \tag{4.5}$$

where

$$F_L(v_0) = \int_0^\infty dv v^3 f_L(v)\widetilde{\sigma}_q^{k,k_1}(j,v) \tag{4.6}$$

It should be emphasized, that $F_L(v_0)$ depends on the multiple moment of the distribution function and the velocity of the incident beam.

From the properties of the Clebsch-Gordan[9] coefficients one can easily obtain that the rate constant of alignment creation

$$\left\langle v\sigma_0^{2,0}(j)\right\rangle = \int_0^\infty dv v^3 f_2(v)\widetilde{\sigma}_0^{2,0}(j,v) \tag{4.7}$$

where that is the transformation of the inclined alignment into the orientation

$$\left\langle v\sigma_1^{1,2}(j)\right\rangle = \int_0^\infty dv v^3 f_2(v)\widetilde{\sigma}_1^{1,2}(j,v) \tag{4.8}$$

which depends on the quadrupole moment of distribution function

4.2 Direct excitation of a state for high velocities.

Introducing a frame of reference analogous to the one of the previous section (see fig. 4) for evolution of the polarization moments in the frame $\widetilde{X}\widetilde{Y}\widetilde{Z}$ on can write (see(3.10)).

$$\frac{\partial}{\partial t}\widetilde{\rho}_q^k(j) = n_0 v\widetilde{\sigma}_q^k(j,v) \tag{4.9}$$

Summing up the inputs from all solid angles one can write an expression for the evolution of polarization moments in the laboratory frame of reference.

$$\frac{\partial}{\partial t}\rho_0^k(j) = n_0\left\langle v\sigma_0^k(j,v)\right\rangle \tag{4.10}$$

We suppose as above than the excitation cross section depends only on the relative velocity value. For excitation rate constant one can write

$$\left\langle v\sigma_0^k(j,v)\right\rangle = \int_0^\infty dv v^3 f_k(v)\widetilde{\sigma}_0^k(j,v) \tag{4.11}$$

where $f_k(v)$ is the multiple moment of distribution function (4.4).

From this relation it is clear that the rate constant for collisional creation of the alignment ordering by collisions is determined by the quadrupole moment of the distribution function.

It is clear from relations (4.5) and (4.11) that the ordering of the angular momenta created by collisions depends on the ordering of the relative velocity vectors. In other words the process of the transformation of the macroscopic ordering of distribution of relative velocities on the microscopic properties of atomic ensemble takes place in this case.

5 Spectropolaremetric effects in the angular correlation experiments.

The sketch of such an experiment is given in fig. 5, where the detector of emission of particles, scattered at a particular angle is illustrated. The specificity of such a problem is in absence of axial symmetry. The registration devise fixes the trajectory of the scattered particle. Hence, the collisional process is symmetric with respect to an operation of reflection in the plane of collision (ZX plane).

As was mentioned in section 1 this symmetry property together with the symmetry property expressed by the operation of the complex conjugation leads to polarization moments of the even rank and pure imaginarily of that's with odd rank. Since the emission of the dipole radiation involve the polarization moments of the rank non higher than two, one can say, that the characteristics of polarized emission in the angular correlation experiments are defined by five polarization moments: the

polarization moment of the zero rank ρ_0^0, three components of alignment tenser ρ_q^2 $(q = 0, 1, 2)$ and one component of orientation vector ρ_1^1.

This can be illustrated by the Stokes parameters for the emission scattered in the solid angle $d\Omega = \sin\vartheta d\vartheta d\varphi$:

$$IQ = -I_0 \left\{ \begin{array}{ccc} 1 & 1 & 2 \\ j & j & j_0 \end{array} \right\} \left[3\sin^2\vartheta \rho_0^2(j) + \sin 2\vartheta \cos\varphi \rho_1^2(j) + \left(\cos^2\vartheta + 1\right) \cos 2\varphi \rho_2^2(j) \right] \tag{5.1a}$$

$$IU = 2I_0 \left\{ \begin{array}{ccc} 1 & 1 & 2 \\ j & j & j_0 \end{array} \right\} \left[\sin 2\vartheta \cos\varphi \rho_1^2(j) + \cos\vartheta \sin 2\varphi \rho_2^2(j) \right] \tag{5.1b}$$

$$IV = -2I_0 \left\{ \begin{array}{ccc} 1 & 1 & 1 \\ j & j & j_0 \end{array} \right\} \sin\vartheta \sin\varphi Im \left(\rho_1^1(j)\right) \tag{5.1c}$$

This expression can be used for considering the inverse problem, Determination of the unknown polarization moments by the measuring of the Stokes parameters. For instance, for determination of polarization moment ρ_1^1 (see (5.1c) it is sufficient to measure the Stokes parameter V in the direction with $\varphi \neq 0$. The same way, for determining the alignment tensor components it is sufficient to measure the Stokes parameter Q at four angles.

In conclusion of this section it should be mentioned that for some particular transitions when the additional symmetry is present, the number of independent parameters can be reduced. For instance, for the transition $j = 1 \to j_0 = 0$ with three wave functions of excited state $\psi_{1,m}$ $(m = 0, \pm 1)$ one can construct two functions ψ_x and ψ_z - that are even with respect to reflection in ZX plane and one odd function ψ_y (see fig. 6). Then the function of the lower state with the zero momentum, which is even with respect to the operation of reflection in the plane ZX, will mix with even functions ψ_x and ψ_z. It is clear that $\psi_y = (\psi_{1,1} + \psi_{1,-1})/\sqrt{2} = 0$. This leads to the additional property of the symmetry of the density matrix $\rho_{1,1} = \rho_{-1.-1}$ and $\rho_{m,1} = -\rho_{m,-1}$; $\rho_{1,m} = -\rho_{-1,m}$ $(m = 0, \pm 1)$. This condition reduces the number of independent parameters to four.

6 Spectropolarimetric manifestations of the higher order polarization moments

Let us consider an isolated level with $j = 3/2$ that at $t = 0$ is excited by the pulses of non-polarized light incident along OY axis, whereas along OZ axis the system is affected by a beam of precipitating particles. We shall consider that the rate constants of the collisional creation and distruction of the ordering of momenta $\left\langle v\sigma_q^{k,k'} \right\rangle$ are symmetric with respect to the transposition of the upper indexes. As was mentioned above (see (3.8)), the rate constant $\left\langle v\sigma_0^{2,0} \right\rangle = 0$, and population and longitudinal alignment, represented by the polarization moments ρ_0^0 and ρ_0^2, undergo independent relaxation

$$\rho_0^0(3/2; t) = \rho_0^0(3/2; 0) \exp(-\gamma_0 t) \tag{5.2}$$

$$\rho_0^2(3/2;t) = \rho_0^2(3/2;0)\exp(-(\gamma_0 + n_0\left\langle v\sigma_0^{2,2}\right\rangle)t)$$

where γ_0 is the radiation damping constant.

The polarization moment ρ_2^2 will "mix" with that's ρ_2^3 such a mutual relaxation is described by the system of equations

$$\frac{d}{dt}\rho_2^2(3/2;t) = -\left(\gamma_0 + n_0\left\langle v\sigma_2^{2,2}\right\rangle\right)\rho_2^2(3/2;t) + n_0\left\langle v\sigma_2^{2,3}\right\rangle\rho_2^3(3/2;t) \tag{5.3}$$

$$\frac{d}{dt}\rho_2^3(3/2;t) = n_0\left\langle v\sigma_2^{2,3}\right\rangle\rho_2^2(3/2;t) - \left(\gamma_0 + n_0\left\langle v\sigma_2^{3,3}\right\rangle\right)\rho_2^3(3/2;t)$$

The character of solutions of this system is depended on the roots of the characteristic equation, which can be complex because the rate constant $\left\langle v\sigma_2^{2,2}\right\rangle$ is purely imaginary. The presence of the complex roots will lead to oscillations in the solution of this system. This effect is illustrated in fig.7, where the temporal dependence of the signal of longitudinal alignment for a certain velocities of the incident beam is represented (the time is measured in the atomic units and λ is the ratio of the velocity of the atomic beam to the thermal one). From this plot one can see, that at $\lambda = 2$ ($v_0 = 2v_{termal}$) the alignment signal is represented by oscillations modulated by the damping exponent. Similar polarization beats can be expected in the orientation signal to be determined by the mutual relaxation of the polarization moments ρ_1^1 and ρ_1^2.

7 Collisional relaxation of polarization moments excited by a laser beam.

Let us consider the system that consists of a mixture of atoms of sorts "a" and "b" with masses m_a and m_b respectively. The distribution of velocities of the atoms of both sorts will be suggested as Maxwellian. If such an ensemble is affected by a monochomatic laser beam of the frequency ν only atoms with fixed value of velocity's projection on the direction of the laser beam will be in resonance. The z projection of velocity of these atoms v_0 is connected with ν_0 - the value of frequency of the center of Doppler's contour, by the following expression:

$$v_0 = \frac{c}{\nu}(\nu - \nu_0) \tag{7.1}$$

Hence, the radiation ofthe laser corresponding to the center of Doppler's contour of atoms of sort "a" creates the anisotropy in the distribution of the relative velocities and thereby generates an alignment of the ensemble of atoms of sort "a". The velocity distribution function of atoms of sort "a" may be written as

$$f_a(\overrightarrow{v}_a) = \frac{m_a}{2\pi kT}\exp\left[-\frac{m_a}{2kt}(v_{ax}^2 + v_{by}^2)\right]\delta(v_{az} - v_0) \tag{7.2}$$

The distribution function of velocities of relative motion $\overrightarrow{v} = \overrightarrow{v}_a - \overrightarrow{v}_b$ takes the form

$$f(\overrightarrow{v}) = \left(\frac{\xi}{v_0}\right)^3 \sqrt{\frac{\eta^3}{\pi(1-\eta)}} \exp\left[-\frac{\xi^2\eta}{v_0^2}\left(v_x^2 + v_y^2 + \frac{(v_z - v_0)^2}{1-\eta}\right)\right] \tag{7.3}$$

where $\xi = v_0\sqrt{m_a/2kT}$ and $\eta = m_b/(m_a + m_b)$.

The surface of the equal probability in the velocity's space is given by the following equation

$$v_x^2 + v_y^2 + \frac{(v_z - v_0)^2}{1-\eta} = const \tag{7.4}$$

It is represented by the ellipsoids shifted along the OZ axis by the value v_0.If $\eta \to 0$ ($m_b << m_a$), these ellipsoids transform into spheres. The physical meaning of parameter η is that it characterizes the dispersion of the relative velocities $D(v_x) = D(v_y) = kT/m_a\eta$ and $D(v_z)) = (1-\eta)/m_a\eta$. In the case $\eta << 1$ the dispersions over all axes approximately equals $D(v_x) \sim D(v_y) \sim D(v_z)) \sim 1/m_a\eta$, and the distribution of relative velocities is close to the Maxwellian one. In the opposite case of $\eta \to 1$ ($m_a << m_b$), the surfaces of equal probabilities are transformed into discs: $D(v_x) \sim D(v_y) \sim const$ and $D(v_z)) \sim 1 - \eta$. This is illustrated in fig. 8, where the shape of the surface of equal probability is represented for the values of parameter $\eta = 0.1$, 0.5, and 0.9.

With the use of formula (4.6) one can obtain the multipole moments of distribution function and calculate the rate constants of relaxation process. This formulas are quite similar to represented above:

$$\left\langle v\sigma_q^{k,k_1}(j)\right\rangle = \sum_{q'.L}(-1)^{q+q'}\begin{bmatrix} k & k' & L \\ q & -q & 0 \end{bmatrix}\begin{bmatrix} k & k' & L \\ q' & -q' & 0 \end{bmatrix} S_L(v_0) \tag{7.5}$$

where

$$S_L(v_0) = \int_0^\infty dv v^3 f_L(v)\widetilde{\sigma}_q^{k,k_1}(j,v) \tag{7.6}$$

with $f_L(v)$ being the multipole moment of the distribution function. From this relations one can see that the rate constants of processes of transformation longitudinal alignment from the population and the orientation from the inclined alignment is defined by the quadrupole moment of the distribution function.

8 Evolution of polarization moments in the presence of a magnetic field.

The evolution of the density operator is described by the Liouville equation,

$$\frac{d}{dt}\widehat{\rho} = -\widehat{\Gamma}_0\widehat{\rho} - \frac{i}{\hbar}\left[\widehat{\rho}, \widehat{H_0}\right] + \frac{i}{\hbar}\left[\widehat{\rho}, \widehat{V}_f\right] + \widehat{N} \tag{8.1}$$

Here first term on the right hand side describes the radiation damping process, $\widehat{H_0}$ is the Hamilton's operator of the free atom, $\widehat{V}_f$ operator describes the interaction with magnetic field and the last term describes the excitation process.

If the Zeeman splitting is less than the width of the fine structure (in the weak field case) the value of the total momentum conserves and the operator $\widehat{V}_f$ takes the form [14]

$$\widehat{V}_f = \mu_0 g_J \left(\overrightarrow{J}, \overrightarrow{H}\right) \tag{8.2}$$

where μ_0 is the Bour's magneton and g_j is the Lande's factor. Equation (8.1) in the $k-q$ representation may be written as

$$\frac{d}{dt}\rho_q^k(j;t) = (-1 - i\omega_z q)\,\rho_q^k(j;t) + \frac{1}{2}\left[\omega^* \sqrt{(k-q)\,(k+q+1)}\rho_{q+1}^k(j;t) - \right.$$

$$\left. + \omega \sqrt{(k+q)\,(k-q+1)}\rho_{q-1}^k(j;t) + N_q^k\right] \tag{8.3}$$

where $\omega = \omega_y + i\omega_x$ and $\omega_i = \mu_0 g_j H_i \tau_o/\hbar$ $(i = x, y, z)$ is a dimensionless Larmour frequency dependent on lifetime of an excited state τ_0. As follows from the last equation, the uniform magnetic field mixes the components of polarization moments of the same rank. Therefore the system of equations (8.3) splits into blocks, each of which describes the evolution of components of the polarization moment for a certain rank. Hence, for the description of the evolution of alignment tenser it is sufficient to consider the block with $k = 2$. In other words, the uniform magnetic field can not create a new type of ordering. Its role reduces to the destruction of the ordering, that had been created by any external mechanism.

Let us consider an atomic system that is excited by an external process, which has an axial symmetry with respect to the OZ axis, and a weak magnetic field is applied to the system in the direction of OY axis.

In this case, the excitation process $N_q^2 \sim \delta_{q,0}$, which is the stationary solution of equation (8.3) takes the form

$$\rho_0^0 = N_0^0 \tag{8.4}$$

$$\rho_2^2 = N_0^2 \sqrt{\frac{3}{2}} \frac{\omega_L^2}{(1+4\omega_L^2)}; \qquad \rho_1^2 = -N_0^2 \sqrt{\frac{3}{2}} \frac{\omega_L}{(1+4\omega_L^2)}; \qquad \rho_0^2 = N_0^2 \frac{1+\omega_L^2}{(1+4\omega_L^2)}; \tag{8.5}$$

These expressions can be used to evaluate the signals of longitudinal and inclined alignment observed from the direction of the OX axis:

$$\Delta I_x = I_z - I_y = I_0 N_0^2 K_2 \sqrt{\frac{3}{2}} \frac{1+2\omega_L^2}{1+4\omega_L^2} \tag{8.6a}$$

$$\Delta I_{yz} = I_{zy+} - I_{zy-} = \sqrt{6} I_0 N_0^2 K_2 \frac{\omega_L}{(1+4\omega_L^2)} \tag{8.5b}$$

From these formulas, one can see that the signal of longitudinal alignment has the Lorenzian form whereas that of the inclined alignment has the dispersive form (see fig 9). This effect in known as the Hanle effect [15] .

In the case of a strong magnetic field when the Zeemans splitting is on the order of the width of the fine structure, only the projection of the spin and orbital moments on the direction of magnetic field will be conserved (here we will considered that

this direction coincides with the OY axis). For the operator the V_f from (8.1) one can write [14]

$$\widehat{V} = \mu_0 H(L_y + 2S_y) \tag{8.7}$$

As was mentioned above, the total electronic quantum number is not conserved in presence of the strong magnetic field. Therefore eigenfunctions of the operator (8.7) take the form of linear combinations of eigenfunctions of the squares of orbital momenta, spin, and their projections $\psi_{l,m}$, χ_σ:

$$\Psi_M(\overrightarrow{r}) = \sum_{m,\sigma} c^M_{m,\sigma} \psi_{l,m}(\overrightarrow{r}) \chi_\sigma \quad (M = 1, 2, 3, ..., 2(2l+1)) \tag{8.8}$$

Within the basis of functions (8.8) the density matrix takes the form

$$\rho_{M,M'} = \langle M | \widehat{\rho} | M' \rangle = \sum_{m,\sigma} \left(c^M_{m,\sigma} \right)^* c^{M'}_{m',\sigma} \rho_{m,m'} \tag{8.9}$$

where $\rho_{m,m'}$ is the matrix element of an "orbital" density matrix that is independent of the spin variables.

The evolution of density matrix is described by

$$\frac{d}{dt}\rho_{M,M'} = -(\gamma_0 + i\omega_{M',M})\rho_{M,M'} + N_{M,M'} \tag{8.10}$$

where γ_0 is a natural damping constant, $\omega_{M',M} = (E_{M'} - E_M)/\hbar$ is a frequency separation between magnetic sublevels, and $N_{M,M'}$ is an excitation matrix. In the case of axial symmetric excitation process ($N^k_q(l) \sim \delta_{q,0}\widetilde{N}^k_q(l)$) The latter may be written as

$$N_{M,M'} = \sum_k T^k_0(l; M, M') \widetilde{N}^k_0(l). \tag{8.11}$$

where

$$T^k_q(l; M, M') = \sum_{m,m',\sigma} \left(c^M_{m,\sigma} \right)^* c^{M'}_{m',\sigma} (-1)^{l-m'} \begin{bmatrix} l & l & k \\ m & -m' & q \end{bmatrix}, \tag{8.12}$$

Under the broad line detection of approximation, the intensity of emission, polarized along the direction $\overrightarrow{e}$ of atomic transitions between levels with orbital momentum l and l_0 may be expressed as

$$I_e = \sqrt{(2l+1)(2l_0+1)} \sum_{K,Q} (-1)^K \Phi^K_Q(\overrightarrow{e}) \begin{Bmatrix} 1 & 1 & k \\ l & l & l_0 \end{Bmatrix} R^K_Q(l) \tag{8.13}$$

where $\Phi^K_Q(\overrightarrow{e})$ is a polarization tensor that depends on the a_q coefficients of expansion of the unit vector $\overrightarrow{e}$ in a circular orthogonal basis [9]:

$$\Phi^K_Q(\overrightarrow{e}) = \sum_{q,q'} (-1)^{1-q'} a_q a^*_{q'} \begin{bmatrix} 1 & 1 & K \\ q & -q' & Q \end{bmatrix} \tag{8.14}$$

The term

$$R_Q^K(l) = \sum_{M,M'} T_Q^K(l; M, M')\, \rho_{M,M'} \tag{8.15}$$

may be considered as the relation of the polarization moments in the presence of the strong magnetic field. The comparison of relations (8.13) and (1.23) illustrates that the relation for the difference of intensities and the Stokes parameters in the strong magnetic field differ from what is described by relation (1,23) by the substitution $\rho_q^k \to R_Q^K$. Fig. 9, illustrates the dependence of the polarization characteristics of H_α emission induced by a proton beam on the value of the magnetic field strength.

References

[1] Blum K. Density Matrix Theory and Applications. Plenum Press, New York and London, 1981.

[2] Kazantsev S A and Henoux J-C Polarization Spectroscopy ofIonizsd Gases, Kluver Academic Publishers. Dordrecht, London, Boston, 1995

[3] Kazantsev S A, Petrashen A G and Firstova N M Impact Spectropolarimetric Sensing. Plenium Publishing Corporation New York, London, 1999.

[4] Kazantsev S A, Petrashen A G, Rebane V N, Rebane T K
JETP,1994, v.106, n3(9), p. 698-714.

[5] Kazantsev S A , Firstova N M , Petrashen A G , Henoux J-K
Optica and Spectroscopy 1996, v.80, n. 4, p. 595-603.

[6] Kazantsev S A, Petrashen A G
Optica and Spectroscopy 2000, v.88, n4, p. 556-559.

[7] Kazantsev S A, Petrashen A G , Pudovkin M I
Aeronom. and Geomagn. 2001, v.41, n. 1, p. 50-56.

[8] Lomont J. S. Applications of the finite groups New York 1959.

[9] Jucys A, Bandzaitis A The angular momentum theory in the quantum mechanics, Vilnius, 1965.

[10] Fano U , Macek Ch.
Rev. Mod. Phys.,1973, v.45, p.553

[11] Fano U
Phys. Rev., 1964, v. 133, p. B828

[12] Rebane V N
Optica and Spectroscopy 1968, v.24, n .3, p.309.

[13] Chamoun E , Lombardi M , Carre M, Gaillard M
J. de Phys v.38, n. 6, p. 581

[14] L.D.Landau E.M.Livshitz Theoretical Physics. Quantum mechanics, v. III Moscwa 1963

[15] Hanle W.
Z. Phis, Bd. 30, S. 93-97,1924.

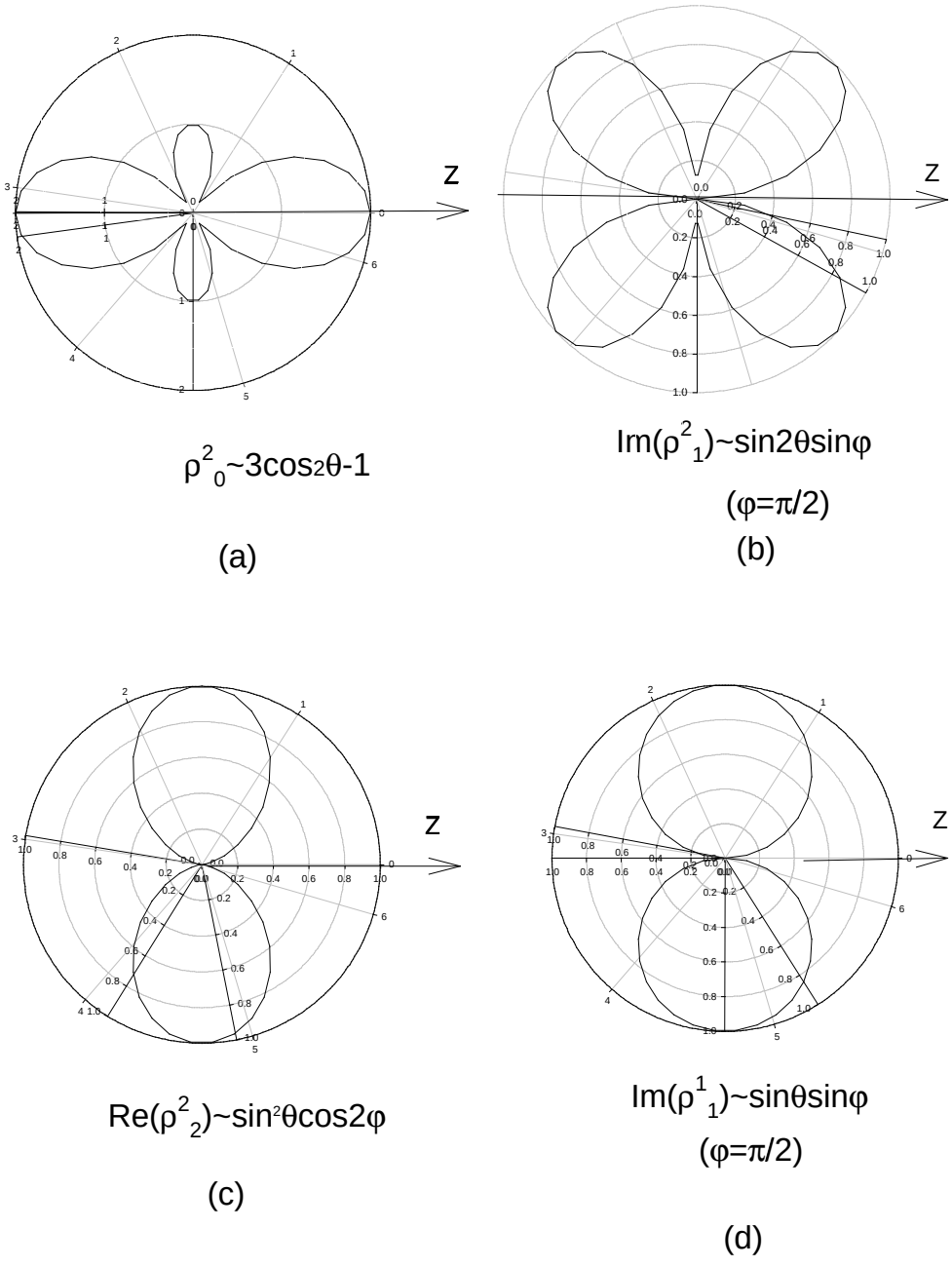

$\rho^2_0 \sim 3\cos^2\theta - 1$

(a)

$\mathrm{Im}(\rho^2_1) \sim \sin 2\theta \sin\varphi$

$(\varphi = \pi/2)$

(b)

$\mathrm{Re}(\rho^2_2) \sim \sin^2\theta \cos 2\varphi$

(c)

$\mathrm{Im}(\rho^1_1) \sim \sin\theta \sin\varphi$

$(\varphi = \pi/2)$

(d)

Figure 1: Schematic image of components of the polarization moments.

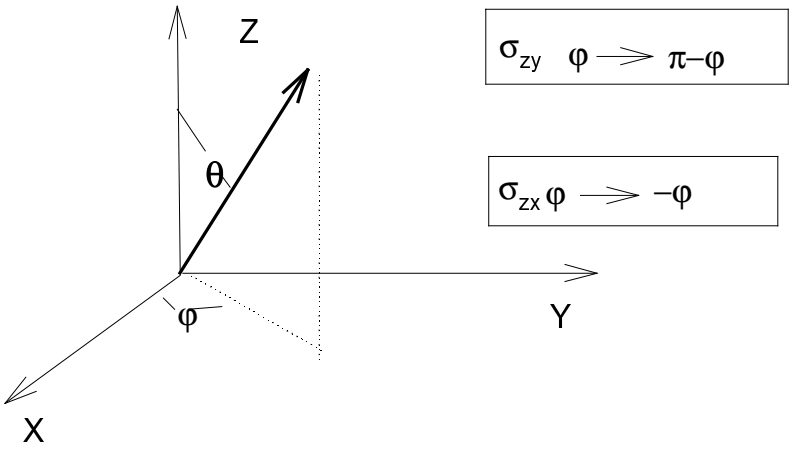

Figure 2: Variation of the azimuthal angle under the operation of reflection.

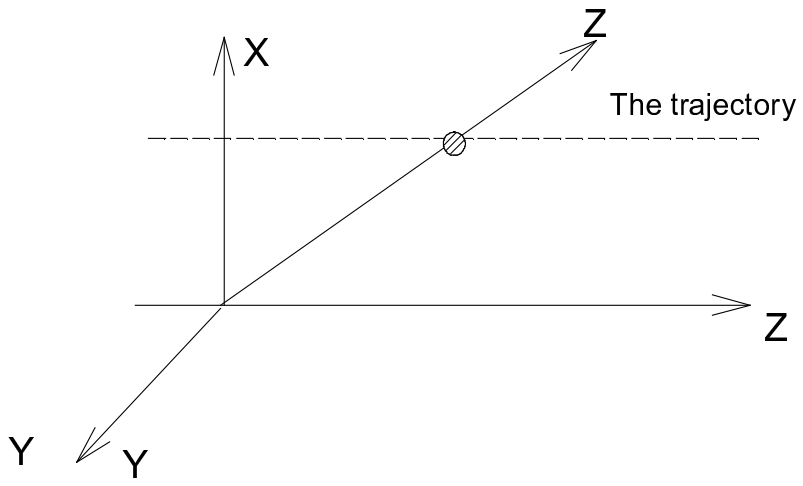

Figure 3: Systems of reference that introduces for the description of collisional processes.

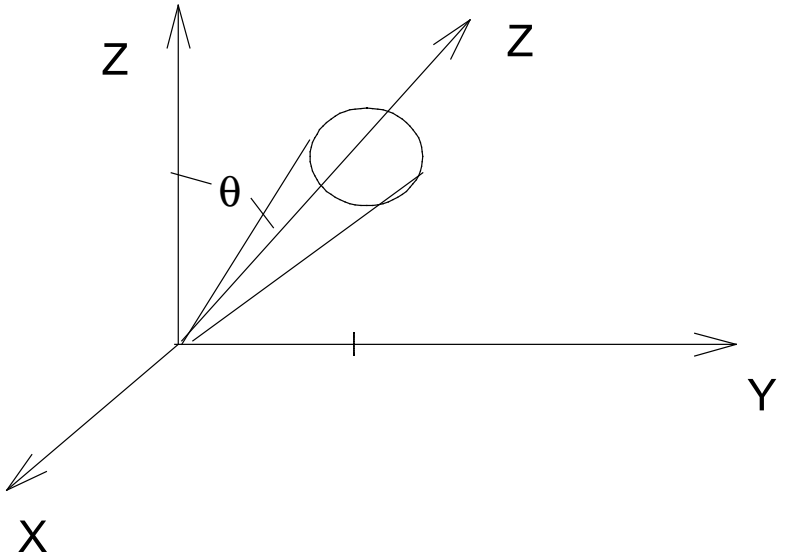

Figure 4: Frames of reference used for averaging over the velocities of excited atoms.

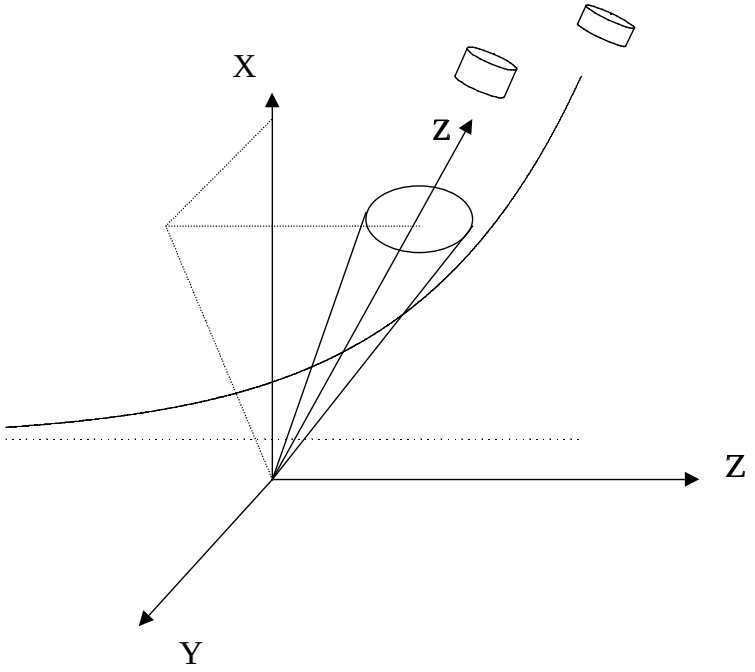

Figure 5: Schematic of an angular correlation experiment.

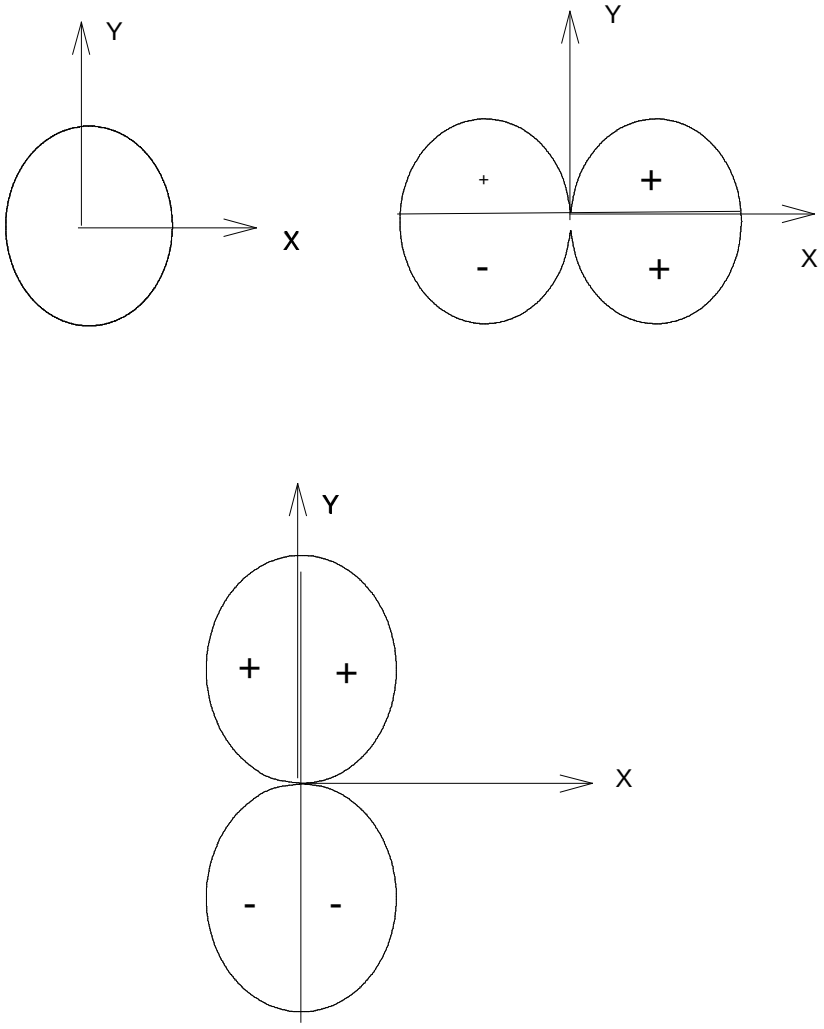

Figure 6: Schematic representation of the P-state function, that has definite properties with respect to the operation of reflection in the collision plane.

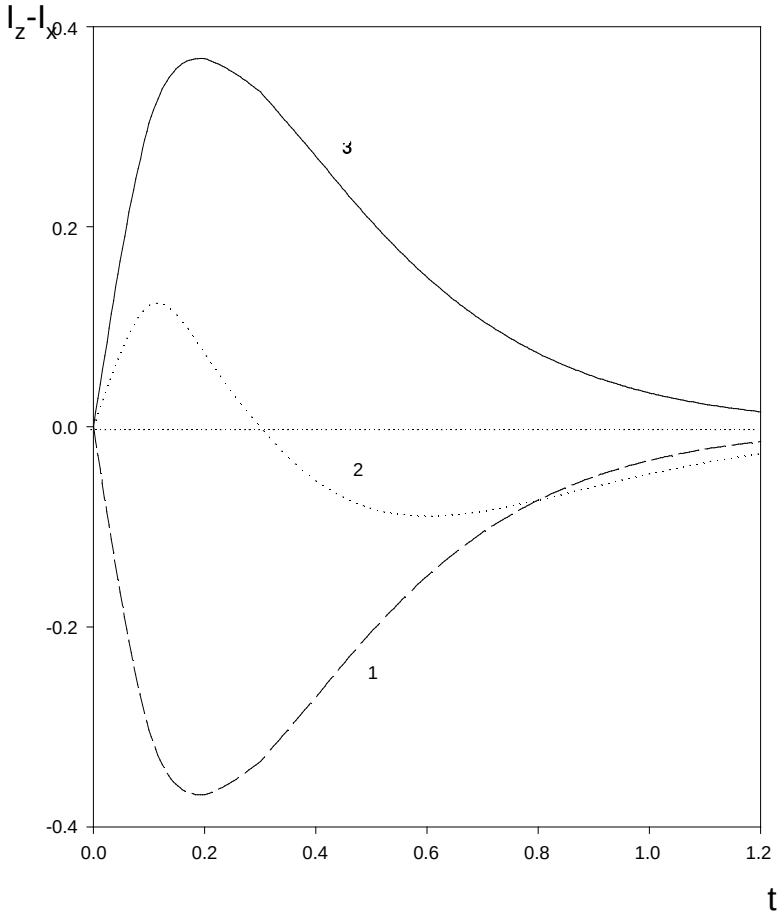

Figure 7: Polarization beats in the signal of longitudinal alignment of the $n^2P_{3/2}$ state of the ensemble of Cs atoms. Solid line -$n = 6$; dashed line - $n = 7$.

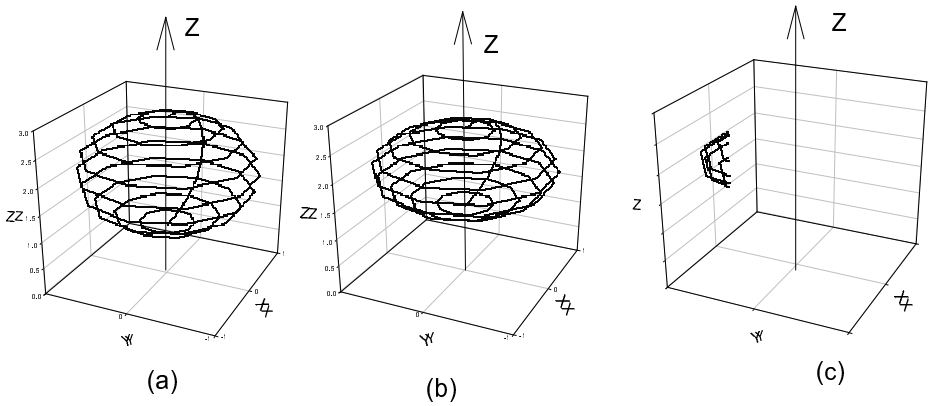

Fig. 8.

Figure 8: Form of the surfaces of constant probabilities for different values of parameter $\eta = 0.1, 0.5$ and 0.9

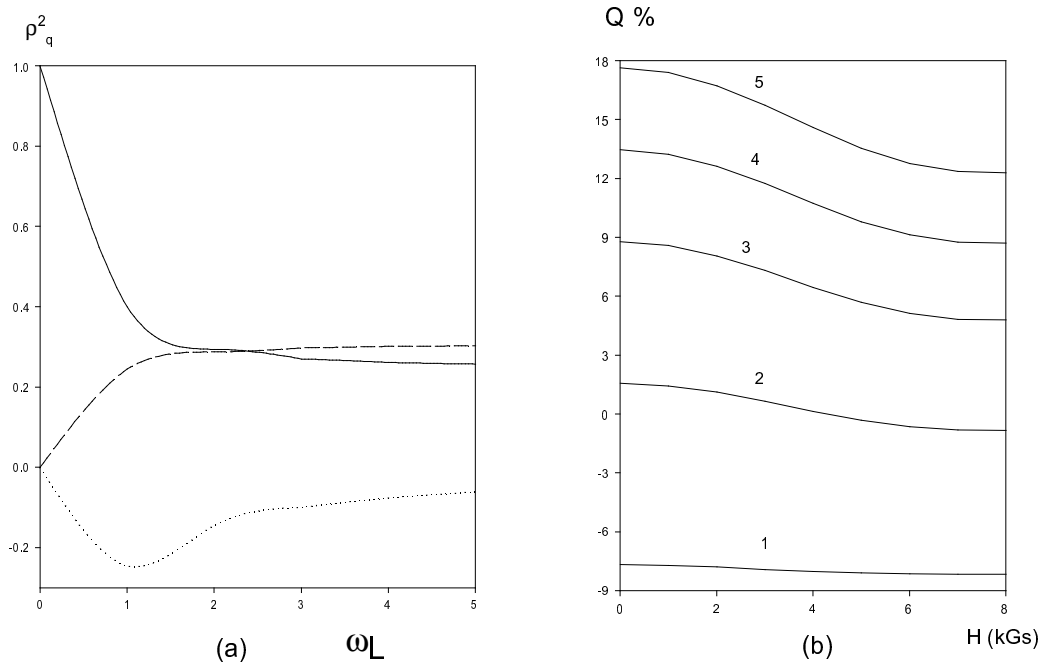

Figure 9: a: The illustration of the Hanle effect. Curves (1-3) show the dependencies of inclined, transverse, and longitudinal alignments on the value of the Larmour frequency; b: The dependence of the Stokes parameter Q for the transition $2^2P_{3/2} - 3^2D_{3/2}$ on the value of the magnetic field for some values of energy of an exciting proton beam: (1)- $E = 55.8\ keV$; (2)- $E = 155\ keV$; (3)- $E = 303.8\ keV$; (4)- $E = 502.8\ keV$; (5)- $E = 892.6\ keV$.

QUANTITATIVE SPECTROPOLARIMETRIC SENSING OF IONIZED MEDIA.

S.A. Kazantsev *, A.G.Petrashen **, Pudovkin M.I. ***

* Observatoire de Paris, DASOP, F-92195,Meudon Cedex, France

** S-Petersburg Institute of the Fine Mechanics and Optics,199101, S-Petersburg, Russia.

*** Institute of Physics of S-Petersburg State University, S-Petersburg, Russia.

CONTENTS

1. Determination of ion drift velocity in a gas discharge plasma.

2. Determination of directive proton velocities in the solar chromosphere.

3. Polarization of optical flash emission in the luminescence of the night sky.

4. Polarization of HeII ions, created under charge exchange of $\alpha-$ particles on hydrogen atoms.

5. Spectropolarimetric diagnostics of the strength of a magnetic field.

5.1 Measurement of the longitudinal alignment signal under different angles.

5.2 Diagnostics of the magnetic field strength by utilizing the ratio of the Stokes parameters Q and U.

5.3 Diagnostics of a weak magnetic field strength by exploiting the parameters of the relaxation process.

5.4 Diagnostics of the strength of a magnetic field by sensing the polarization characteristics under the pulse excitation.

6. Measurement of the magnetic field from remote objects.

6.1 Spectropolarimetric sensing of the geomagnetic field.

6.2 Influence of *field*-aligned at the region of polar cusps on the polarization characteristics of auroral emission.

6.3 Application of polarization spectroscopy to the diagnostics of aerosol clouds.

1 Introduction

Application of spectropolarimetric methods for sensing ionized media is based on the fact that the model under consideration should be adequately created and the evolution of polarization moments in the frame of this model should be specified thereby. Characteristics of polarized emission are calculated at the second stage. Theoretical data are compared with the experimental or observational spectropolarimetric characteristics. Criterion for the quality of this model may be the coincidence of the calculated and the measured polarization characteristics. The methods of the polarization spectroscopy were applied to investigation of the gas discharge plasma, non-thermal process in the Solar chromosphere, studies in the Z-pinch and tokamak plasmas and for investigation of optical process in the upper atmosphere of the Earth. Some structural physical phenomena in the ionized media and the methods of the practical polarization spectroscopy will be considered here.

2 Determination of the ion drift velocity in a gas discharge plasma.

A sketch of this experiment that was performed for the investigation of polarized emission [1] is illustrated in fig 1. We used a hollow cathode diameter approximately 1SM. The cathode contained an argon plasma at a pressure with a few tenths of a torr. The intensities, I_z and I_y, for the transitions between states $4p^2D_{3/2}-4d^2P_j$ and $4s^2P_{1/2}-4p^2P_j$ $(j=1/2,3/2)$ were measured at different parts of the discharge along the radius. From this the ratios

$$A_d=\frac{12.5\,(I_y-I_z)_{1/2}}{5\,(I_y+0.5I_z)_{3/2}-(I_y+0.5I_z)_{1/2}}\quad transition\quad 4p^2D_{3/2}-4d^2P_j \qquad (2.1a)$$

$$A_p=\frac{(I_y-I_z)_{3/2}}{5\,(I_y+0.5I_z)_{3/2}-2\,(I_y+0.5I_z)_{1/2}}\quad transition\quad 4s^2P_{1/2}-4p^2P_j \qquad (2.1b)$$

were calculated. The main results of this experiment are:

1. Lines with the value of the sum of intensities I_y+I_z is maximized near the center of cathode.

2. The value of alignment signal, I_y-I_z, of the lines increases as the distance from the cathode's center increases. This value is maximized near the edge of the region with negative glow (see fig 1).

3. The value of the alignment signal of atomic lines is very small upon comparing them to the lines of ions.

The fact that the value of I_y+I_z has a maximum near the center of the cathode can be explained by the assumption that the excitation of the ion and atom lines are reshaped by the fast electrons, the velocity of which increases from the wall of the cathode to the center. Because the movement of the is directed in the opposite side, from the center to it's edge, the assumption is that the creation of the alignment is due to the ion drifting among the ensemble of the neutral argon atoms helps to

explain the presence of a maximum in the alignment signal near the edge of the cathode.

Interaction of the ions with the neutral atoms leads to the mixing of populations of doublet ^2P_j magnetic sublevels $j = 1/2$ and $j = 3/2$ ion states. In other words, collisional interaction with neutral atoms provides a means of mixing the polarization moments of the ensemble $\rho_0^0(1/2)$, $\rho_0^0(3/2)$ and $\rho_0^2(3/2)$ or connected with them the values $n_{1/2}$ and $n_{2/2}$-, populations of $j = 1/2$ and $j = 3/2$ states and $a_{3/2} = 2\rho_0^2(3/2)$, - the alignment of the state $j = 3/2$ .The mutual evolution of these values are represented by the system of equations

$$\begin{aligned}
\frac{d}{dt}n_{1/2} &= n_0\left[-\left(\gamma_0 + \langle v\sigma_p\rangle\right)n_{1/2} + \frac{\langle v\sigma_p\rangle}{2}n_{3/2} + \frac{\langle v\sigma_a\rangle}{2}a_{3/2}\right] + N_{1/2} \\
\frac{d}{dt}n_{3/2} &= n_0\left[\langle v\sigma_p\rangle\, n_{1/2} - \left(\gamma_0 + \frac{\langle v\sigma_p\rangle}{2}\right)n_{3/2} - \frac{\langle v\sigma_a\rangle}{2}a_{3/2}\right] + N_{3/2} \qquad (2.2) \\
\frac{d}{dt}a_{3/2} &= n_0\left[\langle v\sigma_a\rangle\, n_{1/2} - \frac{\langle v\sigma_a\rangle}{2}n_{3/2} - \left(\gamma_0 + \frac{\langle v\sigma_d\rangle}{2}\right)a_{3/2}\right]
\end{aligned}$$

where n_0 is the density of the argon atoms and $\langle v\sigma_p\rangle = -\sqrt{2}\left\langle v\sigma_0^{0,0}(1/2,3/2)\right\rangle$, $\langle v\sigma_a\rangle = -\sqrt{2}\left\langle v\sigma_0^{2,0}(3/2,1/2)\right\rangle$, $\langle v\sigma_d\rangle = \left\langle v\sigma_0^{2,2}(3/2,3/2)\right\rangle$.

Under stationary conditions one can obtain from the third equation

$$\frac{a_{3/2}}{n_{1/2} - \frac{n_{3/2}}{2}} = \frac{\langle v\sigma_a\rangle\, p}{\langle v\sigma_d\rangle\, p + kT\gamma_0} \qquad (2.3)$$

Where $p = n_0/kT$ is the pressure of ions.

With the help of the relations for the intensities of dipole emission and the numerical values of $6j-$ coefficients, one can find that

$$\frac{\langle v\sigma_a\rangle\, p}{\langle v\sigma_d\rangle\, p + kT\gamma_0} = A_{p,d} \qquad (2.4)$$

Where A_p and A_d are defined by formulas (1a) and (1b) for the transitions of $4d^2P_j - 4p^2D_{3/2}$ and $4p^2P_j - 4s^2P_{1/2}$ respectively.

The rate constants of the collisional ordering and destruction of the ordering of the angular moments depend on the ratio $\lambda = v_0/v_T$ where v_0 is the velocity of ion's drift and v_T is associated with their thermal movement. Therefore, for a certain pressure range the drift velocity can be obtained by adjusting the parameter λ in left hand side of (2.4) in order to create an equality with the left hand side to the right hand side which is known from the measurements. Results of the determination of the drift velocity utilizing the polarization characteristics of both at the transitions $4p^2D_{3/2} - 4d^2P_{3/2}$ and $4s^2P_{1/2} - 4p^2P_j$ are represented in table 1.

Table 1. The anisotropy parameters and drift velocities in the gas discharge Ar plasma at $T = 330K$.

The pressure in torr	Parameter of anisotropy	The values of the drift velocities in 10^5 cm/sek	
		$4s^2P_{1/2} - 4p^2P_{3/2}$	$4p^2D_{3/2} - 4d^2P_{3/2}$
0.02	4.34	2.35	2.22
0.04	4.07	2.30	2.09
0.06	3.83	2.27	1.97
0.08	3.62	2.09	1.83
0.10	3.42	1.89	1.79
0.12	3.25	1.68	1.70

From this table one can see that the values of drift velocities obtained from utilizing the data for different transitions are close to each other.

3 Determination of directive proton velocities in the solar chromosphere.

About ten years ago it was proposed that the thermal heating of the Solar chromosphere is provided by proton beams of energy around 200 kev [2]. In fig. 2 the magnetic loop of a Solar flare is illustrated and the proton tracks that are supposed to penetrate downwards along the magnetic field lines are drawn. A relatively thin (approx. 10 km !) dashed region of this sketch represents the upper layer of the chromosphere that is responsible for formation of hydrogen emission lines. Polarization of the H_α line is measured by the ground based observer. Therefore the problem of comparing the observed and calculated data for H_α polarization can be divided into the following steps:

1. Solution to the collisional problem and the determination of the polarization moments to be created by these collisions.

2. Comparison of the theoretical and the observational data with respect to position of the flare at the Solar surface [3, 4].

Evolution of polarization moments under the impact interaction are characterized by the cross sections $\tilde{\sigma}_0^k$

$$\frac{d}{dt}\tilde{\rho}_0^k = n_o v \tilde{\sigma}_0^k \tag{3.1}$$

The numerical values of $\tilde{\sigma}_0^k$ are the cross sections for the impact excitation of an excited hydrogen atom with $n = 3$. This cross section was calculated in the frame of approximation of impact parameter method in the base of 14 orbital wave functions $\psi_{n,l,m}(r)$ $(n = 1,2,3; \quad l = 0,1,...l-1; \quad m = 0,1,2,...l)$. The result of these calculations is illustrated in fig. 3, where the dependence of polarization characteristics of H_α emission on the energy of the exciting proton beam is ploted. The experimental curve and the theoretical curve are calculated in the frame of the base at ten functions are represented here as well.

The second principle question of the quantitative remote spectropolarimetric sensing is the comparison of the calculated polarization characteristics with the ones measured by an observer located at the Earth surface. In fig. 3, the $O\tilde{Z}$ axis in the frame of reference $\tilde{X}\tilde{Y}\tilde{Z}$ is connected with the exciting proton beam that

propagates in the direction perpendicular to the Solar surface. The values of the Stokes parameters calculated above are related to this system. The measurments, performed by the Earth observer, refer to the system XYZ, the plane ZY of which belongs to the plane of the Solar disk, the OZ axis is the projection of the $O\tilde{Z}$ axis on this plane and the OX axis is directed at the observer. The polarization moments in these two systems are connected with Wigner D-matrixes that depends on the mutual orientation of these systems. If Q and U denote the values of the Stokes parameters in the frame of reference XYZ, one can obtain the relations between the values of the Stokes parameter $\tilde{Q}$ with Q and U:

$$Q = \frac{\tilde{Q}\cos^2\beta\cos 2\alpha}{1-\tilde{Q}\sin^2\beta}$$
$$U = \frac{\tilde{Q}\cos^2\beta\sin 2\alpha}{1-\tilde{Q}\sin^2\beta} \qquad (3.2)$$

Where β is the angle between the OZ and the $O\tilde{Z}$ axis, and α is the angle between the spectrometer and the OZ axis.

With spectropolarimetric sensing we utilize the dependance of the $\tilde{Q}$ parameter on the velocity of a proton beam. For the fixed values of angles α and β, which define the position of the flare at the solar disc, one can find the value of the velocity of proton beam that provides the coincidence of the calculated and observed values of the Stokes parameters.

The results of just such a procedure are represented in the table . Below it should be mentioned that the dependence of the parameter $\tilde{Q}$ on the velocity of the exciting proton beam is calculated in this table with the basis of ten functions: $\psi_{n,l,m}(r)$ $(n = 1, 3)$.

Table 2. The results of diadnosics of the velicities of proton beams.

Angle β	60^o	63^o	68.5^o	49.2^o	21.5^o	61.9^o
Observed values of polarization $(in\%)$	(4.5 $\pm$1.2)	5.5 $\pm$1.7)	(3.5 $\pm$0.9)	(2.3 $\pm$0.9)	6.5 $\pm$2.0)	(3.6 $\pm$0.6)
The intervals of the value of proton beam (in kev)	(280 $\pm$70)	> 280	> 300	(50 $\pm$30)	50 $\pm$30)	(220 $\pm$80)

4 Polarization of optical flash emission in the luminescence of the night sky.

The optical flashes are known as the short $(10^{-3}s < t < 1s)$ light emissions of the night sky. The nature of this phenomenon is not completely known as of now. These flashes were observed primarly in the higher latitudes and further in the middle ones [6]-[7]. A rather large value of the oxygen $^3P_2 - ^1D_2$ line polarization was registered.

Excitation of an oxygen atom in the $^1D_2$ state by an electron beam is the basic collisional process and the value of polarization that can be expected at this impact transition will be considered here.

First, it should be mentioned that the pure electron impact (coulomb interaction) cannot excite the $^1D_2$ state of oxygen atom from the ground stale $^3P_2$, because these

states have different spin. We should suggest, that the spin interaction is violated by the magnetic field which is created by the precipitating electrons [8].

With this assumption, the atomic Hamilton may be written

$$H = H_0 + V_c(r, R) + V_{L,S}(r, R) \tag{4.1}$$

Where V_c is the operator of the pure Coulomb interaction

$$V_c(r, R) = \frac{e}{\left|\overrightarrow{r} - \overrightarrow{R}\right|} \tag{4.2}$$

and $V_{L,S}$ describes the interaction of the total spin of the outer shell of the oxygen atom with the magnetic field of the incident electron beam.

$$V_{L,S}(r, R) = \frac{e}{2mc}(\mathcal{H}, \mathcal{S}) \qquad \mathcal{H} = \frac{\rceil}{\rfloor}\left(\nabla \times \frac{\overrightarrow{v}}{\left|\overrightarrow{r} - \overrightarrow{R}\right|}\right) \tag{4.3}$$

The wave function $\Psi(r)$ of the oxygen atom is presented as a linear combination of the functions $\Psi_M(L, S, J; r)$, the eigenfunctions of the square of the total moment J and its projection. (M are eigenvalues of $\widehat{J}_z$)

$$\Psi(r) = \sum_{M_0} C_{M_0}\Psi_{M_0}(1, 1, 2; r)e^{-iE_p t} + \sum_{M} A_M \Psi_M(2, 0, 2; r)e^{iE_d t} \tag{4.4}$$

After the solution of the system of differential equations of the impact parameter method, the density matrix can be constructed as

$$\rho_{M,M'} = \langle A_M A^*_{M'}\rangle \tag{4.5}$$

Then the polarization characteristics of magneto-dipole transition ${}^3P_2 - {}^1D_2$ can be calculated.

Results of such calculations are illustrated in fig. 5, from which one can see that this model provides a large number of polarization parameters for emission of the red oxygen line.

5 Polarization of HeII ions: Interaction of X particles and hydrogen atoms [9].

This problem arised in connection to diagnostics of a tokamak plasma. where x particles are present as an impurity [10]. Utilizing a hydrogen beam for diagnostics of the tokamak plasma, hydrogen atoms undergo the recharge on $x = alpha$ particles of the plasma impurity according to reaction

$$\alpha + H \rightarrow HeII + p \tag{5.1}$$

and the emission of $HeII$ ions can be used for plasma diagnostics.

The positions of the hydrogen atom (center a), $\alpha-$ particle (centre b) and electron (center e) may be characterized by the set of vectors $\{\overrightarrow{R}_a, \overrightarrow{R}_b, \overrightarrow{R}_e\}$(see fig 6.a). These coordinates are not suitable for the description of collisions. It is well known

that the variables for the problem of three bodies are expanded over the Jacoby coordinates $\{\vec{r}_a, \vec{R'}_a, \vec{R}_c\}$ or $\{\vec{r}_b, \vec{R'_b}, \vec{R}_c\}$ where $\vec{R}_c$ is the coordinate of the center of mass and the origin of the vector $\vec{R'}_a$ ($\vec{R'_b}$) is in the mass center of the system center a (b). With the first triplet of coordinates and the assumption, that the mass of electron is much smaller than masses of atomic particles a and b, the Hamiltonian of the system takes the form

$$H_I = -\frac{\hbar^2}{2m}\Delta_{r_a} - \frac{\hbar^2}{2\mu}\Delta_{R'_a} - \frac{\hbar^2}{2M}\Delta_c + V(r_a) + V(r_b) + V_{ab} =$$
$$H_a - \frac{\hbar^2}{2\mu}\Delta_{R'_a} - \frac{\hbar^2}{2M}\Delta_c + V(r_b) + V_{ab} \tag{5.2}$$

Where μ is the reduced mass of the centers a and b , $M = m_a + m_b$, $V(r_i)$ is the operator of attraction of electron and the center i ($i = a, b$) and H_a is the operator of the one electron atom localized at the center a (the hydrogen atom).

Similarily with the second triplet of coordinates and the same assumption about the masses of the particles one can write for the Hamiltonian of the system:

$$H_{II} = -\frac{\hbar^2}{2m}\Delta_{r_b} - \frac{\hbar^2}{2\mu}\Delta_{R'_b} - \frac{\hbar^2}{2M}\Delta_c + V(r_a) + V(r_b) + V_{ab} =$$
$$H_b - \frac{\hbar^2}{2\mu}\Delta_{R'_b} - \frac{\hbar^2}{2M}\Delta_c + V(r_a) + V_{ab} \tag{5.3}$$

Where H_b is the Hamiltonian of the hydrogen-like helium atom located at the center b .

It should be emphasized that the Hamiltonians (5.2) and (5.3) are equivalent if the precise wave functions are used.

Introducing the notations $\psi_a(r_a)$ and $\psi_{4,l,m}(r_b)$ for the wave functions of the hydrogen atom in the ground state and $HeII$ ion in the state with $n = 4$, the wave function of theelectron in the field of the two centers may be written as a linear combination of the functions $\psi_a(r_a)$ and $\psi_{4,l,m}(r_b)$

$$\Psi = a_o\psi_a(r_a)e^{-iE_at} + \sum_{l,m} c_{l.m}\psi_{4,l,m}(r_b)e^{-iE_bt} \tag{5.4}$$

Since the functions $\psi_a(r_a)$ and $\psi_{4,l,m}(r_b)$ are not orthogonal, the substitution of the last expansion into the Schroedinger equation leads to the non-normal system of the differential equations for the coefficients a_o and $c_{l.m}$. As far as we know there are no suitable programs for the integration of such systems. So, before the substitution of the expansion in (5.4) into the Schrodinger equation, the set of functions $\{\psi_a(r_a), \psi_{4,l,m}(r_b)\}$ should be orthogonalized. This leads to significant difficulties for expressing the matrix elements. These elements can be calculated utilizing either Hamiltonian (5.2) or (5.3).

After obtaining the solution to the system of differential equations and the calculation of the polarization moments of the ensemble of ions $HeII$ in the state with the principal quantum number $n = 4$, the "partial" Stokes parameter Q_{l,l_0} for the transition $4l \to 3l_0$ can be calculated according the formula

$$Q_{l,l_0} = \frac{3\left\{\begin{array}{ccc} 1 & 1 & 2 \\ l & l & l_o \end{array}\right\}\rho_o^2(l)}{2\sqrt{2}\left\{\begin{array}{ccc} 1 & 1 & 0 \\ l & l & l_o \end{array}\right\}\rho_o^0(l) - \left\{\begin{array}{ccc} 1 & 1 & 2 \\ l & l & l_o \end{array}\right\}\rho_o^2(l)}, \tag{5.5}$$

With the analogous value for the transition between the states with the principal quantum numbers $n = 4$ and $n = 3$

$$Q = \frac{3\sum_l W^2(l)\rho_o^2(l)}{\sum_l \left[2\sqrt{2}W^0(l)\rho_o^o(l) - W^2(l)\rho_o^2(l)\right]}, \tag{5.6}$$

Where the coefficients W^k depend on the vector coupling coefficients and r_{l,l_o} is the matrix element of the operator $\hat{r}$ calculated on the wave functions of the state with the momentum l and l_0.

$$W^k(l) = \sum_{l_0}(2l+1)\left[\begin{array}{ccc} l & 1 & l_0 \\ 0 & 0 & 0 \end{array}\right]^2\left\{\begin{array}{ccc} 1 & 1 & k \\ l & l & l_o \end{array}\right\}[r_{l,l_o}]^2 \tag{5.7}$$

The results of the calculations are illustrated in fig. 6b. From this plot one can see that the Stokes parameters for the transition $4p \to 3d$ is approximately constant. The emission of the $4d \to 3p$ transition is mostly polarized. It should be mentioned that the cross sections for alignment creation in the $4d$ state are rather small. The polarization of the alignment signal for the $4f \to 3d$ transition is rather large.

The dependence on the energy of relative motion of colliding particles of the Stokes parameter Q for the $4f \to 3d$.

6 Spectropolarimetric diagnostics of magnetic field strength

The first straightforward idea is to use the Hanle effect for magnetic field diagnostics. Indeed, the stationary solution of the Liouville equation for the polarization moments may be written in a way

$$\rho_2^2 = N_0^2\sqrt{\frac{3}{2}}\frac{\omega_L^2}{(1+4\omega_L^2)}; \qquad \rho_1^2 = -N_0^2\sqrt{\frac{3}{2}}\frac{\omega_L}{(1+4\omega_L^2)}; \qquad \rho_0^2 = N_0^2\frac{1+\omega_L^2}{(1+4\omega_L^2)}; \tag{6.1}$$

Where $\omega_L = \mu_0 g_j \mathcal{H}\tau_l/\hbar$ denotes the dimensionless Larmour frequency. Utilizing this formula one can obtain the relations for the signal of the longitudinal alignment and the Stokes parameter Q

$$\Delta I = I_z - I_y = I_0 N_0^2 K_2\sqrt{\frac{3}{2}}\frac{1+2\omega_L^2}{1+4\omega_L^2} \tag{6.2}$$

$$Q = \frac{I_y - I_z}{I_y + I_z} = \frac{3\rho_0^2 + \sqrt{6}Re(\rho_2^2)}{2\sqrt{2}\rho_0^0\frac{N_0^0 K_0}{N_0^2 K_2} - \rho_0^2 + \sqrt{6}Re(\rho_2^2)} =$$

$$\frac{3(1+\omega_L^2)}{2\sqrt{2}\frac{N_0^0 K_0}{N_0^2 K_2}(1+4\omega_L^2)-1+2\omega_L^2} \tag{6.3}$$

Where a factor is introduced

$$K_k^{-1} = (-1)^{j+j_0+1}\sqrt{3(2j+1)}\left\{\begin{array}{ccc} 1 & 1 & k \\ j & j & j_0 \end{array}\right\}. \tag{6.4}$$

It seems that these relations likely can be directly applied for the diagnostics of the magnetic field because formula (6.2x) contains the unknown factor N_0^2 whereas formula (6.3) contains the ratio of the unknown factors N_0^0 and N_0^2. In other words, these signals depend on the excitation process. Of course these parameters can be calculated in the frame of particular assumptions, but this will introduce additional errors in the results of the diagnostics. Special methods that free us from this difficulty will be explained here.

6.1 Diagnostics of a magnetic field strength by utilyzing the ratio of the Stokes parameters Q and U.

An ensemble of atoms affected by a strong magnetic field will be considered here. Substituting the stationary solution of the Liouville equation $\rho_{M,M'} = N_{M,M'}/(1 + i\omega_{M',M})$ for the relation of the polarization moment for $l = 1$, one obtains

$$R_q^2(l) = \widetilde{N}_0^2(l)\sum_{M,M'}\frac{T_q^2(l;M,M')\,T_0^k(l;M,M')}{1+i\omega_{M',M}}, \tag{6.5}$$

Where the coefficients $T_q^k(l;M,M')$ are a linear combination of the products of $c_{m,\sigma}^M$, coefficients of decomposition of the wave function over the set of orbital and spine functions.

$$T_q^k(l;M,M') = \sum_{m,m',\sigma}\left(c_{m,\sigma}^M\right)^* c_{m',\sigma}^{M'}(-1)^{l-m'}\left[\begin{array}{ccc} l & l & k \\ m & -m' & q \end{array}\right] \tag{6.6}$$

With the help of the program *Mathematica* 4.0 the analytical expressions for the eigenfunctions of the Hamiltonian operator and for the values $T_q^2(l;M,M')$ have been computed. At the second stage the analytical expressions for the polarization moments (6.5) have been obtained. Substitution of this moment results into the formulas for the Stokes parameters,

$$QI = -N_0^2\left[16+48a^2+27a^4+352\eta^2+400a^2\eta^2+192a^4\eta^2+\right.$$

$$\left.+2448\eta^4+432a^2\eta^4+5184\eta^6\right] \tag{6.7a}$$

$$UI = -N_0^2 8\sqrt{2}\eta\left[(4-a^2+9a^4+88\eta^2-109a^2\eta^2+64a^4\eta^2+\right.$$

$$\left.+612\eta^4-720a^2\eta^4+1296\eta^6\right], \tag{6.7b}$$

Where the dimensionless parameters $a = A/\hbar\gamma_0$ (A is the fine structure constant) and $\eta = \mu_0\mathcal{H}/\zeta\gamma_l$, that characterize the width of the fine structure and the value of the magnetic field strength, are introduced.

From the relations in (6.7) one can infer that the Stokes parameters Q and U are dependent not only on parameters a and η, but on the value N_0^2, that characterizes the efficiency of the longitudinal alignment creation under the excitation process. Since this value is incorporated into the relations (6.7) as a factor, the ratio of the Stokes parameters

$$\Lambda = \frac{U}{Q} = \frac{8\sqrt{2}\eta(4 - a^2 + 9a^4 + 88\eta^2 - 109a^2\eta^2 + 64a^4\eta^2 + }{16 + 48a^2 + 27a^4 + 352\eta^2 + 400a^2\eta^2 + 192a^4\eta^2 + } \\ \frac{+612\eta^4 - 720a^2\eta^4 + 1296\eta^6}{+2448\eta^4 + 432a^2\eta^4 + 5184\eta^6} \tag{6.8}$$

Will depend only on a and η but not on the particular properties of the excitation process.

Let us mention that the right hand part of relation (6.7b) and the nominator of ratio (6.8) with a fixed value of the parameter a is a polynomial of sixth order with respect to η. With $a > 1.74106$ it has two real roots $\eta_1^{(0)}$ and $\eta_2^{(0)}$. The localization of these roots is given by the asymptotic formulas

$$\eta_1^{(0)} \approx \frac{1}{3}a \qquad \eta_2^{(0)} \approx \frac{2}{3}a, \tag{6.9}$$

which represent the localization of the roots at $a > 3$.

From fig. 7, where the dependence of ratio (6.8) on the variable η for some values of $a = 1, 10, 20, 40$ are presented. One can see, that the simple diagnostics for a magnetic field and feasible for the values of the η parameter located in the right hand side with respect to the larger root (6.9) i.e. $\eta > 2a/3$. The ratio U/Q in the rather wide region in the right hand side with respect to this root may be approximated by the relation

$$\Lambda \sim \frac{24\sqrt{2}}{11}(\eta - \frac{2}{3}a). \tag{6.10}$$

In conclusion we should mention two peculiarities. First, owing to the fact that the strength of a magnetic field of some tens of kilogauss invokes the Zeeman splitting of some inverse centimeters. The diagnostics of the magnetic field in the frame of the above theory is possible only for the narrow multiplets of the fine and the hyperfine structures. From our point of view one example of such a narrow multiplet may be the set of levels of the state $n = 4$ of a $HeII$ ion. Since for the $4p$ state of this ion $\tau_0 = 0.77\,10^{-9}$ cek [12], the width of the fine stricture is about 0.1 cm^{-1}, the value of the parameter a is about 14, that will provide an opportunity to measure the magnetic field no less than $3\,kGs$.

6.2 Diagnostics of a weak magnetic field strength by exploiting the parameters of the relaxation process [13].

Let us consider the case, when excitation of a certain system is switched out at $t = 0$.

The evolution of the alignment tensor components of the system is described in the frame of the Couchy problem.

$$\frac{d}{dt}\rho_q^2(j;t) = -\rho_q^2(j;t) + \frac{\omega}{2}\left[\sqrt{(2-q)\,(3+q)}\rho_{q+1}^2(j;t) - \right.$$
$$\left. +\sqrt{(2+q)\,(3-q)}\rho_{q-1}^2(j;t)\right] \qquad \rho_q^2(j;0) = \delta_{0,q}N_0^2 \tag{6.11}$$

A solution of this problem is quite simple

$$\rho_{\pm 2}^2 = \frac{1}{2}\sqrt{\frac{3}{2}}N_0^2 e^{-t}\sin^2\omega t; \quad \rho_{\pm 1}^2 = \mp\frac{1}{2}\sqrt{\frac{3}{2}}N_0^2 e^{-t}\sin 2\omega; \quad \rho_{\pm 1}^2 = \mp\frac{1}{2}\sqrt{\frac{3}{2}}N_0^2 e^{-t}\sin 2\omega \tag{6.12}$$

Due to reality of these functions it is clear, that Stokes parameters Q_x and Q_y may be measured in OX and OZ directions, whereas both Stokes parameters may be inferred from the spectropolarimetric data at OY direction. Substituting (6.12) into the relations for intensities one have:

$$Q_x \sim -\sqrt{\frac{3}{2}}N_0^2 e^{-t}\cos^2\omega t \qquad Q_z \sim -\sqrt{\frac{3}{2}}N_0^2 e^{-t} sin^2\omega t$$
$$Q_y \sim -\sqrt{\frac{3}{2}}N_0^2 e^{-t}\cos 2\omega t \qquad U_y \sim -\sqrt{\frac{3}{2}}N_0^2 e^{-t}\sin 2\omega t \tag{6.13}$$

All Stokes parameters (6.13) contain a factor N_0^2, that depends on specific properties of the excitation process. Ratios of these parameters do not depend on the properties of the excitation process being the functions of the magnetic field strength only. For example:

$$\tilde{\Lambda}_y = \frac{U_y}{Q_y} = tg2\omega t \tag{6.14}$$

Decomposing these functions over the Taylor sets in the vicinity of $t = 0$ one obtains an approximate formula:

$$\tilde{\Lambda}_y = 2\omega t + \frac{8\omega^3 t^3}{3} \tag{6.15}$$

which can be used for the diagnostics of the magnetic field strength as the inclination of the curve of dependence (6.14) at $t = 0$.

Similar expansion can be obtained in the case of strong magnetic field

6.3 Diagnostics of the magnetic field strength by sensing the polarization characteristics under the pulse excitation.

If the OZ axis of the laboratory frame of reference is fixed as the direction of the axially symmetric excitation of the atomic ensemble and the magnetic field is directed along the OY axis, the block with $k = 2$, that describes the evolution of the alignment tenser takes the form

$$\frac{d}{d\tilde{t}}\rho^2_{-1}(j) = -\rho^2_{-1}(j) + \omega\left(-\rho^2_{-1}(j) + \sqrt{\frac{3}{2}}\rho^2_0(j)\right),$$

$$\frac{d}{d\tilde{t}}\rho^2_0(j) = -\rho^2_0(j) + \omega\sqrt{\frac{3}{2}}\left(-\rho^2(j) + \rho^2_1(j)\right) + N^2_0, \tag{6.16}$$

$$\frac{d}{d\tilde{t}}\rho^2_1(j) = -\rho^2_1(j) + \omega\left(-\sqrt{\frac{3}{2}}\rho^2_0(j) + \rho^2_2(j)\right),$$

$$\frac{d}{d\tilde{t}}\rho^2_2(j) = -\rho^2_2(j) - \omega\rho^2_1(j),$$

where $\omega = \mu_0 g_j \mathcal{H}/\gamma_\prime\zeta$ is the dimensionless Larmour frequency, N^2_0 - the efficiency of creation of the longitudinal alignment by the external source and the $\tilde{t} = t\gamma_0$ is the time, measured in the units of time of life.

If at $t = 0$ the system is excited by the rectangular impulses of the length τ

$$N^2_0 = \begin{cases} 0 & \tilde{t} < 0 \\ 1 & 0 < \tilde{t} < \tilde{\tau} \\ 0 & \tilde{t} > \tilde{\tau} \end{cases}, \tag{6.17}$$

where $\tilde{\tau} = \tau\gamma_0$.

With the help of Laplace transformation one can obtain the solution of the system (6.16) in the form

$$\rho^2_0(\tilde{t}) \sim \frac{1+\omega^2}{1+4\omega^2} - \frac{e^{-\tilde{t}}\left[1+4\omega^2+3\cos(2\tilde{t}\omega) - 6\omega\sin(2\tilde{t}\omega)\right]}{4\left(1+4\omega^2\right)} +$$

$$\left\{-\frac{1+\omega^2}{1+4\omega^2} + \frac{e^{-(\tilde{t}-\tilde{\tau})}\left[1+4\omega^2+3\cos(2(\tilde{t}-\tilde{\tau})\omega) - 6\omega\sin(2(\tilde{t}-\tilde{\tau})\omega)\right]}{4\left(1+4\omega^2\right)}\right\}\Theta\left(\tilde{t}-\tilde{\tau}\right)$$

$$\rho^2_1(\tilde{t}) \sim \frac{\sqrt{\frac{3}{2}}\omega}{(1+4\omega)^2}\left(1-\Theta(\tilde{t}-\tilde{\tau})\right) +$$

$$\frac{\sqrt{\frac{3}{2}}e^{-\tilde{t}}}{16\sqrt{\omega}\,(1+4\omega)^2}\left[2\sqrt{\omega}\left(\tilde{t}+4\tilde{t}\omega-8\omega\right)\cos(2\tilde{t}\sqrt{\omega}) - (1+12\omega+4\omega\tilde{t}+16\tilde{t}\omega^2)\sin(2\tilde{t}\sqrt{\omega})\right] -$$

$$\frac{\sqrt{\frac{3}{2}}\omega e^{-(\tilde{t}-\tilde{\tau})}}{16\sqrt{\omega}\,(1+4\omega)^2}\left[2\sqrt{\omega}\left((\tilde{t}-\tilde{\tau})+4(\tilde{t}-\tilde{\tau})\omega-8\omega\right)\cos(2(\tilde{t}-\tilde{\tau})\sqrt{\omega}) - \right. \tag{6.18}$$

$$\left.(1+12\omega+4\omega(\tilde{t}-\tilde{\tau})+16(\tilde{t}-\tilde{\tau})\omega^2)\sin(2(\tilde{t}-\tilde{\tau})\sqrt{\omega})\right]\Theta(\tilde{t}-\tilde{\tau})$$

$$\rho^2_2(\tilde{t}) \sim \frac{\sqrt{\frac{3}{2}}\omega^2}{1+4\omega^2}\left(1-\Theta(\tilde{t}-\tilde{\tau})\right) + \frac{e^{-\tilde{t}}\sqrt{6}\left[-1-4\omega^2+\cos(2\tilde{t}\omega) - 2\omega\sin(2\tilde{t}\omega)\right]}{8\left(1+4\omega^2\right)} -$$

$$\frac{e^{-(\tilde{t}-\tilde{\tau})}\left[-1-4\omega^2+\cos(2(\tilde{t}-\tilde{\tau})\omega) - 2\omega\sin(2(\tilde{t}-\tilde{\tau})\omega)\right]}{8\left(1+4\omega^2\right)}\Theta(\tilde{t}-\tilde{\tau})$$

where $\Theta(x) = 0$ if $x < 0$ and $\Theta(x) = 1$ if $x > 0$.

From the last relations one can obtain the expression for the inclined alignment that is observed from the OY axis (along the direction of the field)

$$A_{in}^{(y)} = (I_{xz-} - I_{xz+}) \sim 2Re\left(\rho_1^2(\tilde{t})\right) \tag{6.19a}$$

and the signal of longitudinal alignment that is observed at the same direction

$$A_{l}^{(y)} = (I_x - I_z) \sim \frac{3}{\sqrt{6}}\rho_0^2(\tilde{t}) - Re\left(\rho_2^2(\tilde{t})\right) \tag{6.19b}$$

as well as the signal of the longitudinal alignment observed at OX axis (perpendicular to the direction of the magnetic field)

$$A_{l}^{(x)} = (I_y - I_z) \sim \frac{3}{\sqrt{6}}\rho_0^2 + Re(\rho_2^2) \tag{6.19c}$$

where I_i are the intensities of emission polarized at the direction of $i-$ axis $(i = x, y, z)$ whereas I_{zx+} and I_{zx-} are that's polarized in the direction of diagonals of first and the second quarters of ZX plane.

Firstly it should be mentioned, that because of the decomposition of $A_{in}^{(y)}(\tilde{t})$ at the small $\tilde{t}$

$$A_{in}^{(y)}(\tilde{t}) \sim \omega\tilde{t}^4/8\sqrt{/}6 + O\left(\tilde{t}^5\right) \tag{20},$$

the determination of the value of magnetic field by the slop of the function $A_{in}^{(y)}(\tilde{t})$ is likely possible.

At the fig. 8a the dependence of the inclined alignment observed at OY direction (along the magnetic field strength) on time is represented for the duration of excited impulses $\tau = 1$ and $\omega = 0.1, 1, 2$ and 3. From this plot one can see that these dependencies are of the oscillative character. Therefore the diagnostics of magnetic field can be fulfilled by the positions of the zeros and extrema of these dependencies.

The function $\omega = \omega\left(\tilde{t}\right)$, that is the solution of equation $A_{in}^{(y)}(\tilde{t}) = 0$, for $\tilde{t} > \tilde{\tau}$ is represented at fig. 8b. From this plot one can see that the function $A_{in}^{(y)}(\tilde{t})$ is not equal to zero for the time span $\tilde{t} \leq 0.6$. For large values of ω the parameters ω and $\tilde{t}$ are coupled by the approximate relation $\omega = x_k/4\tilde{t}^2$, where x_k is the $k-$th root of the equation $\tan x = x$. For arbitrary values of ω the pairs $\left\{\omega, \tilde{t}\right\}$ that make zero the value of the inclined alignment are represented by the solutions of the transcendent equation

$$f_c \cos(2\tilde{t}\sqrt{\omega}) + f_s \sin(2\tilde{t}\sqrt{\omega}) = 0 \tag{6.21}$$

where

$$f_c = \left[2\sqrt{\omega}\left(\tilde{t} + 4\tilde{t}\omega - 8\omega\right) - 2\sqrt{\omega}e^{\tilde{\tau}}\left((\tilde{t} - \tilde{\tau}) + 4(\tilde{t} - \tilde{\tau})\omega - 8\omega\right)\cos(2\tilde{\tau}\sqrt{\omega}) - \right.$$
$$\left. e^{\tilde{\tau}}(1 + 12\omega + 4\omega(\tilde{t} - \tilde{\tau}) + 16(\tilde{t} - \tilde{\tau})\omega^2)\sin(2\tilde{\tau}\sqrt{\omega})\right] \tag{6.22}$$
$$f_s = \left[-1 - 12\omega + 4\omega\tilde{t} - 16\tilde{t}\omega^2 + e^{\tilde{\tau}}(1 + 12\omega + 4\omega(\tilde{t} - \tilde{\tau}) + \right.$$
$$\left. 16(\tilde{t} - \tilde{\tau})\omega^2)\cos(2\tilde{\tau}\sqrt{\omega}) - 2\sqrt{\omega}e^{\tilde{\tau}}\left((\tilde{t} - \tilde{\tau}) + 4(\tilde{t} - \tilde{\tau})\omega - 8\omega\right)\sin(2\tilde{\tau}\sqrt{\omega})\right.$$

Differentiation of expression (6.19a) gives that in the interval $\tilde{t} > \tilde{\tau}$ the pairs $\{\omega, \tilde{t}\}$, that makes the zero for the derivative of the function $A_{in}^{(y)}(\tilde{t})$ may be found. These pairs are the solution of transcendent equation

$$\Big[-2\tilde{t}\sqrt{\omega} + e^{\tilde{\tau}}\Big(2\sqrt{\omega}(\tilde{t}-\tilde{\tau})\cos(2\tilde{\tau}\sqrt{\omega}) + \sin(2\tilde{\tau}\sqrt{\omega})\Big)\Big]\cos(2t\sqrt{\omega}) +$$
$$\Big[1 + e^{\tilde{\tau}}\Big(-\cos(2\tilde{t}\sqrt{\omega}) + 2\sqrt{\omega}(\tilde{t}-\tilde{\tau})\sin(2\tilde{\tau}\sqrt{\omega})\Big)\Big]\sin(2t\sqrt{\omega}) = 0 \qquad (6.23)$$

The solution of this equation is represented at the fig. 8c, where symbols plus or minus denote the sign of the derivative within the corresponding areas. Quite analogues one can find that in the region $\tilde{t} < \tilde{\tau}$ positions of extrema of the function under consideration are given by the equation $2\sqrt{\omega}t\cos 2\sqrt{\omega} - \sin 2\sqrt{\omega} = 0$, therefore with use of the position of the first maximum the Larmour frequency may be denoted by the relation $\omega = (2.25/t)^2$.

Analogous to this the diagnostics of the magnetic field strength can be made on the basis of positions of extrema of longitudinal alignment (expression (6.19c)) observed from the OY direction (perpendicular to the direction of magnetic field).

7 Measurement of the magnetic field of the remote objects.

The geomagnetic fields can be measured with the help of the quantum magnetometers, that provide high accuracy of data on the Earth's surface. If this devise is fixed on the satellite significant errors, originating from the non stability of its trajectory may take place. Satellite based quantum magnetometers can examine not only the Earth magnetic field, but weaker fields that are inducted by auroral currents.

In this section the opportunity of the methods of polarization spectroscopy will be applied to the problem of the measurement of the geomagnetic field.

7.1 Spectropolarimetric sensing of the geomagnetic field [14].

Analysing the influence of constant geomagnetic field on the polarization characteristics of ensemble of fluorescent particles, one should take into account two factors: first is the small value of geomagnetic field; the second is large value of the alignment crated by the excitation process and probable presence of polarization in the exiting radiation. In the other words observations should distinguish rather small input from magnetic field at the background of the alignment induced by the excitation and the one from the polarization of the exiting radiation. From geometrical point of view it is clear, that two last factors will dominate at the registration of the Stokes parameter U at the direction perpendicular to the excitation direction.

Indeed, if OZ axis of laboratory frame of reference is connected with the axis of the axial symmetry of the excitation process and the vector of the magnetic field strength belongs to the meridian plane (plane ZY) and makes the angle α with OZ axis: $\overrightarrow{H} = H(\sin\alpha\overrightarrow{e_y} + \cos\alpha\overrightarrow{e_z})$ (see fig. 9a), then in stationary regime the block with $k = 2$ of system of differential equations, that discribes the evolutuion of polarisation moments, takes the form

$$-\rho_q^2(j) + \omega_L \left\{ -iq\rho_q^2(j)\cos\alpha + \frac{\sin\alpha}{2}\left[\sqrt{(2-q)(3+q)}\rho_{q+1}^2(j) - \sqrt{(2+q)(3-q)}\rho_{q-1}^2(j)\right]\right\} = -N_q^2, \quad (7.1)$$

where $\omega_L = \mu_0 g_j H\tau_0/\hbar$.

It should be reminded, that the axial symmetrical excitation process creates only the population and the longitudinal alignment in the ensemble of particles. Then, according to (7.1), at $\alpha \neq 0$ the magnetic field will mix the components of polarization moments that leads to appearance in the ensemble new types of ordering: the inclined and the perpendicular alignment. The inclined alignment (polarization moment ρ_1^2) defines the Stokes parameter U. Hence, considering the "inverse" problem one can determinate the value of magnetic field if parameter U is known from the experiment.

Results of solution of the equation (7.1) in the stationary regime for the transitions $3^5S_2 - 4^5P_3$, $3^3S_1 - 4^3P_2$ and $3^5P_2 - 4^5D_2$ of the oxygen atoms, excited by the non polarized Solar light, are illustrated in fig 9b and 9c. This transitions was selected because on one hand they can be observed in the auroral emission [15] and on the other hand upper states of this transitions has rather large time of life (193 $10^{-9}sec$, 160 $10^{-9}sec$ and 96 $10^{-9}sec$ for $^5P_3$, $^3P_2$ and $^5D_2$ consequently), therefore weak geomagnetic field has time to "untwist" atomic moments. Fig 9c illustrates the dependence of parameter U on the value of magnetic field for the value of angle $\alpha = 30^o$. From this plot one can see, that the value this parameter is rather sensible for the value of magnetic field and the value of the Stokes parameter U is as large as some tenths of percent at the value of magnetic field about $0.3Gs$. At the fig. 9b the dependence of the Stokes parameter mentioned above on the value of angle α is represented for the value of the magnetic field strength $0.5Gs$. From this plot one can see that for each transition the optimal value of angle α exists, that provides the extremely value of parameter U.

8 The influence of field-aligned currents at the region of polar cusps on the polarization characteristics of auroral emission.

The current's distribution in the North Polar Cap obtained from the data of satellite TRIAD [16, 17], is represented on the fig. 10a. From this plot one can see, that the field-aligned currents are observed as a rather extend layers (curtain currents) stretched along the geomagnetic parallels.

The detail of the current system and induced by it magnetic fields are represented in fig. 10b. field-aligned currents are closed in ionosphere by the Pedersen's currents, the distribution and the altitude of which depends on the distribution of conductivity, i.e. on location, time, season and intensity of geomagnetic activity. In addition to Pendersen's currents the intensive Hall's currents are generated in ionosphere. This currents are directed along parallels and named the auroral electrojets (δH_{jet}) .

The magnetic field of electrojet is directed over the geomagnetic meridian and can be observed on the Earth's surface as the disturbance of the geomagnetic field. In the region above the electojet this field changes sign.

The field of field-aligned and Pedercen's currents (δH_{fac}) can not be observed on the Earth's surface. This field are directed along parallel and located in the region between field-aligned currents.

According to scheme mentioned above atomic system located in the zone of influence of the electrojet and Pedersen's fields, is affected by the field

$$\overrightarrow{H} = (\delta H_{fac})\,\overrightarrow{e_x} + (\delta H_{jet})\,\overrightarrow{e_y} + H_{geo}\,\overrightarrow{e_z}. \tag{8.1}$$

Here H_{geo} is the geomagnetic field, directed along OZ axis. It's direction coincides with that's of excitation, provided by the Solar wind particles, propagating along the magnetic field strength lines. Then introducing the dimensionless frequencies $\omega_{geo} = \mu_o g_j H_{geo}\tau_0/\hbar$ and $\omega_0 = (\mu_o g_j \tau_0/\hbar)\,[\delta H_{jet} + i\delta H_{fac}]$, the evolution of components of alignment tenser enforced by the field (9) is given by equation

$$(-1 - i\omega_{geo} q)\,\rho_q^2 + \frac{1}{2}\left[\omega_0^* \sqrt{(2-q)(3+q)}\rho_{q-1}^2 - \omega_0 \sqrt{(2+q)(3-q)}\rho_{q+1}^2\right] - N_q^2 = 0. \tag{8.2}$$

In should be noticed that because of the characteristic values of δH_{jet}, δH_{fac} and H_{geo} that are consequently equal to 0.015 Gs, 0.005 Gs and 0.5 Gs, Larmour's frequencies of these fields are connected by the relation $\omega_{fac} < \omega_{jet} << \omega_{geo}$.

The decomposition of the ratio $U/Q \sim Im\rho_2^2/Re\rho_2^2$ over the small parameter ω_{fac} takes the form

$$\frac{Im\rho_2^2}{Re\rho_2^2} \sim -\frac{3}{4\omega_{geo}^2} + \frac{2\omega_{fac}}{\omega_{jet}} \tag{8.3}$$

From this relation one can see, that the dependence of the right hand part of (8.3) on ω_{fac} practically begins on the origin of the frame of reference. The dependence of the ratio U/Q on the value δH_{fac} for the transition $2^3P_1 - 3^5S_2$ of oxygen atom ($\tau_0 = 1.8\,10^{-4}\,sek$ $\omega_{geo} = \mu_0 g \tau_0 H_{geo}/\hbar = 3164 H_{geo}$) is represented at the fig. 11a. One can see that this dependence is in a good agreement with formula (8.3).

From formulas (8.3) one can obtain the value of δH_{fac} if values of the ratio U/Q and that's of the fields δH_{jet} and δH_{geo} are known. But the practical realization of this methodic is connected with significant difficulty.

It is clear that the diagnostic of the value δH_{fac} may be successful if the source of emission is localized in ionosphere above the current layer . The ionosphere's currents at least in the night part of auroral zone flows in the region of maximal conductivity i.e. in the region of Aurora Borealis where is the transition $2^3P_1 - 3^5S_2$ exists and can be used for the diagnostics of magnetic field. The exited 3^5S_2 of oxygen atom has the time of life $\tau_0 = 1.8\ 10^{-4}\ sec$ and in this state the spine alignment can be induced. At the altitudes less then 120 km this state effectively extinguished by the collisions [18]. Therefore the emission $\lambda = 1357\ \mathring{A}$ correspondent to this transition, will came from the altitudes above the current's layer. Unfortunately the ultraviolet radiation $\lambda < 2500\mathring{A}$ almost completely absorb by the Earth's atmosphere.

More favorable situation is provided in the Polar cusps region where the altitude of Aurora Borealis is about 250 km. Here the Pedersen's conductivity at night is very small and field-aligned currents close in the E - region. This condition provides the opportunity of measuring the value of the field δH_{fac}.

9 Application of polarization spectroscopy to diagnostics of the aerosol clouds.

Intensity of radiation scattered by an ensemble of the macroscopic particles orientated in a certain way is given by a relation:

$$I_{e,e_0} \sim |(\overrightarrow{e}, \beta \overrightarrow{e_o})|^2 \tag{9.1}$$

where $\beta_{i,j}$ $(i,j = x,y,z)$ are components of the scattering tensor and $\overrightarrow{e}$ and $\overrightarrow{e_0}$ are the orths connected with the directions of observation and the incident radiation. The tensor $\beta_{i,j}$ depends on the shape, structure and the sizes of particles. If the size of scattering particles is small comparing to the wavelength, the scattering tenser coincide with the tenser of dipole polarizability.

A specificity of the formula (9.1) is that it "mixes" characteristics of ensembles of particles as to be typically described by the scattering tenser and observation conditions: a nature of incident radiation field and the observation geometry. In order to split these principally different contributions into (9.1) and to connect optical observables with the scattering properties of ensemble of aerosol particles, it is worthwhile to expand the unit vectors $\overrightarrow{e}$ and $\overrightarrow{e}_0$ over the circular orth base: $\overrightarrow{e} = \sum_q b_q \overrightarrow{e_q}$, $\overrightarrow{e_o} = \sum_q a_q \overrightarrow{e_q}$, where $(q = 0, \pm 1)$.

Then introducing tenserial values

$$A^l_m = \sum_{q,q'} (-1)^{1-q'} \begin{bmatrix} 1 & 1 & l \\ q & -q' & m \end{bmatrix} a_q a^*_{q'}, \tag{9.2}$$

and

$$\beta^\lambda_\mu = \sum_{q,q'} (-1)^{1-q'} \begin{bmatrix} 1 & 1 & \lambda \\ q & -q' & \mu \end{bmatrix} \beta_{q,q'} \tag{9.3}$$

where expressions in square brackets are the Clebsch-Gorgan coefficients, after some cumbersome transformations exploiting the momentum coupling technique the formula (9.1) may be written in a way

$$I_{e,e_0} \sim \sum_{L,l,l'\lambda,\lambda',\mu,\mu'} (-1)^{L+M+\lambda+\mu} \Phi^{L,M}_{l,l'} (\overrightarrow{e}, \overrightarrow{e_0}) \sqrt{(2l+1)(2\lambda+1)(2\lambda'+1)}$$

$$\begin{bmatrix} \lambda & \lambda' & L \\ \mu & -\mu' & M \end{bmatrix} \begin{Bmatrix} 1 & \lambda' & 1 \\ l & L & l' \\ 1 & \lambda & 1 \end{Bmatrix} \beta^\lambda_\mu \beta^{\lambda'*}_{\mu'} \tag{9.4}$$

where notation $\{\}$ is a $9j$ coefficient [?] and a term

$$\Phi_{l,l'}^{L,M}\left(\overrightarrow{e},\overrightarrow{e_0}\right)=\sum_{m,m',m_1}\left(-1\right)^{m_1+m}A_{m_1}^{l'}B_{-m}^{l}D_{m,m_2}^{l}\left(\alpha,\beta,\gamma\right)$$

$$\sqrt{2l'+1}\begin{bmatrix} l & l' & L \\ m_2 & -m_1 & M \end{bmatrix} \tag{9.5}$$

that is known as the polarization tenser, contains D_{m,m_2}^{l} is an element of the rotation matrix, depending on the Euler's angles α,β, and γ. These angles characterize an orientation of the system of reference XYZ with $OZ-$ axis connected to a direction of an incident light beam and an observation system $X_1Y_1Z_1$ with OZ_1 axis as a direction of observation.

The coefficients A_m^l are defined by the formula (9.2) and the coefficients B_m^l are described by the similar expression with a substitution of b_q instead of a_q. As a result, all observation conditions are reflected in the polarization tenser $\Phi_{l,l'}^{L,M}\left(\overrightarrow{e},\overrightarrow{e_0}\right)$, whereas the scattering properties of an ensemble of particles are incorporated in the factor $\beta_\mu^\lambda\beta_{\mu'}^{\lambda'*}$ on the right hand part of formula (9.4). The values β_μ^λ may be considered as components of a scattering tenser within the basis of spherical functions $Y_{\lambda,\mu}\left(\lambda=0,1,2;\ \mu=0,\pm1,...\pm\lambda\right)$.

In case when radiation is scattered by an ensemble of arbitrary orientated particles, an averaging over orientations of the scattering particles should be performed in formula (9.4). Axial symmetry in the space orientation of the ensemble of scattering particles will be assumed for simplicity. This means that if $\widetilde{X}\widetilde{Y}\widetilde{Z}$ is the frame of reference with $O\widetilde{Z}$ axis connected to the symmetry axis of a solid angle within which all particle can be considered as oriented in the similar way, the distribution function will depend only on angle ϑ between OZ and $O\widetilde{Z}$ axes. Averaging of (9.4) one may obtain

$$I_{e,e_0}\sim\sum_{L,l,l'}\left(-1\right)^L\Phi_{l,l'}^{L}\left(\overrightarrow{e},\overrightarrow{e_0}\right)T_{l,l'}^{L} \tag{9.6}$$

where

$$T_{l,l'}^{L}=\sum_{\lambda,\lambda',\mu}\left(-1\right)^{\lambda+\mu}\sqrt{\left(2l+1\right)\left(2\lambda+1\right)\left(2\lambda'+1\right)}\begin{Bmatrix} 1 & \lambda' & 1 \\ l & L & l' \\ 1 & \lambda & 1 \end{Bmatrix}$$

$$\begin{bmatrix} \lambda & \lambda' & L \\ \mu & -\mu & 0 \end{bmatrix}\ f^L\ \tilde{\beta}_\mu^\lambda\tilde{\beta}_\mu^{\lambda'} \tag{9.7}$$

The symbol tilde over some values denotes that these values are referred to the system $\widetilde{X}\widetilde{Y}\widetilde{Z}$, f^L is a coefficient of expansion of distribution function over Legendre polynomials

$$f^L=\frac{2}{2L+1}\int P_L\left(\cos\vartheta\right)f\left(\vartheta\right)d\vartheta, \tag{9.8}$$

and according to (9.5):

$$\Phi_{l,l'}^{L}\left(\overrightarrow{e},\overrightarrow{e_0}\right)=\Phi_{l,l'}^{L,0}\left(\overrightarrow{e},\overrightarrow{e_0}\right)=\sum_{m,m_1}\left(-1\right)^{m_1+m}A_{m_1}^{l'}B_{-m}^{l}D_{m,m_1}^{l}\left(\alpha,\beta,\gamma\right)$$

$$\sqrt{2l'+1}\begin{bmatrix} l & l' & L \\ m_1 & -m_1 & 0 \end{bmatrix}. \tag{9.9}$$

Utilizing the property of the transversely of the electromagnetic radiation one can calculate the values of coefficients A_q^l and B_q^l $(l = 0, 1, 2.)$ and finally write the relation for the Stocks parameter Q :

$$Q = \frac{I_{x_1} - I_{y_1}}{I_{x_1} + I_{y_1}} = \frac{\sum_{L,l_1}(-1)^L \left[\Phi^L_{2,l'}(\overrightarrow{e_{x_1}}, \overrightarrow{e_0}) - \Phi^L_{2,l'}(\overrightarrow{e_{y_1}}, \overrightarrow{e_0})\right] T^L_{2,l_1}}{\sum_{L,}(-1)^L \left\{\frac{2}{\sqrt{3}} A^L_0 T^L_{0,L} + \sum_{l_1}\left[\Phi^L_{2,l'}(\overrightarrow{e_{x_1}}, \overrightarrow{e_0}) + \Phi^L_{2,l'}(\overrightarrow{e_{y_1}}, \overrightarrow{e_0})\right] T^L_{2,l_1}\right\}}. \tag{9.10}$$

This formula is applicable for an arbitrary orientation of the system of reference XYZ with respect to $X_1Y_1Z_1$. In the simplest case when axes OY and OY_1 coincide the matrix element of the rotation matrix on the right hand side of (36) depends only on the angle β $\left(D^2_{2,m_1} = D^2_{2,m_1}(0, \beta, 0)\right)$ and because of transversality of incident radiation the possible values of m_1 are 0 and ± 2 . Therefore a right hand part of (39) depends on $\cos^2\beta$.

As en example the case of excitation of aerosol particles by the unpolarized incident light propagating along OZ direction will be considered. It will be suggested that the direction of observation is $O\tilde{Z}$ one (see fig. 11b). In this case the relation for the Stokes parameter Q takes the form

$$Q = \frac{\Delta_2 \sin^2\beta}{\Delta_1 + \Delta_2 \cos^2\beta} \tag{9.11}$$

where

$$\Delta_2 = \frac{1}{2}T^0_{2,2} + \frac{1}{2}T^2_{2,0} - \sqrt{\frac{5}{14}}T^2_{2,2} + \frac{3}{\sqrt{14}}T^4_{2,2} \tag{9.12}$$

$$\Delta_1 = \frac{2}{3}T^0_{0,0} + \frac{\sqrt{10}}{3}T^2_{0,2} - \frac{1}{3}\Delta_2$$

The angle β contains all information about conditions of observations and all internal properties of scattering ensemble is contained in tensers $T^L_{k,k'}$. The expression ( ) depends on five tensors: $T^0_{0,0}$, $T^0_{2,2}$, $T^2_{2,0}$, $T^2_{2,2}$ and $T^4_{2,2}$. Therefore for determination of these tensers one needs not less then fife measurements of parameter Q under different angles β. Making special assumptions about the shape of the scattering particles one can predict the properties of the scattering ensemble.

References

[1] Kazantsev S.A., Petrashen A.G., Rebane V.N., Rebane T.K.// JEPT, 1994, v.106, n,3(9), p.698-724.

[2] Henoux J-K, Chamble G., Smith D., Tamres D., Feantrier N., Rovira M., Sahal-Brechot// Astrophys. J. 1990, v.73, p.303-311.

[3] Kazantsev S.A. and Henoux J-C. Polarization Spectroscopy of Ionizsd Gases, Kluver Academic Publishers. Dordrecht, London, Boston, 1995.

[4] Kazansev S.A., Petrashen A.G. and Firstova N.M Impact Spectropolarimetric Sensing. Plenium Publishing Corporation New York, London, 1999.

[5] Schöller O., Briggs J.S., Dreizler R.M. // J. Phys. B 1986, v.19, p.2505-2517.

[6] Nadubovich,Yu.A., //Geomagnetism and Aeronomy v.10, p.926, 1970.

[7] Ermilov,S.Yu., Mikhalev,A.V., Journ. Atmospher. and Terresrial Phys., 1991, v. 53, p.1157.

[8] Kazansev S.A., Mikhalev,A.V., Petrashen A.G. // Optica and Spectroscopy v.80, n.4, p.559-561, 1999.

[9] Kazansev S.A., Petrashen A.G. // Optica and Spectroscopy v.88, n.4, p.556-559, 2000.

[10] Ida K., Hidekuma S. // Rev. Sci. Instrum. v.60, n. 50, p.867-871, 1989.

[11] Shlyaptseva A.S., Kantsyrev V.L., Bauer B.S. at. al.// Abst. 12-th APS Topical Conf. on Atomic Processes in Plasma, Reno, NV, March 19-23, 2000, p. 156-157.

[12] Fritsch W. //Phys.Rev.A ,v. 38, p 2664-2666, 1988.

[13] Kazansev S.A., Petrashen A.G. // Optica and Spectroscopy v.89, n.3, p. 382-385, 2000.

[14] Kazansev S.A., Petrashen A.G., Pudovkin M.I. // Geomagnetism and Aeronomy v.41, n. 1, p.50-56, 2001.

[15] J.W.Chamberlain, Physics of Aurora and Airglow. New York, 1967

[16] Iijima T.,Potemra T.. //J.Geophys. Res. 1976. V. 81. P. 5971-5979.

[17] Potemra T.. // Space. Sci.Rev.,1985, V.42. P. 295-311.

[18] Alpert Ja. L. The propagation of electromagnetic waves in the atmosphere , Nauka, 1972, 328 p.

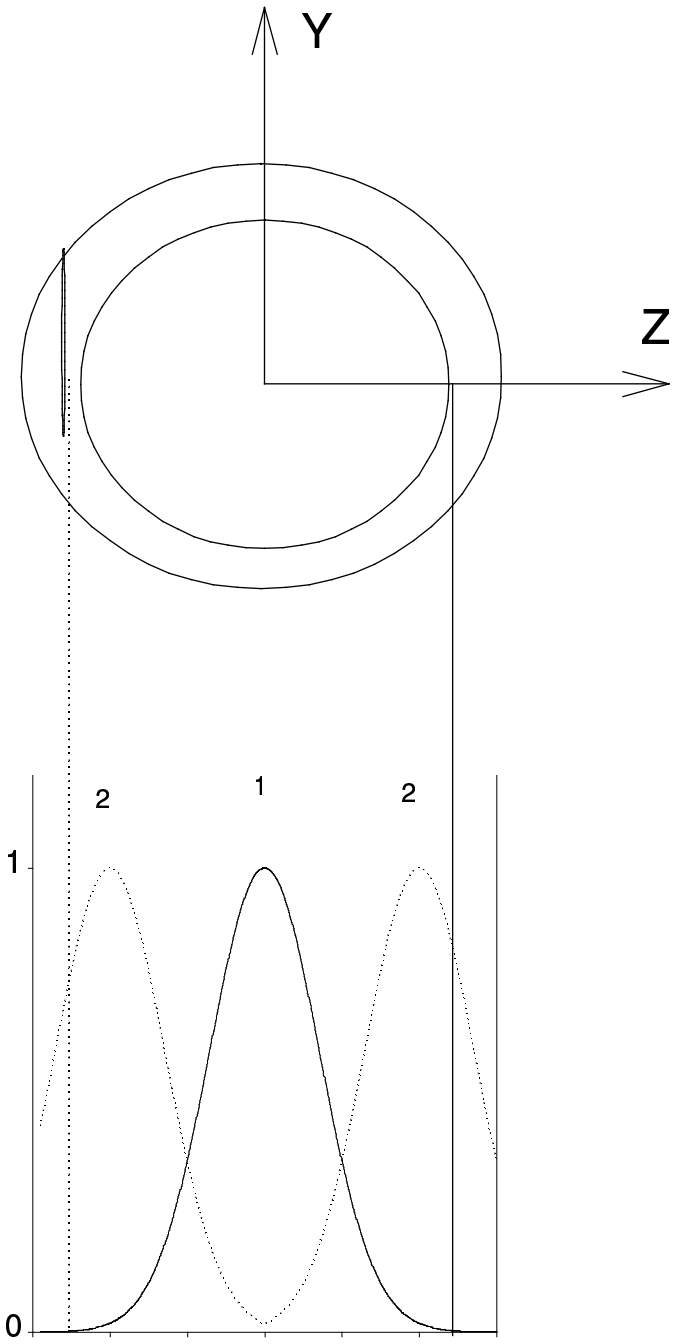

Figure 1: (a) The hollow cathode and the system of reference linked with it; (b) curve (1)-the radial dependence of the sum of intensities, curve (2)- the radial dependence of the alignment signal.

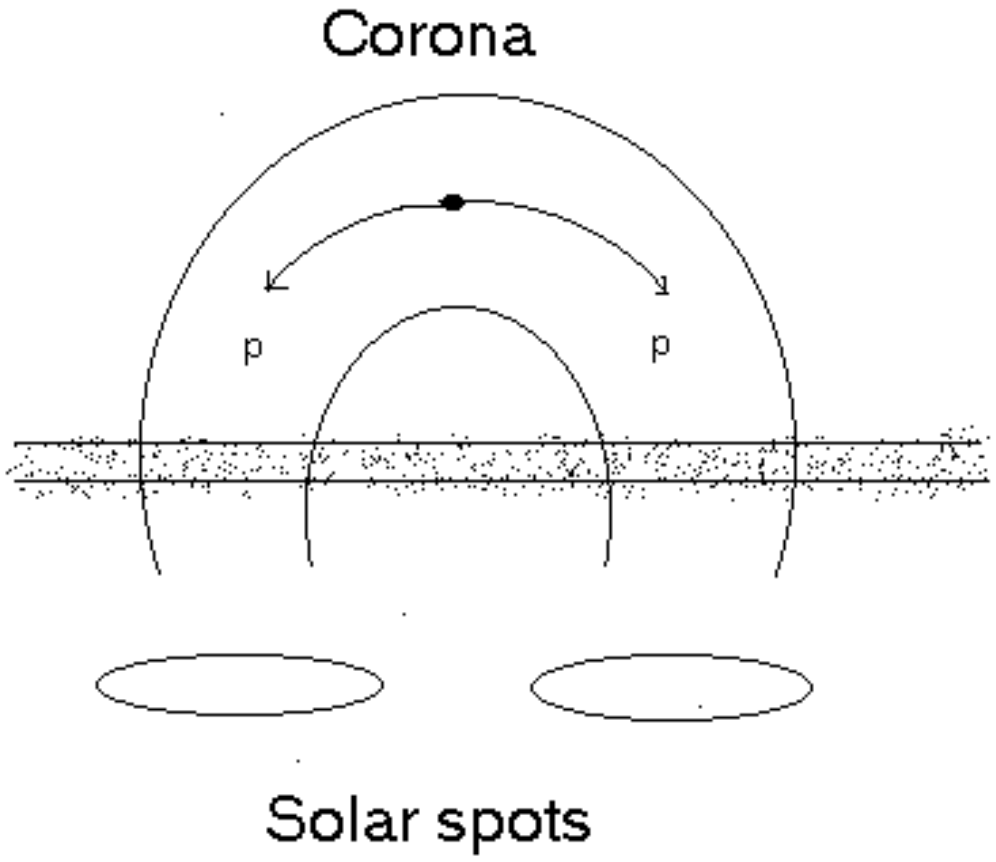

Figure 2: The schematic imagination of the magnetic loop of the solar flare.

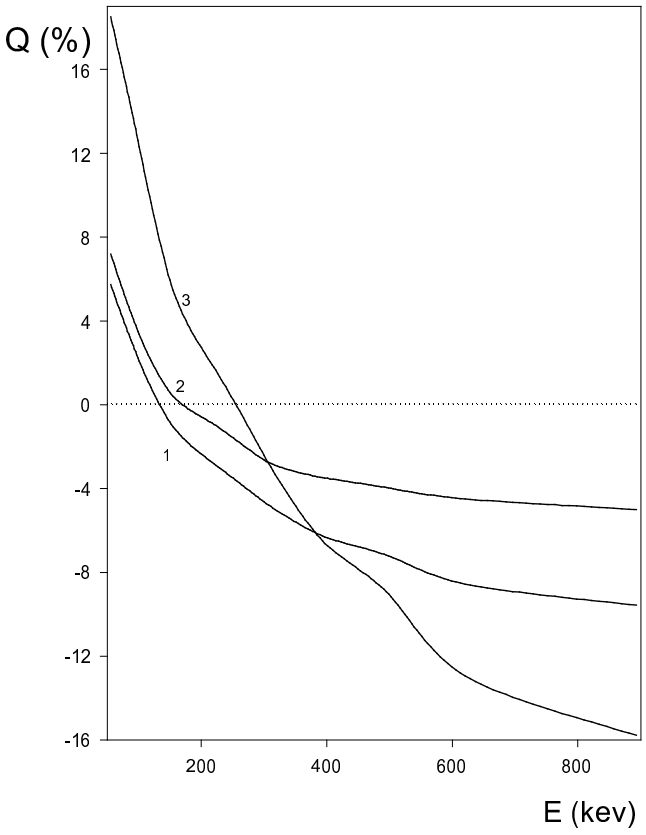

Figure 3: System of reference that was introduced for the interpretation of experimental data.

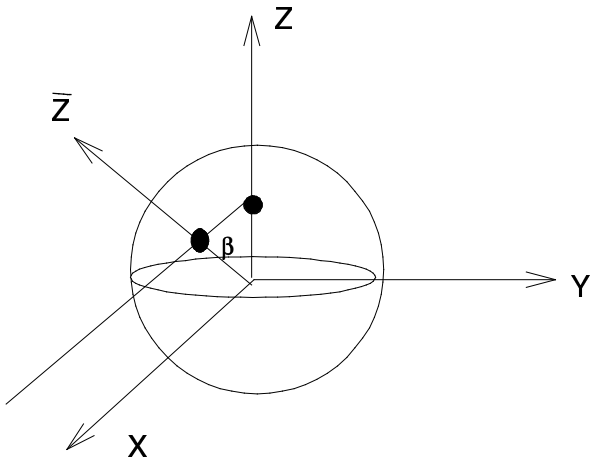

Figure 4: The dependence of the Stokes parameter $\tilde{Q}$ of the H_α emission on the value of the energy of proton beam: curve (1) the result of calculation in the base of 14 ($n = 1, 2, 3$) wave functions; curve (2) the experimental dependence [5]; curve (3) the result of calculation in the base of 10 ($n = 1, 3$) wave functions.

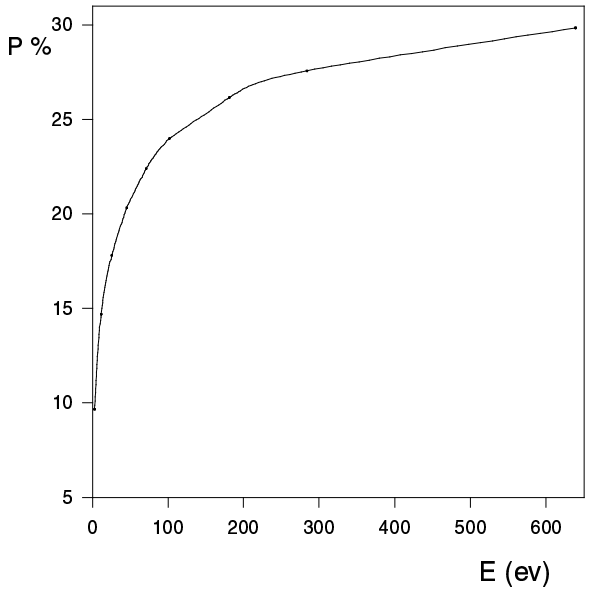

Figure 5: (a) The dependence of the polarization moments ρ_0^0 (curve 2) and ρ_0^2 (curve 1)on the value of the energy of the incident electron beam; (b) the dependence on the same value of the polarization characteristics of $^2P_3 - ^1D_2$ transition of oxygen atom.

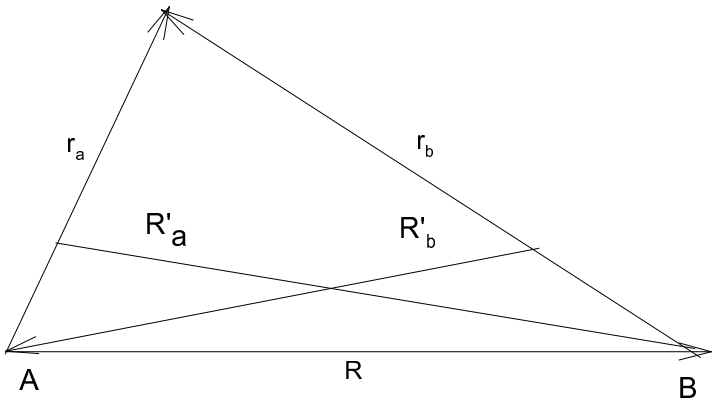

(a)

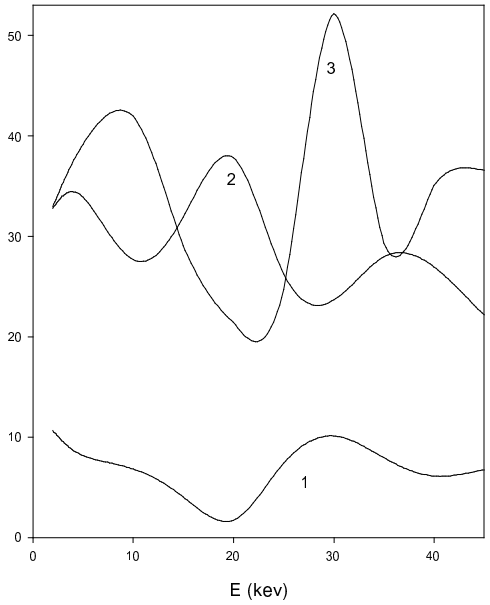

(b)

Figure 6: (a)- The systems of vectors that was introduced for the description of the position of electron th the field of two centers; (b) -the dependence of the Stokes parameters on the energy of relative motion for the partial transitions (1)- $4p \to 3d$, (2)- $4f \to 3d$ and (3)- $4d \to 3p$.

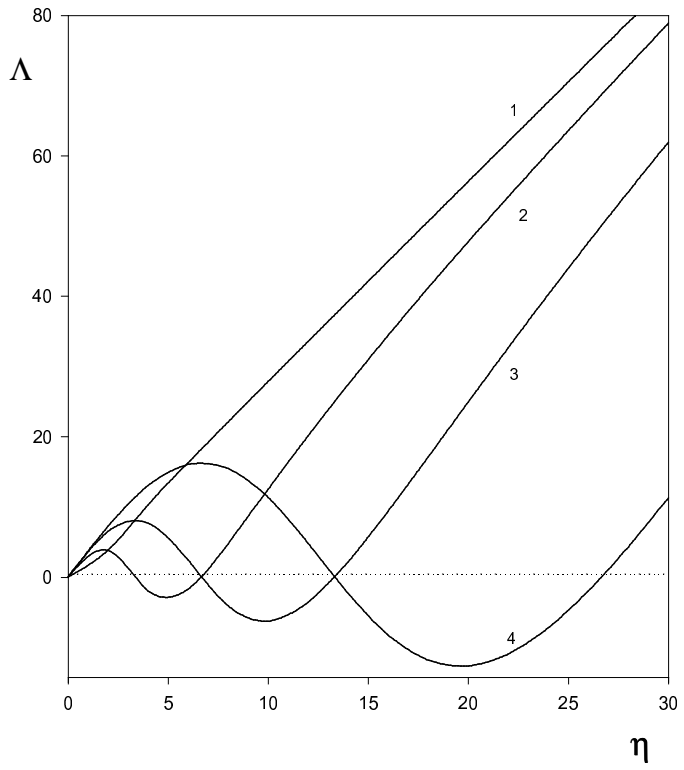

Figure 7: The dependence of value $\Lambda = U/Q$ on the value of the parameter η: curve (1) $a = 1$, curve (2) $a = 10$, curve (3) $a = 20$, curve (4) $a = 40$.

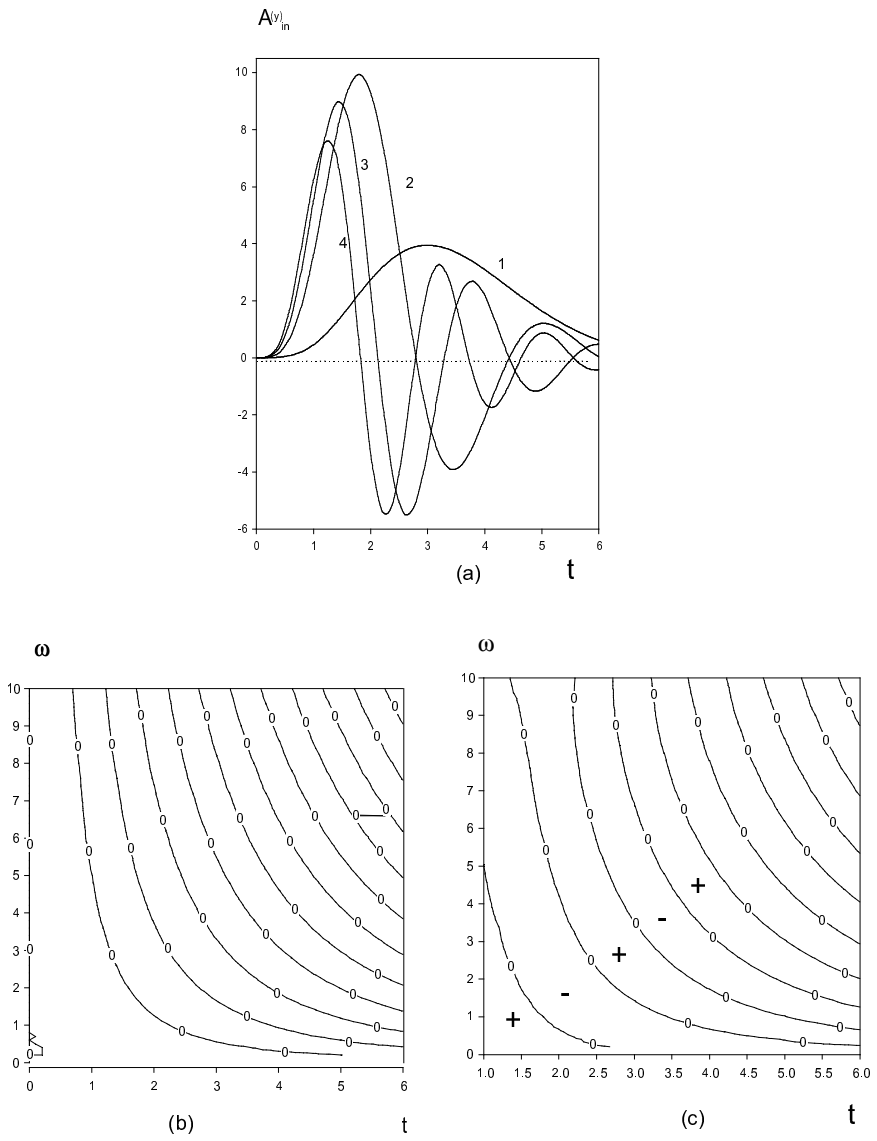

Figure 8: (a)- the dependencies of the inclined alignment, observed from the direction of the magnetic field, for the duration of the excited impulses $\widetilde{\tau} = 1$ and for some values of Larmor frequency ω ($\omega = 0.1$ curve 1, $\omega = 1$ curve 2, $\omega = 2$ curve 3, $\omega = 3$ curve 4; (b)-the solution equation $A_{in}^{(y)}(\omega, \widetilde{t}) = 0$. (c) - curves $\omega = \omega(t)$ on which the derivation of the function $A_{in}^{(y)}(\omega, \widetilde{t})$ is zero. The symbols plus or minuses denotes the sign of this derivation in corresponding area.

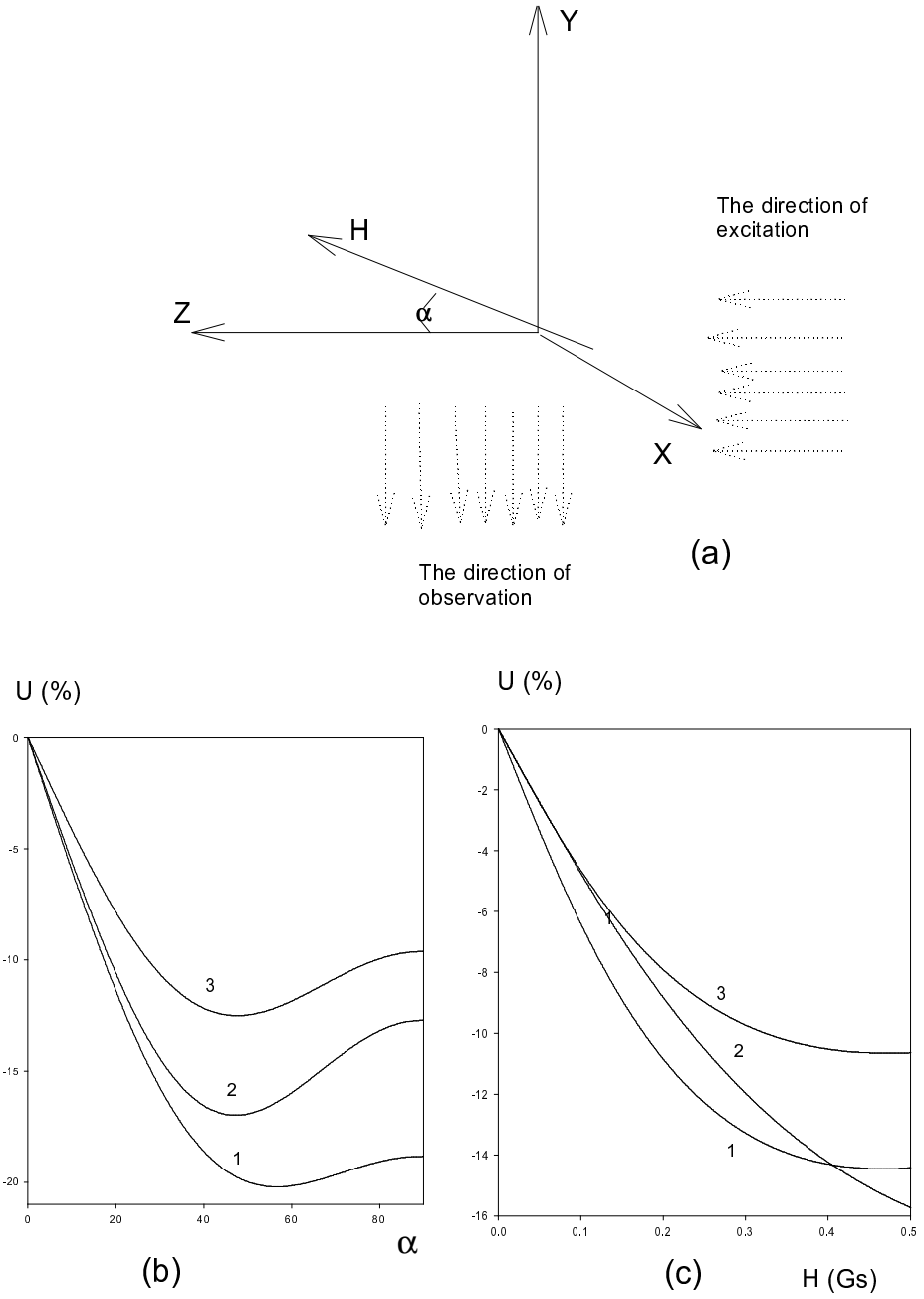

Figure 9: (a) the scheme of observation. (b) - the dependence of the Stokes parameter Q on the angle of inclination of the direction of geomagnetic field. The value of geomagnetic field is 0.5 Gs. Curve (1) - transition $3p^5S_2 - 4d^5P_3$, curve (2) - transition $3p^5P_2 - 4d^5D_3$ and curve (3) - $3s^3S_1 - 4p^3P_2$; (c) - the dependence of the Stokes parameter Q on the value of geomagnetic field. The angle of inclination is 30^o. Curve (1) - transition $3p^5S_2 - 4d^5P_3$, curve (2) - transition $3p^5P_2 - 4d^5D_3$ and curve (3) - $3s^3S_1 - 4p^3P_2$.

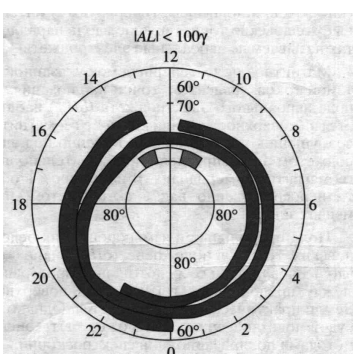

(a)

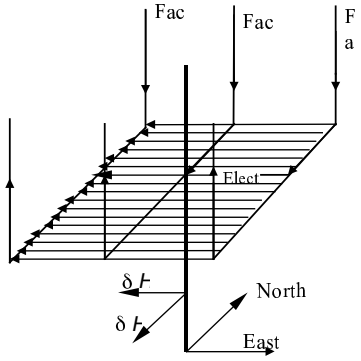

(b)

Figure 10: (a) - the distribution ot the file-aligned currents; (b)- the schematic imagination of current system and inducted by it the magnetic fields.

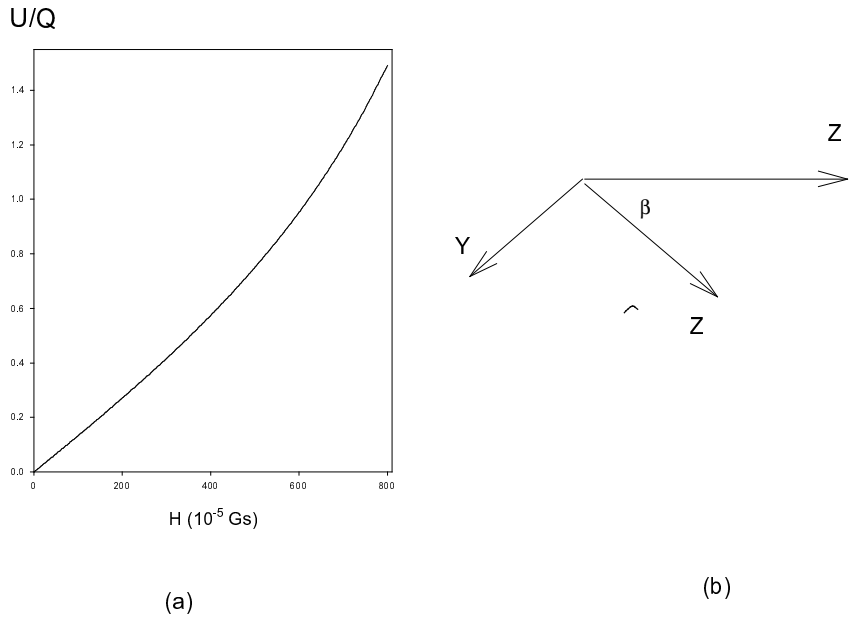

Figure 11: (a)- the dependence of the ratio U/Q for the transition $2^3P_1 - 3^5S_2$ of oxygen atom on the value of δH_{fac}, (b) - the system of reference that was introduced for the description of the light scattering by aerosol particles.

Density-Matrix Description of Atomic Radiative Emission from Autoionizing States in Electric and Magnetic Fields

V. L. Jacobs

Center for Computational Materials Science, Code 6390.2,
Materials Science and Technology Division,
Naval Research Laboratory,
Washington, D. C. 20375-5345

ABSTRACT

A polarization-density-matrix description has been developed for the investigation of the radiative emission during single-photon atomic transitions from autoionizing states in the presence of a general arrangement of static (or quasi-static) electric and magnetic fields. This description can be applied to the excitation of the autoionizing states by electrons with an anisotropic velocity distribution, which may be produced in an electron-ion beam experiment or in a non-equilibrium plasma environment. It is essential to allow for the coherent excitation of a particular subspace of the atomic autoionizing resonances. We present a general expression for the matrix elements of the detected-photon density operator, which provides a unified framework for the analysis of the total intensity, angular distribution, and polarization of the Stark-Zeeman spectral patterns. By means of this polarization-density-matrix description, a unified treatment of radiative and dielectronic recombination can be included. In order to incorporate environmental collisional and radiative relaxation (decoherence) processes, on an equal footing with the relevant autoionization and radiative decay processes, a more comprehensive quantum-opens-systems (reduced-density-matrix) formulation has been developed. This formulation provides a fundamental foundation for the self-consistent treatment of the non-equilibrium (coherent) autoionizing-state kinetics and the (homogeneous) spectral-lines shapes of the dielectronic-satellite transitions.

I. INTRODUCTION

Polarized atomic radiative emission is usually a result of a non-uniform (or non-statistical) distribution of the population densities among the degenerate (or nearly degenerate) angular-momentum magnetic (M) sublevels of the excited atoms (or ions). A non-uniform distribution of M-sublevel populations can be created by directed-electron excitation, laser- or optical-photon excitation, or by the action of electric or magnetic fields. The measurement and analysis of polarized radiative emission from bound-bound atomic transitions has been widely exploited to provide information on the nature of the various anisotropic (non-equilibrium) excitation mechanisms and the strength of the electric or magnetic fields. In the present investigation, a theoretical analysis of the total intensities, angular distributions and polarizations is developed specifically for atomic radiative transitions from autoionizing states in the presence of electric and magnetic fields.

Using a density-matrix approach, we have developed a very general quantum-mechanical description of polarized atomic radiative emission from autoionizing states in the presence of electric and magnetic fields. By means of this approach, we can take into account the quantum-mechanical interference phenomena associated with the coherent excitation of the autoionizing states. The present investigation may be regarded as a natural extension of our previously developed density-matrix description for atomic radiative emission in electric and magnetic fields [1], for which the primary emphasis was on bound-bound atomic radiative transitions. The electric-field induced enhancement of the radiation emitted in the dielectronic-recombination processes, which can be understood in terms of the electric-field induced modification of the radiationless-caputre and autoionizing rates,

has been theoretically predicted [2-4] and experimentally observed [5-7]. Recently, the alteration of electric-field enhanced dielectronic recombination by a perpendicular magnetic field has been theoretically investigated [8-10] and experimentally identified [11-13]. In our analysis of polarized atomic radiative emission from autoionizing states, we shall allow for a general set of steady-state (possibly coherent) atomic-excitation processes in the presence of an arbitrary arrangement of static (or quasi-static) electric and magnetic fields.

The spectroscopic observation of polarized atomic radiative emission in perpendicular (crossed) electric and magnetic fields is illustrated in Fig. 1. The special case of perpendicular electric and magnetic fields is encountered in numerous experimental arrangements. In their rest frame of reference, atomic systems moving in a magnetic field will be under the influence of a Lorentz (or motional) electric field. In any reference frame, an electromagnetic field can be treated as composed of perpendicular electric and magnetic field components, which are also perpendicular to the photon propagation direction. In both charged-particle beam and plasma environments, the total electric or magnetic field acting on the radiating atomic system must often be determined as the sum of an external (applied) field and an internal (possibly dynamical) field. In a high-density plasma, the action of the relatively slowly moving ions has been customarily treated (in the quasi-static approximation) in terms of an isotropic (nearly equilibrium) statistical distribution of static electric fields, but it is often necessary consider an anisotropic (non-equilibrium) component corresponding to turbulent electric fields. In a tokamak plasma, a dynamical (poloidal) magnetic field is generated perpendicular to the externally applied (toroidal) magnetic field. In a tokamak plasma, the viewing angle θ may be selected to be perpendicular to the known toroidal magnetic field. In an electron-ion beam experiment, the most convenient angle of observation is usually at a direction perpendicular to the electron beam. However, it has been recognized that more detailed spectroscopic investigations can

only be made by a variation of the angle of observation away from the perpendicular direction.

In the theoretical description of polarized atomic radiative emission, it is convenient to distinguish between a simple polarization-density-matrix description [1], which is applicable to an isolated atomic system combined with the relevant mode of the electromagnetic field, and a more difficult quantum-opens-systems reduced-density-matrix formulation [14], in which the influence of the larger system (environment) of charged particles and photons is treated in terms of relaxation (or decoherence) processes and spectral-line broadening mechanisms. The ordinary Hilbert-space quantum theory of polarized radiative emission, following directed-electron collisional excitation of an isolated atomic system (in the absence of electric and magnetic fields), was first presented by Oppenheimer [15] and subsequently refined by Percival and Seaton [16]. A polarization-density-matrix approach to this theory of radiative emission has been presented by Inal and Dubau for ordinary bound-bound atomic transitions [17] and subsequently extended to dielectronic recombination radiation [18]. A polarization-density-matrix description for dielectronic recombination radiation (in the absence of electric and magnetic fields) has been developed by Shlyaptseva, Urnov, and Vinogradov [19, 20] and applied by Shlyaptseva et al. [21] to spectroscopic observations on the electron beam ion trap EBIT at the Lawrence Livermore National Laboratory. Radiative emission from atomic transitions excited by electrons spirally in magnetic fields, where the electrons with velocity components perpendicular to the common electron-beam and magnetic-field direction acquire a helical trajectory, has been treated by Gu, Savin, and Beiersdorfer [22], using a polarization-density-matrix approach. In our previously-developed polarization-density-matrix description, which was primarily directed at bound-bound radiative transitions [1], we have exploited the methods and techniques advanced in our earlier density-matrix descriptions of the angular distribution and polarization in single-photon and multi-photon ionization

processes [23, 24], as well as in the density-matrix analyses presented by Inal and Dubau [17, 18]. The present more comprehensive reduced-density-matrix formulation has been based on a fundamental (Liouville-space) quantum-open-systems approach. This formulation provides a detailed description for a general set of steady-state non-equilibrium (possibly coherent) excitation and de-excitation processes involving the atomic autoionizing states, in the presence of an arbitrary arrangement of static (or quasi-static) electric and magnetic fields and under the influence of environmental collisional and radiative relaxation (or decoherence) processes.

II. POLARIZATION-DENSITY-MATRIX DESCRIPTION

Various versions of the polarization-density-matrix formalism has been discussed by Fano [25], Jacobs [23, 24], Blum ([26], and by Kazantsev and J.-C. Hénoux [27]. In our density-matrix description of polarized radiative emission, we have assumed that the matrix of the total Hamiltonian operator, describing the many-electron atomic system in the presence of an arbitrary arrangement of static (or quasi-static) electric and magnetic fields, has been diagonalized in a basis set of field-free atomic eigenstates. The complete atomic basis set consists of discrete bound states, discrete autoionizing resonances, and non-resonant continuum (electron-ion scattering) states. The autoionizing-state excitation and spontaneous radiative emission processes will be treated as independent events. However, in a generalized collisional-radiative model, all important excitation and de-excitation processes must be taken into account in the determination of the initial autoionizing-state density matrix. The initial excitation process is accordingly treated in terms of a density matrix, whose diagonal elements give the familiar population densities of the autoionizing states and whose non-diagonal elements correspond to the autoionizing-state coherences.

The steady-state (frequency-dependent) intensity, angular distribution, and polarization of the radiation that is emitted in the atomic transitions $\gamma_i \rightarrow \gamma_f$ can be determined from the photon-polarization density operator. In terms of the transition operator T, whose lowest-order contribution is given by the electromagnetic-interaction operator V, the matrix elements of the photon-polarization density operator can be expressed in the form

$$\left\langle \lambda | \rho^R | \lambda' \right\rangle = \sum_{f,\, i,\, i'}{}' \left\langle \gamma_f, \vec{k}\lambda | T | \gamma_i, 0 \right\rangle \left\langle \gamma_i | \rho^A | \gamma_{i'} \right\rangle \left\langle \gamma_{i'}, 0 | T | \gamma_f, \vec{k}\lambda' \right\rangle. \qquad (1)$$

The photon-helicity quantum numbers may have the numerical values $\lambda, \lambda' = \pm 1$, corresponding the right and left circular polarization along the direction of observation. The summations over f, i, and i' include the quantum numbers specifying degenerate or nearly degenerate sublevels of the field-dependent final and initial states in the atomic radiative transitions $\gamma_i \rightarrow \gamma_f$. These restricted summations are indicated by the prime above the summation symbol in Eq. (1). ρ^A is the density operator representing the field-dependent atomic autoioning states. The quantum-mechanical interference between radiative and dielectronic recombination can be incorporated by taking into account the autoionizing-state coherences, which correspond to the non-diagonal elements of ρ^A. In order to determine the precise spectral distribution of the possibly overlapping Stark and Zeeman components, it is necessary to retain the high-order contributions in the perturbation expansion for the transition operator T. These high-order contribution give rise to energy shifts and spectral widths of the dielectronic satellite lines.

Since polarization is intimately related to angular momentum, it is advantageous to employ the angular-momentum representation for the discrete bound states, discrete

autoionizing resonances, and non-resonant continuum atomic states. We also employ the electromagnetic-multipole expansion for the quantized radiation field. Accordingly, we will assume that the field-dependent initial atomic eigenstates can be expanded in a basis set of field-free angular-momentum eigenstates:

$$|\gamma_i\rangle = \sum_{\Delta_i J_i M_i} |\Delta_i J_i M_i\rangle\langle\Delta_i J_i M_i|\gamma_i\rangle. \qquad (2)$$

Here J_i is the total electronic angular momentum, M_i is the component along a suitably chosen atomic quantization axis, and Δ_i denotes the set of remaining quantum numbers. Hyperfine structure will be ignored in our analysis. The field-dependent final atomic eigenstates can be represented by an expansion in the same form as Eq. (2). We emphasize that the complete basis set of field-free atomic states must include the bound states, the autoionizing resonances, and the non-resonance electron-ion-scattering (continuum-channel) states. It is also well know that the field-free unperturbed-eigenstate expansion, while formally complete, may not provide an economical representation for atomic systems under the influence of strong fields.

The photon-polarization parameters, which are most naturally defined with respect to the direction of spectroscopic observation, can be conveniently related to the fundamental electromagnetic-transitions amplitudes, which are usually defined with respect to the atomic quantization axis. This can be most readily accomplished by introducing the expansion of the radiative-transition matrix elements in terms of the matrix elements of effective electric and magnetic multipole operators:

$$\left\langle \Delta_f\, J_f\, M_f\,,\, \vec{k}\lambda | T | \Delta_i\, J_i\, M_i\,,\, 0 \right\rangle = \sum_j \sum_m \left(\frac{2j+1}{4\pi} \right)^{1/2} A(j) D^{(j)}_{\lambda m}(\hat{k}) \times (-1)^m \left\langle \Delta_f\, J_f\, M_f \left| \tilde{Q}^{(j)}_{-m} \right| \Delta_i\, J_i\, M_i \right\rangle . \tag{3}$$

Here $\tilde{Q}^{(j)}_{-m}$ denotes the irreducible spherical-tensor form of the effective electromagnetic-multipole-moment operator, whose lowest-order value is the usual electromagnetic-multipole-moment tensor operator $Q^{(j)}_{-m}$. The quantities $D^{(j)}_{\lambda m}(\hat{k})$ designate the matrix elements $D^{(j)}_{\lambda m}(\phi,\theta,0)$ of the Wigner rotation operator that corresponding to the desired coordinate rotation. The multiplying factors A(j) are defined in accordance with the particular types of electromagnetic-multipole components. The matrix elements of the effective electromagnetic-multipole-moment operator can be evaluated in the angular-momentum representation, in terms of Wigner 3-j symbols and reduced electromagnetic-multipole-moment matrix elements, using the Wigner-Eckart theorem:

$$\left\langle \Delta_f\, J_f\, M_f \left| \tilde{Q}^{(j)}_m \right| \Delta_i\, J_i\, M_i \right\rangle = (-1)^{J_f - M_f} \begin{pmatrix} J_f & j & J_i \\ -M_f & m & M_i \end{pmatrix} \times \left(\Delta_f\, J_f \left\| \tilde{Q}^{(j)} \right\| \Delta_i\, J_i \right). \tag{4}$$

In order to take into account both the electric and the magnetic multipole contributions associated with a given value of j, $\tilde{Q}^{(j)}_{-m}$ should be defined to include the contributions associated with all permissible values of the photon parity.

For ordinary bound-bound radiative transitions, our expression for the photon-polarization density matrix has been presented by Jacobs and Filuk [1]. In the derivation of this expression, we retained only the lowest-order contribution in the perturbation-theory

expansion of the electromagnetic-transition operator T. In order to provide a more detailed spectral description for radiative transitions from autoionizing states, as well as to incorporate the quantum-mechanical interference phenomena, we now consider the entire electromagnetic-transition operator and employ the effective electromagnetic-multiple-moment operators $\tilde{Q}^{(j)}_{-m}$. The corresponding generalized expression for the photon-polarization density matrix elements may be presented in the form:

$$
\begin{aligned}
\langle \lambda | \rho^{R} | \lambda' \rangle \;=\; & {\sum_{i,i',f}}' \langle \gamma_i | \rho^{A} | \gamma_{i'} \rangle \\
& \times \sum_{\Delta_f J_f M_f} \sum_{\Delta_f' J_f' M_f'} \langle \gamma_f | \Delta_f J_f M_f \rangle \langle \gamma_f | \Delta_f' J_f' M_f' \rangle^{*} \\
& \times \sum_{\Delta_i J_i M_i} \sum_{\Delta_i' J_i' M_i'} \langle \Delta_i J_i M_i | \gamma_i \rangle \langle \Delta_i' J_i' M_i' | \gamma_{i'} \rangle^{*} \\
& \times \sum_{j,m} \sum_{j',m'} \sum_{J,M,M'} \left(\Delta_f J_f \| \tilde{Q}^{(j)} \| \Delta_i J_i \right) \left(\Delta_f' J_f' \| \tilde{Q}^{(j')} \| \Delta_i' J_i' \right)^{*} \\
& \times \left(\frac{1}{4\pi} \right) (2j+1)^{1/2} (2j'+1)^{1/2} (2J+1)\, A(j)\, A(j')^{*} \\
& \times (-1)^{J_f + J_f' - M_f - M_f' - m - m' + \lambda' - m' + 2j - 2j' - M - M'} \\
& \times \begin{pmatrix} J_f & j & J_i \\ -M_f & -m & M_i \end{pmatrix} \begin{pmatrix} J_f' & j' & J_i' \\ -M_f' & -m' & M_i' \end{pmatrix} \qquad (5) \\
& \times \begin{pmatrix} j & j' & J \\ \lambda & -\lambda' & -M \end{pmatrix} \begin{pmatrix} j & j' & J \\ m & -m' & -M \end{pmatrix} D^{(J)}{}_{MM'} \left(\hat{k} \right).
\end{aligned}
$$

The prime above the summation symbol is used to indicate that the summations over f, i, and i' are to be taken over quantum numbers specifying degenerate or nearly degenerate field-dependent sublevels, as in Eq. (1). Although we are primarily concerned with electric-dipole transitions from the autoionizing levels, we find it advantageous to retain the generality for arbitrary electromagnetic-multipole interactions, including the interference between different multipole amplitudes. We also emphasize that this expression can be employed for an arbitrary arrangement of electric and magnetic fields and for a general set

of steady-state (non-equilibrium) excitation processes. If we neglect field-induced mixing of the atomic eigenstates, our general expression for the photon-polarization density matrix may be reducible to the result obtained by Inal and Dubau [18], who investigated the directed electron excitation of polarized atomic radiative emission during dielectronic-recombination satellite transitions in the absence of electric and magnetic fields. However, it should be pointed out that the density-matrix formulation used here is based on a boundary condition in which the initial atomic states are taken as the autoionizing resonances. This leads to a formulation that is different than the one presented by Inal and Dubau [18], which is based on the boundary condition involving the initial electron-ion continuum states. In the application of our formulation to electron-ion beam experiments, the dependence on the electron direction would occur in the generalized collisional-radiative-model determination of the initial autoionizing-state density–matrix elements.

The matrix elements of photon-polarization density operator have been expressed in a non-perturbative form, in terms of the reduced matrix elements of the effective electromagnetic-multiple-moment operators, by means of Eq. (5). These matrix elements are explicitly given as functions of the photon-emission direction, in terms of which the photon-helicity quantum number λ is defined. Following Fano and Racah [28], Happer [29], Omont [30], and Baylis [31], this photon-polarization density operator may be presented as an expansion in terms of the irreducible spherical-tensor operators $T^{(J)}_M(j,j')$:

$$\rho^R = \sum_{j,j'} \sum_{J,M,M'} \rho^R(j,j';J,M') T^{(J)}_M(j,j') D^{(J)}_{MM'}(\hat{k}). \qquad (6)$$

The coefficients $\rho^R(j,j';J,M')$ are referred to as the irreducible spherical-tensor components of the photon-polarization density operator. The irreducible spherical-tensor

representation of the photon density operator is advantageous, because only a very few electromagnetic multipoles are normally involved in any atomic radiative-emission process. In contrast, the irreducible spherical-tensor representation of the field-dependent atomic autoionizing-state density operator, which may be expressed in the form

$$\rho^{A} = \sum_{\Delta_i \Delta_i'} \sum_{J_i J_i'} \sum_{K,N} \rho^{A}(\Delta_i \Delta_i' J_i J_i'; K, N)\, T^{(K)}{}_{N}(J_i J_i'), \tag{7}$$

involves two expansions that should be taken over the entire basis set of unperturbed field-free atomic eigenstates. Consequently, the irreducible spherical-tensor representation of the atomic density operator could be advantageous for weak fields or perhaps for parallel electric and magnetic fields. For atomic systems with axially symmetry, in which case N = 0, it is useful to introduce a representation of the atomic autoionizing-state density operator in terms of components describing orientation (corresponding to odd values of K) and alignment (corresponding to even values of K).

The photon-polarization density operator is most commonly presented in a representation based on the Stokes parameters. This representation can be expressed as follows [26]:

$$\rho^{R} = \left(\frac{I}{2}\right)\begin{pmatrix} 1+\eta_2 & -\eta_3 + i\eta_1 \\ -\eta_3 - i\eta_1 & 1-\eta_2 \end{pmatrix}. \tag{8}$$

The total spectral intensity I, summed over all photon-polarization states, is determined by the normalization condition on ρ^{R}. The parameters η_1 and η_3 specify linear polarization, while η_2 represents circular polarization. Using the non-perturbative approach, involving the entire electromagnetic-transition operator T rather than the lowest-order contribution V,

the 4 photon-polarization parameters can be determined, as functions of the frequency and direction, by means of our polarization-density-matrix formulation.

The complex dependence on the electric and magnetic fields is incorporated in the coefficients $\langle \Delta_i J_i M_i | \gamma_i \rangle$ and $\langle \Delta_f J_f M_f | \gamma_f \rangle$, which must be determined by a diagonalization, in the field-free angular-momentum basis representation, of the Hamiltonian H describing the atomic system in the presents of the electric and magnetic fields. The electric-field induced mixing of the autoionizing states can significantly alter the radiationless electron capture and autoionization rates [2], which occur in the collisional-radiative model used in the determination of the autoionizing-state populations. Physically, the enhancement of the dielectronic-recombination radiation in the presence of an electric field may be understood as a redistribution of population among the outer-electron nl levels toward higher-l states, which have negligible field-free autoionization rates and radiative decay rates that are essentially independent of l.

III. REDUCED-DENSITY-MATRIX FORMULATION

The quantum-open-systems, reduced-density-matrix approach can provide the fundamental basis for a non-perturbative and non-equilibrium quantum-statistical description of electromagnetic interactions involving many-electron atomic systems in electron-ion beam interactions and in high-temperature laboratory and astrophysical plasmas. Specifically, account can be taken of the multitude of additional interactions that arise from the influence of the much larger system (environment) of charged-particles and photons. The environment is assumed to be not significantly affected by the interactions with the much smaller (relevant) atomic system. However, the dynamical evolution and electromagnetic transitions of the atomic system can be significantly altered by the

environmental collisional and radiative interactions. Within the context of the quantum-open-systems approach, these environmental interactions are treated as relaxation or decoherence processes and spectral-line broadening mechanisms.

The partition of the entire, interacting quantum system into a relevant subsystem (consisting of the atomic system and the observed photon mode) and an environment is by no means unique. In addition, the appropriate decomposition may strongly depend on the particular type of measurement that is desired. In the ordinary Hilbert-space quantum-mechanical perturbation theory, different partitions of the total Hamiltonian operator H into an unperturbed Hamiltonian operator H_0 and an interaction operator V would be equivalent if the interaction could be taken into account to all orders in the perturbation expansion. In contrast, different partitions in the quantum-open-systems reduced-density-matrix description are intrinsically inequivalent and will inevitably lead to different approximations.

A general statistical state of the combined, interacting quantum system is represented by the complete density operator ρ, which is conventionally assumed to be initially expressible as the uncorrelated, tensor-product of the density operators representing the initial state of the relevant quantum system and the initial quantum state of the very large collisional and radiative environment. The relevant quantum system will consist of the many-electron atomic system (which is initially in a set of autoionizing states) combined (entangled) with the relevant (observable) modes of the quantized radiation field. The final state of the entire, interacting quantum system corresponds to the final state of the atomic system (in the set of final states following the stabilizing radiative transitions from the autoionizing states), combined with that of the detected photons. The radiative transitions occur under the simultaneous influence of the environmental collisional and radiative relaxation (decoherence) phenomena.

The statistical state of the quantum subsystem of interest (consisting of the many-electron atomic system and the detected photons) can be most generally expressed by means of the reduced, relevant density operator ρ^r, which is defined most directly in terms of an average (trace) operation over the quantum numbers specifying the environmental degrees of freedom. Alternatively, it is advantageous to formally introduce the reduced description by adopting an abstract procedure based on the Zwanzig Liouville-space projection operators. We emphasize that, in the reduced-density-operator description, the interactions of the quantum subsystem of interest with the environment are treated stochastically, as collisional and radiative relaxation (decoherence) processes and spectral-line broadening mechanisms. For the treatment of coherent interactions, the reduced, relevant system must obviously be defined to include all coherently coupled (entangled) subsystems.

In the time-independent (frequency-domain) version of our reduced-density-operator description, the radiative-transition rate is expressed in the generalized golden-rule form [14]

$$\begin{aligned} A_{\mathrm{Rad}}(i \to f, \omega) &= -i \lim_{\varepsilon \to 0} \left\langle\!\left\langle P_f{}^r \middle| \overline{T}^r(+i\varepsilon) \middle| \rho_i{}^r \right\rangle\!\right\rangle \\ &= -i \lim_{\varepsilon \to 0} \left\langle\!\left\langle P_f{}^r \middle| \overline{V}^r + \overline{V}^r \, \frac{1}{+i\varepsilon - \overline{L}^r - \overline{\Sigma}(+i\varepsilon)} \, \overline{V}^r \middle| \rho_i{}^r \right\rangle\!\right\rangle . \end{aligned} \tag{9}$$

The quantity $\overline{T}^r(+i\varepsilon)$ is the Liouville-space analogue of the ordinary Hilbert-space transition operator T, and the asymptotic (scattering-theory) boundary condition is indicated by the $\varepsilon \to 0$ limit. The relevant Liouville-space operator $\overline{L}^r$ (or Liouvillian operator) is defined in terms of the commutator of the full (relevant) subsystem Hamiltonian operator

H^r describing the many-electron atomic system together (entangled) with the restricted set of observed photons. The relevant Liouville-space interaction operator $\overline{V}^r$ includes the electromagnetic interaction of the atom system, together with the interaction responsible for autoionization. The initial state of the relevant subsystem is represented by the density operator $\rho_i{}^r$. In this investigation, the initial-state density operator represents the autoionizing-state populations and coherences. The Liouville-space self-energy operator $\overline{\Sigma}$, which is the result of the quantum-open-systems (reduced-density-operator) description, represents the effects of the environmental electron-electron, electron-ion, and electron-photon relaxation processes. The single-photon spontaneous emission process is formally described by means of the final-state projection operator $P_f{}^r$. For single-photon absorption or multi-photon processes, the relevant final-state projection operators will have different definitions. The Zwanzig Liouville-space projection operators, which occur in the explicit expression for the Liouville-space self-energy operator, introduce (quantum-statistical) averages over the environmental degrees of freedom. Although these averages are often carried out assuming Maxwellian and Boltzmann equilibrium distributions for the free and bound electrons, respectively, and Bose-Einstein equilibrium distributions for the photons, our general formulation is applicable to non-equilibrium distributions.

The general (tetradic-matrix) form of the expression given by Eq. (9) can be used to determine the spectral-line shape for an array of (possibly overlapping) emission lines due to radiative transitions among the sublevels from two groups of closely-spaced upper (autoionizing) and lower (bound) atomic levels. The Liouville-space self-energy operator $\overline{\Sigma}$, which occurs in Eq. (9) as a correction to (renormalization of) the unperturbed (environment-free) Liouville-space resolvent operator, is defined in the reduced, relevant subspace spanned by the eigenstates representing the many-electron atomic system combined (entangled) with the observed photon states. Consequently, the Liouville-space

self-energy operator is in general a function of the emitted photon energy (or frequency ω). In the widely used isolated-line approximation, the standard Lorentzian spectral-line shape can be recovered from the general expression. In the perturbation expansion for the Liouville-space self-energy operator, in powers of the full Liouville-space interaction operator, only the lowest-order contribution is usually taken into account in the determination of the total (isolated-line) shift and width. In this approximation, the isolated-line shift and width can be expressed as the sums of the partial contributions from the individual collisional and radiative relaxation processes acting alone. Quantum-mechanical interference between the individual collisional and radiative transition amplitudes can occur in the high-order perturbation-theory contributions to the isolated-line width and shift and in our more general (matrix) profile expressions describing overlapping lines. In order to include Stark and Zeeman broadening, the spectral-line-shape formula must be evaluated in a basis of electric-field and magnetic-field dependent atomic eigenstates, as discussed in the preceding section. The atomic states could be determined taking into account a quasi-static (ion-produced) plasma electric microfield and a (poloidal+toroidal) magnetic field or an arbitrary arrangement of externally applied static (or quasi-static) electric and magnetic fields. In order to make comparisons with experimental observations, it is usually necessary to include either the equilibrium or non-equilibrium Doppler effect, which is a major source of inhomogeneous broadening.

The time-dependent (time-domain) version of our reduced-density-operator description is based on the equation of motion for the reduced, relevant density operator. The reduced equation of motion can be derived from the Liouville-von Neumann equation for the combined, complete density operator. The reduced equation of motion can be expressed in the generalized-Master-equation form [14]:

$$\frac{\partial}{\partial t}\rho^{r}(t) \;=\; -i\,\overline{L}^{r}(t)\rho^{r}(t) - i\int_{t_0}^{t} dt'\,\overline{\Sigma}(t,t')\rho^{r}(t')\;. \qquad (10)$$

The self-energy operator kernel $\overline{\Sigma}(t,t')$, which represents the time-dependent renormalization due to the environmental interactions, can be formally related to the frequency-dependent self-energy $\overline{\Sigma}$ operator occurring in the time-independent (resolvent-operator) formulation. The formal relationship, which involves a Fourier transformation, serves as the fundamental basis for a self-consistent treatment of non-equilibrium (possibly coherent) atomic-state kinetics and (homogeneous) spectral-line shapes. Fig. 2 provides an illustration emphasizing the role of this relationship in connecting the time-domain (equation-of-motion) and the frequency-domain (resolvent-operator) versions of the reduced-density-matrix approach. In the commonly adopted Markov (short-memory-time) approximation, the self-energy operator kernel is assumed to be independent of time. In this approximation, the corresponding frequency-domain self-energy operator, which gives rise to the spectral-line shifts and widths of the dielectronic satellite transitions, is independent of the frequency. (For the treatment of ultra-short-pulse optical-laser interactions, the Markov approximation may not be valid.) A set of (further reduced) quantum-kinetics equations for the atomic-level population densities (corresponding to the diagonal reduced-density-matrix elements), together with the atomic-state coherences (represented by the non-diagonal reduced-density-matrix elements), can be derived from Eq. (10) by performing the average (trace) operation over the (relevant) degrees of freedom specifying the observed photon states. The result may be described as a generalized collisional-radiative model, which can be used to determine the populations of the autoionizing states and as well as the autoionizing-state coherences. In addition, the corresponding quantum-kinetics equation for the reduced density matrix describing the observed radiation field can be obtained from Eq. (10) by carrying out the average (trace) operation over the relevant atomic states. If the radiation-field coherences are neglected, the

quantum-kinetics equation for the spectral intensity of the radiation field can be obtained in the form of the familiar equation of radiation transport. The usual (in-out) asymptotic boundary condition of scattering theory, upon which the time-independent (resolvent-operator) description is based, may not be what is desired, especially in the description of ultra-short-pulse optical-laser interactions. Consequently, the time-dependent (equation-of-motion) formulation is often viewed as providing a more flexible foundation for the investigation of general electromagnetic interactions. In order to obtain the generalized Master equation in a closed form rather than as a part of correlation hierarchy, it is necessary to invoke the conventional assumption that the initial-state density operator, referring to the entire interacting system of charged particles and electromagnetic radiation fields, can be expressed in the factorized, tensor-product form. This assumption implies that initial-state correlations can be neglected. However, correlations between collisional and radiative processes are introduced as a result of the general time evolution of the density operator.

As in the time-independent (resolvent-operator) formulation, it is convenient to expand the self-energy operator kernel $\overline{\Sigma}(t,t')$ in a perturbation expansion in powers of the full Liouville-space interaction operator. The time-dependent perturbation-theory analysis is most generally carried out in the Liouville-space interaction representation, in place of the Schrödinger representation adopted in the derivation of Eq. (10). Since the full Liouville-space interaction operator is the sum of electron-electron, electron-ion, and electron-photon interaction operators, the (tetradic) matrix elements of the self-energy operator kernel can involve quantum-mechanical interference terms. Taking into account only the lowest-order perturbation-theory contributions to the self-energy operator kernel, the equation of motion for the atomic-state population densities can be expressed in terms of the familiar collisional and radiative transition rates that are obtained from an evaluation of the standard golden-rule formula of ordinary Hilbert-space perturbation theory. The optical Bloch equations

correspond to the extended set of equations, taking into account the atomic-state coherences.

IV. SUMMARY AND CONCLUSIONS

A polarization-density-matrix description has been under development for the investigation of the total intensity, angular distribution, and polarization of atomic radiative emission from autoionizings levels in an arbitrary arrangement of static (or quasi-static) electric and magnetic fields. A general set of steady-state (possibly coherent) excitation and de-excitation processes may be taken into account in the determination of the (non-equilibrium) populations and coherences of the initial autoionizing states. The quantum-mechanical interference between radiative and dielectronic recombination is described by allowing for the coherent steady-state excitation of the autoionizing states. A quantum-open-systems (reduced-density-matrix) formulation has also been developed to self-consistently treat the influence of the environmental collisional and radiative relaxation (decoherence) processes on the time evolution of the autoionizing-state density operator and on the spectral-line shapes of the Stark-Zeeman spectral patterns. Further details of this investigation will be presented in a more extensive paper.

ACKNOWLEDGMENTS

This work has been supported by the Department of Energy and by the Office of Naval Research.

REFERENCES

[1] V. L. Jacobs and A. B. Filuk, Phys. Rev. A **60**, 1975 (1999).

[2] V. L. Jacobs, J. Davis, and P. C. Kepple, Phys. Rev. Letters **37**, 1390 (1976).

[3] K. LaGattuta and Y. Hahn, Phys. Rev. Letters **51**, 558 (1983).

[4] D. C. Griffin, M. S. Pindzola, and C. Bottcher, Phys. Rev. A **33**, 3124 (1986).

[5] A. Muller, D. S. Belic, B. D. DePaola, N. Djuric, G. H. Dunn, D. W. Mueller, and C. Trimmer, Phys. Rev. Letters **56**, 127 (1986).

[6] P. F. Dittner, S. Datz, P. D. Miller, P. L. Pepmiller, and C. M. Fou, Phys. Rev. A **33**, 124 (1986).

[7] D. W. Savin, L. D. Gardner, D. B. Reisenfeld, A. R. Young, and J. L. Kohl, Phys. Rev. A **53**, 280 (1996).

[8] F. Robicheaux and M. S. Pindzola, Phys. Rev. Letters **79**, 2237 (1997).

[9] D. C. Griffin, F. Robicheaux, and M. S. Pindzola, Phys. Rev. A **57**, 2708 (1998).

[10] K. LaGattuta and G. Borca, J. Phys. B **31**, 4781 (1998),

[11] D. W. Savin et al., Phys. Rev. A **53**, 280 (1996).

[12] T. Bartsch et al., Phys. Rev. Letters **99**, 3779 (1999).

[13] V. Klimenko and T. F. Gallagher, Phys. Rev. Letters **85**, 3357 (2000).

[14] V. L. Jacobs, J. Cooper, and S. L. Haan, Phys. Rev. A **50**, 3005 (1994).

[15] J. R. Oppenheimer, Z. Phys. **43**, 27 (1927).

[16] I. C. Percival and M. J. Seaton, Phil. Trans. R. Soc. A **251**, 113 (1958).

[17] M. K. Inal and J. Dubau, J. Phys. B **20**, 4221 (1987).

[18] M. K. Inal and J. Dubau, J. Phys. B **22**, 3329 (1989).

[19] A. S. Shlyaptseva, A. M. Urnov, and A. V. Vinogradov, P. N. Lebedev Physical Institute of the U. S. S. R. Academy of Sciences Report No. **194**, 1981.

[20] A. V. Vinogradov, A. M. Urnov, and A. S. Shlyaptseva, in *Atomic and Ionic Spectra and Elementary Processes in Plasmas*, Proceedings of the P. N. Lebedev Physics Institute, Academy of Sciences of Russia, Vol. **912**, Edited by I. I. Sobelman (Nova Science Publishers, Commack, New York, 1992), 93.

[21] A. S. Shlyaptseva et al., Phys. Rev. A **57**, 888 (1998).

[22] M. F. Gu, D. W. Savin, and P. Beiersdorfer, J. Phys. B **32**, 5371 (1999).

[23] V. L. Jacobs, J. Phys. B **5**, 2257 (1972).

[24] V. L. Jacobs, J. Phys. B **6**, 1461 (1973).

[25] U. Fano, Rev. Mod. Phys. **29**, 74 (1957).

[26] K. Blum, *Density Matrix Theory and Applications* , Second Edition, (Plenum, New York, 1996).

[27] S. A. Kazantsev and J.-C. Hénoux, *Polarization Spectroscopy of Ionized Gases*, (Kluwer, Dordrecht, 1995).

[28] U. Fano and G. Racah, *Irreducible Tensorial Sets*, (Academic Press, New York, 1959).

[29] W. Happer, Rev. Mod. Phys. **44**, 169 (1972).

[30] A. Omont, Progress in Quantum Electronics **5**, 69 (1977).

[31] W. E. Baylis, in *Progress in Atomic Spectroscopy*, edited by W. Hanle and H. Kleinpoppen (Plenum, New York, 1979).

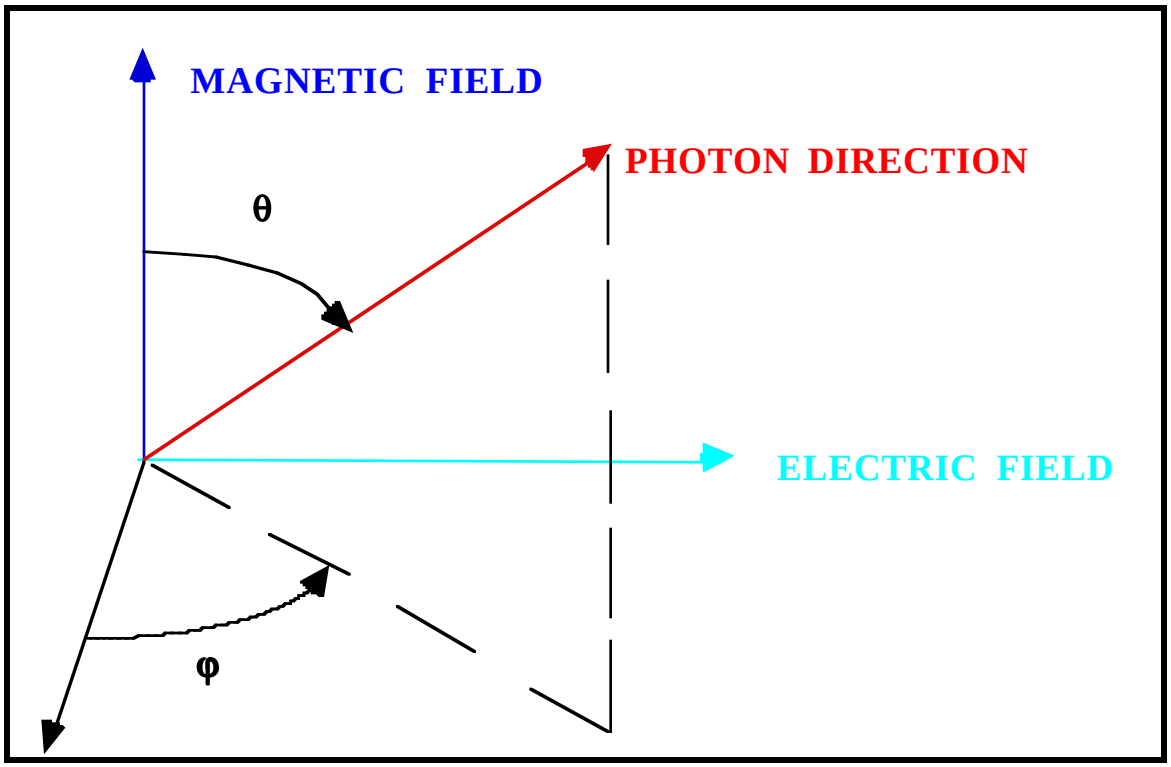

Fig. 1. Viewing angles for spectroscopic observations of polarized atomic radiative emission from autoionizing states in perpendicular (crossed) electric and magnetic fields.

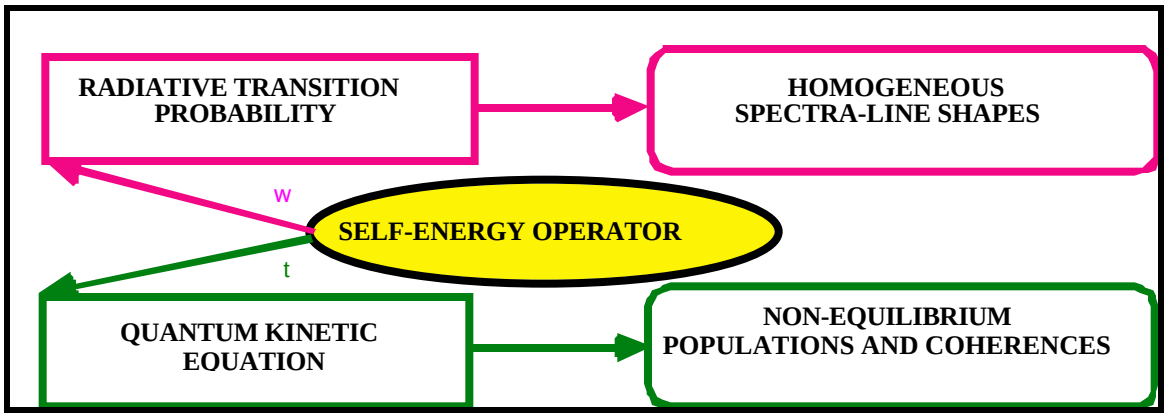

Fig. 2. Influence of environmental collisional and radiative relexation (decoherence) processes on the atomic-state kinetics and the radiative transition probability.

Theoretical development of x-ray line polarization spectroscopy: polarization database and influence of magnetic fields

A.S. Shlyaptseva, S. Hansen, V.L. Kantsyrev
(University of Nevada, Reno, USA)

S. A. Kazantsev
(*Meudon Observatory, France*)

A.G. Petrashen
(*IFMO, Russia*)

U. I. Safronova
(*University of Notre Dame, USA*)

Abstract

Polarization Plasma Spectroscopy (PPS) can substantially complement a usual plasma spectroscopy. It provides important information about anisotropy of plasmas such as the existence and parameters of anisotropic electron beams and magnetic fields. The present paper focuses on the theoretical development of PPS and x-ray line polarization in particular. Specifically, it provides the relevant atomic and polarization characteristics, describes the new collisional-radiative atomic kinetic model which accounts for the effect of anisotropic hot electrons and discusses the influence of magnetic fields on the alignment of the ions. The application of these results to the interpretation of experiments at the NTF and LLNL EBIT is presented in another publication of this volume [1].

I. Introduction

Polarization Plasma Spectroscopy (PPS) provides information about anisotropy of processes occurring in plasmas. The present International Workshop on Plasma Polarization Spectroscopy demonstrated the vitality of this new research field and its unique applications to the plasma diagnostics. It can be used for diagnostics of plasmas with very different density, from a low-density to a dense plasma. This is a multi-step problem, which requires a creation of the new type of the atomic database, the ability of appropriate theoretical modeling and experimental monitoring of the polarization-dependent spectra. The present paper focuses on the theoretical development of PPS and x-ray line polarization in particular. Specifically, it provides the relevant atomic and polarization characteristics, describes the new collisional-radiative atomic kinetic model which accounts for the effect of anisotropic electrons and discusses the influence of magnetic fields on the alignment of the ions. The application of these results to the interpretation of experiments at the NTF and LLNL EBIT is presented in another publication of this volume [1].

II. Atomic and polarization characteristics database

Atomic and polarization characteristics of dielectronic satellites of Li-, Be-, B-, C-, N-, O-, and F-like ions are calculated. The MZ code of Profs. U. Safronova and L. Vainshtein [2, 3, 4] is employed to obtain energy levels, radiative transition probabilities, and amplitudes and total rates of autoionization decays of doubly-excited states for ions in a broad range of nuclear charge Z. The MZ code is based on the perturbation theory method and uses Z-expansion to calculate atomic characteristics. The energy matrix is constructed in a LS-coupling scheme including non-relativistic and relativistic parts. The non-relativistic part takes into account three or four terms of the Z-expansion. The relativistic part is constructed using the Breit-Pauli operators. For one-body operators (for example, Darwin and spin-orbit), zero and first orders of the Z-expansion are calculated. Two-body operators are directly obtained in hydrogenic approximation.

A. Photon density matrix formalism

Using the photon density matrix formalism, the degree of polarization of dielectronic satellites is expressed through autoionization decay amplitudes. The photon density matrix has the following expression [5]:

$$\rho_{\lambda\lambda'} = \frac{\sum_L V_L \times \begin{pmatrix} j_{ph} & j_{ph} & L \\ \lambda & -\lambda' & -\Lambda \end{pmatrix} \times D^{(L)}_{\Lambda 0}(\cos\theta)}{\sum_L V_L \times \begin{pmatrix} j_{ph} & j_{ph} & L \\ 1 & -1 & 0 \end{pmatrix} \times P_L(\cos\theta)} \tag{1}$$

where P_L is a Legendre polynomial of order L and V_L is the "so-called" polarization moment of the ion. In general, the expression for V_L through autoionization decay amplitudes γ in the intermediate coupling scheme has a very cumbersome form:

$$\begin{aligned}
&V_L(Q_a L_a S_a J_a; J_f) = \sum_{Q_1 Q_2 Q_i Q_i' Q_a' L_1 S_1 L_1' S_1' L_i S_i L_i' J_i J_i'} \\
&\times \sum_{M_{L_i} M_{L_i'}} \sum_{a_1 a_2} \sum_{kk'll'} (2L+1) \times (-1)^L \times (-1)^{2a_1 + a_2} \times (-1)^{M_{L_i}} \times \\
&\times (-1)^{J_a + 2J_i' - S_i + 1/2} \times (-1)^{1 + J_f - k} \times \Pi(J_a\, 2 J_a\, 2 J_i J_i' k k' l l' a_1 a_2) \times \\
&\times (a_1 a_2 l') \times (a_1 l L) \times \begin{pmatrix} a_2 & L_i' & L_i \\ 0 & -M_{L_i'} & M_{L_i} \end{pmatrix} \times \begin{Bmatrix} a_2 & L_i' & L_i \\ S_i & J_i & J_i' \end{Bmatrix} \times \begin{Bmatrix} a_1 & l' & a_2 \\ k' & k & J_a' \end{Bmatrix} \times \\
&\times \begin{Bmatrix} a_2 & J_i' & J_i \\ 1/2 & k & k' \end{Bmatrix} \times \begin{Bmatrix} L & J_a & J_a \\ J_f & j_{ph} & j_{ph} \end{Bmatrix} \times \begin{Bmatrix} l & L & a_1 \\ J_a & k & J_a \end{Bmatrix} \times \Pi(J_i J_i' L_1 S_1 k L_1' S_1' k') \times \\
&\times \begin{Bmatrix} S_i & L_i & J_i \\ k & 1/2 & S_1 \end{Bmatrix} \times \begin{Bmatrix} S_i & L_i' & J_i' \\ k' & 1/2 & S_1' \end{Bmatrix} \times \begin{Bmatrix} S_1 & L_1 & J_a \\ l & k & L_i \end{Bmatrix} \times \begin{Bmatrix} S_1' & L_1' & J_a \\ l' & k' & L_i' \end{Bmatrix} \times \\
&\times C^{J_a}(Q_a L_a S_a, Q_1 L_1 S_1) \times \gamma(Q_1 L_1 S_1, Q_i L_1 S_1) \times \\
&\times \gamma(Q_2 L_1' S_1', Q_i' L_1' S_1') \times C^{J_a}(Q_2 L_1' S_1', Q_a' L_a' S_a)
\end{aligned} \tag{2}$$

where a denotes an autoionizing state of the ion; i denotes an initial state of the ion; f denotes a final state of the ion, j_{ph} describes photon; l describes an incident electron, and $\mathbf{C}^{Ja}$ are mixing coefficients.

A degree of polarization is expressed through the elements of the density matrix:

$$P = \sqrt{1 - 4 \times \mathrm{Det}(\rho^{ph})} \tag{3}$$

It was shown that for electric-dipole transitions the sum over L in Eq. (1) in the numerator has only one term with $L=2$ and in the denominator two terms with $L=0$ and 2 [5]. Then, the degree of polarization will depend only on V_0 , V_2 , and an angle of observation with respect to an electron beam θ:

$$P(\theta) = -\frac{3 \times V_2 \times \sin^2\theta}{2\sqrt{10} \times V_0 + (3\cos^2\theta - 1) \times V_2} \tag{4}$$

The maximum degree of polarization $\mathbf{P_0}$ is equal:

$$P(90^o) = \frac{3}{1 - 2\sqrt{10} \times V_0 / V_2} \tag{5}$$

In the case of low-density plasma the expression for V_L for Li-, Be-, and B-like ions has a very simple form and does not require any autoionization decay amplitudes [5,6]. For more complicated ions such as C-like, N-like, and O-like ions even in a case of low-density plasma, there is more than one energy level in a ground state of a target ion and it is necessary to calculate autoionization decay amplitudes. For moderate- and high-density plasmas, calculations of polarization characteristics involve the data on autoionization decay amplitudes. Fig. 1 illustrates the increasing complexity of the description of the autoionization decays for low-density and high-density C-like ions.

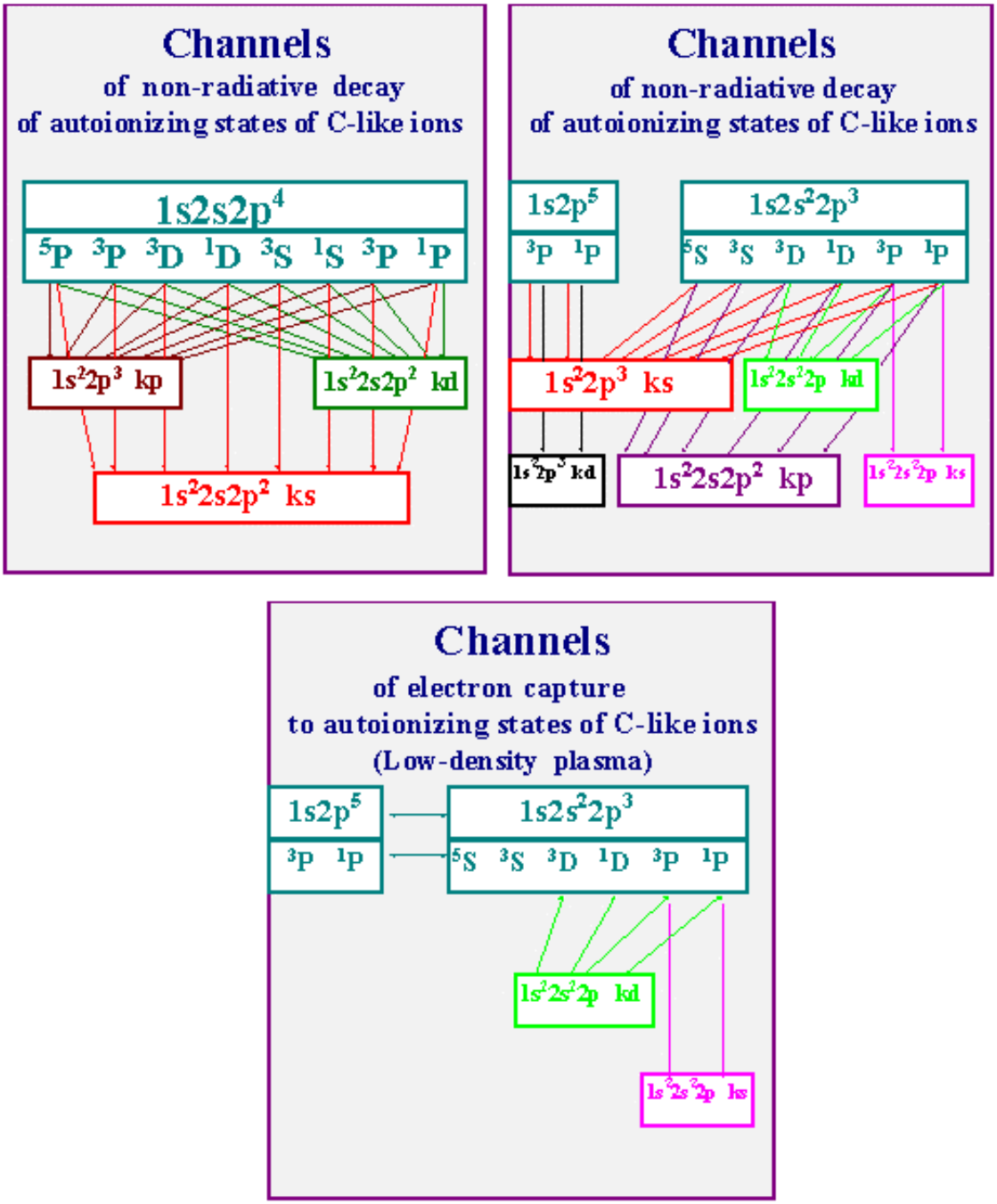

Fig. 1. Channels of autoionization decays of C-like ions for high-density plasmas (top) and low-density plasmas (bottom).

The amplitude of autoionization decay can be expressed through radial integrals $\boldsymbol{R_l(n_1l_1n_2l_2;n_2',l_2',n_1',l_1')}$ specified in Table 1 [7,8]:

$$\gamma(j_1^0 j_2^0[L_{12}S_{12}]j_3^0 \ldots LS, j_1^{0\prime} j_2^{0\prime}[L''_{12}S''_{12}]j_3^{0\prime} \ldots LS]$$

$$= \sqrt{\frac{2\pi}{k_0}} \times \frac{1}{2(n-2)!} \times$$

$$\times \sum_{j_1 j_2 j_1' j_2'} \sum_{L_{12}S_{12}} \sum_{l} (-1)^{L_{12}+l-1/2(l_1+l_1'-l_2-l_2')}$$

$$\times (ll_1l_1') \times (l_2l_2'l) \times \sqrt{(2l_1+1)(2l_2+1)(2l_1'+1)(2l_2'+1)} \times \quad (6)$$

$$\times R_l(n_1l_1n_2l_2;n_2'l_2'n_1'l_1') \times$$

$$\times \sum_{j_3 \ldots j_n} \sum_{L_{13}S_{13} \ldots L_{1n-1}S_{1n-1}} C^{j_1^0 j_2^0 j_3^0 \ldots j_n^0}_{j_1^0 j_2^0 j_3^0 \ldots j_n^0}(L_{12}S_{12}, L''_{12}S''_{12}, \ldots LS)$$

$$\times C^{j_1^{0\prime} j_2^{0\prime} j_3^{0\prime} \ldots j_n^{0\prime}}_{j_1^{0\prime} j_2^{0\prime} j_3^{0\prime} \ldots j_n^{0\prime}}(L'_{12}S'_{12}, L''_{12}S''_{12}, \ldots LS)$$

In the intermediate coupling scheme the partial autoionization rate $\boldsymbol{A^{aut}}$ for the decay into channel *i* can be expressed through the amplitudes [7,8]:

$$A_i^{aut}(Q_aL_aS_aJ_a) = 2\sqrt{2}\pi \sum_{Q_1Q_2} C^{J_a}(Q_aL_aS_a, Q_1L_1S_1) \times$$

$$\times \gamma(Q_1L_1S_1, Q_iL_1S_1) \times \quad (7)$$

$$\times \gamma(Q_iL_1S_1, Q_2L_1S_1) \times C^{J_a}(Q_2L_1S_1, Q_aL_aS_a)$$

For low-density plasmas, there are only two channels of electron capture (EC) to autoionizing states of C-like ions: $1s^2 2s^2 2p$ ks and kd, which can populate four different levels of $1s2s^2 2p^3$ (see Fig. 1). For high-density plasmas, there are eight channels of EC, which can populate sixteen different levels of $1s2s^2 2p^3$, $1s2p^5$, $1s2s2p^4$ (see Fig. 1). All possible channels for the autoionization decays of C-like and O-like ions and the analytical expressions of the amplitudes of autoionization decays through radial integrals are given in Tables 2,3. Similar data for B-like ions are given in [8].

Table 1.

Numerical values of radial integrals used in expressions of amplitudes of autoionization decays.

Designation	Integral	Value
$R_0(ks)$	$R_0(2s2s, 1sks)$	0.016720
$R_0(kp)$	$R_0(2s2p, kp1s)$	0.014778
$R_1(ks)$	$R_1(2p2p, 1sks)$	-0.025217
$R_1(kp)$	$R_1(2s2p, 1skp)$	0.026053
$R_1(kd)$	$R_1(2p2p, 1skd)$	0.061745

Table 2.

Analytical expressions for the decay amplitudes of autoionizing, double-excited states of C-like ions to the ground and single-excited states of B-like ions.

LS	C-like ions autoionizing states	B-like ions ground and single-exc. states	Decay amplitudes Analytical expressions
^1P	$1s2p^5$	$1s^22p^3(^2P)$	$-(\sqrt{2}/3)R_1(ks)$
^1P	$1s2p^5$	$1s^22p^3(^2P)$	$(1/3)R_1(kd)$
^1P	$1s2p^5$	$1s^22p^3(^2D)$	$(1/\sqrt{3})R_1(kd)$
^3P	$1s2p^5$	$1s^22p^3(^2P)$	$(\sqrt{2}/3)R_1(ks)$
^3P	$1s2p^5$	$1s^22p^3(^2P)$	$(1/3)R_1(kd)$
^3P	$1s2p^5$	$1s^22p^3(^2D)$	$(1/\sqrt{3})R_1(kd)$
^5S	$2s^22p^3\,[^4S]1s$	$1s^22p^3(^4S)$	$R_0(ks)$
^5S	$2s^22p^3\,[^4S]1s$	$1s^22p^22s(^4P)$	$\sqrt{3}R_1(kp)]$
^3S	$2s^22p^3\,[^4S]1s$	$1s^22p^3(^4S)$	$-R_0(ks)$
^3S	$2s^22p^3\,[^4S]1s$	$1s^22p^22s(^4P)$	$-(\sqrt{8}/\sqrt{3})[R_0(kp)-(1/3)R_1(kp)]$
^3S	$2s^22p^3\,[^4S]1s$	$1s^22p^22s(^2P)$	$-(1/\sqrt{3})[R_0(kp)-(4/3)R_1(kp)]$
^1D	$2s^22p^3\,[^2D]1s$	$1s^22p^3(^2D)$	$-R_0(ks)$
^1D	$2s^22p^3\,[^2P]1s$	$1s^22s^22p(^2P)$	$(1/\sqrt{5})R_1(k2)$
^1D	$2s^22p^3\,[^2D]1s$	$1s^22p^22s(^2P)$	$-(\sqrt{3}/\sqrt{2})R_0(kp)$
^1D	$2s^22p^3\,[^2D]1s$	$1s^22p^22s(^2D)$	$-(\sqrt{3}/\sqrt{2})[R_0(kp)-(2/3)R_1(kp)]$
^3D	$2s^22p^3\,[^2D]1s$	$1s^22p^3(^2D)$	$R_0(ks)$
^3D	$2s^22p^3\,[^2P]1s$	$1s^22s^22p(^2P)$	$(1/\sqrt{5})R_1(k2)$
^3D	$2s^22p^3\,[^2D]1s$	$1s^22p^22s(^4P)$	$-(1/\sqrt{6})[R_0(kp)+(2/3)R_1(kp)$
^3D	$2s^22p^3\,[^2D]1s$	$1s^22p^22s(^2P)$	$(2/\sqrt{3})[R_0(kp)-(1/3)R_1(kp)]$
^3D	$2s^22p^3\,[^2D]1s$	$1s^22p^22s(^2D)$	$(\sqrt{3}/\sqrt{2})R_0(kp)$
^1P	$2s^22p^3\,[^2P]1s$	$1s^22p^3(^2P)$	$-R_0(ks)$
^1P	$2s^22p^3\,[^2P]1s$	$1s^22s^22p(^2P)$	$-(\sqrt{2}/3)R_1(ks)$
^1P	$2s^22p^3\,[^2P]1s$	$1s^22s^22p(^2P)$	$(1/3)R_1(kd)$

Table 2 (continued)

LS	C-like ions autoionizing states	B-like ions ground and single-exc. states	Decay amplitudes Analytical expressions
^1P	$2s^2 2p^3\,[^2P]1s$	$1s^2 2p^2 2s(^2P)$	$(\sqrt{3}/\sqrt{2})R_0(kp)$
^1P	$2s^2 2p^3\,[^2P]1s$	$1s^2 2p^2 2s(^2D)$	$-(\sqrt{5}/\sqrt{6})[R_0(kp)-(2/3)R_1(kp$
^1P	$2s^2 2p^3\,[^2P]1s$	$1s^2 2p^2 2s(^2S)$	$(\sqrt{2}/\sqrt{3})[R_0(kp)-(2/3)R_1(kp)]$
^3P	$2s^2 2p^3\,[^2P]1s$	$1s^2 2p^3(^2P)$	$R_0(ks)$
^3P	$2s^2 2p^3\,[^2P]1s$	$1s^2 2s^2 2p(^2P)$	$-(\sqrt{2}/3)R_1(ks)$
^3P	$2s^2 2p^3\,[^2P]1s$	$1s^2 2s^2 2p(^2P)$	$(1/3)R_1(k2)$
^3P	$2s^2 2p^3\,[^2P]1s$	$1s^2 2p^2 2s(^2P)$	$(1/\sqrt{6})[R_0(kp)+(2/3)R_1(kp)]$
^3P	$2s^2 2p^3\,[^2P]1s$	$1s^2 2p^2 2s(^4P)$	$-(2/\sqrt{3})[R_0(kp)-(1/3)R_1(kp)$
^3P	$2s^2 2p^3\,[^2P]1s$	$1s^2 2p^2 2s(^2D)$	$(\sqrt{5}/\sqrt{6})R_0(kp)$
^3P	$2s^2 2p^3\,[^2P]1s$	$1s^2 2p^2 2s(^2S)$	$-(\sqrt{2}/\sqrt{3})R_0(kp)$
^1P	$2p^4\,2s[^2P]1s$	$1s^2 2p^3(^2D)$	$(\sqrt{5}/3\sqrt{2})R_1(kp)$
^1P	$2p^4\,2s[^2P]1s$	$1s^2 2p^3(^2P)$	$-(1/\sqrt{6})R_1(kp)$
^1P	$2p^4\,2s[^2P]1s$	$1s^2 2p^2 2s(^2P)$	$(1/3)R_1(ks)$
^1P	$2p^4\,2s[^2P]1s$	$1s^2 2p^2 2s(^2P)$	$-(\sqrt{2}/3)R_1(kd)$
^3P	$2p^4\,2s[^2P]1s$	$1s^2 2p^3(^2D)$	$-(\sqrt{10}/3)[R_0(kp)+R_1(kp)/6]$
^3P	$2p^4\,2s[^2P]1s$	$1s^2 2p^3(^2P)$	$-(\sqrt{2}/\sqrt{3})[R_0(kp)+R_1(kp)/6]$
^3P	$2p^4\,2s[^2P]1s$	$1s^2 2p^3(^4S)$	$(\sqrt{8}/\sqrt{3})[R_0(kp)-R_1(kp)/3]$
^3P	$2p^4\,2s[^2P]1s$	$1s^2 2p^2 2s(^2P)$	$-(1/3)R_1(ks)$
^3P	$2p^4\,2s[^2P]1s$	$1s^2 2p^2 2s(^2P)$	$(\sqrt{2}/3)R_1(kd)$
^3P	$2p^4\,2s[^4P]1s$	$1s^2 2p^3(^2D)$	$(\sqrt{20}/3)[R_0(kp)-R_1(kp)/3]$
^3P	$2p^4\,2s[^4P]1s$	$1s^2 2p^3(^2P)$	$-(2/\sqrt{3})[R_0(kp)-R_1(kp)/3]$
^3P	$2p^4\,2s[^4P]1s$	$1s^2 2p^3(^4S)$	$-(4/3)[R_0(kp)-R_1(kp)/12]$
^3P	$2p^4\,2s[^4P]1s$	$1s^2 2p^2 2s(^4P)$	$(1/3)R_1(ks)$
^3P	$2p^4\,2s[^4P]1s$	$1s^2 2p^2 2s(^4P)$	$(\sqrt{2}/3)R_1(kd)$
^5P	$2p^4\,2s[^4P]1s$	$1s^2 2p^3(^4S)$	$(1/3)R_1(kp)]$
^5P	$2p^4\,2s[^4P]1s$	$1s^2 2p^2 2s(^4P)$	$(1/3)R_1(ks)$
^5P	$2p^4\,2s[^4P]1s$	$1s^2 2p^2 2s(^4P)$	$-(\sqrt{2}/3)R_1(kd)$

Table 2 (continued)

LS	C-like ions autoionizing states	B-like ions ground and single-exc. states	Decay amplitudes Analytical expressions
^1S	$2p^4\,2s[^2S]1s$	$1s^2 2p^3(^2P)$	$-(2\sqrt{2})[R_0(kp)-R_1(kp)/6]$
^1S	$2p^4\,2s[^2S]1s$	$1s^2 2p^2 2s(^2S)$	$-(2/3)R_1(ks)$
^1S	$2p^4\,2s[^2S]1s$	$1s^2 2p^2 2s(^2D)$	$-(\sqrt{2}/3)R_1(kd)$
^3S	$2p^4\,2s[^2S]1s$	$1s^2 2p^3(^2P)$	$(\sqrt{2}/3)R_1(kp)]$
^3S	$2p^4\,2s[^2S]1s$	$1s^2 2p^2 2s(^2S)$	$(2/3)R_1(ks)$
^3S	$2p^4\,2s[^2S]1s$	$1s^2 2p^2 2s(^2D)$	$(\sqrt{2}/3)R_1(kd)$
^1D	$2p^4\,2s[^2D]1s$	$1s^2 2p^3(^2D)$	$-\sqrt{6}[R_0(kp)-R_1(kp)/6]$
^1D	$2p^4\,2s[^2D]1s$	$1s^2 2p^3(^2P)$	$\sqrt{2}[R_0(kp)-R_1(kp)/6]$
^1D	$2p^4\,2s[^2D]1s$	$1s^2 2p^2 2s(^2D)$	$-(1/3)R_1(ks)$
^1D	$2p^4\,2s[^2D]1s$	$1s^2 2p^2 2s(^2D)$	$-(\sqrt{28}/\sqrt{90})R_1(kd)$
^1D	$2p^4\,2s[^2D]1s$	$1s^2 2p^2 2s(^2S)$	$-(\sqrt{2}/\sqrt{45})R_1(kd)$
^3D	$2p^4\,2s[^2D]1s$	$1s^2 2p^3(^2D)$	$(1/\sqrt{6})R_1(kp)]$
^3D	$2p^4\,2s[^2D]1s$	$1s^2 2p^3(^2P)$	$-(1/3\sqrt{2})R_1(kp)]$
^3D	$2p^4\,2s[^2D]1s$	$1s^2 2p^2 2s(^2D)$	$(1/3)R_1(ks)$
^3D	$2p^4\,2s[^2D]1s$	$1s^2 2p^2 2s(^2D)$	$(\sqrt{28}/\sqrt{90})R_1(kd)$
^3D	$2p^4\,2s[^2D]1s$	$1s^2 2p^2 2s(^2S)$	$(\sqrt{2}/\sqrt{45})R_1(kd)$

Table 3.

Analytical expressions for the decay amplitudes of autoionizing, double-excited states of O-like ions to the ground and single-excited states of N-like ions.

LS	O-like ions autoionizing states	N-like ions ground and single-exc. states	Decay amplitudes Analytical expressions
^3P	$1s2s^22p^5$	$1s^22p^5$ (^2P)	$R_0(ks)$
^3P	$1s2s^22p^5$	$1s^22s^22p^3(^2P)$	$(\sqrt{2}/3)R_1(ks)$
^3P	$1s2s^22p^5$	$1s^22s^22p^3(^2P)$	$(1/3)R_1(kd)$
^3P	$1s2s^22p^5$	$1s^22s^22p^3(^2D)$	$(1/\sqrt{3})R_1(kd)$
^3P	$1s2s^22p^5$	$1s^22s2p^4(^4P)$	$(\sqrt{8}/\sqrt{3})[R_0(kp)-R_1(kp)/3]$
^3P	$1s2s^22p^5$	$1s^22s2p^4(^2P)$	$(1/\sqrt{3})[R_0(kp)+2R_1(kp)/3]$
^3P	$1s2s^22p^5$	$1s^22s2p^4(^2S)$	$(1/\sqrt{3})R_0(kp)$
^3P	$1s2s^22p^5$	$1s^22s2p^4(^2D)$	$(\sqrt{5}/\sqrt{3})R_0(kp)$
^1P	$1s2s^22p^5$	$1s^22p^5$ (^2P)	$R_0(ks)$
^1P	$1s2s^22p^5$	$1s^22s^22p^3(^2P)$	$-(\sqrt{2}/3)R_1(ks)$
^1P	$1s2s^22p^5$	$1s^22s^22p^3(^2P)$	$(1/3)R_1(kd)$
^1P	$1s2s^22p^5$	$1s^22s^22p^3(^2D)$	$(1/\sqrt{3})R_1(kd)$
^1P	$1s2s^22p^5$	$1s^22s2p^4(^2P)$	$\sqrt{3})R_0(kp)$
^1P	$1s2s^22p^5$	$1s^22s2p^4(^2S)$	$-(1/\sqrt{3})[R_0(kp)-2R_1(kp)/3]$
^1P	$1s2s^22p^5$	$1s^22s2p^4(^2D)$	$-(\sqrt{5}/\sqrt{3})[R_0(kp)-2R_1(kp)/3]$
^3S	$1s2s2p^6$	$1s^22s2p^4(^2S)$	$(1/\sqrt{3})R_1(ks)$
^3S	$1s2s2p^6$	$1s^22s2p^4(^2D)$	$-(\sqrt{2}/\sqrt{3})R_1(kd)$
^3S	$1s2s2p^6$	$1s^22p^5(^2P)$	$-(1\sqrt{3})R_1(kp)$
^1S	$1s2s2p^6$	$1s^22s2p^4(^2S)$	$(1/\sqrt{3})R_1(ks)$
^1S	$1s2s2p^6$	$1s^22s2p^4(^2D)$	$-(\sqrt{2}/\sqrt{3})R_1(kd)$
^1S	$1s2s2p^6$	$1s^22p^5(^2P)$	$-(2\sqrt{3})$ $[R_0(kp)-R_1(kp)/3]$

B. Polarization-dependent spectra of dielectronic satellites of Ti ions

Atomic and polarization characteristics of dielectronic satellites of Li- and Be-like Ti ions are listed in Table 4. These atomic and polarization characteristics are used as input data to calculate polarization-dependent spectra of dielectronic satellites, i.e., the spectral intensity distribution of lines associated with a given polarization state, parallel or perpendicular to the electron beam.

The intensity of lines associated with the parallel polarization state can be written as

$$I_{II} = \frac{3}{2} \times \langle I \rangle \times \left(\frac{1+P}{3-P} \right) \tag{8}$$

whereas the intensity of lines associated with the perpendicular polarization state is

$$I_{\perp} = \frac{3}{2} \times \langle I \rangle \times \left(\frac{1-P}{3-P} \right) \tag{9}$$

For dielectronic satellite lines the 4π-averaged intensity **<I>** is expressed through the ***Qd*** factor and the electron distribution function ***f(Eb)*** :

$$\langle I \rangle = f(E_b) \times Q_d \tag{10}$$

Theoretical polarization-dependent spectra of dielectronic satellites of Ti ions are presented in Fig. 2. These spectra are calculated for two values of the energy of the electron beam: Eb=3300 eV and 3400 eV. These values of electron beam energies provide the prominence of Li-like and Be-like satellites lines, respectively. Two different traces are calculated at each value of Eb reflecting two different polarization states parallel and perpendicular to the electron beam. These two traces differ from each other at each Eb energies. Thus, the x-ray K-shell spectrum of Ti ions is significantly polarized when produced by a monoenergetic EB, and two polarization-dependent spectra associated with parallel and perpendicular polarization states have different intensity distributions at different EB energies.

Table 4.

Atomic and Polarization Characteristics of Dielectronic Satellite Lines of Ti Ions

a) Li-like Ti

TRANSITION	WL(Å)	Ar($10^{13}s^{-1}$)	Aa($10^{13}s^{-1}$)	Qd($10^{13}s^{-1}$)	Eaut(eV)	P
F 212-P 234	2.6201	1.08E+01	3.01E+00	4.34E+00	3354.9	0.0
C 232-S 212	2.6212	6.35E+00	1.01E+01	7.80E+00	3304.8	0.0
K 232-S 212	2.6302	1.84E+01	2.08E+00	3.74E+00	3288.8	0.0
M 234-P 234	2.6302	3.21E+01	2.82E+00	1.01E+01	3336.7	-0.75
F 254-P 232	2.6320	1.55E+01	1.58E+01	3.06E+01	3325.9	0.6
F 256-P 234	2.6354	1.17E+01	1.77E+01	4.23E+01	3327.3	0.5
M 436-P 234	2.6458	6.74E-01	1.03E+00	2.44E+00	3309.0	0.5
E 212-P 234	2.6816	5.52E-01	1.50E+01	1.04E+00	3246.3	0.0

Designations: K, C = $1s2s2p$ F, M = $1s2p^2$ E = $1s2s^2$
S = $1s^22s$ P = $1s^22p$

b) Be-like Ti

TRANSITION	WL(Å)	Ar($10^{13}s^{-1}$)	Aa($10^{13}s^{-1}$)	Qd($10^{13}s^{-1}$)	Eaut(eV)	P
K 333-P 335	2.6366	9.06E+00	2.35E+00	2.73E+00	3399.0	0.0
K 155-P 335	2.6374	4.05E+00	1.19E+01	6.24E+00	3397.5	-1.0
K 313-P 333	2.6387	4.75E+00	5.31E+00	3.36E+00	3389.9	0.0
K 111-P 133	2.6425	1.15E+01	7.44E+00	2.44E+00	3418.1	0.0
K 353-P 333	2.6470	1.26E+01	9.32E+00	1.06E+01	3375.2	-0.43
Q 333-P 331	2.6472	1.77E+01	9.20E+00	1.43E+01	3372.9	0.6
Q 335-P 335	2.6478	2.36E+01	2.56E+00	8.77E+00	3379.0	-0.6
K 355-P 333	2.6482	1.46E+01	1.64E+01	3.55E+01	3373.2	0.33
K 353-P 335	2.6500	6.23E+00	9.32E+00	5.22E+00	3375.2	0.07
K 357-P 335	2.6507	1.16E+01	1.84E+01	4.57E+01	3373.9	0.44
Q 333-P 335	2.6513	3.73E+00	9.20E+00	3.01E+00	3372.9	0.07
K 155-P 133	2.6541	7.83E+00	1.19E+01	1.20E+01	3397.5	0.6

Designations: K, Q = $1s2s2p^2$ P = $1s^22s2p$

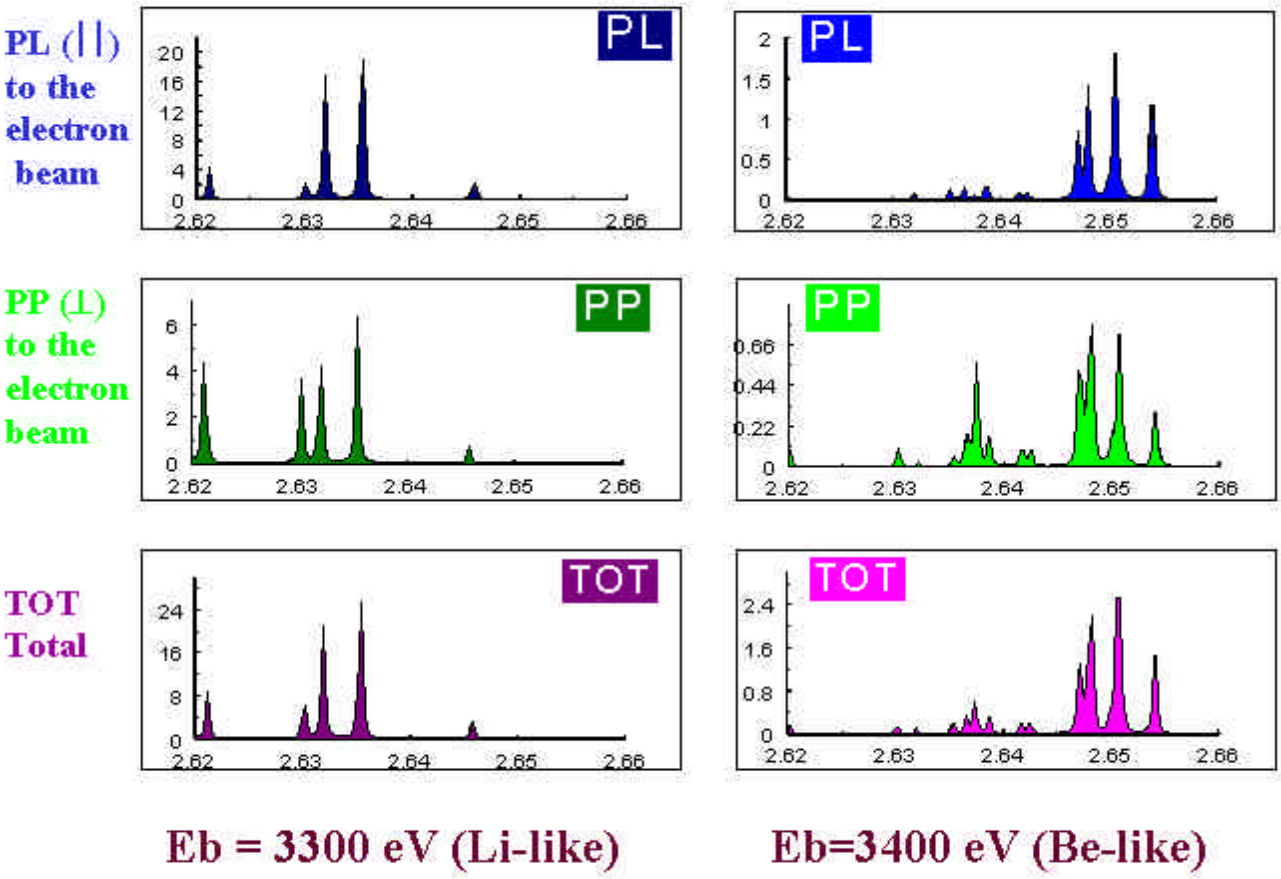

Fig. 2. Theoretical polarization-dependent spectra of dielectronic satellites of Ti ions.

III. Modeling of Ti K-shell spectra with inclusion of hot electrons

The development of K-shell spectropolarimetry requires detailed plasma modeling with inclusion of hot electrons. A collisional-radiative atomic kinetic model has been developed to model Ti K-shell spectra produced at the Nevada Terawatt Facility (NTF). Specifically, it aims to diagnose the electron temperature and electron beam characteristics of various emitting regions of Ti x-pinch plasmas produced at the NTF. Steady-state populations of Ti ionization stages and fine structure energy levels are found and used to construct synthetic spectra for comparison with experimental data. The kinetic model and diagnostic techniques are discussed below. The results of modeling of the NTF Ti x-pinch spectra are presented in another publication of this volume [1].

The collisional-radiative atomic kinetic model includes the ground states of every ionization stage of Ti from the bare ion with no electrons to neutral Ti with 22 electrons. Detailed atomic structure is included for ionization stages from H to O. Each fine structure state is linked to other states within its ionization stage via collisional excitation, collisional de-excitation, and radiative decay. Ground states and low-lying non-autoionizing excited states of ions are linked via collisional ionization, three-body recombination, and radiative recombination. Autoionizing states of ions with charge z are linked to the ground state of the ion with charge z+1 via Auger decay and dielectronic recombination. These processes and the Ti model energy level structure are shown in Fig. 3. The number of states modeled in each ionization stage is shown next to that stage in parentheses.

The energy level structure and radiative and Auger decay rates for all ions were calculated with Safronova and Vainstein 's MZ code [2-4] and the Cowan code [9]. Cross sections for collisional excitation between ground states and excited levels were calculated with the code ATOM for H-, He-, and Li-like Ti [10]. The Van Regemorter formula is used to calculate the excitation cross sections of optically allowed transitions between excited states in all ions and for optically allowed ground to excited transitions for Be-like to O-like Ti. A modified Lotz formula [11] is used to calculate collisional ionization cross sections. Radiative recombination cross sections are calculated with Kramer's approximation. Reverse rates are found using detailed balance.

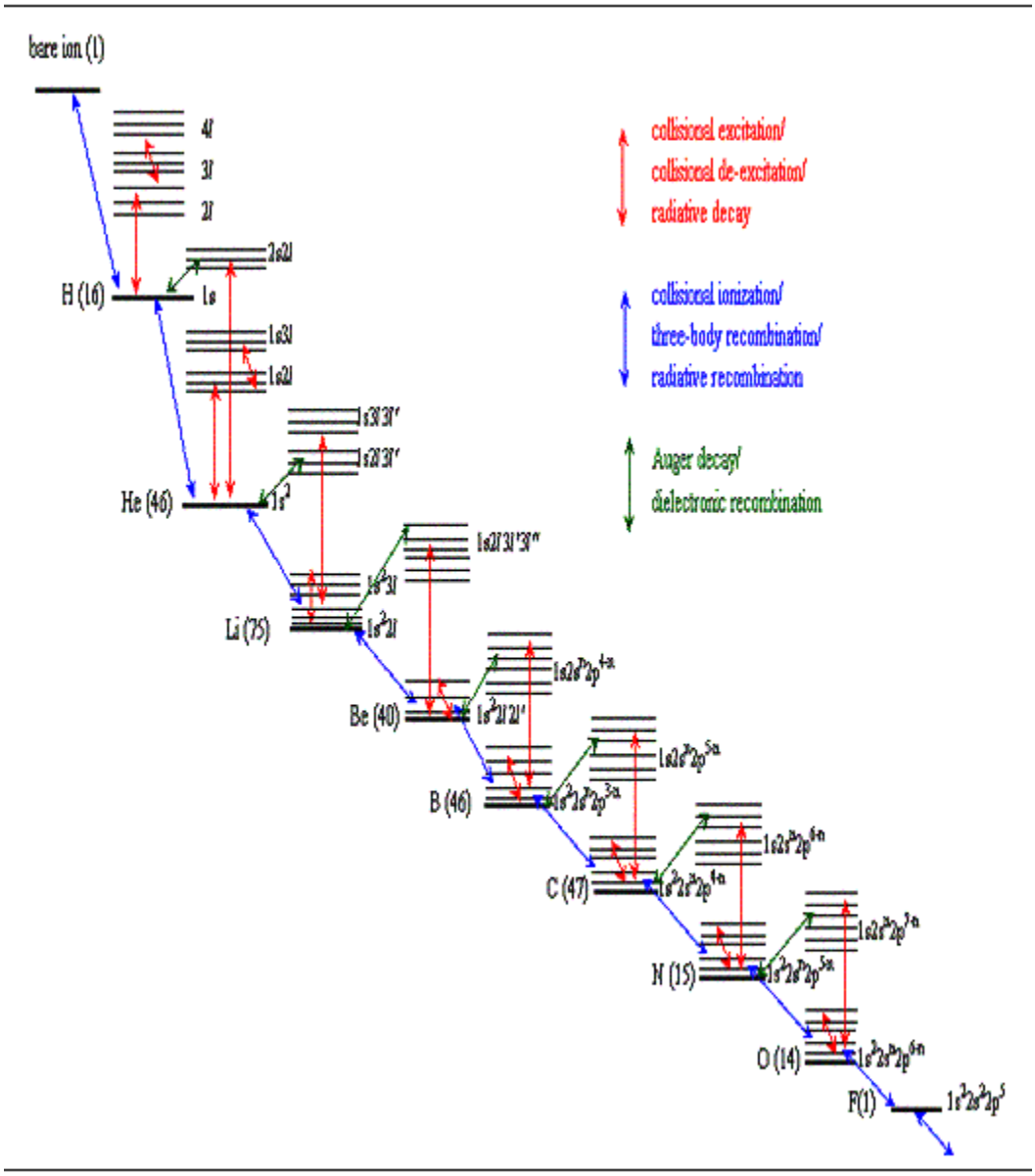

Fig. 3. Energy level structure and atomic processes included in Ti model.

All cross sections are integrated over an electron energy distribution function (EDF), which depends on the Maxwellian electron temperature (T_e), the percentage of hot electrons (f), and the energy of hot electrons (T_{hot}). Fig. 4 shows a typical EDF with a Gaussian distribution of hot electrons. The integrated total cross sections are multiplied by N_e to obtain collisional rates. Together with the spontaneous rates, they form a set of N~300 coupled equations, which can be solved for the population of each state by standard matrix methods. Knowing these populations gives the ionization balance and the intensity of spectral lines.

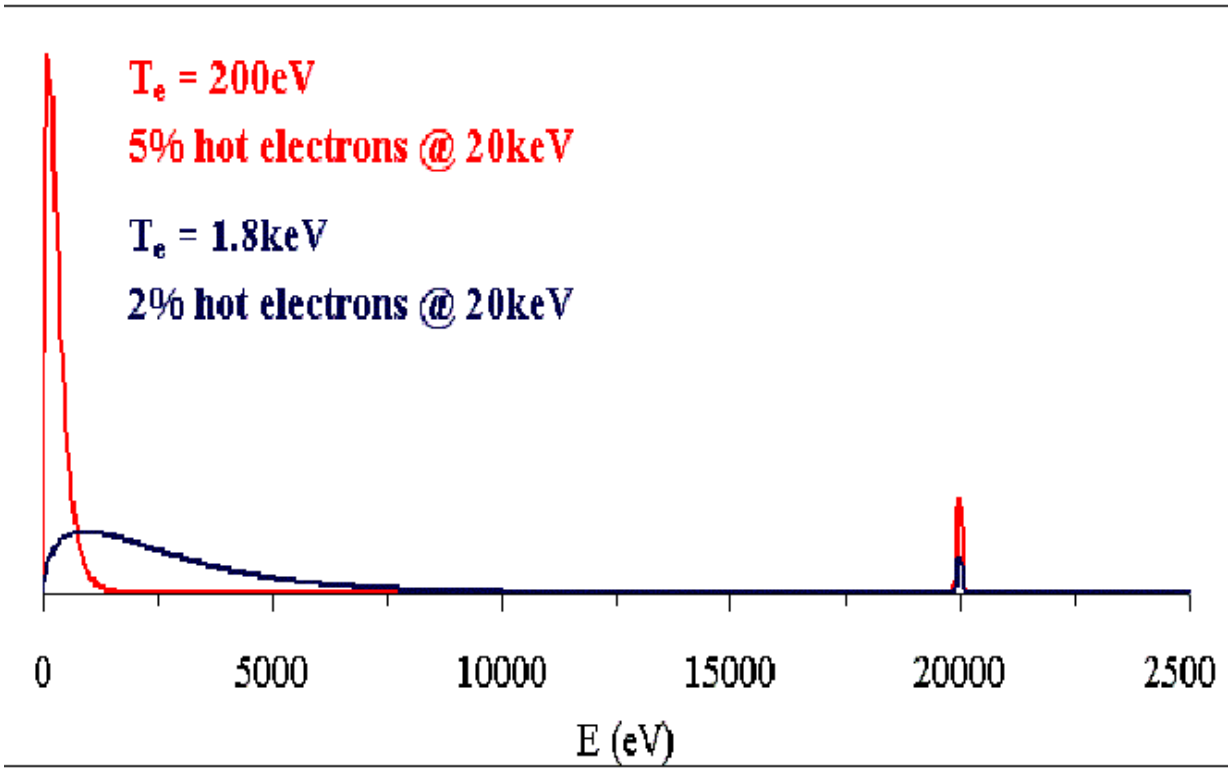

Fig. 4. Typical EDF with a Gaussian distribution of hot electrons.

Four variables (T_e, N_e, f, and T_{hot}) determine the population of states and therefore the spectral line intensities. A good diagnostic spectral feature will be sensitive to one of these plasma parameters and relatively independent of the others. All features are relatively

insensitive to T_{hot} and it is generally straightforward to separate density effects from temperature effects. It is not as easy to isolate temperature effects from electron beam effects, since both alter collisional rates in a similar way. However, it is shown that synthetic spectra do not fit the experimental spectra without hot electrons.

Two main difficulties should be anticipated. The effect of hot electrons on K-shell spectra of multiply-charged ions has been studied for Al x-pinch plasmas [12] and Ar plasma focus plasmas [13]. Specifically, it has been shown that three plasma regions with hot electrons are required to adequately describe the spectra of Ar plasma focus experiments [13], which exhibit spectral features from He-like Ar to Ar K_α. The NTF Ti spectra exhibit features from H-like Ti to Ti K_α produced at least by two different plasma regions, a hot, dense region with hot electrons that contributes all of the H-like and most of the He-like radiation, and a cooler, less dense region also with hot electrons that contributes the satellite radiation from lower ionization stages. Although this is a reasonable picture of the plasma, it introduces flexibility and decreases the robustness of the spectroscopic diagnostics, since synthetic spectra with a range of parameters can fit the experimental spectra. The precision of each diagnostic is discussed below.

The second and more serious difficulty is the plasma opacity. It has been shown [14] that optical depth can decrease the intensity of Al He_α by a factor of two for plasmas at densities 10-100 times lower than those considered here. Other lines are also affected, but they are treated here as optically thin. Opacity will be added to this model in the near future, but until then, the fit near the He_α line and nearby structures are ignored and best fits are found to both sides.

Synthetic spectra with narrow lines show that the He_α resonance to intercombination line ratio is sensitive to electron density. Unfortunately, the intercombination line is very close to Li-like satellite lines and is not resolved in the experimental spectra, so this ratio cannot be used as a density diagnostic. The ionization balance is also slightly sensitive to density, but it is far more sensitive to T_e and electron beam characteristics. Thus, there is no unambiguous spectroscopic density diagnostic in this region. The electron density is taken to be $10^{22}cm^{-3}$ in the hot region and $10^{21}cm^{-3}$ in the cooler regions.

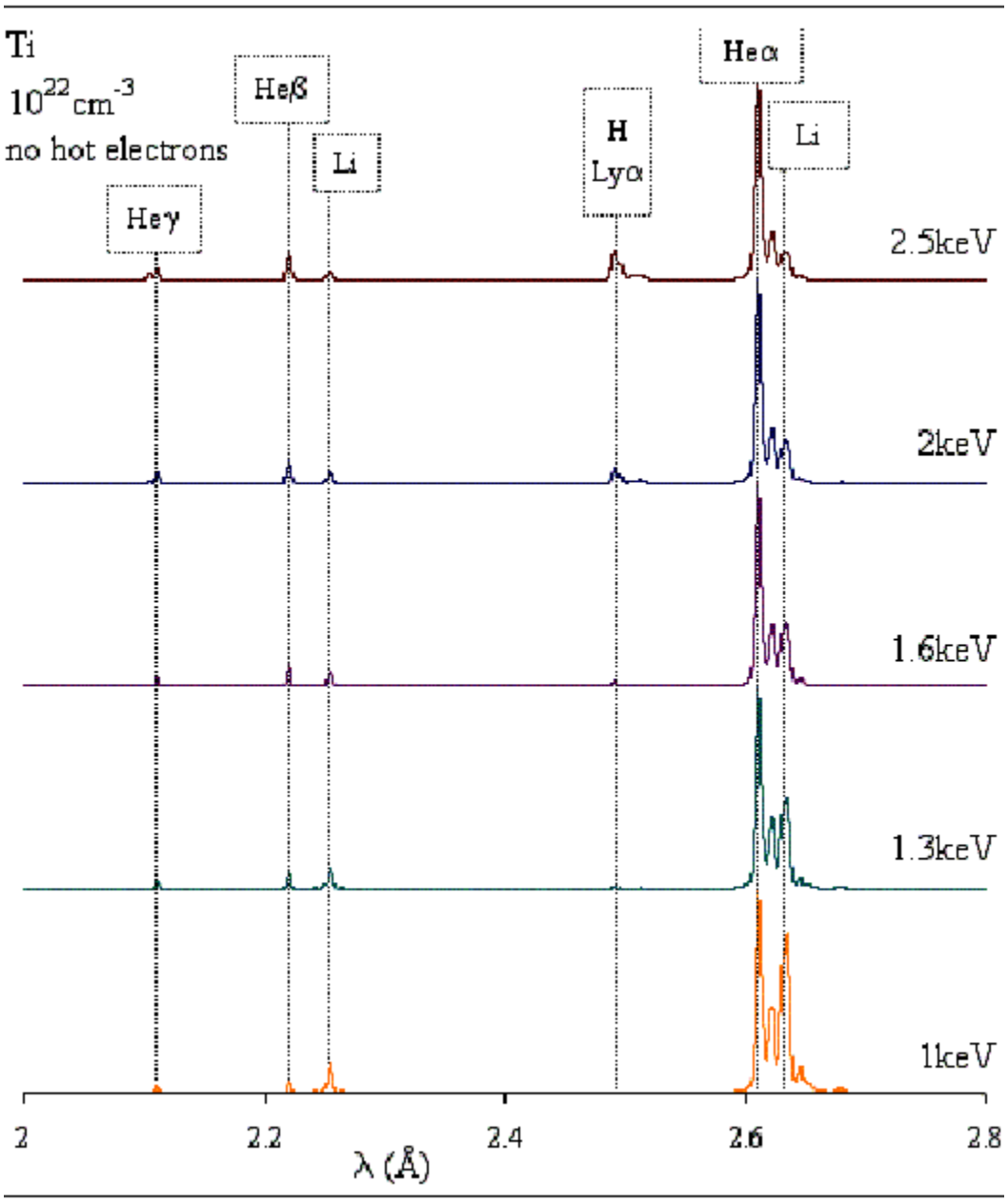

Fig. 5. Effect of Te on the "hot region" Ti spectra.

There are three major T_e-sensitive line ratios involving the resonance lines of He-like ions, He and He , and H-like line Ly and their satellites that have sufficient intensity in the experimental spectra to be useful as temperature diagnostics for the high temperature plasma region. These Ti spectral features are labeled and their dependence on T_e is shown in Fig. 5.

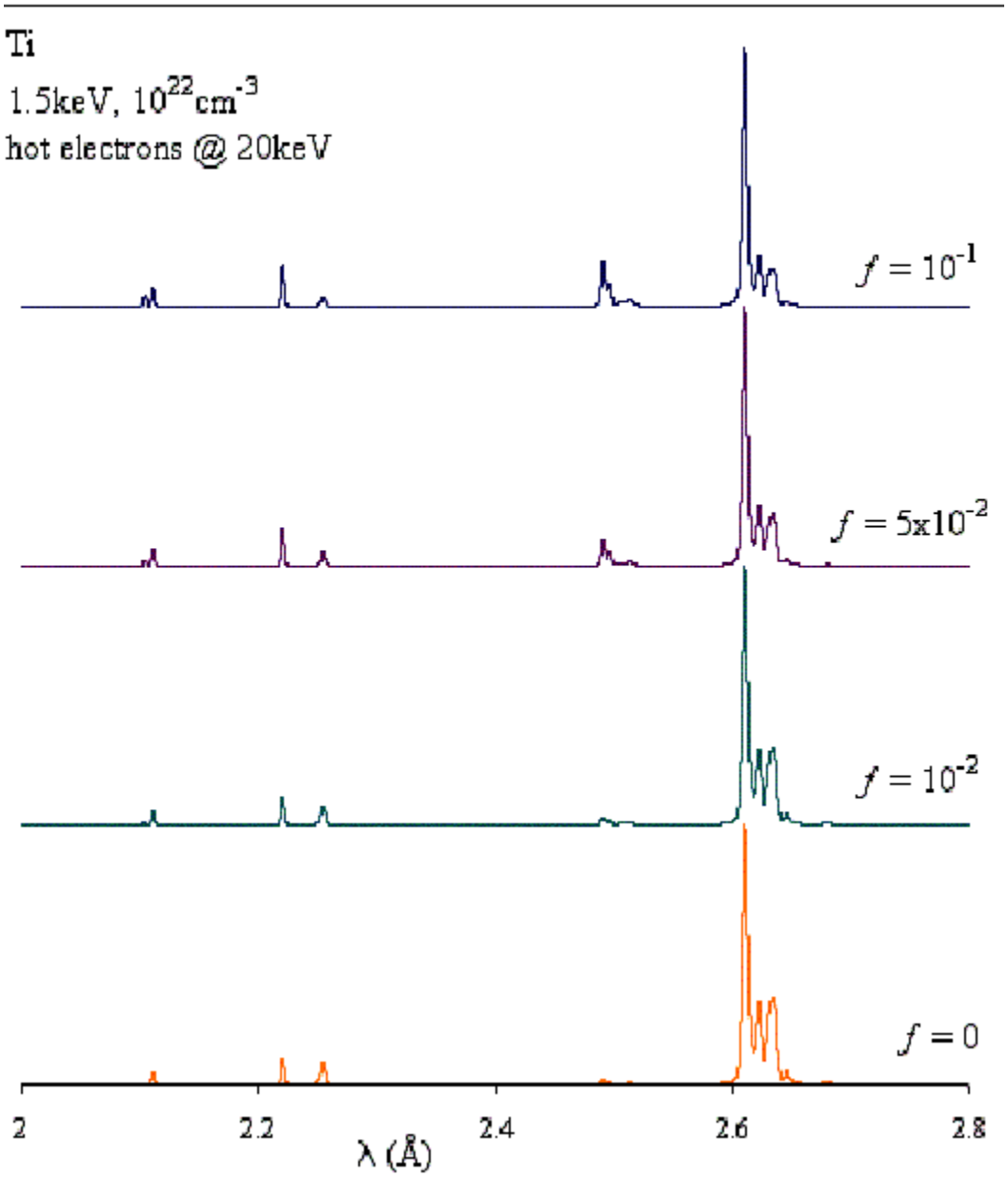

Fig. 6. Effect of hot electrons on the "hot region" of Ti spectra.

Fig. 6 illustrates that the effects of hot electrons are similar to the effects of increasing Te.

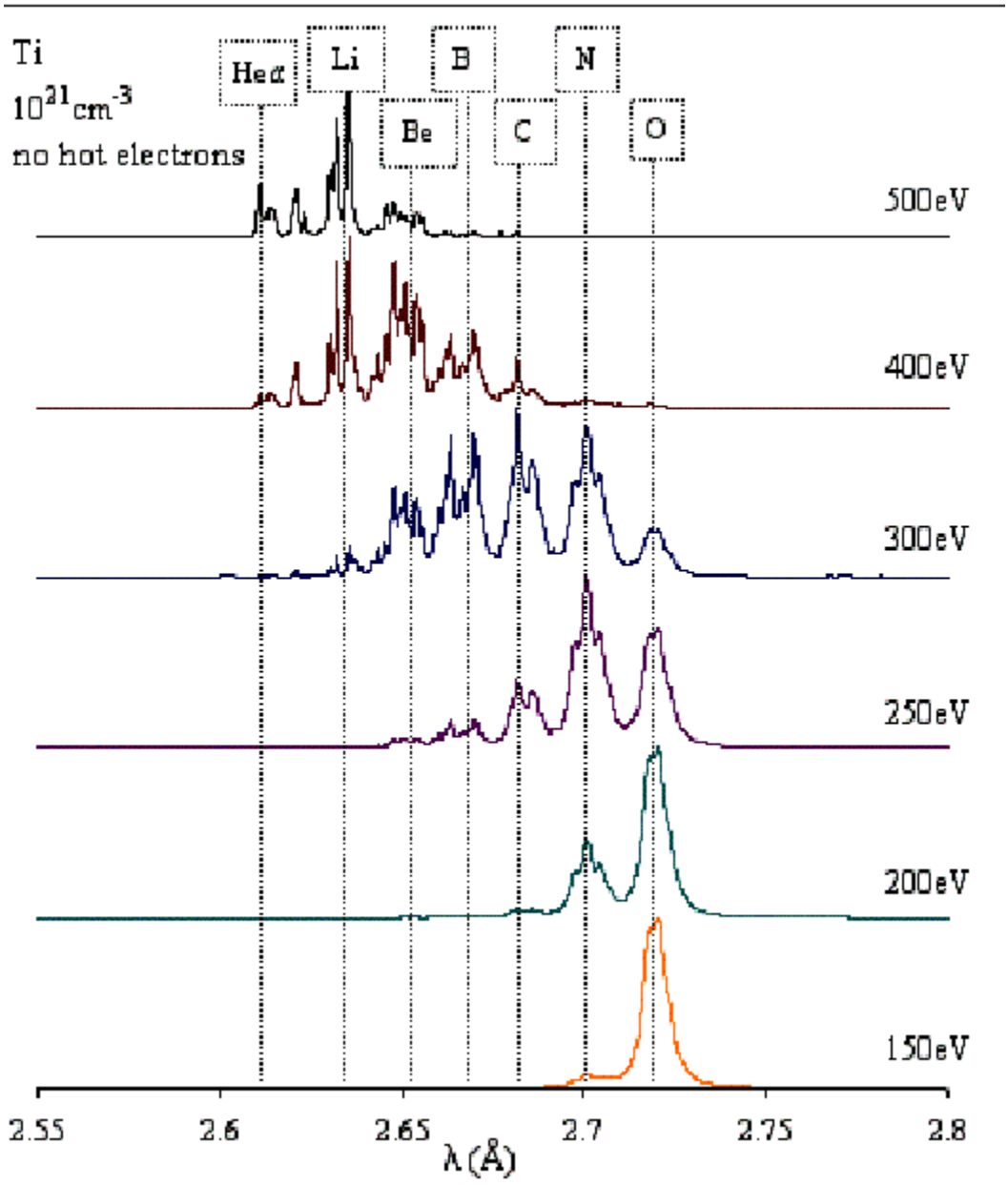

Fig. 7. Te dependence of Li-O-like satellites of Ti ions

The spectra of satellite structures of Li-like to O-like Ti ions are very sensitive to the electron temperature of a cooler plasma region (see Fig. 7). At low temperatures Te=150-200 eV, O-like emission dominates. As T_e increases, so does the ionization balance, the emission is shifted to higher energies, and Li-like emission dominates at Te=400-500 eV.

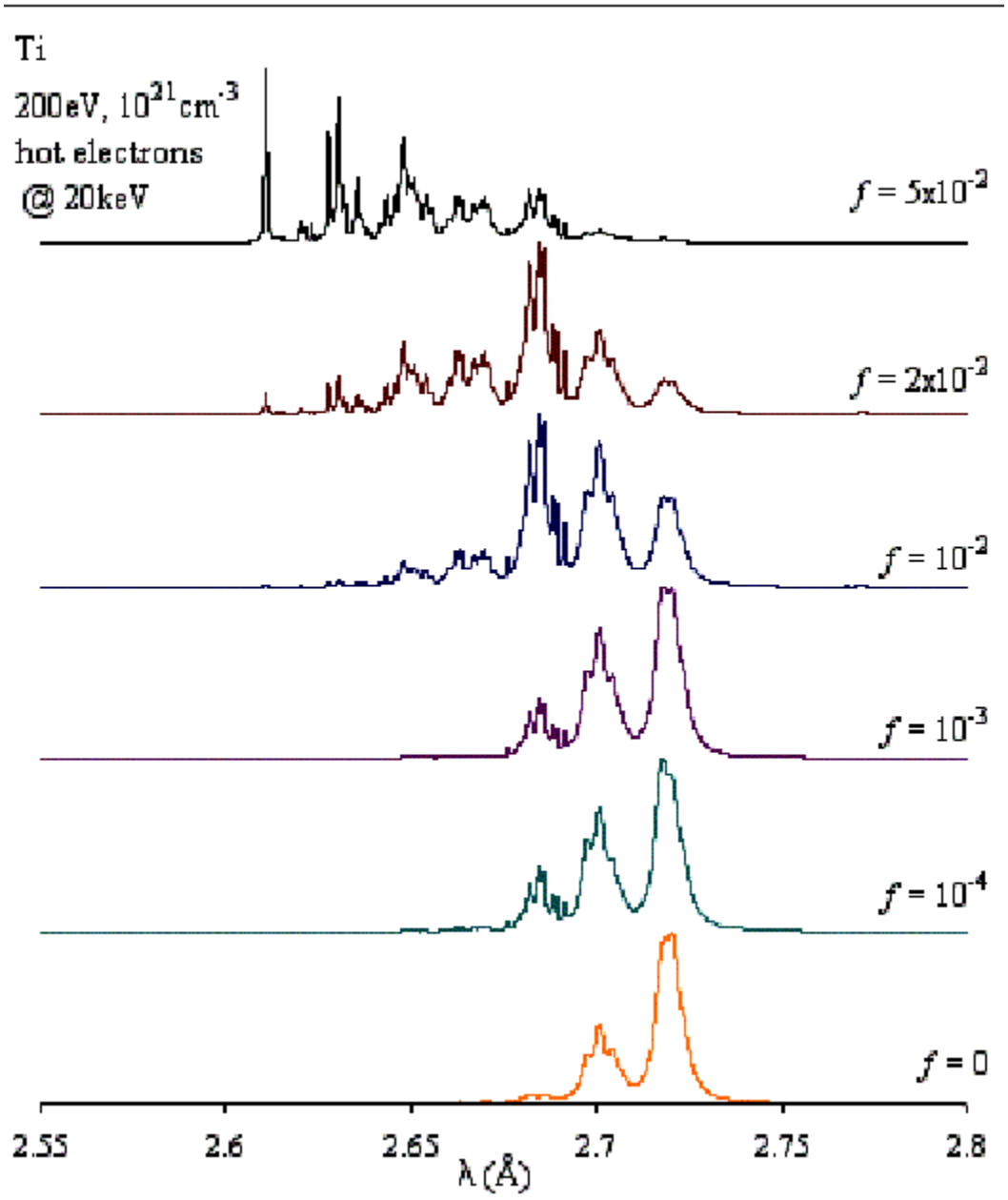

Fig. 8. Effect of hot electrons on the satellite structures of Li-like to O-like of Ti ions.

Figs. 8 and 9 show the effect of an electron beam (f and T_{hot}) on the satellite structures of Ti ions. Increasing f has an effect similar to increasing T_e. It should be noted that even a very small fraction (10^{-4}) of hot electrons has a significant effect on the ionization balance at low T_e.

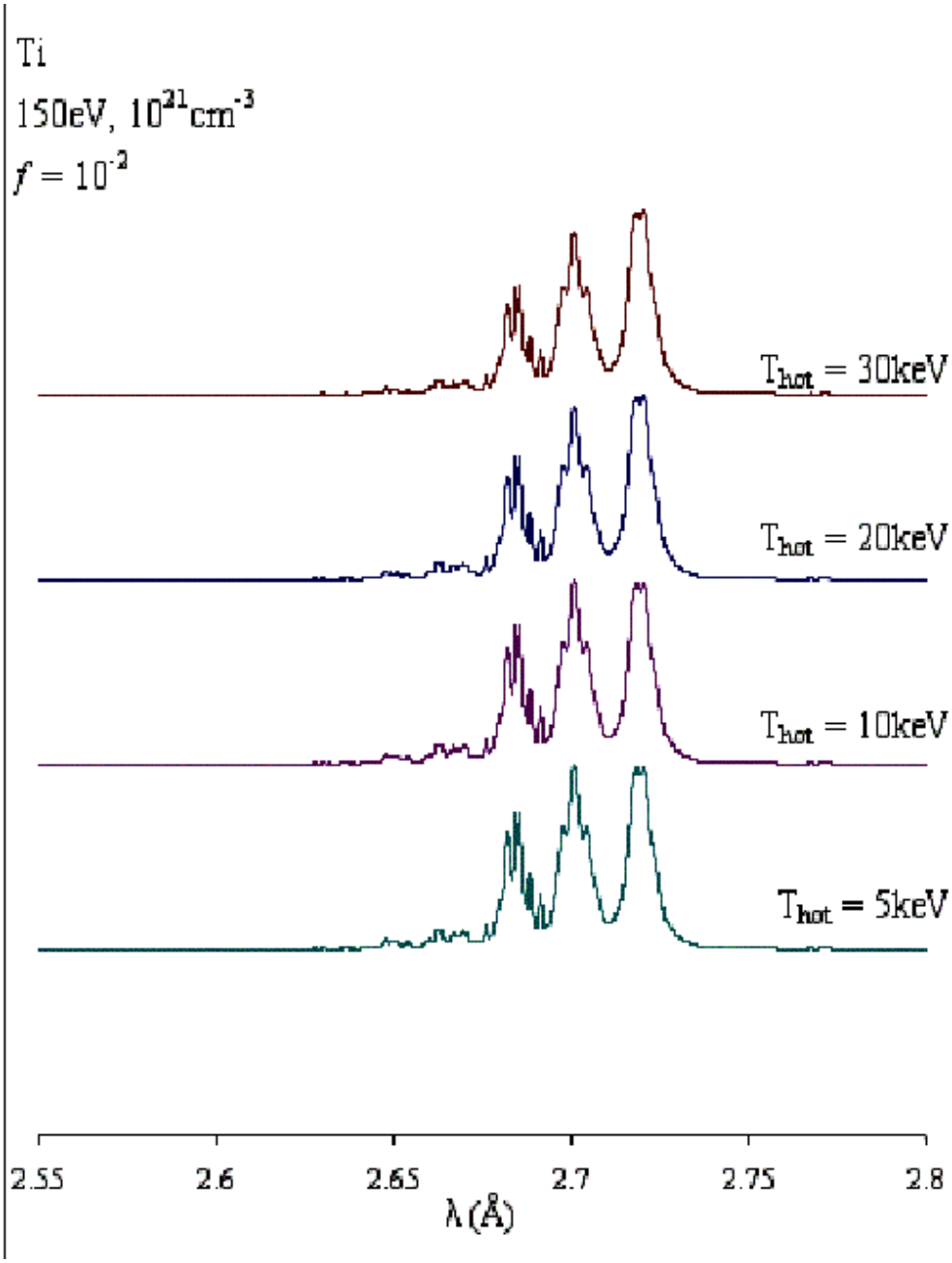

Fig. 9. Effect of the energy of hot electrons on the satellite structures of Li-like to O-like of Ti ions.

The effect of hot electrons described by a Gaussian distribution is not particularly sensitive to the energy of the electron beam (T_{hot}) and actually decreases slightly with increasing beam energy, as illustrated in Fig. 9.

IV. Influence of magnetic fields on the alignment of ions

Our preliminary theoretical estimates have shown that to solve a complex problem of diagnostics of the magnetic field through anisotropy of z-pinch plasma, we need to consider simultaneously two important effects: the creation of the alignment of the excited states by the anisotropic electron beam or other anisotropic sources; the influence of the magnetic field on this alignment. This section shows the results of the theoretical development of density matrix formalism including magnetic fields (for more details see [15], [16]).

The evolution of the density matrix depends on the radiation damping , a non-uniform magnetic field, and an excitation process:

$$\frac{d}{dt}\rho_q^k(j,j') = -\frac{(\gamma_j + \gamma_{j'})}{2}\rho_q^k(j,j') + \tag{11}$$

$$+ \sum_{j_1, j_1', k_1, q_1} W_{q,q_1}^{k,k_1}(j,j';j_1,j_1')\rho_{q_1}^{k_1}(j_1,j_1') + N_q^k(j,j')$$

The matrix element W is expressed through the expansion of the operator of interaction of the atomic system with a non-uniform magnetic field over the irreducible tensor operators:

$$W_{q,q_1}^{k,k_1}(j,j';j_1,j_1') = (-1)^{j+j'+k} \sum_{k_2,q_2} \sqrt{(2k_1+1)(2k_2+1)} \begin{bmatrix} k_1 & k_2 & k \\ q_1 & q_2 & q \end{bmatrix} \times \tag{12}$$

$$\times \left[\begin{Bmatrix} j' & j & k \\ k_1 & k_2 & j_1' \end{Bmatrix} V_{q_2}^{k_2}(j_1',j')\delta_{j_1,j} - (-1)^{k_1+k_2+k} \begin{Bmatrix} j' & j & k \\ k_2 & k_1 & j_1' \end{Bmatrix} V_{q_2}^{k_2}(j,j_1)\delta_{j_1',j'} \right]$$

From these equations it follows that the non-uniform magnetic field is mixing the ranks of the polarization moments and can create the ordering of the angular moments from the population. For the uniform magnetic field in a weak field approximation and for the steady case, the expression of the evolution of the density matrix results in:

$$-\rho_q^k(j,j') + \frac{\omega_L}{2}\left[\sqrt{(k-q)(k+q+1)}\rho_{q+1}^k - \sqrt{(k+q)(k-q+1)}\rho_{q-1}^k\right] + N_q^k = 0 \tag{13}$$

where $\omega_L = \mu_0\tau_0 H/\hbar$ is the dimensionless Larmor frequency, and N^k_q is the efficiency of induction of the ordering of angular moments of ions. From this equation it follows that the uniform magnetic field mixes the components of the polarization moments of the same rank. The uniform magnetic field cannot create a new type of the ordering, and its role is in destruction of already existing ordering.

For a uniform magnetic field, the orthogonal alignment signal is defined as:

$$\Delta I_x = \left(I_z - I_y\right) \sim \sqrt{\frac{3}{2}}\rho_0^2 + \rho_2^2 \tag{14}$$

whereas the incline alignment signal measured at the angle α with the electron beam axis is:

$$\Delta I_\alpha \sim \sqrt{\frac{3}{2}}\sin^2\alpha\,\rho_0^2 + \sin 2\alpha\,\rho_1^2 + \left(1+\cos^2\alpha\right)\rho_2^2 \tag{15}$$

The polarization moments in a uniform magnetic field can be estimated from Eq. (13):

$$\rho_0^2 = N_0^2\frac{1+{\omega_L}^2}{1+4{\omega_L}^2} \quad \rho_1^2 = -\sqrt{\frac{3}{2}}N_0^2\frac{\omega_L}{1+4{\omega_L}^2} \quad \rho_2^2 = \sqrt{\frac{3}{2}}N_0^2\frac{{\omega_L}^2}{1+4{\omega_L}^2} \tag{16}$$

Using Eqs. (14-16), the ratio of intensities sensitive to the magnetic field may be found:

$$\frac{\Delta I_{\alpha}}{\Delta I_{x}} = 1 - \frac{\cos\alpha + \omega_L \sin 2\alpha}{1 + 2\omega_L{}^2} \tag{17}$$

It is very important to emphasize that this ratio does not depend on the process of excitation and is the function only of the value of the Larmor frequency and the angle α.

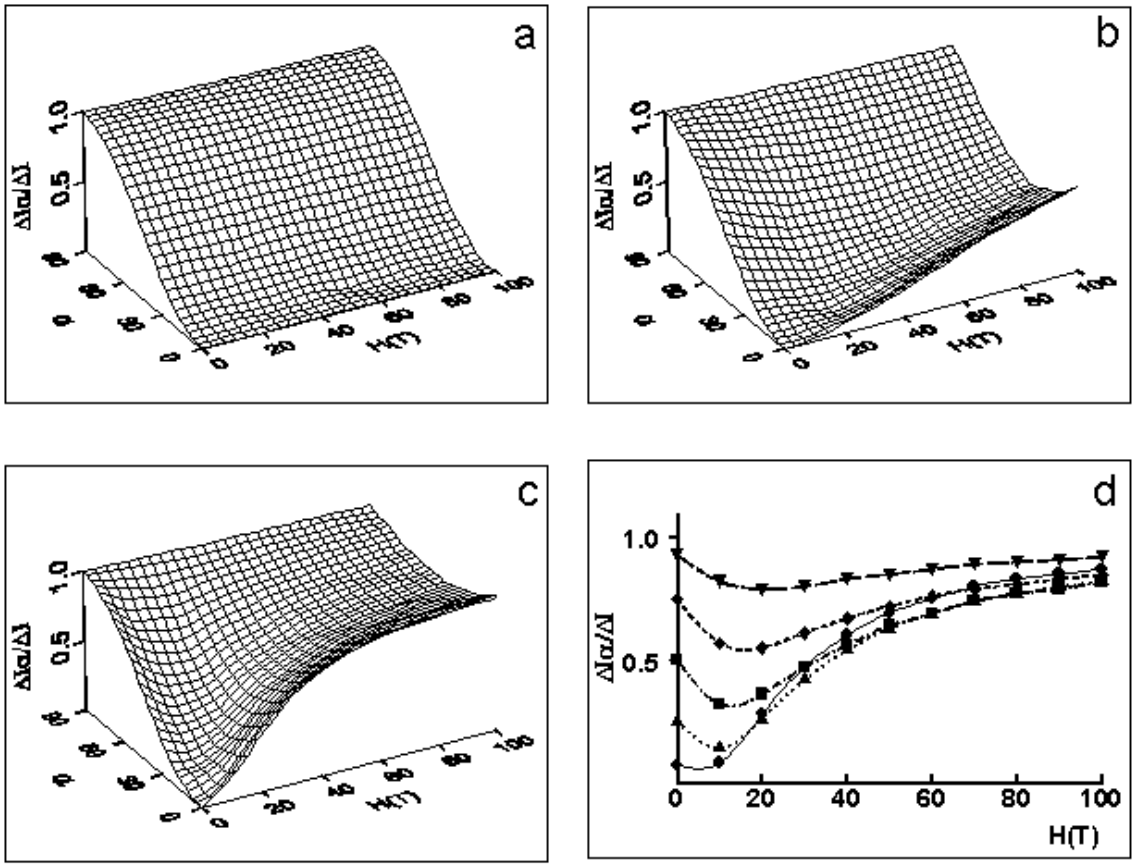

Fig. 10.
3D plot of the dependence of the ratio of the intensities $\Delta I_{\alpha} / \Delta I_{x}$ on the value of a magnetic field H and the angle of observation α calculated for the following transitions in Ti ions: a) the K-shell resonance transition $1s^2$-1s2p $^1P_1$, b) the L-shell transition 2p-3d $^1P_1$, c) the L-shell transition 2s-3p $^1P_1$; and d) 2D plot of the dependence displayed in (c) calculated for the following values of the angle α: 15º , 30º, 45º, 60º, and 75º.

For diagnostics purposes, K- and L-shell transitions in Ti ions are considered. For example, for the He-like resonance line Heα $1s^2$-1s2p $^1P_1$, the lifetime is τ_0=4.5x 10^{-15} s, and for Ne-like transitions 2l-3l', the lifetimes are 1.0x 10^{-13} s (for the transition 2p-3d $^1P_1$,3C) and 3.4 x10^{-13} s (for the transition 2s-3p $^1P_1$, 3A). For the value of magnetic field of about 10 T, the corresponding values of ω_L vary from 0.003 to 0.3. In Fig. 10 a-d, the theoretical values of the ratio $\Delta I_\alpha / \Delta I_X$ are presented in a form of 3D-plots calculated for the specified K- and L-shell transitions. For K-shell transitions, because of the particular small value of ω_L in the range of the value of a magnetic field from 10 T to 100 T, the polarization characteristics do not depend on the value of magnetic field (see Fig.10a). On contrary, for L-shell transitions, the ratio $\Delta I_\alpha / \Delta I_X$ for lines 3A and 3C significantly depends on the value of the magnetic field for small values of an angle $\alpha \leq 45^o$ (see Figs.10 b, c). Fig.10 d illustrates the sensitivity of this ratio for 3A line to the value of the magnetic field calculated for different values of the observation angle α. It is important to emphasize that lines sensitive to this diagnostic method should have not only moderate values of lifetimes but should be polarized by the electron beam excitation. In Ref. [1], similar calculations for L-shell lines of Fe ions are presented and the future experimental development of this method is discussed.

References

1. A.S. Shlyaptseva, V.L. Kantsyrev, B.S. Bauer, P. Neill, C. Harris, D.A. Fedin, S. B. Hansen, N. Ouart, P. Beiersdorfer, A.G. Petrashen, U.I. Safronova, "X-ray spectropolarimetry studies at the Nevada Terawatt Facility and LLNL EBIT", ibid.

2. V.L. Vainshtein, and U.I. Safronova, *Atomic Data and Nuclear Data Tables*, vol. 21, 44 (1978); U.I. Safronova and A.M. Urnov, *J. Phys. B*, vol. 12, 3171 (1979).

3. V.L. Vainshtein, and U.I. Safronova, *Atomic Data and Nuclear Data Tables*, vol. 25, 311 (1980).

4. V.L. Vainshtein, and U.I. Safronova, *Physica Scripta*, vol. 31, 519 (1985).

5. A.S. Shlyaptseva, R.C. Mancini, P. Neill, P. Beiersdorfer et al., "Polarization-dependent spectra of x-ray dielectronic satellite lines of Be-like Fe", *Phys. Rev. A*, vol. 52, 888-898 (1998).

6. A.S. Shlyaptseva, R.C. Mancini, P. Neill, P. Beiersdorfer, “Polarization properties of dielectronic satellite lines in the K-shell x-ray spectra of B-like Fe XXII”, *J. Phys. B*, vol. 32, 1041-1051 (1999).

7. E.V. Aglitskii and U.I. Safronova, *Spectroscopy of Autoionizing States of Multiply-charged Ions*, Energoatomizdat, Moscow (1985).

8. U.I. Safronova, A.S. Shlyaptseva, M. Cornille, J. Dubau, “Autoionization rates for $1s2s^22p^3$, $1s2s2p^3$, $1s2p^4$ states of B-like ions ($6 \leq Z \leq 54$) for decay via different channels”, *Physica Scripta*, vol. 57, 395-409 (1998).

9. R.D. Cowan, *The Theory of Atomic Structure and Spectra*, University of California Press, Berkley, CA, USA (1981).

10. V.P. Shevelko and L.A. Vainshtein, *Atomic Physics for Hot Plasmas*, IOP Publishing, London (1993).

11. V.A. Bernshtam *et al*., "Empirical formula for cross section of direct-electron-impact ionization of ions." *J. Phys. B*, vol. 33, 2025-5032 (2000).

12. J. Abdallah *et al*., "Electron beam effects on the spectroscopy of satellite lines in Aluminum x-pinch plasmas," *Physica Scripta*, vol. 53, 705-711 (1996).

13. J. Abdallah *et al*., "Electron beam effects on the spectroscopy of multiply charged ions in plasma focus experiments," *Journal of Quantitative Spectroscopy & Radiative Transfer*., vol. 62, 85-96 (1999).

14. D. Duston and J. Davis, "Line emission from hot, dense aluminum plasmas," *Phys. Rev. A*, vol. 21, 1664-1676 (1980).

15. A.S. Shlyaptseva, S. B. Hansen, V.L. Kantsyrev, B.S. Bauer, D.A. Fedin, N. Ouart, S.A. Kazantsev, A.G. Petrashen, U.I. Safronova, “X-ray spectropolarimetry of high-temperature plasmas”, *Rev. Sci. Instrum*., vol. 72, 1(II), pp. 1241-1244, 2001.

16. S.A. Kazantsev , A.G.Petrashen, M.I. Pudovkin, “Quantitative Spectropolarimetric Sensing of the Different Ionized Media”, ibid.

QUASICLASSICAL THEORY OF DIELECTRONIC RECOMBINATION IN PLASMAS

L. A. Bureyeva*, T. Kato**, V. S. Lisitsa**+ and C. Namba**

*Scientific Council on Spectroscopy of the RAS, Leninski Pr. 53, Moscow, 119991, Russia

**National Institute for Fusion Science, Toki, Gifu 509-5292, Japan

**+Permanent address: RRC "Kurchatov Institute", Kurchatov Sq., 46, Moscow, 123182, Russia

Abstract

Effects of plasmas on dielectronic recombination (DR) rates are under consideration. Effects of plasmas electric fields on DR rates are analyzed in details in the space of parabolic quantum numbers. A quasiclassical approach is used to obtained general analytical expressions for DR rates in the parabolic basis for arbitrary types of ions having transitions without change of core principal quantum numbers ($\Delta n = 0$ transitions) responsible for the main contribution to DR rates. The approach makes it possible to investigate scaling lows for dependencies of both total and differential DR rates on atomic parameters. Effects of electron collisions and ionization are taken into account with the help of cut off procedures. Numerical data are presented for Li- and Na-like ions under typical plasma conditions. A comparison with numerical calculations for specific ions is presented.

1 INTRODUCTION

Effects of electric fields on dielectronic recombination (DR) rates are under broad investigations in last two decades, see [1] - [5] and references there. These effects are connected with an evolution of highly excited atomic states populated in the DR capture of an electron colliding with ions having complex cores. The main contribution to the process comes from transitions without change of cores principle quantum numbers ($\Delta n = 0$ transitions). The electric field and plasma effects can be separated into three groups:
1) enhance of the phase space volume contributing to the recombination due to a transformation of the ion atomic energy states from the spherical quantization to the parabolic one under the action of the field;
2) decrease of a quantity of excited atomic states responsible for DR because of ionization and energy mixing effects in the electric field;
3) kinetic effects due to electron collisions after (or during) core stabilization.

The effects mentioned are usually taken into account with the help of specific numerical calculations for a particular ion. At the same time the ion energy states responsible for DR are of universal Rydberg type so DR effects must follow general scaling lows. It is a goal of the present paper to investigate general properties of plasmas electric field effects on DR rates. Note that we are interested here in the action of a plasma microfields which are much more strong as compared with laboratory electric fields. So the atomic states mixing effects can be considered to be full, an account of partial mixing being described by a simple cut off receipt. The first group mentioned above is taken into account in the frame of a quasiclassical approach.

To make clear the reasons for applications of quasiclassical methods it is to note that plasma electrons responsible for a strong dielectronic capture are generally classical ones. Really let us consider a multicharged ion with an ion charge Z and a complex atomic core having transitions without changing of its principle quantum number n ($\Delta n = 0$ transitions). The energy of these transitions is of order of Z atomic units (a u) so the energy $E = mv^2/2$ (v is the electron velocity) of the captured electron must be smaller than Z. At the same time the ionization potential of the ion is of order of Z^2 that is much larger than the electron energy E. These conditions are just the conditions of classical electron motion in the field of the multicharged ion:

$$E < Z \ll Z^2 \quad \text{or} \quad Ze^2/\hbar v \gg 1. \tag{1}$$

2 QUASICLASSICAL THEORY FOR AUTOIONIZATION DECAY RATES

The general formula for DR recombination rates takes the form [1] - [5], [10]:

$$Q_{DR}(n) = \left(\frac{4\pi Ry}{T}\right)^{3/2} \frac{g_f}{g_i}(a_0)^3 W_R$$
$$\times \exp(-\frac{\omega}{T} + \frac{Z^2}{2n^2T}) \sum_{k,m} \frac{W_A(n,k,m)}{W_R + W_A(n,k,m)}, \tag{2}$$

where T is an electron temperature, $g_{i,f}$ are statistical wages on initial (i) and finite (f) atomic core states, W_R is a radiative transition probability inside an ion core, W_A is an autoionization decay rate of the excited atomic energy level with a principal quantum number n and parabolic electrical k and magnetic m quantum numbers, ω is a frequency for a transition with $\Delta n = 0$ inside the core. Atomic units (a u) will be used below.

The radiative decay rate is simply expressed in terms of an oscillator strength f_{if} for the transition in the core (c is the speed of light):

$$W_R = 2\omega^2 f_{if}/c^3. \tag{3}$$

The autoionization decay rate $W_A(n,l)$ is calculated usually in spherical quantum numbers and the transition to parabolic ones is performed numerically with the help of summing with Clebsh-Gordan coefficients, see [1] - [5]. To obtain a general expression for DR rates we'll use a quasiclassical representation for both DR rates in spherical coordinates and for Clebsh- Gordan coefficients as well.

A quasiclassical expression for autoionization decay rate W_A may be obtained by different ways which result in the same formulas. The first way is a direct transition to the classical limit in general formulas for matrix elements of the radius-vector taken with Coulomb wave functions. Note that in the case of Rydberg states ($n \gg 1$) there is no difference which types of electron transitions (free-bound, bound-bound or free-free) are considered.

The first results were obtained by Zommerfeld [11] for free-free radiative transition in a Coulomb field. He made also a transition to classical limit and obtained quasiclassical formulas for matrix elements as functions of the scattering angle. With accounting for the relationship between the scattering angle and the electron orbital momentum l one reproduces at fast a total analogues of Kramers classical formulas from the Zommerfeld results. The same results were obtained in [12] by direct calculation of free- bound matrix elements with further transition to the classical limit. The second way is connected with the relationship between the rate W_A and the partial electron excitation cross section near threshold [13]:

$$(2l+1)g_f W_A(nl) = Z^2 n^{-3} \omega g_i \sigma_{exc}(l)/\pi^2 a_0^2, \tag{4}$$

where $g_{i,f}$, ω are statistical wages and transition frequency equal to the difference of initial and final energies of the core energy levels.

The electron excitation cross section for $\Delta n = 0$ transitions can be also calculated in the frame of pure classical mechanics:

$$\sigma^l_{exc} = \frac{8\pi^3}{3}(\hbar/mv)^2 \omega_0^2 |d_{if}|^2 g_f v^{-4}(l+1/2)$$
$$\times \left\{ \left[H^{(1)'}_{i\nu}(i\nu\varepsilon) \right]^2 - (\varepsilon^2 - 1)\varepsilon^{-2} \left[H^{(1)}_{i\nu}(i\nu\varepsilon) \right]^2 \right\}. \tag{5}$$

where v is the electron initial velocity, $H^{(1)}_{i\nu}$ is Hankel function, ε is the eccentricity:

$$\varepsilon = 1 + 2EM^2/Z^2; \;\; \nu = \omega Z/v^3; \;\; E = v^2/2; \tag{6}$$

E and M are the energy and angular moment of the incident electron, respectively.

Thus we obtain the result in the KrED domain:

$$\sigma^l_{exc} = (8\pi/3)(\hbar/mv_e)^2 (g_f/g_i) f_{if} Z^{-2}$$
$$\times (l+1/2)^2 G[\omega(l+1/2)^3/3Z^2], \tag{7}$$

where

$$G = u[K^2_{1/3}(u) + K^2_{2/3}(u)], \tag{8}$$

where $K_{1/3,2/3}$ are McDonald functions, and f_{if} is the oscillator strength for the transition considered, and g_i is the statistical weight of lower level.

The classical result (5) for the excitation cross section must be used in eq. (4) for the determination of the autoionization decay rate.

The most interesting case corresponds to the large value of the parameter $\nu \gg 1$. For large values of ν one obtains finally

$$W_A = \frac{f_{if}}{\pi n^3} lG\left(\frac{\omega_0 M^3}{3Z^2}\right), \tag{9}$$

where f_{if} is the oscillator strength for the core transition, $M = mv\varrho$ is the electron orbital momentum.

The result (5) presents the autoionization decay rate $W_A(n,l)$ in the frame of the classical approximation. It coincides with the limiting case of quantum mechanical consideration [12] after the standard substitution $l \to l + 1/2$. One can see the sharp decrease of the autoionization decay rate with the increase of the electron orbital momentum l describing by the function G. Taking into account that the essential values of the argument of G-function is never close to zero it is possible for practical applications to change the function G by its asymptotic expansion

$$G(u) \approx \pi \exp(-2u). \tag{10}$$

To obtain the total autoionization decay rate it is necessary to multiply the eq.(9) by $(2l+1)$ and sum (or integrate) over l that gives

$$W_A(n) = 4Z^2 \left|d_{if}\right|^2 g[(Z^2/8\omega)^{1/2}] 3^{-1/2} n^{-3}. \tag{11}$$

The dependence of W_A on Z is practically absent if one takes into account that $d_{ij}^2 \propto Z^{-2}$, the argument of Gaunt-factor is large if one scales $\omega \propto Z$ that means that the value of g is close to 1 (practically however the argument is not so large).

3 TRANSFORMATION TO PARABOLIC BASIS IN THE FRAME OF QUASICLASSICAL THEORY

The transformation to parabolic basis may be obtained from a consideration of quasiclassical limit of Clebsh-Gordan coefficients. Really the parabolic and spherical quantum numbers are connected by the sum with Clebsh-Gordan coefficients

$$< n_1 n_2 m | n l m' >^2 = C^2 \left[\frac{n-1}{2}, \frac{n-1}{2}, l; \frac{m+n_2-n_1}{2}, \frac{m+n_1-n_2}{2}, m' \right]. \qquad (12)$$

The squared coefficients may be considered as a joint probability $P(n,l,k,m)$ of the presence of specific quantum numbers. Making a transition to large values of all quantum numbers [16] one arrives to the following approximation

$$P(n,l,k,m) = C^2[(n-1)/2, (n-1)/2, l; (m-k)/2, (m+k)/2, m] = 2l[(l^2 - l^2_{\min})(l^2_{\max} - l^2)]^{-1/2}/\pi, \qquad (13)$$

where

$$\begin{aligned} l^2_{\min} &= [(n-1)^2 + m^2 - k^2]/2 \\ &-\{[(n-1)^2 + m^2 - k^2]^2 - 4(n-1)^2 m^2\}^{1/2}/2, \\ l^2_{\max} &= [(n-1)^2 + m^2 - k^2]/2 \\ &+\{[(n-1)^2 + m^2 - k^2]^2 - 4(n-1)^2 m^2\}^{1/2}/2, \end{aligned} \qquad (14)$$

or, when $m \ll n$

$$\begin{aligned} l^2_{\min} &\approx (n-1)^2 m^2 [(n-1)^2 + m^2 - k^2]^{-1}, \\ l^2_{\max} &\approx [(n-1)^2 + m^2 - k^2] = (n-1)^2 m^2 / l^2_{\min}. \end{aligned} \qquad (15)$$

The normalization of $P(n,l,k,m)$ (13) is equal to 1. Really, the integration (13) over l^2 gives the expression

$$-\pi \arcsin \frac{-2l^2 + l^2_{\max} + l^2_{\min}}{l^2_{\max} + l^2_{\min}} \Bigg|_{l^2_{\min}}^{l^2_{\max}} = 1.$$

The parabolic representation of a autoionization decay rate is obtained by the multiplication of the rate in spherical basis (9) by the probability (13) and integrating (summing) over l

$$W_A(n,k,m) = \int_{l_{\min}}^{l_{\max}} dl P(n,l,k,m) W_A(n,l), \qquad (16)$$

where l_{min}, l_{max} are defined by eq. (14) or (15).

Substituting the expressions (9), (13) for functions $W_A(n,l)$ and $P(n,l,k,m)$ and making a transformation to dimensionless variables $t = l/l_{ef}$, $l_{ef} = (3Z^2/\omega)^{1/3}$ it is possible to obtain:

$$W_A(n,k,m) = \pi^{-1} n^{-3} f_{if} I(n,k,m), \qquad (17)$$

where the universal function $I(n,k,m)$ is

$$I(n,k,m) = I(t_{\min}, t_{\max})$$

$$= 2l_{ef}/\pi \int\limits_{t_{\min}}^{t_{\max}} dtt^2 G(t^3)(t^2 - t_{\min}^2)^{-1/2}(t_{\max}^2 - t^2)^{-1/2}, \tag{18}$$

where G was defined by (8), $t_{\min} \propto (n-1)m[(n-1)^2 + m^2 - k^2]^{-1/2}$, $t_{\max} = (n-1)m/t_{\min} \propto n$.

Below we will use the approximation (10) for our particular calculations.

One can see that for the case $t_{max} \approx n \gg 1$ eq. (18) may be transformed to:

$$I(t_{\min}, t_{\max}) \approx 2l_{ef}/\pi t_{\max} \int\limits_{t_{\min}}^{t_{\max}} dtt^2 G(t^3)(t^2 - t_{\min}^2)^{-1/2}$$

$$\approx 2l_{ef}/t_{\max} \int\limits_{t_{\min}}^{t_{\max}} dtt^2 \exp(-2t^3)(t^2 - t_{\min}^2)^{-1/2}$$

$$= I(t_{\min}) 2l_{ef}/t_{\max}. \tag{19}$$

The universal function $I(x)$ is presented on Fig. 1.

Limiting cases of the function $I(x)$ are as follows:

$$I(x) \approx \begin{cases} \Gamma(2/3)3^{-1}2^{-2/3} \approx 0.284 \, for \, x \ll 1, \\ (\pi/12)^{1/2} x^{1/2} \exp(-2x^3) \, for \, x \gg 1. \end{cases} \tag{20}$$

$(I(0) = 0.284)$.

The function $I(x)$ can be approximated with a good precision by the simple exponent:

$$I(x) = 0.284 \exp(-2x^3). \tag{21}$$

We will use below the asymptotic expression for the function $I(x)$ for particular calculations.

The dependences of dimensionless autoionization decay rate $I(n,k,m)(\pi)^{-1}$ from eq. (18) on "electric" quantum number k for different values of magnetic quantum number m are presented on Fig. 2 for *Li*- like ion $ZnXXVIII$ $(Z = 30)$. One can see that the most contribution into k-phase space comes from small values of m.

4 DIFFERENTIAL DR RATES

To obtain differential (as regard to principal quantum numbers n) and total DR decay rates it is necessary to perform two (or three) summings in the eq. (2). It is convenient to deal with reduced DR rates $q^*(n)$ equal to the term with the sum in the eq. (2) that is

$$q^*(n) = Q_{DR}(n)/B(Z,T,\omega,n) = \sum_{k,m} \frac{W_A(n,k,m)}{W_R + W_A(n,k,m)}, \tag{22}$$

where

$$B(Z,T,\omega,n)$$
$$= \left(\frac{4\pi Ry}{T}\right)^{3/2} \frac{g_f}{g_i}(a_0)^3 W_R \exp(-\frac{\omega}{T} + \frac{Z^2}{2n^2T})$$

Let us take into account that the autoionization decay rates in the eq. (22) are expressed in terms of the universal function (21) with the argument depending on parameters l^2_{min} and l^2_{max} in accordance with eq. (16). To do this let us change the sum in eq. (22) by the integral over corresponding quantum numbers and then make a transformation to the variables l^2_{min}, l^2_{max}. The Jakobian J of the transformation is obtained by a direct calculation:

$$J(n, l^2_{\rm min}, l^2_{\rm max}) = \frac{l^2_{\rm min} - l^2_{\rm max}}{4 l_{\rm min} l_{\rm max} (n-1)^2}$$
$$\times \left[1 + \frac{l^2_{\rm min} l^2_{\rm max}}{(n-1)^4} - \frac{l^2_{\rm min} + l^2_{\rm max}}{(n-1)^2}\right]^{-1/2} \tag{23}$$

Extracting in the sum (22) the dependence on the principal quantum number n we arrive to the expression:

$$q^*(n) = 2 \int_0^{(n-1)^2} dl^2_{\rm max} \int_0^{l^2_{\rm max}} dl^2_{\rm min} \frac{J(n, l^2_{\rm min}, l^2_{\rm max})}{1 + [n/n^*(l_{\rm max}, l_{\rm min})]^3} \tag{24}$$

where the effective value of the principle quantum number n^* is introduced with the account of eqs. (3), (17), (19), (21):

$$n^{*3} = 0.284 \frac{c^3 l^2_{ef}}{\pi \omega^2 l_{\rm max}} \exp(-2 l^3_{\rm min}/l^3_{ef})$$
$$= L(n-1)^{-1} z^{-1/2} \exp(-A_n y^{3/2}),$$
$$L = 0.284 c^3 l^2_{ef} \pi^{-1} \omega^{-2}, \;\; A_n = 2(n-1)^3 l^{-3}_{ef} \gg 1 \tag{25}$$

Here the dimensionless variables $y = l_{min}^2/(n-1)^2$ and $z = l_{max}^2/(n-1)^2$ and parameters L, A_n are introduced also.

Making further the transformation to the variables y and z in eq. (24) we obtain

$$q^*(n) = \frac{1}{2}(n-1)^2 \int_0^1 \frac{dz}{\sqrt{z}} \int_0^z \frac{dy(z-y)}{[y(1+zy-z-y)]^{1/2}[1+n^3(n-1)\sqrt{z}exp(A_n y^{3/2})/L]} \tag{26}$$

The eq. (26) solves the problem of the distribution of DR rates over principal quantum numbers n.

To make clear the dependence let us take into account that under condition $A_n \gg 1$ effective values of the variable y are small as compared with z being of order of unity. Neglecting where it is possible the magnitudes of y as compared with z, expanding the integration over y to infinity and changing variables one arrives to the expression

$$q^*(n) = \frac{1.57 l_{ef}}{2^{4/3}3} n \int_0^\infty \frac{du}{u^{2/3}}(1+n^4 e^u/L)^{-1} \tag{27}$$

One can see that the dependence of DR rates on n is described by the universal function $J(\alpha)$ such that

$$Q_{DR}(n) = B(Z,T,\omega,n)q^*(n), \tag{28}$$

where

$$q^*(n) = 1.25 l_{ef} n J[n^4 \pi \omega^2/(0.284 c^3 l_{ef}^2)] \tag{29}$$

and

$$J(\alpha) = \alpha \int_1^\infty dx \ln^{1/3}(x)/(1+\alpha x)^2$$
$$\approx \begin{cases} \ln^{1/3}(1/\alpha) & if \quad \alpha \ll 1 \\ \alpha^{-1} \int_1^\infty dz z^{-2} \ln^{1/3} z & if \quad \alpha \gg 1 \end{cases} \tag{30}$$

The function $J(\alpha)$ is presented in Fig. 3.

Let us apply a general results (28)-(30) to the case of Li-like carbon ion C^{+3} and make a comparison with the particular calculations [3]. Substituting all numerical constants into the eqs. (28)-(30) one obtains the distribution of DR rates (in units $10^{-12} cm^3/s$ for the electron temperature $T_e = 10^5 K$) over principle quantum numbers presented in Fig. 4 (solid curve).

From the quasiclassical consideration it follows that the conditions for the C^{+3} ion are very close to the conditions for Mg^{+1} presented in [1]. Really one can check that both ions mentioned above have the same radiation decay rates and the arguments of J-function in eq. (29) are also very close for them. The only difference is the value of the parameter l_{ef} equal to 4.6 for C^{+3} and to 2.7 for Mg^{+1}. The corresponding results are presented in Fig. 5. The close correspondence of both data in Fig. 4 and Fig. 5 is a confirmation of the classical scaling low following from the general result (29).

5 TOTAL DR RATES

To obtain total recombination rates one must integrate a differential distribution over all values of principle quantum numbers from small value (put to be zero below) up to a particular value n_{max} depending on the cut off conditions in plasmas. Corresponding results can be also expressed in term of a universal function:

$$Q_{DR}^{tot} = B(Z, T, \omega, n) q^{*tot}, \tag{31}$$

where

$$q^{*tot} = 0.04 c^{3/2} \frac{l_{ef}^2}{\omega} P[n_{\max}^2 \omega \sqrt{\pi}/(0.533 c^{3/2} l_{ef})] \tag{32}$$

and

$$P(x) = \int_0^1 \frac{dz}{\ln^{2/3}(1/z)} \arctan \frac{x}{z}$$
$$\approx \begin{cases} \frac{\pi}{2} \int_0^1 \frac{dz}{\ln^{2/3}(1/z)}, & if \quad x \gg 1; \\ 3x \ln^{1/3}(1/x), & if \quad x \ll 1. \end{cases} \tag{33}$$

The universal function $P(x)$ is presented in Fig. 6.

Using the data (31)-(33) it is possible to investigate a dependence of DR rates on electric field strengths expressing the value of n_{max} as a function of an electric field strength F. We will pick up below the value of n_{max} in accordance with [3] to make more clear the comparison with numerical data, that is

$$n_{\max} = (6.8 \times 10^8 Z_i^3/F)^{1/4} \tag{34}$$

Fig. 7 presents the dependence of DR rates (multiplied by the factor 2 in accordance with mentioned above discrepancy between the data of the papers [2] and [3]) on the field strength (V/cm) in logarithmic scale. The data [2] are also presented in the Fig. 7. These data demonstrate the typical maximum in the increase of the DR rates which corresponds to an essential increase of phase space due to the action of the field. The field ionization results in a decrease of DR rates with the increase of field strengths. Our model corresponds to relatively large values of electric field strengths that is to the full mixing of atomic states, so the only decrease due to ionization is seen on the Fig. 7.

The simple way to take into account plasma density effects is to connect the value of n_{max} with the electron plasma density. It can be done at fast by substitution into eq. (34) the Holsmark field strength given by the formula

$$\begin{aligned} F(V/cm) &= 1.3 \times 10^{-6} Z_i N_i^{2/3} (cm)^{-3}, \\ n_{\max} &= (5.23 \times 10^{14} Z_i^2/N_i^{2/3})^{1/4}, \end{aligned} \tag{35}$$

where one can take into account the relationship $N_e = Z_i N_i$ for one component plasmas or substitute independent value N_i for many component plasmas (for example $N_e = N_{H^+}$ for hydrogen plasmas considered in [2], [3]) The comparison between of our and data [3] is presented in Fig. 8. One can see a good correspondence between universal formulae (31)-(33) and the specific calculation.

The kinetic effects due to electron collisions can be also taken into account in the following approximate manner. The main effect of electron collisions is the decrease of recombination effects due to secondary ionization of the captured electron by other plasma electrons. These effects are described by an attenuation factor $j(n, N_e, T_e)$ equal to a probability for the electron captured to reach a ground atomic state. The probability can be estimated as the ratio of the radiative decay rate A_n from the captured atomic state and the ionization frequency $N_e < v\sigma_i >$ from the state due to electron collisions. These both rates are estimated for Rydberg atomic states as follows [17]

$$\begin{aligned} A_n(s^{-1}) &= 2.4 \times 10^{10} Z_i^4/n^5, \\ < v\sigma_i > &= 10^{-7} n^2 Z_i^{-2} (Ry/T_e)^{1/2}. \end{aligned} \tag{36}$$

Using these approximation one obtains for the attenuation factor

$$j(n, N_e, T_e) = [1 + (n/n_0)^7]^{-1},$$
$$n_0 = Z_i[2.4 \times 10^{17}(T_e/Ry)^{1/2}/Z_i N_e]^{1/7} \quad (37)$$

It is seen the sharp dependence of the factor on the principle quantum number value that means that the electron secondary ionization effects can be also taken into account with the help of a cut off procedure. So the value n_0 can be used as the cut off parameter together with the n_{max} accounting for ion field ionization effects described by eq.(35) because both effects result in the ionization of the captured electron. So the specific value of n_{max} in eq. (32) must be put to be the minimum of two magnitudes (35) and (37).

The effects of both plasma ion microfield and electron collisions on DR rates for C^{+3} ions is presented in Fig. 9 as a function of electron densities for electron temperature $T_e = 10^5 K$. One can see that the ionization by electrons produces more large effect on DR rates than ionization by the electric field. The results of the resent simplified consideration are also in a reasonable correspondence with numerical data [3].

6 CONCLUSION

The consideration above results in the general quasiclassical formulas (17), (29) - (33) for differential and total DR rates as functions of atomic and cut off parameters. It describes effects of relatively strong electric fields (full mixing of atomic states) on DR rates accompanied by transitions in atomic cores without change of their principle quantum numbers ($\Delta n = 0$ transitions). These transitions are responsible for the most contribution to atomic processes in collisions of plasma electrons with complex ions. The present results make it possible to calculate DR rates in a simple way for every ions having $\Delta n = 0$ transitions in the cores.

The results above can be generalized on the case of partial l-mixing by the following way. Let us write down the condition of total mixing comparing the energy shift due to quantum defect δ_l and the matrix elements of the atom-electric field interaction:

$$3n(n^2 - l^2)^{1/2} F > Z^3 \delta_l / n^3 \quad (38)$$

The condition (38) determines a minimum value of orbital momentum l consistent with full mixing conditions. The value must be substituted instead of the parameter l_{min} into eq. (16). A contribution of atomic states with $l < l_{min}$ from the eq.(38) is taken into account in eq. (2) by the usual manner as in the conventional spherical basis.

Let us estimate an enhanced factor for DR rates. To do it one can calculate the DR rate in a spherical basis with account of eq. (9). The general expression for the effective DR rate $q^*_{sph}(n, l)$ into particular values n, l in a spherical basis takes the form [10], [11]:

$$q^*_{sph}(n,l) = (2l+1)[(n/n^*)^3 + 1]^{-1}, \tag{39}$$

where

$$n^*(l) = \{3c^3(2l+1)G[\omega(l+1/2)^3/3Z^2]/(2\pi\omega f_{if})\}^{1/3} \tag{40}$$

Using the asymptotic expression for the function $G(u)$ one can present eq. (40) in the form (see value l_{ef} in eqs. (16) - (18)):

$$n^*(l) = n^*(0)\exp[-(l/l_{ef})^3] \tag{41}$$

$$n^*(0) = c[3l_{ef}/(2\omega^2)]^{1/3} \gg 1 \tag{42}$$

When integrating eq.(39) over l it is natural to change variabls to $n^*(l)$ according eq. (40). Neglecting in this integration by slow logarithmic dependences one can obtain the following simple estimation for the total effective DR rate $q^*_{sph}(n)$:

$$q^*_{sph}(n) \approx l^2_{ef}[3l\, n\, n^*(0)]^{2/3} \tag{43}$$

that is practically doesn't depend on values of n. This value must be compared with the one in the parabolic basis given by eq. (29). Neglecting slow logarithmic dependencies we arrive to the simple estimation:

$$q^*_{par}(n)/q^*_{sph}(n) \approx n^*(0)/l_{ef} \tag{44}$$

where we have introduce the designation "par" for the result (29) above obtained in the parabolic basis. The same estimation is approximately true for the total DR recombination rates.

It is seen from the estimations that the enhanced factor for DR in an electric field is approximately equal to the ratio of the effective volume in n-space to the effective volume in l-space for the spherical basis. This ratio depends on a specific atomic structure of a recombining ion determining effective values of parameters in eq. (44). Practically for most ions the value of l_{ef} changes from 3 up to 10 whereas $n^*(0)$ is of order of 10^2 that means the enhanced factor is near $20-30$ which is in a reasonable correspondence with numerical calculations [1] - [5].

ACKNOWLEDGMENTS

We are gratefull to Prof. R. More for helpfull discussions.

This work was supported in part by the grant from the Russian Ministry of Industry, Science and Technology and in part by the grant 01-02-16305 from the RFBR.

References

[1] K. LaGattuta and Yu. Hahn, Phys. Rev. Lett. **51**, 558 (1983).

[2] D. R. Rosenfeld, Astroph. J. **398**, 386 (1992).

[3] J. Li and Yu. Hahn, Z. Phys. **D41** 19 (1997).

[4] D. C. Griffin, F. Robicheaux and M. S. Pindzola, Phys. Rev. **57** 2708 (1997).

[5] P. Krstic and Yu. Hahn, JQSRT **55** 499 (1996).

[6] L. D. Landau and L. M. Lifshits: Quantum Mechanics. (Oxford, Pergamon 1977).

[7] L. D. Landau and E. M. Lifshits: The Classical Theory of Field. (Oxford, Pergamon 1975).

[8] V. I. Kogan, A. B. Kukushkin and V. S. Lisitsa, Phys. Rep. **213** 1 (1992).

[9] L. A. Bureyeva and V. S. Lisitsa : A Perturbed Atom. (Gordon and Breach 2000).

[10] I. I. Sobelman, L. A. Vaishtein and E. A. Yukov: Excitation of Atoms and Broadening of Spectral Lines. (Springer 1980).

[11] A. Zommerfeld: Atombau und Spektrallinien. Band II, Friedr. (Viewegand Sohn Braunschweig 1960).

[12] I. L. Beigman, L. A. Vainstein and B.N. Chichkov, Sov. Phys. JETP **53** 490 (1981).

[13] V. A. Bazylev and M. I. Chibisov, Sov. Phys. Uspekhi. **24** 276 (1981).

[14] E. Fermi, Z. Physik **29** 315 (1924).

[15] J. Jackson: Classical Electrodynamics, (Wiley, N.Y. 1975).

[16] D. A. Varshalovich, A. N. Moskalev and V. K. Khersonskii: Quantum Theory of Angular Momentum. (Word Scientific, Singapore-New Jersy-Hong Kong 1980).

[17] V. P. Zhdanov, In: Reviews of Plasma Physics, Ed. By M.A. Leontovich (Consultant Bureau, N.Y.) **12** 104 (1987).

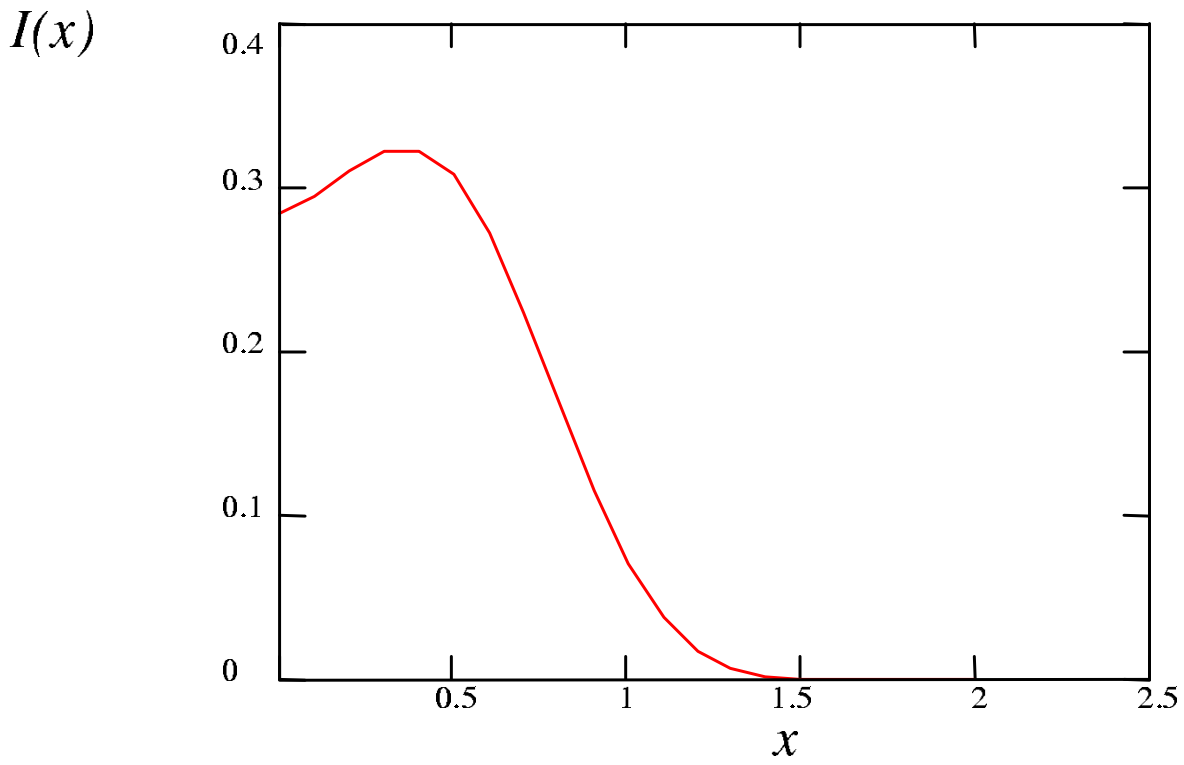

Figure 1: The universal function $I(x)$ discribing the dependence of autoionization decay rates on paabolic quantum number, see eqs. (17) -(19).

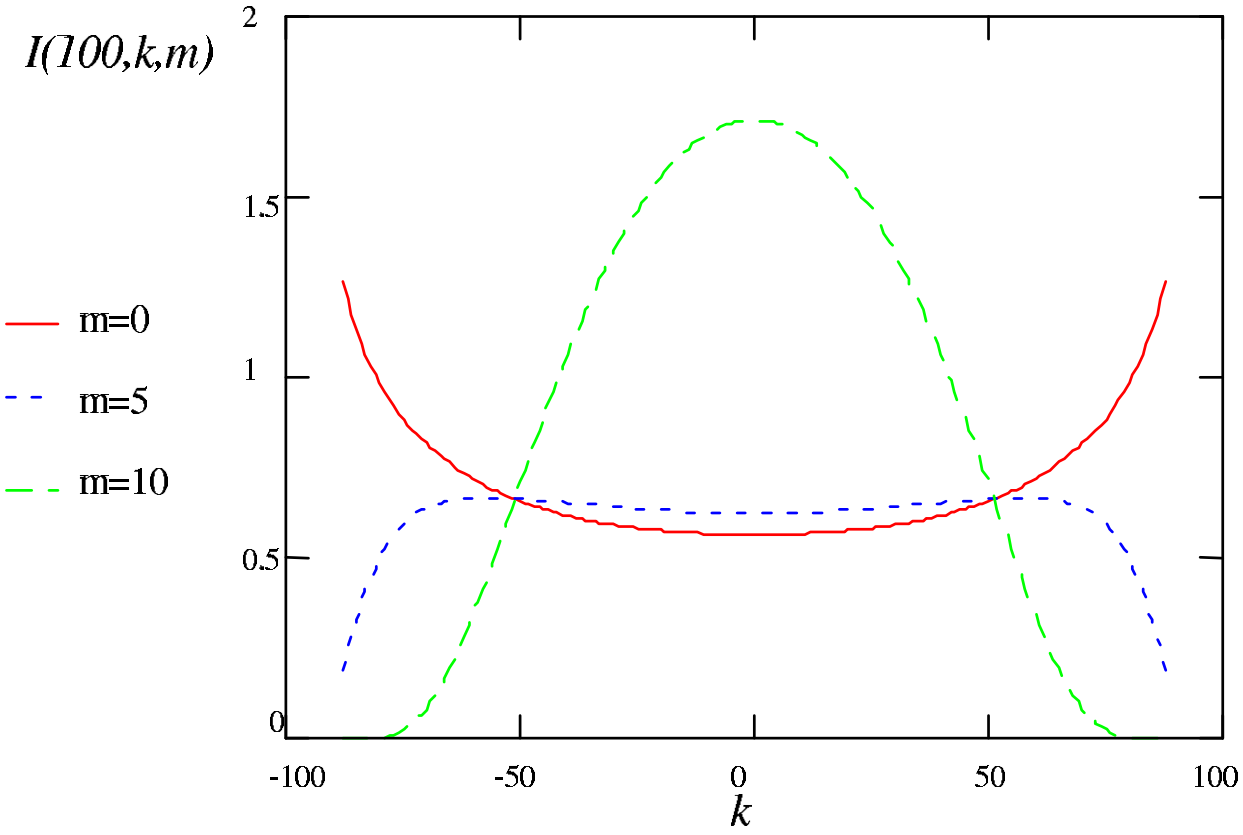

Figure 2: Distribution of autoionization decay rates over "electric" quantum numbers k at different values of magnetic quantum numbers m for Li-like ion ZnXXVIII at the principal quantum number $n = 100$. Here the scale for $I(100, k, 10)$ equals to the scale for $I(100, k, 0)$ multiplied by 10^1.

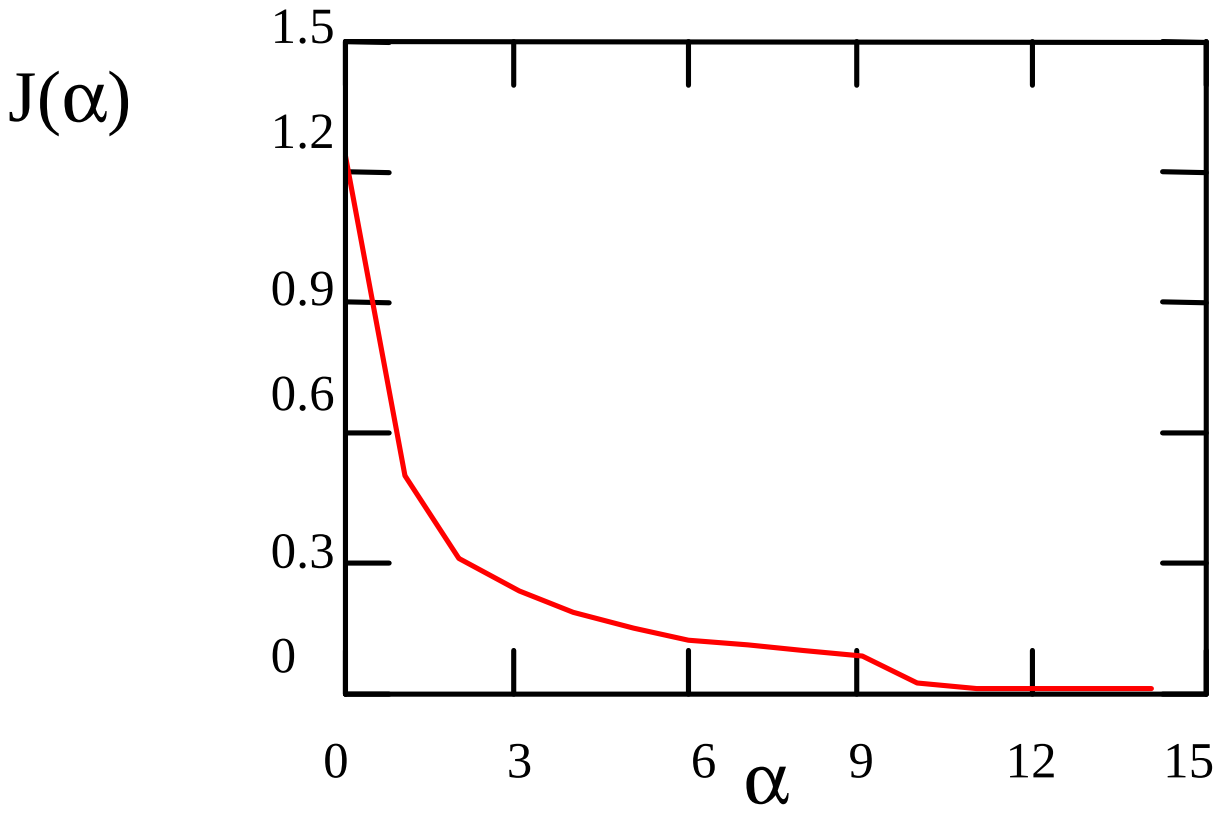

Figure 3: The universal function $J(\alpha)$ describing the distribution of DR rates over principle quantum numbers n, see eqs. (29), (30).

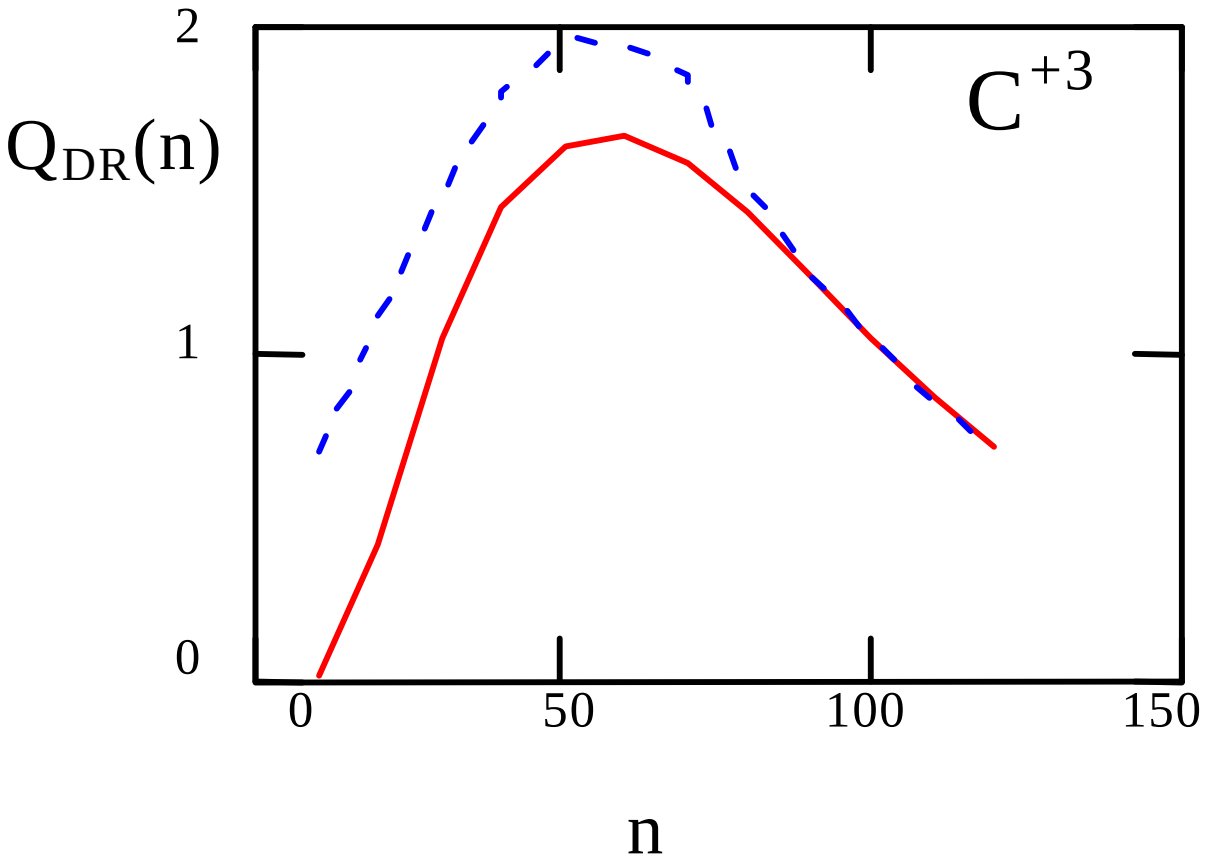

Figure 4: Distribution of DR rates (in units $10^{-12} cm^3/s$) over n for C^{+3} ion at the electron temperature $T_e = 10^5 K$: full curve - universal quasiclassical formula (28)-(30), dotted line - calculation [3].

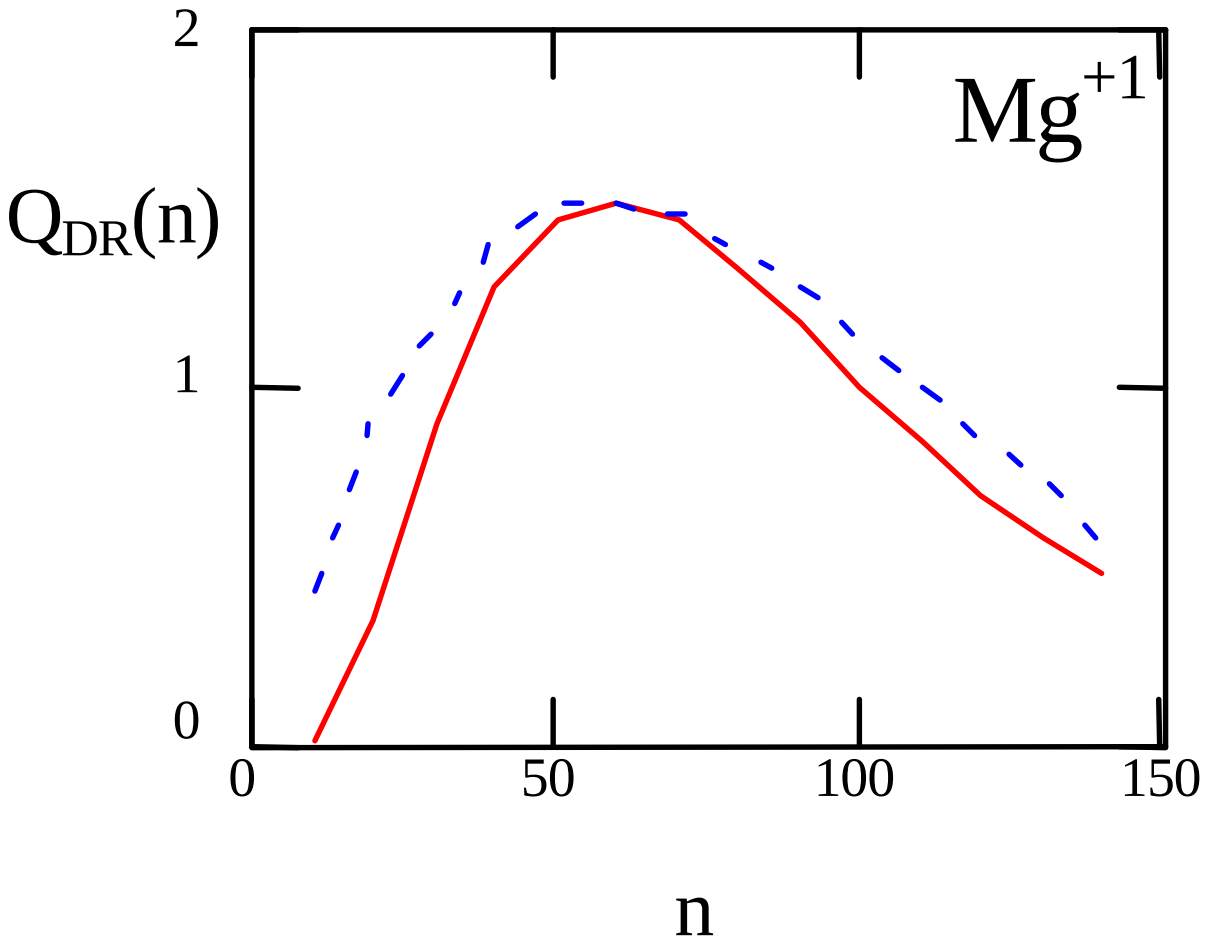

Figure 5: The same as in Fig. 4 but for Mg^{+1}-ion: full curve - quasiclassical formula (28)-(30), dotted line - calculation [1].

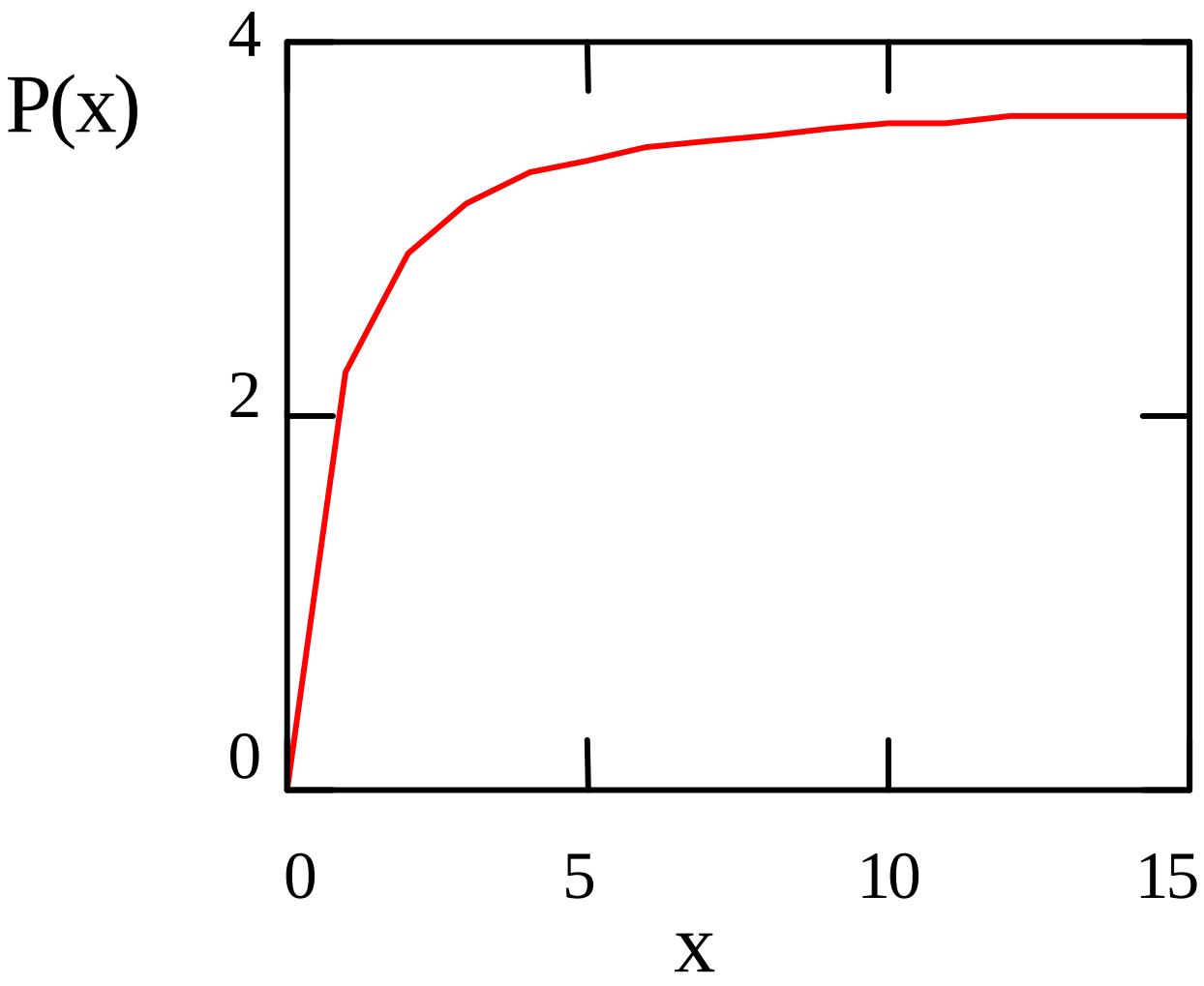

Figure 6: The universal function $P(x)$ (33) describing the dependence of total DR rates on cut off parameters.

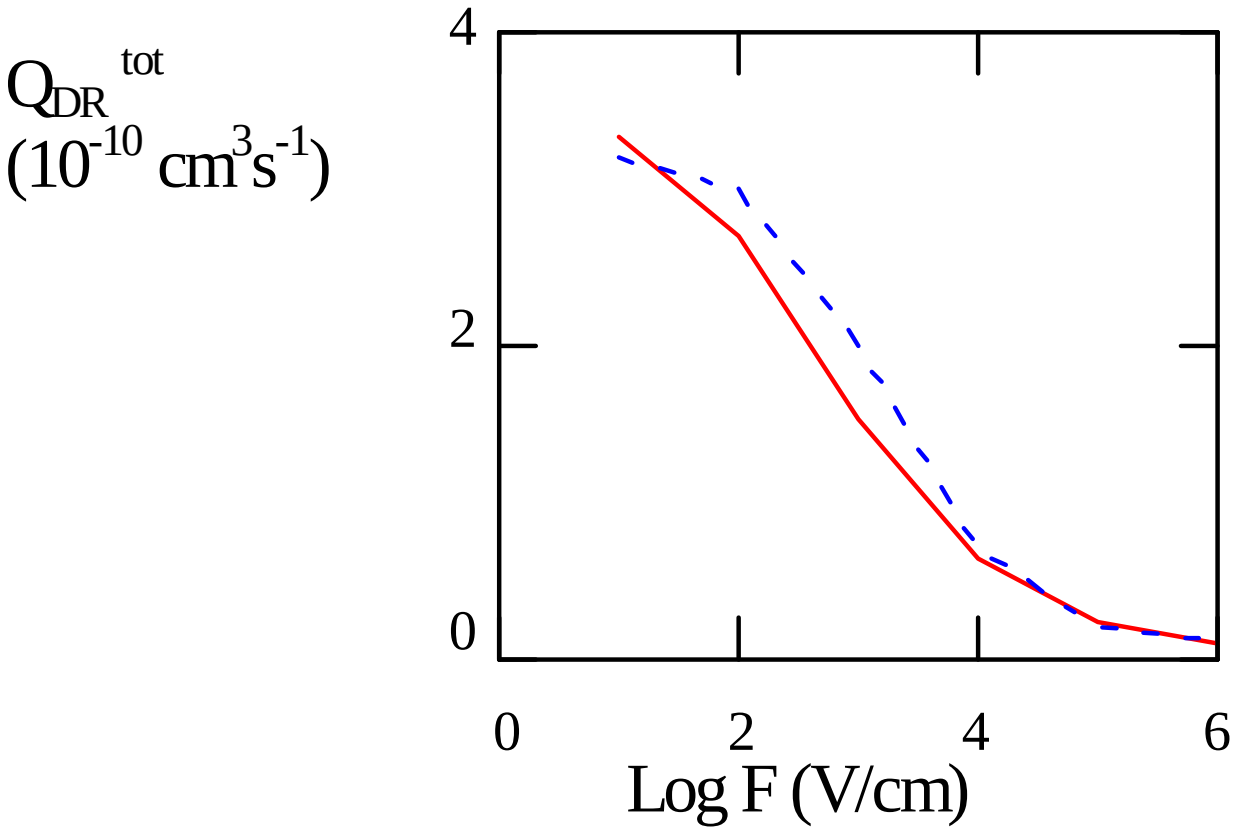

Figure 7: The dependence of total DR rates (31) for C^{+3} ion on the electric field strength: full line - quasiclassical formula (31), (32) multiplied by factor 2, dotted line - calculations [2].

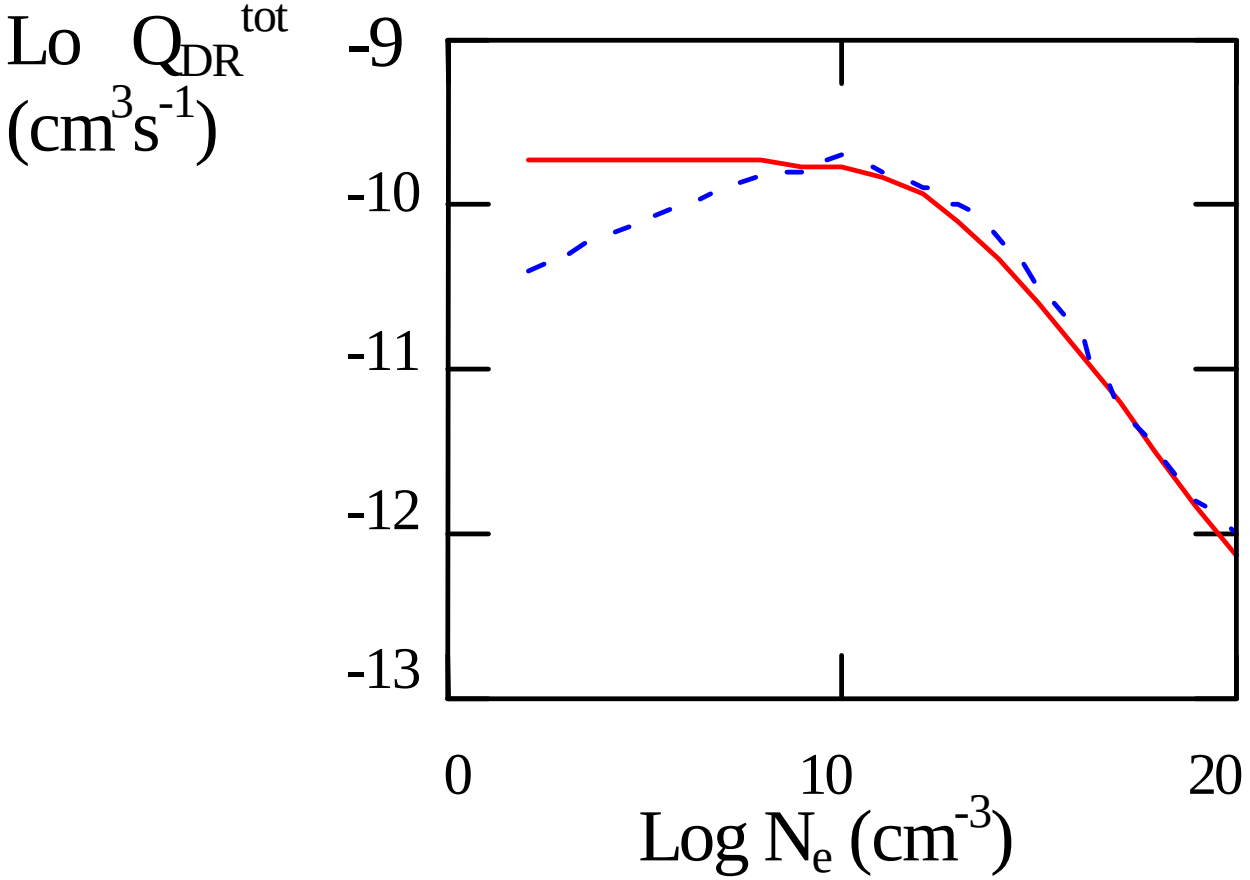

Figure 8: Effect of plasma electron density Ne on DR rate for the C^{+3} ion for the electron temperatures $T_e = 10^5 K$ (full line - quasiclassical formula (31), dotted line - calculations [3]).

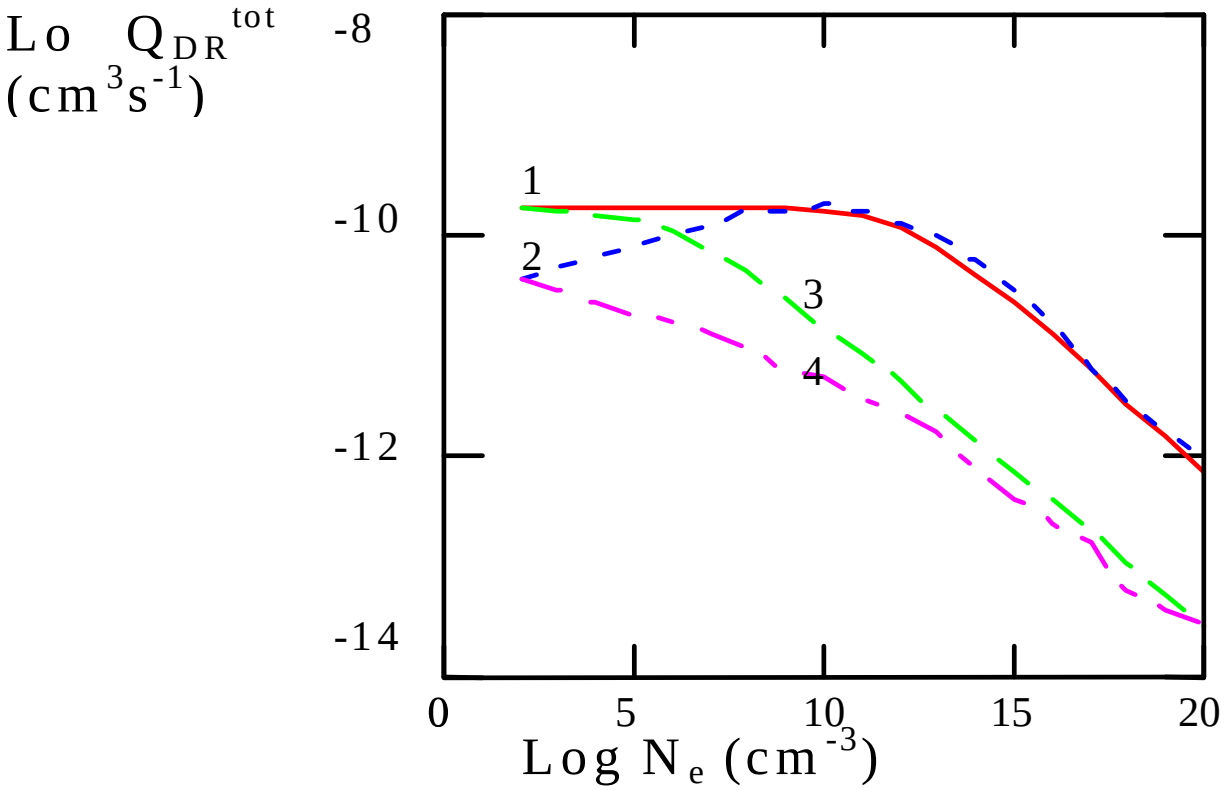

Figure 9: Effects of ion electric field (upper curves: 1 - quasiclassical formula (31), 2 - calculation [3]) and electron collisions (lower curves: 3- quasiclassical formula (31), 4 - calculation [3]) on DR rates for C^{+3} in a hydrogen plasma with $T_e = 10^5 K$.

Effect of Charge Exchange on Spectral Line Intensity of Multicharge Ions in Plasmas

L. Bureyeva[1], V. Lisitsa[2], V. Sergeev[3], R. Stamm[4] and S.Sudo[3]

[1]*Scientific Council on Spectroscopy of the RAS, Leninski Pr. 53, Moscow, 119991, Russia*
[2]*National Institute for Fusion Science, Toki, Gifu 509-5292, Japan*
(Permanent address: RRC "KI", Kurchatov Sq., 46, Moscow, 123182, Russia)
[3]*National Institute for Fusion Science, Toki, Gifu 509-5292, Japan*
[4]*UMR 6633-case 32, Université de Provence, Centre St. Jérôme, 13397 Marseille Cedex 20, France*

I. Introduction

Effects of charge exchange on intensities of multicharged ions spectral lines are of interest in magnetically confined thermonuclear devices. These spectra are subjects for investigation both in edge and bulk plasmas especially under conditions of neutral beam (NB) injection. The reason for the investigation are closely connected with a determination of multicharged ion diffusion coefficients as well as plasma attachment or detachment conditions

The change exchange spectroscopy is of a special interest for experimental investigations because it results in a population of highly excited states of multicharged ions which make it possible to observe spectral lines of ions in visible spectral ranges. So it is of interest to elaborate a kinetic model for the determination of intensities of spectral lines due to charge exchange in thermonuclear plasmas.

It is a distant goal to elaborate a differential kinetic model taking into account polarization effects in charge exchange spectroscopy. Really a neutral beam injected into thermonuclear plasmas determines a specific direction resulting in the orientation of ion electronic states populated by charge exchange on beam's atoms. So the charge exchange effect results in a selective population of both orbital and magnetic quantum numbers resulting in its turn in a polarization of spectral lines irradiated by the ions. The determination of the polarization state of the excited ion's energy levels is a complicated problem connected with effects of depolarization collisions as well as plasma microfield effects changing the quantization direction of the energy levels.

We'll consider as a first step the effects of charge exchange population on intensities of spectral lines of multicharged ions in thermonuclear plasmas.

To do this the estimations of different atomic energy level population channels are to be done together with ionization balance of impurities in such a plasma [1] shall limit ourselves by a comparison of different population sources which are as follows:

electron impact excitation (*ext*) from a ground atomic state;

radiative recombination (*rr*) of an electron on the impurity ion;

dielectronic recombination (*dr*) of an electron on an impurity ion with a complex atomic core;

charge exchange (*cx*) population of excited impurity atomic levels in collisions of impurity ions with fast hydrogen atoms from NB;

polarization recombination (*PlR*) for ions with heavy cores [2].

The electron ionization (*ion*) must be also taken into account for a determination of ionization state of impurity atoms observed.

The dielectronic recombination rates α^{dr} must be corrected with account for plasma density effects connected with the plasma microfield effects, secondary ionization by plasma electrons, etc. [3].

The PlR channel with a rate α^{PlR} can be estimated with the help of its ratio R( ) to the standard radiative recombination channel with a rate α^{rr}. The ratio $R(\omega)$ of both channels at a given transition frequency ω is determined by the ration of the effective number $N(\omega)$ of electrons inside the ions core to the effective ion charge $Z(\omega)$ that is [2]:

$$R(\omega)=\alpha^{PlR}/\alpha^{rr}=[N(\omega)/Z(\omega)]^2$$

So the contribution of the polarization recombination channel can be taken into account by the correction of the RR-channel with the help of the multiplication of the rate ^{rr} by the factor $[1+R(\omega)]$. Practically the factor is close to the unity for small and average values of nuclear charges typical for thermonuclear investigations mentioned above.

Let us make general remarks before detail calculations. The light quanta observed are determined by the sources mentioned above. These sources to a particular energy level n are due to excitation of the A^{+Z}-ion and recombination of the $A^{+(Z+1)}$-ion that is

$$q(n) = \alpha_n^{ext} N_{A^{+Z}} + \alpha_n^{rec} N_{A^{+(Z+1)}}$$

where $\alpha_n^{ext}, \alpha_n^{rec}$ are rates of excitation and all recombination processes including charge exchange recombination to level *n*, $N_{A^{+z}}$ is a density of A^{+Z}-ions. To make a comparison between two members one must take into account the ionisation balance equation:

$$-\alpha^{rec} N_{A^{+(Z+1)}} + \alpha^{ion} N_{A^{+z}} = 0,$$

where $\alpha^{rec}, \alpha^{ion}$ are total recombination and ionisation collision rates.

These two equation must be considered together. Expressing from the last equation the density $N_{A^{+(Z+1)}} = N_{A^{+z}} \alpha^{ion} / \alpha^{rec}$ and substituting it into the first equation one obtains:

$$q(n) = N_{A^{+z}} [\alpha_n^{ext} + \alpha^{ion} \alpha_n^{rec} / \alpha^{rec}]$$

One can see that the recombination source contains the ration of recombination rates to the particular energy level *n* to the total recombination rate. The relationship between excitation and recombination sources depends on a specific atomic structure of the ion and its principle quantum number *n* observed as well as on plasma conditions. When the recombination source dominates the effect is proportional to the density $N_{A^{+(Z+1)}}$. At the same time the increase of recombination channels results in the increase of both nominator (responsible for energy states populations) as well as denominator (responsible for ionisation balance shift). So the recombination source results in a *saturation* effect.

2. Kinetic models

We will take into account four population channels as it has been pointed above:

$$q(n) = q^{exc}(n) + q^{rr}(n) + q^{dr}(n) + q^{cx}(n), \quad (1)$$

where

excitation by electron impact from ground state described by $q^{exc}(n)$;

radiative recombination described by $q^{rr}(n)$;

dielectronic recombination described by i;

charge exchange channel described by $q^{cx}(n)$.

The first three channels are well known and they are taken into account with the help of numerical data presented in [1]. The charge exchange term takes into account a population of an impurity ion A^{+Z}-levels in collisions with neutral H-atoms that is

$$q^{cx}(n) = N_{A^{+(Z+1)}} N_H <v\sigma_n^{cx}>_{A^{+(Z+1)}H} = N_{A^{+(Z+1)}} N_H k_n^{cx} = N_{A^{+(Z+1)}} \alpha_n^{cx}, \quad (2)$$

where $N_{A^{+(Z+1)}}$ is the density of impurity atoms with the charge $Z+1$, N_H is atomic neutral H-atoms density in plasmas, $k_n^{cx} = <v\sigma_n^{cx}>$ is the charge exchange coefficient rate, $\alpha_n^{cx} = N_H k_n^{cx}$ is the rate of charge exchange, σ_n is charge exchange cross sections from the H-atoms to the n-level of A^{+Z}, v is a velocity of neutral H-atoms with the typical value of their energy. For low energy H-atoms one must take into account charge-exchange from excited states of H-atom populated y electron impacts.

The A^{+Z} level population kinetics must be solved together with an ionisation balance kinetics describing a balance between A^{+Z} and $A^{+(Z+1)}$ ion densities. Really the sources mentioned above (1) are proportional to different ion densities, namely: $q^{exc}(n) \sim N_e N_{A^{+Z}}, q^{rr}(n) \sim N_e N_{A^{+(Z+1)}}, q^{dr}(n) \sim N_e N_{A^{+(Z+1)}}, q^{cx}(n) \sim N_H N_{A^{+(Z+1)}}$

The ratio N_H/N_e is a parameter of the problem whereas $N_{A^{+Z}}$, $N_{A^{+(Z+1)}}$ are connected by the ionisation balance equation

$$-\alpha^{rec} N_{A^{+(Z+1)}} + \alpha^{ion} N_{A^{+Z}} = 0, \quad (3)$$

where $\alpha^{rec} = \alpha^{rr} + \alpha^{dr} + \alpha^{cx}$, α^{ion} are total recombination and ionization collision rates.

It is seen from eq.(3) that the density $N_{A^{+(Z+1)}}$ is equal to

$$N_{A^{+(Z+1)}} = N_{A^{+Z}} \alpha^{ion} / (\alpha^{rr} + \alpha^{dr} + \alpha^{cx}) \quad (4)$$

It follow from eq.(4) also that the cx recombination source $q^{cx}(n)$ is equal to

$$q^{cx}(n) = N_{A^{+Z}} \alpha^{ion} N_e \frac{k_n^{cx} N_H / N_e}{k^{rr} + k^{dr} + k^{cx} N_H / N_e} \quad (5)$$

As we can see from (5) in the case of large values of N_H/N_e the source $q^{cx}(n)$ doesn't depend on N_H at all. However one must take into account that the neutral density in nominator and denominator can be different because the density in the nominator is a local one (responsible for a radiative decay from a specific atomic energy level n) whereas the density in denominator must be averaged over a magnetic surface that means its multiplication by an slightly unknown geometrical factor $g<1$.

The detail kinetic equation for specific n energy level populations of A^{+Z}-ion is:

$$\left(N_{A^{+Z}} N_e k_n^{ext} + N_{A^{+(Z+1)}} N_H k_n^{cx} + N_{A^{+(Z+1)}} N_e k_n^{rr} + N_{A^{+(Z+1)}} N_e k_n^{dr}\right)$$
$$\left(N_{A^{+Z}} N_e k_n^{ion} + N_{A^{+Z}} N_{H^+} k_{A^{+Z}(n)H^+}^{cx} + N_{A^{+Z}} N_e k_n^{rr} + N_{A^{+Z}} N_e k_n^{dr}\right) = 0 \qquad (6)$$

The detail kinetic equation (6) shows that the full flux on level n of A^{+Z} may be written as

$$q_{A^{+Z}}(n) = N_{A^{+Z}} N_e k_n^{ext} + N_{A^{+(Z+1)}} N_H k_n^{cx} + N_{A^{+(Z+1)}} N_e (k_n^{rr} + k_n^{dr}) \qquad (7)$$

Using (4) we will write the expression for the flux to level n of A^{+Z} as:

$$q_{A^{+Z}}(n) = N_{A^{+Z}} N_e \left[k_n^{ext} + k^{ion} \frac{k_n^{rr} + k_n^{dr} + k_n^{cx} N_H / N_e}{k^{rr} + k^{dr} + g k^{cx} N_H / N_e}\right] \qquad (8)$$

Equation (8) contains rate coefficients to a particular value of principle quantum number in nominator and total rate coefficients in the denominator. Let us extract the general dependence on principle quantum numbers in the eq.(8).

The expressions for rate coefficients as functions of atomic and plasma parameters with corresponding numerical data for coefficients χ, χ' have been taken from [3]:

$$k_n^{ext} = 10^{-8} \frac{1}{2l_0 + 1} \left[\frac{Ry}{E} \frac{E_1}{E_0}\right]^{\frac{3}{2}} G(\beta) e^{-\beta}; \qquad (9)$$

where

$$G(Z>1) = \frac{A\sqrt{\beta}(\beta+1)}{\beta+\chi}; \beta = \frac{E}{T} = Z_i^2 Ry / n_1^2 T;$$

$$k^{ion} = 10^{-8} \frac{1}{2l_0 + 1} Q_i \left(\frac{Ry}{|E_Z|} \right)^{\frac{3}{2}} G(\beta) e^{-\beta};$$

(10)

where

$$G(Z>1) = \frac{A\sqrt{\beta}}{\beta + \chi}, \quad \beta = \frac{E_Z}{T} = \frac{Z^2 Ry}{n_1^2 T};$$

$$k_n^{rr} = \frac{32\sqrt{\pi} a_0 \hbar}{3\sqrt{3} m (137)^3} Z n_1 \beta_1^{\frac{1}{2}} \left[\ln(1{,}78\beta_1) - e^{\beta_1} Ei(-\beta_1) \right] \left(1 + \frac{\beta_1}{n_1} \right) = {}_{0n}^{Kr} \frac{Z^4}{n^3}; \qquad (11)$$

where ${}_{n0}^{Kr}$ is the Kramer's rate coefficient of radiation recombination [1], $\beta_1 = \frac{Z^2 Ry}{n_1^2 T}$.

The general formula for charge exchange cross section is absent for the energy range of interest. We will use below a classical scaling for the cx rates in collisions with fast *H*-atoms with the energy 150 keV which are in a reasonable correspondence with numerical data for the energy range [4]

$$k^{cx} = 0.510^{-5} [(Z+1)/25]^3,$$

(12)

The distribution of the cx rate over principle quantum numbers is rather broad. From an analysis of numerical data we will put it below to be uniform in the range of principle quantum numbers of order of *(Z+1)/2*, that is

$$k_n^{cx} = 10^{-5} [(Z+1)/25]^3 / (Z+1) \qquad (13)$$

For the dielectronic recombination one has [5]

$$k^{dr} \quad 510^{-10} [(Z+1)^2 Ry / T]^{3/2} f(\omega, eV/(13.6)^2)^{3/4} (Z+1)^{-2} \exp(-\omega / T), cm^3 s^{-1}$$

(14)

The distribution of DR rates over principle quantum numbers is also very broad in the domain of order of effective quantum number n^* being typically of order of 10^2. However the value of principle quantum number doesn't contribute to DR in plasmas because of secondary ionization processes. The numerical calculations show that practically only values *n=10-20* contribute to the DR rates. So we will put it to be uniformly distributed inside the range of *n=10*. It is necessary to note that the real value of DR can be changed strongly by the action of plasma

microfields on the highly excited ions energy states. The action of all these effects must be taken into account simultaneously. Fortunately their action is partially compensated.

Substituting typical values of collision rates into eq. (8) one arrives to the estimation of the total source responsible for a population of excited impurity energy levels:

$$q(n) = N_{A^{+z}} N_e \{k_n^{ext} + k^{ion} \frac{10^{-14}(Z+1)n_1(n_1/n)^3 + 4\ 10^{-14}(Z+1)^2 f/0.1n^* + (N_H/N_e)10^{-5}(Z+1)^2/25^3}{10^{-14}(Z+1)n_1 + 4\ 10^{-14}(Z+1)^2 f + g(N_H/N_e)0.5\ 10^{-5}(Z+1)^3/25^3}\}$$

(15)

where n_1 is a principal quantum number of a ground state ($n_1=1$ for *H, He*-like ions and $n_1=2$ for *Li*- and more complex ions), n^* is a typical quantum number for DR equal to 10^2, g is the geometrical factor accounting for contribution of charge exchange processes into the impurity ionization stage.

Extracting the ionization cross section out of the brackets and taking into account relationships (9,10) one obtains:

$$q(n)[cm^{-3}s^{-1}] = B\ q^*(n), \qquad (16)$$

where

$$B = 10^{-8} N_{A^{+z}} N_e (Z+1)^{-3} G((Z+1)^2 Ry/n_1^2 T)\exp[-(Z+1)^2 Ry/n_1^2 T)],$$

and the reduced source:

$$q^*(n) = V \left(\frac{n_1}{n}\right)^3 + \frac{10^{-14}(Z+1)n_1(n_1/n)^3 + 4\ 10^{-14}(Z+1)^2 f/0.1n^* + (N_H/N_e)10^{-5}(Z+1)^2/25^3}{10^{-14}(Z+1)n_1 + 4\ 10^{-14}(Z+1)^2 f + g(N_H/N_e)0.5\ 10^{-5}(Z+1)^3/25^3},$$

The function *G(x)* is given by eq.(10) and *V* is a slowly varying function of order of unity.

3. Conclusion

The equation (16) is an estimation of the total population source into a specific energy level n due to four types of processes mentioned above.

The intensities I_{nk} of radiative transitions between atomic states $n \to k$ of A^{+Z} are calculated by

$$I_{nk} = \hbar\omega_{nk} N(n) W_{nk} .$$

The probabilities W_{nk} are pure atomic characteristics whereas populations N(n) depend on conditions of plasma. Under corona conditions the source is simply equal to the quantity of quanta radiated by the impurity.

The consideration above demonstrates the essential effect of charge exchange on the intensities of ions spectral lines under neutral beam injection conditions. The interesting effect is connected with partial canceling of the neutral density effects due to shift of ionization balance between $A^{+(Z+1)}$ and A^{+Z} ions under the conditions of charge exchange recombination resulting in the saturation effect mentioned above. This is why the data with and without account charge exchange processes are of the same orders of magnitudes.

Really let us put the value of principle quantum numbers n in eq. (16) to be large enough so that the energy of quanta observed $Z^2/n^3 = 0.1$ a.u. belongs to the visible domain. Then it follows from the eq.(16) that dominant recombination channels are dielectronic and charge exchange recombinations. When $N_H/N_e = 0$ the term $q^*(n)$ in the eq.(16) is approximately equal to 0.1 whereas when $N_H/N_e \rightarrow \infty$ the term is equal to $2/Z$ that is not so distant from the first value for $Z<30$. So a contrast with the action of the beam is not so large. The dependence of the reduced source $q^*(n)$ on the value of N_H/N_e is presented on Figs.1,2 at different values of ion charge Z. One can see the saturation effect which is of special importance for large ions charges. It results in the less sensitivity of the population source to the value N_H/N_e for these ions.

One can see also from Fig.2 that the effect of charge exchange increases for diagnostic beams with a small value of geometrical factor g in eq. (16). The rest problem is an observation of small signal produced by the beam in thermonuclear devices.

Figs.1,2 must be analyzed together with the curves on Fig.3 where the most representative ion charges are shown at different values of N_H/Ne.

References

1.Vanstein L.A., Sobelman I.I., Jukov E.A. “Excitation of atoms and broadening of spectral line ”, Springer, 1981

2. L.A. Bureyeva, V.S. Lisitsa: A Perturbed Atom (Gordon and Beach 2000).

3. L.A. Bureyeva, T. Kato, V.S. Lisitsa, C. Namba. NIFS Report –673. Toki. Japan 2000.

4. Janev R.K., Presnyakov L.P. and Shevelko V.P. “Physics of Highly Charged Ions”, Springer, 1985

5. Zhdanov V.P., Dielectronic Recombination. In: Reviews of Plasma Physics, ed by Leontovich M.A. and Kadomtsev , v.12 (Consultants Bureu, New York, London 1987)

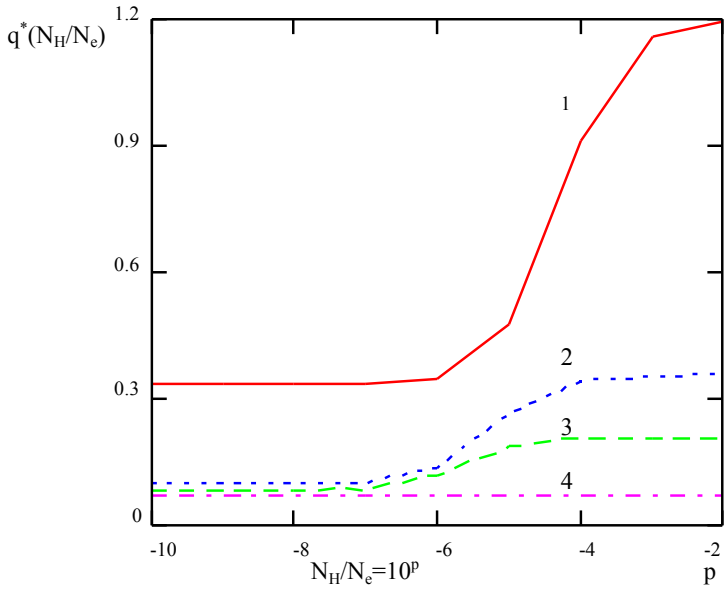

Fig. 1 The dependence of *q*(n)* (equal to the reduced source) on the value of N_H/N_e at different values of ion charge *Z* (curve 1 corresponds to *Z=2*, 2 - *Z=6*, 3 - *Z=10*, 4 - *Z=30*) (for case g=1)

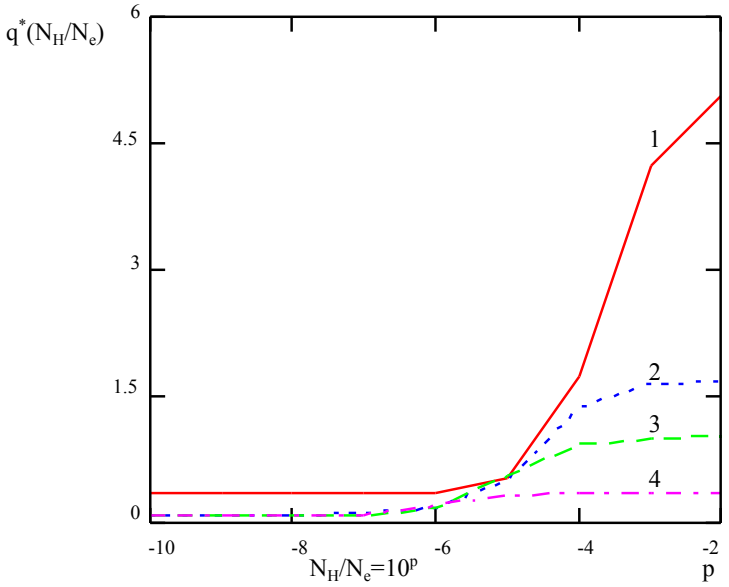

Fig. 2. The same as on Fig.1 but for $g=0.2$.

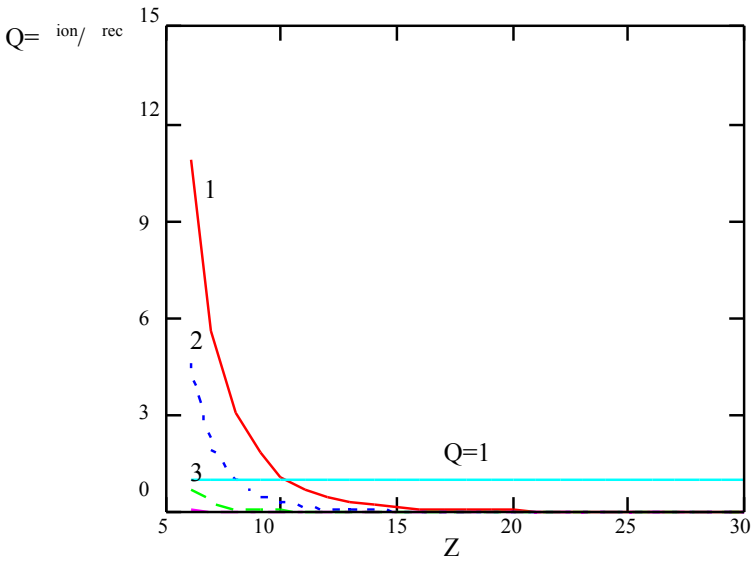

Fig. 3. Ratio Q= $^{ion}/\ ^{rec}$ of ionization rates ^{ion} to recombination ones ^{rec} as functions of ions charges Z for different values on N_H/Ne (1- 10^{-6}, 2 - 10^{-5} , 3- 10^{-4}) and typical plasma parameters $T_e=1keV$ and $N_e=10^{13}\ cm^{-3}$.

The value $Q=1$ corresponds to the most representative ion in plasmas.

Plasma Polarization Spectroscopy for the O V Ion: Relevant Collision Cross Sections for Kinetic Modeling

G. Csanak, D. P. Kilcrease and Honglin Zhang

Los Alamos National Laboratory

Los Alamos, NM 87545

D. V. Fursa and I. Bray

Flinders University of South Australia

G.P.O. Box 2100

Adelaide 5001, Australia

T. Fujimoto and A. Iwamae

Department of Engineering Physics and Mechanics

Graduate School of Engineering, Kyoto University

Kyoto 606-8501, Japan

Abstract

We have performed relativistic distorted wave approximation (RDWA) and close coupling (CC) calculations for electron impact induced magnetic sublevel to magnetic sublevel transitions in OV relevant to the population alignment collisional-radiative model used for the interpretation of polarization spectra taken at Kyoto University. The levels involved were $2s^2\ ^1S_0$, $2s2p\ ^3P_{0,1,2}$ and $2s3p\ ^3P_{0,1,2}$. We have also performed CC calculations for the elastic scattering alignment creation by the $2s2p\ ^3P_1$ level of OV. We will report our RDWA and CC results for the magnetic sublevel to magnetic sublevel cross sections and alignment creation by elastic scattering by the $2s2p\ ^3P_1$ level at one energy.

I. INTRODUCTION

This Report is closely associated to the Report by Iwamae *et al.* in this volume. It has two purposes;

1. To describe the Relativistic Distorted Wave Approximation (RDWA) method which was used in obtaining the rate-coefficients that were used in the population-alignment model of Iwamae *et al.* and compare, in some selected cases, the RDWA results to the close coupling (CC) results.

2. To discuss alignment creation by elastic scattering and give numerical result at one energy for the associated alignment creation cross section.

II. INELASTIC SCATTERING

The first part of the Report deals with the application of the RDWA and the CC method for the calculation of magnetic-sublevel *excitation* and *de-excitation* cross sections that enter the model of Iwamae *et al.* . The system considered is OV, i.e. Be-like Oxygen.

In the RDWA the amplitude for scattering an electron with initial spin m_s and momentum **k**, and final spin m_s' and momentum **k'**, by an atomic ion is given as [1]

$$B^{m_s}_{m_s'}(\beta_t J_t M_t \to \beta_t' J_t' M_t') = \frac{2\pi}{k} \sum_{\substack{l,m_l,j,m \\ l',m_l',j',m'}} \mathrm{i}^{l-l'-1} \exp[\mathrm{i}(\delta_\kappa + \delta_{\kappa'})] Y_l^{m_l^*}(\widehat{k}) Y_{l'}^{m_l'}(\widehat{k}') \times \quad C(l\tfrac{1}{2}m_l m_s; jm) C(l'\tfrac{1}{2}m_l' m_s'; j'm') T(\alpha, \alpha'), \tag{1}$$

where α and α' represent the initial and the final ion states in the uncoupled representation:

$$\alpha = kljm\beta_t J_t M_t, \quad \alpha' = k'l'j'm'\beta_t' J_t' M_t', \tag{2}$$

$\beta_t J_t M_t$ and $\beta_t' J_t' M_t'$ are the initial and the final target ion states, respectively, with β_t and β_t' representing all other quantum numbers required to specify the states of the target ion. In

Eq. (1) the Coulomb phase factors δ_κ and $\delta_{\kappa'}$ can be obtained as described in the Appendix of Ref. [1], and the relativistic quantum numbers κ and κ' are given by Eqs. (3) and (4) in [1].

The T-matrix element can be expressed in terms of the reactance matrix element as

$$T(\alpha,\alpha') = \frac{-2\mathrm{i}R}{1-2\mathrm{i}R} \simeq -2\mathrm{i}R(\alpha,\alpha'). \tag{3}$$

We then obtain the reactance matrix element in the uncoupled representation from the coupled representation by transformation

$$R(\alpha,\alpha') = \sum_{J,M} C(J_t j M_t m; JM) C(J_t' j' M_t' m'; JM) R(\gamma,\gamma'), \tag{4}$$

where the initial and the final ion states are

$$\gamma = klj\beta_t J_t JM, \quad \gamma' = k'l'j'\beta_t' J_t' JM. \tag{5}$$

The reactance matrix element in the coupled representation is given by

$$R(\gamma,\gamma') = \langle \Psi_i \mid \sum_{\substack{q,p \\ q<p}}^{N+1} \frac{1}{r_{qp}} \mid \Psi_f \rangle \ , \tag{6}$$

where the Ψ_i and Ψ_f are the initial and final wave-functions for the total (e + ion) system, as given by Eq. (5) in Ref. [2].

The cross section between the magnetic sublevels is given by

$$Q(\beta_t J_t M_t \to \beta_t' J_t' M_t') = \frac{1}{2} \sum_{m_s, m_s'} \int \mathrm{d}\widehat{k}' \mid B_{m_s'}^{m_s} \mid^2 . \tag{7}$$

Using Eqs. (1), (3), (4) and (6) we obtain

$$\begin{aligned} Q(\beta_t J_t M_t \to \beta_t' J_t' M_t') = \frac{2\pi}{k^2} \sum_{\substack{l,l_1,j,j_1 \\ l',j',m',m_s}} \sum_{J,J_1,M} & \mathrm{i}^{l-l_1}[(2l+1)(2l_1+1)]^{1/2} \\ \times \quad & \exp[\mathrm{i}(\delta_\kappa - \delta_{\kappa_1})] C(l\tfrac{1}{2}0m_s; jm) C(l_1\tfrac{1}{2}0m_s; j_1 m) \\ \times & C(J_t j M_t m; JM) C(J_t j_1 M_t m; J_1 M) C(J_t' j' M_t' m'; JM) \\ \times \quad & C(J_t' j' M_t' m'; J_1 M) R(\gamma,\gamma') R(\gamma,\gamma_1'). \end{aligned} \tag{8}$$

In addition to the RDWA for some specific excitations we have also used a nonrelativistic momentum space CC method [5] for the calculation of electron scattering from the OV ion.

The close-coupling calculations included 30 states: 4 ^1S, 4 $^1P^o$, 1 $^1P^e$, 4 $^1D^e$, 1 $^1D^o$, 2 $^1F^o$, 3 ^3S, 4 $^3P^o$, 1 $^3P^e$, 3 $^3D^e$, and 2 $^3F^o$ states. These are all low energy discreet spectrum states with major configurations as given in the Moore Tables [4]. The model used for the structure calculations is that of two active electrons above a frozen $1s^2$ Hartree-Fock core. Here we give a few numbers pertinent to this calculation: the ground state ionization energy is -113.7 eV, (the experimental value is -113.9 eV).

For the excitation energies:

$2s2p^3P$ level - 10.2 eV

$2s3p^3P$ level - 72.2 eV .

Relativistic effects have been accounted for in a semirelativistic approximation [6] in which we have used a one-body spin-orbit term and calculated singlet-triplet mixing coefficients for the $2s2p^3P_1$ and $2s3p^3P_1$ states. We have found that the $2s2p^3P_1$ state is described very well in the nonrelativistic approximations, while for the $2s3p^3P_1$ state the mixing between nonrelativistic $2s3p^3P_1$ and $2s3p^1P_1$ states is small but not negligible. The mixing coefficients are:

a = 0.997 and b = 0.02237 .

The semirelativistic integrated cross section (ICS) for the $2s3p^3P_1$state (ignoring a small interference term) is given by

$$\mathrm{ICS} = a^2\mathrm{ICS}(2s3p^3P_1) + b^2\mathrm{ICS}(2s3p^1P_1) \tag{9}$$

where $\mathrm{ICS}(2s3p^3P_1)$ and $\mathrm{ICS}(2s3p^1P_1)$ are the cross sections for the nonrelativistic states.

In Figures (1) and (2) we compare the results from the RDWA and CC calculations for the excitation cross sections from the 2s^2 $^1S_0$ state to the magnetic sublevels of the 2s2p $^3P_{0,1,2}$ levels as an example. As can be seen comparison is quite good except for the unresolved resonance structures found just above threshold in the CC calculations. For other cases we found similar agreement.

III. ELASTIC SCATTERING

The second part of the Report deals with alignment creation by *elastic* scattering for positive ions in general and for OV in particular. The elastic scattering amplitude consists of two parts; the well known pure Coulomb (Rutherford) part and the correction term which we calculate by the CC method. The differential cross section (the magnitude squared of the scattering amplitude) will have three parts: The Coulomb (Rutherford) cross section, the interference term and a small correction term. Here we discuss the correction term to the scattering amplitude.

First lets consider how the LS coupling amplitude can be converted to the intermediate coupling (or uncoupled) representation, so that we have an amplitude for a nonrelativistic final (initial) state with orbital angular momentum l_i (l_f), and spin s_f (s_i). We want to have an amplitude for the coupling $(l_f s_f)J_f M_f$ ($(l_i s_i)J_i M_i$) to describe transitions between fine-structure levels $J_f M_f$ and $J_i M_i$,

$$f^{\sigma_f,\sigma_i}_{\pi_f J_f M_f,\pi_i J_i M_i}(\theta,\varphi) = \sum_{m_f,q_f,m_f,q_f,S} C^{J_f M_f}_{l_f m_f,s_f q_f} C^{SM_S}_{\frac{1}{2}\sigma_f,s_f q_f} C^{J_i M_i}_{l_i m_i,s_i q_i} C^{SM_S}_{\frac{1}{2}\sigma_i,s_i q_i} \times f^S_{\pi_f s_f l_f m_f,\pi_i s_i l_i m_i}(\theta,\varphi). \tag{10}$$

Here σ_f and σ_i are final (initial) projectile spin projections.

The nonrelativistic amplitude $f^S_{\pi_f s_f l_f m_f,\pi_i s_i l_i m_i}$ is written below simply as $f^S_{m_f m_i}(\theta,\varphi)$ in a partial wave expansion.

$$f^S_{m_f m_i}(\theta,\varphi) = \frac{2\pi^2}{\sqrt{\pi}}\sqrt{\frac{k_i}{k_f}} \sum_{L_f,L_i,L} i^{L_i-L_f}\sqrt{2L_i+1}\, C^{Lm_i}_{L_f m_i-m_f,l_f m_f} \times C^{Lm_i}_{L_i 0,l_i m_i}\, T^{LS}_{L_f l_f L_i l_i}\, Y^{L_f}_{m_i-m_f}(\theta,\varphi), \tag{11}$$

where $k_i(k_f)$ and $L_i(L_f)$ are projectile initial (final) linear and orbital angular momenta, L is the total orbital angular momentum, S is the total spin. The spherical polar angles of the detected electron are θ and φ. (Note that we removed $1/\sqrt{2l_i+1}$ from the definition of the amplitude and that the Coulomb phase factor is contained in the T-matrix elements.)

Now, for a general case, all that is required is to substitute the second equation into the first one and run summations over all indices except of L_f in order to convert it to the form which will be convenient for future considerations.

The Coulomb amplitude is diagonal in the projectile magnetic spin sublevels indexes σ_f, σ_i. Therefore the interference term will be diagonal in σ_f, σ_i too, so we need only the amplitudes with $\sigma_f = \sigma_i = \sigma$. Actually the Coulomb amplitude is identical for both values of σ, so the close-coupling amplitudes in the interference term must be summed over σ.

Lets consider our case of elastic scattering. We choose:

$J_i = J_f = J, \quad l_i = l_f = l, \quad s_i = s_f = s,$

$M_i = M_f = M, \quad \sigma_f = \sigma_i = \sigma.$

Therefore in Eq. (10) we have:

$m_f = m_i = m, \quad q_f = q_i = q$ and it follows from Eq. (11)

$$f^S_{mm}(\theta, \varphi) = f^S_{mm}(\theta) \tag{12}$$

Thus Eq. (10) becomes:

$$f^{\sigma,\sigma}_{JM,JM}(\theta) = \sum_{m,q,S} [C^{JM}_{lm,sq}]^2 \, [C^{SM_S}_{\frac{1}{2}\sigma,sq}]^2 \, f^S_{m,m}(\theta). \tag{13}$$

Note that there is no dependence on angle φ.

As we noted earlier there should be a summation in the interference term over σ. This will give:

$$\sum_\sigma f^{\sigma,\sigma}_{JM,JM}(\theta) = \sum_{m,S} \frac{2S+1}{2s+1} \, [C^{JM}_{lm,sq}]^2 \, f^S_{m,m}(\theta), \quad (q = M - m). \tag{14}$$

Let us write partial wave expansion for elastic amplitude $f^S_{m,m}(\theta)$

$$f^S_{mm}(\theta) = \sum_{L_f, L_i, L} i^{L_i - L_f} \sqrt{2L_i + 1} \, \sqrt{2L_f + 1} \, C^{Lm}_{L_f 0, lm} \, C^{Lm}_{L_i 0, lm} \, T^{LS}_{L_f l L_i l} \, P_{L_f}(\theta), \tag{15}$$

and substitute it into Eq.(14), with result:

$$\sum_\sigma f^{\sigma,\sigma}_{M,M}(\theta) = \sum_{L_f} B(L_f, M) P_{L_f}(\theta) \tag{16}$$

where

$$B(L_f,M)=\sum_{L_i,L}\left\{\sum_m [C^{JM}_{lm,sq}]^2\ C^{Lm}_{L_f0,lm}\ C^{Lm}_{L_i0,lm}\right\} i^{L_i-L_f}\sqrt{2L_i+1}\ \sqrt{2L_f+1}\ \sum_S \frac{2S+1}{2s+1}T^{LS}_{L_flL_il} \tag{17}$$

$(q=M-m)$.

The coefficients $B(L,M)$ can be easily calculated.

Now let us turn to the calculation of the interference term. The total Coulomb plus CC amplitude F is

$$F^{\sigma_f,\sigma_i}_{M_f,M_i}(\theta,\varphi)=\delta_{\sigma_f,\sigma_i}\ \delta_{M_f,M_i}\ f^{Coul}(\theta)+f^{\sigma_f,\sigma_i}_{M_f,M_i}(\theta,\varphi). \tag{18}$$

The differential cross section (DCS) for a transition between magnetic sublevels is given by:

$$DCS_{M_f,M_i}(\theta,\varphi)=\frac{1}{2}\sum_{\sigma_f,\sigma_i}|F^{\sigma_f,\sigma_i}_{M_f,M_i}(\theta,\varphi)|^2, \tag{19}$$

and for excitation of the sublevel M:

$$\begin{aligned} DCS_M(\theta,\varphi) &= \frac{1}{2J+1}\ \sum_{M_i} DCS_{M,M_i}(\theta,\varphi) \\ &= |f^{Coul}(\theta)|^2+DCS^{CC}_M(\theta,\varphi)+\ \frac{1}{2J+1}\ Re\left[f^{Coul}(\theta)\ \sum_\sigma\ f^{\sigma,\sigma*}_{M,M}(\theta)\right] \\ &= DCS^{Coul}_M(\theta)+DCS^{CC}_M(\theta,\varphi)+DCS^{intf}_M(\theta), \end{aligned} \tag{20}$$

where

$$DCS^{intf}_M(\theta)=\frac{1}{2J+1}\ Re\left[f^{Coul}(\theta)\ \sum_\sigma\ f^{\sigma,\sigma*}_{M,M}(\theta)\right]. \tag{21}$$

Alignment creation is then determined by

$$DCS_1(\theta,\varphi)-DCS_0(\theta,\varphi)=DCS^{CC}_1(\theta,\varphi)-DCS^{CC}_0(\theta,\varphi)+DCS^{intf}_1(\theta)-DCS^{intf}_0(\theta). \tag{22}$$

We can see that the pure Coulomb DCS terms have canceled removing the problem of their divergences at $\theta=0$. For the Coulomb amplitude in the interference term small θ values will not be important for two separate reasons: first plasma screening will introduce a cut-off

in the scattering impact parameter at the Debye screening length. This corresponds to a lower cut-off in the DCS integration over angle θ. Second in the partial wave expansion used below there is a reduction in the CC amplitude as l grows allowing the introduction of an $lmax$ to terminate the series.

Then we integrate over spherical angles

$$\begin{aligned} ICS_1 - ICS_0 &= \int d\Omega \, [DCS_1(\theta,\varphi) - DCS_0(\theta,\varphi)] \\ &= ICS_1^{CC} - ICS_0^{CC} + \int d\Omega \, [DCS_1^{intf}(\theta) - DCS_0^{intf}(\theta)]. \end{aligned} \tag{23}$$

Therefore we need to calculate:

$$\int d\Omega \; DCS_M^{intf}(\theta) = \int d\Omega \; \frac{1}{2J+1} \; Re \left[f^{Coul}(\theta) \; \sum_{\sigma} \; f_{M,M}^{\sigma,\sigma *}(\theta) \right]. \tag{24}$$

In order to do this we use partial wave expansions for both the Coulomb and CC amplitude:

$$\sum_{\sigma} f_{M,M}^{\sigma,\sigma}(\theta) = \sum_{l=0}^{lmax} B(l,M) P_l(\theta), \tag{25}$$

see Eq. (17) for $B(l,M)$,

$$f^{Coul}(\theta) = \sum_{l} (2l+1) C(l) P_l(\theta), \quad C(l) = \frac{e^{i\sigma_l} - 1}{2i}. \tag{26}$$

Therefore

$$\begin{aligned} \int d\Omega \; DCS_M^{intf}(\theta) &= \frac{1}{2J+1} \; Re \left[\sum_{l=0}^{lmax} \sum_{l'} C(l') B(l,M) \int d\Omega \; P_l(\theta) P_{l'}(\theta) \right] \\ &= \frac{4\pi}{2J+1} \; \sum_{l=0}^{lmax} C(l) B(l,M). \end{aligned} \tag{27}$$

Finally the alignment creation cross section $Q_1^{(2)}$ is given by Ref. (3) as:

$$Q_1^{(2)} = \sqrt{\frac{2}{3}} \, (ICS_1 - ICS_0) \tag{28}$$

where

$$ICS_1 - ICS_0 = ICS_1^{CC} - ICS_0^{CC} + \frac{4\pi}{2J+1} \; \sum_{l=0}^{lmax} C(l)[B(l,1) - B(l,0)]. \tag{29}$$

We have used the CC method to calculate $Q_1^{(2)}$ for elastic scattering by the $2s2p\ ^3P_1$ level of a 29.81 eV incident electron. The result obtained was

$$Q_1^{(2)} = 8.32 \times 10^{-18}\text{cm}^2. \tag{30}$$

This appears to be two orders of magnitude larger than the largest values we obtained for the same ion for inelastic processes which were around $Q^{(2)} \sim 5 \times 10^{-20}$ cm^2. This indicates that alignment creation by elastic scattering by ions may be of significant importance.

Acknowledgments

This work was partially funded at Los Alamos National Laboratory by the US Department of Energy, in Japan by a Grant-in-Aid for Scientific Research by the Ministry of Education, Culture, Sports, Science and Technology, and in Australia by the Australian Research Council, Flinders University of South Australia, and the Australian Center for High Performance Computing and Communications.

References

1. H.L. Zhang, D.H. Sampson, and R.E.H. Clark, Phys. Rev. A **41**, 198 (1990).

2. H.L. Zhang, D.H. Sampson and A.K. Mohanty, Phys. Rev. A **40**, 616 (1989).

3. D.V. Fursa and I. Brey. Phys. Rev. A **52**, 1279 (1995).

4. C. Moore, *Atomic Energy Levels*, NBS Circ. No. 467, Vol. lll (1949).

5. S. Trajmar, I. Kanik, M.A. Khakoo, L.R. LeClair, I. Bray, D. Fursa and G. Csanak, J. Phys. B **32**, 2801 (1999).

6. D.V. Fursa, S. Trajmar, I. Bray, I. Kanik, G. Csanak, R.E.H. Clark and J. Abdallah, Phys. Rev. A **60**, 4590 (1999).

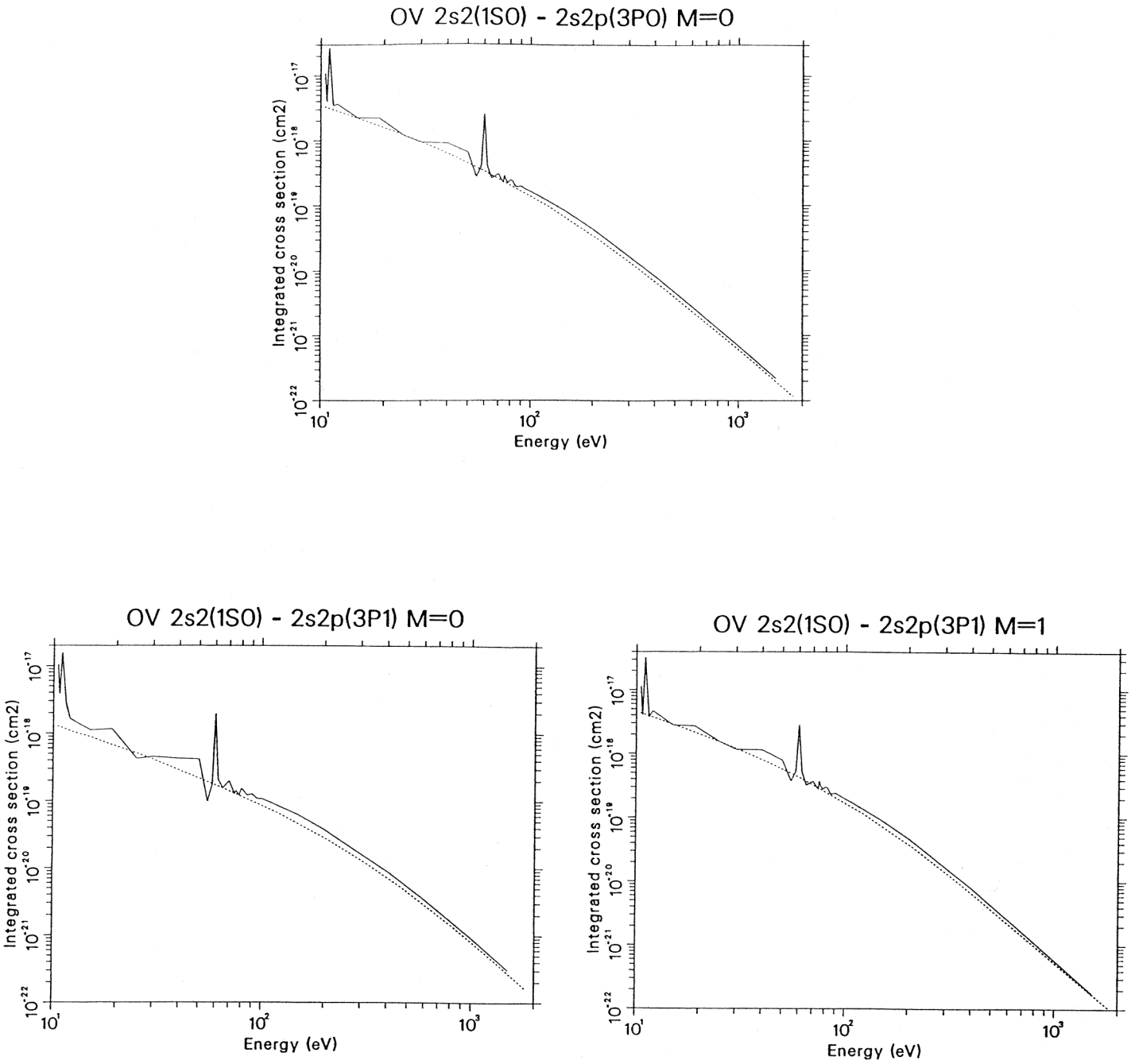

Figure 1. Comparison of the RDWA (dotted line) and CC (solid line) calculations for the excitation cross sections from the $2s^2\ ^1S_0$ state to the magnetic sublevels of the $2s2p\ ^3P_{0,1}$ levels.

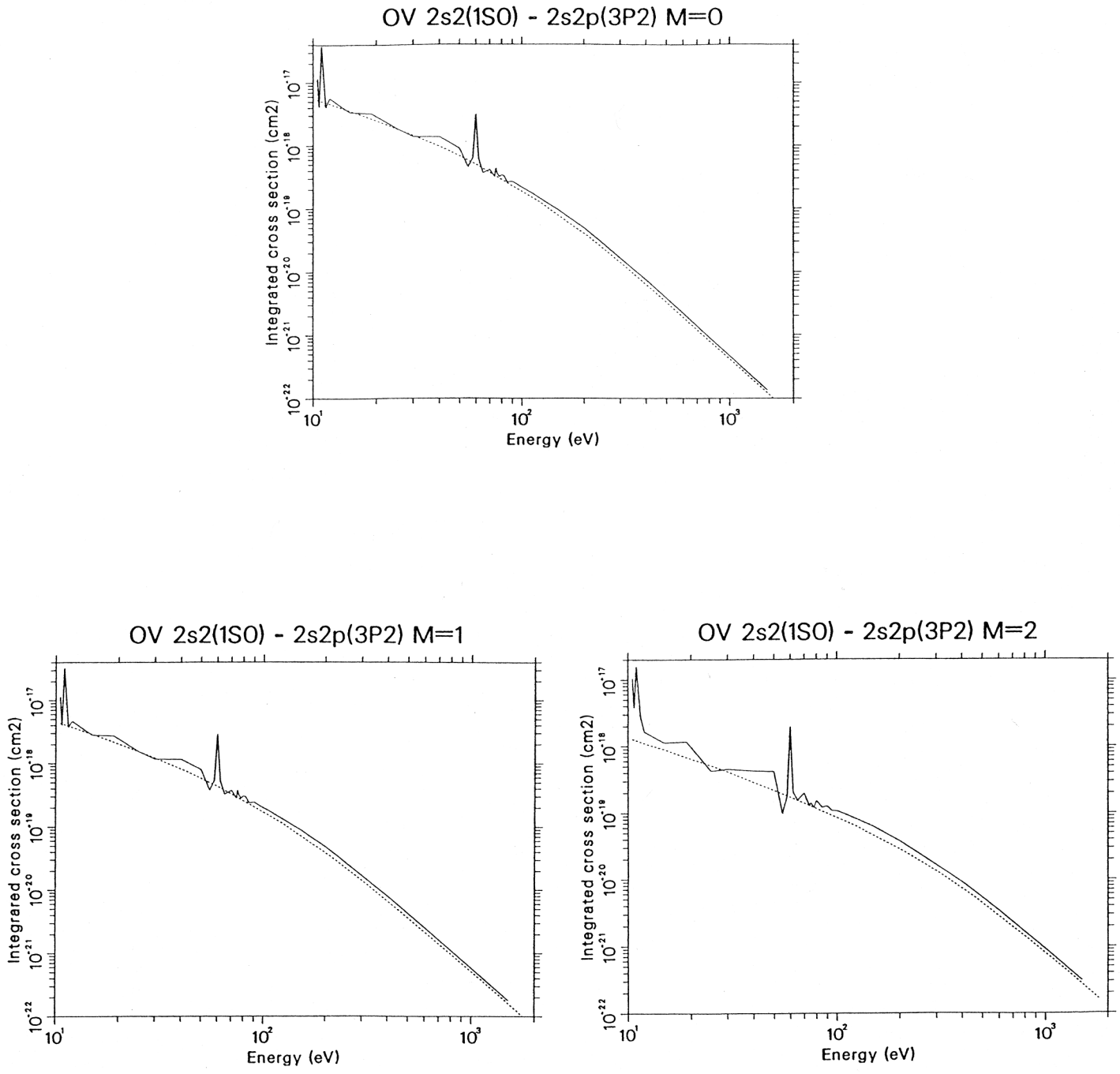

Figure 2. Comparison of the RDWA (dotted line) and CC (solid line) calculations for the excitation cross sections from the $2s^2\ {}^1S_0$ state to the magnetic sublevels of the 2s2p ${}^3P_2$ levels.

Polarization of emission lines from beryllium-like oxygen OV: Analysis based on the Population-Alignment Collisional-Radiative model

Atsushi Iwamae, Akihiro Tanaka, Takeru Inoue and Takashi Fujimoto

Department of Engineering Physics and Mechanics, Graduate School of Engineering, Kyoto University

Kyoto 606-8501, Japan

Honglin Zhang, David P. Kilcrease and George Csanak,

Los Alamos National Laboratory, Los Alamos, NM, 87545, U.S.A.

Abstract

Longitudinal alignment of OV triplet lines for the ($2s3s\ ^3S_1 - 2s3p\ ^3P_{0,1,2}$) transitions is studied on the basis of a population-alignment collisional-radiative (PACR) model, which correlates quantitatively the observed polarization of emission lines from ions and atoms in a plasma with an anisotropy in the electron velocity distribution. The results are compared with measurements on the WT-3 tokamak at Kyoto University. The measured negative values of the longitudinal alignment are qualitatively explained from the anisotropic velocity distributions that have higher speed in the poloidal direction than that in the toroidal direction.

1. Introduction

It has been reported that emission lines may be polarized in magnetically confined plasmas [1,2,3]. This fact means that in addition to the intensity and the spectral profile of a line, we can use its polarization information in interpreting the conditions in the plasma. The triplet lines ($2s3s\ ^3S_1$ $2s3p\ ^3P_{0,1,2}$) of beryllium-like OV ions are often used in plasma diagnostics since the lines rather strong and the wavelengths are in the ultraviolet-visible region. It has been reported that the intensity ratio between the component having the electric fields oscillating in the direction of the quantization axis, toroidal direction, and the component of the J=1 – 2 transition in the triplet lines changed during the discharge time [1]. This indicates that the ensemble of the upper levels ions is aligned. It is suggested that the spatially anisotropic collisional excitation by electrons having an anisotropic velocity distribution creates the alignment. In order to interpret the observed polarization of emission lines in terms of the anisotropic velocity distribution, we have constructed a kinetic model for the OV ions: the population-alignment collisional-radiative (PACR) model.

2. PACR model for OV ions

The levels of the $2s^2$, 2s2p, $2p^2$, 2s3s, 2s3p, and 2s3d configurations for OV (twenty levels) are considered in our model. Figure 1 shows the relevant part of the energy level diagram. The label numbers (1) to (20) are used to refer to the levels. The population densities are calculated for these twenty levels under the assumption that all transitions considered are optically thin and the plasma is the ionizing plasma.

In a PPS observation, the population and the alignment are determined for the upper level. The observed line intensity is given by the upper-level population and the radiative transition probability, and the degree of polarization of the observed line is given by the alignment, or the degree of the population imbalance, of the upper level. Thus a population $n(p)$ and alignment $a(p)$ are assigned to each level p. Transition probabilities and collision cross sections between the singlet levels are taken from the previous CR model for OV [4]. The alignment is considered only for the triplet levels. The excitation and deexcitation cross sections between a magnetic sublevel and a magnetic sublevel concerning anisotropic collisions are calculated by the distorted wave approximation for the transitions between levels (1)– (2), (3), (4) and (1) – (14), (15), (16) and (2), (3), (4) – (14), (15), (16) and for transitions between the different J levels in the same configuration i.e. (2) – (3), (4) and (3) – (4) and (14) – (15), (16) and (15) – (16).

For excitation and deexcitation of $a\,J \neg a\,J$ ($a\,J$ $a\,J$) or r p (r p), the cross section data are the collision cross sections $Q_{a\,JM,a\,J\,M}$ from a magnetic sublevel $a\,J\,M$ to a magnetic sublevel $a\,JM$. As examples, the magnetic-sublevel-to-magnetic-sublevel cross sections $Q_{a\,JM,a\,J\,M}$ from the ground state (1) $2s^2\ ^1S_0$ to (16) $2s3p\ ^3P_2$ and from (4) $2s3p\ ^3P_2$ to (16) $2s3p\ ^3P_2$ are tabulated in Table 1.

The collision cross sections employed in the PACR model are denoted by $Q_0^{kk}(r,p)$. The cross section $Q_0^{00}(r,p)$ is the cross section from the population of level r to the population of level p; this is nothing but the conventional excitation cross section under isotropic collision conditions, $Q_0^{20}(r,p)$ is from population of level r to alignment of level p, $Q_0^{02}(r,p)$ from alignment of level r to population of level p,

and $Q_0^{22}(r,p)$ from alignment of level r to alignment of level p. These cross sections are related to the magnetic-sublevel-to-magnetic-sublevel cross sections as follows; [3]

$$Q_0^{00}(r,p) = (2J+1)^{-1} \sum_{MM'} Q_{a\,JM,a\,JM'} \tag{2.1}$$

$$Q_0^{20}(r,p) = (2J+1)^{-1} \sum_{MM'} (-1)^{J-M} \langle JJM \quad -M \,|\, 20 \rangle \; Q_{a\,JM,a\,JM'} \tag{2.2}$$

$$Q_0^{02}(r,p) = \sum_{M} (-1)^{J-M} \langle JJM \quad -M \,|\, 20 \rangle \sum_{M'} Q_{a\,JM,a\,JM'} \tag{2.3}$$

$$Q_0^{22}(r,p) = \sum_{MM'} (-1)^{J+J+M+M'} \langle JJM \quad -M \,|\, 20 \rangle \langle JJM' \quad -M' \,|\, 20 \rangle \; Q_{a\,JM,a\,JM'} \tag{2.4}$$

where $\langle JJM \quad -M \,|\, kq \rangle$ is the Clebsch-Gordan coefficient.

The converted excitation cross sections are plotted in Figure 2 (a) – (d) for the transition of (4) to (16) as an example. The plotted lines of the cross sections are the results of smooth spline interpolations for the calculated data. These cross sections concerning the alignment $a(p)$: $Q_0^{02}(r,p)$, $Q_0^{20}(r,p)$, $Q_0^{22}(r,p)$ may take negative values in contrast to the population to population cross sections $Q_0^{00}(r,p)$.

One example of the anisotropic electron velocity distributions is the existence of a beam component superimposed on bulk electrons having an isotropic distribution [5,6]. Another example is a Maxwellian distribution with different temperatures in different directions [7,8]. In order to quantify a velocity distribution,

it is expressed by $f(v,\theta)$, which satisfies the normalization condition, $\int f(v,\theta) v^2 \sin\theta \, dv \, d\theta = 1$. Axial symmetry is assumed around the z-axis, the quantization axis. It is convenient to expand the velocity distribution in terms of Legendre polynomials,

$$f(v,\theta) = \sum_K f_K(v) P_K(\cos\theta) \tag{2.5}$$

where $P_K(\cos\theta)$ is the K th Legendre polynomial. The expansion coefficients are obtained by

$$f_K(v) = \frac{2K+1}{2} \int f(v,\cos\theta) P_K(\cos\theta) \sin\theta \, d\theta \; . \tag{2.6}$$

Since it is impossible to distinguish between $\cos\theta$ and $\cos(\pi - \theta)$ components in an actual observation, only the K = (even) terms are considered.

We take the quantization axis in the magnetic field direction. In practice, the quantization axis is regarded as parallel to the toroidal direction. Two anisotropic velocity distribution models are assumed in the PACR model. In the first model, most of the electrons are described by the isotropic Maxwell velocity distribution and some of them have a shifted Maxwell distribution along the quantization z-axis centered at a high velocity V_z. These two parts are called the main $f_M(v,\theta)$ and the child $f_C(v,\theta)$ components;

$$f(v,\theta) = f_M(v,\theta) + f_C(v,\theta) \tag{2.7a}$$

$$f_{\mathrm{M}}(v,\theta) = \frac{2\pi}{1+\delta}\left(\frac{m}{2\pi k_{\mathrm{B}}T_{\mathrm{eM}}}\right)^{3/2} \exp\left(-\frac{m}{2k_{\mathrm{B}}T_{\mathrm{eM}}}v^2\right) \tag{2.7b}$$

$$f_{\mathrm{C}}(v,\theta) = \frac{2\pi\delta}{1+\delta}\left(\frac{m}{2\pi k_{\mathrm{B}}T_{\mathrm{eC}}}\right)^{3/2} \exp\left(-\frac{m}{2k_{\mathrm{B}}T_{\mathrm{eC}}}\left(v^2 - 2vV_z\cos\theta + V_z^2\right)\right), \tag{2.7c}$$

where δ is the electron number ratio between the child and main components. This velocity distribution corresponds to the model of the runaway electrons in a main plasma in a tokamak.

In the second model, the electron velocity distribution is described by different electron temperatures; parallel and perpendicular to the quantization axis: the toroidal temperature T_{t} and the poloidal temperature T_{p}. The electron velocity distribution $f(v,\theta)$ is expressed as

$$f(v,\theta) = \left(\frac{m}{2\pi k_{\mathrm{B}}}\right)^{3/2} \left(\frac{1}{T_{\mathrm{p}}^2 T_{\mathrm{t}}}\right)^{1/2} \exp\left(-\frac{m}{2k_{\mathrm{B}}}v^2\left(\frac{\sin^2\theta}{T_{\mathrm{p}}} + \frac{\cos^2\theta}{T_{\mathrm{t}}}\right)\right) . \tag{2.8}$$

It is noted that these two parameters called *temperature* here are not real temperatures, since the concept of electron temperature is based on the assumption that electrons obey the isotropic Maxwell velocity distribution. Temperature cannot be defined when we introduce the anisotropic velocity distribution. The shape of the equi-velocity surface of the distribution becomes "rugby-ball like" when the toroidal temperature is higher than the poloidal one, $T_{\mathrm{t}} > T_{\mathrm{p}}$, and "pancake-like" when $T_{\mathrm{t}} < T_{\mathrm{p}}$. Examples of the Legendre expansion coefficients $f_K(v)v^3$ (K=0,2,4) are shown in Figure 2 (e) – (f) for the distribution with two temperatures of T_{t} = 40 eV and T_{p} = 100 eV.

The excitation rate coefficients for the transitions $a\,J \to a\,J$, or $r \to p$, are defined with the following formula in the PACR model [3]:

$$C^{00}(r,p) = Q_0^{00}(r,p)2\,f_0(v)v^3\mathrm{d}v \tag{2.9a}$$

$$C^{20}(r,p) = Q_0^{20}(r,p)\frac{2}{5}f_2(v)v^3\mathrm{d}v \tag{2.9b}$$

$$C^{02}(r,p) = Q_0^{02}(r,p)\frac{2}{5}f_2(v)v^3\mathrm{d}v \tag{2.9c}$$

$$\begin{aligned} C^{22}(r,p) = {} & [Q_0^{22}(r,p) + Q_1^{22}(r,p) + Q_2^{22}(r,p)]\frac{2}{5}f_0(v)v^3\mathrm{d}v \\ & + [2Q_0^{22}(r,p) + Q_1^{22}(r,p) - 2Q_2^{22}(r,p)]\frac{2}{35}f_2(v)v^3\mathrm{d}v \\ & + [6Q_0^{22}(r,p) - 4Q_0^{22}(r,p) + Q_0^{22}(r,p)]\frac{2}{105}f_4(v)v^3\mathrm{d}v \end{aligned} \tag{2.9d}$$

where the $f_K(v)$ functions are the Legendre expansion coefficients defined above. The cross sections and the corresponding expansion coefficients in the integrands above are displayed in Figure 2.

Spontaneous radiative transition processes are isotropic, and we have only the two corresponding rates: for $r \to p$ ($p \to r$).

$$A^{00}(r,p) = A(r,p) \tag{2.10a}$$

$$A^{22}(r,p) = (-1)^{J_r + J_p + 1}(2J_r + 1)\begin{Bmatrix} J_r & J_r & 2 \\ J_p & J_p & 1 \end{Bmatrix} A(r,p) \tag{2.10b}$$

where $A(r,p)$ is the usual Einstein A coefficient and $\{\}$ is the 6-j symbol.

We have two sets of rate equations for the ensemble of atoms. For population we have a rate equation

$$\begin{aligned} \frac{dn(p)}{dt} = & \sum_{r \neq p} C^{00}(r,p) n_e + A^{00}(r,p) \; n(r) \\ & - \sum_{r \neq p} C^{00}(r,p) + S(p) \; n_e + \sum_{r \neq p} A^{00}(p,r) \; n(p) \\ & + \sum_{r \neq p} C^{02}(r,p) n_e a(r) \\ & - C^{02}(p,p) n_e a(p) \end{aligned} \tag{2.11}$$

and for alignment we have

$$\begin{aligned} \frac{da(p)}{dt} = & \sum_{r \neq p} C^{20}(r,p) n_e n(r) \\ & - C^{20}(p,p) n_e n(p) \\ & + \sum_{r \neq p} C^{02}(r,p) n_e + A^{22}(r,p) \; a(r) \\ & - C^{22}(p,p) n_e + \sum_{r \neq p} A^{00}(p,r) \; a(p) \end{aligned} \tag{2.12}$$

where n_e is the electron density, $C^{20}(p,p)$ is the alignment production rate coefficient as given by the sum of the rate coefficient for the unequal depopulation from different magnetic sublevels and alignment production by elastic collisions, $C^{02}(p,p)$ is the rate of alignment decay by depopulation from the magnetic sublevels, and $C^{22}(p,p)$ is the rate coefficient for alignment destruction. The alignment destruction process has two components: inelastic and elastic collisions. The former is depopulation. The latter process may be called disalignment. At the moment, these rate coefficients are not available, so that we set $C^{02}(p,p) = 0$, $C^{20}(p,p) = 0$ and $C^{22}(p,p) = \sum_{r \neq p} C^{00}(p,r) + S(p)$. This corresponds to the assumption that the cross sections for the depopulation rate from the magnetic sublevels a_{JM} are all equal.

The population $n(p)$ and the alignment $a(p)$ for OV twenty levels are determined after solving the simultaneous equations under the steady state condition. The population $n(p)$ of the 2s3p $^3P_{0,1,2}$ levels; $n(14)$, $n(15)$ and $n(16)$ as a function of the electron density are shown in Figure 3 for the distribution with temperature components of T_t = 40 eV and T_p = 100 eV.

An ensemble of atoms is excited to the level p and the emission line for transition $p \rightarrow s$ is then observed from the direction perpendicular to the quantization axis. The intensity which is proportional to the population

$$I_0 = \frac{1}{4\pi l^2} n(p) A(p,s) \hbar\omega , \tag{2.13}$$

where l is the distance from the emitting atoms to the detector, is given by

$$I_{0\delta} = \frac{2}{3}(I_{\delta} + 2I_{\acute{o}}). \tag{2.14}$$

The longitudinal alignment is defined as

$$A_{\mathrm{L}} = \frac{(I_{\delta} - I_{\acute{o}})}{(I_{\delta} + 2I_{\acute{o}})}, \tag{2.15}$$

and the degree of polarization is related to the longitudinal alignment by

$$P = \frac{3A_{\mathrm{L}}}{A_{\mathrm{L}} + 2}. \tag{2.16}$$

The intensities of the and polarization components are given as [3]

$$I_{\delta} = \frac{1}{8\pi l^2} n(p) A(p,s) \hbar w [1 + (\quad)^{J_P + J_s} \sqrt{6} (2J_p + 1) \begin{matrix} J_p & J_p & 2 \\ 1 & 1 & J_s \end{matrix} \frac{a(p)}{n(p)}] \tag{2.17a}$$

$$I_{\acute{o}} = \frac{1}{8\pi l^2} n(p) A(p,s) \hbar w [1 \quad (\quad)^{J_P + J_s} \frac{\sqrt{6}}{2} (2J_p + 1) \begin{matrix} J_p & J_p & 2 \\ 1 & 1 & J_s \end{matrix} \frac{a(p)}{n(p)}]. \tag{2.17b}$$

From equations (2.15) and (2.17) the population $n(p)$ and alignment $a(p)$ are related to the longitudinal alignment,

$$A_L(p,s) = (\quad)^{J_P + J_s} \sqrt{\frac{3}{2}} (2J_p + 1) \begin{matrix} J_p & J_p & 2 \\ 1 & 1 & J_s \end{matrix} \frac{a(p)}{n(p)}. \tag{2.18}$$

For the observed lines OV 2s3s $^3\mathrm{S}_1$ 2s3p $^3\mathrm{P}_{1,2}$ the longitudinal alignments are calculated from

$$A_L(J=1 \quad 1) \quad \sqrt{\frac{3}{8}} \frac{a(^3\mathrm{P}_1)}{n(^3\mathrm{P}_1)}, \quad A_L(\neq \quad 2 \quad =1) \quad \sqrt{\frac{7}{8}} \frac{a(^3\mathrm{P}_2)}{n(^3\mathrm{P}_2)}. \tag{2.19}$$

The longitudinal alignment of the 2s3p $^3\mathrm{P}_{0,\,1,\,2}$ levels; $A_{\mathrm{L}}(15,11)$ and $A_{\mathrm{L}}(16,11)$ as a function of the electron density are shown in Figure 3 for the two temperatures Maxwell distribution of equation (2.8) with T_{t} = 40 eV and T_{p} = 100 eV. The absolute values of A_{L} for both the transitions become large as n_{e} decreases and reach a plateau between 10^{18} and 10^{21} m^{-3}. The contour map of the longitudinal alignment $A_{\mathrm{L}}(16,11)$ is displayed in the three dimensional plot in Figure 4 for $n_{\mathrm{e}} = 10^{18}$ m^{-3}. The range of T_{p} and T_{t} is between 10 and 300 eV.

The A_{L} value changes from 0.05 to –0.02 in the varied temperature range. Absolute values of A_{L} larger than 0.01 are realized only when the anisotropy of the velocity distribution is extremely large. From a close look into the calculation it is found that the alignment creation from the ground state plays the dominant role to produce polarization of the emission line. One third of $A_{\mathrm{L}}(16,11)$ is due to the alignment creation from the ground state, level (1), population to alignment of level (16). The next dominant contribution is alignment creation from the 2s2p $^3\mathrm{P}_{0,1,2}$ (2),(3),(4). Alignment to alignment transitions are less important.

For the double Maxwell distribution having a high velocity component given by equation (2.7), the calculated longitudinal alignment is less than 0.005 in absolute value for d values up to 0.2.

3. Experimental Observations

The WT-3 tokamak at Kyoto University is a middle-size toroidal plasma machine with a major radius of 0.65 m and a minor radius of 0.21 m. Typical discharge times are about 100 ms with $n_e = 3\times10^{18}$ m^{-3} and $T_e = 100$ – 300 eV. The plasma was produced in the joule-heating mode with a toroidal current of 60 kA to reach a stationary state at the one turn loop voltage of 2 V. The discharges are performed with hydrogen as a filling gas, and oxygen was the most common impurity.

The plasma was observed from slightly above the equatorial plane through a 15 mm-thick fused silica plate. Knife-edge blades light dump was equipped on the counter wall of the view port. Two plane mirrors and one concave mirror reduced the plasma image by a factor of one eighth which was focused on the entrance slit of a spectrometer. A one-meter focal length spectrometer (f/10) was equipped with a 3600 grooves/mm grating giving a reciprocal linear dispersion of 0.25 nm/mm at 280 nm. The spectrum was detected by an intensified CCD camera of 512×512 pixels (Princeton Instruments IMAX512T). Just behind the entrance slit we placed a calcite plate with thickness 5 mm. The crystal optic axis was in the horizontal direction at 30 ^{o} with respect to the surface normal. The normal incident light was separated into the ordinary (o) ray and the extraordinary (e) ray according to the polarization. Since the quantization axis in the toroidal direction, the polarized component of the emission line is the e-ray (having the electric fields oscillating in the direction of the quantization axis) and the *s* light is the o-ray. The e-ray ( ) was displaced parallel form the o-ray ( ) by about 0.5 mm. The polarization resolved spectral line intensity of the OV triplet lines (2s3s $^3S_1$ – 2s3p ^3P_J) 278.104 nm (J = 2), 278.803 nm (J = 1) and 278.986 nm (J = 0) was obtained. A typical spectral image is shown in Figure 5 which was recorded with an exposure time of 100 ms. The vertical y-axis corresponds to the distance over the plasma from the toroidal axis up to 80 mm. The sum of the counts over the y-axis is shown in Figure 6. Since several Fe II lines are observed with substantial intensity around the dominant OV triplet lines, the OV lines are fit with a nonlinear least square fitting routine over restricted fitting regions so as to eliminate the Fe II lines. Apparently the components of the spectral lines were stronger than the components; this was due to the different reflectivities of the mirrors and grating for different polarized components. The relative sensitivity was calibrated by means of the unpolarized OV J=1-0 line (279.0 nm): The spontaneous emission of the transition from the J = 0 level to the J = 1 level is never polarized since there is only one upper magnetic sublevel (M_J = 0) and the relative intensity of and light is equal in the observation perpendicular to the quantization axis. The relative sensitivity for the / light components was determined to be 1.25 in the centeral region of the image and depens only slightly on the y-axis of the spectral image.

Ten pixels from the top in every one hundred pixels were binned in order to reduce the data transfer time. It made it possible to perform position and time resolved polarization spectroscopy. The six regions labeled (a) to (f) in Figure 5 correspond to plasma regions with 18.75 mm distant each in position from the plasma center. Each shot with 100 ms discharge period produced four frames of spectrum at six different positions in

plasma. The time evolution of the polarization resolved spectra of the region (b) is shown in Figure 7. This was taken with the exposure time of 3 ms with a 25.6 ms interval. Changes in relative intensity of the and components are clearly seen, particularly for the $J = 1 - 2$ transition, indicating a change in the polarization degree of this line during the course of time. For instance, in the frame 3 (64.0 – 67.0 ms) of Figure 7, the apparent intensity of the light is comparable to the light. Considering the relative sensitivity of our system, we conclude that the light intensity is stronger than the light.

Each of the line intensities of the mutiplet spectra were evaluated after performing least square fits to the observed spectra. The relative sensitivity was corrected for, and the longitudinal alignment A_L was obtained according to equation (2.15). The longitudinal alignment A_L for the $J = 1 - 0$ line was confirmed to be 0 within the statistical uncertainty. This confirms that the relative sensitivity calibration was correct. Figure 8 shows the time evolution of the longitudinal alignments A_L for the $J = 1 - 2$ transition in six different positions in the plasma. A_L vary values between 0.050±28 and –0.078±16.

5. Comparison of calculation with measurement and discussion

The relatively large observed longitudinal alignment seen in an experiments was qualitatively explained in terms of the anisotropic electron distribution having the Maxwellian distribution with two temperature components rather than the double Maxwellian distribution with a high energy electron components. The higher toroidal temperature relative to the poloidal temperature causes the positive longitudinal alignment. The negative longitudinal alignment suggests that the poloidal component of the electron velocity distribution has a higher temperature than the toroidal one.

However the observed longitudinal alignment was at least four times larger than that simulated. This quantitative discrepancy may be explained by the following reasons: (i) The resonance structure of the cross section near the threshold energy may substantially contribute to alignment creation. (ii) The alignment creation by elastic scattering for the ion may play an important role. (iii) Alignment creation from the other triplet states, for example $2p^2\ ^3P_{0,1,2}$; (6), (7), (8), may be important.

Acknowledgment

This work is supported by the Grant-in-Aid for Scientific Research by Ministry of Education, Culture, Sports, Science and Technology. Work at Los Alamos National Laboratory has been performed under the auspices of the U.S. Department of Energy.

Reference

[1] T. Fujimoto, H. Sahara, T. Kawachi, T. Kallstenius, M. Goto, H. Kawase, T Furukubo, T. Maekawa and Y. Terumichi, Phys. Rev. E **54** R2240 (1996).

[2] T. Fujimoto and S. A. Kazantsev, Plasma Phys. Control. Fusion **39** 1267 (1997).

[3] T. Inoue, M. Nakai, A. Tanaka, K. Kawakami, A. Iwamae, T. Fujimoto, M. Yoshikawa and T. Tamano, Plasma Phys. Control. Fusion **43** L9 (2001).

[4] T. Kato, J. Lang and K.A. Berrington, NIFS-DATA-2 (1990).

[5] L. Pieroni and S. E. Segre, Phys. Rev Lett. **34** 928 (1975).

[6] B. Coppi, F. Pegoraro, R. Pozzoli and G. Rewoldt, Nucl. Fusion **16** 309 (1976).

[7] J. C. Kieffer, J. P. Matte, H. Pépin. M. Chaker, Y. Beaudoin, T. W. Johnston, C. Y. Chien, S. Coe, G. Mourou and J. Dubau, Phys. Rev. Lett. **68** 480 (1992).

[8] M. D. Bowden, T. Okamato, F. Kimura, H. Muta, K. Uchino, K. Muraoka, T. Sakoda, M. Maeda, Y. Manabe, M. Kitagawa and T. Kimura, J. Appl. Phys. **73** 2732 (1993).

[9] T. Fujimoto and F. Koike, K. Sakimoto, R. Okasaka, K. Kawasaki, K. Takiyama, T. Oda and T. Kato, NIFS-DATA-16 (1992).

Table 1. The cross section between a magnetic sublevel to a magnetic sublevel for the transitions from (a) (1) – (16) the ground state $2s^2\ ^1S_0$ (M_J' = 0) to $2s3p\ ^3P_2$ (M_J = 0, ±1, ±2) and (b) (4) – (16) $2s2p\ ^3P_2$ (M_J' = 0, ±1, ±2) to $2s3p\ ^3P_2$ (M_J = 0, ±1, ±2). Axial symmetry is assumed.

(a)

Electron energy E / eV	Cross section from M_J' = 0 to M_J = 0	to M_J = ±1	to M_J = ±2
		$Q(E)$ / cm^2	
12.0403	1.04521E-19	8.17786E-20	1.35507E-20
12.0715	1.03336E-19	8.08635E-20	1.34462E-20
12.1951	9.90237E-20	7.74690E-20	1.28051E-20
12.3984	9.24614E-20	7.22801E-20	1.17364E-20
12.6775	8.47100E-20	6.60254E-20	9.97166E-21
13.4432	6.49552E-20	5.08011E-20	8.33905E-21
14.4471	4.72833E-20	3.69040E-20	5.76629E-21
15.6435	3.23014E-20	2.53166E-20	4.36215E-21
19.2021	1.11021E-20	8.88879E-21	2.24898E-21
23.3392	3.60141E-21	2.99308E-21	1.16808E-21
27.7258	1.24059E-21	1.08102E-21	6.02280E-22
32.3221	4.63036E-22	4.24347E-22	3.08281E-22
41.7698	8.59680E-23	8.64815E-23	8.80221E-23
51.4268	2.18730E-23	2.36907E-23	2.91437E-23
61.1941	7.02377E-24	8.04687E-24	1.11162E-23

(b)

Electron energy E / eV	Cross section from $M_J' = 0$ to $M_J = 0$	to $M_J = \pm 1$	to $M_J = \pm 2$
		$Q(E)$ / cm^2	
11.1485	2.34744E-18	1.70406E-19	4.52239E-20
11.1821	2.33830E-18	1.68291E-19	4.46328E-20
11.3155	2.30395E-18	1.60609E-19	4.27339E-20
11.5343	2.23967E-18	1.48155E-19	4.00266E-20
11.8338	2.15643E-18	1.32003E-19	3.60549E-20
12.6507	1.94774E-18	1.00423E-19	2.86709E-20
13.7128	1.71506E-18	7.11771E-20	2.20616E-20
14.9680	1.48109E-18	4.91073E-20	1.72482E-20
18.6558	9.84364E-19	1.98474E-20	1.17041E-20
22.8919	6.48249E-19	9.14213E-21	9.75923E-21
27.3503	4.42624E-19	4.85780E-21	8.54905E-21
32.0006	3.13724E-19	2.82647E-21	7.41573E-21
41.5216	1.76636E-19	1.14160E-21	5.43006E-21
51.2254	1.11539E-19	5.17039E-22	3.83851E-21
61.0249	7.64851E-20	2.54041E-22	2.68155E-21

(b) continued

Electron energy E / eV	Cross section from $M_J' = \pm 1$ to $M_J = \mp 2$	to $M_J = \mp 1$	to $M_J = 0$	to $M_J = \pm 1$	to $M_J = \pm 2$
			$Q(E)$ / cm^2		
11.1485	4.42067E-20	5.02090E-20	1.83033E-19	2.38336E-18	8.56024E-20
11.1821	4.35935E-20	4.96339E-20	1.80678E-19	2.37253E-18	8.49790E-20
11.3155	4.14134E-20	4.74677E-20	1.72540E-19	2.33132E-18	8.25821E-20
11.5343	3.84410E-20	4.42557E-20	1.58711E-19	2.26060E-18	7.93536E-20
11.8338	3.47546E-20	4.04043E-20	1.40189E-19	2.16821E-18	7.53451E-20
12.6507	2.56123E-20	3.23935E-20	1.05692E-19	1.94552E-18	6.54321E-20
13.7128	1.78667E-20	2.58278E-20	7.36013E-20	1.70114E-18	5.61203E-20
14.9680	1.17713E-20	2.13637E-20	4.96543E-20	1.46314E-18	4.82568E-20
18.6558	3.82307E-21	1.63479E-20	1.87129E-20	9.77051E-19	3.47444E-20
22.8919	1.20622E-21	1.43055E-20	8.15900E-21	6.54495E-19	2.49855E-20
27.3503	4.36052E-22	1.26892E-20	4.27116E-21	4.55852E-19	1.76000E-20
32.0006	1.77791E-22	1.10585E-20	2.51004E-21	3.29384E-19	1.21229E-20
41.5216	4.12122E-23	8.12613E-21	1.05132E-21	1.91294E-19	5.76967E-21
51.2254	1.29206E-23	5.75125E-21	4.88330E-22	1.23528E-19	2.79306E-21
61.0249	4.89951E-24	4.01978E-21	2.43474E-22	8.60392E-20	1.41691E-21

(b) continued

Electron energy E / eV	Cross section from $M_J' = \pm 2$ to $M_J = \mp 2$	to $M_J = \mp 1$	to $M_J = 0$	to $M_J = \pm 1$	to $M_J = \pm 2$
			$Q(E)$ / cm^2		
11.1485	5.84639E-39	4.42067E-20	9.98760E-20	1.65487E-19	2.31378E-18
11.1821	5.90279E-39	4.35935E-20	9.87813E-20	1.63880E-19	2.30161E-18
11.3155	6.09932E-39	4.14134E-20	9.36142E-20	1.57303E-19	2.25192E-18
11.5343	6.35860E-39	3.84410E-20	8.63724E-20	1.46792E-19	2.18515E-18
11.8338	6.76808E-39	3.47546E-20	7.90231E-20	1.34667E-19	2.09816E-18
12.6507	7.56812E-39	2.56123E-20	5.96823E-20	1.06966E-19	1.88068E-18
13.7128	8.81844E-39	1.78667E-20	4.33781E-20	8.22747E-20	1.64370E-18
14.9680	1.05388E-38	1.17713E-20	3.14257E-20	6.35210E-20	1.41796E-18
18.6558	1.55036E-38	3.82307E-21	1.65816E-20	3.73499E-20	9.77370E-19
22.8919	1.84060E-38	1.20622E-21	1.14654E-20	2.47243E-20	6.89876E-19
27.3503	1.83840E-38	4.36052E-22	9.17029E-21	1.70476E-20	5.07921E-19
32.0006	1.64056E-38	1.77791E-22	7.65435E-21	1.17287E-20	3.86336E-19
41.5216	1.20535E-38	4.12122E-23	5.47278E-21	5.63198E-21	2.42758E-19
51.2254	4.72630E-38	1.29206E-23	3.84814E-21	2.74538E-21	1.65318E-19
61.0249	1.83779E-37	4.89951E-24	2.68418E-21	1.39847E-21	1.19392E-19

Figure Captions

Figure 1 Energy level diagram of the levels included in the present PACR model calculation. The spectroscopic transitions observed are from levels (14), (15), (16) to (11).

Figure 2 An example of the cross sections for 2s2p $^3P_2$ level (14) and 2s3p $^3P_2$ level (16). (a) population to population $Q_0^{00}(r,p)$, (b) population to alignment $Q_0^{20}(r,p)$ (c) alignment to population $Q_0^{02}(r,p)$ and (d) alignment to alignment $Q_0^{22}(r,p)$ The Legendre expansion coefficients of the velocity distribution having two temperatures T_p, = 100 eV and T_t = 40 eV that are used to obtain the rate coefficients are plotted under the corresponding cross sections. See equation (2.9) (e) $f_0(v)v^3$. (f) $f_2(v)v^3$. (g) The dash-dotted line is $f_4(v)v^3$ with $f_0(v)v^3$ and $f_2(v)v^3$.

Figure 3 The electron density n_e dependence of (a) the population of level (14) (dash-dotted line), level (15) (broken line) and level (16) (thick line). (b) the longitudinal alignment $A_L(15,11)$ (broken line) and $A_L(16,11)$ (thick line) for the two temperatures T_p = 100 eV and T_t = 40 eV

Figure 4 The dependence of the longitudinal alignment $A_L(16,11)$ on the toroidal and poloidal temperatures. The electron density n_e is 10^{18} m^{-3}.

Figure 5 A full image of the polarization resolved OV triplet lines (2s3s $^3S_1$ 2s3p $^3P_{0,1,2}$), 278.104 nm (J = 1 – 2), 278.803 nm (J = 1 – 1) and 278.986 nm (J = 1 – 0) obtained from WT-3. The right of each pair is the -light having the electric fields oscillating in the direction of the toroidal axis, left s -light. The exposure time is 100 ms. The ordinate corresponds to the distance from the plasma center. The labelled (a)-(f) regions are binned over 10-pixels each for the position- and time-resolved polarization measurements.

Figure 6 A polarization resolved spectrum of the OV triplet with the fitting.

Figure 7 Time evolution of the OV triplet spectra of the region b (Shot No 83831). Note that in frame 3 (64.0-67.0 ms) for the 1-2 transition the intensity of the light is weaker than that of light i.e. longitudinal alignment is substantially negative.

Figure 8 Longitudinal alignment of the J = 1 – 2 emission line observed from different positions in the plasma.(a) line of sight crosses at 86 mm (b) 67 mm, (c) 48 mm, (d) 30 mm (e) 11 mm and (f) –8 mm from the center.

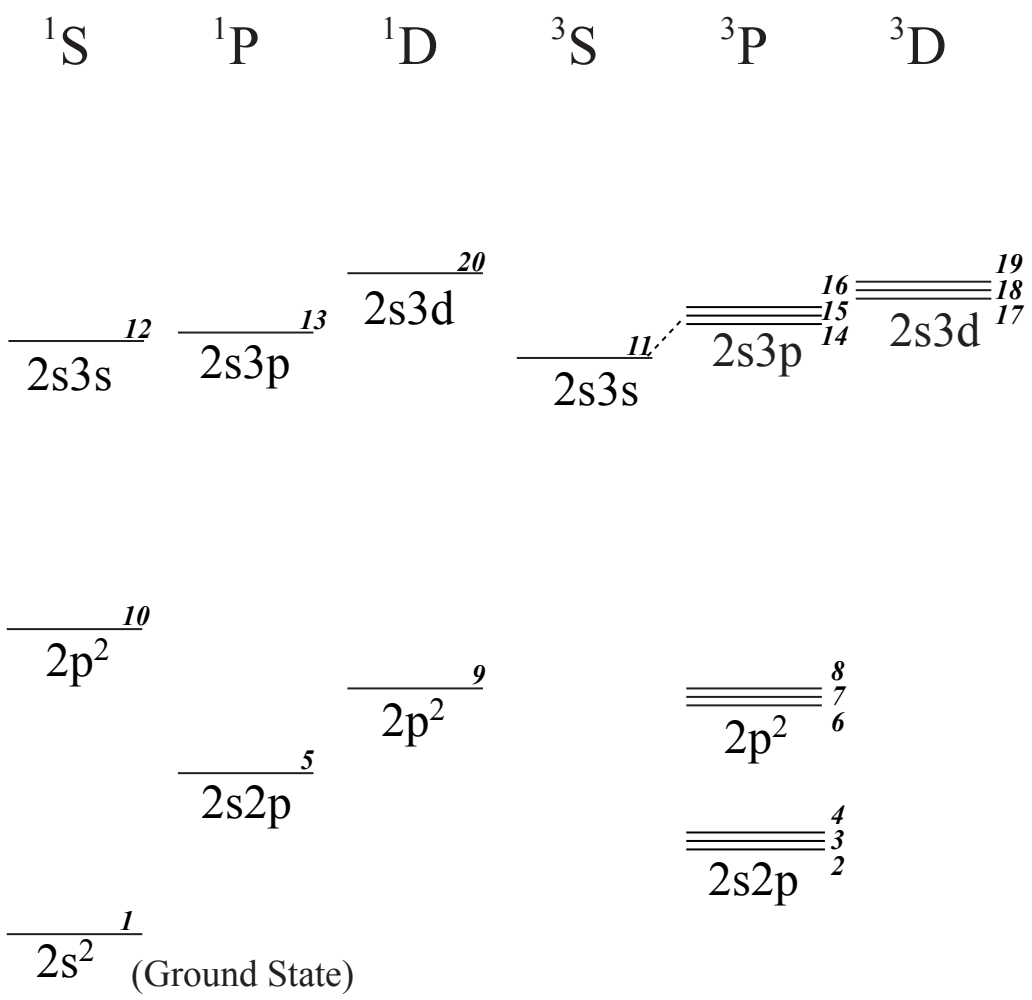
1S
1P
1D
3S
3P
3D
20
2s3d
12
2s3s
13
2s3p
11
2s3s
16
15
14
2s3p
19
18
17
2s3d
10
2p2
9
2p2
8
7
6
2p2
5
2s2p
4
3
2
2s2p
1
2s2
(Ground State)

Figure 1

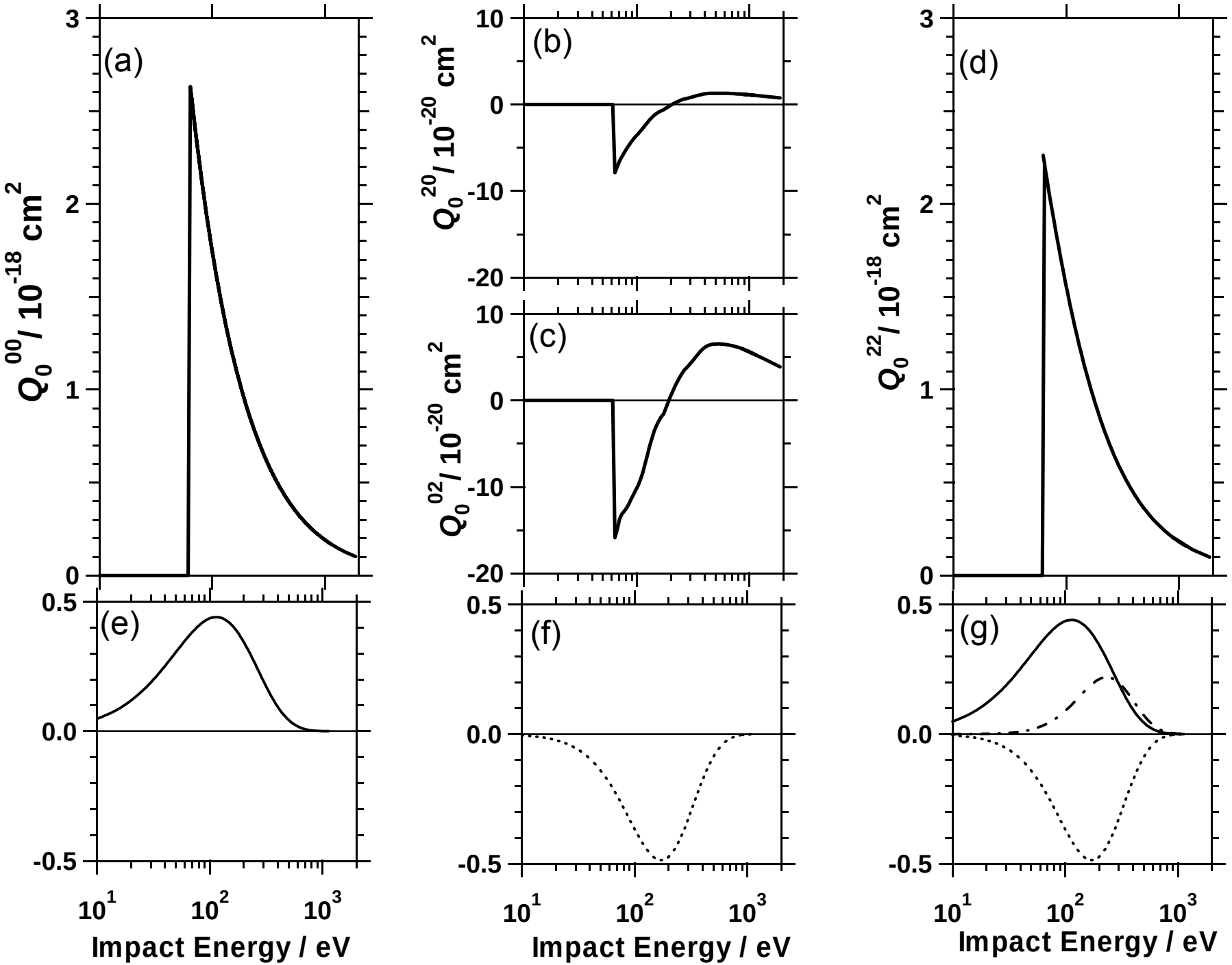
(a)
(b)
(c)
(d)
(e)
(f)
(g)
Q_0^{00} / 10^{-18} cm^2
Q_0^{20} / 10^{-20} cm^2
Q_0^{02} / 10^{-20} cm^2
Q_0^{22} / 10^{-18} cm^2
Impact Energy / eV
Impact Energy / eV
Impact Energy / eV

Figure 2

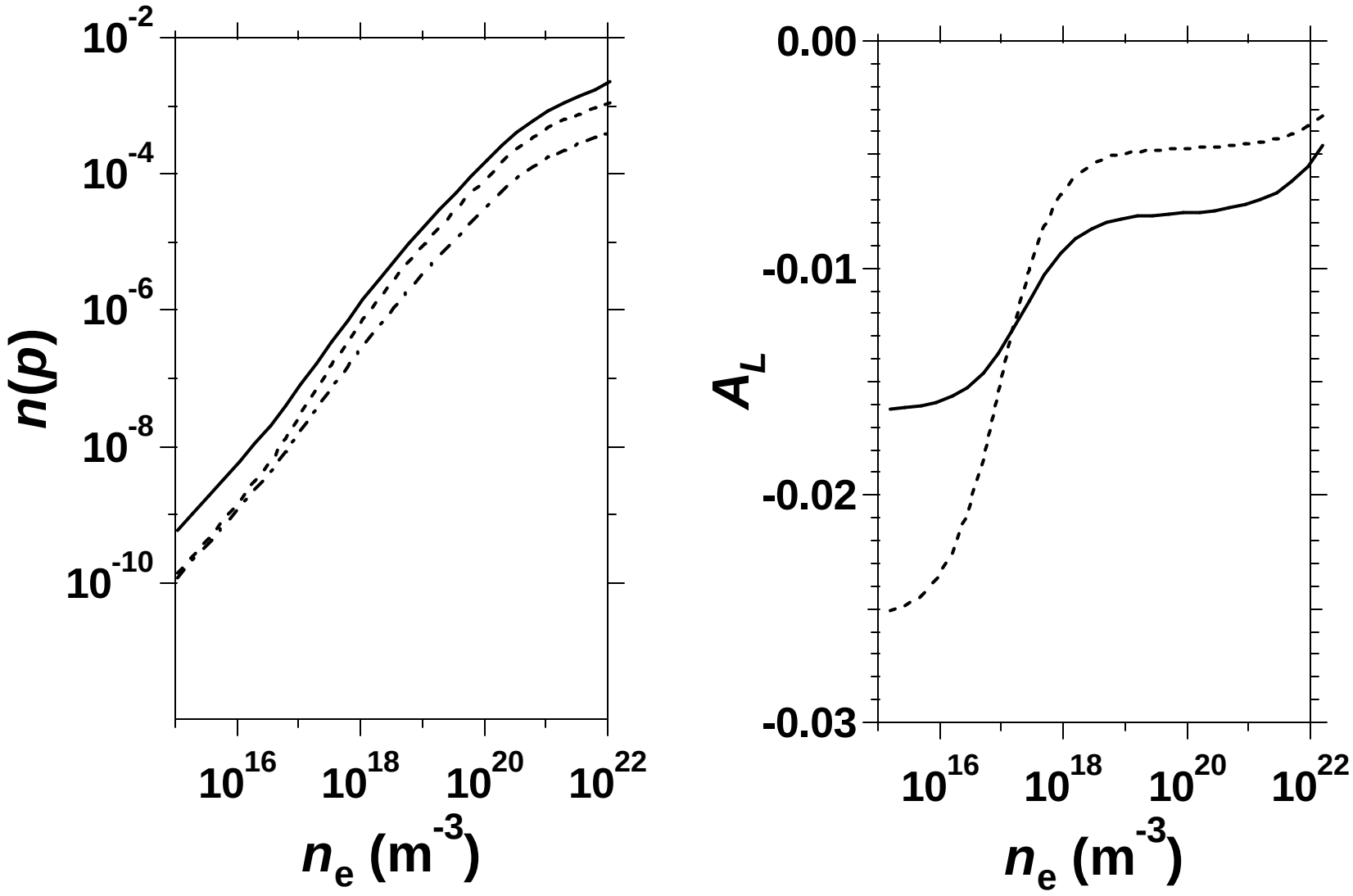
10^-2
10^-4
10^-6
10^-8
10^-10
n(p)
10^16
10^18
10^20
10^22
n_e (m^-3)
0.00
-0.01
-0.02
-0.03
A_L
10^16
10^18
10^20
10^22
n_e (m^-3)

Figure 3

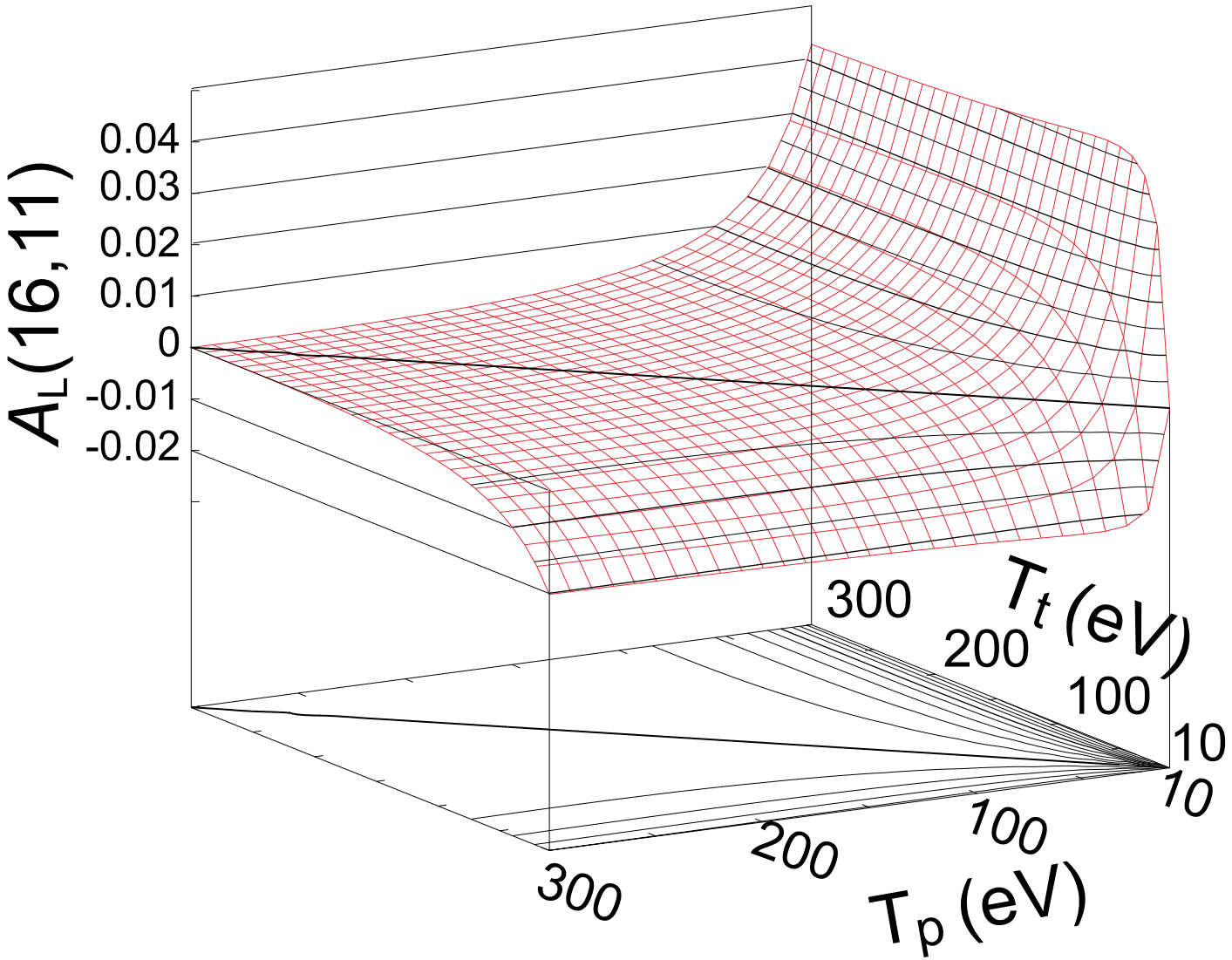
$A_L(16,11)$
0.04
0.03
0.02
0.01
0
-0.01
-0.02
300
200
100
10
T_t (eV)
300
200
100
10
T_p (eV)

Figure 4

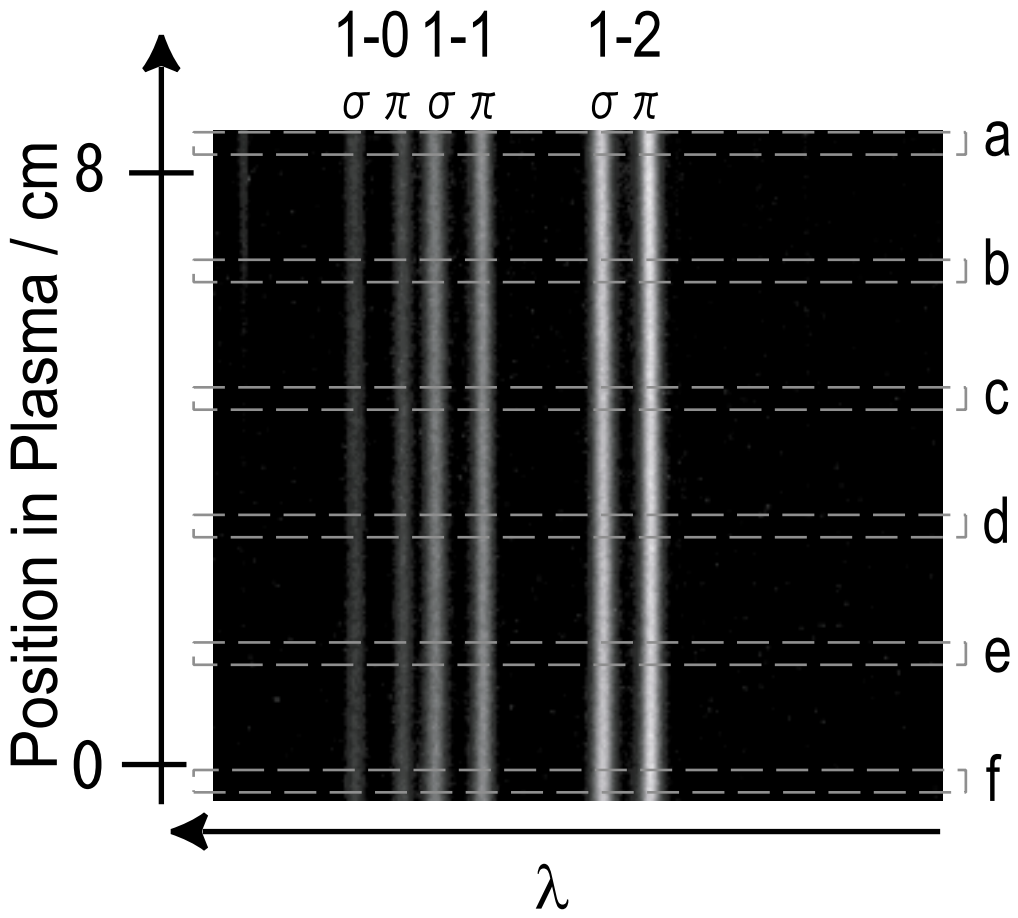

Figure 5

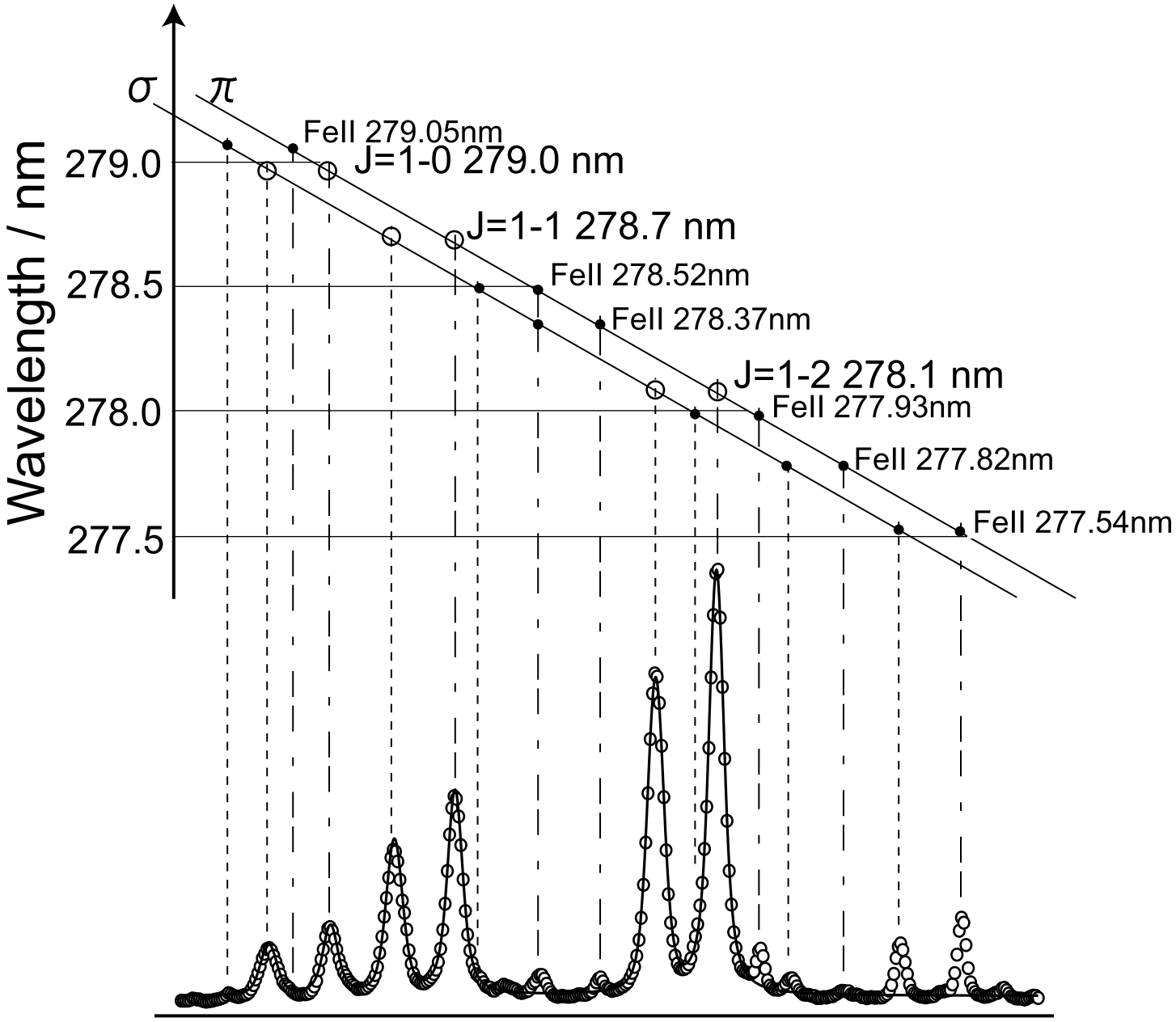
σ
π
Wavelength / nm
279.0
278.5
278.0
277.5
FeII 279.05nm
J=1-0 279.0 nm
J=1-1 278.7 nm
FeII 278.52nm
FeII 278.37nm
J=1-2 278.1 nm
FeII 277.93nm
FeII 277.82nm
FeII 277.54nm

Figure 6

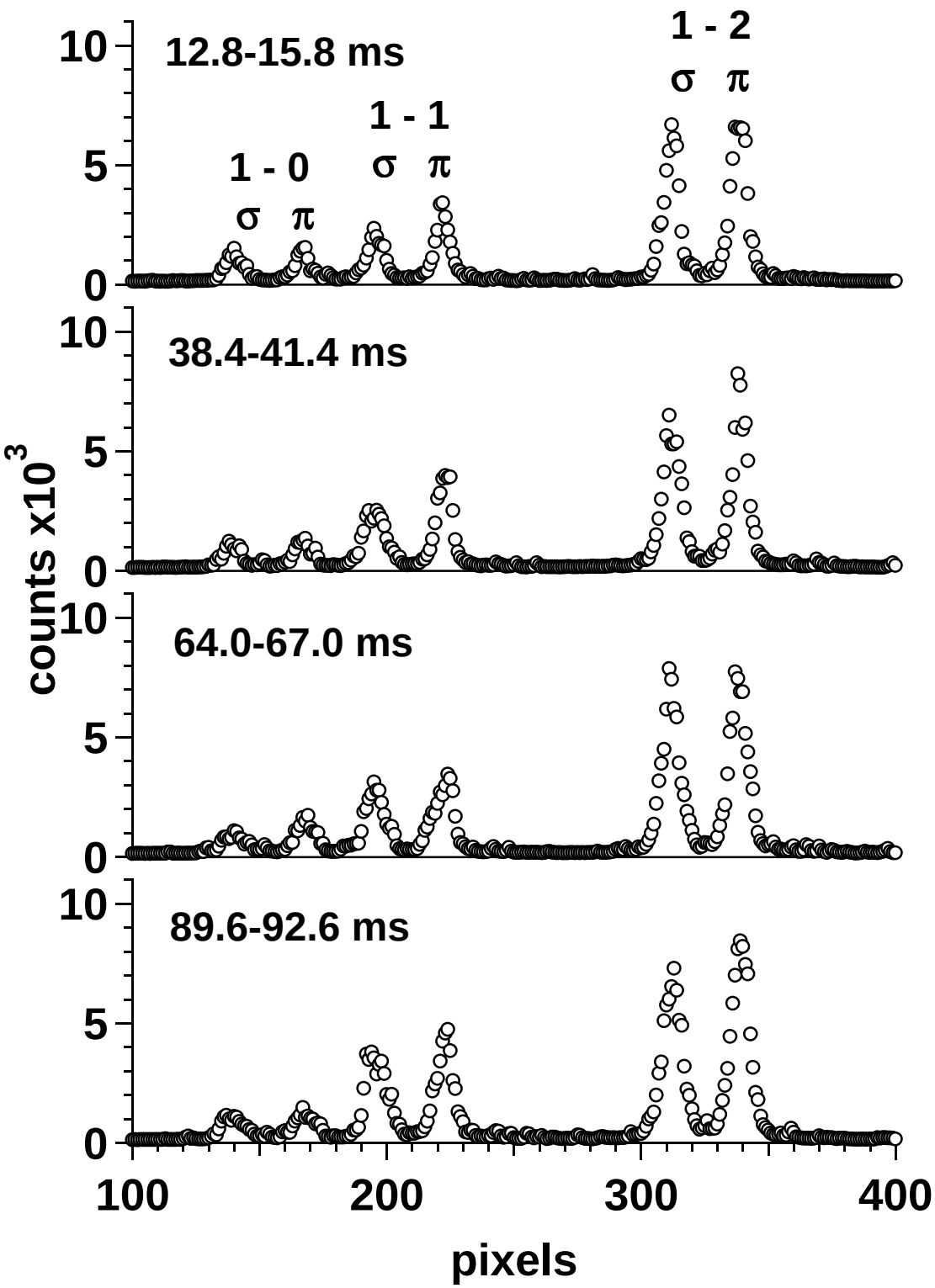
12.8-15.8 ms
1 - 0
σ π
1 - 1
σ π
1 - 2
σ π
38.4-41.4 ms
64.0-67.0 ms
89.6-92.6 ms
counts x10^3
pixels
0
5
10
100
200
300
400

Figure 7

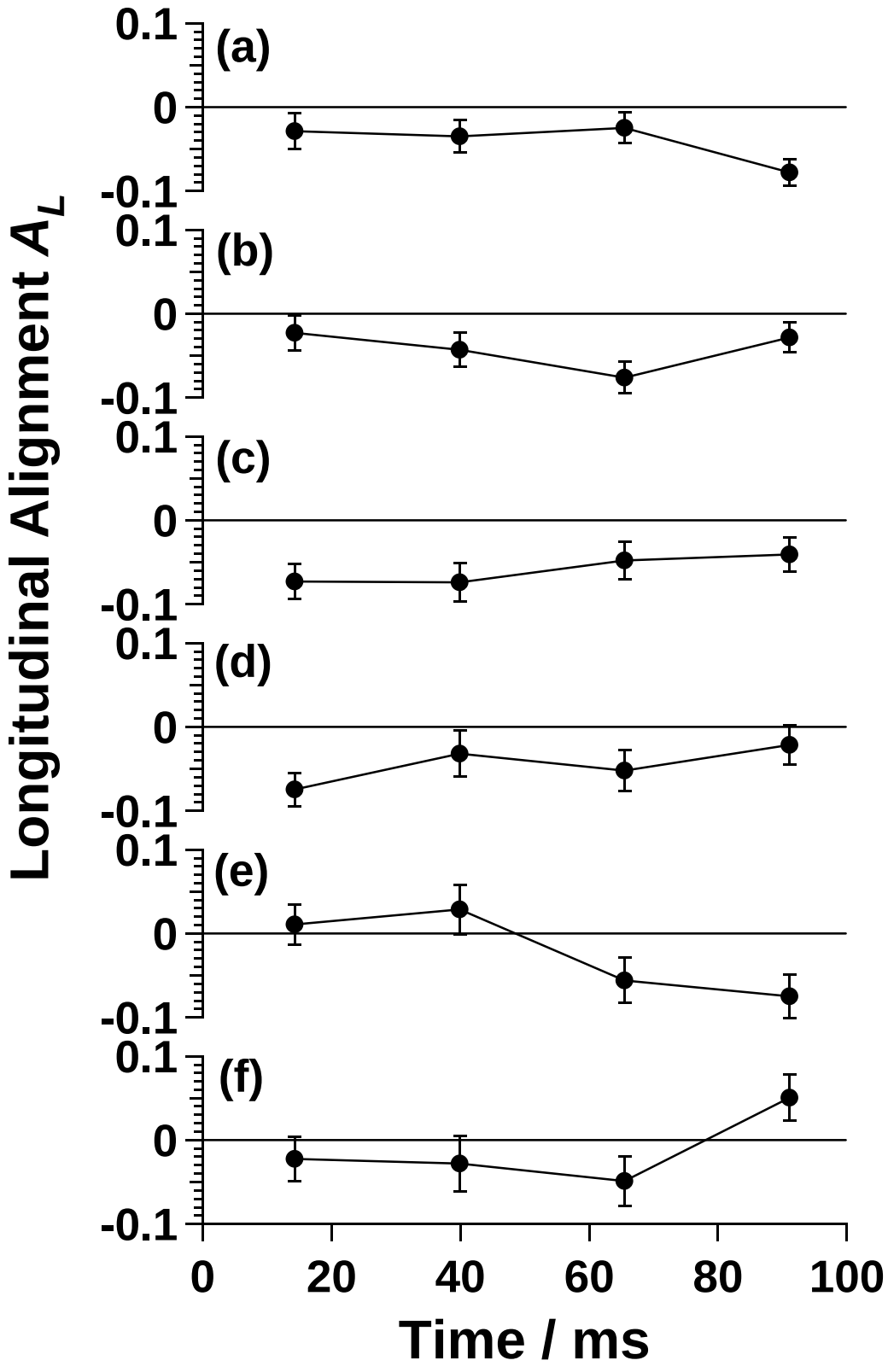
Longitudinal Alignment A_L
(a)
(b)
(c)
(d)
(e)
(f)
0.1
0
-0.1
0
20
40
60
80
100
Time / ms

Figure 8

Monte Carlo calculation of collisions of directionally-incident electrons on highly excited hydrogen atoms

K.Kawakami and T. Fujimoto

Department of Engineering Physics and Mechanics, Graduate School of Engineering, Kyoto University, Kyoto 606-8501, Japan

We treat classically the n-,l- and m_l-changing transitions and ionization. Excitation cross sections against the final state energy continues smoothly to the"ionization cross sections". The steady state populations determined by elastic collisions among the degenerate states in the same n level show higher populations in the m_l=0 states, suggesting positive polarizations of Lyman lines emitted from plasmas having directional electrons. For ionization, the two outgoing electrons have large relative angles, suggesting reduced three body recombination rates for these plasmas.

Yoneda *et al* [1] observed polarization-resolved spectra from hydrogenlike and heliumlike fluorine ions in a laser-produced plasma. The intensity distribution over the series spectral lines indicates that these ions are in a recombination phase, or they are recombining plasma (Fujimoto [2]). The presence of the recombination continuum supports this conclusion. Most significant with this experiment is that the recombination continuum terminating on the heliumlike 1^1S state is polarized, that is, the π component, the electric field of which oscillates in the direction parallel to the quantization axis, is stronger than the σ component, where we take the quantization axis in the direction of the target surface normal. This clearly indicates that the velocity distribution of the recombining electrons is anisotropic: a positive polarization degree means that the distribution is more parallel to the quantization axis (Lamoureux [3], Milchberg [4]). The heliumlike ion lines ($1^1S_0 - n^1P_1$) are also found to be positively polarized. This indicates that the upper levels of these lines are aligned, or the magnetic sublevel $m_J = 0$ has a higher population than those of $m_J = 1$.

For thermal electrons having a Maxwellian velocity distribution with a certain temperature, the detailed mechanism of recombination of these electrons with ions, *i.e.*, the collisional-radiative recombination, and the population kinetics of excited levels in such a recombining plasma are well understood (Fujimoto [5]): Step 1. An electron is captured by an ion radiatively (radiative recombination) or collisionally (three-body recombination) to form an excited (or the ground state) ion. If the temperature of the electrons is low and the density is high three-body recombination dominates and produces predominantly very highly excited state ions. Step 2. Subsequent electron collisions deexcite, excite or even ionize these ions. In other words, these ions are re-distributed among these high-lying levels (and the continuum states). An LTE (local thermodynamic equilibrium) population distribution is established with respect to the electron and ion densities for this temperature. If the electrons are non-Maxwellian, or even the velocity distribution is anisotropic, as is the case in the above experiment, the above picture should be modified: Step 1. For anisotropic radiative recombination the polarization characteristics of the recombination continuum and the alignment of the product ion state have been investigated (Milchberg [4], Scofield [6,7]). However, nothing is known concerning three body recombination. A formula has been proposed (Ditmire [8]) for the three body recombination rate, but this formula is based on two assumptions which are not supported by the calculations reported here. Step 2. Since we cannot define a temperature any more the LTE population distribution loses its significance. Furthermore, there can be a population imbalance among the magnetic sublevels in the same n, l level, leading to polarized emission lines.

If we reverse the direction of time in a three body recombination event this is nothing but an ionization event. Thus, an investigation of directional electron collisions on high-lying excited ions, resulting in excitation, ionization and elastic transitions, should form a basis for understanding the characteristics of a recombining plasma for electrons with an anisotropic velocity distribution. We choose a hydrogen atom with principal quantum number $n = 10$, which is impacted by an electron traveling in the direction of the quantization axis. We neglect the electron spin. Since we treat a highly excited state, we use a classical Monte

Carlo calculation (Olson [9]) .

The proton is fixed at the origin and the atomic electron (electron 1) is in an elliptic orbit. Electron 2 travels from the minus z-direction, where the z-axis is the quantization axis. Initially the trajectory is parallel to the z-axis with a certain impact parameter which is given by random numbers. The orbit of the atomic electron and its initial position are also chosen randomly. We treat the system classically, and follow the trajectories of the two electrons.

Figure 1 shows an example of the excitation and ionization cross sections: The "cross sections" for producing the final states per unit energy interval are given. The initial atomic state is $(n, l, m_l) = (10, 6, 3)$ having energy of -0.14 eV and the incident electron has the speed of 0.2 a.u. (energy 0.54eV). In the calculation the maximum value of the impact parameter is 3000 a.u. The number of trajectories is 5×10^5. For electron 1 the negative energy part corresponds to deexcitation (< -0.14eV), elastic collisions (the peak at -0.14eV) and excitation (> -0.14eV), and the positive part to ionization. The small cross sections for energies higher than 0.41eV corresponds to excitation, elastic collisions and deexcitation with exchange of the two electrons. The curve for electron 2 is symmetrical to that for electron 1 with respect to energy (-0.14+0.54)/2 eV. It is seen that the cross sections per unit energy interval for excitation continue smoothly to ionization. It is noted that the conventional ionization cross section corresponds to the integration of the cross sections for electron 1 or those for electron 2 from 0 eV to 0.41 eV. Our conventional ionization cross section ($6.9\ 10^{-13}$cm^2) compares well with the formula ($8.4\ 10^{-13}$cm^2) given by Lotz [10]. In the region of ionization, we also show the average of the cross sections for electron 1 and for electron 2; this "cross section" will be mentioned later.

In the case of excitation, deexcitation and elastic transitions the final atomic state is specified by its energy, angular momentum and its projection onto the quantization axis. In our present calculation these quantities are continuous. We quantize these quantities or the atomic states. Our quantization scheme is given in Fig. 2 ;twice the energy of the state $2E$ multiplied by the duration of one revolution of the electron over the orbit, with the sign

reversed, corresponds to nh where h is Planck's constant. λ is the absolute value of the angular momentum and μ_λ is its z-component. To the atomic states having n between, say, 2.5 and 3.5, we assign the principal quantum number $n = 3$, as shown in Fig. 2. Integer values of l and m_l are assigned similarly, as shown in Fig 2. As is obvious in Fig. 2, $-2E\tau$, $2\pi\lambda$ and $2\pi\mu_\lambda$ all have the units of h. Thus, the volume of the quantization cell is h^3. This may be regarded as a quantum cell, the states within which cannot be distinguished. Figure 2 shows examples of the quantum cells for $(n, l, m_l) = (3, 1, 0)$ and $(3, 2, 2)$. It is noted that the volume of the "quantum cell" of extremity states, *ie.*, $m_l = n - 1$ is $1.04h^3$ rather than h^3. This small anomaly may be a natural consequence of quantization of a classical system.

In Fig. 3, we compare our excitation cross section with the semiempirical cross section by Vriens [11]. It is seen that smaller l values tend to give smaller excitation or deexcitation cross sections. Overall good agreement is obtained.

Figure 4 shows an example of the cross sections for inelastic and elastic collisions. The initial state is (10,6,3) and the incident electron speed is 0.2 a.u. A cross section value is expressed with the volume of the sphere placed on each (n, l, m_l) point of the final state. The cross sections for elastic collisions are much larger than that for inelastic collisions. See also Fig. 1. Among the elastic collisions within same l the cross sections leading to smaller m_l values are larger than those leading to larger m_l values. This means that, the atomic electron tends to drift to smaller m_l states under the condition of the beamlike electron collisions.

We made similar calculations for all $(10, l, m_l)$ states. Of course, we assumed symmetry between the m_l and -m_l states. We found that the states with smaller m_l values have larger cross sections for elastic collisions. Since the cross sections for elastic collisions are much larger than those for inelastic collisions, we here assume that the population distribution among the same n states is determined solely by the elastic collisions. We solve the simultaneous equations for steady state. The result is shown in Fig. 5. It is seen that the populations of the m_l=0 states are larger than those of other states. For example, population $N(l = 1, m_l = 0)$ is about twice $N(l = 1, m_l = 1)$. This is consistent with experiment on an

excited barium atom (Trajmar [12]). The emission from the m_l=0 state to the ground state is π polarized. That is, if the velocity distribution is more parallel to the quantization axis, the π light is stronger for the Lyman lines. This is consistent with the Yoneda's experiment.

In the case of ionization, two electrons leave the proton. The excess energy (0.41 eV in Fig. 1) is partitioned by the two electrons. We rotate the coordinate system around the z-axis so that the final trajectory of the electron having higher energy (electron 3) is included in the plane with $\phi = 0$, or the final trajectory is expressed by angle (θ_3, ϕ_3=0). (We use the spherical coordinate.) The lower energy electron (electron 4) has (θ_4, ϕ_4). Figure 6 shows the distribution of (θ_4, ϕ_4), or the differential cross section per unit solid angle, in the case of $0 < \theta_3 < 10°$.

Figure 1 indicates that in majority of the ionization events the incident electron 2 becomes electron 3. This means that the case of Fig. 6 is for collisions in which the incident electron follows an almost straight path. In this case, electron 4 is distributed mostly in the area where θ_4 is larger than 60°.

It is noteworthy that θ_4 cannot have small values. Figure 7 shows the distribution of the relative angles of the two electrons, for several initial states and incident electron speeds. It is interesting to note that the two electrons rarely fly away in the directions relative angle of which is smaller than 60°. When we reverse the direction of time in the ionization process, we have a three body recombination process. Thus, we reach a conclusion that electrons travelling in similar directions cannot recombine, so that the three body recombination rate is reduced under the condition of directional electrons.

As mentioned earlier the three body recombination rate formula proposed by Ditmire is based on two assumptions. 1. The three body recombination rate is independent of the relative angle of the two recombining electrons, or the curves in Fig. 7 are flat. This assumption is not valid. 2. The "ionization cross section" per unit energy interval is constant, i.e., in Fig. 1 the curve (-) is flat. This assumption is also invalid. A new formula is needed which takes into account these features.

We are indebted to Professor R. More for the quantization scheme given in Fig. 2. This

work is supported by the Grant-in-Aid for Scientific Research, by Ministry of Education, Sports and Culture.

[1] H. Yoneda *et al.*, Phys. Rev. E **56**, 988 (1997).

[2] T. Fujimoto, J. Phys. Soc. Japan, **47**, 265 (1979).

[3] M. Lamoureux, L. Jacquent, and R. H. Pratt, Phys. Rev. A **39**, 6323 (1989).

[4] H. M. Milchberg and J. C. Weisheit, Phys. Rev. A **26**, 1023 (1982).

[5] T. Fujimoto, J. Phys. Soc. Japan, **49**, 1569 (1980).

[6] J. H. Scofield, Phys. Rev. A **40**, 3054 (1989).

[7] J. H. Scofield, Phys. Rev. A **44**, 139 (1991).

[8] T. Ditmire, Phys. Rev. E **54**, 6735 (1996).

[9] R. E. Olson and A. Salop, Phys. Rev. A **16**, 531 (1977).

[10] W. Lotz, Z.Phys. **220**, 466 (1969).

[11] L. Vriens and A. H. M. Smeets, Phys. Rev. A **22**, 940 (1980).

[12] S. Trajmar *et al.*, J. Phys. B **31**, L393 (1998).

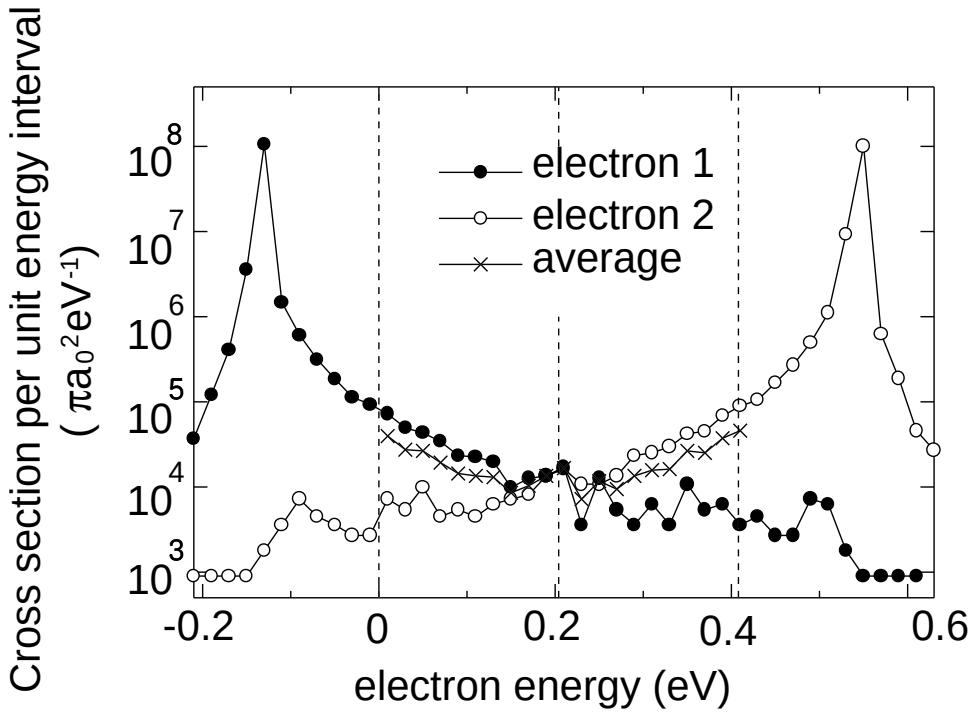

FIG. 1. Cross section for transitions to the final states per unit energy interval. The initial atomic state (electron 1) is (n, l, m_l) = (10,6,3), and the speed of the incident electron (electron 2) is 0.2 a.u. For electron 1 the negative energy part corresponds to deexcitation (< -0.14eV), eleastic collisions (the peak at -0.14eV) excitation (> -0.14eV), and the positive part to ionization. The curve for electron 2 is the mirror image for that for electron 1. Average of the "ionization cross section" (0 <E< 0.41eV) are also given.

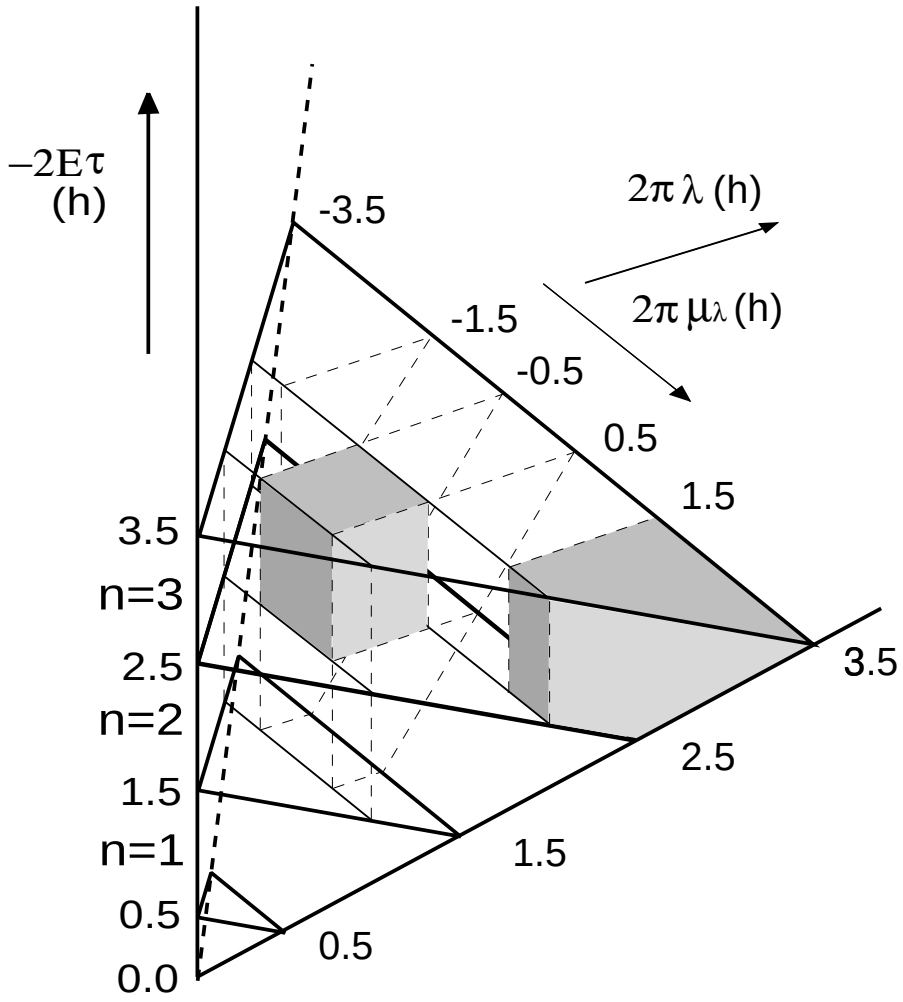

FIG. 2. The quantization scheme. The quantity $-2E\tau$ corresponds to the principal quantum number, where E is the energy of the electron state and τ is the duration of one revolution of the atomic electron over the orbit. $2\pi\lambda$ and $2\pi\mu_\lambda$ is determined by the angular momentum and its z-component. Atomic states included in an (n, l, m_l) volume are assigned the quantum numbers (n, l, m_l). Two examples are shown for (n, l, m_l)=(3, 1, 0) and (3, 2, 2).

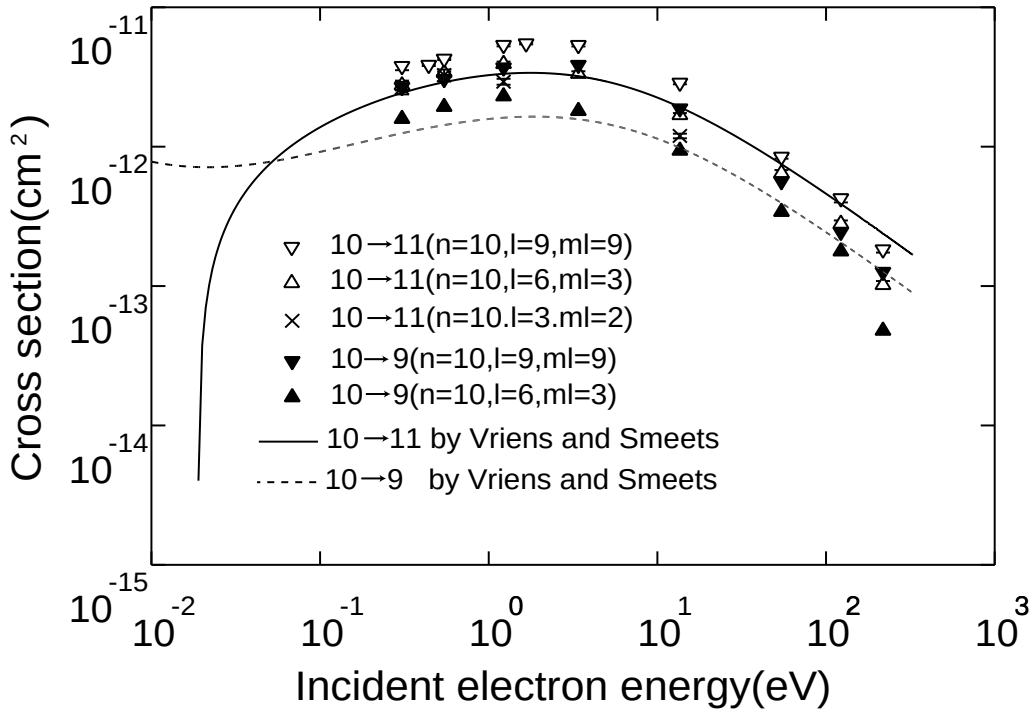

FIG. 3. The conventional excitation and deexcitation cross sections vs incident electron energy. We show also semiempirical cross sections by Vriens [11].

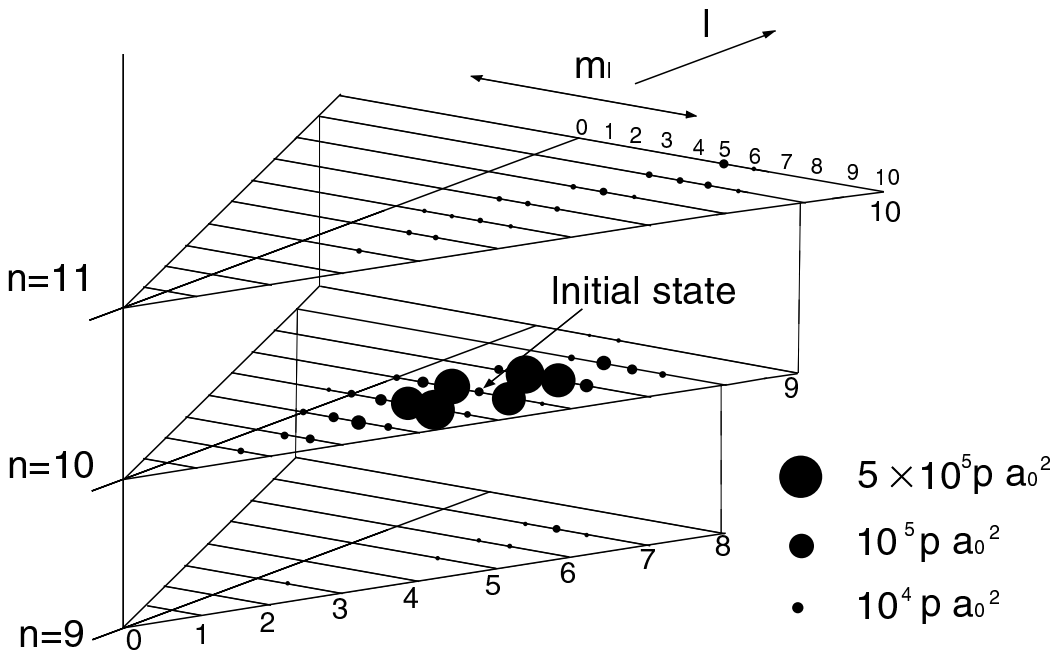

FIG. 4. The cross sections for excitation ($n = 10 \rightarrow n = 11$), the elastic collision and deexcitation ($n = 10 \rightarrow n = 9$). The initial state is (10,6,3) and $v = 0.2$ a.u. A cross section value is expressed with the volume of the sphere placed on each final state.

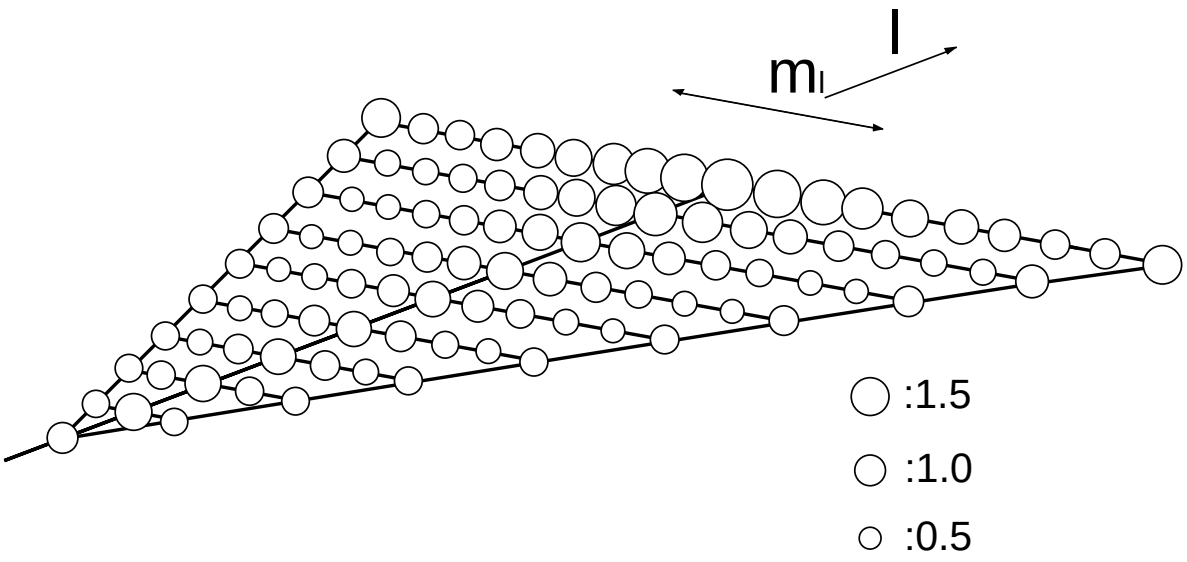

FIG. 5. The population distribution among the $n = 10$ states for elastic collisions by the beamlike electrons with $v = 0.2$ a.u. A population is expressed by the area of the circle placed on each state.

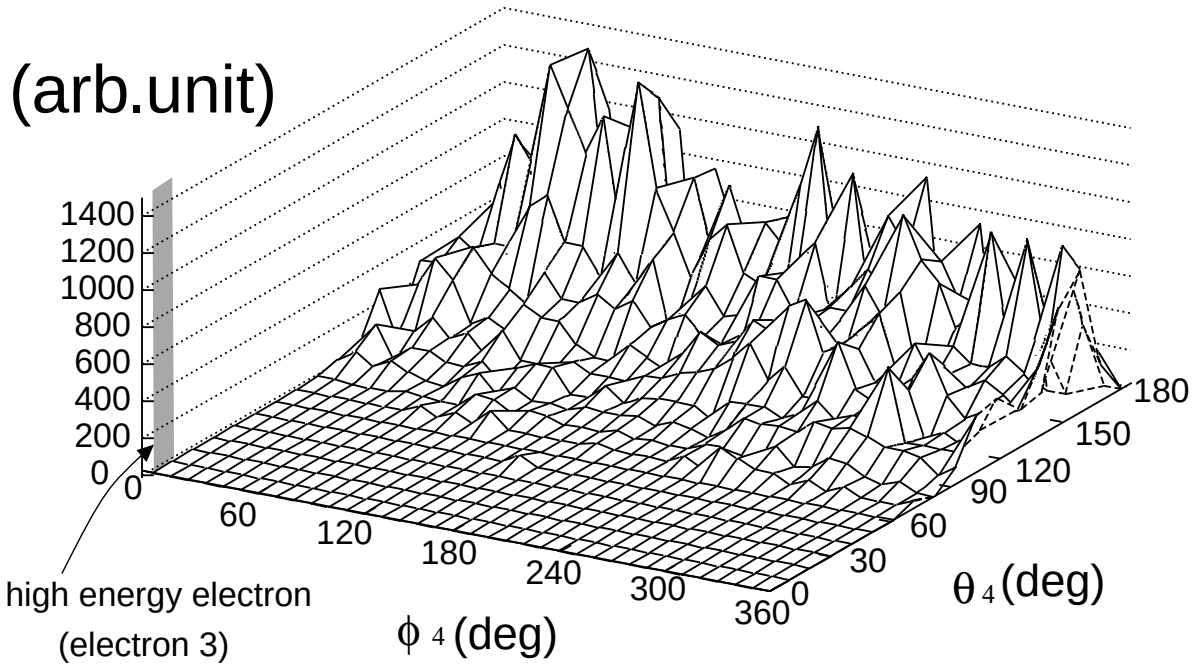

FIG. 6. Angular distribution of the directions of the lower-energy electron in the case of ionization, or the differential cross section per unit solid angle. The higher energy electron has $0° \leq \theta_3 < 10°$ and $\phi_3 = 0$. The initial state is (10,6,3).

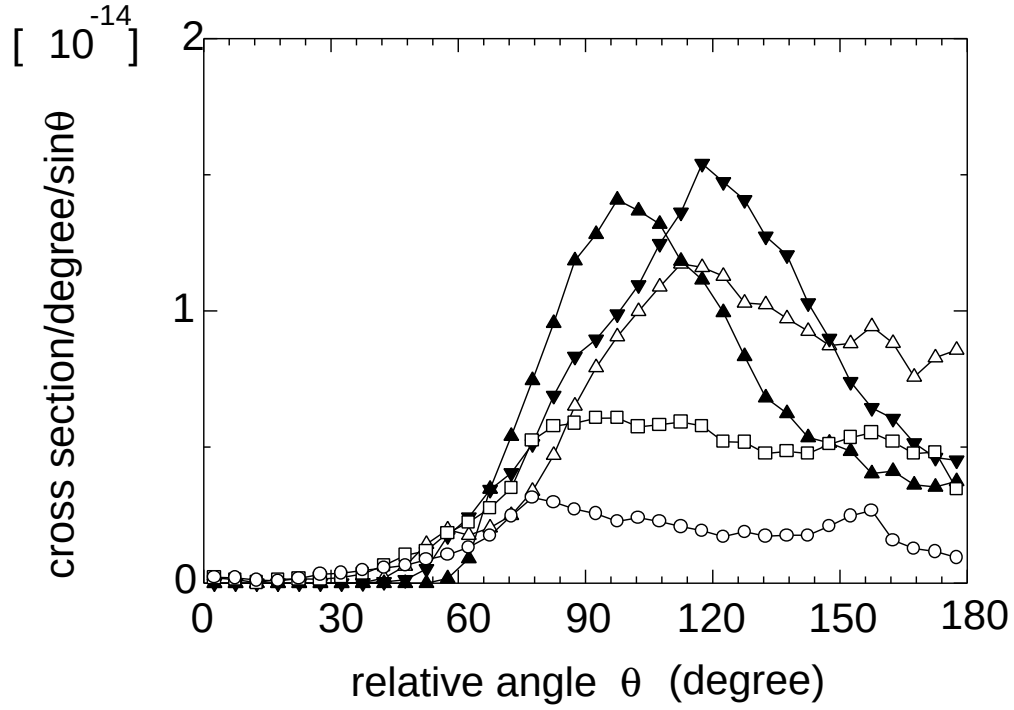

FIG. 7. The distribution of relative angles of the two outgoing electrons, or the cross section per unit degree per $\sin\theta$. Solid triangle: the initial state $(10, 9, 9)$ and $v = 0.2$ a.u. Inverted triangle: $(10, 9, 5)$, $v = 0.2$ a.u. $\triangle$: $(10, 6, 3)$, $v = 0.2$ a.u. $\square$: $(10, 6, 3)$, $v = 0.3$ a.u. $\bigcirc$: $(10, 6, 3)$, $v = 0.5$ a.u.

Hydrogen spectra in microwave fields

Richard More
NIFS

Hydrogen spectra from fusion machines do not always show the expected intensities for Zeeman split lines. Such spectra have been collected by Fujimoto and Goto.[1] Such spectra may be due to improper alignment of the spectrometer or to effects of reflected light. Is there another process able to produce anomalous Zeeman spectra? We examine the possible perturbation of hydrogen spectra by high-power microwaves.

In certain experiments, several Megawatts of 82.6 GHz electron cyclotron resonance heating is pumped into the LHD machine. This intense microwave radiation is nearly resonant with the hydrogen Zeeman splitting in a 6T field. We performed a numerical calculation to understand the effect of this radiation.

The calculation uses one-electron basis states with quantum numbers $n, \ell, m, \ldots$. The isolated-atom Hamiltonian H_o includes the non-relativistic binding energy and fine structure energy. Static electric and magnetic fields give a perturbation $H_s = - \mu \cdot \mathbf{B}_o - e\mathbf{r} \cdot \mathbf{E}_o$, where $\mu = {}_o\mathbf{L} + 2\ {}_o\mathbf{S}$ is the sum of orbital and spin magnetic moments (${}_o = e\hbar/2mc$ is the Bohr magneton). The dynamic perturbation $H_d(t)$ has the same form as H_s but uses the time-dependent electric and magnetic fields $\mathbf{E}(t)$, $\mathbf{B}(t)$ of the microwave heating. The Hamiltonian is not diagonal. In our code, we can use two sets of basis states: a large set, 1s through 4f, with spin (60 states), and a small set, 2s through 3d, without spin (13 states).

The code contains matrices for X, Y, Z, L_X, L_Y, L_Z, S_X, S_Y, S_Z, H(t), and ρ_o where H(t) is the total Hamiltonian and ρ_o is the (initial) density matrix. The code solves the time-dependent Schroedinger equation:

$$i\hbar \frac{d}{dt} U(t) = H(t) \circ U(t) \qquad (1)$$

H(t) has the time-dependence of the microwave electric and magnetic fields. From U(t), the spectrum is calculated by forming the dipole autocorrelation function,

$$\rho_x(t) = Tr\left[\hat{x}\, \hat{U}^{+}(t)\ \hat{x}\, \hat{U}(t)\ \hat{\rho}_o\right] \qquad (2)$$

The emission spectrum [2] is:

$$P(\omega) = \frac{2e^2\omega^4}{3c^3} \mathrm{Re} \int_0 e^{i\omega t} e^{-\lambda t} \left[\rho_x(t) + \rho_z(t) \right] dt \qquad (3)$$

Eq. (3) gives the radiation seen from the y-direction having electric vector in the x or z directions; the polarizations are easily separated.

We evaluate ρ (t) for times up to ~ 40 psec in order to resolve Zeeman splittings, but require a time-step dt ~ .4 10^{-17} seconds to resolve the K-shell. This means the code must take 10 million time-steps. For stability and accuracy, several matrix operations are needed for each time-step. Therefore, it is important to carefully organize the calculation; we use various numerical

tricks and use the small set of states for most calculations. We collected the necessary atomic data and checked it for consistency.

There are several ways to use the code. We can calculate the effect of microwaves on Zeeman or Stark spectrum. We are most interested to see if there is a new way to measure the local microwave intensity in the plasma.

The code can easily calculate the DC Stark effect, DC Zeeman effect, Stark-Zeeman mixtures, or the spectrum from aligned or polarized input populations. In these cases there are only static electric or magnetic fields.

The code can also calculate harmonic production in laser interaction with H-like ions, and can calculate cross-sections for excitation by the pulsed microfield E(t) which arises in an ion-ion collision.

The calculations performed so far show that the code reproduces the expected Stark effect in a strong DC electric field, gives the expected Zeeman effect (, components) for static B-field and show that alignment changes ratio of these components. For an oscillating electro-magnetic field of resonant frequency having microwave power ~30 kW/cm^2, we find a 6% change in the Zeeman profile. This power is in the range of the intensities that exist in some fusion machines.

References:

(1) Professor T. Fujimoto and Dr. M. Goto, unpublished communication.

(2) H. Griem,, **Principles of Plasma Spectroscopy**, Cambridge University Press, Cambridge, 1997.

Spectral Motional Stark Effect Measurement of |B| in Low-Field Devices

D. J. Den Hartog. D. Craig, G. Fiksel, and the MST group
Department of Physics, University of Wisconsin—Madison

V. I. Davydenko, A. A. Ivanov, and A. A. Lizunov
Budker Institute of Nuclear Physics, Novosibirsk , Russia

*We have made first-time measurements of the magnetic field magnitude in the core of low-field (< 0.5 T) magnetic fusion energy research devices. This is a direct measurement of the motional Stark splitting of the Balmer-α emission from a 30 keV neutral hydrogen beam injected into the plasma. These spatially localized non-perturbative measurements of |**B**| were made in the MST reversed-field pinch at the University of Wisconsin–Madison and the GDT magnetic mirror at the Budker Institute of Nuclear Physics.*

In many low-field (< 0.5 T) magnetic fusion energy research devices such as reversed-field pinches, magnetic mirrors, and spherical tori, the magnitude of of the magnetic field in the core of the plasma is an important constraint for equilibrium modeling. In these devices the vacuum magnetic field profile can be greatly altered by dynamo, diamagnetic, or other plasma driven mechanisms. Thus non-perturbative spatially localized measurements of |**B**| are valuable to an understanding of the physical mechanisms determining the behavior of the plasma.

In order to measure |**B**| in a high temperature fusion research plasma, we have implemented a technique we call spectral motional Stark effect, or spectral MSE for short.[1] This is a direct measurement of the Balmer-α Stark spectrum emitted by the neutral hydrogen atoms injected as a 30 keV beam into the plasma.[2] The beam atoms are excited by collisions with the plasma and emit statistically mixed line radiation. We measure the separation of the π manifolds (polarized parallel to the motional $\mathbf{E} = \mathbf{v} \times \mathbf{B}$) of the Stark split Balmer-α line at 656.3 nm. Since the beam velocity is accurately known, the measured separation is directly analyzed for local |**B**|. As a side note, measuring field line pitch via MSE polarimetry[3] is not suitable for low-field (<0.5 T) devices. The π and σ manifolds are not sufficiently spaced in wavelength to allow for separation with a filter polarimeter.

Since the initial implementation of this technique was on the MST Reversed-Field Pinch at the University of Wisconsin–Madison, we shall report results from that device. The RFP is a toroidal magnetic confinement device similar to the tokamak, but with toroidal field $B_\phi \approx$ poloidal field B_θ, with |**B**| < 0.5 T everywhere. The magnetic field configuration of the MST RFP is shown below in Fig. 1. Note the extensive modification of the vacuum magnetic field, which is entirely toroidal, by the the RFP plasma. MST has a major radius R = 1.5 m, minor radius a = 0.52 m, with torodial plasma current less than 500 kA, electron temperature ≤ 1 keV, and electron density typically 1×10^{19} m^{-3}. Discharge duration is usually 60 ms with a 25 ms current flat-top.

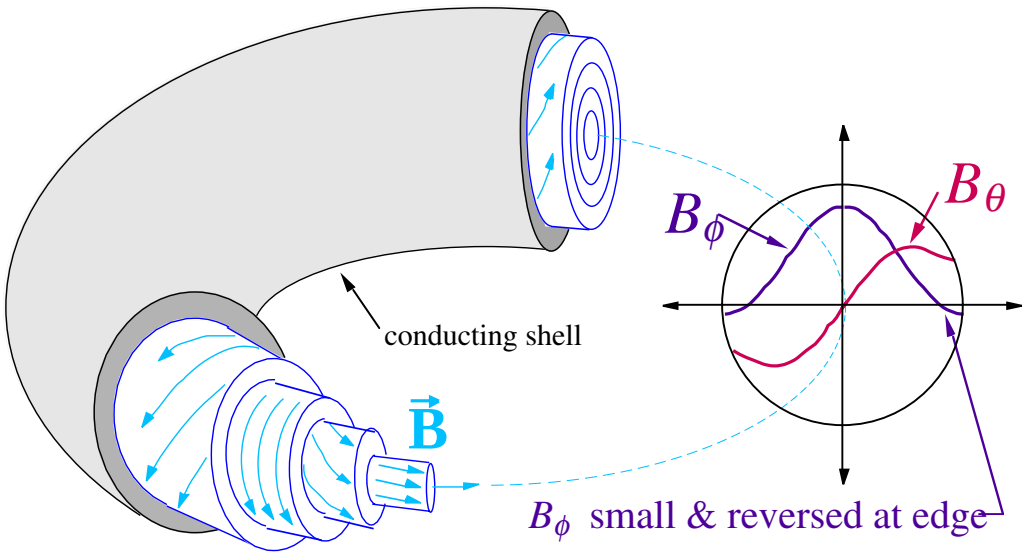

Fig. 1. Self-generated currents drive the RFP plasma to a relaxed state in which the toroidal field reverses direction at the edge.

For our 30 keV neutral hydrogen beam, the π+ and π- manifolds of the Balmer-α Stark manifold are separated by approximately 0.2 nm for |**B**| = 0.5 T. Measuring the splitting at this level and smaller requires a high quality neutral beam and good collection optics. The first order spectral line measurement smearing mechanisms are finite beam temperatures, both parallel and perpendicular to the direction of beam propagation, and a finite collection solid angle for the beam emission. On MST, low beam temperatures and carefully designed light collection optics result in a total line smearing of FWHM ≈ 0.1 nm, enabling measurement of |**B**| down to about 0.2 T. Our neutral beam, which was designed and built by our collaborators at the Budker Institute of Nuclear Physics, has excellent operational characteristics. The equivalent beam current is 4 A and the beam current density at focus is 0.4 A/cm^2 with a smooth current density profile. Beam energy and current are very stable for the entire 3 ms beam pulse. The high beam current and current density are crucial for MSE measurements as they result in sufficient beam emission to overcome Poisson statistical noise.

Figure 2 shows a typical measured Stark spectrum from MST. All nine Stark components are fit to account for incomplete rejection of the perpendicularly polarized σ components. Each of the individual components is fit as a Gaussian-broadened line with the relative amplitudes of the components fixed. A set of MSE data for central |**B**| on MST is shown is Fig. 3. The central axial |**B**| provides a strong constraint for equilibrium reconstruction and is important for differentiating between standard and improved confinement discharges. Note the deviation from the linear fit for the measurement below 0.2 T in Fig. 3. This may reflect actual behavior of the plasma, or may be due to the fact that the fine structure of the Balmer-α transition is no longer negligible at these low motional electric fields. One of our remaining analysis needs is to calculate the effect of fine structure on the Stark spectrum at low fields. Another analysis question arises from a small asymmetry we record in the amplitude of the π+ and π- manifolds. These amplitudes are definitely not equal, as predicted by a simple calculation of the Stark spectrum.[4] Speculation is that some part of the beam-plasma excitation process causes this asymmetry, but the definitive answer is not yet known.

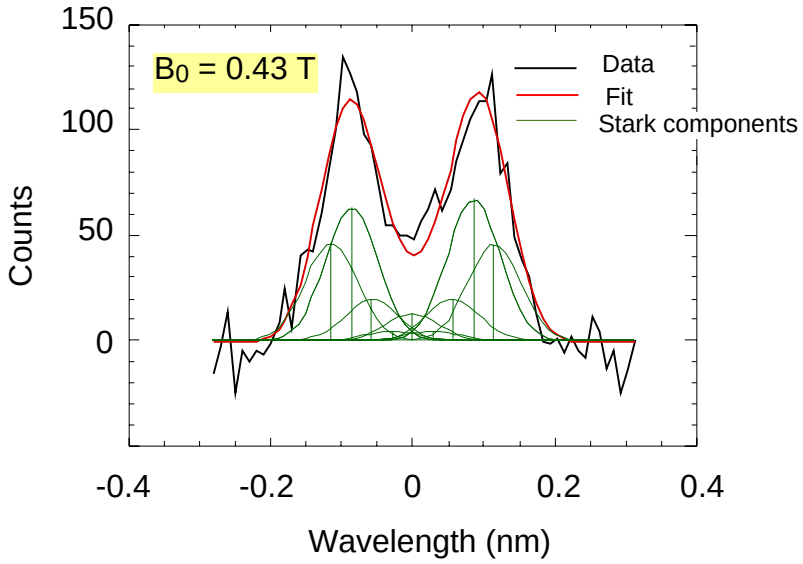

Fig. 2. A typical motional Stark spectrum from MST.

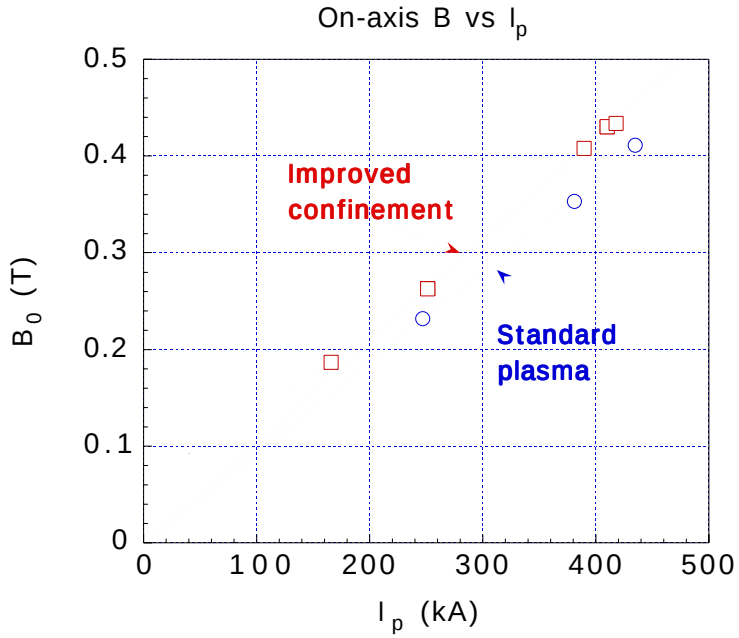

*Fig. 3. Measurements of central |**B**| for standard and improved confinement MST discharges.*

The next step for MSE measurements on MST is the addition of time resolution. Much of the data taken to this point simply integrated the Stark spectrum over the 3 ms beam pulse. However, this integration misses features of the magnetic equilibrium that can evolve on a 100 μs timescale. To capture these features we are implementing the experimental setup shown in Fig. 4. The same central volume of beam emission will be viewed as previously, but instead of just one light collection chord, we will now have seven individual chords. The view through each chord is controlled by an individual ferroelectric liquid crystal (FLC) shutter[5] capable of an effective exposure time of < 100 μs. FLC shutters effectively polarize the collected light,

eliminating the need for a separate polarizer. These shutters will be fired in sequence during the 3 ms beam pulse, effectively exposing each horizontal strip of the spectrometer CCD in sequence. Thus we will capture seven individual Stark spectra for analysis of |**B**| at specific timepoints in the evolution of the magnetic equilibrium. This new capability is made possible by recent acquisition of a CCD camera with very low read noise and flexible hardware binning.

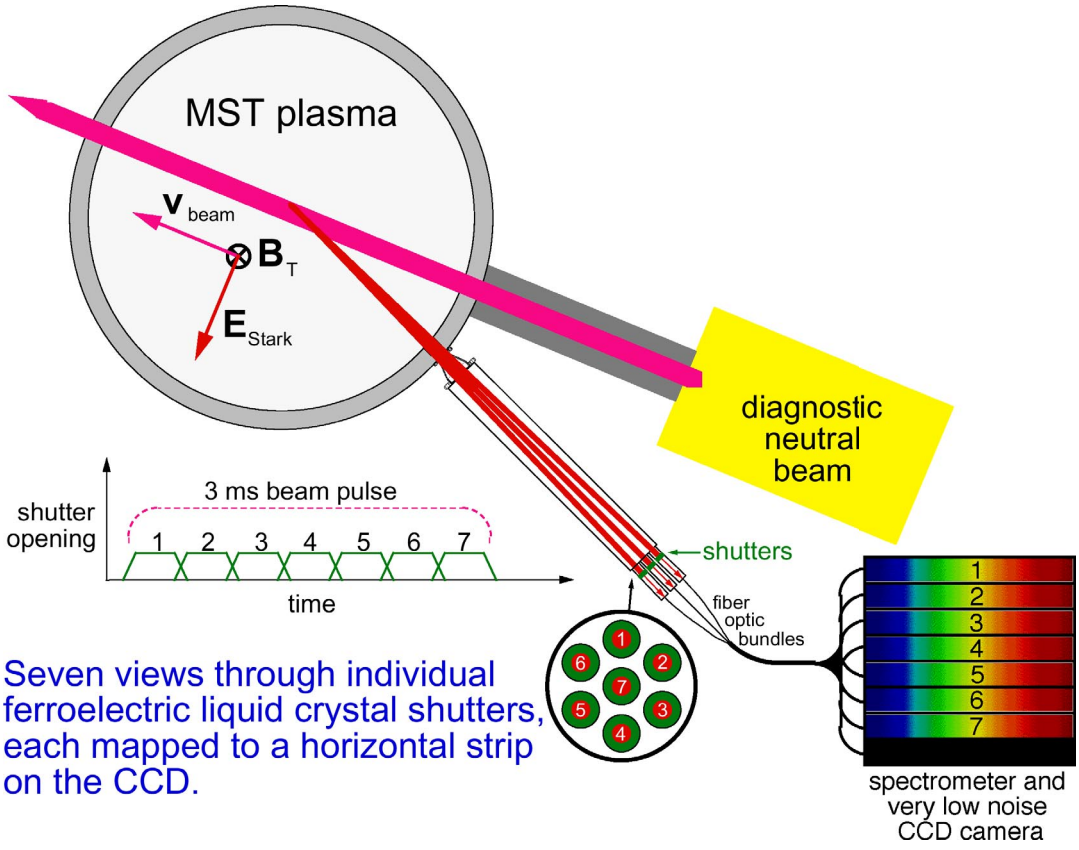

Fig. 4. Setup for time-resolved MSE measurements on MST.

We acknowledge contributions to this work from the entire MST research group, particularly B. Chapman, C. Forest, S. Prager, and J. Sarff. This research is funded by the U. S. Department of Energy

---

[1] A. Boileau, M. von Hellermann, W. Mandl, H. Weisen, and A. Zinoviev, *J. Phys. B: At. Mol. Opt. Phys.* **22**, L145 (1989).

[2] D. Craig, D.J. Den Hartog, G. Fiksel, V.I. Davydenko, and A.A. Ivanov, *Rev. Sci. Instrum.* **72**, 1008 (2001).

[3] F. M. Levinton, R. J. Fonck, G. M. Gammel, R. Kaita, H. W. Kugel, E. T. Powell, and D. W. Roberts, *Phys. Rev. Lett.* **63**, 2060 (1989).

[4] H. Mark and R. Wierl, *Z. Phys.* **55**, 156 (1929).

[5] Displaytech, Inc., Longmont, CO; http://www.displaytech.com/.

Determination of the line emission locations in the LHD on the basis of the Zeeman effect

M. Goto and S. Morita
National Institute for Fusion Science, Toki 509-5292, Japan

Neutral helium HeI λ728.1 nm (2^1P-3^1S) and λ667.8 nm (2^1P-3^1D) emission lines have been observed with an array of optical fibers which covers the entire poloidal cross section of the plasma. The Zeeman profile yields a magnetic field strength, and the locations of the emission regions are identified on the well established map of the magnetic field of the plasma. It is found that the emission region forms a closed zone just outside the region, so called, the 'ergodic layer' where the magnetic field line structure is chaotic. A collisional-radiative model calculation for an inward atom flux suggests a peaked emission profile of about 3.5 cm in FWHM, and this is consistent with the experimental result. The inward atom flux is found to decay before reaching the last closed flux surface and this implies a screening effect of the ergodic layer.

I. INTRODUCTION

In fusion devices such as tokamaks and helical machines, determination of neutral particle influx from the plasma edge region to the main plasma is extremely important for the purpose of studying, e.g., the H-mode[1, 2] and the formation of density profiles[3]. In this regard, the emission line intensity is the only source of information. In conventional spectroscopy, we measure the intensity of an emission line which is integrated over the line of sight. When we can assume, say, cylindrical symmetry, we can convert the measured chord dependence of the emission line intensities to the radial distribution of the intensity. Even in the case that we can assume cylindrical symmetry for the plasma, however, this may not be the case for the neutral atom influx, because the distribution of the neutral atoms depends on the structure of the plasma vessel and on the operation of the plasma. For plasmas with a large non-circular shape like divertor-configuration tokamaks and helical devices, the cylindrical symmetry is not valid even for the plasma. We thus seek to develop a method to determine the local intensities from the line integrated emission intensity. One candidate for such a method is to use the Zeeman splitting of spectral lines. A work in this direction tried in the Alcator C-Mod tokamak device has been reported recently[4, 5]. In the following we report our attempt on a helical device.

II. EXPERIMENT AND ANALYSIS

The Large Helical Device (LHD) is a heliotron type device of a double null divertor configuration[6]. The major and averaged minor radii are 3.5–3.9 m and 0.54–0.64 m, respectively. Because of the absence of inductive current, the magnetic field is determined accurately by coil currents. The maximum magnetic field strength on the magnetic axis $B_{\rm ax}$ could be as high as 3 T. The field structure is saddle-shaped and the field strength near the helical coils is twice or more higher than the lowest field near the X points (see Fig. 1). In the confinement region the field lines form closed magnetic surfaces and the outermost surface is called the last closed flux surface (LCFS). Outside the LCFS both ends of the field lines are connected to the divertor plates and generally the length of the field lines are only several meters. In a region having a thickness of several centimeters just outside the LCFS the magnetic field has a chaotic structure and the field line through the layer often has a length of several kilometers[7, 8]. This region is called the 'ergodic layer'. As a result, in this layer there forms a plasma, the parameters of which are high enough to ionize neutral atoms (see Fig. 8 later). Once the atoms are ionized, they are trapped by the magnetic field and guided to the divertor plates unless they are diffused or become neutral again by charge exchange processes. Thus this layer reduces the fueling efficiency[9] by preventing neutral atoms from penetrating into the core region.

Emission from the LHD plasma was observed with a set of parallel optical fibers, the lines of sight of which cover the entire cross section of the plasma which is elongated in the major radial direction as shown in Fig. 1. Each line of sight is collimated by a lens to have a cylindrical shape of about 30 mm diameter. Optical fibers of 5 m length guide the collected UV and visible light to a 1.33 m Czerny-Turner-type spectrometer (McPherson Model 209) having a 1800 grooves/mm grating. The end surfaces of the fibers are aligned along the entrance slit of the spectrometer such that chord-resolved spectra are recorded on a CCD detector.

The measurement was carried out for a 20 s stationary phase of a helium discharge heated by a neutral beam injection (NBI) of 25 s pulse duration. The nominal field strength $B_{\rm ax}$ and the radius of the magnetic axis $R_{\rm ax}$ of the discharge were 2.75 T and 3.6 m, respectively. The actual field strength at the plasma center in this cross section was 2.67 T. The NBI power was 1.2 MW. The gas-fueling rate was controlled so as to keep the line-averaged electron density $\overline{n}_{\rm e}$ constant. In the stationary phase $\overline{n}_{\rm e}$ and the electron temperature at the plasma center were 3×10^{19} m^{-3} and 2 keV, respectively.

Figure 2 shows an example of the observed profiles of the HeI λ728.1 nm (2^1P-3^1S) line obtained on the viewing chord (a) in Fig. 1. Though this line is subjected to the normal Zeeman effect since the transition is between the singlet terms, the observed profile shows a rather complicated structure. This profile can be understood as the superimposed two Zeeman profiles which originate from the different locations on the same viewing chord and are relatively shifted.

In the normal Zeeman effect the unit of the energy level shift ΔE is expressed as[10]

$$\Delta E = \mu_{\rm B} B, \tag{1}$$

where $\mu_{\rm B}$ and B are the Bohr magneton and the magnetic

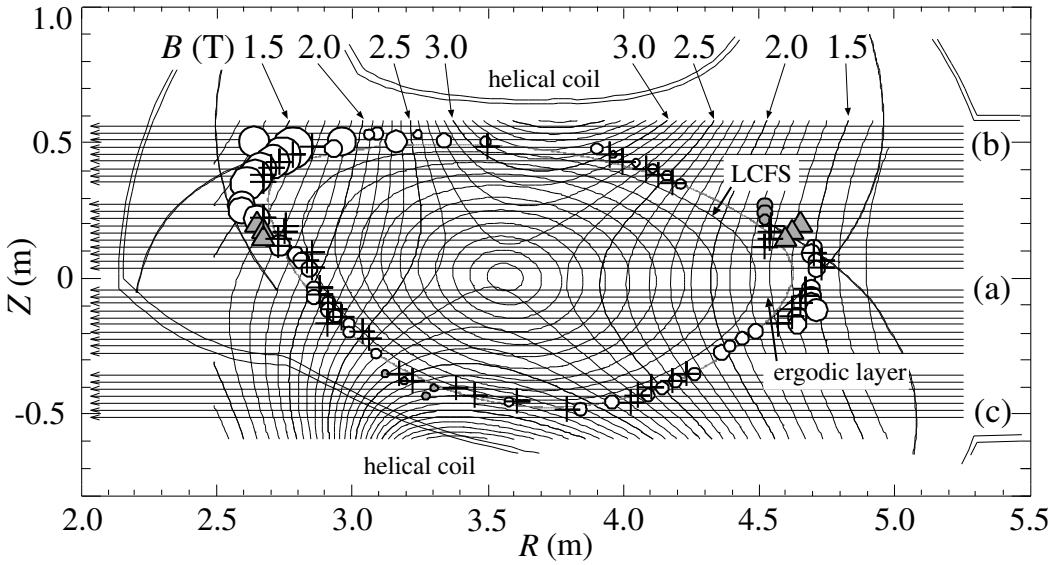

FIG. 1: The map of the magnetic surfaces and field strength for the configuration of $R_{\rm ax} = 3.6$ m and $B_{\rm ax} = 2.75$ T. The R- and Z-axes indicate the major radial direction and the direction perpendicular to the equatorial plane, respectively. Viewing chords are shown with the arrows. The circles and the triangles indicate the location of λ728.1 nm line emission and their size indicates the intensity of the emission. The meanings of the details of the symbols are explained in the text. The crosses are for λ667.8 nm.

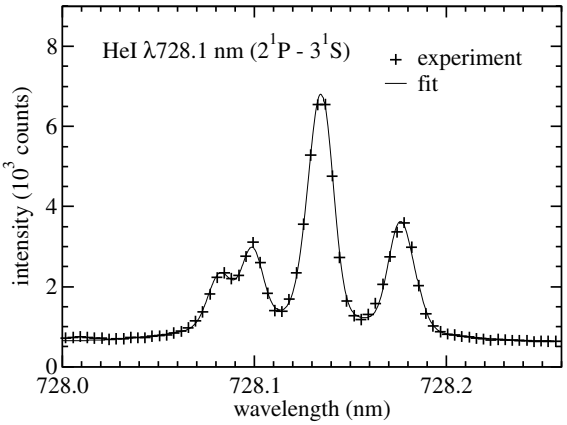

FIG. 2: Emission line profile of HeI λ728.1 nm (2^1P-3^1S) observed with the viewing chord (a) in Fig. 1. The solid line is the result of the least-squares fitting with two sets of Zeeman profiles plus a broad Gaussian profile.

field strength, respectively. The wavelength shift of the σ-component relative to the unshifted π-component, $\Delta\lambda$, is then given as

$$\Delta\lambda = \frac{hc}{E_0}\frac{\Delta E}{E_0 \pm \Delta E}\frac{1}{n_{\rm s}} \simeq \lambda_0 \frac{\Delta E}{E_0}, \qquad (2)$$

where λ_0 and E_0 are the wavelength and the transition energy of the central π-component, respectively, and h, c and $n_{\rm s}$ (≈ 1) are the Planck's constant, the speed of light and the refractive index of air, respectively. Since the viewing chord is almost perpendicular to the direction of the magnetic field, each Zeeman profile consists of one π-component and two half-amplitude σ-components which are symmetrically shifted from the π-component. The total angular momentum quantum number of the upper level is 0, so that the possibility of gross polarization, or a difference in the intensities of the π- and σ-components, is absent. This fact is favorable in reducing the uncertainty in fitting the line profile. Under these constraints we perform a least-squares fitting for the observed profile in Fig. 2 with two sets of Zeeman profiles plus a broad Gaussian profile. Each profile has the independent amplitude, width and center wavelength. The result is shown in Fig. 2 with the solid line. In this case, the broad Gaussian component has the FWHM (Doppler temperature) of 0.12 nm (19 eV) and is about 24 % of the total intensity. The derived field strength values from the sharp Zeeman profiles are $B = 1.99$ T and 1.51 T. The uncertainties are less than 0.01 T. The relative shift is 5.0×10^{-3} nm. The variation of the field strength along the viewing chord is shown in Fig. II. Here, the above derived field strength values are indicated with the horizontal dashed lines. Each of the values has two candidates for the spatial location. Candidates $R = 2.46$ m for $B = 1.51$ T and $R = 4.33$ m for $B = 1.99$ T are discarded because the former position is too far from the plasma boundary and the latter is deep inside the main plasma (see Fig. 1). We thus conclude $R = 4.70$ m for the former and $R = 2.85$ m for the latter. The result of this identification is shown in Fig. 1 with the open circles. In a similar analysis for all the viewing chords we reach a unique identification of the positions in most cases as given in Fig. 1. However, there remains ambiguity for several viewing chords, which are indicated in Fig. 1 with the filled

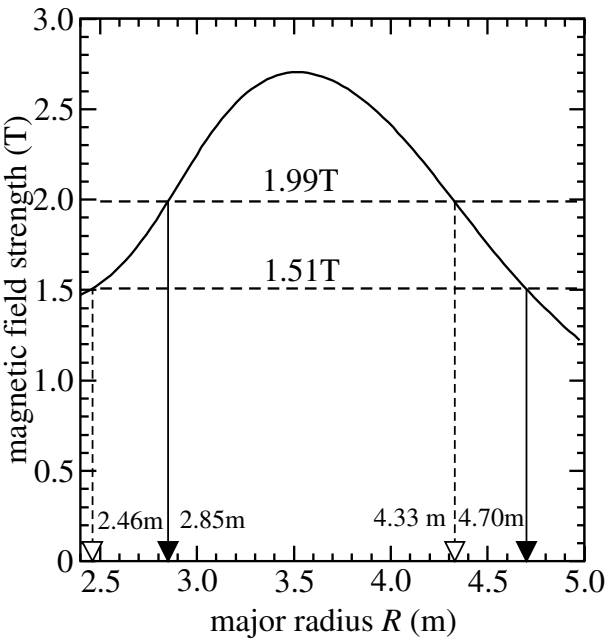

FIG. 3: Variation of magnetic field strength along the viewing chord (a) in Fig. 1. The field strengths derived from the line profile for this viewing chord are shown with the horizontal dashed lines. The identified radial positions are shown with the vertical solid lines with arrows.

triangles; the two magnetic field values are too close. The filled circles indicate the derived field strength values with the uncertainty of about 0.05 T, which is due to the weak signals or the blending of impurity lines. The size of the symbol is proportional to the signal intensity; it is seen that very intense emissions are observed near the inner X point.

A spatial extent of the emission region could make the σ-components broader than the π-component. This broadening is, however, found smaller than 1×10^{-3} nm, or 0.05 T in most cases; this change of the magnetic field corresponds to about 5 cm around the X points, for example. An exception is the chord (b) in Fig. 1, which is nearly tangential to the outer boundary of the ergodic layer. The line profile for this chord is shown in Fig. 4. In this case the profile is fitted with five sets of Zeeman profiles, each of which has the independent amplitude, width and center wavelength, with the field strength values from 1.4 T to 3.1 T. See Fig. 1 for the result.

In most cases a broad Gaussian component is necessary in the fitting. The temperature and the fraction of the total intensity of this component are in the range of 13–20 eV and 24–33 %, respectively. The source of this component is not positively identified but is supposed to be due to charge exchange collisions or the recombining plasma component (see eq. (4) later). It is noted that the temperature of helium ions, which is derived from the Doppler broadening of the λ468.6 nm ($n = 3-4$) line, is found to have similar values.

Though the λ728.1 nm line cannot have gross polarization, some observed profiles exhibit apparent polarization. An example is shown in Fig. 5; this is obtained with the viewing chord (c) in Fig. 1 and the π-component is much stronger than

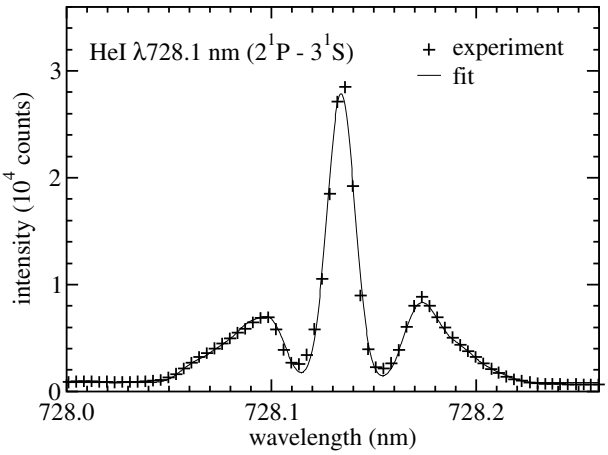

FIG. 4: Similar to Fig. 2 but with the viewing chord (b) in Fig. 1. The profile is fitted with five sets of the Zeeman profiles.

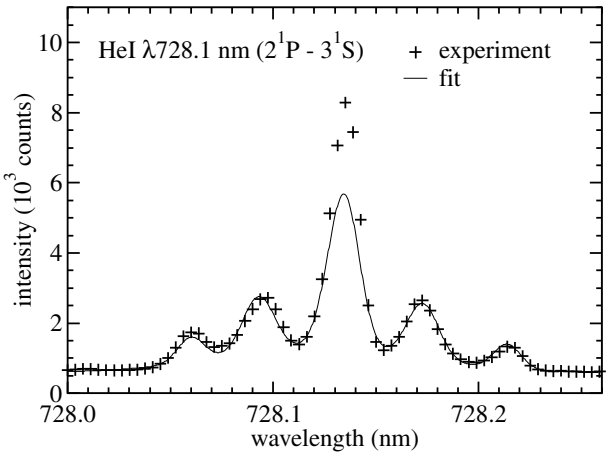

FIG. 5: Similar to Fig. 2 but with the viewing chord (c) in Fig. 1.

expected. This cannot be explained as due to an oblique viewing angle with respect to the direction normal to the magnetic field. If this were the case the apparent polarization would be opposite. The inner components of the profile correspond to the field strength of about 1.5 T, and reasonable locations cannot be found on this line of sight; the location of this field strength falls outside the vacuum vessel or far away from the plasma boundary. Rather, this component is identified as light reflected by the wall surface. For specular reflection the incident angle to the wall surface is larger than 65 degree so that the reflection efficiencies are expected to be different for the two polarized components; suggesting a higher efficiency for the s-polarized component than for the p-polarized component. The anomaly of the intensity ratio could be explained by this, but the complicated plasma vessel geometry prevents us from identifying the source of the reflected light.

We conducted similar measurements with the HeI λ667.8 nm (2^1P-3^1D) line. The description is almost the same as for the λ728.1 nm line. We did not detect any gross polarization except for the reflected light. The result is shown in Fig. 1 with the crosses. The emission locations of these two lines

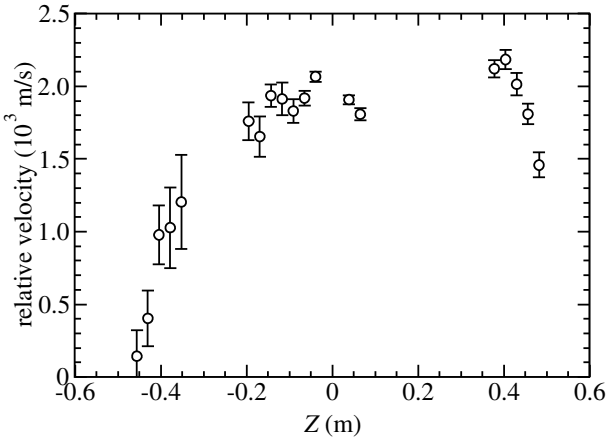

FIG. 6: The chord dependence of the apparent relative speed of the two components of atoms which is derived from the Doppler shift of the observed emission line.

almost coincide each other. The slight differences would be due mainly to the slightly different conditions of the plasma.

Figure 6 shows the relative speed of the atoms which is obtained from the two Zeeman profiles like those in Fig. 2. The emission at the smaller major radius always shifts to the shorter wavelength with respect to that at the larger major radius. Unfortunately, we could not determine the absolute shift. This figure, especially the points in $Z \leq 0$, suggests that the atoms have an inward motion with speeds of $1\text{–}2 \times 10^3$ m/s.

III. DISCUSSION

Figure 1 indicates that the regions of intense line emission form a closed zone, which almost coincides with the outer boundary of the ergodic layer, except for the "dent" at around $Z = 0.05$ m, $R = 2.8$ m. We do not have any explanation for this at present. As mentioned above the spatial extent of the emission region is narrower than or about 5 cm. We consider the emission intensity and the decay of the atom density in the inward atom flux by a one dimensional model. The atom density $n_{\rm He}$ at the penetration depth ℓ in the x direction is expressed as

$$n_{\rm He} = n_0 \exp\left[-\int^{\ell} \frac{n_{\rm e} S_{\rm CR}}{v} {\rm d}x\right], \tag{3}$$

where $S_{\rm CR}$ and v are the effective ionization rate coefficient and the penetration velocity of the atoms, respectively, and n_0 is the atom density at the edge. The ionization flux and the emission intensity for the λ728.1 nm line, taken as an example, are expressed as $S_{\rm CR} n_{\rm e} n_{\rm He}$ and $\varepsilon_{728.1} n_{\rm e} n_{\rm He}$, respectively: both the quantities are defined as the number of events, ionization or photon emission, per unit volume and unit time. $\varepsilon_{728.1}$ is called the emission rate coefficient for the λ728.1 nm line.

$S_{\rm CR}$ and $\varepsilon_{728.1}$ are calculated from the collisional-radiative (CR) model[11, 12]. According to the CR model in which the quasi-steady-state approximation is assumed even for the

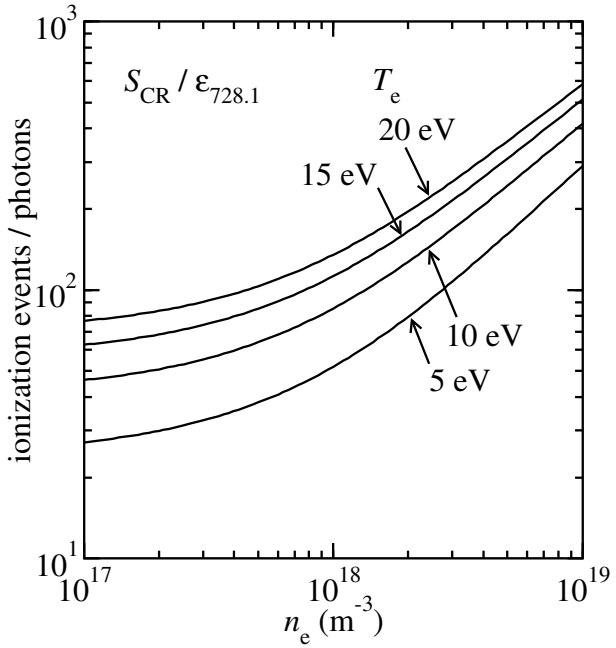

FIG. 7: The $n_{\rm e}$ and $T_{\rm e}$ dependences of the ratio $S_{\rm CR}/\varepsilon_{728.1}$ calculated with the CR model under the assumption that the quasi-steady-state approximation is valid.

metastable levels, 2^1S and 2^3S, the population density of excited level p is expressed as

$$n(p) = R_0(p) n_{\rm e} n_{\rm He^+} + R_1(p) n_{\rm e} n_{\rm He}, \tag{4}$$

where $R_0(p)$ and $R_1(p)$ are the population coefficients of the recombining and ionizing plasma component, respectively, and are functions of $n_{\rm e}$ and $T_{\rm e}$, and $n_{\rm He^+}$ is the helium ion density. It may be assumed that, in the plasma peripheral region, the second term predominates over the first, at least for the sharp components of the observed profiles. In this case $S_{\rm CR}$ and $\varepsilon_{728.1}$ are defined as

$$\begin{aligned} \sum_{\text{all } p} S(p) n_{\rm e} n(p) &= \left\{ S(1) + \sum_{\text{all } p>1} S(p) R_1(p) n_{\rm e} \right\} n_{\rm e} n_{\rm He} \\ &\equiv S_{\rm CR} n_{\rm e} n_{\rm He}, \end{aligned} \tag{5}$$

and

$$\begin{aligned} n(3^1S) A(3^1S \to 2^1P) &= R_1(3^1S) n_{\rm e} n_{\rm He} A(3^1S \to 2^1P) \\ &\equiv \varepsilon_{728.1} n_{\rm e} n_{\rm He}, \end{aligned} \tag{6}$$

respectively. Here, $S(p)$ is the ionization rate coefficient of level p and $A(3^1S \to 2^1P)$ is the spontaneous transition probability from 3^1S to 2^1P. The level "1" stands for the ground state. Figure 7 shows the $n_{\rm e}$ dependence of the ratio $S_{\rm CR}/\varepsilon_{728.1}$ for several $T_{\rm e}$ values. It is seen that the value is rather insensitive to $n_{\rm e}$ and $T_{\rm e}$. This means that the emission intensity could be a good measure of the ionization flux in the range of $n_{\rm e}$ and $T_{\rm e}$ shown in this figure.

By using eq. (5) for $S_{\rm CR}$ we evaluate eq. (3) numerically for positions near the outer X point on the chord (a) in Fig. 1. For

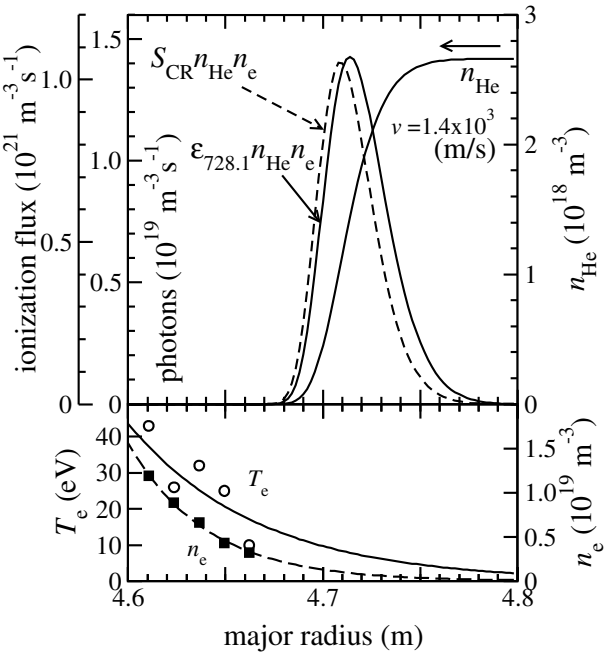

FIG. 8: Profiles of helium atom density $n_{\rm He}$, emission intensity of 728.1 nm line $\varepsilon_{728.1}n_{\rm e}n_{\rm He}$ and ionization flux $S_{\rm CR}n_{\rm e}n_{\rm He}$ in a one dimensional penetration model with the mono-energetic penetration velocity of 1.4×10^3 m/s. The $n_{\rm e}$ and $T_{\rm e}$ profiles are extrapolated exponentially from the measured values with Thomson scattering for a similar discharge.

$n_{\rm e}$ and $T_{\rm e}$ profiles the Thomson scattering data for a similar discharge of the same configuration are extrapolated with an exponential decay, as shown in Fig. 8. The apparent atom temperature is lower than 0.1 eV which is the lower detection limit of the Doppler broadening. We assume a mono-energetic penetration velocity with the thermal velocity of 300 K ($v = 1.4\times10^3$ m/s). So far n_0 has not been determined yet. At the same time we calculate $\varepsilon_{728.1}$ from eq. (6) and integrate the emission intensity over the penetration path

$$I_{728.1} = \int \varepsilon_{728.1} n_{\rm e} n_{\rm He} {\rm d}x. \qquad (7)$$

From the observed value of $I_{728.1}$ (Fig. 2) we determine n_0 to be 2.7×10^{18} m^{-3}. The result is shown in Fig. 8. The spatial dependences of $\varepsilon_{728.1}n_{\rm e}n_{\rm He}$ and $S_{\rm CR}n_{\rm e}n_{\rm He}$ are also shown in the same figure. Both the profiles have similar peaked shapes of about 3.5 cm in FWHM. This width of the emission intensity profile is consistent with the experimental result which suggests that the extent of the emission region is narrower than or about 5 cm. The radial location of the emission is also in good agreement with the experiment. The atom density is found to decay in the region of the strong emission intensity before reaching the LCFS, which is located at $R = 4.5$ m.

We have assumed the quasi-steady-state approximation for the metastable levels. The relaxation time of the 2^3S level as determined from the ionization rate is 5×10^{-6} s for $n_{\rm e} = 10^{18}$ m^{-3} and $T_{\rm e} = 10$ eV. During this time the atoms travel over 0.7 cm, short enough as compared with the scale length of the plasma.

If the penetration velocity were twice the above assumption, the peaks of the emission intensity and the ionization flux would shift by 1 cm to the inward direction and become broader by 10 %. Since the atom density n_0 normalized from eq. (7) decreases by 40 %, the inward particle flux $n_{\rm He}v$ and the total ionization flux $\int S_{\rm CR}n_{\rm e}n_{\rm He}{\rm d}x$ increase by 20 %. This is caused by the $n_{\rm e}$ and $T_{\rm e}$ dependences of the ratio $S_{\rm CR}/\varepsilon_{728.1}$.

Since the neutral atom densities in the light-emitting region and in the outer region are appreciable, the opacity effects may not be neglected; we consider the effect of absorption of the resonance line, HeI λ58.4 nm (1^1S-2^1P). Since the magnetic field strength varies over space, the σ-components would be optically thin throughout, and only the π-component may have a significant optical thickness. On the assumption of the thermal Doppler broadening with temperature of 300 K, the absorption coefficient at the line center is about 30 m^{-1}. In the light-emitting region of several centimeters thickness (Fig. 8), the line is barely optically thick, and effective reduction of the transition probability may be expressed in terms of the escape factor; the transition probability is reduced by a factor of 2[11]. If we average the effect on the π-component with the σ-components, the effect of opacity on the transition probability ($[1/2+1+1]/3$) and thus on the excited-level populations (except perhaps for the 2^1P population) would be minimal. The helium gas in the outer region may be illuminated by the resonance line from the light-emitting region, again only by the π-component, and the 2^1P atoms may be produced there. However, electron temperature and density there are low (see Fig. 8), and further excitation may be minimal, again.

We observed other neutral helium lines; the wavelength of the λ501.6 nm (2^1S-3^1P) line is rather short and the Zeeman splitting is found too small for a similar analysis. For triplet lines the fine structure levels of the 2^3P_J, for example, have the intrinsic energy level separation of $J = 2$ to $J = 0$, 1 of about 1 cm^{-1} and this is of the same order as the Zeeman shifts for these levels under the field strength of the present experiment; $\mu_{\rm B}B \simeq 1$ cm^{-1} for $B = 2$ T. This makes the profiles of the λ706.5 nm (2^3P-3^3S) and the λ587.6 nm (2^3P-3^3D) lines complicated and a similar analysis is difficult. For the other triplet line λ388.9 nm (2^3S-3^3P) the wavelength is too short. Even for the second order light of the λ388.9 nm line the splitting is found small; substituting eq. (1) and $E_0 = hcn_{\rm s}/\lambda_0$ ($n_{\rm s} \approx 1$) into eq. (2) we obtain a relation

$$\Delta\lambda \simeq \lambda_0^2 \frac{\mu_{\rm B}B}{hc}, \qquad (8)$$

and it is found that $\Delta\lambda$ is proportional to λ_0^2. This means the Zeeman splitting for the second order light of the λ388.9 nm line is about 1/2 of that for the first order light for the λ728.1 nm line.

Welch et al. observed a wavelength shift of the Zeeman split Balmer-α line of deuterium atoms in Alcator C-Mod[5]. They identified the Doppler shifts to the different neutral atom flows along the magnetic field lines at the two locations. The LHD has a magnetic field structure different from the tokamaks and has a rather thick ergodic layer outside the LCFS. We may thus conclude that, in our case, the atoms have inward motion with the thermal speed of 1–2 $\times 10^3$ m/s. The relative speeds

in Fig. 6 on the chords $0.4\ \mathrm{m} \leq Z \leq 0.5\ \mathrm{m}$ do not fit in this picture; *i.e.*, they appear too large when compared with those in $Z \simeq -0.4$ m. This is probably due to a structure of atom flows which is caused by the complicated geometry of the plasma vessel.

Finally, similar measurement on the Balmer-α line of hydrogen was also attempted and we encountered difficulties in fitting of the observed profile. The reasons are: (1) The wavelength $\lambda 656.3$ nm is shorter than the $\lambda 728.1$ nm, and the Zeeman splitting is smaller. The reciprocal dispersion of the spectrometer is larger by a factor 1.08. (2) The Doppler broadening of the emission lines is larger: Hydrogen atoms have a higher temperature (~ 0.6 eV) than helium atoms (< 0.1 eV) and the Doppler width becomes larger than the Zeeman splitting. This is possibly due to the hydrogen atoms produced from the dissociation of molecules.

[1] J. A. Snipes *et al.*, Plasma Phys. Control. Fusion **38**, 1127 (1996).
[2] T. Fukuda, Plasma Phys. Control. Fusion **40**, 543 (1998).
[3] S. Morita *et al.*, Proc. 16th International Conference on Fusion Energy, Montreal, 1996, IAEA-CN-64/CP-3 (IAEA, Vienna, 1997).
[4] J. L. Weaver *et al.*, Rev. Sci. Instrum. **71**, 1664 (2000).
[5] B. L. Welch *et al.*, Phys. Plasmas **8**, 1253 (2001).
[6] O. Motojima *et al.*, Phys. Plasmas **6**, 1843 (1999).
[7] N. Ohyabu *et al.*, Nucl. Fusion **34**, 387 (1994).
[8] N. Ohyabu *et al.*, Phys. Rev. Lett. **84**, 103 (2000).
[9] S. Morita *et al.*, Proc. 26th European Conference on Controlled Fusion and Plasma Physics, Maastricht, 1999, **23J**, 1321 (1999).
[10] P. H. Heckmann and E. Träbert, Introduction to the Spectroscopy of Atoms (North-Holland, Amsterdam, 1989).
[11] T. Fujimoto, J. Quant. Spectrosc. Radiat. Transfer **21**, 439 (1979).
[12] M. Goto and T. Fujimoto, NIFS-DATA-43, National Institute for Fusion Science (1997).

Plasma polarization spectroscopy in the tandem mirror GAMMA 10

M. Yoshikawa,[1] T. Furukawa,[1] A. Tanaka,[2] A. Iwamae [2] and T. Fujimoto [2]
[1] Plasma Research Center, University of Tsukuba
[2] Department of Engineering Physics and Mechanics, Kyoto University

Abstract

Polarization of impurity ion emission lines shows us information of the electric fields, strong magnetic fields, and/or angular anisotropy of the plasma. We have started measurements of plasma polarization of impurity ion emissions in the tandem mirror GAMMA 10 plasma in the UV/V wavelength region. We plan to measure polarization spectra in the VUV wavelength region by using calibrated VUV spectrograph. The small polarization was observed in the UV/V wavelength range.

1. Introduction

Polarization of impurity ion emission lines from the GAMMA 10 tandem mirror plasma has been observed [1]. Polarization is a result of angular anisotropy of the ensemble of the ions, and that of the plasma. We used a calcite plate as a polarizer and two columns of optical fiber bundle in the UV/V spectrograph. New polarization spectrograph will be used in VUV wavelength region [2]. We show some results of polarization spectroscopy in the UV/V wavelength region and new plan to observe the polarization spectrum in the VUV wavelength region.

2. Tandem mirror GAMMA 10 device

GAMMA 10 is a 27m long tandem mirror consisting of a 5.6 m long axisymmetric central cell, anchor cells for suppressing MHD instability and axisymmetric end mirrors forming the plug/barrier potentials [2,3]. Plasma in the central cell are produced and heated by ICRH with hydrogen gas puffing and the plug potentials are produced by ECRH. One of the main characters of the tandem mirror is that confinement is achieved by not only magnetic field but also electric field. The typical plasma parameters in the central cell are as follows; the electron density is 2×10^{12} cm^{-3}, electron temperature is 80 eV and the ion temperature is 5 keV. The plasma duration is 0.2 sec and the duration of potential formation is reached to 0.1 sec. We set the UV/V spectrographs at the central cell and anchor cell. The SX or VUV spectrograph is set at the central cell.

3. Polarization spectroscopy system in GAMMA 10

Polarization spectroscopy system in UV/V wavelength region is shown in Fig. 1 [1]. We used calcite plate for polarizer and two columns of optical fiber bundle for dividing P and S lights. Figure 2 is the arrangements of the face of the optical fibers on the entrance and exit surfaces. The exit surface is set on the entrance slit of 1 m Czerny-Turner spectrometer. The output spectral image is amplified by the image intensifier and recorded by the CCD camera. Time resolution of this spectrograph is 30 frames/sec with 10 ms shutter speed.

We plan to use aberration corrected concave grating VUV spectrograph for polarization spectroscopy (Fig. 3) [2]. This spectrograph is absolutely calibrated at the photon factory (PF) in the high energy accelerator research organization (KEK). The light from the plasma goes through the entrance slit and is diffracted by the aberration corrected concave grating. The diffracted light is detected by the MCP and phosphor plate. The

spectral images are recorded by the high-speed camera. Figure 4 shows the absolute sensitivity against polarization of incident lights. The vertical axis shows the wavelength in Å and the horizontal axis shows absolute sensitivity. Blue cross shows the S-polarized light and red circle shows the P-polarized light.

4. Plasma polarization spectroscopy in GAMMA 10

In the GAMMA 10 plasma, Carbon and Oxygen ions are mainly observed. Main radiated wavelength region is VUV region because of plasma temperature. Figure 5 shows typical output image of UV/V polarization spectrograph. Upper side of the photograph shows the -light and lower side shows the -light. In this image, OV and FeII ion lines are observed. Figure 6 shows time dependent polarization spectra in the core region of line of sight in the central cell. Polarization of FeII and OV ion line emissions were observed. The intensity ratio of and light emissions is changed as the time. We decided the longitudinal alignment as following equation.

$$P = (I - I) / (I + I) \quad (1)$$

Figure 7 shows time evolutions of longitudinal alignment of the lines in the core region of the plasma. These show that the longitudinal alignments are randomly observed.

5. Summary.

In GAMMA 10 tandem mirror, polarization spectroscopic measurements were started. UV/V polarization spectroscopic system has been constructed and a VUV spectroscopic system for polarization measurement was indicated. In UV/V polarization spectroscopy, Iron and Oxygen ion emissions were slightly polarized in some cases.

References

[1] T. Inoue, M. Nakai, A. Tanaka, K. Kawakami, A. Iwamae, T. Fujimoto, M. Yoshikawa, T. Ito and T. Tamano, *Plasma Phys. Control. Fusion* **43** (2001) L9.
[2] M. Yoshikawa, Y. Okamoto, E. Kawamori, C. Watabe, Y. Watanabe, T. Furukawa, K. Ikeda, N. Yamaguchi, T. Tamano and K. Yatsu, *Transaction of Fusion Technology,* **39** (2001) 289.
[3] T. Tamano, *Phys. Plasmas*., **2** (1995) 2321.

Figures:

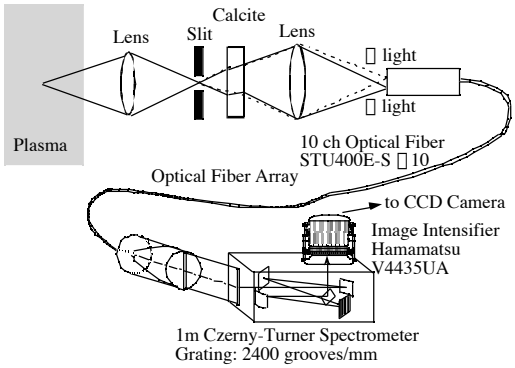

Fig. 1 Polarization spectroscopy system in UV/V wavelength region.

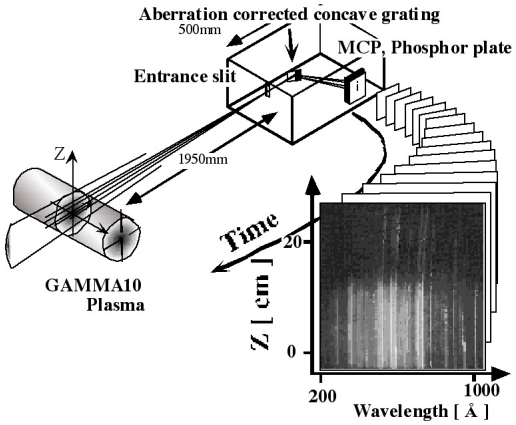

Fig. 2 The arrangements of the face of the optical fibers on the entrance and exit surfaces.

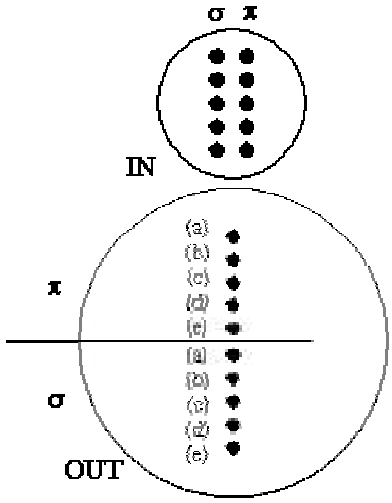

Fig. 3 Polarization spectroscopy system in the VUV wavelength region.

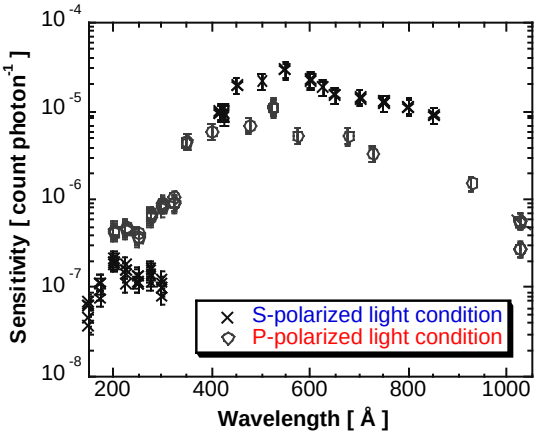

Fig. 4 Absolute sensitivity of VUV spectrograph.

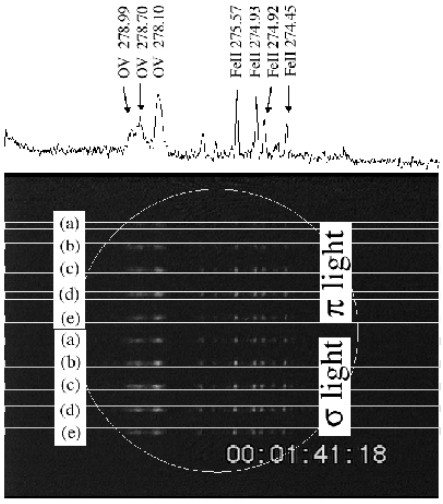

Fig. 5 Typical polarization spectroscopic image of UV/V spectrograph.

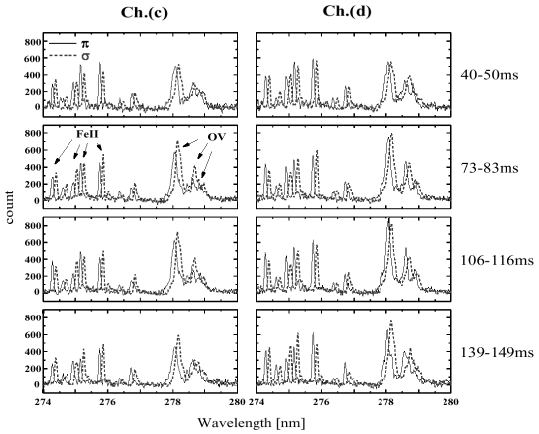

Fig. 6 Time evolution of polarization spectra in the UV/V wavelength range.

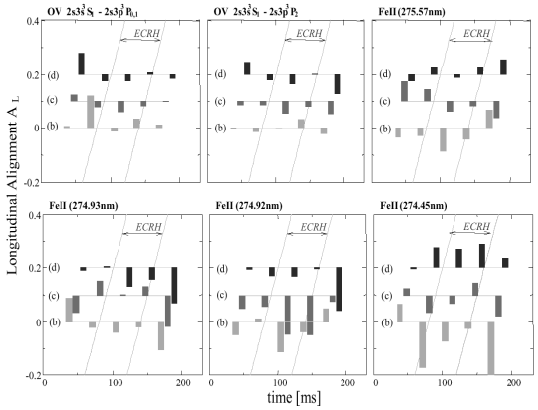

Fig. 7 Time and space dependences of longitudinal alignment.

Plasma Polarization Spectroscopy on an Optical-Field-Ionization Plasma

Tetsuya Kawachi
Advanced Photon Research Center, Japan Atomic Energy Research Institute (JAERI)
8-1, Umemidai, Kizu, Soraku-gun, Kyoto, 619-0215, JAPAN

Atsushi Iwamae and Takashi Fujimoto
Department of Engineering Physics and Mechanics, Kyoto University, Kyoto, Japan

Abstract Helium gas target was irradiated by a linearly polarized ultra-short pulse of Ti:Sapphire laser light with duration of 50fs and energy of 150 mJ. We changed the direction of the polarization of the incident laser light and observed the emission of the Lyman series lines and continuum from the plasma in the recombining phase.

I. INTRODUCTION

Recent advent of ultra-short-pulse lasers makes it possible to generate highly charged ions ionized by the high laser electric field; this mechanism is called the optical field ionization (OFI). [1-4] Characterization of the plasmas thus produced, especially that of the electron velocity distribution, is essential for the purpose of developing a novel x-ray source such as x-ray lasers. Therefore, clarification of the electron velocity distribution is an important objective of plasma polarization spectroscopy (PPS). In the high laser field, an electron in an atom is quivered by the periodic laser field and has a pondermotive potential energy. With an increase in the laser electric field strength, the pondermotive potential energy becomes comparable with or even exceeds the ionization potential of the atom, and tunneling ionization occurs with a substantial probability. In the case that the laser light is linearly polarized, ionized electrons would have velocities only in the direction of the laser field, so that the electron velocity distribution would be strongly anisotropic. The emission lines and continuum of ions in such a plasma may be polarized. It is known that OFI plasmas emit radiation in the recombining plasma phase. It is thus expected that, by observing the temporal change of the emission polarization, we can investigate relaxation process of the anisotropic electron velocity distribution due to electron-electron and electron-ion scattering.

In th e following , we report on our preliminary experiment toward the polarization measurement of the OFI plasma.

II. PRELIMINARY EXPERIMENT

A schematic diagram of our laser system is given in Fig. 1. The seed light at wavelength of 800 nm with 20 fs duration and 80 MHz repetition rate is generated by a mode-locked Ti:sapphire oscillator (Femto-source technology) pumped by a 5 W diode-pumped solid state laser (Spectra Physics Millenia V). The typical power of the seed light is 250 mW and the spectral bandwidth is 40 nm (full-width at half maximum (FWHM)). A four-path stretcher

based on a spherical mirror and a grating with 1200 grooves/mm (Richardson grating) generates a chirp of 50 ps/nm. Due to the limitation by the grating size, the spectral bandwidth after the stretcher is 30 nm. The regenerated amplifier is a 10 Hz Ti:sapphire laser pumped by a Nd:YAG laser (B.M. Industries). In order to reduce the ASE level and to achieve a high contrast ratio, we have optical shutters just before and after the regenerative amplifier. The typical output energy and the spectral bandwidth of the regenerative amplifier is 1 mJ and 30 nm (FWHM), respectively. The output laser pulse is further amplified by the two stage amplifiers, a 4 path and a 3 path Ti:Sapphire amplifiers, both pumped by Nd:YAG lasers, and the maximum output energy is 300 mJ/pulse. A pulse compressor, which is placed in a vacuum chamber, has an efficiency of about 60 % and provides an output laser pulse with maximum energy of 180 mJ, diameter of 50 mm, and pulse duration of 50 fs.

The laser pulse was steered by a plane mirror, went through a zero-order l/2 wave-plate (CVI optics), and was focused by an off axis parabolic mirror with *f* number of 4. The focus spot size was measured to be about 50 μm-diameter (FWHM) with an imaging system having magnification of 10. The maximum irradiance was estimated to be 2 10^{17} W/cm^2. The target gas was helium, which was injected into the focusing area by a pulse gas nozzle (General Valve) having an output aperture size of 800μm. This gas valve was synchronized with the pumping YAG laser and was opened at 400 μs before the laser pulse and was closed at 600μs after the pulse. Backing pressure of the nozzle could be varied from 1 atm through 20 atm. Gas density was determined from the line density map taken with a Mach-Zehnder type interferometer at wavelength of 633 nm for several backing pressures. [5]

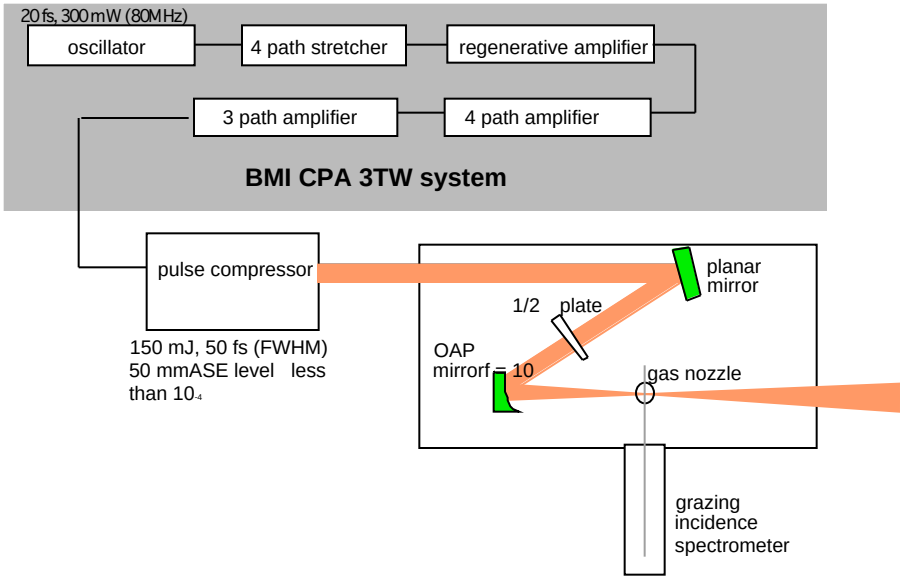

Fig.1 Schematic diagram of 3 TW TiS laser system and focusing system.

Figure 2 shows experimental set-up. OFI plasma is observed using a grazing incidence:

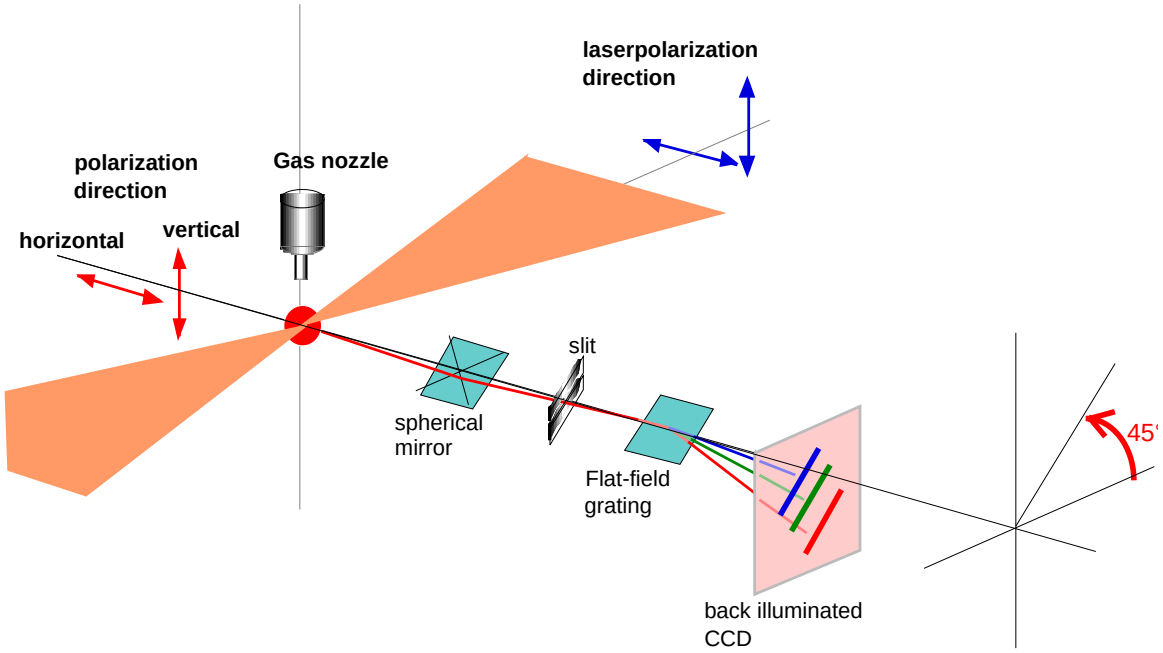

Fig.2 Experimental set-up

The emission from the plasma was observed by use of a grazing incidence spectrometer in the direction of 90° with respect to the laser propagation direction. It consisted of a concave mirror with curvature of 3240mm (angle of incidence: 86°), a 200 μm-width entrance slit and an uneven spacing flat-field grating with 1200 grooves/mm (HITACHI). The grazing incidence mirror and the grating may have different reflectivities or efficiencies for different polarization directions. Emission radiation was expected to be polarized in the direction parallel or perpendicular to the laser propagation direction. In order to compensate the differences, we rotated the spectrometer by 45° around the observation axis. We attempted to observe temporally resolved spectra by using an x-ray streak camera. We found, however, that our streak camera had a too low sensitivity in the wavelength region of interest. Instead we used a CCD in the present experiment. This was a back-illuminated CCD and we took time-integrated spectra.

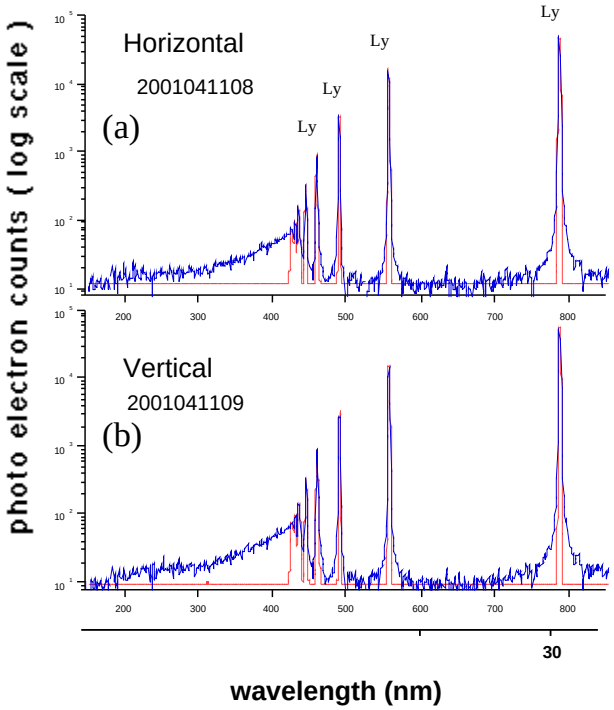

Fig.3. Typical spectra of the hydrogenlike helium ions in recombining OFI plasmas. "Horizontal" and "vertical" is shown in Fig.2.

By rotating the zero-order /2 wave-plate, the polarization direction of the linearly polarized laser light was set to be horizontal or vertical, and we compared the spectra of the plasma emission between the horizontal and vertical cases. Since the recombination continuum terminates on the 1s state, its polarization characteristics are exactly the same as those of the classical oscillator [6]. Figure 3 shows typical spectra for the helium gas target. The laser intensity was 5 10^{16} W/cm^2, and gas density is estimated to be 3 10^{18} cm^{-3}. The Lyman series lines and continuum of hydrogen-like helium ions are seen. We took similar spectra under the gas density of 4 10^{16} cm^{-3}. We derived the excited level populations of the upper levels of the hydrogen-like helium ions using the corresponding transition probabilities, where we took into account the wavelength dependence of sensitivity of our diffraction grating and that of our CCD. Figure 4 (a) and (b) shows the Boltzmann plots of the excited level populations for the gas density of 3 10^{18} cm^{-3} and 4 10^{16} cm^{-3}, respectively. In the high gas density case (a), no significant difference is seen between the two polarization cases, whereas in the low gas density case (b), a slight difference appears in the slope of the population distribution.

Here, we assume that the electron temperature (or average electron energy), T_e, is 20 eV and electron density, n_e, is 2 times the gas density. This leads to the electron-electron thermalization rate, which is $t_{ee} \sim T_e^{3/2}/[(n_e/10^{20})\ln\ ]$ (T_e and n_e are in KeV and in m^{-3}, respectively.), of order of ps for the high gas density case and 100 ps for the low density case. Since the transition probabilities of Lyman series lines are 10 ~ 100ps, it would not be unreasonable that anisotropy in the electron velocity distribution can be observed for the low density case even under the time-integrated observation. At the present preliminary stage, however, we cannot draw any definite conclusion. We plan to conduct a time-resolved observation in near future.

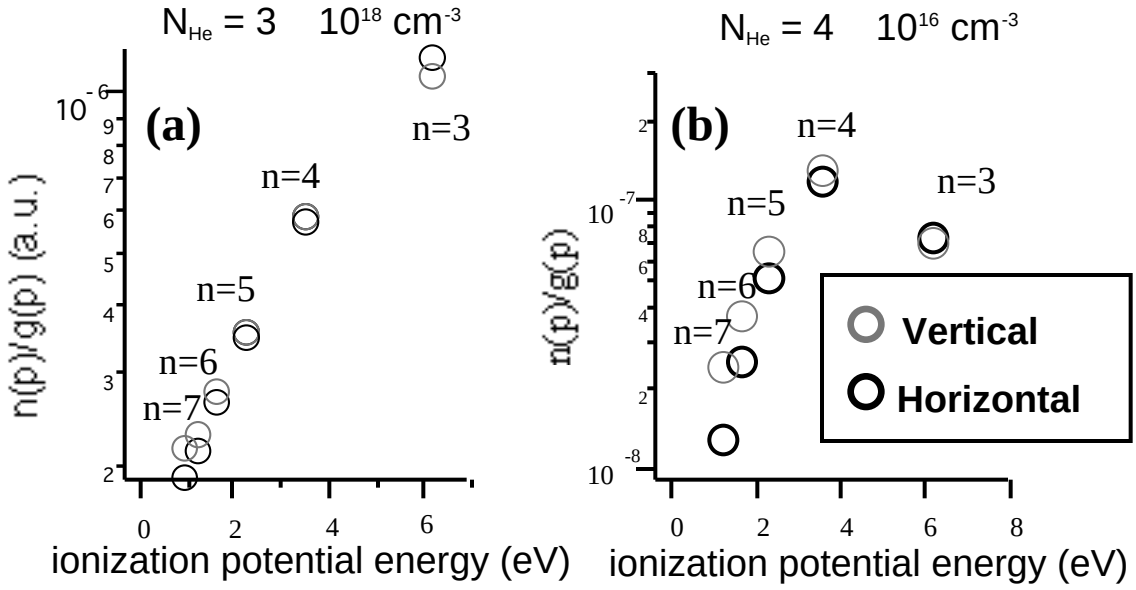

Fig.4 Boltzmann plot of the excited level populations divided by the statistical weights for the high gas density case (a); and the low gas density case (b).

References

[1] P.B. Corkum, N.H. Burnett and F. Brunel, Phys. Rev. Lett., **62**, 1259 (1989)

[2] L.V. Keldish, Zh.Eksp. Teor. Fiz. **47**, 1945 (1964) [Sov. Phys. JETP **20**, 1307 (1965)]

[3] M.V. Ammosov, N.B. Delone and V.P. Krainov, Zh.Eksp. Teor. Fiz. **91**, 2008 (1986) [Sov. Phys. JETP **64**, 1191 (1986)]

[4] S. Augst, D. Strickland, D.D. Meyerhofer, S.L. Chin, and J.H. Eberly, Phys. Rev. Lett. **63**, 2212 (1989)

[5] H. Kotaki, proc. of 10th International Symposium on Applied Electromagnetics and Mechanics (ISEM2001) (in press)

[6] H. M. Milchberg and J. C. Weisheit, Phys. Rev. A **26**, 1023 (1982)

Measurement of polarization of atomic helium lines due to strong caviton fields caused by IREB-plasma interactions

M. Yoshikawa,[1] F. Osawa,[2] R. Ando,[2] K. Kamada[2] and M. Masuzaki[2]
[1] Plasma Research Center, University of Tsukuba
[2] Department of Physics, Kanazawa University

Abstract

When an intense relativistic electron beam (IREB) is injected into plasma, the strong Langmuir turbulence is occurred. We have been studied IREB-plasma interactions by measuring a broadband high power microwave radiation and strong electric fields in cavitons. We have constructed plasma polarization spectroscopy system in order to measure the polarization of atomic helium lines due to strong caviton field in IREB-plasma system.

1. Introduction.

When an intense relativistic electron beam (IREB) is injected into plasma, the strong Langmuir turbulence is occurred [1-3]. In the plasma, there are cavitons which have dipole high frequency electric field. Strong Langmuir turbulence is occurred when IREB is injected to plasma. In the strong Langmuir turbulence state, generation, collapse and burnout of cavitons are repeated by nucleation process. Here a caviton is a localized solitonlike Langmuir wave packet with density depletion. For such strong Langmuir turbulence state, the dimensionless electrostatic wave energy density $W = {}_0\langle E^2\rangle / (2n_pT_e)$ should be larger than $(k_0 {}_D)^2$. Here n_p , T_e are the plasma density and electron temperature, respectively, and k_0 is the resonance wave number ${}_p / v_p$, ${}_p$ is plasma frequency, v_p is the beam velocity, and ${}_D$ is the Debye length. The previous works show that W ~ 1.1 from spectroscopic measurements of the high frequency electrostatic fields [1-3]. Then the plasma was in the strong Langmuir turbulence state in our IREB-plasma system. Moreover, the results form measurements of beam dispersion of the IREB and polarization of microwave emission show the cavitons electric field direction is parallel to IREB direction. Then, main purpose of this study is measurements of cavitons electric field direction by using polarization spectroscopy.

2. Experimental setup

Experimental setup is shown in Fig. 1 (a) [1]. The drift chamber, 60 cm long and 16 cm in diameter, was filled with 20 mTorr He gas for spectroscopy. Carbon plasma was generated by two rail-type plasma guns set opposite to each other at 10 cm downstream from the anode foil. The experiment was carried out changing the delay time of the beam injection after the gun firing. This delay time is denoted as . The plasma density n_p was measured by triple Langmuir probe and a microwave interferometer. The measured plasma density is shown in Fig. 2 as a function of . The range of the plasma density for this experiment was from 8 10^{11} ~ 1.3 10^{13} cm^{-3}. A modified Pulserad 110A was used to generate an IREB. The diode used consisted of carbon cathode of 3.6 cm in diameter and a titanium foil anode of 20 μm thick. The typical wave forms of the diode voltage and the diode current are shown in Fig. 1 (b). The diode voltage is 1.4 MV and the diode current is 27 kA with 30 ns pulse duration.

Polarization of line radiation from the atomic helium in the plasma was measured by the newly constructed plasma polarization spectroscopic system (Fig. 3). It consisted of

calcite plate as a polarizer, lenses, a slit, two channel of bundle fibers, a monochromator, a prism and two PMTs. Output of each PMT was led to an input terminal of 1 GSa / s digitizing oscilloscopes. We decided the Z-axis is parallel to the electric filed, parallel to it is -light, and perpendicular to it is -light. Polarization of HeI forbidden emission of 663.2 nm will be observed. We show the polarization parameter, P, as follows,

$$P = (I_{\parallel} - I_{\perp}) / (I_{\parallel} + I_{\perp}). \quad (1)$$

Here, $I_{\parallel}$ and $I_{\perp}$ are the emission intensities of -light and -light, respectively. If polarization of forbidden line is parallel to the electric field direction, P = 0.447. We measured two atomic helium line emissions, allowed line of 501.6 nm and forbidden line of 663.2 nm.

3. Results of polarization spectroscopy

Figure 4 shows the dependence of HeI allowed line of 501.6 nm. Figure 4 (a) shows the allowed line output signals both - and -lights. The polarization of allowed line is shown in Fig. 4 (b). It shows that almost P = 0.0. This shows that polarization is not observed in the allowed line. In Fig. 5 (a), dependence of forbidden line emission of 663.2 nm is shown with both - and -lights. This shows that forbidden line emission has some dependence on that means plasma density. Figure 5 (b) shows the polarization of forbidden line against . It seems that small polarization of forbidden line was observed, but there are not clear dependence on . However, there are very low signal to noise ratio in our experiments. Then we check our polarization value according to signal to noise ratio. Even for the fully polarized emission, i.e. P = 0.447, if the ratio of noise component to output signal is equal to 1, observed polarization, P', decreases to 0.22. Then we have to increase the ratio of signal to noise, by improving the optical collection system of the spectrometer and reduction of electromagnetic noises.

4. Summary

We have constructed plasma polarization spectroscopy system in order to measure the polarization of atomic helium lines due to strong caviton field in IREB-plasma system. There is plasma density dependence of forbidden line output of atomic helium. Small polarization of forbidden line was observed, but there were not clear dependence on , because of low signal to noise ratio in these experiments. We plan to improve the spectroscopic system, reduction of noises and collection of large output signals, etc.

References

[1] M. Yoshikawa, M. Masuzaki, R. Ando, et al., J. Phys. Soc. Jpn., **65** (1996) 2081.
[2] R. Ando, M. Masuzaki, H. Morita, et al, J. Phys. Soc. Jpn., **65** (1996) 2518.
[3] H. Koguchi, M. Masuzaki, R. Ando, et al., J. Phys. Soc. Jpn., **67** (1998) 1273.

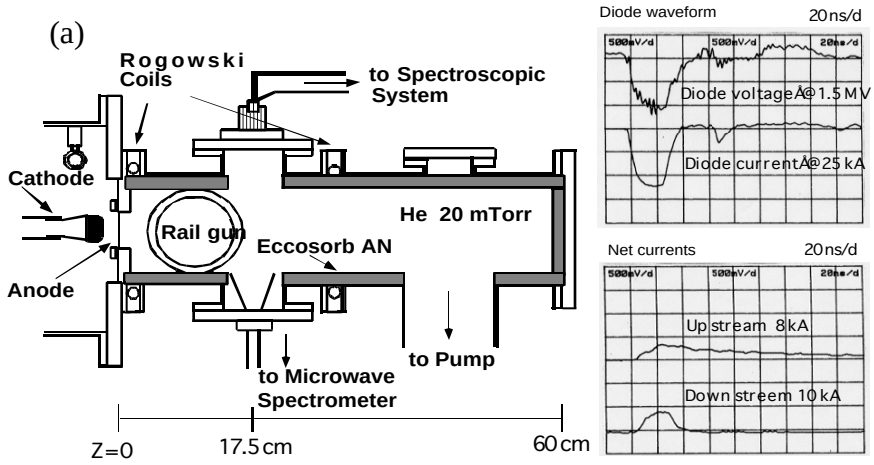

Fig. 1: IREB-plasma system. (a) shows experimental setup and (b) shows typical diode waveform and net currents.

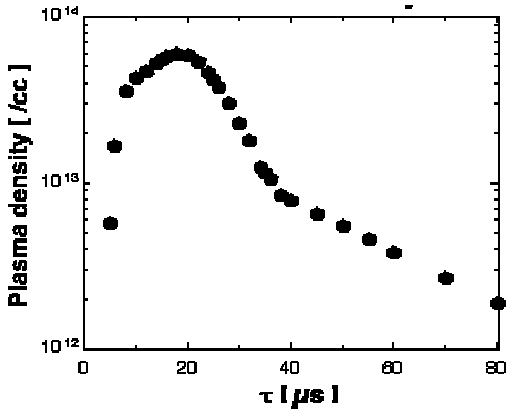

Fig. 2: Plasma density against .

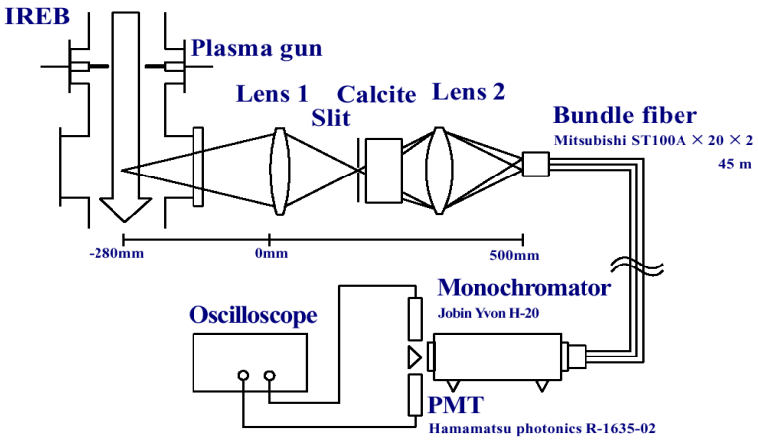

Fig. 3: Polarization spectroscopy system in the IREB-plasma system.

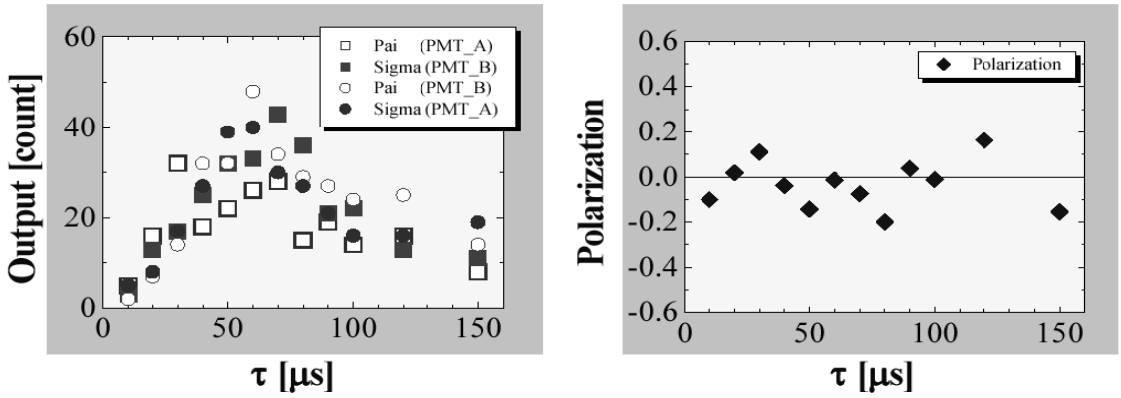

(a) (b)

Fig. 4: (a) shows the allowed line output against and (b) shows polarization.

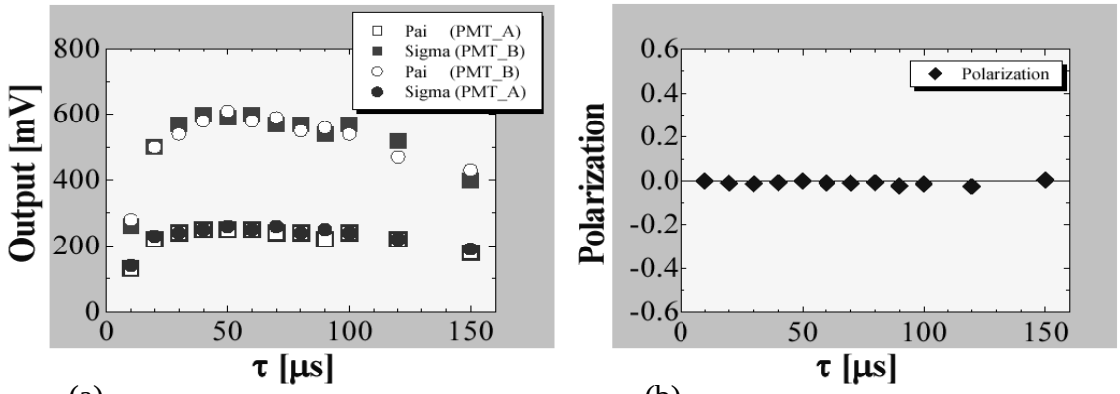

(a) (b)

Fig. 5: (a) shows the forbidden line output against t and (b) shows polarization.

Analysis of Charge Separation in Neutral Gas-Confined Laser-Produced Plasmas by Polarization Spectroscopy

Yong W. Kim
Department of Physics, Lehigh University
Bethlehem, PA 18015, USA

Abstract

Nonideal plasmas present interesting open problems in plasma physics. One of them has to do with the breakdown of the Debye scaling at high plasma densities. The Debye length underestimates the screening distance of the Coulomb potential due to free charges in the plasma to the extent that it becomes shorter than the inter-particle distance. Well-characterized dense plasmas are needed for critical examination of the breakdown and its remedies. We have investigated neutral confinement of laser produced plasmas to attain such nonideal plasmas. The confinement concept works but at neutral argon densities in excess of 20 atm at room temperature it precipitates interfacial instability for the expanding plasma plume. By means of two newly devised plasma diagnostic methods, we have uncovered the growth of the luminous interface and established its Rayleigh-Taylor nature. In order to elucidate further the microscopic processes of the instability, we have examined the feasibility of visualizing the local electric field by means of plasma polarization spectroscopy. We report on a preliminary study by polarization spectroscopy of charge separation in laser-produced plasma plumes, which are confined by low-density neutral argon.

1. The Context

High-density plasmas are of great interest from the standpoints of inertial confinement fusion, stellar dynamics and reaction processes involving energetic materials. The Coulomb potential energy for a charged particle pair becomes no longer negligible compared with the thermal kinetic energy of a single particle. The equation of state must include the nonideality contributions and the transport properties similarly corrected for. First-principle understanding of these plasma properties is essential in formulating the optimal strategies for utilization of such dense plasmas, on the one hand, and in making realistic assessment of the structure and dynamics of given plasmas, on the other. The fundamental theoretical framework is in a state of flux, however, because the basic measure of Debye shielding is no longer accurately given by the Debye length. At densities where the nonideality corrections are no longer negligible, the Debye length becomes shorter than the mean spacing between nearest-neighbor particles in the plasma, as shown in Fig. 1, negating the basis of the analysis. The question is how to bridge the

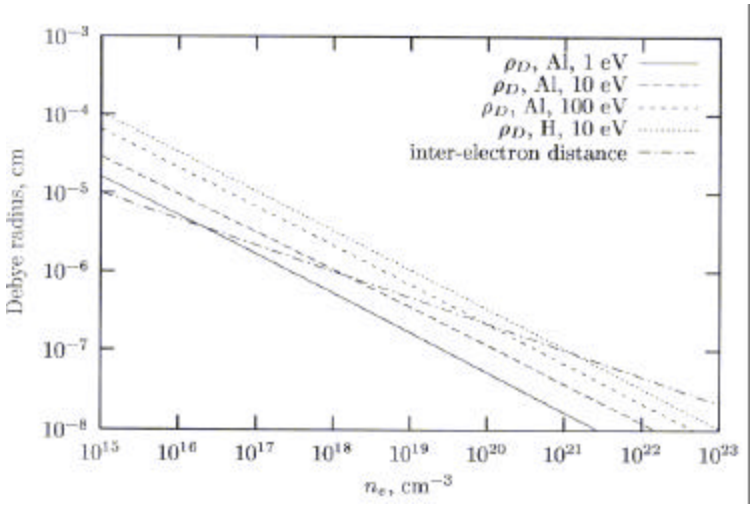

Figure 1. Inter-particle distance and Debye radius in aluminum plasmas as functions of electron density at different temperatures. The Debye radius is calculated for aluminum plasmas at 1, 10 and 100 eV. The Debye radius in hydrogen plasma at a temperature of 10 eV is also shown for comparison.

transition from the states of ideal plasmas to those of weakly, and then strongly, nonideal states. The existing formalism developed for ideal plasmas must be replaced by new formulation. One of the major obstacles to this undertaking had been the scarcity of well-characterized nonideal plasmas. Another obstacle was the lack of clear delineation of the relative importance of the consequences from the breakdown of the Debye length scaling.

We have devoted a considerable length of time to make headway into overcoming the above two major obstacles. The efforts have resulted in a significant program on weakly nonideal laser-produced plasmas (LPP) from metallic targets, including alloys. Specifically, the focus of our program has been on the basic effects of the plasma nonideality on the ionization potential lowering, plasma self-absorption, laser-plasma interaction and plasma diagnostics. The temperature and number density of the plasma, comprised of multiply ionized species, ranged up to 60 eV and 10^{21} cm^{-3}, respectively. Confinement of the LPP plume by inert gas at densities up to 50 times the standard density helped increase the plasma density but precipitated Rayleigh-Taylor interfacial instability. This has presented us with two opportunities for plasma diagnostics: weak nonideality of the LPP plumes,[1,2] as intended, and the loss of plasma symmetry that was unintended.[3,4] We have subsequently developed two new diagnostic methods, based entirely on plasma's continuum luminosity. The time-resolved 3-D profile of plasma density and temperature is reconstructed from the 2-D luminosity profiles at selected times by incorporating full equilibrium plasma calculations and imposing independently measured plasma energy and mass, plasma self-absorption and laser energy scaling as constraints.[1] The second method provides the algorithm for reconstruction of Rayleigh-Taylor unstable plasmas resulting in irregular shape.[3] In section 2 we present a review of the two new plasma diagnostic methods.

2. Nonideal Plasmas and their 3-D Plasma Structure Reconstruction

Our LPP research program has been focused on developing experimental tests of new theories of plasma transport properties and atomic structures appropriate for the plasma density regime where the nonideality of the equation of state becomes significant. The formulation of Coulomb screening breaks down in that the Debye shielding length becomes shorter than the mean inter-particle distance. New estimates for the screening length[2,5,6] need to be examined in order to facilitate accurate calculation of the lowering of ionization potentials and the equation of state, both necessary for equilibrium plasma calculations. Plasma absorption is substantially affected, as we have discovered,[2,7] and this plays out in the evolution of LPP plume. Delineation of the consequences is necessarily circuitous due to the fact that many competing processes within the plasma are manifested in plasma diagnostics.

We have waged a two-pronged attack in the pursuit of weakly nonideal LPP plumes. On the one hand, a comprehensive diagnostic method is developed for time-resolved reconstruction of 3-D plasma profiles in terms of specific continuum emission intensity for stable LPP plumes in a vacuum. On the other, the nonideality effects are purposely accentuated by confining the LPP plumes by means of a dense neutral gas blanket.

A. Weakly nonideal LPP plumes in a vacuum

The early-time spectral emissions from weakly non-ideal LPP plumes are essentially a continuum, consisting of bremsstrahlung radiation and severely Stark-broadened line emissions.[8-10] Our plasma diagnostic method is novel in that the LPP plume is imaged entirely with the continuum plasma emissions. Due to the presence of significant self-absorption, the analysis leading to the plasma's density and temperature as function of space and time is carried out in close coupling to plasma equilibrium calculations. We start from the scaling relations relating the specific continuum intensity I at a point within the LPP plume to the local temperature T and pressure p: $T = S_T I^{\alpha}$ and $p = S_P I^{(\alpha + \beta)}$. The LPP plume is completely specified once the specific continuum intensity is found together with the scaling exponents α and β and the scaling constants S_T and S_p. The observable side-view plasma luminosity profile arises from a line-of-sight integration of the specific continuum intensity profile across a cross-sectional plane of the plume [see Fig. 2a], and as such, must be inverted in order to reconstruct the 2-D specific continuum intensity profile. At the same time, the inversion requires the local plasma absorption coefficient, which is derived from specific plasma continuum intensity through the scaling relations.

The program of continuum-based plasma diagnostics has consisted of measuring the side-view plasma luminosity profiles as function of time; these are in the form of streak photographs taken at different distances from the target surface [see Fig. 2b]. The attenuation by the plasma plume of laser beams, at its fundamental and second harmonic frequencies, is measured as function of time by using a pinhole at the center of the aluminum target. The total mass contained in each LPP plume is determined from

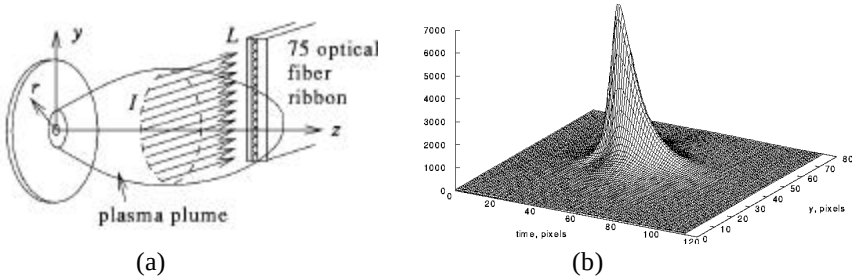

(a) (b)

Figure 2. (a) Schematic diagram of the arrangement for streak measurement of a side-view luminosity profile at distance z from the target surface. (b) Luminosity profile at 0.5 mm from the aluminum target surface as function of time when the laser pulse energy is 2.3 J.

measuring the mass lost by the target by each laser ablation. The total energy deposited into the plume is determined by subtracting the energy expended in evaporation of the mass and the energy lost by reflection by the plume, target and the optical elements. Finally, the entire measurement is repeated at four different laser pulse energies. These measurements are used as constraint conditions, which the inversion process must satisfy.

The basic steps of the process are shown in Fig. 3. The two scaling constants and two scaling exponents are first selected. The inversion of the detected luminosity L(y, z) into the specific continuum intensity I(r, z, t), emanating from a differential plasma volume element, then proceeds for one cross-sectional slice at a time at distance z from

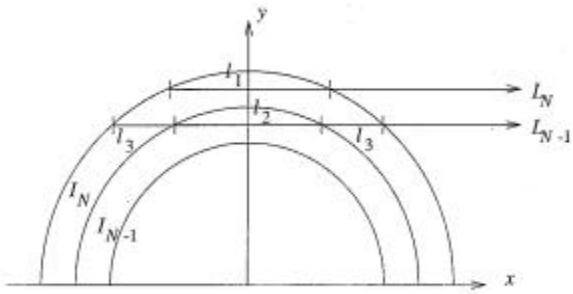

$$L_N = \frac{I_N}{k_N}\left(1 - e^{-k_N l_1}\right)$$

$$L_{N-1} = \frac{I_N}{k_N}\left(1 - e^{-k_N l_3}\right) e^{-k_{N-1} l_2} e^{-k_N l_3} + \frac{I_{N-1}}{k_{N-1}}\left(1 - e^{-k_{N-1} l_2}\right) e^{-k_N l_3} + \frac{I_N}{k_N}\left(1 - e^{-k_N l_3}\right)$$

$$\vdots$$

Figure 3. Modified Abel inversion algorithm that includes the effect of self-absorption on the line-of-sight integration of the specific plasma continuum intensity. The cross-sectional slice of A selected cross-sectional slice of the LPP plume is divided into N equal-width shells, and the specific continuum intensity I_i is integrated along the line of sight for i = N to i = 1. Self-absorption is included, assuming that the plasma absorption coefficient is constant within a given shell. The absorption coefficient k_N is calculated according to the plasma temperature and density of the shell by solving the full set of 13 Saha equations. The intensity and plasma properties are found iteratively using the relationship shown in the figure.

the target surface at time t of the LPP plume. For a LPP plume produced in a vacuum, it is axially symmetric but the plasma medium is optically thick and the measured luminosity is complicated by self-absorption of the plasma emissions on the way out of the plasma. We have thus developed a modified Abel inversion algorithm to properly

correct for the effect of self-absorption. The plasma temperature and density and the specific continuum intensity from each differential plasma volume element are found self consistently by iteration. The energy loss from each volume element by radiation and thermal conduction is included. The inversion proceeds from the outermost shell toward the inner shells.

The basic equations used in the algorithm are assembled in Fig. 4 with descriptions of the optimization process. The inversion calculation is continued to successive time intervals for the entire lifetime of each LPP plume. In the end, we have on hand a full set of calculated plasma mass, plasma energy, transmitted intensities of the probing laser beams at two wavelengths, all as a function of time. The results are compared with the corresponding measurements. The search for the optimal values of the scaling constants and scaling exponents takes place in a hierarchical manner - namely, coarse-grained searches followed by fine-grained searches. The final values for the

- **Saha equations for aluminum**

$$\frac{\alpha_i(1-\alpha_{i+1})}{(1-\alpha_i)} = \frac{2kT\,(2\pi m_e kT)^{3/2}}{p_e h^3}\frac{Q_i}{Q_{i-1}},\quad i = 12\ldots 1$$

$$\frac{\alpha_{13}}{(1-\alpha_{13})} = \frac{2kT\,(2\pi m_e kT)^{3/2}}{p_e h^3}\frac{Q_{13}}{Q_{12}}$$

$$\overline{Z} = \alpha_1 + \alpha_1\alpha_2 + \alpha_1\alpha_2\alpha_3 + \cdots + \alpha_1\alpha_2\alpha_3 \cdots \alpha_{11}\alpha_{12}\alpha_{13}$$

$$p_e = p\frac{\overline{Z}}{(1+\overline{Z})} \qquad \Gamma = \frac{\overline{Z}e^2 n_e^{1/3}}{kT}$$

- **Debye length ⟹ Screening length**

$$\rho_D = \sqrt{\frac{kT}{4\pi(n_e + \sum_s z^2 n_s)e^2}}$$

$$\frac{r_s}{\rho_D} = 1 + \frac{\Gamma^{3/2}\sqrt{\overline{Z}}\pi^{3/2}}{\sqrt{2}}\ln\left[1 + \left(\frac{r_s}{\rho_D}\right)^2 \frac{2\overline{Z}}{3\pi\Gamma^3}\right]$$

- **Lowering of ionization potentials**

$$\Delta IP_{\text{Debye}} = (Z+1)\,e^2/\rho_D$$

$$\Longrightarrow \Delta IP = n_e kT \int_0^{r_s} \left(e^{-\Phi_{ei}/kT} - 1\right) d^3r$$

- **Plasma absorption coefficient**

$$k = \frac{2\omega}{\sqrt{2}c}\left[\sqrt{\left(1 - \frac{\omega_p^2}{\omega^2+\nu^2}\right)^2 + \left(\frac{\nu}{\omega}\frac{\omega_p^2}{\omega^2+\nu^2}\right)^2} - \left(1 - \frac{\omega_p^2}{\omega^2+\nu^2}\right)\right]^{1/2}$$

$$\nu = \frac{n_e}{(kT)^{3/2}}\frac{\overline{Z}\pi^{3/2}e^4}{m_e^{1/2}2^{5/2}\gamma(\overline{Z})}\ln(\Lambda)$$

$$\gamma(\overline{Z}) \sim \frac{\overline{Z}n_e}{kT}\ln\left(\frac{kT\rho_\omega}{\overline{Z}e^2}\right)$$

Figure 4. Basic equations used in the equilibrium plasma calculation. Altogether 13 stages of ionization of aluminum atom are included for a given set of plasma pressure and temperature values. The Saha equations are parameterized using the electron pressure p_e as floating parameter and solved iteratively for the degrees of ionization $_{i.}$ Q_i denotes the electronic partition function of *i*th ion. The cutoff of the sum over states is found by calculating the lowering of ionization potential according to the Debye model, while any impending breakdown of Debye length $_D$ due to nonideality in the plasma is checked for against the screening radius r_s. The self -absorption coefficient *k* is calculated to obtain the luminosity over the detector's spectral response and to track the energy loss by radiation as function of frequency . is Spitzer's correction factor.[11,12] , Z, k and T are the collision frequency, ion charge number, Boltzmann constant and the plasma temperature, respectively. is the nonideality parameter given by the ratio of mean Coulomb energy at mean interparticle distance to k_B T and the Coulomb length.

scaling exponents and scaling constants, which are globally applicable to the entire system of data are: $\alpha = 0.45 \pm 0.03$, $\beta = 1.0 \pm 0.03$, $S_T = 0.190 \pm 0.003$ and $S_p = 340 \pm 5$. The resulting optimization shows evidence for significant modifications to the plasma absorption coefficient through revisions to the collision frequency, whereas only modest corrections to the Debye model of ionization potential lowering are indicated thus far.[2,7]

B. Interfacial instability in neutral gas confinement of dense LPP plumes

In an attempt to gain even higher plasma density, another study of neutral gas confinement of the LPP plume had been undertaken. The confinement was noticeably effective at modest gas pressures of helium or argon. When the pressure was raised beyond about ten atmospheres at room temperature, the LPP plume became less and less reproducible in the evolution of its shape and luminosity and the attenuation of the intensities of the probing laser beams through the plume. A full-scale investigation of the instability has established that the neutral gas confinement precipitates the interfacial instability of the Rayleigh-Taylor nature.[3,4,13] We summarize the primary findings and a new diagnostic method developed for study of such unstable non-axisymmetric plasmas.

In the presence of the interfacial instability, the structure of the LPP plume, as presented in plasma continuum emission intensity, is no longer symmetric about the laser beam axis. This renders the Abel inversion algorithm unworkable as a tool for inverting the 1-D plasma luminosity profile seen from the side into the 2-D cross-sectional profile of the plasma's specific continuum intensity. We have subsequently developed another modified inversion algorithm, which is applicable to non-axisymmetric plasma plumes. The new method consists of taking two mutually orthogonal side views of plasma luminosity at a fixed distance from the target by means of streak photography. The two side views are insufficient for unique reconstruction of the 2-D plasma profile. To overcome this limitation, a snapshot image of the front view of the plume is also taken at the start. Fig. 5 shows four sets of such measurements, one each at the neutral gas pressure of 1, 10, 20 and 50 atmospheres at room temperature. This approach is different from the Cormack-Hounsefield algorithm in medical x-ray imaging, where many side views are taken in a scan, but is equally effective.[14]

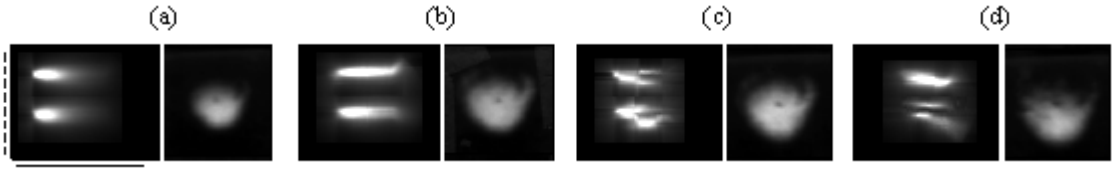

Figure 5. A set of two side-view streaks at 0.5 mm from the target surface (left) and a front-view photograph (right) is shown for four different LPP plumes, one each from an aluminum target placed in argon at: (a) 1 atm; (b) 10 atm; (c) 20 atm; and (d) 50 atm. The laser pulse energy is fixed at 2.5 J. The solid horizontal line at the bottom on the left hand side corresponds to 1 μs along the time axis while the broken vertical line indicates 14.6 mm in width in each of the two mutually orthogonal directions on the target plane.

The basic sequence of the algorithm is summarized in Fig. 6. The new inversion algorithm reconstructs the 2-D cross-sectional section of the LPP plume at a given time iteratively by proposing a trial profile and correcting it according to the two side view luminosity profiles. The front view image is used as a 2-D weighting factor to be multiplied into the error signals constructed from the difference between the calculated side-view profiles and the measured ones. The final reconstructed 2-D profile at one time is used as the weighting factor for the next time step. This is continued for the entire life of the plume.

Fig. 7 gives a summary of the data for the LPP plumes from an aluminum target immersed in argon at four different pressures. For each run, two mutually orthogonal side-views streaks are recorded. With increasing argon density, the run to run variation

1. ***Organize the two streak images into two time-resolved mutually orthogonal luminosity profiles, $L_{side}(i; t)$ and $L_{top}(j; t)$.***
2. ***Construct a 2-D array of weighting factors from front-view snap shot:***

$$W_2(i,j;t) = \frac{W_{front}(i,j;t)}{\sum_i W_{front}(i,j;t)}$$

$$W_1(i,j;t) = \frac{W_{front}(i,j;t)}{\sum_j W_{front}(i,j;t)}$$

3. ***Select an initial trial 2-D continuum intensity profile at time t, $I_{plasma}(i,j;t)$.***
4. ***Calculate temporary luminosity profiles:***

$$\mathrm{temp}L_{side}(i;t) = \sum_j I_{plasma}(i,j;t)$$

$$\mathrm{temp}L_{top}(j;t) = \sum_i I_{plasma}(i,j;t)$$

5. ***Calculate a revised 2-D continuum intensity profile:***

$$I_{plasma}(i,j;t) = I_{plasma}(i,j;t) - [\mathrm{temp}L_{top}(j;t) - L_{top}(j;t)]\, W_2(i,j;t)$$

$$I_{plasma}(i,j;t) = I_{plasma}(i,j;t) - [\mathrm{temp}L_{side}(i;t) - L_{side}(i;t)]\, W_1(i,j;t)$$

6. ***Calculate an rms error from the temporary and measured luminosity profiles:***

$$RMS = \sqrt{\frac{\sum_j [\mathrm{temp}L_{top}(j;t) - L_{top}(j;t)]^2 + \sum_i [\mathrm{temp}L_{side}(i;t) - L_{side}(i;t)]^2}{M_{max} + N_{max}}}$$

7. ***Repeat the sequence from 3 to 6 until rms error is minimized.***
8. ***Calculate new weighting factors using $I_{plasma}(i,j;t)$ for next time step.***
9. ***Repeat the sequence 3 to 8 until the end of the luminosity streak***

Figure 6. The basic sequence of the inversion algorithm for reconstruction of non-axisymmetric 3-D LPP plumes from two-mutually orthogonal side-view luminosity streaks and a front-view snapshot image.

in each set of streaks and image grows larger. At the same time, the intensity of the laser beam transmitted through a pinhole in the target exhibits increasingly larger fluctuations.

In Fig. 8 the reconstructed 2-D profiles of specific continuum intensities of aluminum LPP plumes in argon are shown for seven selected times. The two constant intensity contours, one at 50% and another at 20% of the local maximum intensity in one atmosphere argon, grow larger but remain approximately axisymmetric as the time advances. At higher pressures, the contours exhibit increasingly larger distortions with increasing time. It also shows that evolution of the intensity contours is increasingly less reproducible from one run to the next. These trends have been quantified by first carrying out a 2-D Fourier decomposition of the reconstructed specific intensity profiles and analyzing the run-to-run variations in the mode amplitudes. The rms values of such mode amplitude variations, computed from a set of eight runs under identical condition, are plotted as a function of the wavenumber of the respective modes in Fig. 11. We find the rms values scale as the square root of the wavenumber, a well-established signature of Rayleigh-Taylor instability.[13] The wavenumber of rectangular modes is expressed by the geometric mean of the two wavenumbers associated with each rectangular mode.

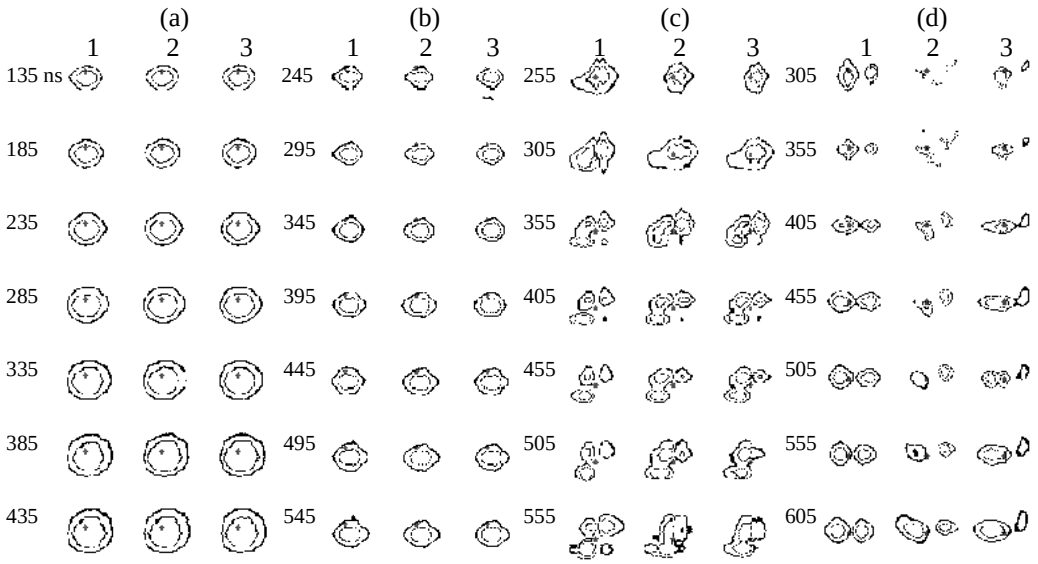

Figure 7. Evolution of the constant intensity contours of reconstructed 3-D LPP plume profiles at 50% and 20% of the local maximum is shown at 0.5 mm from the aluminum target surface, which is placed in argon at: (a) 1 atm; (b) 10 atm; (c) 20 atm; and (d) 50 atm. Each column of contours shows development of a single LPP plume at 50 ns intervals. The number above each column of contours corresponds to the repeat run number.

3. Polarization Spectroscopy of Neutral Gas Confined LPP Plumes

Our interest lies in taking images of the full LPP plumes by means of polarization-resolved emissions from the plasma, be a continuum or line emission, in order to elucidate further the nature of the interfacial structures such as those shown in Fig. 7. The continuum intensity variation in space signifies the existence of large gradients in plasma temperature and pressure, which in turn will drive the plasma flows

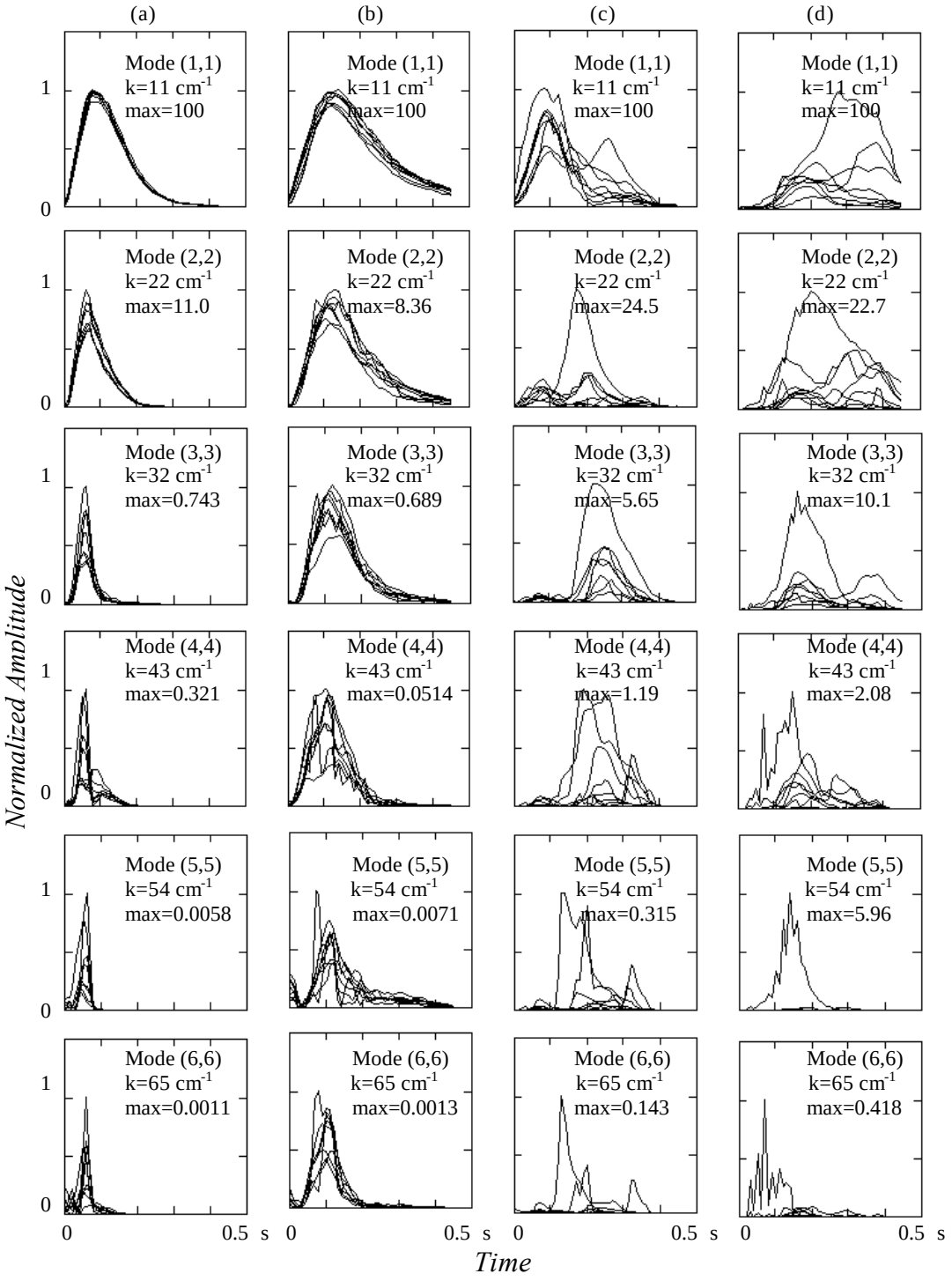

Figure 8. The normalized power amplitudes of 6 selected single modes as a function of time for aluminum plasmas produced in argon at four different pressures: a) 1 atm; b) 10 atm; c) 20 atm; and d) 50 atm. At each pressure, eight LPP plume shots under identical incident power laser conditions have been analyzed. k is the wavenumber of the single mode indicated by the mode number (n,n), where n = 1 to 6. The zero of the time axis corresponds to the plasma onset time, t_{onset} = 36nsec. The maximal value within each group of eight laser shots are normalized with respect to the average maximal value of mode (1,1) set at 100.

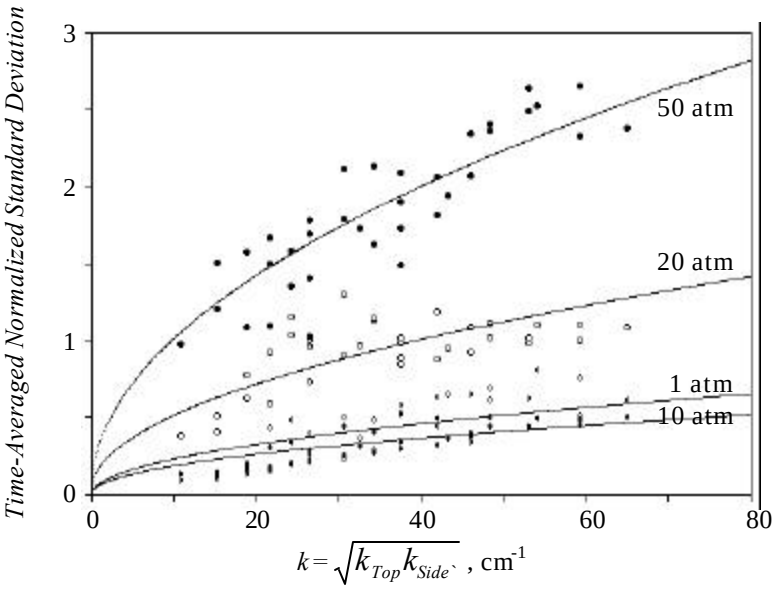

Figure 9. The standard deviation, normalized by the mean and then averaged over time from t_{onset}+20nsec to t_{onset}+120nsec, is plotted against wavenumber. The wavenumber used is the geometric mean of the two wavenumber of each 2-D mode, i.e., $k=(k_{Top}k_{Side})^{0.5}$. Results include 39 lowest-order single modes, from (1,1) to (6,6). The solid line is the best fit to the data points according to $y \sim k^{0.5}$.

of complex topology. We anticipate separation of charges throughout the plasma plume, and polarization-resolved imaging will help visualize development of such structures.

The feasibility experiment makes use of an experimental arrangement, shown in Fig. 10. The vacuum chamber contains an aluminum target mounted on an electrically floating stage. The emissions from the LPP plume can be detected and analyzed either

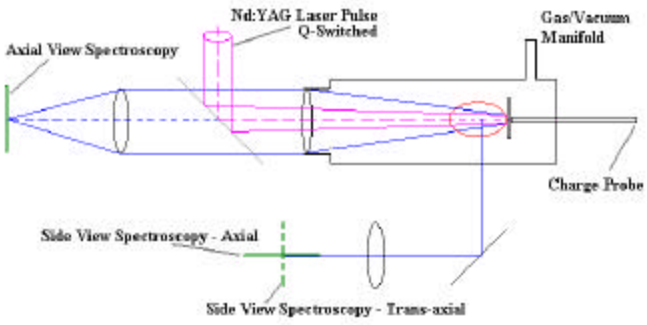

Figure 10. Schematic diagram of the experimental setup used for polarization spectroscopy. Three different orientations of the spectrograph's entrance slit are used to probe the local electric field and particle velocity. The electric potential, to which the target has been driven, is measured by a means of a 10x probe and a potential divider.

across the cross-section of the LPP plume by looking down on the target through the laser beam focusing lens or from the side through the side wall of fused quartz. We will refer to the first view as an axial view and the latter as a side view. The full uv to near ir spectral range is accessible for both views. The ambient neutral gas density remains

much lower, in the range from high vacuum to one atmosphere at room temperature, than in the case of high density LPP plume runs. Argon is used as the confining gas.

There are basically three measurement configurations. The plasma plume is imaged onto the entrance slit of a spectrograph either for an axial view of the plasma or a side view. In the arrangement of an axial view of the plasma, the center of the plume's image is positioned in the middle of the slit. One half of the slit is covered with an analyzer with its polarization axis parallel to the slit, and the second half is covered with another analyzer with its axis perpendicular to the slit. The central portion of the slit between the two analyzers is blocked from the LPP plume emissions. Given that at these neutral gas densities the LPP plume retains the axial symmetry, the polarization property of the plume's emission are measured at once both wavelength and radial position-resolved.

The side view arrangement entails placing the image of the LPP plume on the slit plane with the plasma axis aligned either parallel or perpendicular to the slit. The first of these alignments is referred to as an axial side view, and the latter as a trans-axial side view. In the trans-axial side view, the axial symmetry of the plasma plume can be exploited: two analyzers can be placed on the slit in two mutually orthogonal directions. In the trans-axial arrangement, the analyzer can be alternated from an alignment with its axis parallel to the slit to another that it orthogonal to it. All three configurations for polarization-resolved imaging are indicated schematically in Fig. 10.

Figure 11 shows the time-resolved target potentials due to charge separation in the expanding LPP plumes. Altogether eleven different argon pressures are indicated. Using

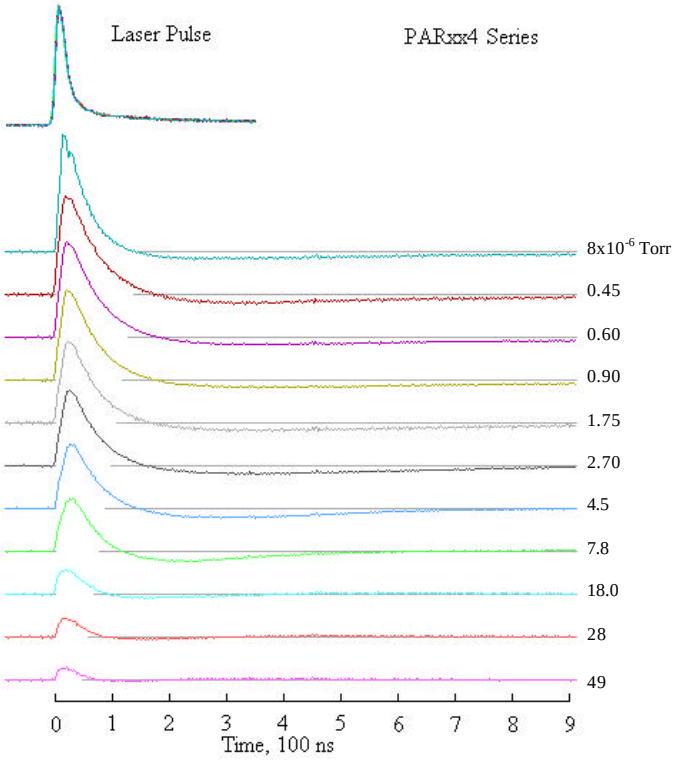

Figure 11. Measured time-resolved target potential as resulting from charge separation within the expanding laser-produced plasma plume from an aluminum target. The target is placed inside the vacuum chamber, which is filled with argon to varying pressures. The conducting target holder is electrically insulated from ground and connected to a potential divider. Its potential is measured by using a 10x probe. The intensity profile of each laser pulse used to generate the plasma is plotted at the top, one above the other.

the common time base the laser intensity is shown as function of time for these runs. They overlap closely, indicative the reproducibility of the laser pulse. The scale of the potential is common to all runs, and the peak value of the potential reaches 14.7 kV.

Fig. 12 shows a set of axial-view measurements for the LPP plume in 4.5 Torr argon. The polarization-resolved spectrum is taken using a gated intensified CCD detector placed at the exit plane of the spectrograph. It represents 400 ns integration starting at 300 ns from the onset of the laser pulse indent on the aluminum target. The

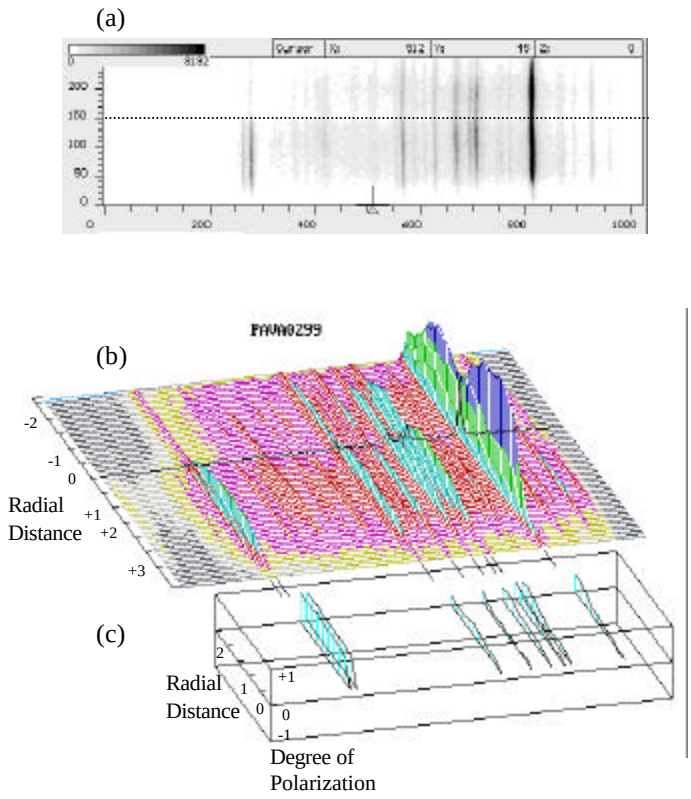

Figure 12. Polarization and radial position-resolved axial-view spectrum of the laser-produced plasma plumes from an aluminum target. The target vacuum chamber is filled with argon to 4.5 Torr. See the caption of Fig. 10 for more details. The spectrum (a) shows the spectrum, which is displayed as function of radial position, in spatial resolution of 0.025 mm per vertical pixel. Two mutually orthogonal polarization components are obtained simultaneously, the upper part being parallel to the radial direction and the lower part perpendicular to the first. The wavelength is shown in pixels, which runs from 0 (389.5 nm) to 1023 (447.3 nm). The intensity scans (b) run as function of wavelength at each radial position. The dark line in the middle indicates the plume's center. The line intensities for the two polarization directions are used to evaluate the degree of polarization at each radial position. The results are shown in (c) for eight emission lines. The short solid lines identify the line positions in the spectrum of (b).

dotted line in the middle of Fig. 12a makes the center of the plume and the boundary between the two mutually orthogonal polarization analyzers. The wavelength-resolved emission intensity is shown at different radial distances from the plume's axis in Fig. 12b. The dark line running in the middle shows the demarcation for the two polarization directions. Fig. 12c shows the degree of polarization computed from the spectral intensity data of Fig. 12b for a selected group of emission lines. The degree of polarization is shown as function of radial distance from the plume's axis. The positive value means that the line is polarized preferentially in the radial direction. The results show a dependence of the degree of polarization on the wavelength of the emission lines as well as on the radial position from which the plasma emissions emanate.

Fig. 13 compares the two polarization-resolved spectra from the axial-view imaging of the LPP plume at two different argon pressures, 48 Torr (a) and 4.5 Torr (b),

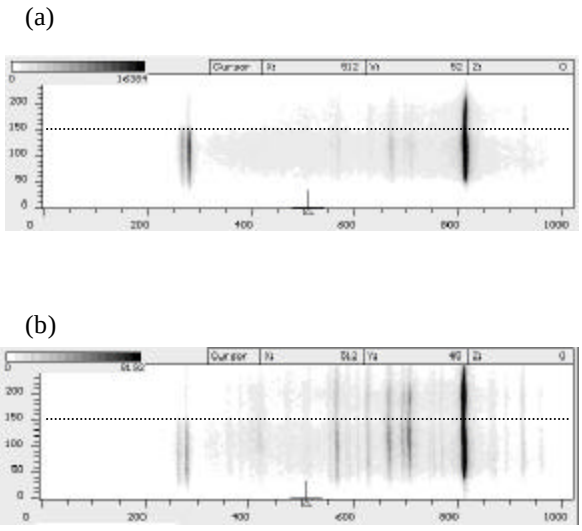

Figure 13. Polarization and radial position-resolved axial-view spectrum of the laser-produced plasma plumes from an aluminum target. The target vacuum chamber is filled with argon to two different pressures: a) 48 Torr and b) 4.5 Torr. The LPP plume is viewed from the direction of the incident laser beam and is imaged onto the entrance slit of the spectrograph such that the slit cuts through the center of the plume. The dotted lines indicate the plume's center, which divides one polarization analyzer parallel to the slit (bottom) from another perpendicular to it (top). The emissions from the plume's core have been blocked at the slit. The vertical axis indicates the radial distance from the plasma axis, given in detector pixels at resolution of 0.025 mm per pixel. The wavelength axis is displayed horizontally in detector pixel addresses running from 0 (387.4 nm) to 1023 (477.4 nm).

respectively. They show a significant density dependence of the degree of polarization. Also careful inspection of the individual spectral lines as function of the radial distance from the plume's axis shows that the line centers are blue shifted by amounts that are both wavelength and radial position dependent.

A sampler of the side-view polarization spectroscopy of the LPP plumes, on the other hand, is given in Fig. 14 for two different neutral gas densities, one at 4.5 Torr and another at 48 Torr. Here one can surmise that the preferred polarization axis is trans-

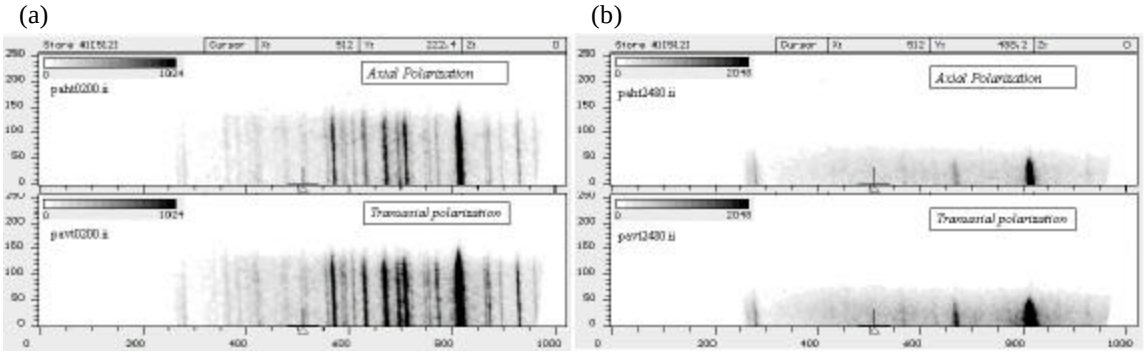

Figure 14. Polarization and axial position-resolved side-view spectrum of laser produced plasma emissions. The aluminum target is placed in the vacuum chamber filled with argon to two different pressures: a) 2.5 Torr and b) 48 Torr. The side view of the plume is imaged with its axis parallel to the entrance slit of the spectrograph. The upper frames show spectra taken with the polarization analyzer aligned along the plasma axis ('axial polarization'), while the lower frames correspond to the analyzer aligned normal to the plasma axis ('trans-axial polarization'). The vertical axis indicates the distance along the plasma axis, given in detector pixels at resolution of 0.050 mm per pixel. The aluminum target is located 4 mm below the bottom in each frame. The wavelength axis is displayed horizontally in detector pixel addresses running from 0 (387.4 nm) to 1023 (477.4 nm).

axial, i.e., perpendicular to the plasma axis or in the radial direction at each given axial position within the plume. It also demonstrates strong blue Doppler shifts, growing larger with increasing axial distance from the target, whose plane is located below the bottom edge of the spectrogram.

The neutral gas density dependence of the degree of polarization is summarized in Fig. 15 for three emission lines, one each from the neutral atoms, singly ionized ions and doubly ionized ions of aluminum, respectively. Fig. 16 shows a summary of the corresponding dependence of the Doppler shifts on the neutral gas density and the originating species and emission line wavelength. The three emission lines are chosen to

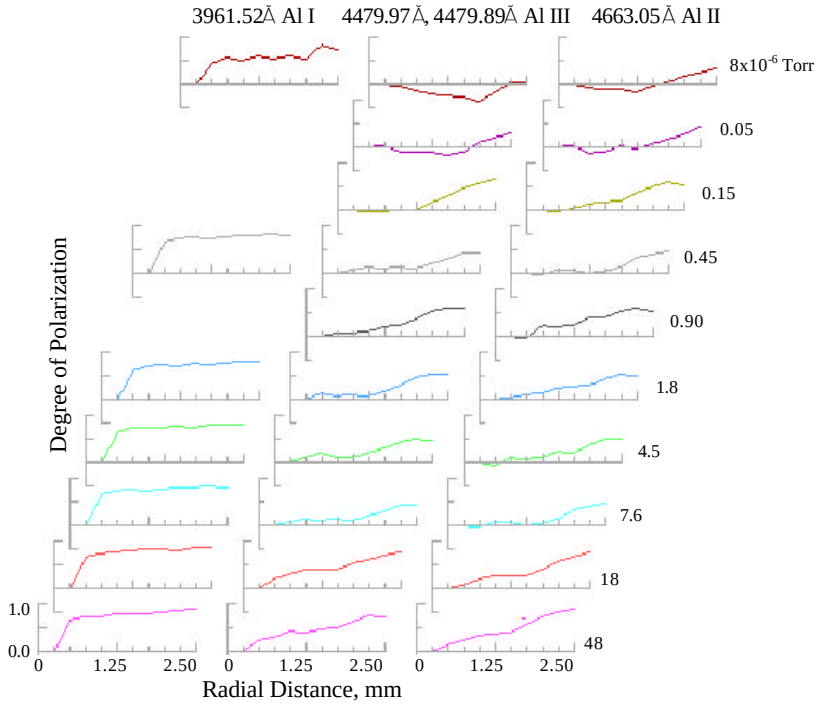

Figure 15. Radial position resolved degree of polarization for three emission lines of laser-produced aluminum plasma. The neutral gas pressure is varied from high vacuum to 48 Torr, as shown on the right-hand side. The lines are selected from the neutral (3961.52Å Al I), singly ionized (4663.05Å Al II) and doubly ionized aluminum (4479.97Å, 4479.89Å Al III).

in order to probe different aspects of charge separation. The emission lines at 3961.52Å Al I, 4663.05Å Al II and 4479.97Å, 4479.89Å Al III belong to the multiplets, $^2P^o$-^2D of the neutral aluminum atom, ^1D-$^1P^o$ of the singly ionized aluminum ion and $^2P^o$-^2D of the doubly ionized aluminum ion, respectively.

4. Analysis and Discussion

The results of the axial view spectroscopy indicate that the emission lines are significantly polarized with the plane of polarization predominantly in the radial direction, while the degree of polarization grows larger with the radial distance. The

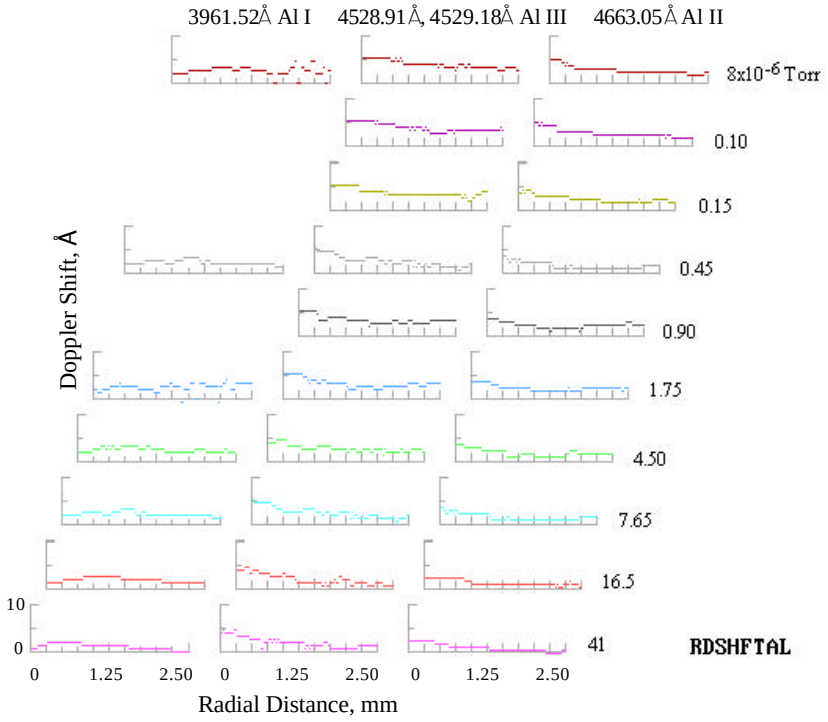

Figure 16. Radial position resolved Doppler shifts for three emission lines of laser-produced aluminum plasma. The neutral gas pressure is varied from high vacuum to 41 Torr, as shown on the right-hand side. The lines are selected from the neutral (3961.52Å Al I), singly ionized (4663.05Å Al II)and doubly ionized aluminum (4479.97Å, 4479.89Å Al III).

Doppler shifts tend to be greater for doubly ionized ions than for the singly ionized ions. The side view spectroscopy indicates that the emission lines are polarized preferentially in the trans-axial direction but with smaller degrees of polarization. The Doppler blue shifts grow larger as one moves away from the aluminum target surface, which suggests that the electrostatic acceleration of charged species takes place near the periphery of the plasma plume. This is consistent with the view that the charge separation takes place in the expanding front of the plume where steep density gradients exist. A domed plasma pillar is covered with a sheath of positive charges while a negative charge layer of electrons expands away rapidly. The region of charge separation is lower in plasma density, and the line emissions dominate the plasma spectrum. At the same time the strong electric fields propel charged species and the electric dipole moments become aligned with the field despite considerable thermal fluctuation. Our earlier studies, we have determined that the core temperature of the comparable LPP plumes reaches 50 eV at the peak. This translates to a temperature in the range of 10 eV in the outer layers of the plasma where charge separation takes place.

The question is how the dipole moments of the neutral aluminum atoms remain so well aligned radially and their line emissions exhibit such strong Doppler blue shifts. It has been suggested that the line emissions from the neutral atoms result from recombination of the singly ionized species.[15] This bodes well with the fact that at the

peak of the LPP plume the aluminum ions are three to ten fold ionized across the core of the plasma plume.[2]

The fact that the side-view spectroscopy (see Fig. 14) indicates significant levels of trans-axial polarization is a puzzle at first sight. The emitting species whose dipole moments are aligned radially would show little polarization when viewed from the side. The explanation may be found in the fact that due to the finite size of the imaging optics the plume's image on the slit plane contains plasma emissions in directions other than the direct line of sight. The measured polarization reflects the polarized emissions from the part of the plasma, which is off the line of sight but still within the finite-size solid angle of acceptance of the spectrograph. Fig. 17 shows a sketch of the plasma particle movement and the alignment of the electric dipole moments of the radiating species that includes the above observations.

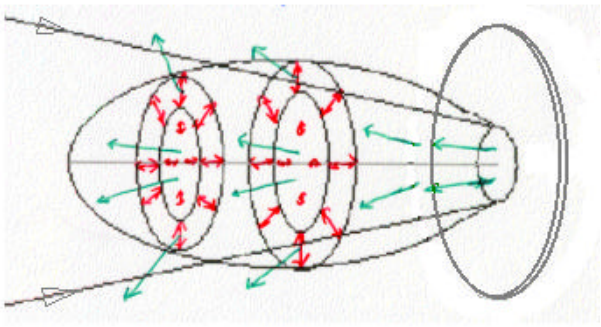

Figure 17. A sketch of the alignment of the electric dipole moments (double headed arrows) of radiating neutral and ionized aluminum atoms with the local electric field and the directions of motion (single headed arrows) of super-thermal radiating species. The two large hollow arrows on the left-hand side show the rays of the laser beam directed toward the aluminum target.

5. Summary and Conclusions

The observed Doppler shifts indicate that the energies of neutral aluminum atoms and singly and doubly ionized ions are in the range as large as 15 keV. This far exceeds the peak thermal energy of $k_B T = 50$ eV, suggesting that the species are driven electro-magnetically as well as gas-dynamically and thermally. The energy distribution function has an appearance of being bimodal due to the fact that plasma particles are driven spuriously by the electric field. Laser-produced plasmas from atomic clusters are reported to contain MeV-class species through a process known as Coulomb explosion, which results in charge separation.[16-18] Charge separation is sensitive to other physical processes involved in LPP plume generation, such as the detail of laser-matter interaction in terms of materials structure and transport properties.[20-22]

The dipole moments of the radiating species are by and large aligned radially. This is a direct consequence of the large electrostatic field resulting from the charge separation during the plume's expansion. The preponderance of the large observed degree of polarization suggests that $\mathbf{d} \cdot \mathbf{E} \gg k_B T$, according to the Langevin function, which gives the mean value of the dipole moment when an ensemble of atomic dipoles with moment **d** is in thermal equilibrium in the presence of an applied electric field **E**. The distribution of the electric field in magnitude and direction, however, will have to

await a full reconstruction of the 3-D plasma structure by the algorithms presented earlier.

By the same token, plasma diagnosis by means of spectral line broadening does not illuminate beyond this point because the apparent emission line profiles are actually the results of line of sight integration through the plasma of strong nonuniformity. Full-scale reconstruction of the 3-D plasma structure is needed.

The presence of the neutral background gas confines the plasma plume. The size and shape varies as strong functions of gas pressure at a given moment of the plasma evolution, while strongly influencing the persistence of the electrostatic field due to charge separation. It appears highly likely that the interfacial instability in strongly neutral gas confined LPP plumes imposes complex electric fields near the interface. The robustness of the polarization of emission lines adds to the confidence that plasma polarization spectroscopy can be further developed as a useful diagnostic tool for analysis of a precipitation of the interfacial instability and the ensuing development of 3-D plasma structure.

J.-C. Oh and C.D. Lloyd-Knight contributed significantly in the development of the two diagnostic methods applicable to a large class of weakly nonideal and non-axisymmetric plasmas. Financial support of the work by the CTU 5-2 Consortium for Laser Produced Plasmas and Lehigh University is acknowledged

References

[1] Y.W. Kim and C. Lloyd-Knight, "Continuum-Based Diagnostics of Weakly Nonideal Laser-Produced Plasmas," *Rev. Sci. Instr.* **72**, 944 (2001).
[2] C.D. Lloyd-Knight, "Experimental Investigation of the Effects of Plasma Nonideality on Ionization Potential Lowering and Plasma Absorption," Ph.D. dissertation, Lehigh University (2000).
[3] Y.W. Kim and J.-C. Oh, "Reconstruction of Time-Resolved Continuum Intensity Profile of Non-axisymmetric Laser-Produced Plasma," *Rev. Sci. Instr.* **72**, 948 (2001).
[4] J.-C. Oh, "Interfacial Instability in Dense Neutral Gas Confinement of Laser-Produced Plasmas," Ph.D. dissertation, Lehigh University (1999).
[5] R.B. Mohanti and J.G. Gilligan, "Electrical Conductivity and Thermodynamic Functions of Weakly Nonideal Plasma," *J. Appl. Phys.* **68**, 504 (1990).
[6] B.V. Zelener, G.E. Norman and V.S. Filinov, "Statistical Theory of a Nonideal Plasma," *Soviet Physics High Temperature* **10**, 1160 (1972).
[7] Y.W. Kim and C.D. Lloyd-Knight, "New Estimates for Absorption Coefficients in Weakly Nonideal Laser-Produced Plasmas," 42nd Annual DPP/ICPP Meeting, Quebec, October 23-27,2000, *Bull. Am. Phys. Soc.* **45**, 299 (2000).
[8] Y.W. Kim, "Fundamentals of Analysis of Solids by Laser Produced Plasmas," in *Laser-Induced Plasmas and Applications*, L.J. Radziemski and D.A. Cremers, eds. (Marcell Dekker, New York 1989). Chapter 8.
[9] Y.W. Kim, "Composition Determination at High Temperatures by Laser Produced Plasma Analysis," *High Temp. Sci.* **26**, 57-70 (1990).
[10] Y.W. Kim, K.-S. Lyu and J.C. Kralik, "Shock Formation in a Laser Produced Plasma," in *Current Topics in Shock Waves*, Y.W. Kim, ed. (American Institute of Physics, 1990). p.353.
[11] L. Spitzer, Jr. and R. Haerm, "Transport Phenomena in a Completely Ionized Gas," *Phys. Rev.* **89**, 977 (1953).
[12] H. Hora, *Physics of Laser Driven Plasmas*, Wiley, New York (1981).

[13] H.J. Kuhl, "Theory of the Rayleigh-Taylor Instability," *Physics Reports* **206**, 197 (1991).
[14] H.H. Burrett and W. Swindell, *Radiological Imaging*, Vol. 1 and 2, Academic Press, New York (1981).
[15] D.P. Kilcrease, unpublished comment (2001).
[16] C. Brechignac and J.P. Connerade, "Giant resonances in free atoms and in clusters," *J. Phys. B: At. Mol. Opt. Phys.* **27**, 3795 (1994).
[17] T. Ditmire, T. Donnelly, A.M. Rubenchick, R.W. Falcone and M.D. Perry, "Interaction of intense laser pulses with atomic clusters," *Phys. Rev.* **A53**, 3379 (1996).
[18] M. Lesius, S. Dobosz, D. Normand and M. Schmidt, "Explosion Dynamics of Rare Gas Clusters in Strong Laser Fields," *Phys. Rev. Lett.* **80**, 261 (1998).
[19] H.S. Robertson, *Statistical Thermophysics*, Prentice Hall, Englewood, NJ (1992).
[20] Y.W. Kim, "Thermal Diffusivity Measurement at High Temperatures by Laser-Produced Plasmas," in *Thermal Conductivity **25**/Thermal Expansion **13***, C. Uher and D. Morelli, eds., (Technomic Publishing, Lancaster, PA, 2000). p. 15.
[21] Y.W. Kim, "Depth-Resolved Surface Thermophysical Property Measurement by Laser-Produced Plasmas," Int. J. Thermophysics **20**, 1313-1323 (1999).
[22] Y.W. Kim, "Effects of Surface Morphology and Composition Modification on the Depth Dependence of Thermal Diffusivity at High Temperatures," *Int. J. Thermophys.*(in press).

Polarized X-ray satellite line emission in non-equilibrium transient Si plasmas

Peter Hakel and Roberto C. Mancini
Department of Physics, University of Nevada, Reno, USA

Jean-Claude Gauthier
Laboratoire pour l'Utilisation des Lasers Intenses, Palaiseau, France

Emilio Mínguez
Instituto de Fusión Nuclear, Universidad Politécnica de Madrid, Spain

Jacques Dubau and Marguerite Cornille
Observatoire de Paris, Meudon, France

Abstract

We have performed model calculations aimed at studying the formation and properties of polarized X-ray line emissions from Si plasmas driven by high-intensity (10^{16} – 10^{18} W/cm^2), ultrashort-duration (300 fs) laser pulses. Our focus is on the He-like Si 2l 2l' → 1s 2l satellite transitions of the Ly-α line. The calculated polarization effect is due to an anisotropic component in the electron distribution. Time histories of line intensities and polarization degrees were obtained from magnetic sublevel populations computed by the time-dependent collisional-radiative atomic kinetics code POLAR. This model and code is the final step in the employed suite of codes that model laser-target interaction using hydrodynamics, electron kinetics, and atomic kinetics simulations. The degree of polarization is due to the competition between several atomic processes that drive alignment creation, transfer, and destruction. We identify lines that can be used as polarization markers of plasma anisotropy as well as the main channels responsible for the creation of alignment in magnetic sublevels.

Introduction

Line polarization can arise in plasmas that exhibit some type of anisotropy. A special spatial direction can, for example, be defined by an external electric or magnetic field. In our studies we consider the anisotropy caused by a non-thermal, directional component in the distribution of plasma electrons. Such "hot electrons" are known to be produced in experiments where a solid target is irradiated by a high-intensity, short-duration (subpicosecond) laser pulse [1,2]. These electrons then drive atomic processes that can create alignment, i.e. unequal population distribution of magnetic sublevels within a given fine structure atomic level. Radiative decay of aligned levels results in emission of partially polarized electromagnetic radiation. Therefore polarization characteristics of line emissions are indicative of plasma anisotropy.

Model and code POLAR

POLAR is a time-dependent, collisional-radiative magnetic-sublevel atomic kinetics model and code. It evaluates rates of atomic processes (both spontaneous as well as driven by electron-ion collisions) based on plasma conditions and then computes magnetic-sublevel populations and line intensities arising from the mutual interplay of these processes. The main characteristic that sets POLAR apart from other models is that it is applied in the context of anisotropic plasmas and its goal is the calculation of polarization properties of line emissions. In turn, this polarization effect can be used to characterize plasma anisotropy. This requires the magnetic-sublevel level of description of the atomic energy level structure and similarly determines the nature of other atomic data (such as cross sections) needed for the model. The second hallmark of POLAR is its

automatic treatment of multi-level (cascade) effects in the sublevel population kinetics. This is a step beyond previous theoretical work regarding line polarization that has been done within the scope of "two-level" models. In these types of models only the two energy levels involved in the transition are considered and possible cascade effects on the populations of upper magnetic sublevels from other states require special treatment (such as the use of effective excitation rates [3]). While this approach has been successful in low-density, atomic-spectroscopy-type experimental situations [4-6], in the context of dense plasmas it is necessary to address the complex multi-level and multi-atomic-process nature of level-population kinetics in a different way. To this end we combined the calculation of polarization properties of line emissions with the need of systematic treatment of multi-level (cascade) effects on sublevel population. This we accomplished by building a time-dependent collisional-radiative, magnetic-sublevel atomic kinetics model and code POLAR.

In our model the normal to the target surface defines also the axes of symmetry and quantization in the problem. Non-thermal electrons are assumed to be moving along this direction and the line of sight is perpendicular to it. The ultimate results of POLAR calculations are polarization-dependent total line intensities $I_{\parallel}$ and $I_{\perp}$ (the parallel and perpendicular directions of linear polarization are also relative to the axis of symmetry). In terms of these intensities, the degree of polarization defined as,

$$P = \frac{I_{\parallel} - I_{\perp}}{I_{\parallel} + I_{\perp}} \tag{1}$$

can then be calculated. Intensities $I_{\parallel}$ and $I_{\perp}$ are calculated for line transitions between fine-structure energy levels, that are formed as an incoherent superposition of all possible transitions between magnetic sublevels of the two energy levels. The resulting line

emissions have the same energy due to degeneracy with respect to the magnetic quantum number and are linearly polarized because of the conservation of angular momentum [7,8]. Sublevel populations in isotropic plasmas are evenly distributed within each fine-structure level, thus line emissions contain both polarization states with equal intensities, which leads to P=0. The polarization effect can appear in anisotropic plasmas as a consequence of sublevel population imbalance favoring emission of photons of one polarization state over the other. Under axial symmetry only the diagonal elements of ion density matrix are non-zero [2]. These are the magnetic sublevel populations and their calculation is therefore of central importance in modeling of polarized line emissions. The effect of hyperfine interaction on the polarization does not need to be considered in this case, since the most abundant Si isotope lacks nuclear magnetic moment.

POLAR sets up and numerically integrates the set of rate equations,

$$\frac{d\vec{g}}{dt} = A\vec{g} + \vec{b} \tag{2}$$

where $\vec{g}$ are the fractional populations of magnetic sublevels formed by the 2l 2l' configurations containing upper levels of the spectral lines of interest (satellites of Ly-α, see Table 1). The matrix A consists of rates of processes linking these sublevels to one another as well as their total depopulation rates. The vector $\vec{b}$ represents processes originating from the ground states of the He-like (collisional excitation) and H-like (electron capture) ions. The populations of these two ground states are extracted from the ionization balance calculation ($\vec{f}$ from M3R) that considers all Si ionization stages starting from Ne-like through the fully-stripped ion [9]. The chief source of atomic data for our kinetics models are the Los Alamos structure and collision codes CATS, ACE and

Level	Configuration	LSJ	Energy (eV)
1	$1s^2$	$^1S_0$	0.0
2	1s 2s	$^3S_1$	1840.2
3	1s 2p	$^3P_0$	1854.1
4	1s 2p	$^3P_1$	1854.5
5	1s 2s	$^1S_0$	1854.7
6	1s 2p	$^3P_2$	1855.4
7	1s 2p	$^1P_1$	1865.4
8	1s 3s	$^3S_1$	2176.8
9	1s 3p	$^3P_0$	2180.6
10	1s 3s	$^1S_0$	2180.7
11	1s 3p	$^3P_1$	2180.7
12	1s 3p	$^3P_2$	2181.0
13	1s 3d	$^3D_1$	2183.0
14	1s 3d	$^3D_2$	2183.0
15	1s 3d	$^3D_3$	2183.1
16	1s 3d	$^1D_2$	2183.2
17	1s 3p	$^1P_1$	2183.7
18	$2s^2$	$^1S_0$	3821.7
19	2s 2p	$^3P_0$	3824.6
20	2s 2p	$^3P_1$	3825.1
21	2s 2p	$^3P_2$	3826.3
22	$2p^2$	$^3P_0$	3837.2
23	$2p^2$	$^3P_1$	3837.8
24	$2p^2$	$^3P_2$	3838.8
25	$2p^2$	$^1D_2$	3845.7
26	2s 2p	$^1P_1$	3846.4
27	$2p^2$	$^1S_0$	3865.9

Table 1. POLAR energy level structure for He-like Si

"singlet" transitions
$2p^2\ ^1D_2 \rightarrow 1s\ 2p\ ^1P_1$
$2s\ 2p\ ^1P_1 \rightarrow 1s\ 2s\ ^1S_0$
"triplet" transitions
$2s\ 2p\ ^3P_{0,1,2} \rightarrow 1s\ 2s\ ^3S_1$
$2p^2\ ^3P_1 \rightarrow 1s\ 2p\ ^3P_{0,1,2}$

Table 2. He-like satellites of Ly-α

GIPPER [10], although our codes have the flexibility to accommodate atomic data of any other origin. Both POLAR and M3R codes take as input the time histories of the electron distribution characteristics calculated by the hydrodynamic code FILM [11] and the particle-in-cell (PIC) code EUTERPE [12], with α characterizing the fraction of non-thermal electrons. Model-calculations are performed in two steps. First, FILM, EUTERPE and M3R are used to compute time-dependent plasma environmental conditions and overall ionization balance for the magnetic-sublevel atomic kinetics model. Second, the code POLAR is used to calculate time-dependent collisional-radiative magnetic-sublevel atomic kinetics. These four codes thus form a suite that starts with the modeling of laser-target interaction and concludes with the calculation of polarization-dependent synthetic spectra (see Figure 1).

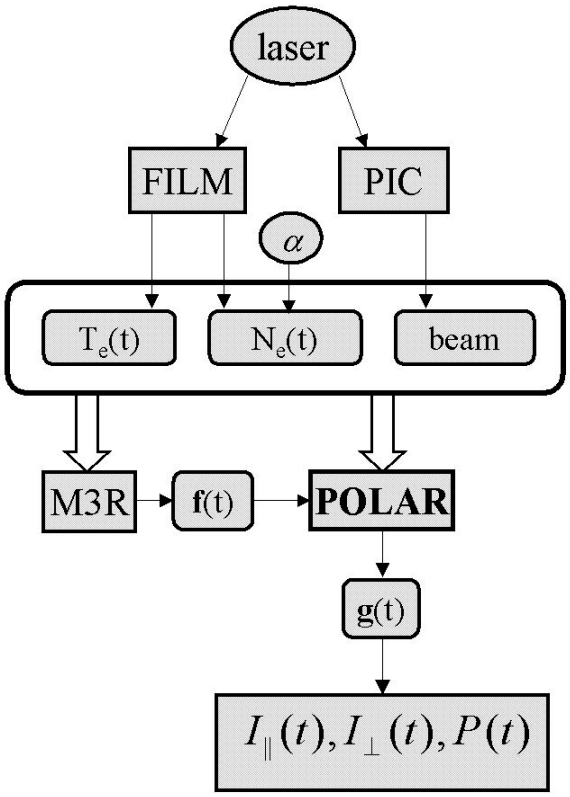

Figure 1. Suite of codes

Results

Figure 2 shows the time histories of polarization degrees P for the 2l 2l' → 1s 2l He-like Si satellites of Ly-α emitted from a fluid element within the skin-depth region of the Si target. The laser pulse has a Gaussian temporal profile with the peak at 400 fs and FWHM of 300 fs. The traces split into two groups (see Table 2): 1) two "singlet" transitions that develop significant polarization degree later in time (i.e. during the recombination of the plasma), and 2) "triplet" lines that remain essentially unpolarized. FILM hydrodynamic simulations indicate that the electron temperature qualitatively follows the laser pulse time-history (i.e. it peaks around 400 fs) and that electron number density drops below 10^{23} cm^{-3} rather early in time due to a rapid decompression. Thus, the depolarizing influence of thermal electrons is strongest early in time. On the other hand, PIC simulations show that the alignment-driving anisotropic (non-thermal) part of the electron distribution develops quickly and then remains essentially unchanged throughout the 1 ps time interval of interest. (We note that the PIC simulations used here are non-collisional and hence cannot account for the thermalization of non-thermal electrons.) It is the interplay between the atomic kinetics effects driven by these two groups of electrons that allows for polarization development only later in time.

The atomic process considered in POLAR can be classified in two groups: anisotropic and isotropic. Anisotropic atomic processes are driven by non-thermal (directional) electrons, and include collisional excitation (within He-like Si sublevels) and electron capture (from H-like Si ground state). These processes can create alignment. Isotropic atomic processes are either spontaneous or driven by thermal electrons and transfer or destroy alignment. These include spontaneous radiative decay

(within He-like Si sublevels), autoionization and electron capture (to and from H-like Si ground state), and collisional excitation and deexcitation (within He-like Si sublevels). In addition, collisional elastic scattering within the sublevels of a given fine structure level is also taken into account. We emphasize that within the context of this model the degree of polarization is due to the competition between anisotropic and isotropic atomic processes. This is important for polarization studies of laser-produced plasmas where, in general, different atomic processes can become important at different times.

In order to understand in more detail the main channels leading to the emergence of the polarization effect in the two singlet lines, we repeated the POLAR calculations including only a selection of energy levels defined in Table 1. Through the use of such "reduced models" we can "turn-off" the influence of selected atomic processes on the sublevel kinetics and assess their importance by comparing these simulation outcomes with the "full" result in Figure 2.

Figure 3 shows the time history of polarization degree for the $2s\,2p\ ^1P_1 \rightarrow 1s\,2s\ ^1S_0$ line calculated from a minimum model that includes only the He- and H-like Si ground states and the two levels forming the transition. The upper level is hence allowed to be fed only by three processes: 1) collisional excitation from the ground state of the He-like ion, 2) collisional excitation from $1s\,2s\ ^1S_0$, and 3) electron capture from the ground state of the H-like ion. The rates of all three processes consist of contributions due to thermal and non-thermal electrons. The application of this reduced model results in considerably smaller polarization values than in the full model. This is dramatically changed by the addition of the $1s\,2s\ ^3S_1$ level (Figure 4). The associated

inner-shell collisional excitation feeding channel is thus shown to be an important alignment-creating process for the 2s 2p $^1P_1$ level.

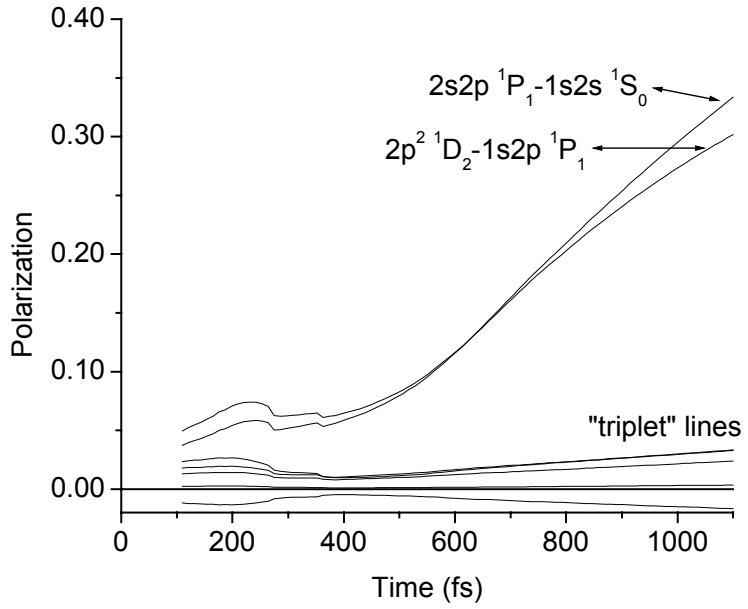

Figure 2. Laser intensity 5×10^{16} W/cm^2, α=0.2, "full model". The non-thermal electrons "turn on" at 100 fs.

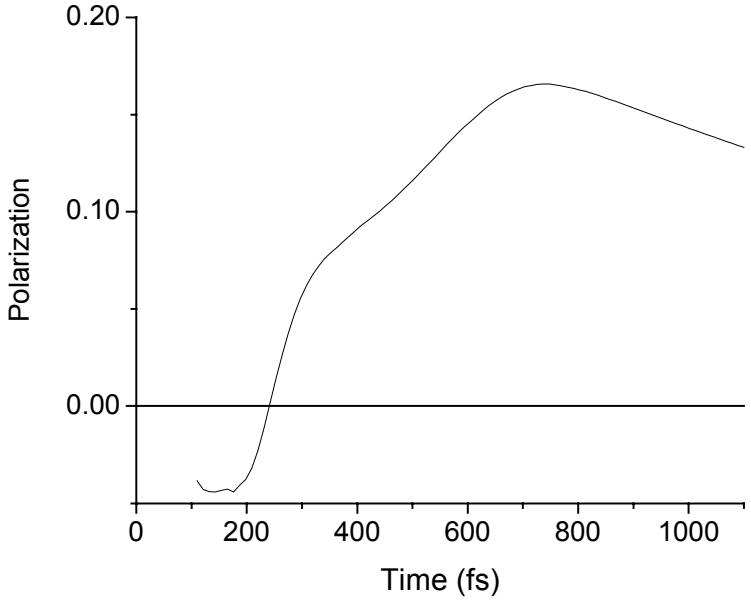

Figure 3. 2s 2p $^1P_1 \rightarrow$ 1s 2s $^1S_0$: reduced model: levels 1,5,26,H only (H represents the ground state of H-like Si)

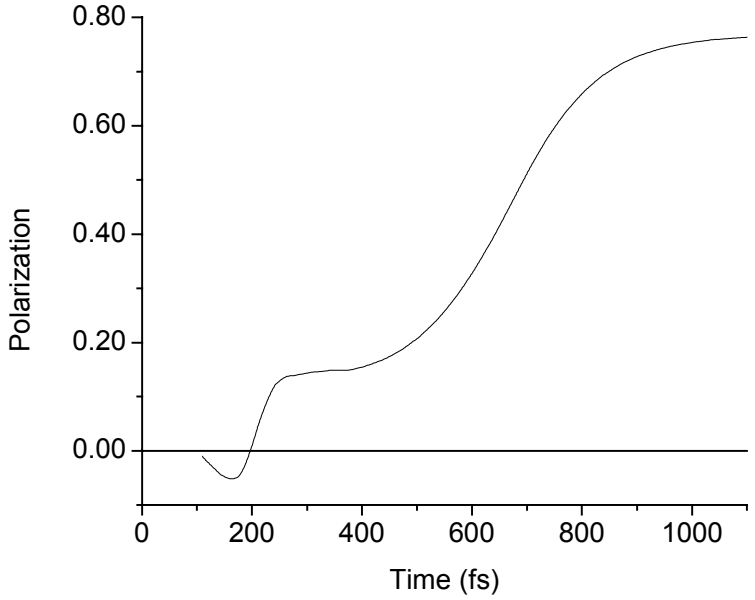

Figure 4. $2s\ 2p\ {}^1P_1 \rightarrow 1s\ 2s\ {}^1S_0$: reduced model: levels 1,2,5,26,H only

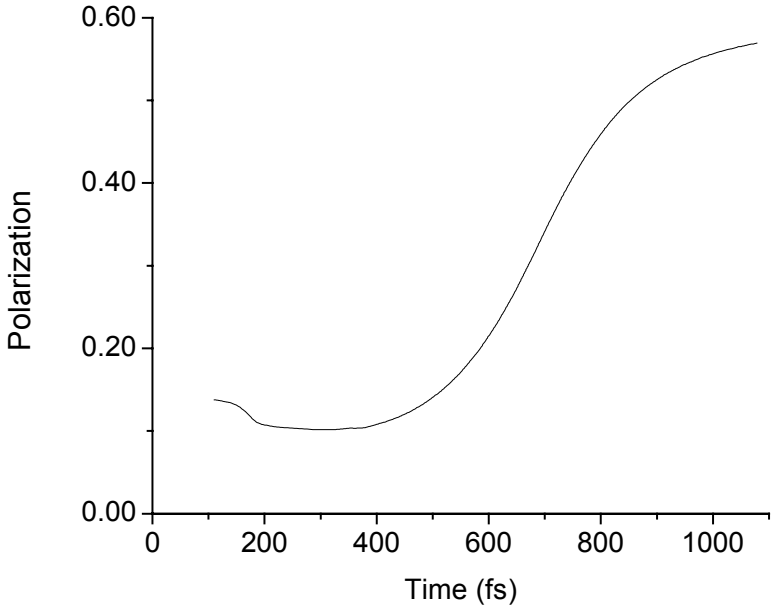

Figure 5. $2p^2\ {}^1D_2 \rightarrow 1s\ 2p\ {}^1P_1$: reduced model: levels 1,6,7,25,H only

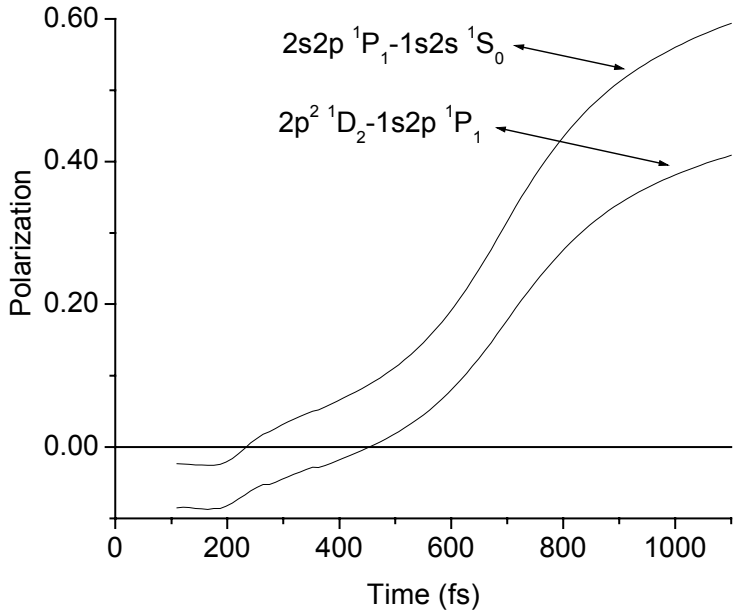

Figure 6. reduced model: levels 1,2,5,6,7,25,26,H only

Similarly we have constructed reduced models to study the other singlet transition, $2p^2\ ^1D_2 \rightarrow 1s\ 2p\ ^1P_1$. The result in Figure 5 is based on a model containing the two ground states, the two levels forming the transition, plus an additional level ($1s\ 2p\ ^3P_2$) from which an important inner-shell collisional excitation channel originates. Finally, a combination of the simpler models for the two singlet lines (Figure 6) yields an approximation to the full model result. In all these models, the inclusion of H-like ground state and the associated electron capture process significantly affects magnetic sublevel atomic kinetics. The $2p^2\ ^1D_2$ level has a strong autoionization/electron-capture connection to the H-like ground state, which can also indirectly influence populations of other autoionizing states [13]. Furthermore, this process (when driven by non-thermal electrons) is an important alignment-creating feeding channel for the 2l 2l' He-like states. This stems from selection rules based on angular momentum conservation that govern the accessibility of various magnetic sublevels through this process [14].

Conclusions

We have constructed a time-dependent, collisional-radiative model and code for the purpose of calculating the characteristics of polarized line emissions from laser produced plasmas. This is accomplished by calculating time histories of magnetic sublevel populations as the final step in a complex modeling of laser-target interaction that involves hydrodynamics, and electron and atomic kinetics. We have studied the formation and polarization properties of the satellite line emissions of the Ly-α in He-like Si. These lines fall into two categories: "singlet" lines that show potential for a polarization effect, and the largely unpolarized "triplet" lines. We have also studied in detail and identified the most important atomic kinetics feeding channels responsible for the appearance of the polarization effect. The multi-level nature of the problem in laser-produced plasmas with many competing atomic processes is addressed and its systematic consideration is shown to be of critical importance.

Acknowledgments

This work was supported by the LLNL contract B503614, by the NATO grant CRG 971588, and by the University and Community College System of Nevada.

References

[1]. J.C. Kieffer, J.P. Matte, M. Chaker, Y. Beaudoin, C.Y. Chien, S. Coe, G. Mourou, J. Dubau, and M.K. Inal, Phys. Rev. E, **48** (6), 4648 (1993).

[2]. F. Walden, H.-J. Kunze, A. Petoyan, A. Urnov, and J. Dubau, Phys. Rev. E, **59** (3), 3562 (1999).

[3]. M.K. Inal and J. Dubau, Phys. Rev. A, **47** (6), 4794 (1993).

[4]. P. Beiersdorfer, D.A. Vogel, K.J. Reed, V. Decaux, J.H. Scofield, K. Widmann, G. Hölzer, E. Förster, O. Wehrhan, D.W. Savin, and L. Schweikhard, Phys. Rev. A, **53** (6), 3974 (1996).

[5]. A.S. Shlyaptseva, R.C. Mancini, P. Neill, P. Beiersdorfer, J.R. Crespo López-Urrutia, and K. Widmann, Phys. Rev. A, **57** (2), 888 (1998).

[6]. A.S. Shlyaptseva, R.C. Mancini, P. Neill, and P. Beiersdorfer, J. Phys. B, **32** (4), 1041 (1999).

[7]. B.W. Shore and D.H. Menzel, Principles of Atomic Spectra, Wiley (1968).

[8]. U. Fano, J. Opt. Soc. Am., **39** (10), 859 (1949).

[9]. R.C. Mancini and E. Mínguez, "M3R: a NLTE atomic kinetics model for plasmas." First International NLTE Atomic Kinetics Workshop, Gaithersburg, MD, August 12-16, 1996.

[10]. J. Abdallah Jr., R.E.H. Clark, and R.D. Cowan, Los Alamos National Laboratory report LA-11436-M vol. I (1988);
R.E.H. Clark, J. Abdallah Jr., G. Csanak, J.B. Mann, and R.D. Cowan, Los Alamos National Laboratory report LA-11436-M vol. II (1988);
R.E.H. Clark, J.B. Mann, G. Csanak, and A.L. Merts, Los Alamos National Laboratory report LA-UR-89-2675, Vol. 2 (1989).

[11]. U. Teubner, P. Gibbon, E. Förster, F. Falliès, P. Audebert, J.P. Geindre, and J.C. Gauthier, Phys. Plasmas, **3** (7), 2679 (1996).

[12]. G. Bonnaud and G. Reisse, Nucl. Fusion, **26** (5), 633 (1986);
E. Lefebvre, Ph.D. dissertation, Université de Paris XI-Orsay, 1996 (unpublished);
Th. Schlegel, S. Bastiani, L. Grémillet, J.-P. Geindre, P. Audebert, J.-C. Gauthier, E. Lefebvre, G. Bonnaud, and J. Delettrez, Phys. Rev. E, **60** (2), 2209 (1999).

[13]. V.L. Jacobs and M. Blaha, Phys. Rev. A, **21** (2), 525 (1980).

[14]. P. Hakel, X-ray Line Spectral Signatures of Plasmas Driven by High-Intensity Ultra-Short Laser Pulses, Ph.D. dissertation, University of Nevada, Reno (2001).

Measurement of the degree of polarization of the spectra from laser produced Al plasmas

Jaehoon Kim* and Dong-Eon Kim

Department of Physics, Pohang University of Science and Technology,

San 31, Hyojadong, Namgu, Pohang,

KyungBuk, 790-784, Republic of Korea

Abstract

Using a polarization-resolved UV/Visible spectrometer, the degree of polarization of the spectra from laser produced Al plasmas was measured. The degree of polarization of Al III 4s $^2S_{1/2}$ - 4p $^2P^o_{3/2}$ transition was measured at different positions from a target surface. To resolve the different polarization components of the emission line, a dichroic polarizer was used in front of the entrance slit of the spectrometer. The degree of polarization was observed to be 2 % 200 μm from target surface and decreased as the distance from the target increased, vanishing about 1.3 mm from the target surface. To avoid the possible error due to the shot-to-shot variation of the line intensity, a calcite crystal was used to simultaneously observe the two polarization components. Both measurements yielded the same result. The plasma parameters, such as the electron temperature and density, were estimated by spectroscopic methods. The measured electron temperature was about 3 eV and the density 2×10^{17} cm^{-3} near the target surface and decreased to 4×10^{16} cm^{-3} 1.3 mm away from the target surface.

*jhoonie@postech.edu

I. INTRODUCTION

Polarization of emissions from a plasma is generated by the presence of an anisotropy in the plasma such as the anisotropy of the election velocity distribution[1]. The measurement of the degree of polarization of an emission line can then be used to find the anisotropy of the plasma. The plasma polarization spectroscopy has been applied to laser produced plasmas[2–5]. Previous studies dealt with high density and high temperature plasmas produced by high power lasers by means of emission lines in the x-ray and soft x-ray region. In this work, the degree of polarization of a spectral line from a low-temperature Al plasma produced by a low power laser was measured using a polarization-resolved UV-visible spectrometer.

II. EXPERIMENTAL SETUP

Figure 1. shows the experimental setup. A Q-switched Nd/Glass was used to generate an Al plasma. The pulse duration of the laser is 3 ns and the energy per pulse of 6 mJ was used. This laser beam was focused onto an Al target surface with a focal spot size of 0.260 mm diameter. The power density on the target surface was then about 4×10^9 W/cm^2. Two imaging lenses were used to image the plasma on the entrance slit of a Czerny-Turner type UV-Visible spectrometer with a focal length of 1 m. This spectrometer was designed in the configuration of near-normal- incidence to the concave mirror to minimize an astigmatism. Hence the overall optical system of the spectrometer and imaging optics could image the plasma in one direction; the imaging direction was the direction of the laser incidence axis as shown in Fig. 1. The spatial imaging property of the system was measured using a 0.4 mm-diameter wire as a fiducial at the position of the plasma following Ref. [6]. The spatial resolution was measured to be about 0.3 mm. All the spatially-resolved data were taken at positions which were at least 0.3 mm apart.

To measure the degree of polarization of an emission line, two methods were used. The first one is to use a dichroic polarizer in front of the entrance slit of a spectrometer. The set-up is easy. The spectrometer system sees the wide region of a plasma, a region of about 1.5 mm from a target surface, with a spatial resolution of 0.3 mm. The disadvantage of this setup is that for the measurement of the degree of polarization, we need two spectra obtained independently with a polarizer set for the horizontal and vertical polarization, respectively.

The measurement of the degree of polarization can be affected by the shot-to-shot variation.

The second one is to use a calcite crystal after the entrance slit. The birefrigent property of properly-cut calcite crystal separates two perpendicular polarizations and allows one to observe two polarizations simultaneously. Hence the possible error due to the shot-to-shot variation can be avoided. This method was also employed to check the variation of the line intensity which may introduce an error in the measurement using the dichroic polarizer.

In our experiment, two polarizations were separated by 1.6 mm vertically after a 20 mm calcite crystal, and imaged and dispersed by imaging concave mirrors and a grating of the spectrometer on a CCD detector. On the detector, then we have two horizontal lines, one spectrum per each polarization as shown in Fig. 2. Since the optical set up in our experiment does imaging in the vertical direction, without the proper limitation of a viewing area, the two spectra overlap each other. To avoid this, we placed a 1-mm-wide slit in front of the entrance slit of the spectrometer.

The direction of polarization is defined as follows: one polarization is parallel to the laser incidence axis and the other polarization is perpendicular to the laser incidence axis. The degree of polarization is then define by $P = (I_{\parallel} - I_{\perp})/(I_{\parallel} + I_{\perp})$, where, $I_{\parallel}$ is the intensity of the light whose direction of polarization is parallel to the laser incidence axis, and $I_{\perp}$ the intensity of perpendicular polarization.

III. RESULTS AND DISCUSSION

The optical system consists of many optical elements such as mirrors, grating, lenses, and windows. It's important to calibrate the sensitivity of the optical system to different polarization components. In this works, Al III (4s ^{2}S$_{1/2}$ - 4p ^{2}P$^o_{1/2}$) transition line was selected to calibrate the polarization sensitivity of the system because this line can never be polarized from quantum-mechanical point of view. But near a target surface, a high density plasma exists, the continuum radiation of which contaminates the line emission. This region was hence neglected. The polarization sensitivity were measured for the region of 0.4 mm to 1.5 mm away from a target surface. The ratio of intensities of two different polarizations, $R = I_{\parallel}/I_{\perp}$ was measured to be about 0.544 in the above region with a standard deviation of 0.002.

Figure 3 shows the polarization-resolved Al III (4s ^{2}S$_{1/2}$ - 4p ^{2}P$^o_{1/2,3/2}$) lines obtained with

a dichroic polarizer. The transition lines were fitted by Voigt profile to find the intensities. Using the calibration of the polarization sensitivity, all the intensities were calibrated. Figure 4 shows the variation of the degree of polarization with respect to the distance from a target surface. The degree of polarization was measured to be 2.5% 200 μm from the target surface, decreased with the distance, vanishing at 1.3 mm. Another series of experiments were performed with a calcite crystal to check the effect of the shot-to-shot variation of intensity on the polarization measurement. Figure 5 is the spectrum at a place of about 400 μm from the target surface obtained with a calcite crystal, and the degree of the polarization was about 2.5%, confirming that the measured polarization was not affected by the shot-to-shot variation of the plasma, but real.

Assuming the local thermodynamic equilibrium[7], the electron temperature was estimated by the intensity ratio of the emission lines from different upper level transitions. The electron temperature was measured to be about 3 eV. To find the electron density, the Stark broadening was used. The spectral line was fitted using Voigt profile and the Lorentzian width. Electron-impact broadening parameter was taken from Ref. [8]. The averaged electron density was measured to be 2.2×10^{17} cm^{-3} at a place of 220 μm away from the target surface and decreased to 4×10^{16} cm^{-3} at a place of 1300 μm.

The electron density and temperature are too low for collisional excitation to be dominant process to the upper level population. Saha equation indicates that Al IV ion is more abundant than Al III ions. This means that the population of the upper level of transition may be populated by recombination process from Al IV ion. For this case, as in Ref. [9], the origin of the polarization of the emission line may be different from that in the case of dominant collisional process. Quantitative calculations including the recombination processes are needed and under progress.

IV. CONCLUSION

The degree of polarization of Al III (4s ^{2}S$_{1/2}$ - 4p ^{2}P$^o_{3/2}$) transition from laser produced Al plasmas were measured using a polarization-resolved UV/Visible spectrometer. The degree of polarization of the emission line was measured along the laser incidence direction. This emission line was polarized to a degree of 2.5% near the target surface and unpolarized far from target surface. The electron temperature and density estimated by the spectroscopic

method indicates that our plasma is in the recombination phase. The further study is needed to understand the behavior of polarization characteristics of emission lines in a recombining plasma.

---

[1] T. Fujimoto and S. A. Kazantsev, Plasma Phys. Control. Fusion **39**, 1267 (1997).

[2] J. C. Kieffer, J. P. Matte, H. Pépin, M. Chaker, Y. Beaudoin, and T. W. Johnston, Phys. Rev. Lett. **68**, 480 (1992).

[3] J. C. Kieffer, J. P. Matte, M. Chaker, Y. Beaudoin, C. Y. Chien, S. Coe, G. Mourou, J. Dubau, and M. K. Inal, Phys. Rev. E **48**, 4648 (1993).

[4] T. Kawachi, K. Murai, G. Yuan, S. Ninomiya, R. Kodama, H. Daido, Y. Kato, and T. Fujimoto, Phys. Rev. Lett. **75**, 3826 (1995).

[5] H. Yoneda, N. Hasegawa, S. Kawana, and K. Ueda, Phys. Rev. E **56**, 988 (1997).

[6] J. Kim and D. Kim, Jap. J. Appl. Phys. **39**, 6062 (2000).

[7] J. T. Knudtson, W. B. Green, and D. G. Sutton, J. Appl. Phys. **61**, 4771 (1987).

[8] M. S. Dimitrijević, Z. Djurić, and A. A. Mihajlov, J. Phys. D **27**, 247 (1994).

[9] T. Fujimoto, Plasma Phys. Control. Fusion **41**, A625 (1999).

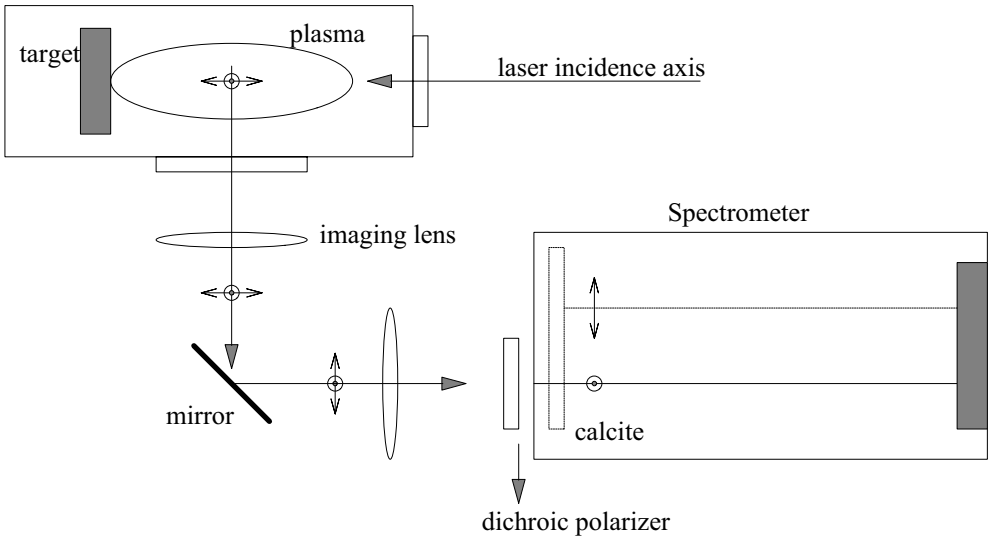

FIG. 1: Experimental setup.

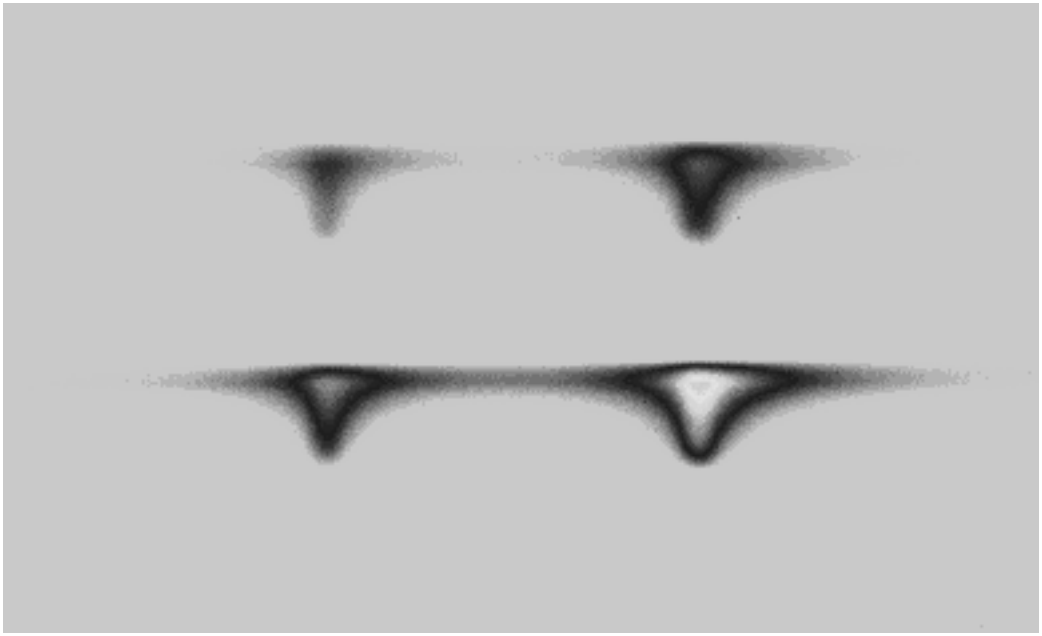

FIG. 2: Polarization resolved spectral image on the CCD camera using a calcite crystal after an entrance slit. Upper part of the spectra is E-ray of the calcite crystal, perpendicular polarization to the laser incidence axis, and lower part is O-ray, parallel to the laser incidence axis.

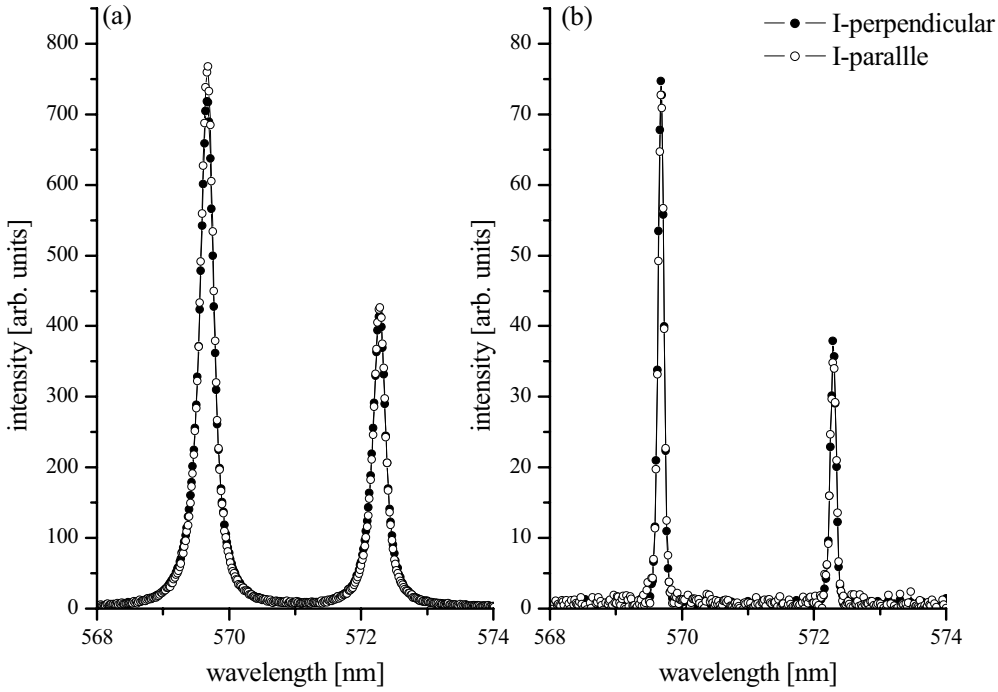

FIG. 3: Polarization resolved spectra using dichroic polarizer. Laser energy is 6 mJ. (a) is taken 220μm from target surface and (b) taken 1.3 mm from target surface. Open circle is the spectra of parallel to the laser incidence axis and dot is perpendicular.

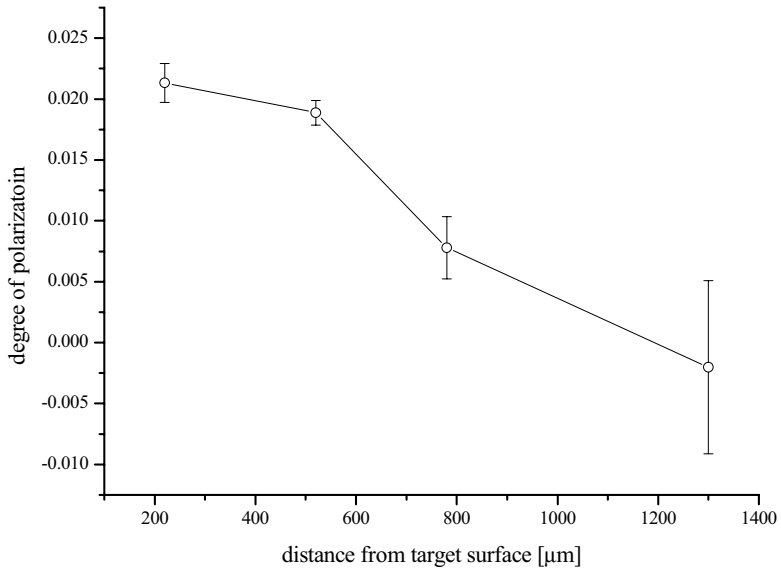

FIG. 4: Degree of polarization as a function of the distance from the target surface)

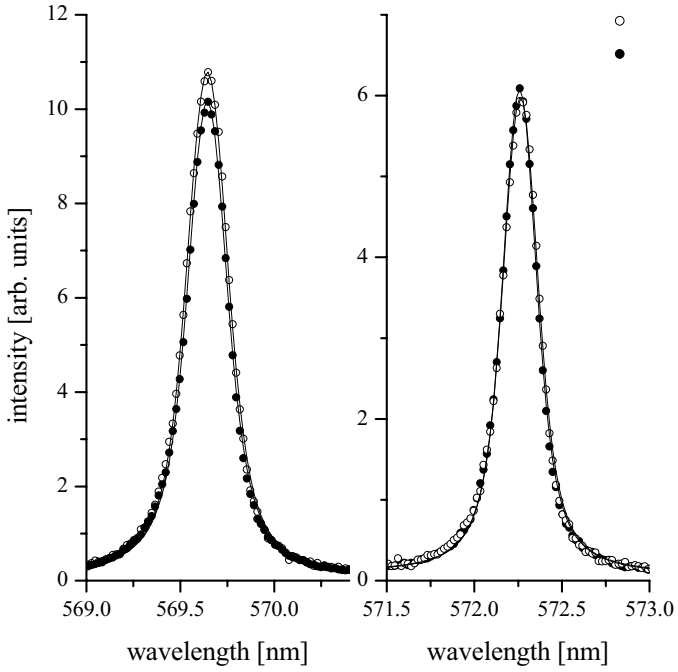

FIG. 5: Polarization resolved spectra using calcite crystal. The experimental condition is same as in Fig. 3

Relativistic Cross Sections for Excitation and Ionization by an Electron Beam and Application to the Polarization of the Subsequent Radiation

D.H. Sampson[1], H.L. Zhang[2], M.K. Inal[3] and C.J. Fontes[2]

[1]Department of Astronomy and Astrophysics, The Pennsylvania State University, University Park, Pennsylvania 16802

[2]Applied Physics Division, Los Alamos National Laboratory, Los Alamos, NM 87545

[3]Université A. Belkaid, Département de Physique, B.P.119, 13000 Tlemcen, Algeria

A fully relativistic distorted-wave method for calculating cross sections for excitation and ionization of ions by impact with a polarized or unpolarized electron beam is described. Some comparisons with semi-relativistic calculations are given. Also some comparisons made at the Lawrence Livermore National Laboratory with their EBIT measurements are discussed. Some predictions made by us of the polarization of the emergent radiation resulting from excitation by both spin polarized and unpolarized directional electrons are given. Improvements in the excitation codes needed for special conditions are described.

I. INTRODUCTION

Out principal purpose in this paper is to describe procedures and codes we have developed to calculate fully relativistic distorted-wave cross sections for excitation and ionization of ions by impact with an electron beam. Also some consideration is given to the expected degree of polarization of the subsequent radiation and to comparisons with measured values for the polarization plus some other theoretical work.

First the approach used for calculating the needed atomic structure data is described. The we outline how the excitation cross sections are determined. This is followed by a description of how the procedure for excitation is modified to give ionization cross sections. Then some comparisons are given of the excitation numerical results we obtain with those of two semi-relativistic distorted-wave codes. In addition, comparisons made at the Lawrence Livermore National Laboratory (LLNL) of the expected degree of polarization based on use of our codes for excitation with electron beam ion trap (EBIT) measurements are presented. Also we give results for excitation by a spin polarized electron beam and the degree of circular polarization of the subsequent radiation expected in that case. This is followed by a discussion of the degree of linear polarization of Se^{24+} lines expected when, in addition to direct excitation, the effects of inner-shell ionization of Se^{23+} and radiative cascades are included. Finally two types of improvements in our excitation code that are required for accuracy in treating special circumstances are described. One of these is the modifications required in treating optically allowed $\Delta n = 0$ transitions. The other is inclusion of the generalized Breit interaction between the active bound electron and the free electron. This is required in considering excitation of ions with large nuclear charge Z, especially when excitation of a 1s electron is involved.

II. THEORY

A. Atomic structure

For the atomic structure data the Dirac-Fock-Slater (DFS) code described in Ref. [1] is used with the improvements of Ref. [2] added. Since the orbitals of all electrons are solution of the Dirac equation, the major relativistic effects are included automatically. However, for large Z it is necessary to include the improvements of Ref. [2]. These are: (1) replacement of the point charge Z with the Fermi charge distribution $Z(r)$, as described in Ref. [3]; and (2) inclusion of the QED corrections, that is the electron self energy, the vacuum polarization and the generalized Breit interaction, the latter being the most important. We note that $Z(r)$ differs from Z only for extremely small r.

First the electron orbitals are calculated self consistently as solutions of the Dirac equation using a central potential $V(r)$. This is the DFS potential given by

$$V(r) = -\frac{2Z(r)}{r} + V_c(r) - \left[\frac{24}{\pi}\rho(r)\right]^{1/3} \quad , \tag{1}$$

where

$$V_c(r) = \sum_{n'\kappa'} w_{n'\kappa'} \int_0^\infty \frac{2}{r_>} \left[P^2_{n'\kappa'}(r_2) + Q^2_{n'\kappa'}(r_2)\right] dr_2, \tag{2}$$

and

$$\rho(r) = \frac{1}{4\pi r^2} \sum_{n'\kappa'} w_{n'\kappa'} [P^2_{n'\kappa'}(r) + Q^2_{n'\kappa'}(r)]. \tag{3}$$

Here $w_{n'\kappa'}$ is the occupation number of subshell $n'\kappa'$, and $P_{n'\kappa'}(r)$ and $Q_{n'\kappa'}(r)$ are the large and small components of the radial part of the wave functions of electrons in that subshell. The relativistic quantum number κ has the values

$$\kappa = l,\ j = l - 1/2; \qquad \kappa = -l - 1,\ j = l + 1/2\ . \tag{4}$$

The final term in Eq. (1) is the exchange energy of an electron in a free electron gas averaged over all possible momenta of the electron. With Eq. (3) we are using for $\rho(r)$ the spherical average of the density of electrons at a distance r from the nucleus.

Single configuration basis state functions are constructed using these orbitals. Then the mixing coefficients and energy level eigenvalues are determined by diagonalizing the complete Hamiltonian with the exact electron-electron Coulomb interaction and QED corrections included. Usually only the mixing among states with the same set of n values, as well as J value and parity, is included.

In determining the central potential given by Eqs. (1) – (3) a single mean configuration is used. For example, in excitation of He-like ions to the $n = 2$ levels we used

$$1s^{1.5}2s^{0.17}2p_{1/2}^{0.17}2p_{3/2}^{0.16} \tag{5}$$

Here, as we usually do, we have split the occupation of the active electron between the initial and final shells. The way in which the occupation is divided among the subshells of a shell has little effect.

B. Excitation cross sections

The procedure we use for calculating cross sections for excitation by an electron beam has been given in Ref. [4]. This procedure is summarized here, but to be consistent with ionization we use the notation of Ref. [5]. The relativistic scattering amplitude $B^{m_s}_{m'_s}$ for scattering an electron with spin m_s, wavenumber k, and direction $\widehat{k}$ into direction $\widehat{k}'$ with wavenumber k' and final spin m'_s accompanied by change in the state of the target ion from $\beta_t J_t M_t$ to $\beta'_t J'_t M'_t$ cab be written

$$B^{m_s}_{m'_s}(\beta_t J_t M_t \to \beta'_t J'_t M'_t) = \frac{2\pi}{k} \sum_{\substack{l,m_l,j,m \\ l',m'_l,j',m'}} \mathrm{i}^{l-l'+1} \exp[\mathrm{i}(\delta_\kappa + \delta_{\kappa'})] Y_l^{m_l^*}(\widehat{k}) Y_{l'}^{m'_l}(\widehat{k}') \times C(l\tfrac{1}{2}m_l m_s; jm) C(l'\tfrac{1}{2}m'_l m'_s; j'm') T(\alpha, \alpha'), \quad (6)$$

where

$$\alpha = kljm\beta_t J_t M_t, \quad \alpha' = k'l'j'm'\beta'_t J'_t M'_t. \quad (7)$$

Here the Y's are spherical harmonics, the C's are Clebsch-Gordon coefficients, the l, m_l, j, m and l', m'_l, j', m' refer in the usual way to initial and final angular momenta of the free electron. The δ's are the relativistic Coulomb phase factors given by Eq. (A2) of [4] with the small corrections due to departure of the potential from a pure Coulomb potential computed as described in the appendix of [4]. J_t and M_t are the ion's initial total angular momentum and its z-component, while β_t represents all additional quantum numbers required to specify the initial state of the ion. Analogous primed quantities refer in a corresponding way to the final state of the ion. The $T(\alpha, \alpha')$ is an element of the T-matrix.

Assuming we are not interested in the final spin of the electron, the excitation cross section is given by

$$Q^{m_s}(\beta_t J_t M_t \to \beta'_t J'_t M'_t) = \sum_{m'_s} \int \mathrm{d}\widehat{k}' \mid B^{m_s}_{m'_s} \mid^2 . \quad (8)$$

In determining Eq. (8) we choose the z axis to be in the direction of $\widehat{k}$. Then $m_l = 0$ and

$$Y_l^{m_l}(\widehat{k}) \to \left(\frac{2l+1}{4\pi}\right)^{1/2} . \quad (9)$$

The integration over scattering electron direction gives

$$\int \mathrm{d}\widehat{k}' Y_{l'_1}^{m'^*_{l1}}(\widehat{k}') Y_{l'}^{m'_l}(\widehat{k}') = \delta_{l'_1 l'} \delta_{m'_{l1} m'_l} . \quad (10)$$

Then after performing the summation over m'_{l1} and l'_1 we can use

$$\sum_{m'_s,m'_l} C(l'\tfrac{1}{2}m'_l m'_s; j'_1 m'_1) C(l'\tfrac{1}{2}m'_l m'_s; j' m') = \delta_{j'_1 j'} \delta_{m'_1 m'} \ . \tag{11}$$

So the dependence on the final phase factors $\delta_{\kappa'}$ drops out. Also we express the T-matrix in terms of the R-matrix

$$T = \frac{-2\mathrm{i}R}{1-2\mathrm{i}R} \simeq -2\mathrm{i}R, \tag{12}$$

where, as is well known, the final form applies for highly charged ions for which the R-matrix elements are very small. Finally we go to the coupled representation so that we can use R-matrix elements calculated by one version of our total cross section code

$$R(\alpha,\alpha') = \sum_{J,M} C(J_t j M_t m; JM) C(J'_t j' M'_t m'; JM) R(\gamma,\gamma'), \tag{13}$$

$$\gamma = klj\beta_t J_t JM, \quad \gamma' = k'l'j'\beta'_t J'_t JM. \tag{14}$$

Thus, collecting results

$$\begin{aligned} Q^{m_s}(\beta_t J_t M_t \to \beta'_t J'_t M'_t) = \frac{4\pi}{k^2} \sum_{\substack{l,l_1,j,j_1 \\ l',j',m'}} \sum_{J,J_1,M} & \mathrm{i}^{l-l_1}[(2l+1)(2l_1+1)]^{1/2} \\ & \times \exp[\mathrm{i}(\delta_\kappa - \delta_{\kappa_1})] C(l\tfrac{1}{2}0m_s; jm) C(l_1\tfrac{1}{2}0m_s; j_1 m) \\ & \times C(J_t j M_t m; JM) C(J_t j_1 M_t m; J_1 M) C(J'_t j' M'_t m'; JM) \\ & \times C(J'_t j' M'_t m'; J_1 M) R(\gamma,\gamma') R(\gamma,\gamma'_1) \ . \end{aligned} \tag{15}$$

In most applications the target ions are initially randomly oriented so the cross section of interest is given by averaging Eq. (15) over initial sublevels

$$Q^{m_s}(\beta_t J_t - \beta'_t J'_t M'_t) = \frac{1}{2J_t+1} \sum_{M_t} Q^{m_s}(\beta_t J_t M_t - \beta'_t J'_t M'_t) \ . \tag{16}$$

In addition, the interest is usually in impact by an unpolarized electron beam so the cross section of interest is

$$Q(\beta_t J_t - \beta'_t J'_t M'_t) = \frac{1}{2(2J_t+1)} \sum_{m_s,M_t} Q^{m_s}(\beta_t J_t M_t - \beta'_t J'_t M'_t) \ . \tag{17}$$

It should be noted that the same potential is used for all electrons, bound and free, so they are all automatically orthogonal. For example, for excitation of He-like ions to the $n = 2$ levels this potential is given by Eqs. (1) – (3) evaluated using the mean configuration given by Eq. (5).

C. Ionization cross sections

As described in Ref. [5], the expression for the cross section for ionization by an electron beam is readily obtained by modification of the expression given in the previous subsection for excitation. In doing this, ejected electron properties are indicated by double primes. Then in order that Eq. (6) be modified to apply for ionization we insert on the right-hand side the quantity $Y_{l''}^{m_l''}(\widehat{k})\,\mathrm{i}^{-l''}\,\exp[\mathrm{i}\,\delta_{\kappa''}]\,C(l''\tfrac{1}{2}m_l''m_s'';j''m'')$ and sum over l'', m_l'', j'' and m''. Also we must divide by $\pi^{1/2}$ to take account of the different normalization for the extra (ejected) free electron, which has replaced the final active bound electron. Thus, the ionization scattering amplitude $B_{m_s'\,m_s''}^{m_s}$ for scattering of an electron with spin m_s, wave number k and direction $\widehat{k}$ into direction $\widehat{k}'$ with wave number k' and final spin m_s' accompanied by a change in the state of the target ion from $\beta_t J_t M_t$ to $\beta_t'' J_t'' M_t''$ with one less bound electron, which has been ejected into direction $\widehat{k}''$ with wave number k'' and spin m_s'', is given by

$$\begin{aligned} B_{m_s'm_s''}^{m_s} = \frac{8\pi^{1/2}}{k} \sum_{\substack{l,m_l,j,m\\ l',m_l',j',m'\\ l'',m_l'',j'',m''}} & \mathrm{i}^{l-l'-l''}\exp[\mathrm{i}(\delta_\kappa+\delta_{\kappa'}+\delta_{\kappa''})]Y_l^{m_l^*}(\widehat{k})Y_{l'}^{m_l'}(\widehat{k}')Y_{l''}^{m_l''}(\widehat{k}'') \\ & \times C(l\tfrac{1}{2}m_lm_s;jm)C(l'\tfrac{1}{2}m_l'm_s';j'm')C(l''\tfrac{1}{2}m_l''m_s'';j''m'') \\ & \times\langle\Psi_i^u \mid \sum_{\substack{q,p\\ q<p}}^{N+1}\frac{1}{r_{qp}} \mid \Psi_f^u\rangle\ . \end{aligned} \tag{18}$$

Here the T matrix in the analogous Eq. (6) has been repaced with

$$T \to -4\mathrm{i}\langle\Psi_i^u \mid \sum_{\substack{q,p\\ q<p}}^{N+1}\frac{1}{r_{qp}} \mid \Psi_f^u\rangle\ , \tag{19}$$

where

$$\langle\Psi_i^u \mid \sum_{\substack{q,p\\ q<p}}^{N+1}\frac{1}{r_{qp}} \mid \Psi_f^u\rangle\ = \langle\beta_tJ_tM_t\epsilon ljm \mid \sum_{\substack{q,p\\ q<p}}^{N+1}\frac{1}{r_{qp}} \mid \beta_t''J_t''M_t''\epsilon''l''j''m''\epsilon'l'j'm'\rangle \tag{20}$$

is the ionization scattering matrix element in the uncoupled representation. The N in these equations is the initial number of bound electrons, while ϵ, ϵ'' and ϵ' are the relativistic kinetic energies of the incident, ejected and scattered electrons, respectively.

If one is not interested in the spins of the scattered and ejected electrons, the differential and total cross sections for ionization from one specific sublevel to a final specific sublevel by directive electrons with spin m_s are

$$\frac{\mathrm{d}^3Q^{m_s}}{\mathrm{d}\widehat{k}''\mathrm{d}\widehat{k}'\mathrm{d}\epsilon''} = \sum_{m_s'',m_s'} \mid B_{m_s'm_s''}^{m_s}\mid^2 \tag{21}$$

and

$$Q^{m_s}(\beta_t J_t M_t - \beta_t'' J_t'' M_t'') = \sum_{m_s'', m_s'} \int_0^{(\epsilon - I)/2} \mathrm{d}\epsilon'' \int \mathrm{d}\widehat{k}' \int \mathrm{d}\widehat{k}'' \mid B^{m_s}_{m_s' m_s''} \mid^2 , \tag{22}$$

where I is the ionization energy.

Our present interest is in Eq. (22). Again we choose the z axis to be in the $\widehat{k}$ direction. Then $m_l = 0$ and Eqs. (9) – (11) apply. Also equations like (10) and (11) apply for the ejected electron so the dependence on $\delta_{k''}$, as well as the dependence on $\delta_{k'}$, drops out. Collecting results we obtain

$$\begin{aligned} Q^{m_s}(\beta_t J_t M_t - \beta_t'' J_t'' M_t'') = \frac{16}{k^2} \sum_{\substack{l, l_1, j, j_1 \\ l', j', m' \\ l'', j'', m''}} & \mathrm{i}^{l - l_1} [(2l+1)(2l_1+1)]^{1/2} \exp[\mathrm{i}(\delta_\kappa - \delta_{\kappa_1})] \\ & \times C(l \tfrac{1}{2} 0 m_s; j m) C(l_1 \tfrac{1}{2} 0 m_s; j_1 m) \\ & \times \int_0^{(\epsilon - I)/2} \mathrm{d}\epsilon'' \langle \Psi_i^u \mid \sum_{\substack{q,p \\ q<p}}^{N+1} \frac{1}{r_{qp}} \mid \Psi_f^u \rangle \ \langle \Psi_{i1}^u \mid \sum_{\substack{q,p \\ q<p}}^{N+1} \frac{1}{r_{qp}} \mid \Psi_f^u \rangle . \end{aligned} \tag{23}$$

We note that the second matrix element in Eq. (23) is given by Eq. (20) with l and j replaced by l_1 and j_1, respectively, and that $m = m_s$ due to the property of the Clebsch-Gordon coefficient.

In evaluating Eq. (23) it is computationally efficient to first evaluate the matrix elements by expressing them in terms of those in the coupled representation using the expression

$$\begin{aligned} \langle \Psi_i^u \mid \sum_{\substack{q,p \\ q<p}}^{N+1} \frac{1}{r_{qp}} \mid \Psi_f^u \rangle \ = \sum_{J, M, J_t', M_t'} & C(J_t j M_t m; J M) C(J_t' j' M_t' m'; J M) \\ & \times C(J_t'' j'' M_t'' m''; J_t' M_t') \langle \Psi_i \mid \sum_{\substack{q,p \\ q<p}}^{N+1} \frac{1}{r_{qp}} \mid \Psi_f \rangle , \end{aligned} \tag{24}$$

where

$$\langle \Psi_i \mid \sum_{\substack{q,p \\ q<p}}^{N+1} \frac{1}{r_{qp}} \mid \Psi_f \rangle \ = \langle \beta_t J_t \epsilon l j J M \mid \sum_{\substack{q,p \\ q<p}}^{N+1} \frac{1}{r_{qp}} \mid \beta_t'' J_t'' \epsilon'' l'' j'' J_t' \epsilon' l' j' J M \rangle . \tag{25}$$

These coupled matrix elements can be obtained using one version of our code for total ionization cross sections, i.e. cross sections given by summing over final sublevels and averaging over initial sublevels.

As in the case of excitation, in our calculations all orbitals for both bound and free electrons are solutions of the Dirac equation using the same potential given by Eqs. (1)

– (3) evaluated using a mean configuration so they are all automatically orthogonal. For example, for inner-shell ionization of Li-like ions the mean configuration used was

$$1s^{1.5}2s^{0.34}2p_{1/2}^{0.33}2p_{3/2}^{0.33}8p_{1/2}^{0.25}8p_{3/2}^{0.25}. \tag{26}$$

Here we represent the state of the ejected electron by the highly excited subshells $8p_{1/2}$ and $8p_{3/2}$. The results are insensitive to the precise subshells used for that purpose, as long as they are much higher than the other subshells involved in the set of transitions being considered. Again analogous to excitation we have split the occupation of the active electron equally between the initial subshells and the subshells representing the ejected electron.

In most applications the target ions are initially randomly oriented so the cross section of interest is given by averaging Eq. (23) over initial target ion subshells

$$Q^{m_s}(\beta_t J_t - \beta_t'' J_t'' M_t'') = \frac{1}{2J_t+1}\sum_{M_t} Q^{m_s}(\beta_t J_t M_t - \beta_t'' J_t'' M_t'') \ . \tag{27}$$

If the ionization is also due to impact with unpolarized directional electrons, the cross section of interest is

$$Q(\beta_t J_t - \beta_t'' J_t'' M_t'') = \frac{1}{2(2J_t+1)}\sum_{m_s,M_t} Q^{m_s}(\beta_t J_t M_t - \beta_t'' J_t'' M_t'') \ . \tag{28}$$

If one also sums over final subshells M_t'' it is readily verified that the usual expression for the total ionization cross section is obtained. A similar statement applies for the excitation results given in the previous subsection.

It is interesting to note that although the numerical results for the case of impact by polarized directional electrons obtained with Eqs. (23) or (27) depend on the final magnetic sublevel M_t'', those obtained with Eq. (28) for unpolarized electrons are found to be almost independent of M_t''. Test cases have indicated that they are completely independent of M_t'' when configuration mixing can be neglected, although we have been unable to prove this analytically. The fact that at least for quite highly charged ions the cross sections for ionization by impact with directional electrons is almost independent of M_t'' is very convenient because it is much faster to calculate total ionization cross sections than those obtained with Eq. (23) in Eq. (28). Thus, approximate values for ionization to specific magnetic sublevels by impact with unpolarized directional electrons are readily obtained by simply dividing the total ionization cross section equally among the final magnetic sublevels.

III. COMPARISONS WITH OTHER WORK

A. Comparison with results of other codes for excitation

To our knowledge there are no other fully relativistic codes, i.e., codes based on the Dirac equation, with which we can compare results for impact by directional electrons. However, there are two semi-relativistic distorted-wave codes, i.e., codes in which all or most relativistic effects are treated perturbatively, with which we can compare results. One of these is the code of Inal and Dubau [6]. This is an extension of the well-known University College London set of programs [7 – 9] to apply for directional electrons. The other is the Los Alamos code of Clark *et al.* [10], which is based on the distorted-wave method of Mann [11]. This uses atomic structure data obtained with the code of Abdallah, Clark and Cowan [12], which in turn is based on Cowan's Hartree-Fock approach [13]. As shown in [4] the agreement is generally good for He-like and inner-shell excitation of Li-like iron. It is also moderately good for neon-like iron and molybdenum ($Z = 42$), which indicates a semi-relativistic treatment is fairly accurate in these ions. We think the larger discrepancies for the neon-like ions are due principally to the different potentials used in the calculations, but for $Z = 42$ relativistic effects on the radial functions might be of some significance. If instead of $n = 2$ excitation, $1s$ excitation were being considered, as would be the case for He-like ions, almost certainly a fully relativistic treatment would be required for $Z = 42$.

As an example of the comparisons, we have included those for He-like iron in Table I, which is taken from Ref. [4]. The results are for impact by unpolarized directional electrons for which Eq. [17] applies. However, the values given are for the collision strengths Ω rather than the cross section Q. The two are related by

$$Q = \frac{\pi a_0^2}{k^2 g}\Omega, \tag{29}$$

where g is the statistical weight of the initial level. For total cross sections

$$g = 2J_t + 1 \ ,$$

but for transitions between magnetic sublevels g is 1. Also the relation between k^2 and ϵ(Ry) is given by

$$k^2 = \epsilon(Ry)[1 + \frac{\alpha^2}{4}\epsilon(Ry)], \tag{30}$$

where $\alpha = 1/137.036$ is the fine structure constant. The second term in the brackets of Eq. (30) is small for the cases considered in Table I. For unpolarized electrons results depend only on $\mid M_t' \mid$ so only values for positive M_t' are given.

B. Comparisons with measured EBIT results

Comparisons of excitation results obtained with our codes have been made with EBIT measurements by Beiersdorfer and coworkers at LLNL. Generally the agreement is found to be good [14, 15]. As an example of the comparisons between measured results and theory we include the polarization comparisons given in Tables II and III. These are taken from Ref. [16] and [17]. Table II gives polarization results for He-like iron for the four lines $1s2p\ ^1P_1 \rightarrow 1s^2\ ^1S_0$, $1s2p\ ^3P_1 \rightarrow 1s^2\ ^1S_0$, $1s2p\ ^3P_2 \rightarrow 1s^2\ ^1S_0$ and $1s2s\ ^3S_1 \rightarrow 1s^2\ ^1S_0$, called w, y, x and z, respectively. Values labeled "Shlyaptseva and coworkers" are predictions based on Coulomb-Born calculations of Ref. [18] and [19]. The values labeled "Inal and Dubau" are based on excitation calculations using the semi-relativistic distorted-wave programs of Ref. [6] and [20]. The values labeled "Present Calculations" are based on use of our code for excitation. One sees that there is very good agreement between theory and measurements with the exception of the Coulomb-Born calculations. Table III gives similar comparisons of the predicted polarization based on using our code for excitation and the EBIT experiments for titanium. In this case results for the Li-like line $1s2s2p\ ^2P_{3/2} \rightarrow 1s^2 2s\ ^2S_{1/2}$ called q are also given. The agreement is again very good with the exception of a larger discrepancy for the w line.

IV. OUR PREDICTIONS OF POLARIZATION

A. He-like ions excited by polarized electrons

Here we give a brief summary of work done in Ref. [21] on the circular polarization of lines of He-like iron excited by longitudinally polarized directional electrons. By longitudinally polarized it is meant that $m_s = +1/2$, that is the impact electron spin is in the same direction as the electron motion so that Eq. (15) with $m_s = +1/2$ is used in determining the cross section. Although no measurements have been done using polarized electrons, it is expected that they will eventually. In contrast to excitation by unpolarized electrons, excitation by longitudinally polarized electrons produces circular polarized, as well as linear polarized, radiation. Also the cross section depends on the sign of the final magnetic sublevel quantum number M_i', as well as its magnitude.

In Ref. [21] results for collision strengths Ω (see Eq. (29) for the relation between Ω and Q) are given for excitation to both the $n = 3$ levels and the $n = 2$ levels. However, in the interests of brevity we sample only some of the results for $n = 2$ excitation in Table IV. The upper entries are semi-relativistic distorted-wave values obtained with the code of Ref. [6], while the lower entries are our fully relativistic distorted-wave values.

With the exception of two extremely weak transitions (not shown in the present sample) the agreement is very good.

In Table V we have sampled part of the results in Ref. [21] for the degree of circular polarization expected when observed along the electron beam direction, where it is a maximum. The upper entries are semi-relativistic results obtained assuming direct excitation from the ground level is the only mechanism populating the upper levels. The second entries are corresponding fully relativistic results. The third entries are semi-relativistic calculations that include the effect of cascades from higher $n = 2$ and $n = 3$ levels. In view of the general agreement between relativistic and semi-relativistic results for He-like Fe we expect the results would be almost unchanged, if the third entries had been calculated fully relativistically. One sees that the degree of circular polarization is large for lines x, y and z, but for x and y the effect of cascades is small. In work now in progress and expected to be completed soon we are doing fully relativistic calculations with inclusion of the effect of inner-shell ionization of Li-Like Fe on the expected degree of polarization.

B. Predicted polarization of Se^{24+} lines

Here we summarize recent theoretical work done in Ref. [5] on the predicted degree of linear polarization of Ne-like Se lines. The lines considered are the magnetic quadrupole transition $(2p^2_{1/2}2p^3_{3/2}3s)_2 - (2p^2_{1/2}2p^4_{3/2})_0$ called 3H and the two electric dipole transitions $(2p^2_{1/2}2p^3_{3/2}3s)_1 - (2p^2_{1/2}2p^4_{3/2})_0$ called 3G and $(2p_{1/2}2p^4_{3/2}3s)_1 - (2p^2_{1/2}2p^4_{3/2})_0$ called 3F. The mechanism considered for populating the upper magnetic sublevels by impact with an unpolarized electron beam are: (1) direct excitation from the ground level; (2) excitation to higher levels followed by radiative cascades; and (3) inner-shell ionization of Na-like Se. The excitation and inner-shell ionization cross sections are calculated fully relativistically using the distorted-wave codes described in Section IIB and IIC.

Assuming the direction of observation is at right angles to the incident electron beam, the degree of linear polarization of the radiation emitted in the electric dipole transitions is related to the populations $N_{M'_t}$ of the upper M'_t-magnetic sublevels by

$$P = \frac{N_0 - N_1}{N_0 + N_1}. \tag{31}$$

For the other line of interest here, namely the magnetic-quadrupole transition that we call 3H, P is given by

$$P = \frac{N_2 - N_1}{N_2 + N_1}. \tag{32}$$

Now we consider the radiative cascades. In doing this it is convenient to use a slightly different notation than used previously in Sec. II. We let

$$\alpha_i = \beta_i J_i M_i, \tag{33}$$

where, similar to Sec. IIB, the β_i represents the quantum numbers in addition to the ion's total angular momentum J_i and its z component M_i that are required to specify a magnetic sublevel in detail. Also we let $\alpha_j = \beta_j J_j M_j$ refer in an analogous way to a higher sublevel. Then assuming that the radiative decays determining the cascade contribution are dipole transitions, the relation

$$A(\alpha_j \to \alpha_i) = \left(C(J_j 1 M_j M_i - M_j; J_i M_i)\right)^2 A(\beta_j J_j \to \beta_i J_i) \tag{34}$$

applies. In Eq. (34) A represents the radiative decay transition probability for the appropriate level or sublevel transition. For very low densities, as in EBIT experiments, and a mono-energetic electron beam we can replace the N_{α_i} in Eqs. (31) and (32) with

$$\sigma^e(g \to \alpha_i) + r\, \sigma^{ii}(g' \to \alpha_i),$$

where g and g' are the ground levels of the Ne-like and Na-like stages of ionization and r is the abundance ratio of these ionization stages. Here $\sigma^{ii}(g' \to \alpha_i)$ is the inner-shell ionization cross section and $\sigma^e(g \to \alpha_i)$ is the sum of the direct excitation cross section $\sigma^{de}(g \to \alpha_i)$ and the effective cross section for indirect excitation from g to α_i via all cascade transitions feeding α_i

$$\begin{aligned} \sigma^e(g \to \alpha_i) \qquad &= \sigma^{de}(g \to \alpha_i) + \textstyle\sum_{\beta_j J_j} R(\beta_j J_j \to \beta_i J_i) \\ &\times \textstyle\sum_{M_j} \sigma^e(g \to \alpha_j)\, \left(C(J_j 1 M_j M_i - M_j; J_i M_i)\right)^2, \end{aligned} \tag{35}$$

where R is the branching ratio for the radiative transition from level j to level i, which we compute using the Babuskin gauge and the relativistic GRASP code of Refs. [22] and [23]. Evidently, in $\sigma^e(g \to \alpha_j)$ cascades are also involved.

Before giving numerical results we note that in determining the central potential given by Eqs. (1) – (3) and used in solving the Dirac equation for the bound and free orbitals we used the mean configurations

$$1s^2 2s^{1.9} 2p_{1/2}^{1.9} 2p_{3/2}^{3.7} 3s^{0.2} 3p_{1/2}^{0.2} 3p_{3/2}^{0.2} 3d_{3/2}^{0.2} 3d_{5/2}^{0.2} 10d_{3/2}^{0.25} 10d_{5/2}^{0.25} \tag{36}$$

and

$$1s^2 2s^{1.9} 2p_{1/2}^{1.9} 2p_{3/2}^{3.7} 3s^{0.1} 3p_{1/2}^{0.1} 3p_{3/2}^{0.1} 3d_{3/2}^{0.1} 3d_{5/2}^{0.1} \tag{37}$$

for inner-shell ionization of Na-like Se and direct excitation to the $n = 3$ levels of Ne-like Se, respectively. In the case of Eq. (36) the $n = 10$ subshells are used to represent the contribution of the ejected electron to the potential.

Tables VI, VII and VIII give results for the basic quantities required in determining the polarization of the lines being considered. There we use the following common abbreviations for the upper levels of the transitions:

$$(2p_{1/2}3s)_1 = (1s^2 2s^2 2p_{1/2} 2p_{3/2}^4 3s)_1 \tag{38}$$

and

$$(2p_{3/2}3s)_1 = (1s^2 2s^2 2p_{1/2}^2 2p_{3/2}^3 3s)_1. \tag{39}$$

For the quadrupole transition Eq. (39) also applies, but with 2 replacing the subscript 1. Results are only given for positive M_i because they depend only on $|M_i|$. One sees from these tables that in all cases σ^{e} considerably exceeds σ^{de}, which indicates that the major contribution to σ^{e} is the cascade contribution. Also it appears, especially for $(2p_{1/2}3s)_1$ and $(2p_{3/2}3s)_1$, that the cascade contribution must yield a nearly uniform population distribution. This occurs as a consequence of the Clebsch-Gordon factor in Eq. (34) and the fact that the major cascade contribution in these cases comes from higher levels with $J_j = 0$. Also one sees that, except for low energies in the case of the upper levels for the dipole transitions, the inner-shell ionization cross section σ^{ii} exceeds the direct excitation cross section σ^{de}. In addition as mentioned in Sec. IIC the ionization cross section is nearly independent of the final magnetic sublevel. Hence, both the effect of inner-shell ionization and radiative cascades tend to diminish the polarization. This is demonstrated by the results for the degree of polarization given in Table IX, where the results are given with and without the radiative cascade contribution and for various values r for the relative abundances of Na-like ions.

V. IMPROVEMENTS REQUIRED FOR SPECIAL CASES

A. Treatment of optically allowed $\Delta n = 0$ transitions

It is well known that for optically allowed $\Delta n = 0$ transitions, which generally have small transition energies, very large angular momenta l and l' for the impact and scattered electrons contribute significantly to the cross section for excitation. For total excitation cross sections, i.e. cross sections summed over final magnetic quantum sublevels M_t' and averaged over initial magnetic sublevels M_t, this large l contribution

can be calculated readily using the Coulomb-Bethe (CB) approximation, as described by Burgess [24]. However, his convenient formula is not valid when the electron radial functions become j-dependent due to relativistic effects and it certainly does not apply at all for transitions between magnetic sublevels produced by impact with directional electrons. In Ref. [25] we have given a procedure for treating this, which we now summarize.

For $l' \geq l_0$, where l_0 is some large number, the relativistic Coulomb-Bethe approximation (RCB) becomes valid. This approximation corresponds to approximating the Coulomb interaction between the active bound electron N and the free electron $N+1$ by

$$\begin{aligned} \frac{1}{\mid \mathbf{r}_N - \mathbf{r}_{N+1} \mid} &= \sum_\lambda \frac{r_<^\lambda}{r_>^{\lambda+1}} C^\lambda(N) \cdot C^\lambda(N+1) \\ &\simeq \frac{r_N}{r_{N+1}^2} C^{(1)}(N) \cdot C^{(1)}(N+1) \; . \end{aligned} \tag{40}$$

In addition exchange is neglected and relativistic Coulomb functions are used for the free electrons. The result, expressed in terms of the collision strength, is

$$\begin{aligned} \Omega_{m_s}^{\mathrm{RCB}}(\beta_t J_t M_t \to \beta_t' J_t' M_t') = 16 S(\beta_t J_t, \beta_t' J_t') & \sum_{\substack{l,l_1,j,j_1 \\ l',j',m'}} \mathrm{i}^{l-l_1}[(2l+1)(2l_1+1)]^{1/2} \\ & \times \exp[\mathrm{i}(\delta_\kappa - \delta_{\kappa_1})] C(l\tfrac{1}{2}0m_s; jm) C(l_1\tfrac{1}{2}0m_s; j_1 m) \\ & \times \sum_k \begin{pmatrix} j & 1 & j' \\ -m_s & k & m' \end{pmatrix} \begin{pmatrix} j_1 & 1 & j' \\ -m_s & k & m' \end{pmatrix} \begin{pmatrix} J_t & 1 & J_t' \\ -M_t & k & M_t' \end{pmatrix}^2 \\ & \times (-1)^{j+j'-2m_s} I(klj, k'l'j') I(kl_1 j, k'l'j') \\ & \times \langle j \parallel C^{(1)} \parallel j' \rangle \langle j_1 \parallel C^{(1)} \parallel j' \rangle \; , \end{aligned} \tag{41}$$

where

$$\langle j_1 \parallel C^{(1)} \parallel j_2 \rangle = (-1)^{j_1+1/2}[(2j_1+1)(2j_2+1)]^{1/2} \begin{pmatrix} j_1 & \lambda & j_2 \\ \frac{1}{2} & 0 & \frac{1}{2} \end{pmatrix} \tag{42}$$

and the ( ) in Eqs. (41) and (42) are Wigner $3j$'s. The I's are relativistic Coulomb integrals

$$I(klj, k'l'j') = \int_0^\infty \frac{1}{r^2}[P_{klj}(r) P_{k'l'j'}(r) + Q_{klj}(r) Q_{k'l'j'}(r)] \; \mathrm{d}r \tag{43}$$

and S is the line strength.

For sufficiently large l' the code of Ref. [25] using Eq. [41] gave numerical error. However, we found that before this region of l' was reached, the ratio of successive partial

wave contributions had become very nearly constant. Assuming this ratio is exactly constant and equal to some value C for a given transition and energy, the contribution of all partial wave with $l' \geq l_0^*$ is given by

$$\Omega^{RCB*}_{l_0^*,\infty} = \Omega^{RCB}_{l_0^*-1} \frac{C}{1-C} \tag{44}$$

where $\Omega^{RCB}_{l_0^*-1}$ is the partial wave relativistic Coulomb-Bethe value for $l' = l_0^* - 1$. Hence, the complete collision strength for transitions between magnetic sublevels is given by

$$\Omega = \Omega^{RDW}_{0,l_0-1} + \Omega^{RCB}_{l_0,l_0^*-1} + \Omega^{RCB*}_{l_0^*,\infty} \tag{45}$$

where Ω^{RDW}_{0,l_0-1} is the relativistic distorted-wave contribution for $0 \leq l' \leq l_0 - 1$ calculated by the procedures discussed in Sec IIB. The value of l_0 is chosen such that the partial wave contribution for $l' = l_0$ calculated by the relativistic distorted-wave method and by the RCB approximation agree to four significant figures. Thus the only uncertainty in use of Eq. (45) for the fully relativistic distorted-wave results is in the final term, which gave quite a large contribution of ~ 20 or 25% in some of our calculations. These were done for He-like ions with $Z = 10$, 26, 56 and 79. In Table X a part of the results for $Z = 56$ are reproduced. The key for the labeling of the transitions is

$$1 - 3 = 1s2s\ ^3S_1 - 1s2p\ ^3P_1 \quad \text{or} \quad (1s_{1/2}2s_{1/2})_1 - (1s_{1/2}2p_{1/2})_1 \tag{46}$$

and

$$1 - 5 = 1s2s\ ^3S_1 - 1s2p\ ^1P_1 \quad \text{or} \quad (1s_{1/2}2s_{1/2})_1 - (1s_{1/2}2p_{3/2})_1 \tag{47}$$

In the table the Σ entries are results for the total collision strength obtained by summing over M_t and M_t'. For the $Z = 10$ results, which we have not been reproduced here, a non-relativistic treatment should be valid for which one can use the convenient Burgess formula [24] in obtaining the total cross section. Results obtained that way with the same atomic structure data do agree with the Σ entries for $Z = 10$ given in Ref. [25] to within a fraction of a percent. This indicates the procedures of Ref. [25] do probably give the distorted-wave results for the individual sublevel transitions to within a few percent despite the fairly large contribution of the final term in Eq. (45) in some cases. In Table X results between some sublevels could be omitted because they can be obtained from the fact that

$$\Omega(\beta_i J_i M_i \rightarrow \beta_f J_f M_f) = \Omega(\beta_i J_i - M_i \rightarrow \beta_f J_f - M_f) \tag{48}$$

It is noted that l_0 and l_0^* used for the three electron energies are also listed in the table.

B. Inclusion of the generalized Breit interaction

For high Z values it is necessary to include the generalized Breit interaction between the electrons in addition to the Coulomb interaction. This has been done in our atomic structure calculations, as mentioned in Sec. IIA. Also in calculating the scattering matrix elements the generalized Breit interaction between bound and free electrons has been included as an option in our codes for total excitation cross sections [26, 27] and total ionization cross sections [28, 29, 30]. More recently it has been added to our code for excitation cross sections for transitions between magnetic sublevels in Ref. [31], which we now briefly discuss.

In order to include the generalized Breit interaction between a bound electron labeled 1 and a free electron labeled 2 one replaces $1/r_{12}$ with $g(1,2)$ in the calculations, where $g(1,2)$ is given by

$$g(1,2) = \frac{1}{r_{12}} - (\boldsymbol{\alpha}_1 \cdot \boldsymbol{\alpha}_2)\frac{\exp(i\omega r_{12})}{r_{12}} + (\boldsymbol{\alpha}_1 \cdot \boldsymbol{\nabla}_1)(\boldsymbol{\alpha}_2 \cdot \boldsymbol{\nabla}_2)\frac{\exp(i\omega r_{12}) - 1}{\omega^2 r_{12}}. \qquad (49)$$

Here $\boldsymbol{\alpha}_1$ and $\boldsymbol{\alpha}_2$ are the usual Dirac matrices and ω is the wave number of the exchanged virtual photon.

In Table XI and XII we have reproduced the results obtained in Ref. [31] for He-like iron and xenon ($Z = 54$). One sees from Table XI that inclusion of the generalized Breit interaction has a small effect for $Z = 26$ except for the highest energies considered, where it can have an effect as large as 15%. However, as seen from Table XII, the effect is often very significant for $Z = 54$. The validity of these results for xenon has been verified by EBIT measurement at LLNL given in Ref. [32], as seen from Table XIII, which is a reproduction of their Table 3.

It is interesting to note that in all cases our calculations indicate the inclusion of the imaginary part of the generalized Breit interaction has a small effect. This is important because the calculations are very lengthy and omitting the imaginary part reduces the computing time by about a factor of 2.

Finally we note that we have not yet put an option to include the generalized Breit interaction into our code for ionization to specific magnetic sublevels, but we expect to do so in future work.

References

1. D.H. Sampson, H.L. Zhang, A.K. Mohanty and R.E.H. Clark, Phys. Rev. A **40**, 604 (1989).

2. D.H. Sampson, H.L. Zhang and C.J. Fontes, At. Data And Nucl. Data Tables **48**, 25 (1991).

3. M.H. Chen, B. Crasemann, M. Aoyagi, K.-N. Huang and H. Mark, At. Data Nucl. Data Tables **26**, 561 (1981).

4. H.L. Zhang, D.H. Sampson, and R.E.H. Clark, Phys. Rev. A **41**, 198 (1990).

5. H.L. Zhang, D.H. Sampson and M.K. Inal, Phys. Rev. A **63**, 52713, (2001).

6. M.K. Inal and J. Dubau, J. Phys. B **20**, 4221 (1987).

7. W. Eissner, M. Jones, and H. Nussbaumer, Comput. Phys. Commun. **8**, 270 (1974).

8. W. Eissner and M.J. Seaton, J. Phys. B **5**, 2187 (1972).

9. H. E. Saraph, Comput. Phys. Commun. **15**, 247 (1978).

10. R.E.H. Clark, J. Abdallah, Jr., G. Csanak, J.B. Mann, and R.D. Cowan, Los Alamos National Laboratory Report No. LA–11436–M, Vol. II (1988) (unpublished).

11. J.B. Mann, At. Data Nucl. Data Tables **29**, 407 (1983).

12. J. Abdallah, Jr., R.E.H. Clark, and R.D. Cowan, Los Alamos National Laboratory Report No. LA–11436–M, Vol. I (1988) (unpublished).

13. R.D. Cowan, *The Theory of Atomic Structure and Spectra* (University of California Press, Berkeley, 1981)

14. K.L. Wong, P. Beiersdorfer, K.J. Reed, and D.A. Vogel, Phys. Rev. A **51**, 1214 (1995).

15. S. Chantrenne, P. Beiersdorfer, R. Cauble, and M.B. Schneider, Phys. Rev. Lett. **69**, 265 (1992).

16. P. Beiersdorfer, D.A. Vogel, K.J. Reed, V. Decaux, J.H. Scofield, K. Widmann, G. Hölzer, E. Förster, O. Wehrhan, D.W. Savin and L. Schweikhard, Phys. Rev. A **53**, 3974 (1996).

17. P. Beiersdorfer, G. Brown, S. Utter, P. Neill, K.J. Reed, A.J. Smith and R.S. Thoe, Phys. Rev. A **60**, 4156 (1999).

18. A.S. Shlyaptseva, A.M. Urno and A.V. Vinogradov, P.N. Lebedev Physical Institute of the USSR Academy of Sciences Report No. 194 (1981) (unpublished).

19. A.V. Vinogradov, A.M. Urno and A.S. Shlyaptseva, in *Atomic and Ionic Spectra and Elementary Processes in Plasma*, Proceedings of the Lebedev Institute Academy of Sciences of Russia Vol. 192, edited by I.I. Sobelman (Nova Science, Commack, N.Y., 1992), p. 93.

20. M.K. Inal and J. Dubau, J. Phys. B **47**, 4794 (1993).

21. M.K. Inal, H. L. Zhang and D. H. Sampson, Phys. Rev. A **46**, 2449 (1992)

22. I.P. Grant, B.J. McKenzie, P.H. Norrington, D.F. Mayers and N.C. Pyper, Comput. Phys. Commun. **21**, 207 (1980).

23. B.J. McKenzie, I.P. Grant and P.H. Norrington, Comput. Phys. Commun. **21**, 233 (1980).

24. A. Burgess, J. Phys. B **7**, L364 (1974).

25. H.L. Zhang and D.H. Sampson, Phys. Rev. A **52**, 3827 (1995).

26. C.J. Fontes, D.H. Sampson and H.L. Zhang, Phys. Rev. A **47**, 1009 (1993).

27. C.J. Fontes, D.H. Sampson and H.L. Zhang, Phys. Rev. A **49**, 3704 (1994).

28. C.J. Fontes, D.H. Sampson and H.L. Zhang, Phys. Rev. A **51**, R12 (1995).

29. C.J. Fontes, D.H. Sampson and H.L. Zhang, Phys. Rev. A **59**, 1329 (1999).

30. C.J. Fontes, D.H. Sampson and H.L. Zhang, At. Data And Nucl. Data Tables **72**, 217 (1999).

31. C.J. Fontes, D.H. Sampson and H.L. Zhang, Phys. Rev. A **59**, 205 (1999).

32. K. Widmann, P. Beiersdorfer, G.V. Brown, J.R. Crespo Lopez-Urrutia, A.L. Osterheld, K.J. Reed, J.H. Scofield and S.B. Utter, in *X-Ray and Inner-Shell Processes*, edited by R.W. Dunford *et al.* (2000 American Institute of Physics 1-56396-713-8), p. 444.

TABLE I. Comparison of results for collision strengths for excitation from the ground level to the magnetic sublevels M_t' of various $1s2p$ levels in He-like iron. In each case upper entries represent fully relativistic values, second entries are from the code of Ref. [10], and third entries are from Ref. [6]. Numbers in the square brackets are power of 10 by which adjacent entries should be multiplied. All transition energies ΔE were approximated by the same value 493Ry in Ref. [6]. Also, for most transitions the present results were calculated for slightly different values for the impact electron energies ϵ(Ry) than those listed.

Excited			ϵ(Ry)				
Level	M_t'	ΔE(Ry)	550	700	900	1200	2000
1s2p ^{1}P$_1$	0	493.2	1.69[-3]	2.37[-3]	3.09[-3]	3.85[-3]	4.94[-3]
or		493.0	1.69[-3]	2.39[-3]	3.07[-3]	3.76[-3]	4.68[-3]
$(1s_{1/2}2p_{3/2})_1$			1.69[-3]	2.38[-3]	3.06[-3]	3.76[-3]	4.69[-3]
	1		4.19[-4]	6.12[-4]	8.84[-4]	1.30[-3]	2.32[-3]
			4.18[-4]	6.20[-4]	8.98[-4]	1.31[-3]	2.30[-3]
			4.06[-4]	5.84[-4]	8.87[-4]	1.35[-3]	2.39[-3]
1s2p ^{3}P$_1$	0	490.7	2.08[-4]	2.42[-4]	2.85[-4]	3.37[-4]	4.20[-4]
or		490.6	2.19[-4]	2.55[-4]	2.99[-4]	3.47[-4]	4.16[-4]
$(1s_{1/2}2p_{1/2})_1$							
	1		2.65[-4]	2.09[-4]	1.76[-4]	1.69[-4]	2.16[-4]
			2.66[-4]	2.09[-4]	1.78[-4]	1.72[-4]	2.20[-4]
1s2p ^{3}P$_2$	0	491.9	2.91[-4]	1.98[-4]	1.27[-4]	7.35[-5]	2.50[-5]
or		491.7	3.08[-4]	2.10[-4]	1.35[-4]	7.76[-5]	2.63[-5]
$(1s_{1/2}2p_{3/2})_2$							
	1		2.37[-4]	1.61[-4]	1.04[-4]	6.04[-5]	2.12[-5]
			2.50[-4]	1.70[-4]	1.10[-4]	6.36[-5]	2.23[-5]
			2.45[-4]	1.65[-4]	1.05[-4]	6.05[-5]	2.10[-5]
	2		7.46[-5]	5.00[-5]	3.32[-5]	2.11[-5]	9.70[-6]
			7.63[-5]	5.13[-5]	3.42[-5]	2.19[-5]	1.02[-5]
			7.55[-5]	4.96[-5]	3.28[-5]	2.09[-5]	9.74[-6]

TABLE II. Comparison of calculated and measured values of the polarization of lines w, x, y, and z at an excitation of 6800 eV. Results are for He-like iron.

Line	Shlyaptseva and co-workers	Inal and Dubau	Present calculations	Measurements
P_{w}	+0.82	+0.584	+0.599	$+0.56^{+0.17}_{-0.08}$
P_{x}	-0.75	-0.518	-0.515	$-0.53^{+0.05}_{-0.02}$
P_{y}	-0.23	-0.196	-0.192	$-0.22^{+0.05}_{-0.02}$
P_{x} (no cascades)	0.000	0.000	0.000	
P_{z} (with cascades)		-0.078	-0.074	$-0.076^{+0.007}_{-0.007}$

TABLE III. Intensities (adjusted for the spectrometer response function) and inferred linear polarization of the helium-like lines w, x, y, and z and of the lithium-like line q for titanium measured with Si(220) and Si(111) crystals. Theoretical polarization values are given for comparison.

Line	Ion	Si(220) (counts)	Si(111) (counts)	Predicted polarization	Measured polarization
w	Ti^{20+}	18976	1820	+0.608	$+0.43^{+0.14}_{-0.12}$
x	Ti^{20+}	3628	185	-0.519	$-0.48^{+0.06}_{-0.06}$
y	Ti^{20+}	4468	268	-0.339	$-0.33^{+0.07}_{-0.07}$
z	Ti^{20+}	6511	470	-0.106	$-0.101^{+0.014}_{-0.013}$
q	Ti^{19+}	5999	569	+0.341	$+0.40^{+0.15}_{-0.10}$

TABLE IV. Collision strengths for transitions from the 1 $^1S_0$ ground level to the different M_t' magnetic sublevels of two of the $n = 2$ levels in Fe^{24+}, assuming the incident electron beam to be completely longitudinally polarized. The upper entries are the semi-relativistic results and the second entries are fully relativistic results. The threshold energies ΔE and the impact electron energies ϵ are in Ry. Here $R[n]$ means $R \times 10^n$.

Upper			ϵ(Ry)		
Level	M_t'	ΔE(Ry)	495	700	2000
1s2p $^3P_1$	-1		1.10[-5]	1.97[-5]	1.49[-4]
			1.13[-5]	2.28[-5]	1.81[-4]
	0	490.74	1.99[-4]	2.39[-4]	4.00[-4]
		490.04	2.13[-4]	2.68[-4]	4.73[-4]
	1		5.72[-4]	3.82[-4]	2.61[-4]
			5.84[-4]	4.03[-4]	3.01[-4]
1s2p $^1P_1$	-1		4.08[-4]	6.61[-4]	2.40[-3]
			3.89[-4]	6.49[-4]	2.34[-3]
	0	493.18	1.42[-3]	2.39[-3]	4.69[-3]
		492.46	1.39[-3]	2.36[-3]	4.94[-3]
	1		3.25[-4]	5.75[-4]	2.34[-3]
			3.19[-4]	5.70[-4]	2.27[-3]

TABLE V. Degree of circular polarization (in %) of the four Fe^{24+} $n = 1 - 2$ lines at three impact energies ϵ(Ry) of the longitudinally polarized incident electrons. For the lines w, x, and y the values in upper and second entries are obtained using semi-relativistic and fully relativistic collision strengths, respectively, and assuming direct excitation from the ground level to be the only population process for the upper levels. The third entries for these lines, as well as the sole entries for the line z, are the results of the semi-relativistic calculations including cascade contributions from the higher $n = 2$ and 3 levels.

	ϵ(Ry)				ϵ(Ry)		
Line	495	700	2000	Line	495	700	2000
	-11.3	-7.0	-1.3		96.2	90.2	27.3
w	-9.9	-6.5	-1.5	y	96.2	89.3	24.9
		-6.1	-1.3			85.7	26.1
	-50.4	-50.8	-46.2	z	64.0	60.4	44.7
x	-50.1	-50.4	-46.0				
		-48.5	-41.0				

TABLE VI. Cross sections (in units of cm^2) versus incident electron energy ϵ(Ry) for direct-excitation $\sigma^{de}_{M_i}$, effective excitation $\sigma^{e}_{M_i}$ and inner-shell ionization $\sigma^{ii}_{M_i}$ involved in the population of the specific magnetic sublevels M_i of the $(2p_{1/2}3s)_1$ level of Ne-like Se. Values for the threshold excitation and ionization energies ΔE(Ry) are also given. $x[y]$ means $x \times 10^y$.

		ϵ(Ry)			
	ΔE(Ry)	190	250	400	800
σ_0^{de}	108.7	3.423[-22]	3.504[-22]	3.190[-22]	2.221[-22]
σ_1^{de}		1.044[-22]	1.016[-22]	1.074[-22]	1.110[-22]
σ_0^{e}		3.561[-21]	2.794[-21]	1.854[-21]	1.011[-21]
σ_1^{e}		3.108[-21]	2.415[-21]	1.604[-21]	9.202[-22]
σ_0^{ii}	184.8	1.365[-22]	1.047[-21]	1.526[-21]	1.331[-21]
σ_1^{ii}		1.360[-22]	1.041[-21]	1.510[-21]	1.319[-21]

TABLE VII. The same as Table VI but for the $(2p_{3/2}3s)_1$ level.

		ϵ(Ry)			
	ΔE(Ry)	190	250	400	800
σ_0^{de}	105.6	5.495[-22]	5.636[-22]	5.119[-22]	3.540[-22]
σ_1^{de}		1.394[-22]	1.502[-22]	1.718[-22]	1.807[-22]
σ_0^{e}		5.773[-21]	4.563[-21]	3.049[-21]	1.678[-21]
σ_1^{e}		5.218[-21]	4.071[-21]	2.676[-21]	1.514[-21]
σ_0^{ii}	181.8	2.263[-22]	1.145[-21]	1.640[-21]	1.406[-21]
σ_1^{ii}		2.213[-22]	1.111[-21]	1.547[-21]	1.339[-21]

TABLE VIII. The same as Table VI but for the $(2p_{3/2}3s)_2$ level.

		ϵ(Ry)			
	ΔE(Ry)	190	250	400	800
σ_0^{de}	105.4	5.963[-23]	3.256[-23]	9.988[-24]	1.362[-24]
σ_1^{de}		5.334[-23]	2.915[-23]	9.138[-24]	1.339[-24]
σ_2^{de}		3.442[-23]	1.889[-23]	6.584[-24]	1.269[-24]
σ_0^{e}		1.589[-21]	9.792[-22]	4.760[-22]	2.029[-22]
σ_1^{e}		1.478[-21]	9.020[-22]	4.299[-22]	1.908[-22]
σ_2^{e}		1.168[-21]	7.476[-22]	4.080[-22]	2.150[-22]
σ_0^{ii}	181.6	2.332[-22]	1.154[-21]	1.654[-21]	1.415[-21]
σ_1^{ii}		2.312[-22]	1.140[-21]	1.617[-21]	1.389[-21]
σ_2^{ii}		2.251[-22]	1.101[-21]	1.508[-21]	1.311[-21]

TABLE IX. Degree of linear polarization P (in %) for the three lines 3F, 3G, and 3H of Se^{24+} at several incident electron energies and for various values of the ratio r of the ground-level ion population Se^{23+}/Se^{24+}. Values labeled (1) are without radiative cascade effects. Values labeled (2) include radiative cascades.

		ϵ(Ry)							
r	line	190		250		400		800	
		(1)	(2)	(1)	(2)	(1)	(2)	(1)	(2)
	3F	53.0	6.8	54.4	7.3	48.4	7.2	31.5	4.7
0.00	3G	58.8	5.0	56.8	5.7	48.0	6.5	29.9	5.1
	3H	-21.9	-11.7	-21.7	-9.4	-16.5	-2.6	-2.6	+6.0
	3F	50.0	6.8	37.3	7.0	28.5	6.7	17.7	4.2
0.10	3G	55.3	5.0	43.5	5.6	33.6	6.3	20.6	4.9
	3H	-14.9	-11.5	-5.3	-8.4	-4.1	-2.9	-2.9	+2.4
	3F	47.2	6.7	28.4	6.8	20.3	6.2	12.4	3.8
0.20	3G	52.2	5.0	35.4	5.5	26.2	6.2	16.0	4.7
	3H	-11.5	-11.4	-3.7	-7.7	-3.8	-3.0	-2.9	+0.9
	3F	40.6	6.7	16.6	6.1	11.0	5.2	6.7	3.0
0.50	3G	44.7	5.0	22.9	5.2	16.4	5.7	10.1	4.3
	3H	-7.1	-10.9	-2.6	-6.3	-3.6	-3.2	-2.9	-0.8

TABLE X. Collision strengths for $\Delta n = 0$ optically allowed transitions between magnetic sublevels with $n = 2$ in He-like barium.

		ϵ'(Ry)					ϵ'(Ry)		
M_t	M_t'	1000	4500	22000	M_t	M_t'	1000	4500	22000
		l_0=23	33	58			l_0=23	33	58
		l_0^*=50	100	190			l_0^*=50	100	190
		1-3 transition, ΔE (eV) = 89.9					1-5 transition, ΔE (eV) = 575		
-1	-1	9.10[-3]	6.57[-3]	2.23[-3]	-1	-1	3.11[-3]	2.82[-3]	2.23[-3]
-1	0	5.63[-3]	1.04[-2]	1.59[-2]	-1	0	1.70[-3]	2.50[-3]	4.42[-3]
-1	1	5.26[-8]	5.50[-8]	2.95[-8]	-1	1	4.73[-5]	4.41[-5]	2.29[-5]
0	-1	5.65[-3]	1.04[-2]	1.59[-2]	0	-1	1.62[-3]	2.45[-3]	4.42[-3]
0	0	8.98[-5]	6.23[-5]	1.78[-5]	0	0	1.75[-4]	1.08[-4]	2.03[-5]
	Σ	4.08[-2]	5.50[-2]	6.80[-2]		Σ	1.31[-2]	1.57[-2]	2.22[-2]

TABLE XI. Comparison of collision strengths for excitation of He-like iron from the ground level to specific magnetic sublevels M_t' for various impact electron energies ϵ(Ry). Σ entries are the total collision strengths. In each case upper, middle, and lower entries are with inclusion of only the Coulomb interaction, Coulomb plus real part of the Breit interaction, and Coulomb plus total Breit interaction, respectively. Note $y[n]$ means $y \times 10^n$.

Excited			ϵ(Ry)				
Level	M_t'	ΔE(Ry)	550	700	900	1200	2000
$1s2s\ ^3S_1$	0	487.75	1.078[-4]	8.206[-5]	5.995[-5]	4.051[-5]	1.880[-5]
or			1.084[-4]	8.359[-5]	6.218[-5]	4.321[-5]	2.163[-5]
$(1s_{1/2}2s_{1/2})_1$			1.084[-4]	8.358[-5]	6.218[-5]	4.320[-5]	2.163[-5]
	1		1.078[-4]	8.206[-5]	5.995[-5]	4.051[-5]	1.881[-5]
			1.072[-4]	8.247[-5]	6.105[-5]	4.206[-5]	2.061[-5]
			1.073[-4]	8.248[-5]	6.106[-5]	4.207[-5]	2.061[-5]
	Σ		3.235[-4]	2.462[-4]	1.799[-4]	1.215[-4]	5.642[-5]
			3.229[-4]	2.485[-4]	1.843[-4]	1.273[-4]	6.284[-5]
			3.229[-4]	2.485[-4]	1.843[-4]	1.273[-4]	6.284[-5]
$1s2p\ ^3P_1$	0	490.04	2.264[-4]	2.677[-4]	3.185[-4]	3.781[-4]	4.729[-4]
or			2.191[-4]	2.553[-4]	2.988[-4]	3.474[-4]	4.132[-4]
$(1s_{1/2}2p_{1/2})_1$			2.192[-4]	2.552[-4]	2.986[-4]	3.471[-4]	4.130[-4]
	1		2.660[-4]	2.130[-4]	1.848[-4]	1.825[-4]	2.408[-4]
			2.726[-4]	2.211[-4]	1.952[-4]	1.968[-4]	2.678[-4]
			2.726[-4]	2.212[-4]	1.953[-4]	1.970[-4]	2.679[-4]
	Σ		7.584[-4]	6.936[-4]	6.881[-4]	7.430[-4]	9.545[-4]
			7.643[-4]	6.975[-4]	6.892[-4]	7.411[-4]	9.489[-4]
			7.643[-4]	6.975[-4]	6.892[-4]	7.411[-4]	9.489[-4]
$1s2p\ ^1P_1$	0	492.46	1.678[-3]	2.357[-3]	3.062[-3]	3.817[-3]	4.940[-3]
or			1.637[-3]	2.287[-3]	2.947[-3]	3.630[-3]	4.536[-3]
$(1s_{1/2}2p_{3/2})_1$			1.634[-3]	2.284[-3]	2.943[-3]	3.626[-3]	4.533[-3]
	1		4.194[-4]	6.095[-4]	8.788[-4]	1.288[-3]	2.304[-3]
			4.146[-4]	6.114[-4]	8.946[-4]	1.332[-3]	2.445[-3]
			4.160[-4]	6.132[-4]	8.966[-4]	1.334[-3]	2.447[-3]
	Σ		2.517[-3]	3.576[-3]	4.820[-3]	6.394[-3]	9.547[-3]
			2.466[-3]	3.510[-3]	4.736[-3]	6.295[-3]	9.426[-3]
			2.466[-3]	3.510[-3]	4.736[-3]	6.295[-3]	9.426[-3]
$1s2p\ ^3P_2$	0	491.12	2.898[-4]	1.971[-4]	1.269[-4]	7.326[-5]	2.495[-5]
or			3.043[-4]	2.099[-4]	1.377[-4]	8.167[-5]	2.980[-5]
$(1s_{1/2}2p_{3/2})_2$			3.040[-4]	2.097[-4]	1.375[-4]	8.162[-5]	2.979[-5]
	1		2.360[-4]	1.603[-4]	1.035[-4]	6.022[-5]	2.114[-5]
			2.377[-4]	1.624[-4]	1.057[-4]	6.227[-5]	2.276[-5]
			2.375[-4]	1.623[-4]	1.056[-4]	6.225[-5]	2.275[-5]
	2		7.429[-5]	4.983[-5]	3.309[-5]	2.104[-5]	9.689[-6]
			7.453[-5]	5.052[-5]	3.404[-5]	2.213[-5]	1.089[-5]
			7.483[-5]	5.071[-5]	3.415[-5]	2.219[-5]	1.090[-5]
	Σ		9.103[-4]	6.173[-4]	4.000[-4]	2.358[-4]	8.661[-5]
			9.288[-4]	6.358[-4]	4.171[-4]	2.505[-4]	9.709[-5]
			9.288[-4]	6.358[-4]	4.171[-4]	2.505[-4]	9.709[-5]

TABLE XII. The same as Table XI except the results are for He-like xenon ($Z = 54$) instead of He-like iron ($Z = 26$) and higher impact electron energies are considered

Excited			ϵ(Ry)				
Level	M_t'	ΔE(Ry)	2400	3000	4000	6000	10000
1s2s ^{3}S$_1$	0	2214.6	3.084[-5]	2.425[-5]	1.716[-5]	9.917[-6]	4.559[-6]
or			3.312[-5]	2.718[-5]	2.070[-5]	1.384[-5]	8.356[-6]
$(1s_{1/2}2s_{1/2})_1$			3.306[-5]	2.713[-5]	2.066[-5]	1.382[-5]	8.345[-6]
	1		3.085[-5]	2.428[-5]	1.720[-5]	9.969[-6]	4.612[-6]
			3.358[-5]	2.777[-5]	2.140[-5]	1.473[-5]	9.866[-6]
			3.376[-5]	2.791[-5]	2.150[-5]	1.478[-5]	9.886[-6]
	Σ		9.255[-5]	7.280[-5]	5.157[-5]	2.986[-5]	1.378[-5]
			1.003[-4]	8.272[-5]	6.350[-5]	4.331[-5]	2.809[-5]
			1.006[-4]	8.296[-5]	6.366[-5]	4.339[-5]	2.812[-5]
1s2p ^{3}P$_1$	0	2220.4	1.309[-4]	1.767[-4]	2.426[-4]	3.436[-4]	4.877[-4]
or			1.245[-4]	1.584[-4]	2.027[-4]	2.568[-4]	3.016[-4]
$(1s_{1/2}2p_{1/2})_1$			1.238[-4]	1.571[-4]	2.007[-4]	2.546[-4]	2.995[-4]
	1		8.201[-5]	8.168[-5]	9.230[-5]	1.310[-4]	2.266[-4]
			9.394[-5]	9.645[-5]	1.141[-4]	1.737[-4]	3.278[-4]
			9.447[-5]	9.730[-5]	1.153[-4]	1.751[-4]	3.292[-4]
	Σ		2.949[-4]	3.400[-4]	4.272[-4]	6.056[-4]	9.410[-4]
			3.124[-4]	3.513[-4]	4.310[-4]	6.042[-4]	9.573[-4]
			3.127[-4]	3.517[-4]	4.314[-4]	6.047[-4]	9.579[-4]
1s2p ^{1}P$_1$	0	2251.5	2.785[-4]	3.926[-4]	5.540[-4]	7.946[-4]	1.136[-3]
or			2.588[-4]	3.585[-4]	4.897[-4]	6.550[-4]	8.123[-4]
$(1s_{1/2}2p_{3/2})_1$			2.545[-4]	3.529[-4]	4.829[-4]	6.474[-4]	8.047[-4]
	1		8.419[-5]	1.096[-4]	1.589[-4]	2.690[-4]	5.012[-4]
			7.737[-5]	1.069[-4]	1.668[-4]	3.106[-4]	6.425[-4]
			7.984[-5]	1.101[-4]	1.706[-4]	3.150[-4]	6.470[-4]
	Σ		4.469[-4]	6.119[-4]	8.717[-4]	1.333[-3]	2.138[-3]
			4.135[-4]	5.723[-4]	8.233[-4]	1.276[-3]	2.097[-3]
			4.142[-4]	5.731[-4]	8.241[-4]	1.277[-3]	2.099[-3]
1s2p ^{3}P$_2$	0	2248.9	6.709[-5]	4.724[-5]	2.874[-5]	1.317[-5]	4.392[-6]
or			8.316[-5]	6.155[-5]	4.058[-5]	2.161[-5]	9.421[-6]
$(1s_{1/2}2p_{3/2})_2$			8.248[-5]	6.108[-5]	4.031[-5]	2.150[-5]	9.386[-6]
	1		5.507[-5]	3.876[-5]	2.364[-5]	1.096[-5]	3.777[-6]
			5.873[-5]	4.272[-5]	2.755[-5]	1.446[-5]	6.836[-6]
			5.841[-5]	4.250[-5]	2.743[-5]	1.442[-5]	6.827[-6]
	2		1.866[-5]	1.298[-5]	8.078[-6]	4.180[-6]	1.867[-6]
			1.936[-5]	1.409[-5]	9.604[-6]	6.242[-6]	4.986[-6]
			2.007[-5]	1.458[-5]	9.879[-6]	6.352[-6]	5.015[-6]
	Σ		2.146[-4]	1.507[-4]	9.219[-5]	4.345[-5]	1.568[-5]
			2.393[-4]	1.752[-4]	1.149[-4]	6.302[-5]	3.307[-5]
			2.394[-4]	1.752[-4]	1.149[-4]	6.304[-5]	3.307[-5]

TABLE XIII. Comparison between the measured ($\sigma_{\rm EE}$) and calculated electron-impact excitation cross section. The calculated values are based on a distorted-wave approach [4]. Relativistic effects certainly play an important role in the interaction between the 112-eV beam electron and the highly charged xenon ion as seen in the large difference between the non-relativistic calculations, $\sigma_{\rm non-rel}$, and the relativistic calculations, $\sigma_{\rm rel}$. Additionally, the impact of the Breit interaction between the free and bound electrons is significant in the excitation process of the heliumlike xenon. Thus, agreement between the measured and calculated cross section values can only be found when the Breit interaction, i.e., the Generalized Breit Interaction [26, 27], is included in the calculations, $\sigma_{\rm GBI}$.

line	$\sigma_{\rm EE}$ barn	$\sigma_{\rm non-rel}$ barn	$\sigma_{\rm rel}$ barn	$\sigma_{\rm GBI}$ barn
Ly-α_1	8.6 ± 1.5		8.256	8.109
Ly-$\alpha_{2,3}$	8.2 ± 3.4		6.541	6.787
w	7.0 ± 2.0	21.64	17.45	8.364
y	3.9 ± 1.5	0.127	7.313	3.842
z	1.08 ± 0.48	0.123	0.172	0.152

Measurement of the Polarization of the Kβ2 Line of heliumlike V^{21+}

A. J. Smith[1], P. Beiersdorfer[2], K. L. Wong[2], and K. J. Reed[2]

[1] *Department of Physics, Morehouse College, Atlanta GA 30314*

[2] *Lawrence Livermore National Laboratory, Livermore, CA 94550*

Abstract

We have measured the polarization of the intercombination line 1s3p $^3P_1$ - 1s^2 $^1S_0$, the so called Kβ2 line, in heliumlike V^{21+} using two Bragg crystal spectrometers. The ions were excited in the Lawrence Livermore National Laboratory electron beam ion trap. We find values which are not significantly different from theoretical predictions based on some admixing of the initial state by the hyperfine interaction. In this short paper we present our results.

1. Introduction

Interest in polarization measurements is increasing as polarization spectroscopy is rapidly becoming the standard technique for determining the existence of directed electron beams in laboratory as well as in astrophysical plasmas. The Lawrence Livermore National Laboratory (LLNL) electron beam ion trap EBIT-II facility uses a unidirectional, nearly monoenergetic electron beam to ionize, trap and excite ions. Various electron-ion interactions are investigated by looking at x-ray emission from the trap in a direction that is perpendicular to the electron beam. In EBIT-II, photon emission is anisotropic and the emitted photons are polarized [1], since the electron beam imposes a directionality on the emission process. The Livermore high resolution spectrometers [2] use Bragg crystals to disperse the x-rays and

these crystals have reflectivities which are polarization dependent. For this reason, measured intensities of x-rays produced in an electron beam ion trap must be corrected for polarization [3]. In most cases we use theoretical values for the polarizations of lines whose intensities we wish to correct. The polarizations are calculated using partial cross sections for excitation into magnetic sublevels σ_m. Thus for E1 transitions the polarization is calculated from

$$P = -\frac{\sigma_1 - \sigma_0}{\sigma_1 + \sigma_0}. \tag{1}$$

We have used the Zhang, Sampson, and Clark [4] code which uses a distorted wave approxiamation (DWA) to calculate σ_m. These calculations show that for V^{21+} ions at electron energies near the Kβ1 excitation threshold of 6118.3 eV the polarization of the Kβ1 line is 0.61 [5], and that this value remains nearly constant for energies up to several hundred eV above threshold. This theory also predicts the polarization of the Kβ2 line to be -0.37 for near-threshold excitation. However, experimental measurements described in Ref. [1], found the polarization of the Kβ2 line of Sc^{19+} to have a value near zero. Since Sc and V are adjacent odd-Z nuclei, we expect the polarization of the Kβ2 line of V^{21+} to be near zero also. This is because the vanadium nucleus, like the scandium nucleus, has a nuclear spin of 7/2, and the hyperfine interaction is expected to cause admixing of the upper levels of the intercombination lines of He-like ions of these elements with other levels, and therefore to change the polarization of these lines to near-zero values [1]. The hyperfine interaction does not seem to cause any admixing of the upper levels of the of the resonance lines of these ions, the polarizations of the resonance lines are not affected by the hyperfine interaction.

We define the polarization of an x-ray line emitted at $\vartheta = 90°$ to the electron beam as

$$P = \frac{I_{||}(90°) - I_{\perp}(90°)}{I_{||}(90°) + I_{\perp}(90°)} \tag{2}$$

where $I_{||}$and $I_{\perp}$ are the intensities of the x-rays polarized parallel and perpendicular to the electron beam, respectively. The actual intensity observed by a spectrometer is given by

$$I^{obs} = R_{||} I_{||}(90°) + R_{\perp} I_{\perp}(90°). \tag{3}$$

Here, $R_{||}$ and $R_{\perp}$ are the integrated reflectivities of the crystal for x-rays polarized parallel and perpendicular to the plane of dispersion. The ratio R = $R_{\perp}/R_{||}$ depends on the Bragg angle θ at which the crystal is set. R varies from $\cos^2(2\theta)$ for mosaic crystals to $|\cos(2\theta)|$ for an ideal crystal. Values of R have been tabulated by Henke, Gullickson, and Davis [6].

The two crystal method for measuring polarization has been described elsewhere [7]. The ratio of the intensities of two lines, Kβ1 and Kβ2 measured by two crystals, say Si and LiF are given by

$$\frac{I^2}{I^1}\ |_{\rm Si} = \frac{I^2_{||} + R_{\rm Si} I^2_{\perp}}{I^1_{||} + R_{\rm Si} I^1_{\perp}} \tag{4}$$

and

$$\frac{I^2}{I^1}\ |_{Lif} = \frac{I^2_{||} + R_{Lif} I^2_{\perp}}{I^1_{||} + R_{Lif} I^1_{\perp}}, \tag{5}$$

where we have assumed that the two lines are close to each other and that R is the same for the Bragg angles spanned by the two lines. We combine the equations 2, 4, and 5 to obtain an expression for the polarization P_2 of Kβ2 in terms the polarization P_1 Kβ1,

$$P_2 = \frac{\frac{I^2}{I^1}\ |_{\rm Si}\ (1 + R_{\rm Si}\frac{1-P_1}{1+P_1})(R_{Lif}+1) - \frac{I^2}{I^1}\ |_{Lif}\ (1 + R_{Lif}\frac{1-P_1}{1+P_1})(R_{\rm Si}+1)}{\frac{I^2}{I^1}\ |_{\rm Si}\ (1 + R_{\rm Si}\frac{1-P_1}{1+P_1})(R_{Lif}-1) - \frac{I^2}{I^1}\ |_{Lif}\ (1 + R_{Lif}\frac{1-P_1}{1+P_1})(R_{\rm Si}-1)}. \tag{6}$$

We have used the values $R_{Lif} \sim 0$ and $R_{\rm Si}$ =0.44, these values are appropriate for an ideal crystals.

2. Measurement and Result

We have used the LLNL EBIT-II electron beam ion trap to measure the polarization of the Kβ2 line emitted by heliumlike V^{21+}. The electron beam energy was initally set at 8 kV for a few milliseconds to produce mainly the heliumlike charge state. It was then switched to 6.6 kV to excite the Kβ1 and Kβ2 lines directly. With this excitation energy (which is just above threshold for direct excitation of Kβ1), we expect that direct excitation is the main mechanism for line formation, in particular we do not expect the upper levels of these

lines to be fed by cascades. The polarizations of the lines are therefore not expected to be modified by cascades.

We have used two EBIT high-resolution spectrometers [2], which were configured in von Hámos geometry, and which both had a plane of dispersion perpendicular to the electron beam. For one spectrometer we used a LiF(220) crystal, with a 2d spacing of 2.848 Å, bent to a radius of 30 cm, and set at a nominal Bragg angle of 45°. This spectrometer had a resolving power of $\lambda/\Delta\lambda = 2500$. In this configuration, the spectrometer has zero quantum efficiency for $I_\perp$, and the signal depends on $I_{||}$ only. For the second spectrometer we used a Si(220), which has a 2d spacing of 3.840 Å, and was bent to a radius of 30 cm. This crystal was set at a nominal Bragg angle of 31.6°, for a resolving power of $\lambda/\Delta\lambda = 2500$. Figure 1 shows the spectra accumulated by the two spectrometers over the same period of time. The intensities of the lines recorded by the LiF(220) spectrometer at a Bragg angle of 45°, are much lower than those recorded by the Si(220) spectrometer. Part of the reason for this is that the former crystal has zero reflectivity for x-rays that polarized perpendicular to the electron beam.

For each spectrum, we have fitted the lines to Gaussian profiles to obtain relative intensities. We inserted the fitted intensities into Eq. 6 and use the theoretical value of 0.61 for the polarization of Kβ1. As a result, we find a polarization of -0.1 $\pm$ 0.2 for the Kβ2 line. The errors in this result come from the fitting procedure, and also from taking into account some perpendicular motion for EBIT electrons. The result is consistent with the expectation that the polarization of the Kβ2 line nearly vanishes because of the hyperfine interaction admixing the upper level of the intercombination line with other levels. The measured value is not consistent with the value of -0.37 predicted by the DWA to be the polarization of the Kβ2 line in the absence of the hyperfine interaction.

3. Acknowledgment

We gratefully acknowledge support by the Office of Basic Energy Science, Chemical Sciences Division, and by the LLNL Research Collaborations Program for Historically Black Colleges and Universities and Minority Institutions. This work was performed under the auspices of the U.S. Department of Energy by the University of California, Lawrence Livermore National Laboratory under contract No. W-7405-Eng-48 and by Morehouse College under contract No. DE-FG02-98ER14877.

4. References

[1] Henderson, J. R. *et al*, Phys. Rev. Lett. **65**, 705 (1990).

[2] Beiersdorfer, P. *et al*, Rev. Sci. Instrum. **61**, 2338 (1990).

[3] Smith, A. J. *et al*, Phys. Rev. A **51**, 2808 (1995).

[4] Zhang, H. L., D. H. Sampson, and R. E. H. Clark, Phys. Rev. A **41**, 198 (1990).

[5] Smith, A. J. *et al*, Phys. Rev. A **61**, 012704 (2000).

[6] Henke, B. L., E. M. Gullickson, and J. C. Davis, At. Data Nucl. Data Tables **54**, 181, (1993).

[7] Beiersdorfer, P. *et al*, Phys. Rev. A **60**, 4156 (1999).

FIGURES

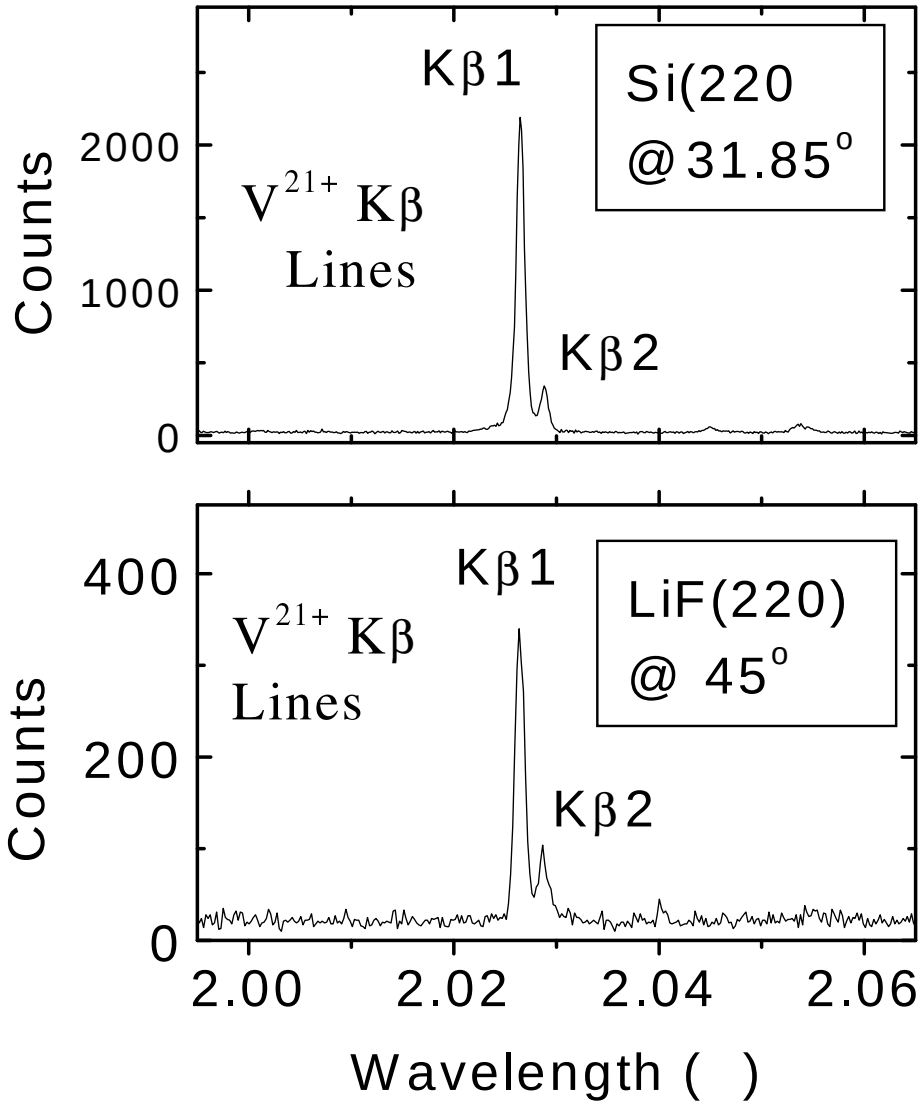

Fig. 1. Kβ spectra of heliumlike V^{21+} excited in the Lawrence Livermore National Laboratory electron beam ion trap EBIT-II. The upper spectrum was accumulated with a Si(220) crystal set at a nominal Bragg angle of 31.63°, while the lower spectrum was obtained with a LiF(220) crystal set at a nominal Bragg angle of 45°.

Relativistic effects on the polarization of line radiation emitted from He-like and H-like ions following electron-impact excitation

K. J. Reed and M. H. Chen

Lawrence Livermore National Laboratory

Livermore, CA 94550

Radiation emitted from ions excited by a directed electron beam can be strongly linearly polarized. Itikawa, et al. [1] reported calculations which indicated that the polarization is independent of atomic number for H-like and He-like ions when expressed as functions of incident - electron energy in threshold units. They calculated the polarization for several low - Z ions and then determined the polarization for the case of the infinite Z approximation. However, they neglected relativistic effects in their calculations. For low-Z ions at low collision energies relativistic effects are not significant. But for higher - Z ions, relativistic effects on the target atomic structure and the high energy scattered waves are not negligible, and these effects can significantly affect the cross sections for electron impact excitation. Since the polarization of the emitted radiation depends upon the cross sections for excitation to magnetic sublevels, relativistic effects on the polarization could be significant for ions with high atomic number.

We made a systematic investigation of relativistic effects on the polarization of radiation emitted following electron impact excitation of the $1s^2 \quad 1s2p(^1P_1)$ transition in He-like ions of Si, A, Ti, Mo, Ba, Au, and U, and the $1s \quad 2p_{3/2}$ transition in H-like ions of these same elements.

Cross sections for excitation to individual magnetic sub-levels were calculated using a distorted wave code developed by Zhang and Sampson [2]. Configuration-interaction type wave functions were used in the target structure calculations which were performed

with a Dirac-Fock-Slater atomic structure code developed for use with the scattering code. These cross sections were then used to determine the polarization of the resulting radiation, and relativistic effects were assessed by comparing results of nonrelativistic and relativistic calculations.

For He-like ions the polarization of radiation emitted at 90 degrees with respect to the electron beam is related to the excitation cross sections by

$$P = (\sigma_0 \quad \sigma_1)/(\sigma_0 + \sigma_1) \ , \qquad (1)$$

where $_0$ and $_1$ are the cross sections for electron impact excitation from the ground state to the m=0 and m=1 magnetic sublevels respectively.

Table 1 shows the polarization of the 1s2p ($^1P_1$) $1s^2$ line for the He-like ions. In the nonrelativistic case the polarization is nearly independent of Z and has approximately the same value as the polarization for infinite Z given in Ref. 1. The situation is clearly quite different when relativistic effects are taken into account. At incident electron energies of twice the threshold energy the polarization is 52.44 for Si and remains fairly constant for the whole range of Z. The nonrelativistic infinite Z value is 53.4. At incident energies 4 times threshold, the polarization for Si is 34.51, which is close to the nonrelativistic infinite Z value of 35.30. However, at these energies, the polarization rapidly increases with increasing Z, and at Z=92 it has increased to 47.43. At incident energies 5 times threshold the polarization for Z=13 is still close to the nonrelativistic infinite Z value, but it increases even more rapidly with increasing Z. Thus for Z=92, at 5 times the threshold energy, the polarization is 44.69, which is quite different from the nonrelativistic infinite Z value of 28.7.

In our investigation we noted that the cross section for excitation to the m=0 sublevel is significantly larger than the cross section for excitation to the m=1 sublevel for all of the ions. This was true for both the nonrelativistic and the relativistic results. This preferential excitation to the m=0 sublevel at lower incident energies occurs because the momentum

transfer is predominantly parallel to the direction of motion of the incident electron at lower collision energies. Since this direction is also along the axis of quantization, the orbital momentum and its projection m, are zero for the incident electron. These quantum numbers are also initially zero for the target ion. At much higher incident energies, the momentum transfer becomes predominantly transverse to this direction. As a result the ratio of the m=0 cross section to the m=1 cross section begins to decrease rapidly at higher energies. We find that for both sublevels the differences between the relativistic and nonrelativistic results become increasingly pronounced as Z increases.

The polarization of the emitted radiation depends on the deviation from statistical population of the magnetic sublevels of the excited states, so the unequal relative changes in the excitation cross sections at a given energy results in a change in the polarization at that energy. There is also a noticeable decrease in the m=1 cross sections as a result of relativistic effects, and this decrease also becomes increasingly significant with increasing Z.

For H-like ions the polarization of the $2p_{3/2} \quad 1s_{1/2}$ is given by

$$P = - 3B_0 / (4 - B_0) , \qquad (2)$$

where

$$B_0 = (\quad _{3/2} - \quad _{1/2}) / (\quad _{3/2} + \quad _{1/2}) . \qquad (3)$$

Table 2 shows relativistic and nonrelativistic polarization for the $2p_{3/2} \quad 1s_{1/2}$ line in H-like ions for impact electron enrgies of 2, 4 and 5 times threshold. As in the case of He-like ions the nonrelativistic results are fairly independent of Z and in close agreement with the infinite Z results from Ref.1. (Note that we have multiplied the infinite Z results from Ref. 1 by 1.5 to account for the fact that Itikawa et al. used spin averaged 2p cross sections, while we used $2p_{3/2}$ cross sections in our calculations.) The trends for the relativistic results are similar to the trends noted for the relativistic results for He-like ions.

In conclusion, we found that relativistic effects alter the magnitude of the polarization for the ions studied in this work. The effects of relativity on the polarization become more important with increasing collision energy and with increasing atomic number.

REFERENCES

1. Y. Itikawa, R. Srivastava and K. Sakimoto, Phys. Rev. A 44, 7195 (1991).
2. H. L. Zhang , D. H. Sampson and R.E.H. Clark, Phys. Rev. A 41,198 (1990).
3. P. Beiersdorfer (private communication).

Table 1. Polarization of the 1s2p ($^1P_1$) $1s^2$ line in He-Like Ions. (Infinite Z values from Ref. 1). X is the incident electron energy in threshold units.

X	Si	A	Ti	Mo	Ba	Au	U	Z=
<u>Non-Relativistic</u>								
2	53.80	53.66	53.62	53.56	52.97	53.47	53.51	53.4
4	35.73	35.36	35.44	35.42	36.06	35.26	35.25	35.3
5	28.96	28.95	28.93	28.97	27.09	28.87	28.81	28.7
<u>Relativistic</u>								
2	52.44	53.81	53.81	53.87	54.23	54.31	53.40	53.4 *
4	34.51	37.82	37.85	38.87	41.37	46.07	47.43	35.3
5	28.29	29.85	30.26	33.59	36.63	41.93	44.69	28.7

* The infinite Z values shown here are nonrelativistic values

Table 2. Polarization of the $2p_{3/2}$ $1s_{1/2}$ line in H-Like Ions. (Infinite Z values from Ref. 1 have been multiplied by 1.5 as explained in text.) X is the incident electron energy in threshold units.

X	Si	A	Ti	Mo	Ba	Au	U	Z=
Non-Relativistic								
2	33.83	33.84	33.87	33.87	33.79	33.80	33.83	31.2
4	19.69	19.69	19.66	19.69	19.67	19.71	19.63	19.3
5	15.52	15.63	15.56	15.59	15.57	15.62	15.69	15.6
Relativistic								
2	33.93	34.04	34.18	35.10	35.98	38.37	38.55	31.2 *
4	19.93	20.21	20.76	22.14	23.92	27.29	29.31	19.3
5	15.84	16.17	16.49	18.57	20.60	23.58	26.76	15.6

* The infinite Z values shown here are nonrelativistic values.

Measurement of the relative intensity of the Ly-α lines in Fe^{25+}

K. L. Wong, P. Beiersdorfer, K. J. Reed, and A. L. Osterheld

Lawrence Livermore National Laboratory,

University of California, Livermore, California 94550

The intensity of the polarized Ly-α_1 ($2p_{3/2}\rightarrow 1s_{1/2}$) transition has been measured relative to that of the unpolarized Ly-α_2 ($2p_{1/2}\rightarrow 1s_{1/2}$) transition in Fe^{25+}. The measurements were made with the Livermore electron beam ion trap EBIT-II for beam energies from threshold to 2.5 times threshold. The results are compared to the corresponding intensity ratio predicted using excitation cross sections from distorted-wave calculations, which includes polarization, the M1 ($2s_{1/2}\rightarrow 1s_{1/2}$) transition, and cascade contributions. Discrepancies are found that tend to confirm recent a recent report of a measurement of the Ly-α lines in Ti^{21+} performed on the Tokyo electron beam ion trap.

I. INTRODUCTION

X-ray polarization is predicted to occur whenever ions collide with non-Maxwellian electron velocity distributions. It has been used as a diagnostic to study bremsstrahlung from a vacuum spark plasma [1], laser-produced plasmas [2], and solar flares [3–6]. Of particular interest has been the ratio of Ly-α_2 ($2p_{1/2}\rightarrow 1s_{1/2}$) and Ly-$\alpha_1$ ($2p_{3/2}\rightarrow 1s_{1/2}$), which is labeled "$B$" by solar physicists [7]. The reason is that this ratio is thought to be well understood and essentially constant as a function of electron temperature. Moreover, one of the two lines, Ly-α_2, is always unpolarized. Hence deviations from the predicted ratio of B is taken as evidence for polarization of Ly-α_1, and thus for the excitation of the ions by electrons in a beam.

A very recent measurement of B in Ti^{21+} was reported by Nakamura et al. [8]. The measurement was performed on the Tokyo electron beam ion trap facility. It showed that B did not agree with predictions even if polarization effects are taken into account. This was taken to be evidence that the calculated polarization values are inconsistent with the experiment by as much as 50%, casting doubt on the accuracy of the calculations.

In this paper we present a measurement of the Ly-α_2 transition relative to the Ly-α_1

transition in hydrogenlike iron using the Livermore EBIT-II electron beam ion trap. We show that B disagrees in a similar way from theory as the Tokyo result, albeit to a smaller extent if radiative cascades are properly taken into account.

II. POLARIZATION EFFECTS

Polarization has two effects on the x rays we measure: (1) since we measure x rays at 90° to the electron beam our detectors and spectrometers are sensitive to the angular distribution of the x rays, and (2) our crystal spectrometer acts as a polarimeter, which preferentially detects x rays polarized perpendicular to the plane of dispersion.

For electric dipole radiation, i.e., the primary type we study in this paper, the expression for the x-ray intensity at 90°, I(90°), and the average over the 4π solid angle, $\langle I \rangle$, is [9]

$$I(90°) = \frac{3}{3-P}\langle I \rangle. \tag{1}$$

P is defined as the linear polarization and is given by

$$P = \frac{I_{\|} - I_{\perp}}{I_{\|} + I_{\perp}}, \tag{2}$$

where $I_{\|}$ and $I_{\perp}$ are the intensities of the x-ray emission components with electric field vectors parallel and perpendicular electron beam, respectively, and

$$I_{\|} + I_{\perp} = I(90°). \tag{3}$$

The x-ray intensity $I^{\rm meas}$ measured with our crystal spectrometer is

$$I^{\rm meas} = R_{\|} I_{\|} + R_{\perp} I_{\perp}, \tag{4}$$

where $R_{\|}$ and $R_{\perp}$ are the integrated reflectivities of the crystal for x rays polarized parallel and perpendicular to the electron beam, which were provided by Gullikson [10].

Combining Eqs. (1)-(4), the intensity ratio we measure for two electric dipole x-ray lines is related to their 4π average by the expression

$$\frac{I_1^{\rm meas}}{I_2^{\rm meas}} = \frac{W_1 \langle I_1 \rangle}{W_2 \langle I_2 \rangle}, \tag{5}$$

where we define W to be

$$\frac{W_1}{W_2} = \frac{R_1(P)A_1(P)}{R_2(P)A_2(P)} = \left(\frac{(1+P_1) + \frac{R_{\perp}^1}{R_{\|}^1}(1-P_1)}{(1+P_2) + \frac{R_{\perp}^2}{R_{\|}^2}(1-P_2)} \right) \left(\frac{3-P_2}{3-P_1} \right), \tag{6}$$

The terms $R(P)$ and $A(P)$ represent the reflectivity and angular distribution terms, repectively. The values for $\frac{R_\perp}{R_\parallel}$ are less than 1. Therefore, positive polarization enhances and negative polarization decreases the intensity of an x-ray line relative to an unpolarized line.

III. EXPERIMENT

EBIT-II consists of a series of three drift tubes [11,12]. It uses an electron beam ($\leq$ 150 mA) to generate, trap, and excite highly charged ions. Low charged ions are injected into the trap from the MeVVA ion source [13], while gases are ballistically injected through the side ports. The ions are trapped radially by the electron beam that is compressed to a radius of roughly 30-μm by a 3-Tesla magnet. They are trapped axially by the two end drift tubes, which are biased positive with respect to the center drift tube.

The x rays generated by the electron-ion collisions are recorded with EBIT-II's curved crystal Bragg spectrometer in the von Hámos geometry [14]. In our experiment we used a LiF(200) crystal with a lattice spacing of 2d = 4.027 Å. The crystal was bent to a radius of curvature of 30 cm. The resolving power of the setup is $\Delta\lambda/\lambda \approx 1500$. The spectrometer was set to a nominal Bragg angle of 26.8° which corresponds to a wavelength of 1.81 Å. The total wavelength covered was 1.77 Å $< \lambda <$ 1.88 Å which contains the hydrogenlike transitions Ly-α_1 ($2p_{3/2} \rightarrow 1s_{1/2}$) at 1.7780 Å and Ly-$\alpha_2$ ($2p_{1/2} \rightarrow 1s_{1/2}$) at 1.7834 Å [15]. A typical x-ray spectrum taken with the electron beam energy set to 15 keV is shown in Fig. 1.

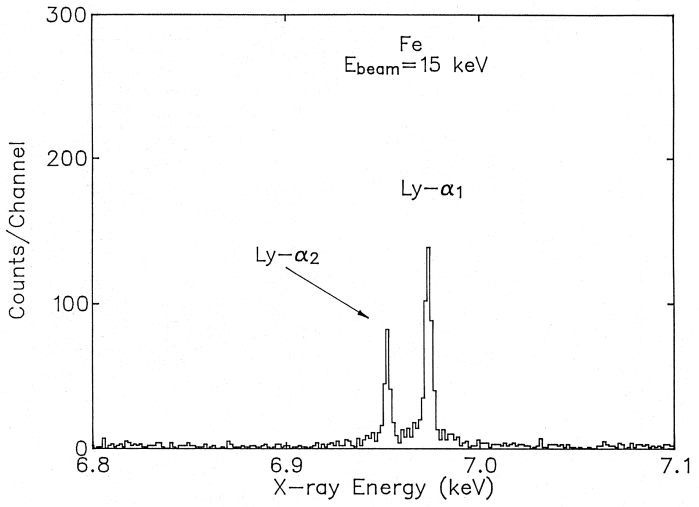

FIG. 1. Direct excitation x-ray spectrum of Fe^{25+} measured with a Bragg crystal spectrometer at an electron beam energy of 15 keV showing Ly-α_1 and Ly-α_2.

The Ly-α_2 intensity has a contribution from an M1 ($2s_{1/2} \rightarrow 1s_{1/2}$) transition, which cannot be resolved from the Ly-α_2 x ray. The separation between the two transitions in iron is a mere 0.03 eV. The $2s_{1/2}$ upper level decays 10% of the time by M1 (magnetic dipole) radiation and 90% of the time by two photon decays [16]. Therefore, the M1 transition results in an x ray which blends with and adds to the effective intensity of Ly-α_2.

We have measured Ly-α_2 and Ly-α_1 in iron as a function of electron beam energy for energies near the excitation threshold of Ly-α_1 at 7.1 keV to 18 keV. The measurements for energies from 10 to 18 keV were made in steady-state at one beam energy, and recording a spectrum of approximately 250 counts in Ly-α_2 and 500 counts in Ly-α_1 typically lasted 50 min. However, the measurements made below 8.828 keV, which is the ionization potential for producing hydrogenlike iron, are made by taking advantage of electron beam ion trap's ability to alternate the electron beam accelerating voltage (5 kV/ms) from one value to another and back. This feature allows us to create the ionization balance at, e.g., 15 keV and to probe the hydrogenlike transitions at energies below 8.828 keV. These spectra took roughly 6 hours each to acquire. The excitation energies of Ly-α_2 and Ly-α_1 in iron are 6.952 keV and 6.973 keV, repectively.

We compare the experimental intensities of Ly-α_2 and Ly-α_1 with those predicted at 90° to the electron beam direction. For Ly-α_2 and Ly-α_1, the predicted x-ray intensities are:

$$I_{\mathrm{Ly}-\alpha 2} = \frac{j_e}{e}(\sigma_{\mathrm{Ly}-\alpha 2} + 0.1\sigma_{\mathrm{M1}}) n_{\mathrm{H}} W_{\mathrm{Ly}-\alpha 2} G, \tag{7}$$

$$I_{\mathrm{Ly}-\alpha 1} = \frac{j_e}{e}\sigma_{\mathrm{Ly}-\alpha 1} n_{\mathrm{H}} W_{\mathrm{Ly}-\alpha 1} G, \tag{8}$$

where j_e is the effective current density, e is the charge of the electron, $\sigma_{\mathrm{Ly}-\alpha 2}$, σ_{M1}, and $\sigma_{\mathrm{Ly}-\alpha 1}$ are excitation cross sections calculated with the distorted-wave code of Zhang et al. [17], n_{H} is the number densities of ground-state hydrogenlike ions, and G is the solid angle subtended by the spectrometer. W, which we derived in the last section, accounts for the angular distribution of the x rays, their linear polarization, and the reflectivity of the LiF(200) crystal. P=0 for Ly-α_2 plus the M1 contribution (J=1/2→1/2 transitions). The polarization for Ly-α_1 is given by:

$$P = \frac{3(N_{1/2} - N_{3/2})}{3N_{3/2} + 5N_{1/2}}, \tag{9}$$

where $N_{1/2}$ and $N_{3/2}$ are the magnetic sublevel populations. This formula was derived by Inal and Dubau [18] for ions excited by an electron beam. It was derived for the lithiumlike line

q $(1s2s(^3S)2p\ ^2P_{3/2} \rightarrow 1s^2 2s\ ^2S_{1/2})$, which is analogous to Ly-α_1 for hydrogenlike ions, for x rays observed at 90° to the electron beam. Line q and Ly-α_1 are both E1 (elecric dipole), J=3/2→1/2 transitions. Because the magnetic sublevel populations are energy dependent, the theoretical value P for Ly-α_1 varies from 0.363 near the excitation threshold of the Ly-α lines at 7.025 keV to 0.250 at 20 keV; the corresponding variation of $W_{\mathrm{Ly}-\alpha 1}$ is from 1.99 to 1.86.

IV. RESULTS

The observed value of B, i.e., the ratio of Ly-α_2 to Ly-α_1, is shown in Fig. 2. The error bars shown reflect the uncertainties associated with determining the relative line intensities given that the two lines are not fully resolved in the observations because of the Lorenztian-shaped wings at the base of each line.

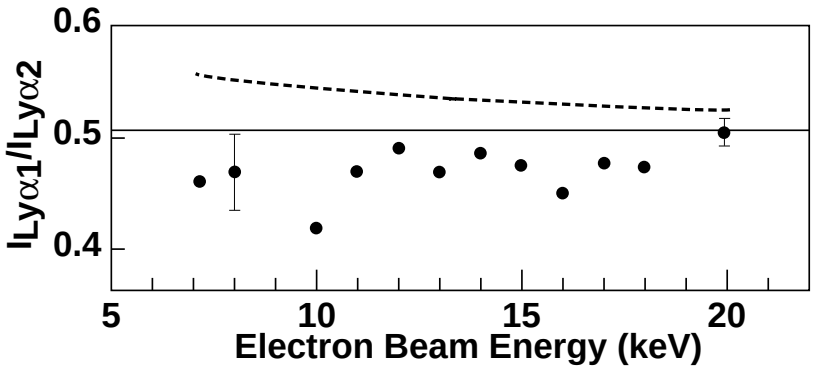

FIG. 2. Dependence of the measured Ly-α_2 to Ly-α_1 ratio on beam energy. Theoretical predictions based on direct electron-impact excitation with and without including the $2s \rightarrow 1s$ magnetic dipole transition are shown as dashed and solid lines, respectively. The predictions do not include polarization effects.

Also shown in Fig. 2 is the ratio of B that results from direct electron-impact excitation of the $2p_{1/2}$ and $2p_{3/2}$ of the $1s$ ground state. From statistical considerations, i.e., excitation to a $j = 3/2$ versus a $j = 1/2$ electron, we expect this ratio to be 0.50. It is slightly higher due to relativistic effects. No polarization effects are accounted for in this prediction. The theoretical ratio is even larger when adding the contribution of the unresolved $2s \rightarrow 1s$ magnetic dipole transition, which enhances the effective intensity of the Ly-α_2 line. Figure 2 shows that the measured value of B is clearly smaller than the predicted values without

polarization.

In Fig. 3 we add polarization effects to the theoretical B ratio. The positive polarization of Ly-α_1 enhances the intensity relative to Ly-α_2 (and the $2srightarrow1s$ contribution) resulting in a smaller value of B. We calculated that B changes by only 4% when the reflectivity of the crystal, $\frac{R_\perp}{R_\parallel}$, is varied by 25% between the upper (0.675) and lower (0.525) limits. The value we use in the calculations is 0.606. The figure shows that now the measured values of B are larger than predicted.

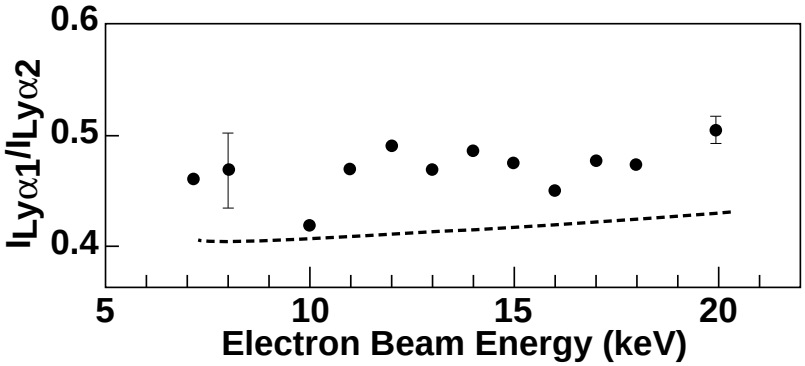

FIG. 3. Comparison of the measured Ly-α_2 to Ly-α_1 ratio with theoretical predictions based on direct electron-impact excitation, including the $2s \rightarrow 1s$ magnetic dipole transition, and polarization effects.

This is the same result Nakamura et al. [8] found in their analysis of the Lyman lines of Ti^{21+}. Clearly, if the polarization of Ly-α_1 was only two-thirds of the predicted values, the theoretical B ratios would have passed through the observations. This is exactly what Nakamura et al. [8] found.

This is however not the end of the story. The lines are not only excited by direct electron-impact collisions. They are also fed by radiative cascades and radiative recombination of beam electrons with bare ions. These effects were studied by Nakamura et al. and found not to change the results significantly. We agree that these effects do not significantly change the predicted unpolarized B value. However, radiative cascades have the effect of depolarizing Ly-α_1 by about 10We have included cascades from levels up to n=5. The primary cascade contributions to Ly-α_2 and Ly-α_1 come from the n=3 levels, while the M1 transition has contributions from n=2, 3, 4, and 5. For example, at an electron beam energy of 12.5 keV cascades are predicted to contribute 7%, 15.8%, and 6.3% to the observed intensity of Ly-α_2, M1, and Ly-α_1, respectively.

The comparison of the theoretical ratios including radiative cascades with the observa-

tions are shown in Fig. 4. The agreement between theory and measurement is improved, but still not perfect.

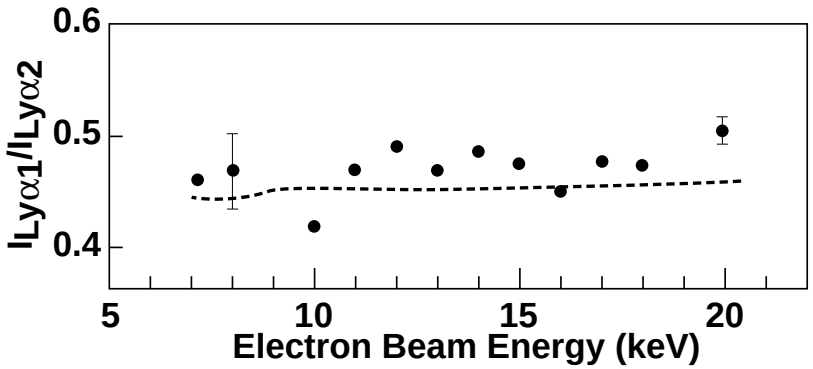

FIG. 4. Comparison of the measured Ly-α_2 to Ly-α_1 ratio with theoretical predictions based on direct electron-impact excitation, radiative cascades from levels $n \leq 5$, blending with the $2s \rightarrow 1s$ magnetic dipole transition, and polarization effects.

V. CONCLUSION

We have measured the ratio of Ly-α_2 and Ly-α_1 as a function of electron beam energy from threshold to 2.5 times threshold. The results are compared to theoretical predictions of B, which includes the polarization, the M1 contributions, and cascades. We find that the measured value of B is larger than predicted. If the polarization of Ly-α_1 was about 20 % less than predicted, good agreement would have been achieved. Our results that agree qualitatively with those obtained by Nakamura et al. [8], who studied the Lyman lines in hydrogenlike titanium.

ACKNOWLEDGMENTS

We wish to thank E. Magee and D. Nelson for their technical assistance in these measurements. This work was performed under the auspices of the U. S. Department of Energy by Lawrence Livermore National Laboratory under contract No. W-7405-ENG-48.

---

[1] R. Beier, C. Bachmann, and R. Burhenn, J. Phys. D **14**, 643 (1981).

[2] J. C. Kieffer, J. P. Matte, H. Pépin, M. Chaker, Y. Beaudoin, T. W. Johnston, C. Y. Chien, S. Coe, G. Mourou, and J. Dubau, Phys. Rev. Lett. **68**, 480 (1992).

[3] R. Novick, Space Science Rev. **18**, 389 (1975).

[4] Ebehard Haug, Sol. Phys. **61**, 129 (1979).

[5] Ebehard Haug, Sol. Phys. **71**, 77 (1981).

[6] Kyo Akita, Katsuo Tanaka, and Tetsuya Watanabe, Sol. Phys. **86**, 101 (1983).

[7] J. M. Laming, Astrophys. J. **357**, 275 (1990).

[8] N. Nakamura, D. Kato, N. Miura, T. Nakahara, and S. Ohtani, Phys. Rev. A **63**, 024501 (2000).

[9] I. C. Percival and M. J. Seaton, Philos. Trans. R. Soc. London **251**, 113 (1958).

[10] E. M. Gullikson, private communication (1990).

[11] M. A. Levine, R. E. Marrs, J. R. Henderson, D. A. Knapp, and M. B. Schneider, Phys. Scr. **T22**, 157 (1988).

[12] R. E. Marrs, M. A. Levine, D. A. Knapp, and J. R. Henderson, Phys. Rev. Lett. **60**, 1715 (1988).

[13] I. G. Brown, J. E. Galvin, R. A. MacGill, and R. T. Wright, Appl. Phys. Lett. **49**, 1019 (1986).

[14] P. Beiersdorfer, R. E. Marrs, J. R. Henderson, D. A. Knapp, M. A. Levine, D. B. Platt, M. B. Schneider, D. A. Vogel, and K. L. Wong, Rev. Sci. Instrum. **61**, 2338 (1990).

[15] W. R. Johnson and G. Soff, At. Data Nucl. Data Tables **33**, 405 (1985).

[16] F. A. Parpia and W. R. Johnson, Phys. Rev. A **26**, 1142 (1982).

[17] H. L. Zhang, D. H. Sampson, and R. E. H. Clark, Phys. Rev. A **41**, 198 (1990).

[18] M. K. Inal and J. Dubau, J. Phys. B **20**, 4221 (1987).

Effect of polarization on the measurements of electron impact excitation cross-section of L-shell Fe in an electron beam ion source

Hui Chen

Department of Physics and Advanced Technologies, Lawrence Livermore National Laboratory, Livermore, CA 94551, U.S.A.

Abstract

The mono-energetic electron beam in an electron beam ion trap excites ions in a preferred direction and this results polarized emission. Polarization affects the line intensity measurement using instruments that collect emission with small solid angle; consequently, it affects the electron excitation cross-section measurements on such an EBIT source. We analyzed quantitatively how large are the various aspects of polarization effects. We considered crystal reflectivity predicted by different models as well as depolarization effects caused by the existence of transverse beam energies. We conclude that the effects of polarization on the excitation cross-sections can be as high as 40% for some of the transitions, and therefore are very important in such measurements.

1. Introduction

Line emission produced by quasistationary ions colliding with electron beam source from an electron beam ion trap (EBIT) is polarized because the electron sources are unidirectional and monoenergetic. Main characteristics of such polarized emission have been described by, for example, Beiersdorfer, et al 1992, 1996 and 1999; Gu et al, 1999. Polarization affects the line intensity measurements using instruments that collect emission with small solid angle; consequently, it affects the electron excitation cross section measurements on such an EBIT source. Based on our measurements of the Fe L-shell excitation cross sections on EBIT-II using both crystal spectrometers and a microcalorimeter, the effects of polarization on the measurements are analyzed quantitatively to demonstrate the importance of such effects.

2. Experimental measurement

Our experiments were carried out on the EBIT-II device (Levine et al. 1988). The instrument setup is shown in Figure 1.

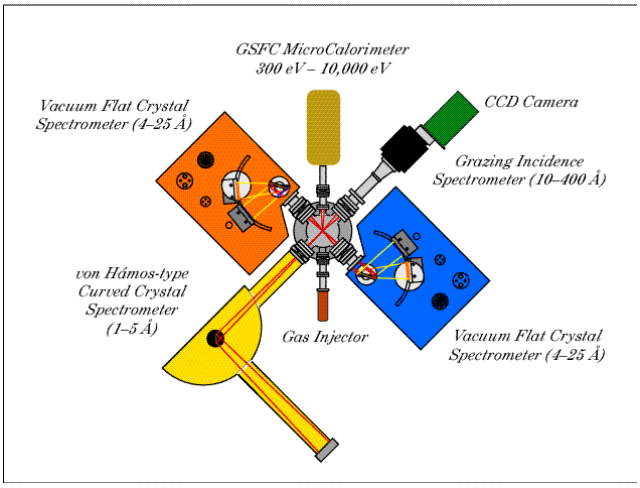

Figure 1: Instrumental setup at EBIT-II. Flat crystal spectrometers and microcalorimeter are used for the measurements discussed in this paper.

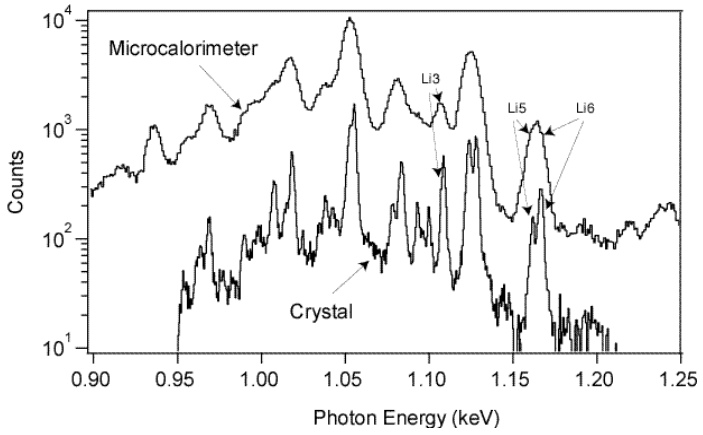

Figure 2: Fe spectra taken by the crystal spectrometer and the microcalorimeter at electron beam energy of 2.1 keV. The three Fe XXIV 3→2 lines marked are: Li3 ($3p_{3/2}\rightarrow 2s_{1/2}$), Li5 ($3p_{1/2}\rightarrow 2s_{1/2}$), and Li6 ($3d_{5/2}\rightarrow 2p_{3/2}$).

In addition to the spare XRS detector, we used the flat-crystal spectrometer described by Brown, Beiersdorfer & Widmann (1999b). The spectrometer employed a 50 mm 25 mm 25 mm thallium acid phthalate crystal at a 26 degree Bragg angle, giving a wavelength coverage from 9.5 Å to 12 Å (0.9 – 1.2 keV). It had a resolving power of 385 (FWHM of 2.6 eV at a photon energy of 1 keV). For comparison, the microcalorimeter (XRS)(Porter et al. 2000) had a bandwidth of 0.3 – 10 keV with moderate resolution: FWHM of about 9 eV at a photon energy of 1 keV. Spectra from both instruments are shown in Figure 2.

This bandwidth allows simultaneous coverage of both Fe L-shell EIE and RR radiation at the electron beam energies used in our experiment (shown in Figure 3). Iron was injected into EBIT-II using a metal vapor vacuum arc source (Brown et al. 1986). The ions were trapped for about five seconds. Then the trap was emptied and filled anew. We chose to analyze only those data collected after ionization equilibrium was reached, i.e., data recorded at least one second after the injection. Measurements were made at three electron beam energies: 2.1, 2.5 and 3.0 keV. The wavelength scale was established using line emission previously measured on EBIT-II (Brown et al. 1999a) and the PLT tokamak (Wargelin et al. 1998).

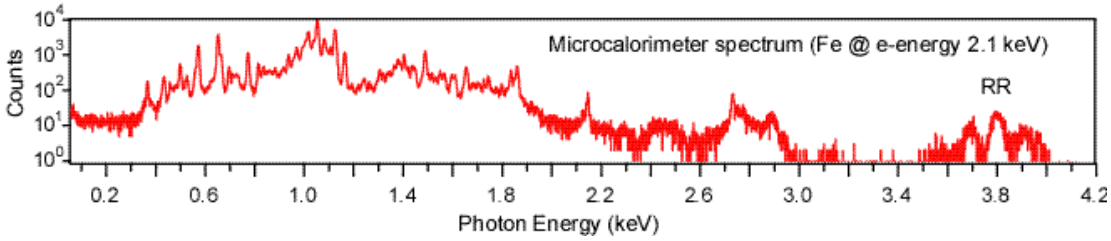

Figure 3: Fe spectrum taken by the microcalorimeter at an electron beam energy of 2.1 keV.

We measured the EIE cross section by directly normalizing the emission line intensities to the radiative recombination (RR) line intensities. For charge-state *i*, the EIE intensity can be described by:

$$I^{EIE} = G^{EIE}(E)\eta^{EIE}T^{EIE}\sigma^{EIE}v_e(E) \quad n_e(r)n_i(r)d^3r \qquad (1)$$

In the case of the micro-calorimeter measurements, *G* represents the effects of the angular distribution of the polarized radiation, η is the quantum efficiency of the detector, and *T* is the filter transmission. σ is the EIE cross section and ν the impact electron velocity. The integral of the electron density n_e and ion density n_i is over the emitting volume seen by each instrument. For the micro-calorimeter, $G = 3/(3 \quad P)$ for electric-dipole transition where *P* is the degree of linear polarization (Beiersdorfer et al, 1996). Among all the parameters, we experimentally measure *I*, η , and *T*. The polarization *P* was calculated using the code of Zhang, Sampson & Clark (1990). We also took into account the depolarizing effect due to transverse beam

energy of ~200 eV. Modification on the polarization parameter due to depolarization is given by (Gu, Savin & Beiersdorfer, 1999b):

$$P = P_0 \frac{1 \quad 3E \,/ 2E}{1 \quad P_0 E \,/ 2E} \qquad (2)$$

Where P_0 is the polarization parameter for an ideal unidirectional beam, E is the transverse energy of the actual beam while E is the total beam energy.

The volume integral needs to be determined by normalizing to the RR intensity.

The RR intensities for each charge state are given by:

$$I^{RR} = \int_j G_j^{RR}(E)\eta_j^{RR} T_j^R \sigma_j^{RR} v_e(E)\ n_e(r) n_i(r) d^3 r \qquad (3)$$

The summation is over the fine structure of a given ion, represented by subscript *j*. For example, in the case of electron capture by Li-like Fe to produce Be-like Fe, the ground state fine structure includes $2s^2{}_{1/2}$ (J=0), $2s_{1/2}2p_{1/2}$ (J=0, J=1), $2s_{1/2}2p_{3/2}$ (J=1, J=2). By measuring the RR and EIE intensity simultaneously with the same instrument, we can eliminate the volume integral and solve for the EIE cross section as:

$$\sigma^{EIE} = \frac{\sum_j G_j^{RR}\eta_j^{RR} T_j^{RR} \sigma_j^{RR}}{G^{EIE}\eta^{EIE} T^{EIE}} \quad \frac{I^{EIE}}{I^{RR}} \qquad (4)$$

However, as illustrated in Figure 1, the XRS could not fully resolve the 3 2 transition lines. As a consequence, we had to rely on the crystal spectrometer to determine the individual EIE line intensities. In this circumstance, the volume integral cannot be eliminated by taking the ratio of Equation (1) and (3) because two separate instruments were used for the RR and the EIE measurements. Instead, we first need to extract the EIE intensity from the crystal data and relate it to that of the micro-calorimeter measurement:

$$I_X^{EIE} = A \ \frac{G_X^{EIE} T_X^{EIE} \eta_X^{EIE}}{G_c^{EIE} T_c^{EIE} \eta_c^{EIE}} I_c^{EIE} \qquad (5)$$

Subscript *c* stands for crystal and *X* for XRS. For the crystal spectrometer, factor *G* includes not only the effect of the angular distribution of the polarized radiation, but also the crystal reflectivity to the polarized radiation (Beiersdorfer et al. 1992 and 1996; Gu et al. 1999a):

$$G_c^{EIE} = \frac{1}{2} R_{//} \ \left(1 + P\right)\Big) + \frac{R}{R_{//}}\left(1 \quad P\right)\div\frac{3}{3 \quad P} \qquad (6)$$

For the crystal reflectivity, we used a value averaged between perfect and mosaic crystals (Henke, Gullikson & Davis 1993). The geometry factor *A* represents the ratio of the plasma volume in the field of the view of the crystal and the micro-calorimeter. We determine this factor by normalizing the intensity of the two Fe XXIV lines $1s^2 3p_{1/2}$ $1s^2 2s_{1/2}$ and $1s^2 3p_{3/2}$ $1s^2 2s_{1/2}$, labeled as Li5 and Li6 in Figure 2. These two lines are well isolated from the other lines and their intensities can be determined accurately.

Figure 4 shows the EIE cross section we measured for various Fe L-shell emission lines.

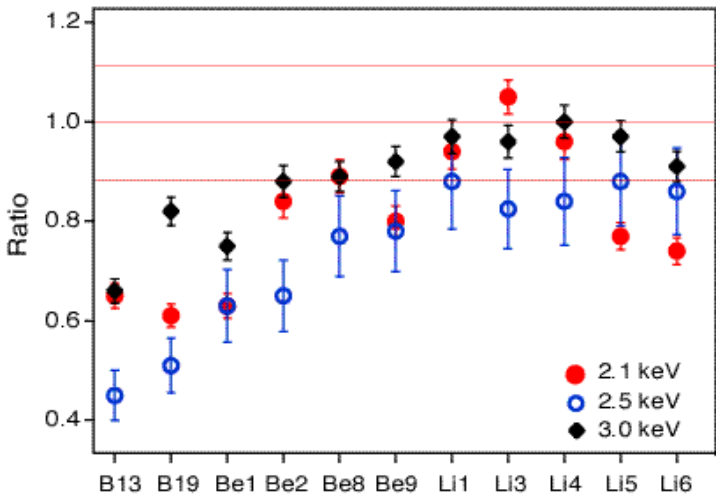

Figure 4: Comparison of EIE cross sections of Fe L-shell lines between present measurements and R-matrix calculations at three electron beam energies.

3. Analysis of the effects of polarization on the EIE cross sections

In order to quantify the effects of polarization on the EIE cross section, we calculated the EIE cross section under different hypothetical conditions. By comparing the changes on the line intensity (which is directly proportional to the EIE cross sections, Equation 4), we can estimate the effect of polarization parameters *G* including the depolarization effect (Equation 2) as well as crystal reflectivity (Equation 6) on the EIE cross section measurements using an EBIT source.

1) If we totally ignore the polarization effect, i. e, set *P*=0, the intensities of electron excitation lines will be altered significantly, as shown in the top curve of Figure 5. As shown in the figure, the changes for each line depend on its degree of polarization: there are no changes for lines Be1, Li1 and Li5 for the lines are not polarized. For Be9 line, the change is over 40%.

2) Two additional factors included in the total polarization effect of the excitation lines are depolarization factor due to the existence of transverse electron beam energy (Equation 2) and crystal reflectivity (Equation 5). If we ignore the depolarization factor, i.e. assume $P=P_0$, we would effectively enhance the polarization effect, as shown in the bottom trace of Figure 5. Similarly, if we assume the crystal has reflectivity $R = R_{//}=1$, i.e. it is not sensitive to polarization, we will have changed on the excitation lines as shown in mid-trace of Figure 5.

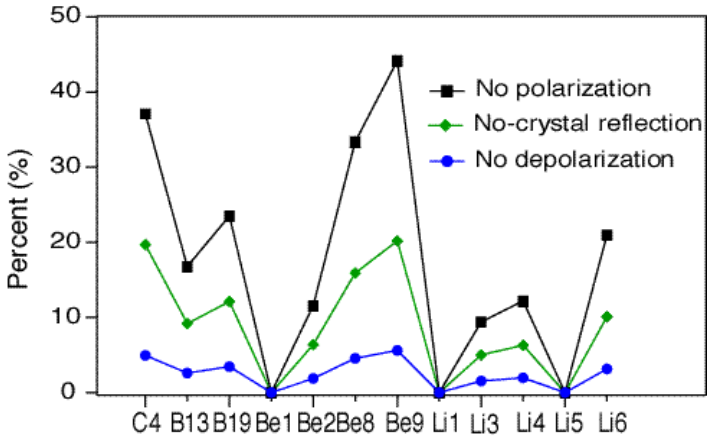

Figure 5. Changes on the Fe L-shell excitation line intensities due to three assumptions: the lines are not polarized (top); crystal reflections are not sensitive to polarization (middle), and the electron beam is perfectly unidirectional (bottom).

More detailed analysis of the crystal reflectivity include using two different model calculations. One calculation is based on an ideal mosaic model for the crystal, and another on a perfect crystal assumption. The actual value for the reflectivity is between the results of the two models, (we used averaged values of the two models in our analysis as shown in Figure 4). The two lower traces of Figure 6 show the change of the excitation lines if we choose each model. It shows that the differences for most lines are less than 5%. This compares to the 10 – 25% change of the line intensities (Figure 6, top curve) if we ignore the reflectivity totally.

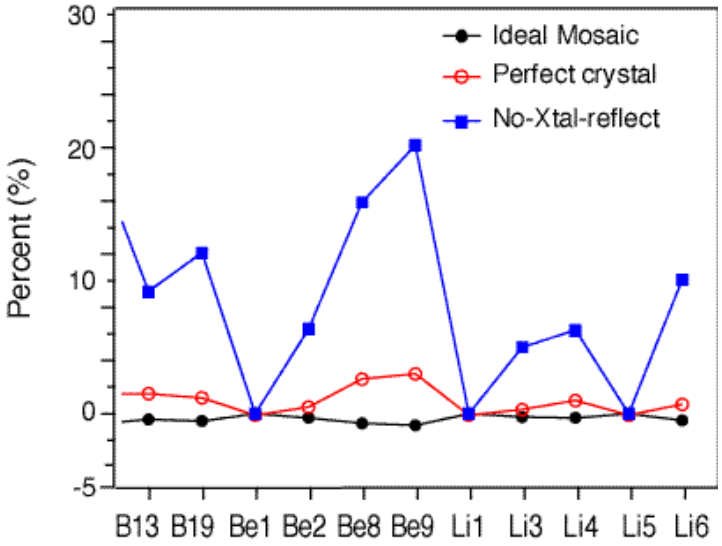

Figure 6. Changes on the Fe L-shell excitation line intensities from crystal reflectivity: crystal reflections are not sensitive to polarization (top); reflectivity using Perfect crystal model, and reflectivity using Ideal Mosaic model (bottom).

3) By converting the polarization effect discussed above to the changes on the EIE cross sections, (as shown in Figure 7 for an electron beam energy of 2.1 keV), we show that for many lines, if we ignore the polarization effects on the excitation lines, the EIE cross sections would be significantly higher than their actual values.

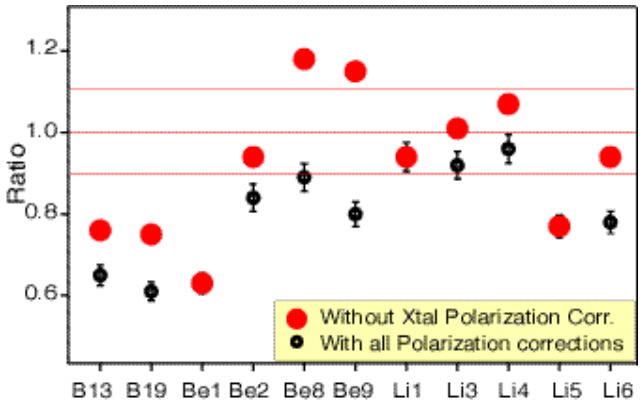

Figure 7. Comparisons of EIE cross section measurements with theory at an electron energy of 2.1keV. Circles with error bars: Polarization considered; Solid dots: the polarization effects ignored.

4) Similarly, we compared the polarization effects on the RR measurements. Because RR was measured using the XRS, G factor includes only the angular distribution of the polarized radiation. Figure 8 shows the changes of the RR line intensities depending two conditions. The upper trace of Figure 8 shows the change of the RR intensities with the condition that polarization effects are ignored. It shows that there is about a 25% change on all the Fe L-shell lines. The lower trace shows that if we do not consider the depolarization factor – there will be about a 5% change of the RR intensities due to this effect for all the lines we measured.

5) Ignoring the polarization effects on the RR measurements for the L-shell lines will result in smaller EIE cross sections than their actual values, as shown in Figure 9. Similar to the case for excitation lines, the changes on the EIE cross sections are significant.

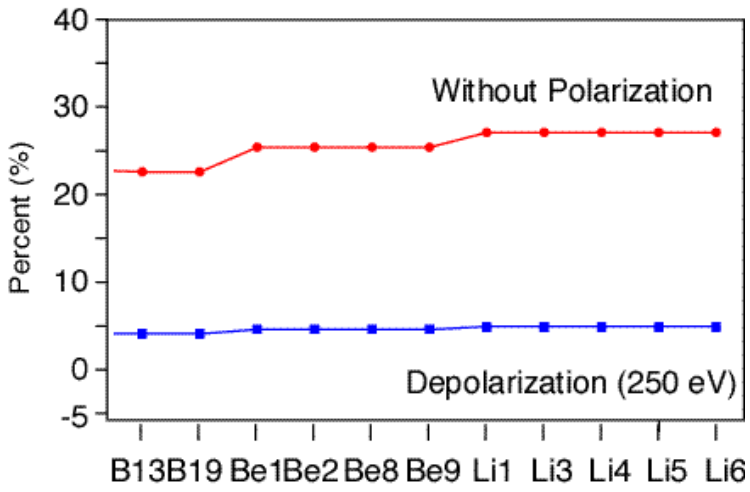

Figure 8. Changes on the RR line intensities from polarization effects: (top) ignore all polarization effects and (bottom) assume perfect unidirectional electron beam, i.e. ignore the depolarization factor.

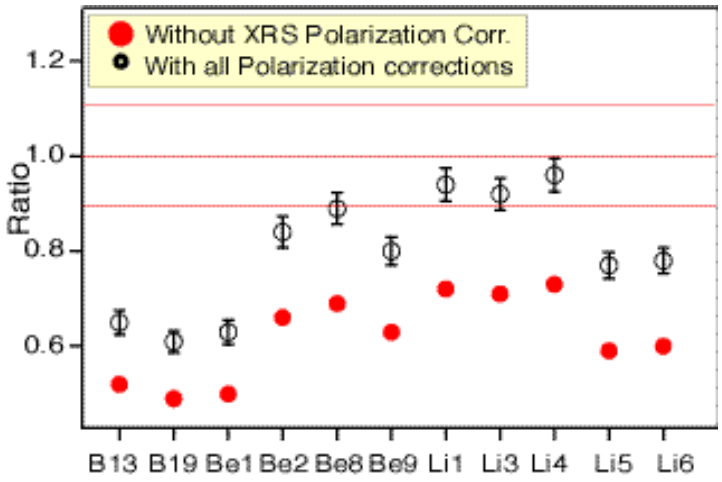

Figure 9. Comparisons of EIE cross section measurements with theory at an electron energy of 2.1keV. Circles with error bars: Polarization considered; Solid dots: the polarization effects ignored.

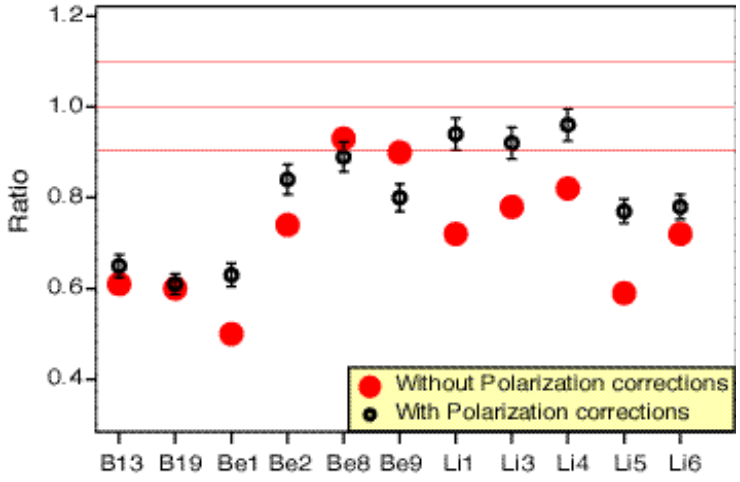

Figure 10. Comparisons of EIE cross section measurements with theory at an electron energy of 2.1keV. Circles with error bars: Polarization considered; Solid dots: the polarization effects on both RR and EIE lines are ignored.

6) The total polarization effects on the EIE cross section measurements are shown in Figure 10. Comparing to Figure 7 and Figure 9, although changes for some lines are reduced in some degree due to the partial cancellation (Equation 4); there are still significant differences present for certain lines relative to their actual value. In summary, based on our analysis, various polarization effects play an important role in the excitation cross section measurements using an EBIT source, and we need to taken them into account in the data analysis.

4. Acknowledgement

This work was performed under the auspices of the U.S. Department of Energy by the University of California, Lawrence Livermore National Laboratory under Contract No. W-7405-Eng-48

Reference

Beiersdorfer, P., Phillips, T. W., Wong, K. L., Marrs, R. E., & Vogel, D. A., 1992, Phys. Rev. A, 46, 3812

Beiersdorfer, P., et al, 1996, Phys. Rev. A. 53, 3974

Brown, G. V., Beiersdorfer, P., Liedahl, D. A., Widmann, K., & Kahn, S. M., 1999a, University of California Lawrence Livermore National Laboratory report No. UCRL-JC-136647.

Brown, G. V., Beiersdorfer, P., & Widmann, K., 1999b, Rev. Sci. Instrum. 70, 280

Brown, I. G., Galvin, J. E., MacGill, R. A., & Wright, R. T., 1986, Appl. Phys. 49, 1019

Gu, M. F., Kahn, S. M., Savin, D. W., Beiersdorfer, P., Liedahl, Brown, G. V., Reed, K. J., Bhalla, C. P., & Grabbe, S. R., 1999a, APJ, 518, 1002

Gu, M. F., Savin, D. W., & Beiersdorfer, P., 1999b, J. Phys. B, 32, 5371

Henke, B. L., Gullikson, K. M. & Davis, J. C., 1993, Atomic Data & Nuclear Data Tables, 54, 181

Levine, M. A., Marrs, R. E., Henderson, J. R., Knapp, D. A., & Schneider, M. B., 1988, Physics Scripta, T22, 157

Porter, F. S., et al, 2000, SPIE 4140, 407

Wargelin, B. J., Beiersdorfer, P., Liedahl, D. A., Kahn, S. M., & von Goeler, S., 1998, APJ 496, 1031

Zhang, H. L., Sampson, D. H., & Clark, R. E. H., 1990, Phys. Rev. A, 41,198

Measurement of the electron cyclotron energy component of the EBIT-II electron beam

Peter Beiersdorfer[1] and Michelle Slater[1,2,†]
[1] *Department of Physics and Advanced Technologies, Lawrence Livermore National Laboratory, Livermore, CA 94551, U.S.A.*
[2] *Spelman College, Atlanta, GA, 30314, U.S.A.*

We used measurements of the linear polarization of the K-shell x-ray lines emitted from heliumlike Mg^{10+} ions to determine the energy component associated with the cyclotron motion of the beam electrons in the EBIT-II electron beam ion trap. The average line polarization was found to be reduced by about 20% from its nominal value. From this we inferred that the electron cyclotron motion accounted for 190 ± 30 eV of the total electron beam energy. The measured value is in good agreement with the predictions of optical electron beam propagation.

I. INTRODUCTION

The electron beam ion trap utilizes a magnetically compressed electron beam to produce, trap, and study essentially any ion from any element of choice [1–3]. Radial slots allow direct, line-of-sight access to the interaction region between the trapped ions and the electron beam. By measuring the radiation produced by the ions excited by the electron beam, cross section determinations for a variety of atomic processes have been possible. Examples are measurements of excitation [4–7], ionization [8,9], and dielectronic recombination [10–15] cross sections.

The use of an electron beam interacting with quasi-stationary ions means that the emitted radiation generally is both anisotropic and polarized [16,17]. As a result, the intensity of a given emission feature from a beam-excited ion depends on the observation angle relative to the axis defined by the electron beam. It also depends on whether or not the emission is analyzed with polarization-sensitive instrumentation.

Adjustments for polarization effects in electron beam ion trap experiments are not without complications. One reason is that a given electron in the electron beam does not simply travel in the direction of beam propagation. Its path instead traces out a helix, as it spirals around the magnetic field lines aligned with the beam propagation axis. Ions, therefore, interact with electrons with velocity vectors that deviate from that of the beam direction. The net result is that the amount of polarization is reduced from what it would be, if all electrons were truly following a straight line along the magnetic field direction.

The amount of depolarization depends on the pitch angle of the electron motion, i.e., on the angle γ between the magnetic field line and electron's velocity vector. This angle is

---

[†]Deceased

determined by the ratio of the electron's velocity component along the magnetic field line and that perpendicular:

$$\tan\gamma = \frac{v_\perp}{v_\parallel} \tag{1}$$

or,

$$\sin\gamma^2 = \frac{E_\perp}{E_{beam}} \tag{2}$$

where E_{beam} is the beam energy and $E_\perp$ is the electron energy in the motion perpendicular to the beam propagation direction. A simple expression that describes the reduction in the polarization of the emitted radiation as a function of the pitch angly was recently given by Gu, Savin, and Beiersdorfer [19]. For electric dipole radiation they showed that the polarization P is reduced to

$$P = P_0 \frac{2 - 3\sin\gamma^2}{2 - \sin\gamma^2 P_0}. \tag{3}$$

Here P_0 is the polarization for a zero pitch angle.

The perpendicular velocity component can be estimated from several considerations. Using the Herrmann theory of optical electron beam propagation we estimated 110 eV for the value of $E_\perp$ in Livermore's EBIT-II electron beam ion trap [20]. Independently, Takács *et al.* estimated a value of 700 eV for the NIST electron beam ion trap using the theory of rigid beam rotation [21]. They estimated an even higher value ($\leq$ 1000 eV) based on the principle of adiabatic magnetic flux invariance.

The large spread in estimates clearly make a measurement of the perpendicular energy component highly desirable in order to discriminate among the models. In the following we employ the techniques of plasma polarization spectroscopy for determining $E_\perp$. Plasma polarization spectroscopy has already been applied to tokamak, solar, and laser-produced plasmas for determining non-equilibrium components of the electron distribution function [25–27]. Our measurement favors the prediction based on the Herrmann theory of optical electron beam propagation, giving a value of 190 $\pm$ 30 eV for $E_\perp$.

II. EXPERIMENT

The measurement is carried out on the EBIT-II electron beam ion trap using the vacuum flat-crystal spectrometer described in [28]. The instrument is mounted on one of six ports viewing the ions in the trap in the direction perpendicular to the beam. The plane of dispersion is parallel to the plane perpendicular to the beam direction, as illustrated in Fig. 1. The opening angle of the detector in the vertical direction is less than 0.8°. This is sufficiently small as to provide a reliable sample of radiation emitted at 90° to the beam propagation direction.

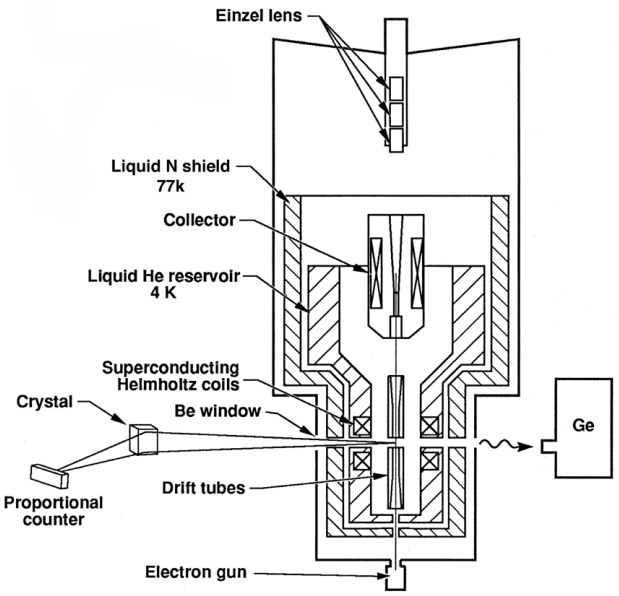

FIG. 1. Layout of the flat-crystal spectrometer on the EBIT-II electron beam in trap. Ions are produced and trapped in a 2-cm long region between the superconducting Helmholtz coils. The ions are excited by an electron beam propagating between the electron gun and the collector. X rays are monitored via the radial ports in the vacuum vessel and are analyzed and dispersed with the crystal spectrometer in the plane perpendicular to the propagation direction of the electron beam.

The spectrometer utilizes a thallium-acid-phtalate crystal (TlAP) with a lattice spacing $2d = 25.76$ Å. This crystal is well suited to record the K-shell x-ray lines of heliumlike spectrum Mg^{10+} and study the effect of polarization. The Mg^{10+} spectrum is centered around 9.25 Å. In first order Bragg reflection, the observation angle is 21.4°. In second order, the observation angle is 45.2°. In the latter position, only the emission component with electric field vector parallel to the plane of the crystal (and parallel to the electron beam propagation) is reflected and counted. In the former position, a mixture of both polarization components are reflected and counted. The present measurement utilizes the differences in the crystal response at these two Bragg angles to determine the polarization of the observed lines. The present method is similar to the two-crystal method employed in earlier measurements on the EBIT-II and SuperEBIT electron beam ion traps [20,29–32].

The observed Mg^{10+} lines comprise the $1s2p\ ^1P_1 \rightarrow 1s^2\ ^1S_0$ resonance line, the blend of the $1s2p\ ^3P_1 \rightarrow 1s^2\ ^1S_0$ intercombination line and the $1s2p\ ^3P_2 \rightarrow 1s^2\ ^1S_0$ magnetic quadrupole line, and the $1s2s\ ^3S_1 \rightarrow 1s^2\ ^1S_0$ forbidden line, which are commonly labeled w, y, x, and z, respectively.

We have chosen the lines in heliumlike magnesium for determining the amount of depolarization because the polarization P_0 of these lines in the absence of depolarization effects is well known from theory and experiment. The polarization of lines w and x is within a few percent the same for all low- and mid-Z heliumlike ions at similar electron-collision energies expressed in threshold units [33,34]. Within a few percent above excitation threshold the polarization of w and x is $P_0(w) = 0.60$ and $P_0(x) = -0.52$, respectively. The accuracy of these calculations have been experimentally verified for several heliumlike ions [20,32,35].

The value of the polarization of x determines the value of the polarization of z. In magnesium, the $1s2p\ ^3P_2$ upper level of x decays 93% of the time to the $1s2s\ ^3S_1$ upper level of z. Following the expression derived in [20], the polarization $P_0(z)$ of z in terms of the polarization $P_0(x)$ of x is

$$P_0(z) = +\frac{3kP_0(x)}{3\sqrt{5/7} - P_0(x)(\sqrt{5/7} + k)}. \tag{4}$$

The factor k is proportional to the fractional excitation of z by cascades from the $1s2p\ ^3P_2$ level [20]. It was shown in [32] to depend only on the branching ratio β_r for radiative decay of the $1s2p\ ^3P_2$ level to the $1s2s\ ^3S_1$ level. For $\beta_r = 0.93$ [36] we find $k = 0.377$.

Another reason to pick heliumlike magnesium for determining the amount of depolarization is that the atomic number of magnesium is low enough so that LS-coupling is valid. This eliminates the uncertainty in ascertaining the polarization of line y, as the $1s2p\ ^3P_1$ upper level of y mixes only negligibly with the $1s2p\ ^1P_1$ upper lever of w. The polarization of y, therefore, equals that of x, and the unresolved blend of y and x has the same polarization as x or y alone.

The spectrum of the magnesium Kα transitions recorded with the TlAP crystal in first order is shown in Fig. 2(a). The spectrum recorded in second order is shown in Fig. 2(b). The second order spectrum has considerably higher resolution than the first order spectrum. This is expected from the higher intrinsic resolving power of the crystal in second order Bragg reflection and the fact that the resolving power increases with the tangent of the Bragg angle. The data were accumulated at a beam energy that was about 50 eV above threshold for direct excitation of the lines of interest, avoiding the above-threshold KMM resonances.

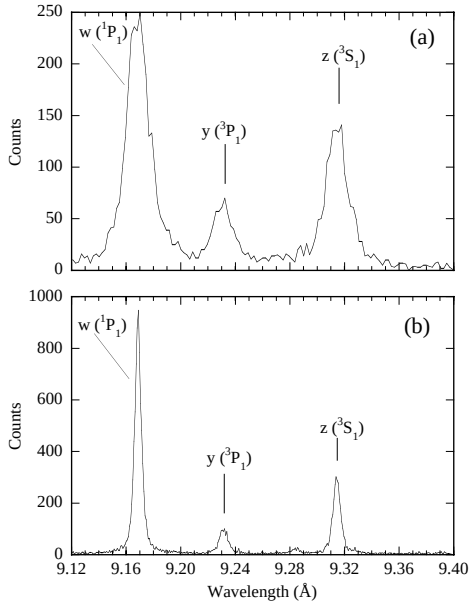

FIG. 2. Crystal-spectrometer spectra of lines w, x, y, and z in Mg^{10+} excited by a 1400-eV electron beam. (a) spectrum obtained with a TlAP crystal in first order reflection at a Bragg angle of 21^o; (b) spectrum obtained with the same crystal in second order reflection at a Bragg angle of 45^o.

III. ANALYSIS

The relative intensities of the heliumlike lines shown in Fig. 1 are clearly different in the two spectra. To obtain a quantitative measure of the intensity of each feature we used least-squares fits of different trial functions to the line: a single Gaussian, a double Gaussian, a Lorenztian, and a mixture of a Lorentzian and a Gaussian trial function. The double trial functions are used to fit the rather narrow peak and the rather wide base of the lower-resolution spectrum obtained in first order Bragg reflection. The intensities determined from the fits with these trial functions are listed in Table I.

The fits with the double trial functions gave much better fits then those with a single function. The use of a Lorenztian function (either alone or in combination with a Gaussian) was somewhat problematic, because the inherently broad tails are poorly constrained and may readily lead to spurious results. This is true even if the residuals intimate an excellent fit. Because of their extensive tails, the fits involving a Lorentzian function result in considerably higher line intensities than using only Gaussian functions.

The intensities in Table I are used to infer the polarization of a given line relative to the polarization of second line. As shown in [32], we can express the polarization P_a of line a in terms of the polarization P_b of line b:

$$P_a = \frac{\frac{I^a}{I^b}|_1(1+R_1\frac{1-P_b}{1+P_b})(R_2+1) - \frac{I^a}{I^b}|_2(1+R_2\frac{1-P_b}{1+P_b})(R_1+1)}{\frac{I^a}{I^b}|_1(1+R_1\frac{1-P_b}{1+P_b})(R_2-1) - \frac{I^a}{I^b}|_2(1+R_2\frac{1-P_b}{1+P_b})(R_1-1)}. \tag{5}$$

Here I^a/I^b is the intensity ratio of lines a and b. The subscripts refer to the order of Bragg reflection in which the ratio is measured. $R = R_\perp/R_{||}$ is the ratio of the integrated crystal reflectivities for x rays polarized perpendicular and parallel to the electron beam directions, i.e., parallel and perpendicular to the plane of dispersion, respectively. Again, the subscripts refer to the order of Bragg reflection. The values of R are taken from [37]: $R_1 = 0.605$ and $R_2 = 0.004$.

Using the iterative procedure described in [32] and the fact that the polarization of z is completely determined by the polarization of x (and thus of y), we can determine the polarizations of all lines from the data in Table I. The results are given in Table II.

TABLE I. Intensities of the heliumlike lines w, $x+y$, and z measured in first and second order with a TlAP crystal obtained with different trail functions.

Line	Single Gaussian		Double Gaussian		Lorentzian+Gaussian		Single Lorenztian	
	1st	2nd	1st	2nd	1st	2nd	1st	2nd
w	2750	7672	2820	7814	3137	8331	3168	8586
x+y	708	1066	707	991	679	1078	679	1168
z	1487	2724	1567	2830	1720	3069	1761	3230

TABLE II. Polarization inferred from the data in Table I. Also listed are the polarization values for an electron beam without a perpendicular component of electron motion.

Line	Single Gaussian	Double Gaussian	Lorentzian+Gaussian	Single Lorenztian	Theory
w	0.46	0.55	0.61	0.64	0.614
x+y	-0.40	-0.37	-0.205	-0.13	-0.519
z	-0.15	-0.14	-0.083	-0.055	-0.185

The polarization values inferred from the four different fitting procedures show interesting trends. The inferred polarization of w increases from $P = 0.46$ to $P = 0.64$ when considering the single and double Gaussian fits, the Gauss-Lorentzian fit, and the single Lorentzian fit. The value inferred from the Lorentzian fit is larger than that predicted by theory, and thus is unphysically large. Similarly, the inferred polarizations of the blend of the intercombination lines x and y steadily increase from $P = -0.40$ inferred from the single-Gaussian fit to $P = -0.13$ inferred from the single Lorentzian fit. The inferred polarizations of the forbidden line z steadily increase from $P = -0.15$ to $P = -0.055$. The result is that the fits involving a Lorentzian function show a strong depolarization of lines x, y, and z, while they show that line w experiences no depolarization or even an increase in its polarization value. The results inferred from fits involving Lorenztian functions are, thus, highly contradictory. By contrast, the polarization values derived from fitting Gaussian functions to the data are self-consistent. All three line features show similar amounts of depolarization.

By comparing the polarization values inferred from the line intensities in Tabel I to those predicted by theory (listed in the last column of Table II), we can determine the amount of depolarization and thus $E_\perp$. Solving Eq. (3) for $E_\perp$, we get

$$E_\perp = \frac{2(P_0 - P_i)}{P_0(3 - P_i)} E_{beam}, \tag{6}$$

where i refers to lines w, $x + y$, and z. The resulting values are listed in Table III.

TABLE III. Values of $E_\perp$ inferred from the data in Table II.

Line	Single Gaussian	Double Gaussian	Lorentzian+Gaussian	Single Lorenztian
	eV	eV	eV	eV
w	277	100	4	-35
x+y	165	229	956	1920
z	154	217	931	1880

The internal inconsistency of the data inferred from the Lorentzian fits is even better seen in when looking at the $E_\perp$ values listed in Table III: The $E_\perp$ values derived for w range from a non-physical -35 eV to $+4$ eV; those derived for the other features range from $+931$ to $+1920$ eV. These inconsistencies arise from the poor constraint on the wide wings afforded by the Lorentzian trial function.

By contrast the Gaussian fits give $E_\perp$ values that range from 100 to 277 eV for w, and from 154 to 229 eV for the three triplet lines. The results are plotted in Fig. 3. These results are clearly consistent with each other. In fact, the results strongly suggest that a fitting function might exist for which all three features yield the same value of $E_\perp$. The average value of $E_\perp$ is 190 ± 30 eV.

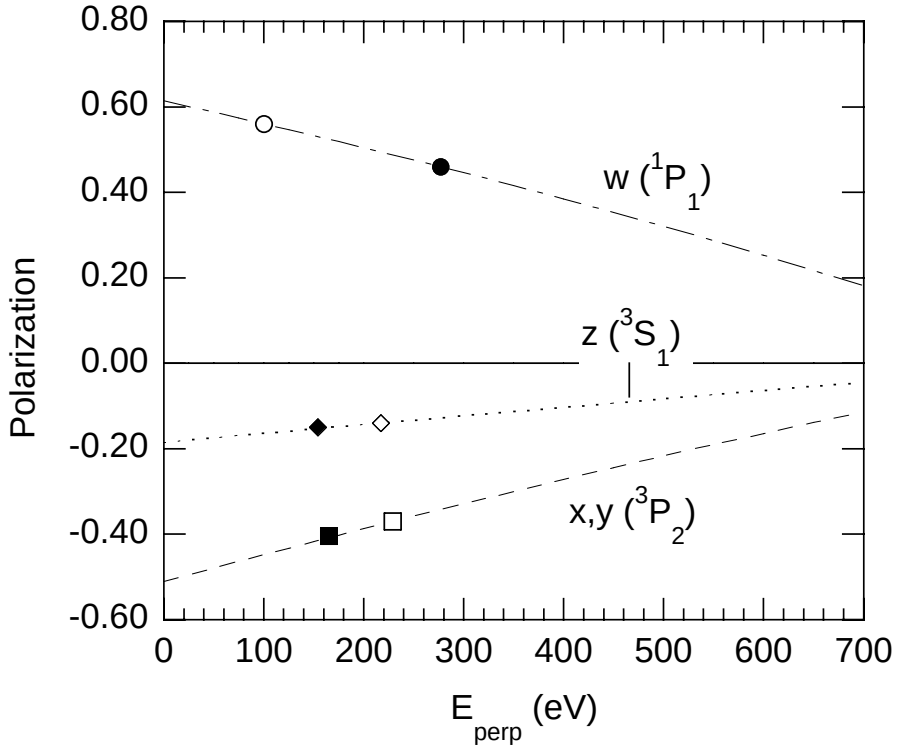

FIG. 3. Dependence of the linear x-ray polarization of lines w, x, y, and z of Mg^{10+} on the size of the electron energy component perpendicular to the beam propagation direction. The total beam energy is set to 1400 eV. Measured values are shown for spectral data analyzed with single Gaussian (solid symbols) and double Gaussian (open symbols) trial function fits.

IV. DISCUSSION

Our result of $E_\perp = 190 \pm 30$ eV is in agreement with the predictions of the optical approach by Herrmann [38]. Herrmann showed that cathode images are formed at various locations along the beam axis, whereby the magnitude of the transverse velocity is inversely proportional to the radii of the images. This means that the product of beam area and tranverse electron energy $E_\perp$ is a constant. $E_\perp$ can thus be estimated from the temperature of the cathode of the electron gun and the areal compression ratio of the beam. The gun

temperature is about 1400 K (0.123 eV), and the beam radius at the cathode is about 1 mm. The beam is compressed to about 25 μm in the trap. Using these values, we obtain $E_\perp = 194$ eV, in full agreement with our measurements. These values, however, are only estimates; they are not well known. But the answer shows that consistency with our measurements can readily be achieved. The temperature of the filament may vary between 1000 to 1600 K, depending on the filament heating current. Similarly, the radius of the electron beam may vary between 25 to 35 μm, depending on such parameters as the beam current and bucking coil setting. As a result, the value of $E_\perp$ predicted by the Herrmann theory may vary between 50 to 250 eV. The estimate of 110 eV provided in [20] falls well within this range.

Our measured value does not agree with the 700-eV prediction provided by the rigid rotator approach employed by Takács et al. to describe the electron beam ion trap at NIST [21]. The rigid rotator approach assumes a uniform electron density within a cylindrical volume [39]. Such an idealized situation is not realized in an electron beam ion trap. Not only are there gradients in the radial electron density, there are strong gradients along the electron beam direction. The magnetic field of the Helmholtz coils is uniform only throughout a relatively small length within the trap region (about 4 cm). The magnetic field, and thus the beam radius and electron density, are highly nonuniform for remaining $\geq 95\%$ of the beam path. There is no reason why the rigid rotor model should be applicable, and our measurements bear this out. The strong magnetic field gradients (from essentially zero field at the gun to 30,000 gauss in the trap) that are traversed by fast moving electrons also invalidate applicability of the principle of adiabatic magnetic flux invariance.

Our measurements provide strong support for the optical beam transport theory derived by Herrmann [38]. This is comforting, as the Herrmann theory was used as one of the underlying principles in the design the electron beam ion trap [1]. The Herrmann theory yields a good upper bound of the energy in the electron cyclotron motion, and thus provides an upper bound on the amount of depolarization of the emitted radiation.

ACKNOWLEDGMENTS

This work was performed by the University of California Lawrence Livermore National Laboratory under the auspices of the Department of Energy under contract W-7405-ENG-48. It was supported by the Office of Basic Energy Sciences, Division of Chemical Physics. Additional support from the Livermore Collaborations Program for Historically Black Colleges and Universities is gratefully acknowledged.

---

[1] M. A. Levine, R. E. Marrs, J. R. Henderson, D. A. Knapp, and M. B. Schneider, Phys. Scripta **T22**, 157 (1988).

[2] M. A. Levine, R. E. Marrs, J. N. Bardsley, P. Beiersdorfer, C. L. Bennett, M. H. Chen, T. Cowan, D. Dietrich, J. R. Henderson, D. A. Knapp, A. Osterheld, B. M. Penetrante, M. B. Schneider, and J. H. Scofield, Nucl. Instrum. Methods **B43**, 431 (1989).

[3] R. E. Marrs, P. Beiersdorfer, and D. Schneider, Phys. Today **47**, 27 (1994).
[4] S. Chantrenne, P. Beiersdorfer, R. Cauble, and M. B. Schneider, Phys. Rev. Lett. **69**, 265 (1992).
[5] P. Beiersdorfer, in *Electron and Atomic Collisions – XVII ICPEAC, Brisbane, 1991*, ed. by W. R. MacGillivray, I. E. McCarthy, and M. C. Standage (Adam Hilgar, Bristol, 1992), p. 313.
[6] K. L. Wong, P. Beiersdorfer, K. J. Reed, and D. A. Vogel, Phys. Rev. A **51**, 1214 (1995).
[7] M.F. Gu, S. M. Kahn, D. W. Savin, P. Beiersdorfer, G. V. Brown, D. A. Liedahl, K. J. Reed, C. P. Bhalla, and S. R. Grabbe, Astrophys. J. **518**, 1002 (1999).
[8] K. Wong, P. Beiersdorfer, M. H. Chen, R. E. Marrs, K. J. Reed, J. H. Scofield, D. A. Vogel, and R. Zasadzinski, Phys. Rev. A **48**, 2850 (1993).
[9] R. E. Marrs, S. R. Elliott, and J. H. Scofield, Phys. Rev. A **56**, 1338 (1997).
[10] P. Beiersdorfer, T. W. Phillips, K. L. Wong, R. E. Marrs, and D. A. Vogel, Phys. Rev. A **46**, 3812 (1992).
[11] P. Beiersdorfer, M. B. Schneider, M. Bitter, and S. von Goeler, Rev. Sci. Instrum. **63**, 5029 (1992).
[12] D. A. Knapp, R. E. Marrs, M. B. Schneider, M. H. Chen, M. A. Levine, and P. Lee, Phys. Rev. A **47**, 2039 (1993).
[13] A. J. Smith, P. Beiersdorfer, V. Decaux, K. Widmann, K. J. Reed, and M. H. Chen, Phys. Rev. A **54**, 462 (1996).
[14] A. J. Smith, P. Beiersdorfer, K. Widmann, M. H. Chen, and J. H. Scofield, Phys. Rev. A **62**, 052717 (2000).
[15] B. J. Wargelin, S. M. Kahn, and P. Beiersdorfer, Phys. Rev. A **63**, 022710 (2001).
[16] J. R. Oppenheimer, Z. Phys. **43**, 27 (1927).
[17] I. C. Percival and M. J. Seaton, Philos. Trans. R. Soc. London **A251**, 113 (1958).
[18] H. G. Berry, L. J. Curtis, D. G. Ellis, and R. M. Schectman, Phys. Rev. Lett. **32**, 751 (1974).
[19] M.-F. Gu, D. W. Savin, and P. Beiersdorfer, J. Phys. B **32**, 5371 (1999).
[20] P. Beiersdorfer, D. A. Vogel, K. J. Reed, V. Decaux, J. H. Scofield, K. Widmann, G. Hölzer, E. Förster, O. Wehrhan, D. W. Savin, and L. Schweikhard, Phys. Rev. A **53**, 3974 (1996).
[21] E. Takács, E. S. Meyer, J. D. Gillaspy, J. R. Roberts, C. T. Chandler, L. T. Hudson, R. D. Deslattes, C. M. Brown, J. M. Laming, J. Dubau, and M. K. Inal, Phys. Rev. A **54**, 1342 (1996).
[22] J. D. Gillaspy, Physica Scripta **T71**, 99 (1997).
[23] E. Träbert, P. Beiersdorfer, and S. B. Utter, Phys. Scripta **T80**, 450 (1999).
[24] P. Beiersdorfer, J. K. Lepson, G.V. Brown, S. B. Utter, S.M. Kahn, D.A. Liedahl, and C. W. Mauche, Astrophys. J. **519**, L185 (1999).
[25] T. Fujimoto, T. Kawachi, T. Kallstenius, M. Goto, H. Kawase, T. Furukubo, T. Maekawa, and Y. Terumichi, Phys. Rev. E **54**, R2240 (1996).
[26] E. Haug, Solar Phys. **71**, 77 (1981).
[27] H. Yoneda, N. Hasegawa, S. Kawana, and K. Ueda, Phys. Rev. E **56**, 988 (1997).
[28] P. Beiersdorfer and B. J. Wargelin, Rev. Sci. Instrum. **65**, 13 (1994).
[29] P. Beiersdorfer, J. Crespo López-Urrutia, V. Decaux, K. Widmann, and P. Neill, Rev. Sci. Instrum. **68**, 1073 (1997).
[30] A. S. Shlyaptseva, R. C. Mancini, P. Neill, P. Beiersdorfer, J. Crespo López-Urrutia, and K. Widmann, Phys. Rev. A **57**, 888 (1998).

[31] A. S. Shlyaptseva, R. C. Mancini, P. Neill, and P. Beiersdorfer, J. Phys. B **32**, 1041 (1999).
[32] P. Beiersdorfer, G. Brown, S. Utter, P. Neill, K. J. Reed, A. J. Smith, and R. S. Thoe, Phys. Rev. A **60**, 4156 (1999).
[33] Y. Itikawa, R. Srivastava, and K. Sakimoto, Phys. Rev. A **44**, 7195 (1993).
[34] K. J. Reed and M. H. Chen, Phys. Rev. A **48**, 3644 (1993).
[35] J. R. Henderson, P. Beiersdorfer, C. L. Bennett, S. Chantrenne, D. A. Knapp, R. E. Marrs, M. B. Schneider, K. L. Wong, G. A. Doschek, J. F. Seely, C. M. Brown, R. E. LaVilla, J. Dubau, and M. A. Levine, Phys. Rev. Lett. **65**, 705 (1990).
[36] C. D. Lin, W. R. Johnson, and A. Dalgarno, Phys. Rev. A **15**, 154 (1977).
[37] B. L. Henke, E. M. Gullikson, and J. C. Davis, At. Data Nucl. Data Tables **54**, 181 (1993).
[38] G. Herrmann, J. Appl. Phys. **29**, 127 (1958).
[39] N. A. Krall and A. W. Trivelpiece, *Principles of Plasma Physics*, (McGraw-Hill, New York, 1973), p. 117.

X-ray spectropolarimetry studies at the Nevada Terawatt Facility and LLNL EBIT

A.S. Shlyaptseva, V.L. Kantsyrev, B.S. Bauer, P. Neill, C.Harris, D.A. Fedin, S. Hansen, N. Ouart
(University of Nevada, Reno, USA)

P. Beiersdorfer
(*LLNL, USA*)

A.G. Petrashen
(*IFMO, Russia*)

U. I. Safronova
(*University of Notre Dame, USA*)

Abstract

Recent results from x-pinches at the NTF provide experimental evidence for the existence of strong electron beams in x-pinch plasmas and motivate the development of a new diagnostic, x-ray spectropolarimetry, for investigating the anisotropy of such plasmas. This diagnostic is based on theoretical modeling of polarization-dependent spectra measured simultaneously by spectrometers with different sensitivity to polarization. Results of the first polarization-sensitive experiments at the NTF are presented. K-shell emission from Ti x-pinches is recorded simultaneously by two identical spectrometers with the dispersion plane perpendicular and parallel to the discharge axis. The spectroscopic analysis of more than eight Ti x-pinch shots show how spectropolarimetry complements the usual diagnostics of a z-pinch plasma. The polarization-sensitive spectra, generated by a Maxwellian electron beam at LLNL EBIT have been collected and analyzed. These data make an important contribution to the plasma polarization spectroscopy program at the NTF. In particular, the study of multiply-charged Ti ion spectra help in the interpretation of the polarization-sensitive spectra from Ti x-pinches at the NTF.

I. K-shell x-ray spectropolarimetry of Ti x-pinch plasma at the NTF.

The first polarization-sensitive experiments at the Nevada Terawatt Facility (NTF) have been preformed and prove that the best object for the x-ray spectropolarimetry of high-density plasma is x-pinch plasma. The core of the NTF is a Zebra z-pinch with a maximum voltage 2 MV, a current 1.2 MA, a rise time 100 ns, and a maximum Marx generator energy of 200 kJ (formerly the HDZP-II z-pinch facility at LANL). A x-pinch produces a bright, small-sized x-ray source, with a well-defined location. It can yield x-ray spectra of numerous ions with very high resolution. X-pinches are made by positioning two thin, straight, crossed wires between the cathode and anode of the Zebra pulsed-power generator, with a wire contact at the axis of the cathode-anode gap. Two typical configurations of x-pinches were tested: a wire twisted (at angle of rotation 30^{o}) and a planar-loop. The most compact, bright source of x-rays was produced using a planar-loop configuration. A schematic view of a x-pinch load with a planar-loop configuration is presented in Fig. 1.

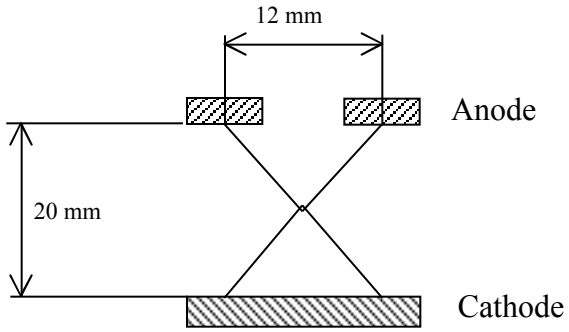

Fig. 1. Planar-loop x-pinch load.

The distinct feature of x-pinches is the existence of a strong electron beam making them attractive objects for spectropolarimetry. A new diagnostic, x-ray spectropolarimetry, applied to x-pinch plasmas, can provide detailed information about the electron distribution function and the magnetic field. Our recent results on x-pinches and x-ray spectropolarimetry have been published [1,2]. Details of K-shell spectroscopy and spectropolarimetry of Ti ions are given below.

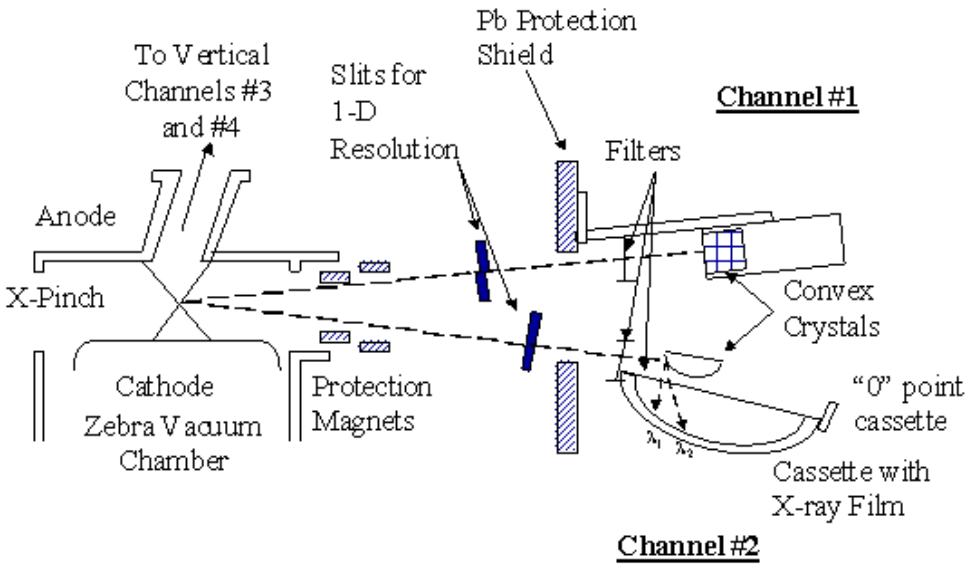

Fig.2. Experimental setup for polarization measurements.

Polarization-sensitive experiments on x-pinch plasmas were performed at the NTF in May-August 2000. The polarization-dependent spectra of K line radiation produced by Ti and Fe x-pinches in more than 15 shots were recorded simultaneously by horizontal (with a slit) and vertical (w/o a slit) spectrometers (see experimental setup by Kantsyrev et al [2], Fig. 2). The horizontal spectrometer with a slit provides a resolution along the z-pinch symmetry axis and has a dispersion plane perpendicular to the discharge axis (channel 1), whereas the vertical spectrometer has a dispersion plane parallel to the discharge axis (channel 2). Both spectrometers are identical LiF (2d=4.027 Å) convex crystal spectrometers. The LiF crystal has a spacing corresponding to the nominal Bragg angle of 40º at the wavelength of 2.6 Å: the Ti lines most likely to be polarized with close to or above 2.6 Å when a strong electron beam is generated.

Time-integrated images of eight selected shots are shown in Fig.3. In these shots, a planar-loop Ti x-pinch was used as the load (see Fig. 1). The anode is at the top of all images. The brightest spot is located in the cross point of the wires. The cathode is not seen at the bottom.

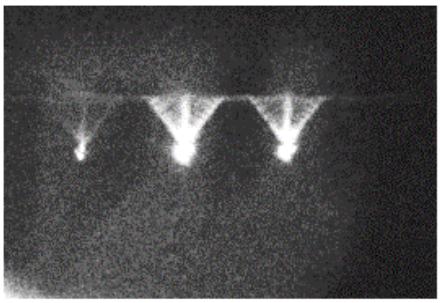

Shot 36 (07/12/00)

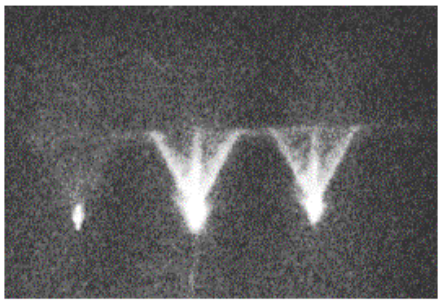

Shot 37 (07/13/00)

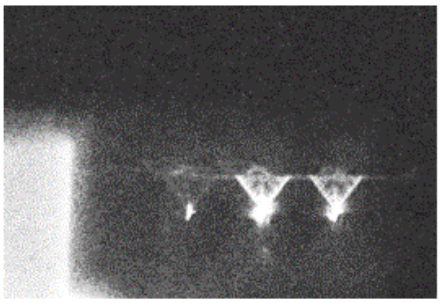

Shot 38 (07/18/00)

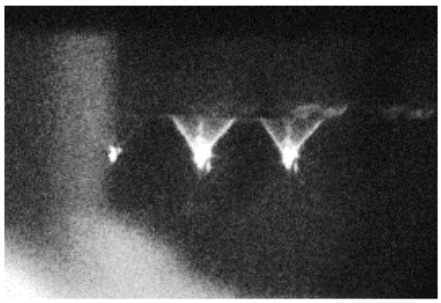

Shot 39 (07/19/00)

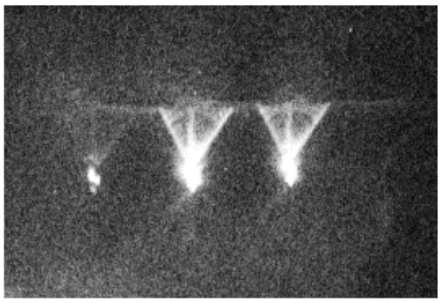

Shot 40 (07/21/00)

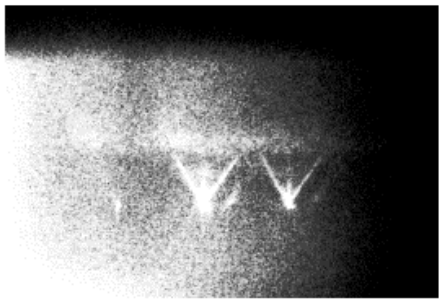

Shot 41 (07/26/00)

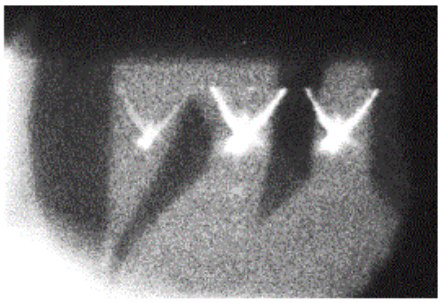

Shot 47 (08/16/00)

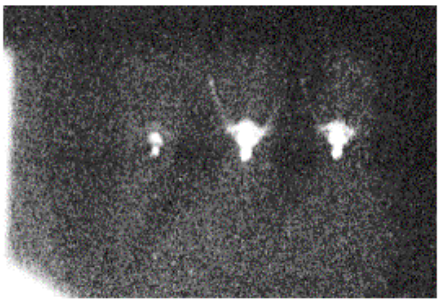

Shot 48 (08/17/00)

Fig. 3. NTF time-integrated x-ray pinhole camera images of Ti x-pinches (shots 36-41, 47 and 48).

The diameter of Ti wires was 30 (for the shots 36-41), 76.2 (for the shot 47), and 152.4 (for the shot 48). The left image in each picture was recorded through the filter providing the maximum of radiation with $_{1/10}$ < 2.6 Å, whereas the center and the right side images were recorded through the filter providing the maximum of radiation with $_{1/10}$ <7.9 Å and $_{1/10}$ <5 Å, respectively. Fig. 3 shows that a x-pinch is a small, almost point source of radiation with 2.6 Å, which was also supported by 1-D spectral line measurements. The structure of a x-pinch includes energetic electron beams directed toward the anode and along the wires [1,2]. The experimental estimation of the widths of the central jet on x-pinch x-ray images and Fe K spectral lines (generated on a steel anode) has shown that the electron beam diameter in a high-current x-pinch may be smaller than 1mm [3, 4]. As a percentage of the x-pinch discharge energy (E 100-120 kJ) the electron beam energy is from 2-3 % (for Ti, Fe) to 15-20 % (Mo and W). This is based on the experimental estimation of the energy needed to generate the observed holes at the points of connection of the wires with the anode of a x-pinch [3,4].

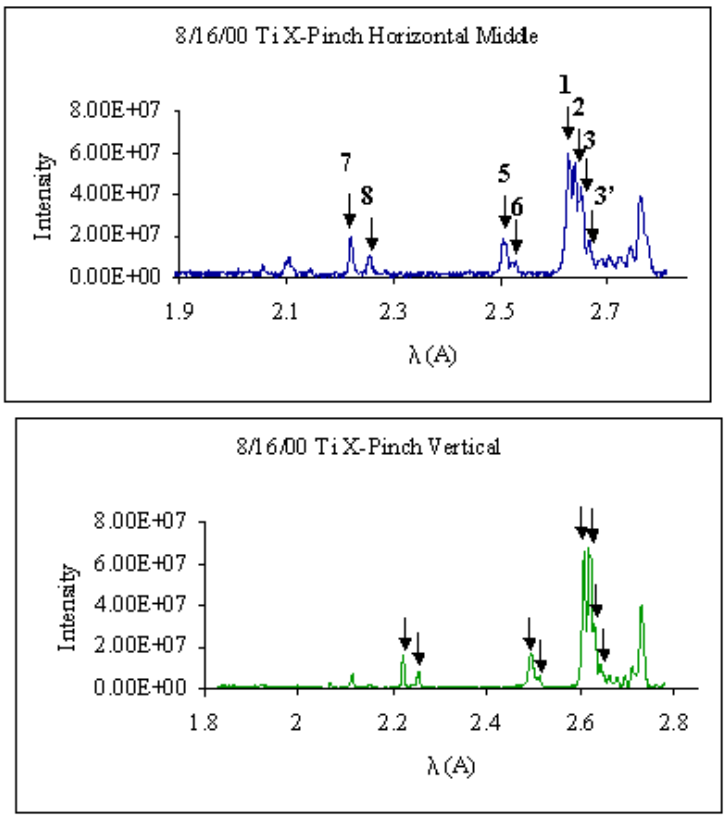

Fig. 4. Polarization-sensitive Ti x-pinch spectra (shot 47).

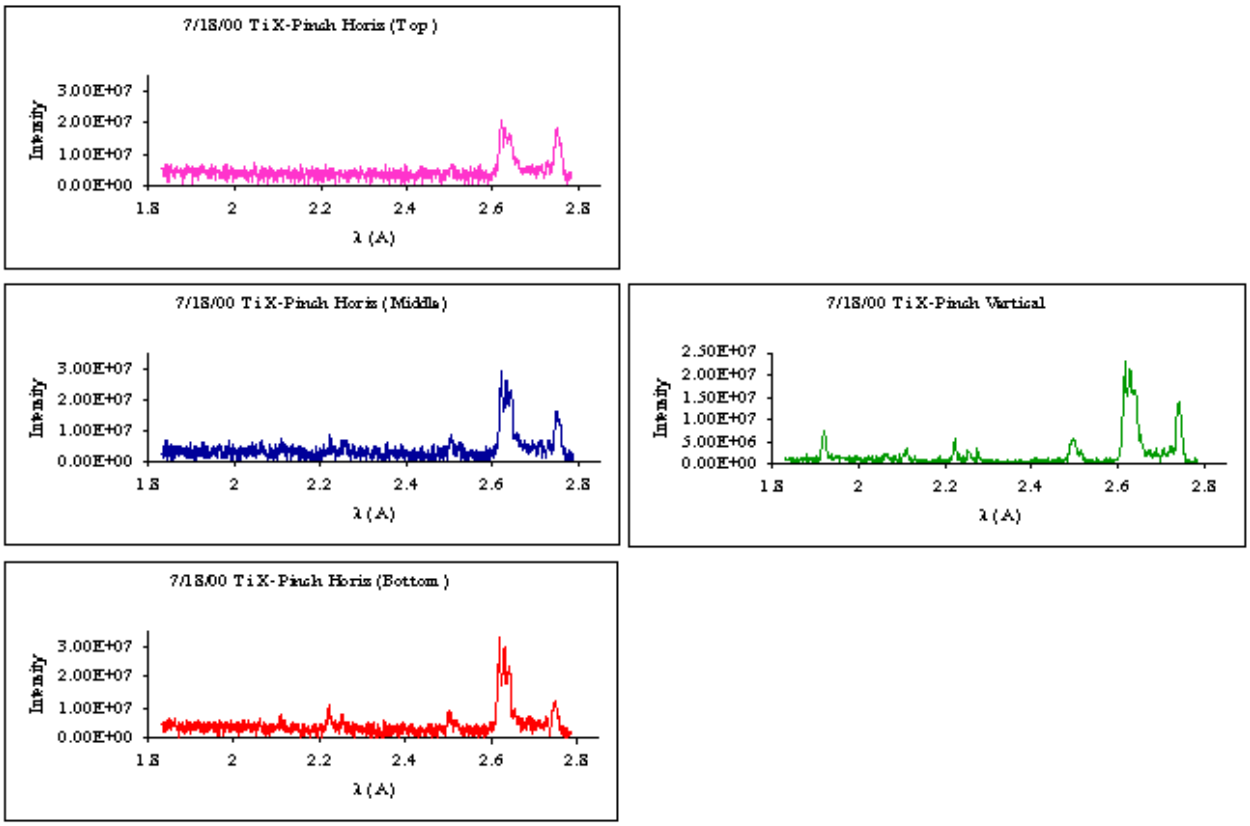

Fig. 5. Polarization-sensitive Ti x-pinch spectra (shot 38).

Typical polarization-sensitive spectra are presented in Figs. 4-5. They include the He-like resonance line He (1), the most intense line in all K-shell Ti spectra, the intercombination He-like line y (2), the Li-like satellite line peak (3), the Be-like satellite line peak (3'), the H-like resonance line Ly (5), the He-like satellite peak (6), the He-like resonance line He (7), and the Li-like satellite peak (8). Also, to the right of the peak 3', the x-ray spectra include satellite structures due to B-, C-, N-, and O-like Ti ions and the most prominent peak at the right, a cold K . Three spatially-resolved spectra recorded by a horizontal spectrometer are presented together with a spectrum recorded by a vertical spectrometer on July 18, 00 (Fig. 5). For the polarization analysis, the horizontal spectra from the middle were chosen. The horizontal spectrometer records mostly parallel polarization state whereas the vertical one records mostly perpendicular polarization state.

Fig. 6 explains the general trends in the polarization of the major lines: the measured ratio of the intensities associated with different polarization states $I_{II}/I_{\perp}$ greater (less) than 1 indicates the positive (negative) polarization of the line. Theoretical calculations estimate that the polarization of the resonance line He decreases from 60% at threshold to 0 (near 7 thresholds). It then becomes negative. Polarization of the intercombination line y increases from about –33% (at threshold) to 0 and at higher energies tends to the polarization of the He line.

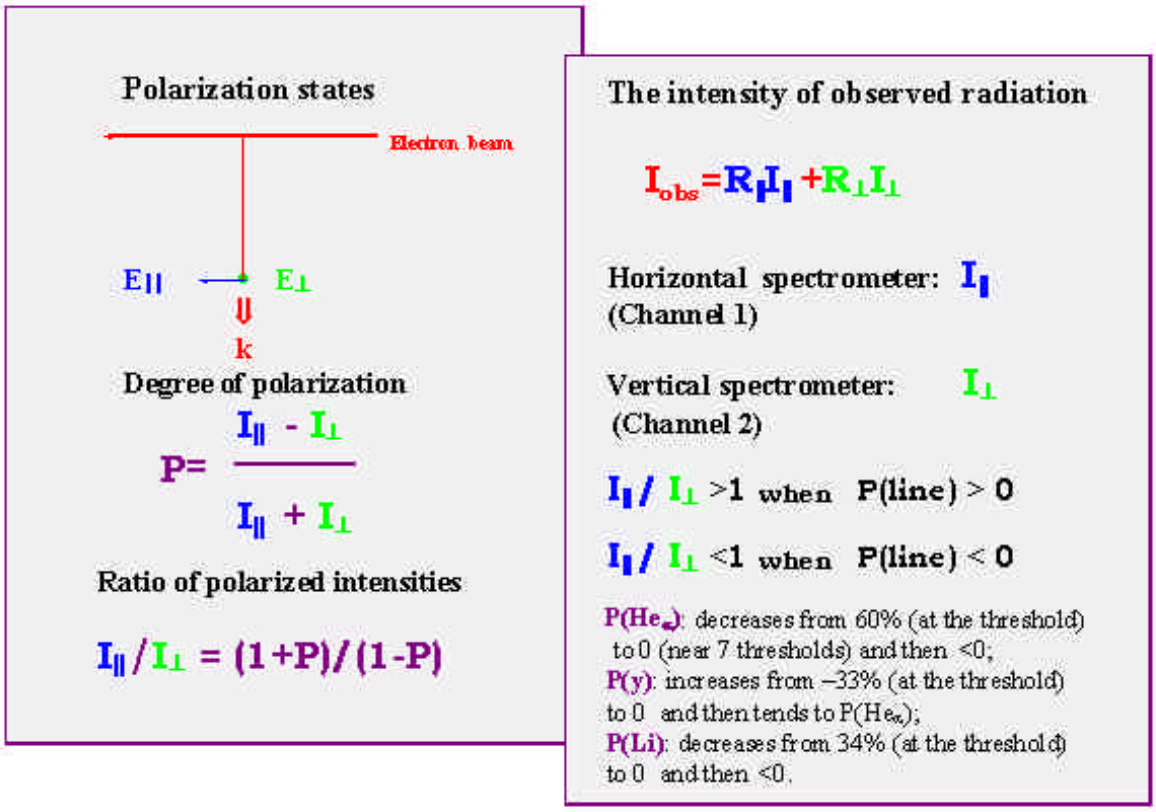

Fig. 6. Identification of the ratio of the intensities of different polarization states ($I_{II}/I_{\perp}$).

Table 1. Illustration of polarization of Ti K-shell lines through the measured ratio of intensities ($I_{\parallel}/I_{\perp}$)

	Line	Ion	λ(Å)	7/12/00	7/18/00	7/19/00	7/21/00
1	Heα	He	2.618	0.93	1.02	0.65	1.09
2	y	He	2.631	1.01	0.98	0.66	1.04
3	q	Li	2.640	1.05	1.12	0.86	1.06
3′	sat	Be	2.655	1.0	1.22	1.07	1.13
5	Lyα	H	2.500	0.97	1.25	1.06	1.02
6	sat	H	2.515	1.29	1.58	1.52	1.14
7	Heβ	He	2.221	0.91	1.29	0.69	1.12
8	sat	He	2.253	1.28	1.75	0.94	1.19

The ratios of intensities associated with different polarization states I_{II}/I for each of the spectral lines (1, 2, 3, 3', 5, 6, 7, and 8), and the line ratios of the intercombination line and satellite lines to their resonance lines (2/1, 3/1, 3'/1, 6/5, and 8/7), from horizontal and vertical are presented in Tables 1,2. Specifically, Table 1 lists the measured ratio of the spectral line intensities associated with different polarization states I_{II}/I for four different shots. The ratios show largest deviation from 1 for the shot on 07/19/00. The ratio for the He-like lines is usually less than 1 (negative polarization), whereas the ratio for most of the satellite peaks is larger than 1 (positive polarization). For example, the data for the shot on 7/19/00 show that the ratio I_{II}/I is 0.65 for the He resonance line, 0.66 for the He-like intercombination line y, 0.69 for the He resonance line, whereas this ratio for the satellite peaks is 1.07 for the peak 3' and 1.52 for the peak 6.

Table 2. Illustration of polarization of Ti K-shell lines through the measured ratio of relative intensities of the lines recorded by a horizontal (H) and vertical (V) spectrometers.

Line	7/12/00			7/18/00			7/19/00			7/21/00		
ratio	H	V	H/V	H	V	H/V	H	V	H/V	H	V	H/V
2/1	0.90	0.83	1.09	0.88	0.91	0.96	0.88	0.88	1.0	0.82	0.86	0.95
3/1	0.77	0.68	1.13	0.79	0.73	1.1	0.79	0.60	1.32	0.62	0.64	0.98
3′/1	0.30	0.27	1.08	0.33	0.28	1.2	0.33	0.20	1.65	0.35	0.33	1.04
6/5	0.56	0.35	1.61	0.68	0.53	1.27	0.66	0.46	1.42	0.80	0.71	1.13
8/7	0.70	0.50	1.41	0.79	0.58	1.37	0.77	0.57	1.35	0.80	0.75	1.06

Table 2 lists the line ratios of the intercombination line and satellite lines to their resonance lines for the same four shots. The first column for the each shot shows the relative intensities in a spectrum recorded by the horizontal spectrometer, whereas the second column shows the relative intensities in a spectrum recorded by the vertical spectrometer. Both spectra were recorded simultaneously. The third column represents the first column ratio divided by the second column ratio. The data for the 2/1 ratio from the third column indicate almost the same polarization for the He and y lines. The ratio for the satellite line peaks to the corresponding resonance lines (3'/1, 6/5, and 8/7) from the third column is larger than 1 for all shots. Summarizing, the data in Tables 1,2 indicate the positive polarization of dielectronic satellite peaks produced by the low energy electron beam (3-5keV) and the negative polarization of resonance lines produced by an electron beam with a much higher energy (>30keV).

X-ray spectral lines of Be-, B-, C-, N-, and O-like Ti ions in the spectral region above 2.6 Å are probably also polarized; relative intensities of corresponding peaks are different in horizontal and vertical spectra.

A collisional-radiative atomic kinetic model has been developed to diagnose the electron temperature and electron beam characteristics of various emitting regions of Ti plasmas produced at the NTF. A detailed description of the model is given in the another publication of this volume (see Shlyaptseva et al , ibid). The NTF Ti spectra exhibit features from H-like Ti to Ti K and it is clear that no single region can describe all these features, even with hot electrons. The NTF Ti plasmas are taken to have three regions: a hot, dense region with hot electrons that contributes all of the H-like and most of the He-like radiation, a cooler, less dense region with hot electrons that contributes He- to C-like radiation, and a cool region without hot electron that contributes N- and O-like radiation (the Ti K line is not modeled). Three intense T_e-sensitive spectral features useful as temperature diagnostics for the high temperature plasma region are labeled and their dependence on T_e and on hot electrons is shown in Fig. 7. The intensity ratios of Li-like satellite lines to He and He decrease with increasing T_e, while the intensity of H-like Ly increases. The effects of hot electrons are similar to the effects of increasing Te. But if T_e and the hot electron fraction *f* are chosen such that the increase in the Ly intensity is the same in both cases, the Li-like satellites will be more intense with hot electrons than with higher T_e. By matching both the Ly and the Li-like satellites to the experimental He line, both T_e and *f* of the hot region can be estimated. The temperature and hot electron dependence of synthetic spectra in the cool region shown in Fig. 8 have a great deal to do with the ionization balance. The regions of emission from the various ionization stages He to O are indicated. At low temperatures, O-like emission dominates. As T_e increases, so does the ionization balance, and the emission is shifted to higher energies. Increasing *f* has an effect similar to increasing T_e, but, as in the higher temperature case, emission from lower ionization stages is retained. It should be noted that even a very small fraction (10^{-4}) of hot electrons has a significant effect on the ionization balance at low T_e. This is not the case for the high T_e regions, where significant changes require a few percent of hot electrons. The development of x-ray spectropolarimetry can complement kinetic modeling with inclusion of hot electrons by providing an important information on electron beam characteristics.

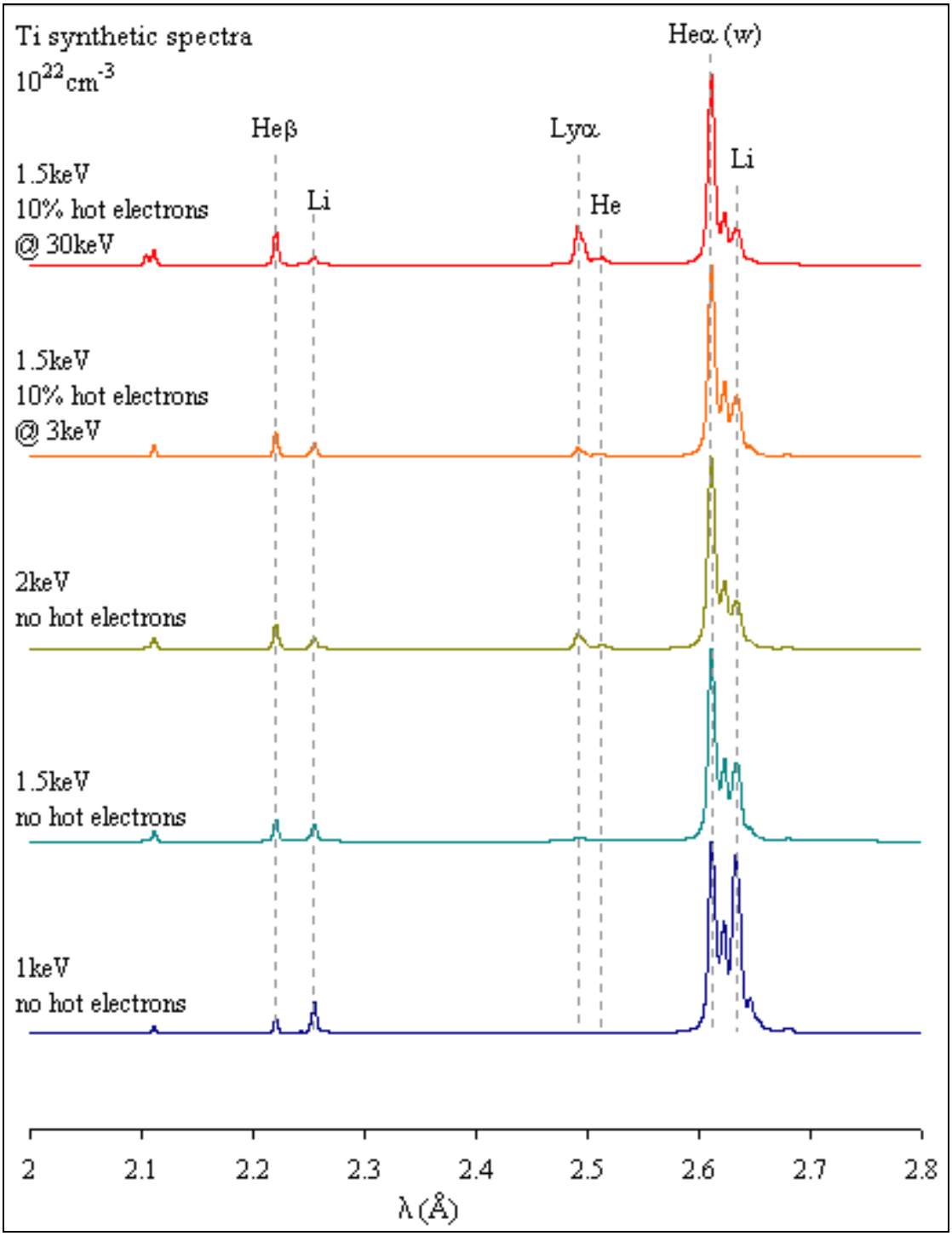

Fig. 7. Effect of Te and hot electrons on the "hot spectral region" of Ti spectra.

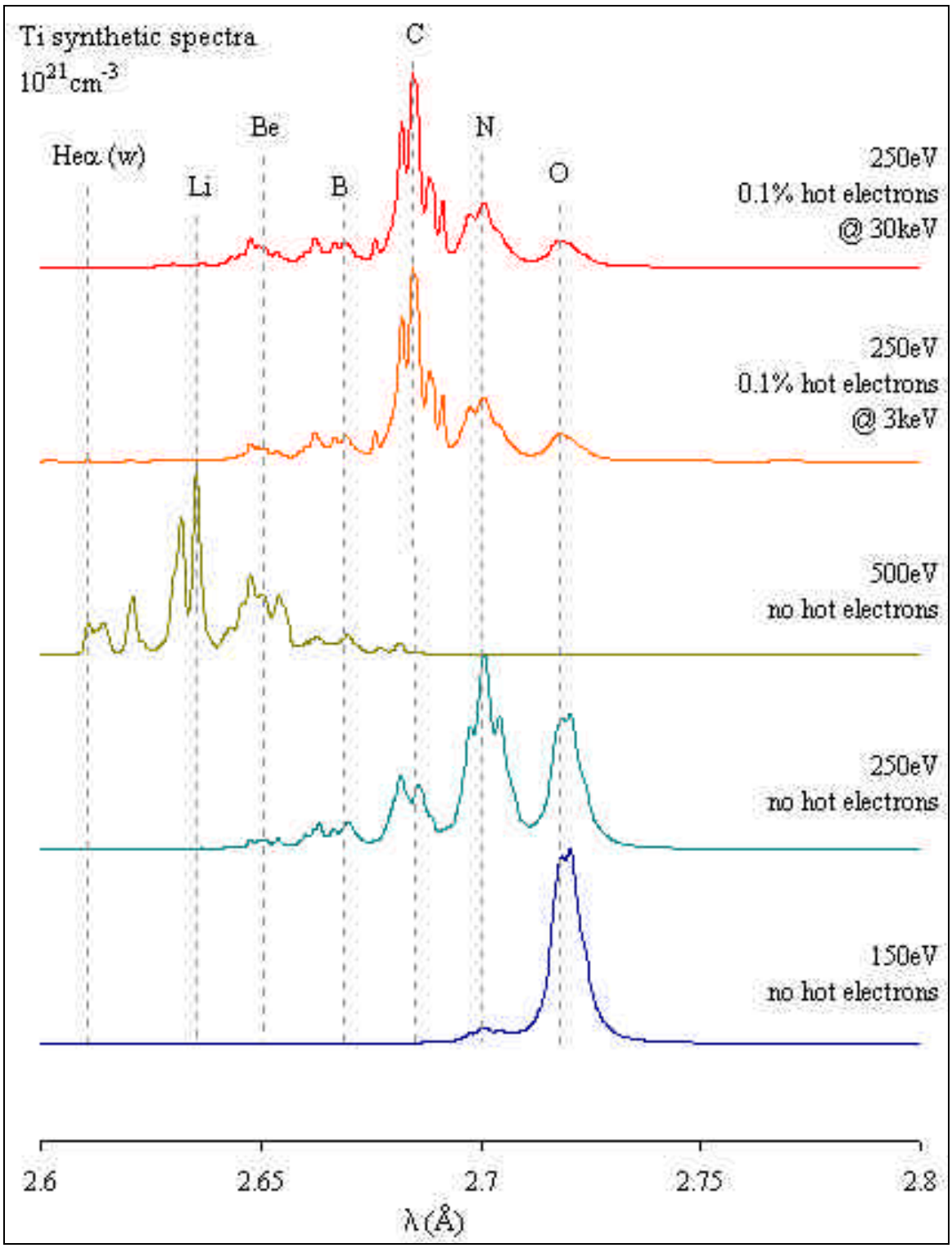

Fig. 8. Effect of Te and hot electrons on the "cooler spectral region" of Ti spectra.

T_e and electron beam fractions were determined for Ti x-pinches. For each experimental spectrum, line shapes were determined. Then, synthetic spectra were constructed with these line shapes over a T_e range of 1-2keV with *f* from 0-10%. The best fits of He , He and satellites, and Ly and satellites in all experimental cases indicate the presence of hot electrons in the hot plasma regions. This fitting procedure only determines T_e to ± 100eV and *f* to a factor of two, since decreasing T_e by 50-100eV and increasing *f* by 0.5-1% in each case gives fits that are only slightly inferior to the ones chosen. The temperature of the cool region without hot electrons was determined by finding the best fit to the N- and O-like features; T_e of the cool region could be thus determined to within 10eV. The hot electron beam fraction in the cool region was varied until a good fit with the rest of the ionization stage features was found. The hot electron fraction in the cool region was determined to within 0.5%. The Ti x-pinch plasma spectrum was determined to have a hot region with T_e = 1.8keV and *f* = 4% hot electrons and a cool region with T_e =200eV and *f* = 6.

In conclusion, the K-shell Ti model developed at the NTF is already useful as a temperature and electron beam fraction diagnostic. Further improvements to increase precision and robustness are necessary and well within sight: efforts to include Ti K , opacity and polarization properties of K-shell lines have already begun. The detailed modeling of the polarization-dependent features of Ti is the subject of another publication.

Polarization in X-ray lines of Fe ions is not observed with these LiF crystals; the corresponding Bragg angle is 27^O , and the measured ratio I_{II}/I for the resonance line He and an intercombination line y is the same in horizontal and vertical spectra.

II. L-shell x-ray spectropolarimetry

Recently, we have shown that polarization of K-shell line emission can be used to diagnose the presence of particle beams in plasmas, whereas the polarization of L-shell line emission can be used to diagnose the magnetic field in plasmas. L-shell spectra of Ti, Fe, and Mo have been calculated to select the spectral lines most suitable for this diagnostic. The typical L-shell Mo x-pinch spectrum is shown in Fig. 9.

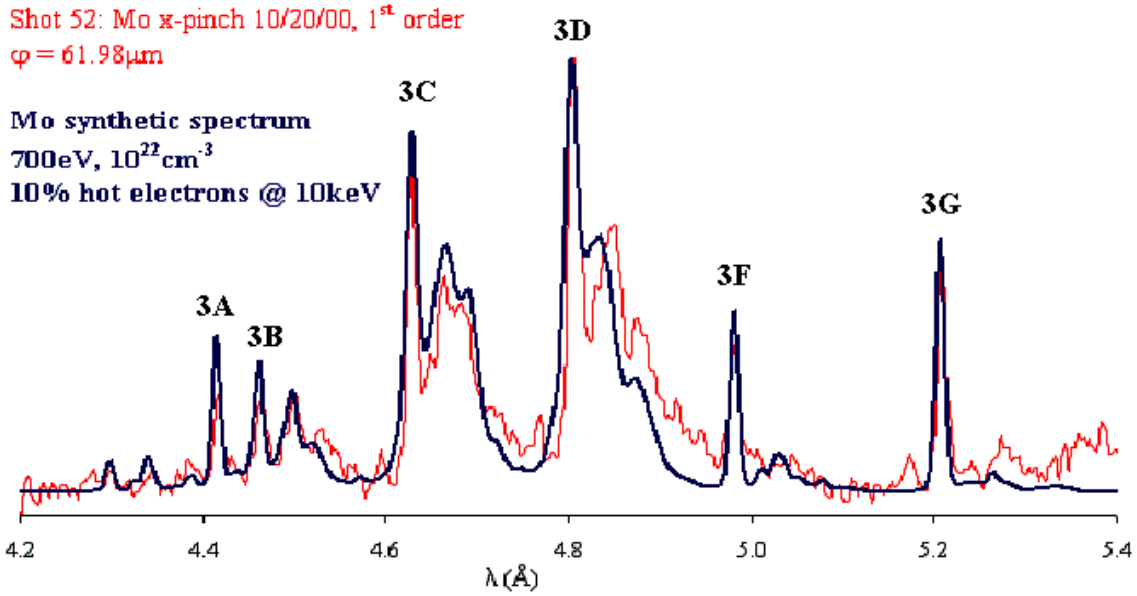

Fig. 9. Comparison of experimental and theoretical spectra of Mo x-pinch plasmas produced on 10/20/2000 (shot 52).

The brightest lines, labeled with letters 3A-3G, belong to Ne-like Mo. The group of lines between 3B and 3C is generated mostly by F-like Mo and the groups between 3C and 3F are mostly Na-like and Mg-like satellite lines. The relative intensities of these features vary from shot to shot and indicate variations of plasma conditions.

Our calculations for Ti are presented in the another publication in this volume (Shlyaptseva at all, ibid). Similar calculations performed for Fe ion lines indicate more L-shell lines suitable for this diagnostic: Ne-like lines 3A (R changes from 0 to 0.63), 3B (R changes from 0 to 0.95), 3C (R changes from 0 to 0.11), and 3D (R changes from 0 to 0.73). The vertical line with channels 3 and 4 (Fig. 2) is ready to be used for L-shell spectropolarimetry. We did not succeed yet to produce a good quality L-shell Fe spectrum in a vertical line: one of the reasons is the strong x-ray beam going upwards. Moreover, an analysis of explosions of different types of Fe-pinches has shown that this element has very different pinching properties from Ti and Mo. In particular, we have found that Mo x-pinches produce the brightest L-shell spectra of all elements investigated. It leads us to the conclusion that Mo

rather than Fe x-pinches will be used in future diagnostics of the magnetic field. Such experiments are under development.

III. X-ray spectropolarimetry of Ti K-shell emission at LLNL EBIT.

A major thrust of the spectroscopy program at EBIT has been to develop techniques to model, more realistically, the effects of plasma electron energy distributions on the spectra. The goal is to look for electron temperature diagnostics, and signatures of Maxwellian and non-Maxwellian energy distributions. To this end Ti spectra were gathered while the electron beam energy was swept through a carefully synchronized pattern to replicate a Maxwellian. The use of two spectrometers with crystals of differing polarization sensitivities to gather spectra simultaneously allows the determination of the line polarizations. These polarization-sensitive spectra, generated by the Maxwellian electron beam at EBIT, are making a very important contribution to the plasma polarization spectroscopy program at the NTF. In particular, the study of multiply-charged Ti ion spectra will help in the interpretation of the polarization-sensitive experiments using Ti x-pinches at the NTF. The ability of post-experiment processing of event-mode EBIT data allows the separation of the dielectronic satellite lines and structures from the direct excitation lines that are strongly blended in the plasma environment. This provides the opportunity to study separately the polarization properties of spectra produced by different processes, and well-defined electron distribution functions, and to apply the results to the diagnostics of z-pinch plasma experiments.

X-ray line polarization of heliumlike Ti^{20+} excited by a monoenergetic electron beam at LLNL EBIT was measured by Beiersdorfer et al [5]. In the present paper we use the same technique to measure polarization-sensitive Ti spectra but they were generated by a quasi-Maxwellian electron beam and were accumulated simultaneously using two individual von Hamos spectrometer setups. The spectrometers observed photons emitted along axes perpendicular to the electron beam axis, and their dispersion planes were also normal to the electron beam axis. One spectrometer used a Si (220) crystal and the other one a Ge (111) crystal. These crystals were chosen because of appropriate integrated reflectivities R_{II} and $R_{\perp}$ for x-rays polarized perpendicular and parallel respectively to the electron beam axis, which in turn is parallel and perpendicular to the spectrometers dispersion plane in the present

experimental setup. In particular, the relative reflectivity, $R=R_{\perp}/R_{II}$ indicates the polarization sensitivity of the crystal, as the intensity of the observed lines is given by the relationship $I_{obs}=R_{II} \times I_{II} + R_{\perp} \times I_{\perp}$, where I_{II} and $I_{\perp}$ are the x-ray intensities for polarization components parallel and perpendicular respectively to the electron beam axis. Using crystals with very different values for R provides the most polarization sensitivity to the experiment. R is strongly dependent on the Bragg angle. The Si (220) and Ge (111) crystals have a spacing corresponding at the wavelengths of interest to nominal Bragg angles of 43^{O} and 23.5^{O}, respectively. Post-experiment processing of event-mode EBIT data produce two different data sets: the first experimental data set includes two spectra recorded simultaneously by two crystals corresponding to the spectral lines produced via electron impact excitation (Fig. 10), and the second experimental data set includes two spectra recorded simultaneously by two crystals corresponding to the satellite lines produced via dielectronic recombination (Fig. 11).

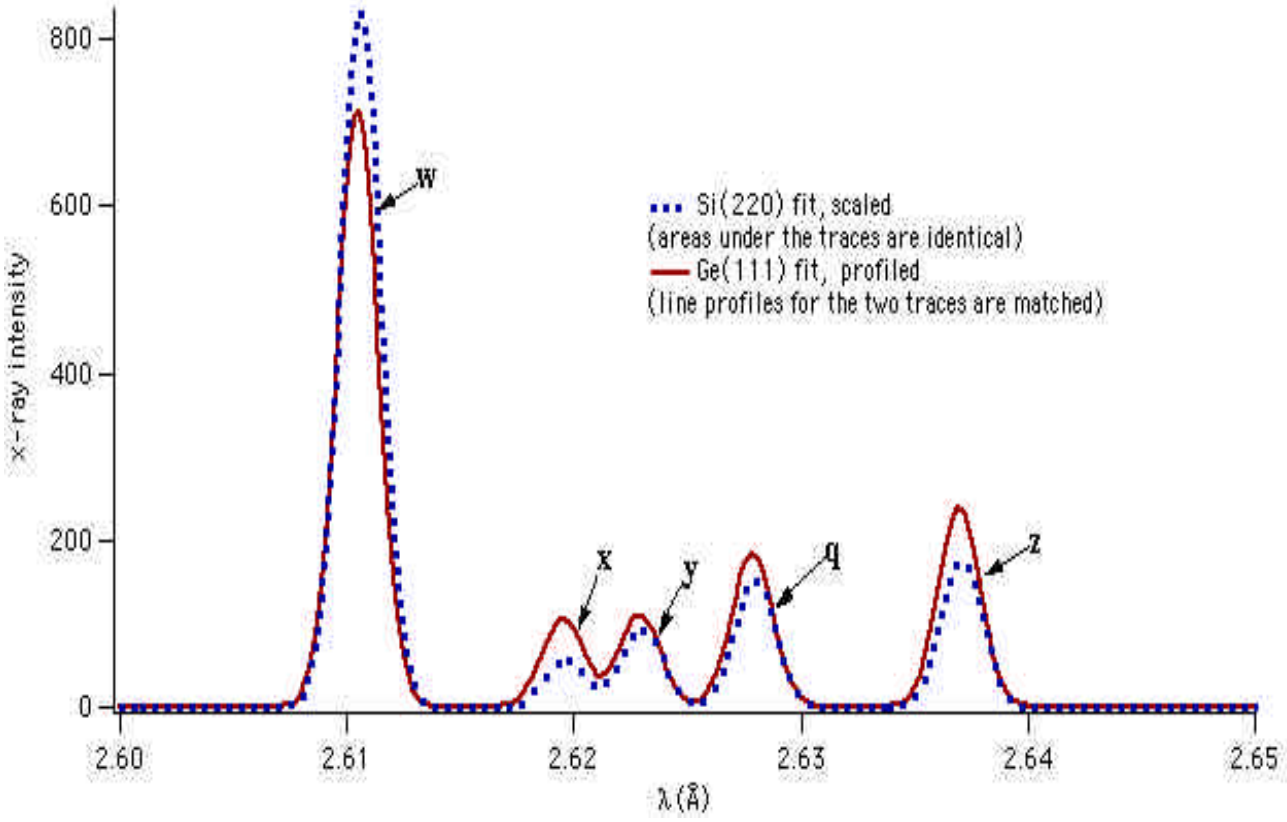

Fig. 10. Experimental direct electron excitation spectra of He-like Ti produced by a quasi-Maxwellian electron beam simultaneously recorded by Si 220 and Ge 111 crystals.

In Fig. 10, the first experimental data set is shown which includes the most prominent He-like resonance line w at =2.6105 Å together with other lines excited by electron impact, such as He-like lines z, x, and y and Li-like inner-shell satellites of Ti ions, produced by the unidirectional electron beam with a quasi-Maxwellian distribution function. The comparison of measured relative intensities of the He-like Ti lines w, z, x, and y, and the Li-like Ti line q produced by the quasi-Maxwellian (present paper) and monoenergetic electron beam [5] is presented in Table 3.

Table 3. The comparison of experimental relative intensities of the He-like Ti lines z, x, and y, and Li-like Ti line q to the line w produced by the quasi-Maxwellian and the monoenergetic electron beam at LLNL EBIT.

	Present paper			Ref. [5]		
	Si(220)	Ge(111)		Si(220)	Si(111)	
	I_1	I_2	I_1/I_2	I_3	I_4	I_3/I_4
z/w	0.212	0.335	0.633	0.258	0.343	0.752
x/w	0.068	0.145	0.469	0.102	0.191	0.534
y/w	0.113	0.153	0.739	0.147	0.235	0.625
q/w	0.184	0.255	0.722	0.313	0.316	0.99

The x-ray spectrum of He-like Ti excited by the monoenergetic electron beam was measured at an energy just above the electron-impact excitation threshold (4800 eV) [5]. From the ratio I_3/I_4 for four lines z, x, y, and q it follows that the line q has a maximum, positive polarization almost equal to the line w and the line x has the lowest, negative polarization. In the present paper, the electron beam was set to model a Maxwellian distribution function with T_M=2.3 keV in the energy range from 0.6 keV up to 11.85 keV. To calculate line polarization, the corresponding cross sections of M-sublevels are integrated over 2.5 times threshold. The polarization of the line w undergoes a small change for these electron energies, the calculated value is equal to 58%, which is close to the value calculated for the monoenergetic beam. The lines z and x have the negative values of polarization at the threshold, which monotonically decrease with the energy. The line y has also the negative polarization at the threshold, but the line y is the only one line which polarization undergoes considerable changes from a negative to a positive value in the range from the excitation threshold up to 2.5 times excitation thresholds. The comparison of I_3/I_4 and I_1/I_2 for the z, x, and y lines proves that: the ratio decreases for the lines z and x and they become more negatively polarized, the ratio increases for the line y, which become more positively polarized. The comparison of these ratios for the line q indicates considerable decrease in the value of polarization, which does not agree with theoretical calculations. To complete the study of polarization properties of these lines produced by a quasi-maxwellian electron beam it is necessary to include the higher-n satellites [6,7]. Specifically, we are estimating the contribution of unresolved dielectronic satellites due to transitions $1s^2 3l$-$1s2l'3l''$ into intensities of polarized w, x, y, and q lines. We have already succeed in the interpretation of the polarization-dependent spectra of Li- and Be-like dielectronic satellites due to transitions with n=2. Using the same experimental data set and the same technique, we have resolved polarization-sensitive dielectronic satellite transitions with n=3 separately from direct excitation lines and are working on their analysis. It will provide us the important answer how the unresolved dielectronic satellite structures from higher Rydberg states can affect the polarization of resonance and forbidden lines in plasma.

By analyzing the second experimental data set (Fig. 11), we studied the polarization properties of dielectronic satellites of Li- and Be-like Ti, produced by the unidirectional electron beam with a quasi-Maxwellian distribution function. The details of calculations of atomic and polarization characteristics of K transitions in Ti ions are discussed in another publication of the same volume (Shlyaptseva at al, ibid.). The comparison of theory and the experimental data shows encouraging agreement.

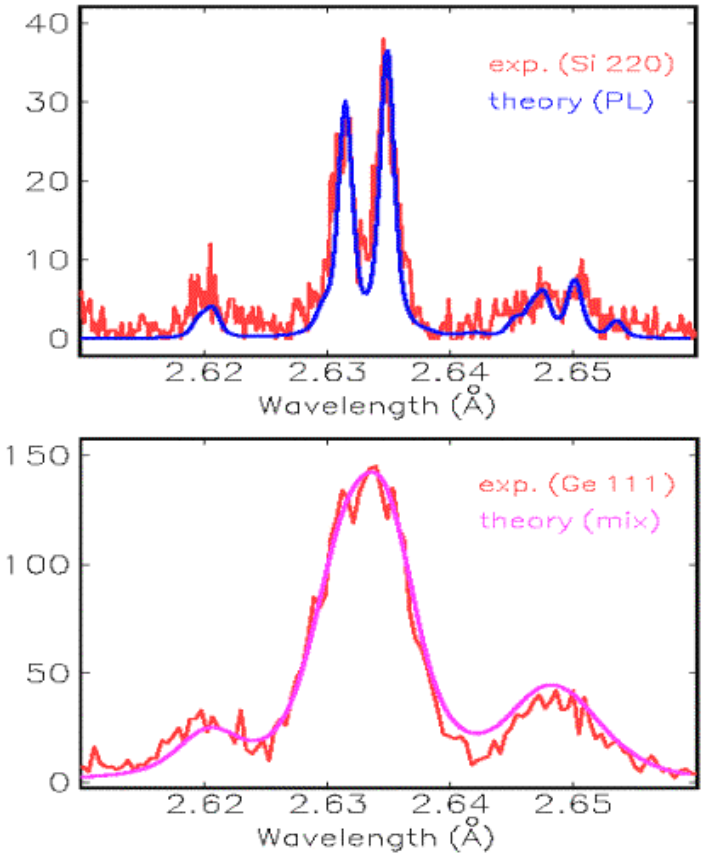

Fig. 11. Comparison of experimental and theoretical dielectronic recombination spectra of He-like Ti produced by a quasi-Maxwellian electron beam simultaneously recorded by Si 220 and Ge 111 crystals.

REFERENCES

1. A.S. Shlyaptseva, S. B. Hansen, V.L. Kantsyrev, B.S. Bauer, D.A. Fedin, N. Ouart, S.A. Kazantsev, A.G. Petrashen, U.I. Safronova, "X-ray spectropolarimetry of high-temperature plasmas", Rev. Sci. Instrum., 72, 1(II), pp. 1241-1244, 2001.

2. V. Kantsyrev, B. Bauer, A. Shlyaptseva, D. Fedin, S. Hansen, R. Presura, S. Batie, A. Oxner, B. LeGalloudec, H. Faretto, D. Chamberlain, N. Ouart, A. Jones, H. LeBeau, M. Gharaibeh, "Advanced x-ray and EUV diagnostics and first application to x-pinch plasma experiments at the Nevada Terawatt Facility", Rev. Sci. Instrum., v.72, 1(II), pp.663-667, 2001.

3. V.L. Kantsyrev, A.S. Shlyaptseva, B.S. Bauer, D.A. Fedin, R. Presura, S. Fuelling, S. Hansen, S. Batie, A. Oxner, H. Faretto, N. Ouart, S. Keely, H. LeBeau, D. Chamberlain, "X-ray temporal, spatial and spectral study of 0.9 MA x-pinch Ti, Fe, Mo, W and Pt radiation sources. Energetic electron beam and hard x-ray generation", PPPS-2001 Conf. Proc. Book, 2001 (in press)

4. V.L. Kantsyrev, B.S. Bauer, A.S. Shlyaptseva, D.A. Fedin, S. Hansen, R.Presura, S. Fuelling, S. Batie, A. Oxner, H. Faretto, N. Ouart, S. Keely, H. LeBeau, D. Chamberlain. "Powerful microfocus x-ray and hard x-ray 1 MA x-pinch plasma source for imaging, spectroscopy, backlighting, and polarimetry". Proc.SPIE , v. 4502, 2001 (in press).

5. P. Beiersdorfer, G. Brown, S. Utter, P. Neill, K.J. Reed, A.J. Smith, and R.S. Thoe, "Polarization of K-shell transitions of Ti $^{19+}$ and Ti $^{20+}$ excited by an electron beam", Phys. Rev. A, v. 60, 5, pp. 4156-4159, 1999.

6. S. Chantrenne, P. Beiersdorfer, R. Cauble, and M.B. Schneider, "Measurement of Electron Impact Excitation Cross Sections for Heliumlike Titanium", Phys. Rev. Let., v. 69, 2, pp. 265-268, 1992.

7. M. Bitter, K.W. Hill, M. Zarnstorff, S. von Goeler, R. Hulse, L.C. Johnson, N.R. Sauthoff, S. Sesnic, and K.M. Young et al., "Satellite spectra for heliumlike titanium. II.", Phys. Rev. A, v. 32, 5, pp. 3011-3029, 1985.

Polarimeter, based on one quartz crystal

E.O.Baronova, M.M.Stepanenko

RRC Kurchatov Institute, 123182, Moscow, Russia

The first X-ray polarimeter, consisting of scattering graphite, viewing at 90 degrees was suggested by Barcla [1]. A multipurpose polarimeter, where the crystal is oriented to reflect the beam in one plane and than rotated to get the second reflection is described in [2]. The polarimeters of the latter type can be used to characterize synchrotron radiation, to analyze polarization in magnetic or resonant scattering experiments, where the X ray sources are stable in space and time.

However for pulsed, irreproducible X-ray sources, like laser produced plasma and Z-pinch devices, it is not correct to rotate one crystal and to compare the two measurements taken in two different shots. One can use a scheme with two crystals [3], simultaneously detecting the radiation in mutually perpendicular directions and at a Bragg angle close to 45 degrees.

This scheme works well for point X-ray sources with the assumption that i) the x-ray source radiates isotropically, ii) the crystals are quite identical, iii) the crystals are used at a Bragg angle of 45°, and iv) both crystals record radiation from the same plasma region.

This paper presents the principle of operation and design of a polarimeter, consisting of a single quartz crystal, simultaneously selecting both polarization components in the two perpendicular directions. With this polarimeter criteria ii) and iiii) are fulfilled automatically; requirements i) and iv) are no longer needed. The polarimeter can be used to select and study polarization for eight fixed wavelengths: for 6 Å, 3.47 Å, 1.32 Å, 0.96 Å in first order of reflection and for 3 Å, 1.74 Å, 0.66 Å, 0.48 Å in second order of reflection. For this group of wavelengths, the Bragg angle is equal to 45° and both reflected components are fully polarized in mutually perpendicular directions. We think this type of polarimeter is presented for the first time.

Principle of operation

We consider here how the ideal polarimeter operates. Let us assume we have two groups of crystal planes, group A and group B, oriented at some angle P one with respect to another. In Fig. 1 the flat crystal sample is shown. On the front surface the particular crystal planes A and B are marked by dotted lines. Investigated radiation comes along ray P_{12} and is reflected in P_1 and P_2 directions by planes A and B, correspondingly.

To select polarization components along P_1 and P_2 directions it is necessary to satisfy two conditions: to reflect each components at a Bragg angle equal to 45 degrees, and in mutually perpendicular directions. Let us find an angle P between planes A and B, which would satisfy the above mentioned conditions. We will use the following notation:

P_1 - polarization component, reflected at 45 degrees from planes B.

P_2 - polarization component, reflected at 45 degrees from planes A,

$_I$ – incident angle with flat crystal surface, i.e. the mechanical plane,

$_B$ – Bragg angle with polarization planes A and B, if this angle is equal to 45 degrees, each polarization component has 100% reflection coefficient in the case of ideal crystal.

P – angle between planes A and B.

From the geometry one can obtain the main relationship for the single-crystal polarimeter:

$$\mathrm{Sin}\ _B = \mathrm{Sin}\ _I * \mathrm{Sin}(P/2) \qquad (1)$$

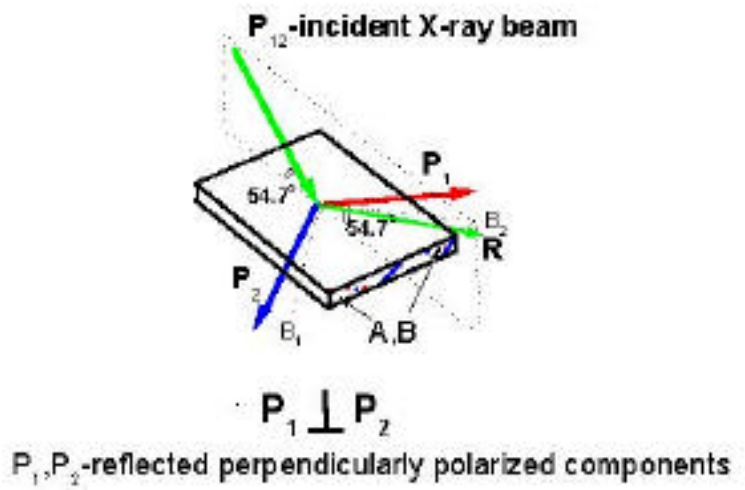

Fig.1. Geometry of polarimeter

where $_B = 45°$, as the first general condition for ideal polarimeter.

Further geometrical considerations give the next expression to an angle between two polarized components P_1 and P_2:

$$\angle P_1OP_2 = 2\arcsin\ (\cos^2\ _B + \sin^2\ _B \cos^2 P/2)^{1/2} \qquad (2)$$

The angle P_1OP_2 should be equal to 90 degrees due to the second condition for an ideal polarimeter. It is easy to see, that equations (1) and (2) are only satisfied if P=120°. Therefore the angle P between reflecting planes A and B should be equal to 120°. **This means that the natural hexagonal structure of quartz crystal is ideally suited for such a polarimeter.**

We present here the fundamental formulas for the polarimeter, based on a single quartz crystal. These formulas describe the basis of the polarimeter and can be applied to determine the geometry of an experiment, i.e., the directions of incoming and reflected beams with respect to the mechanical crystal surface and the positions of the detectors.

Formula (1) for quartz crystal polarimeter looks like:

$$\mathrm{Sin}\ \theta_B = \mathrm{Sin}\ \theta_I * \mathrm{Sin}60 \qquad (3)$$

Therefore if $\theta_B = 45°$, then $\theta_I = 54.7°$. So, the incident angle with the mechanical plane for the investigated radiation should be 54.7°. For a given intermediate crystal distance the wavelength is fixed and can be calculated from Bragg's law at a reflecting angle of 45°.

Formula (2) for quartz crystal:

$$\angle P_1OP_2 = 2\arcsin 0.5(1+3\cos^2\theta_1)^{1/2} \qquad (4)$$

The angle P_1OP_2 should be equal to 90 degrees as it is necessary for an ideal polarimeter.

It is easy to see, that if $\theta_I = \arcsin(\mathrm{Sin}\ \theta_B/\mathrm{Sin}60) = 54.7°$, than $\angle P_1OP_2 = 90°$. This is a build-in check of the formulas presented.

To determine the coordinates of a detector for the P_1 and P_2 components it is useful to know the angle B_1OB_2 between the projections of rays P_1 and P_2 on the mechanical plane:

$$B_1OB_2 = 2\ \mathrm{arctg}(\mathrm{tg}\ \theta_I * \mathrm{tg}30) \qquad (5)$$

If $\theta_B = 45°$, $\theta_I = 54.7°$, $B_1OB_2 = 78.3°$.

In practice, especially when one investigates spectra emitted from plasma, it is not possible to find a crystal plane that reflects the particular wavelength at 45 degrees. In this case formulas (3)–(5) permit a calculation of the exact corresponding angles and coordinates to detect the polarized components. The relative intensities of polarized components is proportional to $\cos 2\theta_B$ for an ideal crystal and proportional to $\cos^2 2\theta$ for a mosaic crystal. Actual crystals are between these two types.

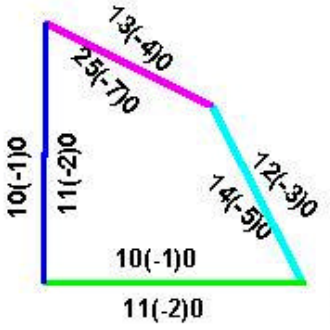

	I order	II order
cut	2d,A	λ,A	λ,A
10(-1)0	8.51	6.0	3.0
11(-2)0	4.91	3.47	1.74
14(-5)0	1.86	1.32	0.66
25(-7)0	1.36	0.96	0.48

$P_1/P_2 = \cos 2\theta$ - for ideal crystals

$P_1/P_2 = \cos^2 2\theta$ - for mozaic crystals

ion	λ,A	cut	θ	cos2θ	cos²2θ
ArXVII	3.94	11(-2)0	53.8	0.3	0.09
K [He]	3.55	11(-2)0	46.23	0.04	0.002

Fig.2. Four-face prism polarimeter

Figure 2 shows the polarimeter, made like a four-face prism. This design allows studying polarization for eight wavelengths in first and second orders of reflection. Each face of the prism is parallel to a particular cut of the quartz crystal, shown outside prism. Corresponding polarizing X-ray planes are marked inside prism. The cuts and wavelengths are presented in above table. The degree of polarization is also calculated for He-like Ar and K, reflected from the 11(-2)0 cut. This polatimeter has been manufactured, and we plan to calibrate it in order to estimate the degree of mosaicity of quartz crystal.

A photo of the polarimeter is shown in Fig.3.

Fig.3. Photo of polarimeter

References.

1. C.G.Barcla, Proc.Roy.Soc., London,77,247 (1906).
2. Qun Shen, K.D.Finkelshtein, Phys.Rev. B45,5075 (1992).
3. Baronova E.O., Sholin G.V., Yakubowski L., JETP letters, v.69,issue 12,25 June 1999.

Polarization studies in fast-ion beam spectroscopy

Elmar Träbert

Lawrence Livermore National Laboratory, Livermore, CA, USA

Université de Liège, Belgium

Ruhr-Universität Bochum, Germany

In a historical review, the observations and the insight gained from polarization studies of fast ions interacting with solid targets are presented. These began with J. Macek's recognition of zero-field quantum beats in beam-foil spectroscopy as indicating alignment, and D.G. Ellis' density operator analysis that suggested the observability of orientation when using tilted foils. Lastly H. Winter's studies of the ion-beam surface interaction at grazing incidence yielded the means to produce a high degree of nuclear orientation in ion beams.

I. INTRODUCTION

For polarization to become observable, either the emitter must be restricted in its spatial orientation (for example, by a magnetic field), or the excitation must show directionality. Here I will give an overview of what in terms of polarization has been seen with (highly directional) fast ion beams that interact with targets in arrangements of various symmetries. Most of the work was done in the mid-1970s, but the topic has fallen dormant again after less than a decade. However, there are a few aspects of that work that are still of interest and that might even become useful again.

Since I have not worked in this particular sub-field myself (although I have worked with fast ion beams), I ask the reader to pardon me for my lack of depth and understanding, as well as for my more casual approach. Details of the formalism will be found, for example, in the contribution by A. Petrashen, and I am happy in not having to duplicate any of that excellent work. Instead of showing pictures from what is not my own work (which also would have required dealing with copyright issues), I shall show only a few sketches and refer to the literature for any details and specific presentations. The reference list is arranged alphabetically and includes the titles of the journal articles. This, I thought, might be more useful for anybody interested than me making up a serpentine presentation just in order to be then able to refer to this or that paper. Also, one finds quite a bit of repetition of the data and graphs presented in the original publications which are then re-hashed for this or that review or conference. Closer study might reveal specific information, if sought for, but I leave that to the interested reader. The list of references is far from complete. It was originally based on a US-based paper trail, and some European references have been added

from memory. For example, my own memory - backed up by recollections of colleagues - has traces of quantum beat work done at Lyon (France) in the late 1970s, by M. Ceyzeriat, A. Denis, and J. Désesquelles, but I have not found the references yet again. Looking up the beam-foil conference proceedings of the time will give further clues and references beyond this report.

I have structured my report along the following topics:

Historical context
Techniques and symmetries
Foil at right angles
- Coherent excitation
- Cylindrical symmetry $\rightarrow$ Alignment
- Best observed with a polarization analyzer
Quantum beats
- Fine structure intervals
- Hyperfine intervals
Tilted foil
- Cylindrical symmetry broken $\rightarrow$ Orientation
- Scattering at grazing incidence
(Ion-Beam Surface Interaction at Grazing Incidence - IBSIGI)
Dirt effects
- Temperature
- Current density
- Surface fields
- Surface contamination
Applications of IBSIGI
- Production of nuclear orientation for nuclear physics
- Probing the band structure of the surface material

II. HISTORICAL INTRODUCTION

At the beginning of the twentieth century, vacuum technology progressed to enable experiments with particle beams, be they electrons (for example, for producing x-rays) or ions (canal rays). Ion beam formation was being studied, both for investigations of the Stark effect and for analyzing the light intensity distribution along such canal rays. Wilhelm Wien realized that such a technique might reveal the lifetimes of atomic levels and derived approximate formulae for atomic level lifetimes long before quantum mechanics became available for that purpose [12].

In the 1930s, ion beams were adapted by nuclear scientists into accelerators (at the time branded/glorified as *atom smashers*) that could produce ions energetic enough to overcome the Coulomb barrier and induce nuclear reactions. Targets were now formed as thin foils which have a much higher areal density than a gaseous target. The ion beams would penetrate the target foil and then be analyzed for energy loss and charge state in a detector downstream, together with possible nuclear reaction fragments. The first ion beams were feeble, and people had difficulty in developing detectors for fast ions and reaction fragments,

and even detectors that would be sensitive enough to note and analyze a particle at all. With continuous development, ion sources improved and ion beams grew in beam current. However, it was only in the early 1960s that some nuclear physicists used their own eyes for detection again. They saw visible light from an ion beam after it had passed through a target foil. Several of them understood the atomic physics value of their observation [19,2] - some only to find themselves reprimanded by their faculty colleagues for straying away from nuclear physics [20].

Energetic ions passing through matter may lose one or more of their electrons. The remaining ones may be shaken into excited levels, or electrons may be captured upon leaving the target. In any case, this was a new way to produce multiply charged ions, populate high-lying or multiply-excited levels, and studying atomic processes with a time resolution of a small fraction of a nanosecond. This time-resolution was easily achieved in beam-foil spectroscopy, by mechanical means, displacing either the foil or the detector along the ion beam trajectory (in those days, tube-based electronics had a hard time in the ns time range). An ion beam of energy 2 MeV/nucleon travels about one centimeter in one nanosecond. Easily achieved mechanical displacements of 10 μm then correspond to one picosecond, without any need for fast electronics (and oscilloscope displays that were poorly suited for showing the traces of rapidly deflected electron beams). If one photographed the light emission that occurred along the ion beam (using a filter to discriminate one spectral line from the others), the change of light intensity was interpreted as an intensity decay curve. The time after excitation strictly correlates with the distance from the foil via the uniform ion beam velocity. After properly converting film blackening back to an intensity scale, one might then determine atomic decay time constants. Photoelectric detectors were rather novel then, but quickly took over.

However, while there were many promises of the new technique [3], there were also many puzzling features that required some time to be recognized and sorted out. For example, some of the intensity decay curves, in particular those from hydrogen atoms or H-like ions, showed oscillations. These were quickly subsumed as resulting from "something like the Hanle effect", invoking stray electric and magnetic fields, or even fields produced by the ion beam itself, as well as the degeneracy of levels in hydrogenlike ions. In 1969, however, Joe Macek (then at Lincoln, Nebraska) suggested that the oscillations might have quite another origin. This origin is what we now call coherent excitation, and would lead to zero-field quantum beats, which are best observed with polarization-sensitive equipment [23]. This concept brings the story to the topic of this polarization spectroscopy workshop. A little more detail is needed to explain the how and why.

III. FOIL AT RIGHT ANGLES

The ion beam trajectory provides a direction, and any sideways orientation in a plane whose normal coincides with the beam direction has no preference over any other. The standard arrangement of an exciter foil in beam-foil spectroscopy is just that, with a foil at right angles, i.e., the foil surface normal pointing along the ion beam (Fig. 1).

Such a thin foil (with an areal density of, say, 10 to 20 μg/cm^2, or about 1/500 of the thickness of writing paper) is being traversed by the ion beam in a time of order 10^{-14} s. This time interval is comparable to the typical lifetimes of K-shell vacancies in (moderately) heavy ions. However, for most of the subsequent discussion, I shall concentrate on visible

light, from the excitation of valence electrons in not so highly charged ions. There the typical lifetimes range from 10^{-9} s to 10^{-11} s, which is orders of magnitude longer than the time the ions spend inside the foil. Inside the bulk of the foil, electronic excitation of the fast ions is very likely, but the cross sections for electron loss are also very high, and excited states are easily destroyed again before the ion leaves this dense environment. Excitation in the surface layer may survive, and more population of excited levels may occur by electron capture after leaving the foil. Therefore the typical excitation has to happen in a time interval that is even shorter than the time it takes to cross the foil, and this puts the time interval close to 10^{-15} s.

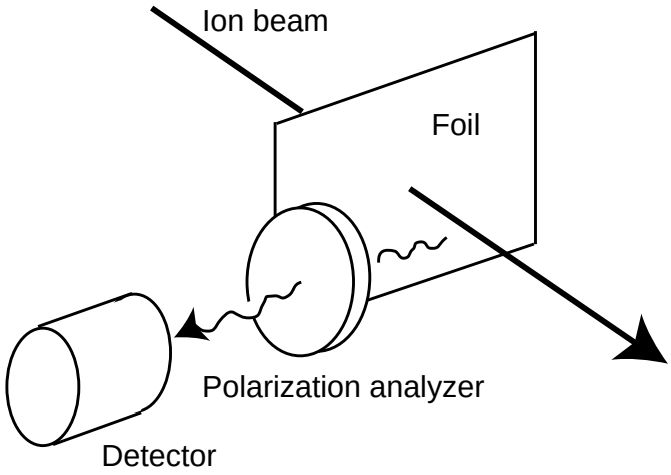

FIG. 1. Geometry with a fast-ion beam and an exciter foil at right angles.

Such considerations paved the ground for a conjecture by Macek [23] who suggested that the oscillations observed on decay curves might relate not to external fields, but be the consequence of coherent excitation. In this picture, via the uncertainty principle, a short time interval corresponds to an uncertainty in excitation energy. Excited levels with an energy separation smaller than this energy spread would be coherently excited, and their decay would possibly display interference effects.

Take two fine structure levels of a given term as an example and consider their decays to another level. As with coupled pendulums in mechanics, the levels develop in time together, and the level energy difference ΔE shows as a frequency ν in the decay curve. As the frequency describes a (lower-frequency) beat pattern between two high frequencies (the actual transition energies) associated with transitions between quantum states (and does not require external fields), the phenomenon has been dubbed *zero-field quantum beats*. In a simple view, this phenomenon results from the non-statistical population (different excitation cross sections) of the magnetic sublevels m_l effected in the ion-foil interaction. With a foil at right angles to the ion beam, the only asymmetry expected may be forward/backward, and this restricts the dependence of the sublevel population effect to a dependence on the absolute values of m_l, $|m_l|$.

Such *alignment* can then only affect terms with levels of $|m_l| > 1/2$. It is thought of to result (semiclassically) in a rotating dipole that is best observed by a polarization analyzer. At a certain *magic angle* (of 54.7°, where the Legendre polynomial P_2 vanishes), it is possible to obtain a signal to which all polarization components contribute in a way that renders the result independent of alignment and which thus is proportional to the total intensity of the decay (the total intensity shows no beat pattern). If one wants to measure the alignment, one measures through a polarization analyzer at two mutually perpendicular orientations (for example, along/across the ion beam) the signal strength and then applies a density operator analysis or uses the Stokes parameters (outlined in Table III). Remember that a J=1/2 - 1/2 transition cannot show polarization (which makes it a useful unpolarized sample), but the 1/2 - 3/2 component can. So in atomic lifetime measurements employing either a fast ion beam and a foil, or short-pulse laser excitation of atoms in a vapor cell, one tries to obtain unperturbed decay curves and thus avoids quantum beats. On the other hand, searching for level population effects or trying to measure small term differences in an otherwise poorly accessible range of level energies, it is advantageous to seek quantum beats.

TABLE I. The Stokes Parameters help in evaluating the measured polarization signal in terms of the density matrix, illuminating the physical situation.

$I = \|E_{\|}\|^2 + \|E_{\perp}\|^2$
$M = \|E_{\|}\|^2 - \|E_{\perp}\|^2$
$C = 2\ \mathrm{Re}\ (E_{\|}E_{\perp}^*)$
$S = 2\ \mathrm{Im}\ (E_{\|}E_{\perp}^*)$
With I being the overall intensity,
$M/I = \langle\ L_y^2 - L_z^2\ \rangle\ /\ \langle\ L_x^2\ \rangle$ relates to the alignment,
$C/I = 2\ \mathrm{Re}\ \langle\ L_y L_z\ \rangle\ /\ \langle\ L_x^2\ \rangle$ measures the correlation of L_y and L_z, and
$S/I = -\ \bar{h}\ \langle\ L_x\ \rangle\ /\ \langle\ L_x^2\ \rangle$ relates to circular polarization.

An experimental problem with quantum beats is their frequency. A decay curve of a level with a multi-nanosecond lifetime may stretch out over a few centimeters along the ion beam. In order to analyze the beat pattern, the frequency has to be high enough to result in many oscillations. Yet the frequency must be low enough to be resolved spatially (which, as mentioned above, corresponds to time resolution). This limits observations largely to low charge states and to ions with a small fine structure, that is with a single electron in the valence shell. For early examples, see the work done in Andrä's group in Berlin and in Bukow's group at Bochum [1,15,33,30]. However, there also are ions in which hyperfine intervals can be seen from quantum beats, and then often quite a number of hyperfine level intervals can be recovered from a Fourier analysis of the beat pattern.

Measurements of alignment do not necessarily require the observation of quantum beats, only of polarization. Still, polarizers with sufficient analyzing power and transmission largely restrict such work to wavelengths in the visible spectrum. A remarkable exception is the Ly_α transition in hydrogen, with a wavelength near 121.5 nm. Several polarizers of different designs have been built for this wavelength, using, for example, a stack of tilted LiF plates (in transmission) or a set of three surface reflections [30]. Much of this work was done by Helmut Winter (Bochum/Lyon/Berlin/Münster/Berlin). He wanted to ascertain the ion-energy variation of the alignment (energy dependence of the relative cross sections of the magnetic sublevels) in order to find the predicted cross-over between positive and negative values of the alignment. He did find a first crossing for about 50 keV H atoms [30], and later on an even lower-energy second crossing. By then he interpreted his data no longer as an energy trend, but, theoretically justified, as a variation with the inverse of the ion velocity [21]. In order to remind the plasma workshop audience of the energy scale: 50 keV protons colliding with the electrons in the foil correspond to 25 eV electrons impinging on protons in a plasma.

IV. TILTED FOIL

Macek's article referred to a much earlier treatment of polarization, by Percival and Seaton [24], who had considered the excitation of atoms by an electron beam, extending the even earlier Oppenheimer-Penney approximation. In 1973, Dave Ellis from Toledo (Ohio) revisited the case and expanded the scope by breaking the dominant symmetry [16]. By tilting the exciter foil (Fig. 2), he suggested, the previously used cylindrical symmetry around the ion beam would be broken, and Percival and Seaton's formalism would lead from the density matrix to a tensor with a main axis tilted away from the ion beam. In this way, *orientation* would be added to the alignment, to be observed as a superposition of linear and circular polarization, resulting in elliptical polarization with a major axis of specific orientation in space. The underlying level population would then no longer depend just on absolute values $|m_l|$, but on m_l itself.

The University of Toledo had an ion accelerator, and the theoretician Dave Ellis and his more experimentally inclined colleagues Gordon Berry, Larry Curtis and Dick Schectman promptly confirmed all these predictions. They then continued on to explore the parameter space, devising 3-D contour plots to follow the Stokes parameters as a function of ion energy and foil tilt angle. Via the coupling of nuclear and electron-shell momenta, it could be shown that the orientation of the electron shell could be transferred to the nucleus, and a beam of oriented nitrogen nuclei could be obtained [7].

One of the first surprises was that the orientation grew with the tilt angle to very high values (then the projection of the foil in the direction of the ion beam increases the ion path through the foil so much that the ions are lost due to energy loss and scattering). This contradicted an earlier model that had assumed excitation to take place mostly inside the foil, and clearly favored a dominance of surface effects. In fact, the observed orientation simply corresponded to what one would expect from the relative motion of ions outside a tilted surface, picking up largely stationary electrons, or from a surface friction picture. In Fig. 2, the observer/detector would see right-hand circular polarization.

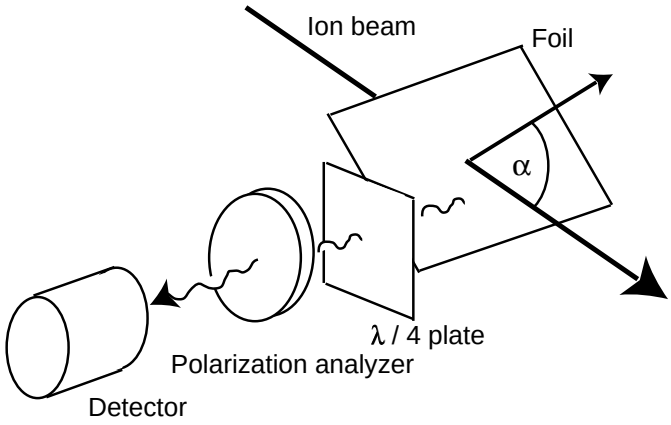

FIG. 2. Geometry with a fast-ion beam and an exciter foil that is tilted from the ion beam by an angle α. Since some of the observations seek for circular polarization, a $\lambda/4$ plate is required to convert this part of the light into linearly polarized light first.

Of course, such pictures must be oversimplified, and thus some rather fierce discussion broke loose, each side having evidence (from perpendicular or tilted foils) supporting their own views and contradicting others. One study found a dependence on the temperature of the foil (that under intense ion bombardment can glow brightly) [17]. Another study claimed this to be a current-density effect instead [29]. In their model, the limited conductivity of carbon foils trying to replenish secondary electrons released by ion bombardment would create a current in the foil, converging onto the ion beam spot, with associated electric and/or magnetic fields. This current-density effect might be influenced by the choice of foil material, special backings, foil holders or supporting grids. A third group found no current-density effect even when varying the current density in a wider range than the second had done [22]. The foil material was varied [11], then finding that carbon and similar non-metals yielded more polarization than metals did. Soon it was found that the ubiquitous contamination of materials under ion bombardment by cracked hydrocarbons of whatever origin clouded the sensitivity of the experiments. And so on.

On the theoretical side, the corrugation of a foil surface, the state density in and above the surface, various intricate models for electron capture, the influence of surface fields, and whatever else were invoked - and made no recognizable impact on the results. However,

a few insights survived, supported by evidence from other experiments: Inner vacancies are mostly produced in the bulk of the foil material, whereas much of the valence electron structure is assembled only in the surface layers of the foil, if not above the surface. Surface fields play a notable role only for hydrogenic (degenerate or near-degenerate) levels.

Orientation was found in multiply charged ions [18], too. However, there was no valid model to describe the various polarization effects of outer electrons theoretically, and for lack of that and for exhaustion of accessible simple atomic systems, the field of polarization studies in beam-foil spectroscopy petered out.

V. SCATTERING AT GRAZING INCIDENCE

Some of the above can be driven to the extreme, and there gain new significance: At very large tilt angles, the ions can no longer penetrate the foil. Instead, one may try to scatter them from the same surface, under grazing-incidence conditions. This then almost implies a surface without a bulk; it also requires ultra-high vacuum and in-situ cleaning of the surfaces by ion sputtering. Again, Helmut Winter tried his hands on this, and again successfully. His IBSIGI technique (Ion-Beam Surface Interaction at Grazing Incidence), begun in collaboration with H.J. Andrä, provided unprecedentedly high degrees of orientation, including a high-yield arrangement for producing a beam of nitrogen ions with nuclear spin polarization [31]. The nuclear spin polarization reached 15% after scattering on one surface, and 20% after scattering off two such surfaces. The technique has also been employed to study surface fields between an incoming ion (with the vertical velocity component reduced by geometry) and the target surface, and it has recently been used to probe the electron band structure of a composite material inside the target bulk. On the fundamental physics side, Winter has demonstrated with individual ion-atom collisions that the aforementioned simple geometrical picture of producing orientation holds. The latest feat of Winter's group is a measurement of the circular polarization of Auger electrons after IBSIGI on magnetized surfaces [25]. If you want more details, look for the extensive Physics Report that he has just finished preparing.

VI. CONCLUSION

Why is polarization spectroscopy of fast ion beams a (largely) closed chapter? Probably because there is no conclusive theory predicting the polarization of specific outer electrons.

Inner-shell vacancies in heavy ions, produced by ion-foil interactions, have occasionally been studied by evaluating angular correlations of the x-ray emission pattern, but hardly by employing polarization-sensitive devices. This may become an interesting field (again), because plasma physics has diagnostic problems at very-high density. In such plasmas, collisions are so frequent that multiple excitation becomes possible - a mainstay of beam-foil spectroscopy for almost four decades. Beam-foil spectroscopy features ion excitation in a dense medium (solid matter), followed by observation in a low-density medium (good vacuum). There may be prospects ...

Acknowledgment: Larry Curtis and his web-based paper mine, with access to his many insightful manuscripts, made it easy to dig into this field. Let me thank Dave Ellis and

Daniel Thorn for checking this manuscript from their very different perspectives.

---

[1] H. J. Andrä, *Zero-field quantum beats subsequent to beam-foil excitation*, Phys. Rev. Lett. **25**, 325 (1970).

[2] Bashkin, S., Meinel, A.B., *Laboratory excitation of the emission spectrum of a Nova*, Astrophys. J. **139**, 413 (1964).

[3] Bashkin, S., *A new method for studying the atom*, Science **148**, 1047 (1965).

[4] H. G. Berry, L. J. Curtis, J. L. Subtil, *Cascade-induced alignment changes of intensity-decay curves*, J. Opt. Soc. Am. **62**, 771 (1972).

[5] H. G. Berry, L. J. Curtis, D. G. Ellis, R. M. Schectman, *Anisotropy in the beam-foil light source* Phys. Rev. Lett. **32**, 751 (1974).

[6] H. G. Berry, S. N. Bhardwaj, L. J. Curtis, R. M. Schectman, *Orientation and alignment of atoms by beam-foil excitation*, Phys. Lett. **50A**, 59 (1974).

[7] H. G. Berry, L. J. Curtis, D. G. Ellis, R. M. Schectman, *Hyperfine quantum beats in oriented* ^{14}N *IV*, Phys. Rev. Lett. **35**, 274 (1975).

[8] H. G. Berry, L. J. Curtis, R. M. Schectman, *Tests of the final surface electrostatic interaction in beam–tilted-foil experiments*, Phys. Rev. Lett. **34**, 509 (1975).

[9] H. G. Berry, L. J. Curtis, D. G. Ellis, R. M. Schectman, *Spatial asymmetries in atomic collisions*, in "Electron and photon interactions with atoms", edited by H. Kleinpoppen and M. R. C. McDowell, Plenum: New York 1976, p. 515

[10] H. G. Berry, L. J. Curtis, D. G. Ellis, R. D. Hight, R. M. Schectman, *The surface interaction in beam foil spectroscopy*, in "Beam-Foil Spectroscopy", Vol. 2, Plenum: New York 1976, p. 755

[11] H. G. Berry, G. Gabrielse, T. Gay, A. E. Livingston, *Material-dependent variations of alignment in beam-foil excitation*, Phys. Scr. **16**, 99 (1977).

[12] L. J. Curtis, *Predictions of the Early Atomic Meanlife Theory of Wilhelm Wien*, J. Opt. Soc. Amer. **63**, 105 (1973).

[13] L. J. Curtis, R. Hallin, J. Lindskog, J. Pihl, H. G. Berry, *Alignment effects in heavy ionized beam foil excited atoms*, Phys. Lett. **60A**, 297 (1977).

[14] L. J. Curtis, *Some current problems in beam-foil spectroscopy*, Nucl. Instrum. Meth. B **9**, 565 (1985).

[15] P. Dobberstein, H. J. Andrä, W. Wittmann, H. H. Bukow, *Zero-field quantum beats in Lyman* α *radiation subsequent to beam-foil interaction of protons*, Z. Phys. **257**, 272 (1972).

[16] D. G. Ellis, *Density-operator description of foil-excited atomic beams: Zero-field quantum beats*

in L-S coupling without cascades, J. Opt. Soc. Am. **63**, 1232 (1973).

[17] T. J. Gay, H. G. Berry, *Temperature dependence of alignment production in He I by beam-foil excitation*, Phys. Rev. A **19**, 952 (1979).

[18] S. Huldt, L. J. Curtis, B. Denne, L. Engström, K. Ishii, I. Martinson, *Observation of strong orientation effects for levels in highly ionized oxygen*, Phys. Lett. **66A**, 103 (1978).

[19] Kay, L., *A van de Graaff beam as a source of atomic emission spectra*, Phys. Lett. **5**, 36 (1963).

[20] Kay, L., *On the origins of beam-foil spectroscopy - I*, Nucl. Instrum. Phys. Res. B **9**, 544 (1985).

[21] E. Kupfer, H. Winter, *Influence of surface electric fields on the alignment of the hydrogen-2p state after beam-foil-excitation*, Z. Phys. A **285**, 3 (1978).

[22] V. Lodwig, Investigation of current density effects (priv. comm.), Bochum

[23] J. Macek, *Interference between coherent emissions in the measurement of atomic lifetimes*, Phys. Rev. Lett. **23**, 1 (1969).

[24] I. C. Percival, M. J. Seaton, *The polarization of atomic line radiation excited by electron impact*, Phil. Trans. Roy. Soc. London, Series A **251**, 113 (1958).

[25] R. Pfandzelter, T. Bernhard, H. Winter, *Spin-polarized electrons in collisions of multicharged nitrogen ions with a magnetized Fe(001) surface*, Phys. Rev. Lett. **86**, 4152 (2001).

[26] R. M. Schectman, L. J. Curtis, H. G. Berry, *Alignment, orientation and the beam-foil interaction*, J. de Physique Coll. C1, suppl. au. no. 2, Tome **40**, C1-289

[27] R. M. Schectman, R. D. Hight, S. T. Chen, L. J. Curtis, H. G. Berry, T. J. Gay, R. Deserio, *Orientation and alignment of the $3p\ ^1P$ and $4d\ ^1D$ levels of neutral helium*, Phys. Rev. A **22**, 1591 (1980).

[28] R. M. Schectman, L. J. Curtis, H. G. Berry, *Alignment, orientation, and the beam-foil interaction*, in *"Coherence and correlation in atomic collisions"*, edited by H. Kleinpoppen and J. F. Williams, Plenum: New York 1980, p. 387

[29] W. Singer, J. C. Dehaes, J. Carmeliet, *Stray electric field due to the carbon foil resistance in hydrogen beam-foil spectroscopy measurements*, Phys. Scr. **21**, 165 (1980).

[30] H. Winter, H. H. Bukow, *Alignment of H (2p) after beam-foil excitation*, Z. Physik A **277**, 27 (1976).

[31] H. Winter, H. J. Andrä, *Nuclear polarized ^7Li and ^{14}N ions via ion beam surface interaction at grazing incidence*, Z. Phys. A **291**, 5 (1979).

[32] H. Winter, R. Zimny, A. Schirmacher, B. Becker, H. J. Andrä, R. Fröhling, *Band structure effects in high energy ion beam surface interaction at grazing incidence*, Z. Phys. A **311**, 267 (1983).

[33] W. Wittmann, K. Tillmann, H. J. Andrä, P. Dobberstein, *Fine-structure measurements of ^4He by zero-field quantum beats*, Z. Phys. **257**, 279 (1972).